RESPONSE SURFACE FUNCTION FOR DETECTING CRACK PARAMETERS IN THIN WALLED BEAMS

A Thesis Submitted in

Partial Fulfillment of the Requirements

for the Degree of

DOCTOR OF PHILOSOPHY

By

Palash Dey

DEPARTMENT OF CIVIL ENGINEERING

INDIAN INSTITUTE OF TECHNOLOGY GUWAHATI

JANUARY, 2017

Certificate

It is certified that the work contained in the thesis entitled **Response Surface Function for Detecting Crack Parameters in Thin-Walled Beams** by **Palash Dey** (Roll No: 126104028), a student of the Department of Civil Engineering, Indian Institute of Technology Guwahati, submitted for the award of the degree of Doctor of Philosophy, has been carried out under my supervision and that this work has not been submitted elsewhere for a degree.

January, 2017

Dr. S. Talukdar
Professor
Department of Civil Engineering
Indian Institute of Technology Guwahati
Assam, India

Dedicated

To

My Parents

for supporting and encouraging me to believe in myself

My Grandparents

for being my first teachers

Acknowledgement

Foremost, I would like to express my sincere gratitude to my supervisor Prof. S. Talukdar for his continuous support to my Ph.D study and research, his patience, motivation, enthusiasm, and immense knowledge. His vast experience in the area and his willingness to impart his knowledge has helped in my research work.

Besides my supervisor, I would like to thank the rest of my Doctoral committee members: Prof. S. K. Dwivedy, Dr. H. B. Kaushik and Dr. H. Sharma for their encouragement and fruitful suggestions.

I would like to thank Prof S. Dutta, Head of Civil Engineering Department for providing financial grant for attending conferences. My sincere thanks also go to Dr. Karuna Kalita and Dr. Dhruba Jyoti Bordoloi for allowing and helping me to conduct experiment in Vibrations and Acoustics Laboratory, Department of Mechanical Engineering and the staffs of Central Workshop of the institute for fabrication of the experimental specimens. I am grateful to Central Library for offering such a vast resource of research material and making it easily accessible.

I am also thankful to my friends, Lalthlamuana, Sulaem, Tanmoy, Nishant and Biswajit for their co-operation and help while carrying out my research works.

Special thanks go to my family members. Words cannot express how grateful I am to my parents, sister and brother for all of their sacrifices that they have made during my research period. Their prayer for me was what sustained me so far.

January, 2017 Palash Dey

Abstract

Damage or crack can be expressed as changes arising in a structure that may affect its ongoing or future performance, concerning its safety and serviceability. Structures have always been susceptible to different kinds of damage during their service life span due to environmental, operational and human-induced factors and these factors are deterioration, degradation, corrosion, fatigue, creep, shrinkage, etc. It needs to be mentioned that damage forming cracks rapidly propagate under repeated and reversal loading. Therefore, early prediction of this damage can help in increasing their life span and avert unexpected modes of failure. Safety information and precautionary maintenance of structures may be guaranteed by application of structural health monitoring (SHM) systems, which can provide valuable information for detail inspection and repair of the structures. Recognizing the significance of the research on damage detection, attempts have been made in this thesis to carry out theoretical and experimental study for the estimation of crack parameters (namely, crack location and crack depth ratio) from the dynamic response of the thin-walled beams.

In the present work, a generalized finite element (FE) model for arbitrary cross-sectional thin-walled uncracked and cracked beams has been developed. Element stiffness and mass matrix have been derived based on energy formulations. The FE model has been improved by including the warping stiffness in the uncracked and cracked beams. Line-spring elements have been assumed to model the cracks. In the present study, beams with one axis of symmetry and with no axis of symmetry have been considered since these types of thin walled beams exhibit coupled bending–torsion behavior. For practical implementation of the FE model, channel and angle section beams of mild steel are considered in the study. Cracks are considered on top flange of the channel section beam, whereas these exist on upper leg of the angle section beams.

A series of experiments in the laboratory on straight and curved beams of channel and angle section for various combinations of crack parameters have been conducted using harmonic excitation. The test specimen of channel and angle section beams of straight and

curved profile has been prepared in the workshop from mild steel plate of thickness 2 mm. The physical properties of the plate were determined in the laboratory tests which serve as input to the FE model. All straight and curved specimens were of length 800 mm. The support conditions of the test specimen were considered fixed-free. For that purpose, a short RC pillar of cross section 150 × 150 mm with base 400 × 400 × 150 mm was used to support the test specimen. The fixity at one end is ensured by embedding the specimen sufficiently inside the RC pillar during casting. In the present study, an artificial crack has been introduced in the channel and angle section beam using saw cut. The crack depth ratio has been maintained in the range of 0.08 to 0.8 in different specimen of channel or angle for the experimental study. The curved beam specimen was prepared for two different degrees of curvature. In one case subtended angle was 25° and in another case it was 50°.

Comparison of finite element and experimental results show that present model of thin walled beams can satisfactorily represent a cracked model. The consideration of warping deformation in the present study shows that experimental results widely differ if warping is neglected in theoretical formulation. Modal features such as natural frequencies, mode shapes and modal curvatures of uncracked and cracked beams are then utilized to detect crack location and crack depth. While very insignificant change of mode shapes between uncracked and cracked beams were observed in the study, absolute difference of curvature of mode shapes between uncracked and cracked beams could indicate the crack location accurately. This approach, however, could not detect the extent of crack. Moreover, information of undamaged beams are necessary for the prediction of the location of the crack

To overcome these difficulties, present study outlines an integrated inverse approach for health monitoring of straight and horizontally curved thin walled open section beam using a combined Finite element method (FEM), Response surface methodology (RSM) and Genetic algorithm (GA) for the detection of crack parameters. Response surface method is a tool used to form an empirical model by finding the association between the response and design variables through statistical fitting approach, which is built on observed data from system response. Finite element (FE) simulations based on Central composite face-centered (CCF) design approach has been chosen in order to obtain the coefficients of a polynomial model for the Response surface function (RSF). These models are trained and tested based on analysis of variance (ANOVA) by means of F-test and P-value. Moreover, the adequacy

of the model has been also determined by evaluating the standard deviation value and coefficient of determination. Once a model has been found significant, the optimum crack parameters are obtained by minimizing an objective function using a searching tool, GA. The objective function has been established by root mean square (RMS) of the residuals between the computed responses from RSFs and measured responses. Several examples are included to illustrate the present integrated approach for crack identification by using free vibration, forced vibration and combination of both. Experimental results obtained in the laboratory for single cracked and multi cracked beams of channel and angle section with straight and curved profile have been used in the present approach to detect crack location and crack depth. The results show that reasonable accuracy in the location of crack and its depth can be achieved in all cases considered in the present study. Use of forced vibration data decreases accuracy of detection compared to only free vibration data. However, heterogeneous data yield better estimate compared to force vibration data. The present identification approach has great potential in crack detection as it does not require the response of an uncracked beam as baseline criteria. Moreover, the present hybrid approach can identify external force satisfactorily through optimization process.

Contents

List of Tables

List of Figures

Nomenclature

The symbols associated with this thesis are classified into Greek and Roman symbol group. Although some symbols can represent multiple quantities. An overview of the most important symbols, operators and abbreviations used in the present thesis:

Greek symbols

α	Distance from the center of the design space to a star point
β	Slope factor
Γ_ω	Warping constant
ζ_n	n^{th} crack length
η_i	i^{th} natural or original predictor variable
$\eta_{i,high}$	Natural value of the variable at high level
$\eta_{i,low}$	Natural value of the variable at low level
θ_s	Subtended angle
θ_{Sn}	Angular distance (in degrees) of n^{th} crack
κ_y	Shearing factor along y direction
κ_z	Shearing factor along z direction
λ	Root of eigen equation
μ	Poisson's ratio
ξ	Local non-dimensional spatial coordinate
ϖ	Sectorial area
ρ	Density of material

ς	Damping ratio
ϕ_d	Theoretical modal vector for damaged beam
ϕ_o	Theoretical modal vector for uncracked beam
χ	Mode shape vector
ω	Natural frequency

Roman symbols

A	Cross-sectional area
a_n	Depth of 'n^{th}' crack
c_0	Model constant
c_i	Linear coefficient
c_{ii}	Quadratic coefficient
c_{ij}	Interaction coefficient
$\boldsymbol{D}$	Global damping matrix for uncracked beam
$\boldsymbol{D_{cr}}$	Global damping matrix for cracked beam
dV	Differential volume
E	Young's modulus
e_{ij}	Strain tensor
EI_{yy}	Bending rigidities of the section about y-axis
EI_{zz}	Bending rigidities of the section about z-axis
e_y	Offset distance between centroid and shear center in y- direction
e_z	Offset distance between centroid and shear center in z- direction
F_{Obj}	Objective function
F_x	Axial force in in x-direction
F_y	Vertical shear force in y-direction
F_z	Transverse shear force in z-direction
G	Shear modulus
GJ	Saint-Venant torsional rigidity
I_s	Polar moment of inertia of the cross-section about shear center
I_{yy}	Moment of inertia about the y axis
I_{yz}	Product moment of inertia
I_{zz}	Moment of inertia about the z axis
$I_{\omega y}$	Warping product of inertia about y-axis

$I_{\omega z}$	Warping product of inertia about z-axis
J	Torsional constant
J	Strain energy release rate
$\boldsymbol{K}$	Global stiffness matrix for uncracked beam
$\boldsymbol{K_{cr}}$	Global stiffness matrix for cracked beam
$\boldsymbol{k^e}$	Element stiffness matrix for uncracked beam
K_I	First mode stress intensity factor
K_{II}	Second mode stress intensity factor
K_{III}	Third mode stress intensity factor
L	Length of the beam along longitudinal axis
l_e	Length of the beam element
L_f	Least-squares function
L_n	n^{th} crack position
L_S	Length of the line-spring
lt	Left node of the line spring element
$\boldsymbol{M}$	Global mass matrix for uncracked beam
$\boldsymbol{M_{cr}}$	Global mass matrix for cracked beam
$\boldsymbol{m^e}$	Element mass matrix for uncracked beam
M_x	Torsion about x-axis
M_y	Bending moment about y-axis
M_z	Bending moment about z-axis
M_ω	Bimoment
N_{ET}	Total number of experimental trials required
P_i	Loading along i^{th} co-ordinate
Q	Displacement vector
R	Radius of curvature
rt	Right node of the line spring element
S_y	First moment of area in the x direction
S_z	First moment of area in the y direction
S_ω	First sectorial moment
T	Kinetic energy
U	Elastic strain energy
u	Axial displacement in x-direction

u_i	Additional displacement in i^{th} co-ordinate
U_S	Strain energy due to crack
v	Flexural translation in y-direction
w	Flexural translation in z-direction
$X_i^{(n)}$	The n^{th} experimental run, the i^{th} variable
$y^{(n)}$	Response value of n^{th} experimental run
y_i	i^{th} predicted responses
y_i^*	i^{th} laboratory measured output response
ε	Error vector
σ_{ij}	Stress tensor
ψ	Torsional rotation

Abbreviations

ANOVA	Analysis of variance
CCC	Central composite circumscribed
CCD	Central composite design
CCF	Central composite faced centered
CCI	Central composite inscribed
CDF	Curvature damage factor
CG	Mass center
DOE	Design of experiments
FEM	Finite element method
FRC	Frequency response curves
GA	Genetic algorithm
LSM	Least-squares method
MAC	Modal assurance criterion
NDT	Non-destructive techniques
RSF	Response surface function
RSM	Response surface method
RSM	Root mean square
SC	Shear center
SHM	Structural health monitoring
SIF	Stress intensity factor

Chapter 1

Introduction

1.1 Overview

All structures in service are liable to be damaged due to overloading, environmental factors and natural as well as man-made hazards. Damage initiates with the formation and propagation of crack and continues till collapse unless structures are freed from overloading and suitably strengthened or repaired. Presence of small cracks in a structure may cause unsatisfactory serviceability, while large cracks may lead the way of undesirable situations such as catastrophic failure of the structures. To prevent extension of a small crack, crack detection and quantification at the preliminary stage of development are very essential but challenging tasks. If such crack detection and quantification are possible at an early stage, then the safety margin may considerably be enhanced while decreasing the maintenance cost too.

Damage or crack is a physical discontinuity in a material or an object. It may be developed either during manufacturing or service stage. The procedure of detecting damage and slowing down its progression in the structure falls under the umbrella of structural health monitoring (SHM). In real field applications, ranging from outer space to deep ocean, various engineering structures such as buildings, bridges, towers, turbine, helicopter and propeller blades are frequently subjected to numerous dynamic excitations in complex environment which may cause vibrations. It needs to be mentioned that damage forming cracks rapidly propagate under repeated and reversal loading. Therefore, it is of particular

importance to detect the early stage of crack so as to ensure reliable, safe and lasting performance on repair and retrofitting of the structures.

Damage detection and SHM have drawn attention among various researchers over the past few decades. In this arena of research non-destructive techniques (NDT) play a major role in assuring that the structural components perform their tasks in a safe, reliable and cost effective manner without affecting the serviceability of the system. Generally, the concepts and uses of NDT are not just limited to industry but also applicable in day to day lives. This method can be explained by the example of a man buying melons in a fruit shop. For this purpose, he will first have a glance over the melons, pick one among them and closely inspect for any type of defects - this is visual NDT. Then, he will test the ripeness by tapping surface and listening for hollow response - this is acoustic NDT. Finally, based on the response of the tests and compliance to the preset NDT criteria, the person will either accept the melon for buying or discard it and look for other one.

NDT have been classified into three categories and these are traditional methods (such as liquid penetrant testing, ultrasonic testing, acoustic emission testing, radiography and eddy-current methods etc.), static based and vibration based methods. Figure 1.1 represents the classification of NDT for damage identification. Static and vibration based non-destructive methods provide the scope to detect and assess crack on a global basis whereas traditional non-destructive tests fall under local basis. Local basis methods focus on a part of the structural element and are generally considered to be more sensitive than global basis methods.

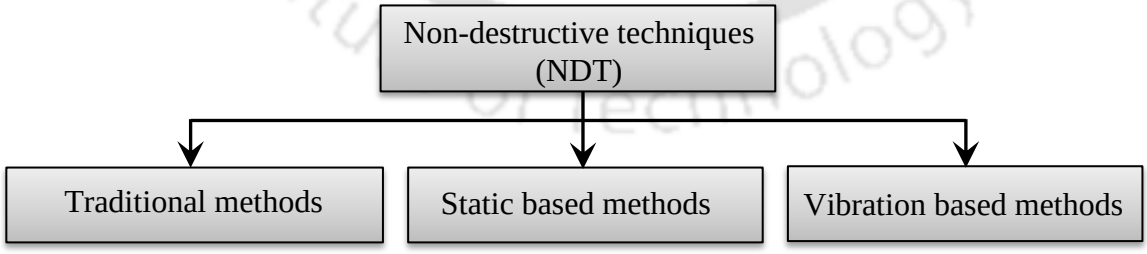

Figure 1.1: Classification of NDT

In addition to this, their application requires a prior knowledge of the position of the cracked area. The global basis methods can examine a relatively large area at once. The global methods are used to infer damage from changes in vibration characteristics of the

system. The basic idea of vibration based detection is that damage in the structure will alter the structural properties (mass, stiffness and damping) and these alters will lead the way of changes in the dynamic characteristics of the global structural response. For these reasons, response of the intact and damaged structures is comparatively different.

In another classification for damage identification methods given by Rytter [1], four levels of damage identification are defined as follows

- Level 1: Determines whether damage is present in the structure.
- Level 2: Level 1 plus determines location of the damage.
- Level 3: Level 2 plus quantifies the severity of the damage.
- Level 4: Level 3 plus predicts the remaining service life of the structure.

The first three levels are mostly connected to identification and modeling of structural and mechanical systems and the last level of detection generally comes under the fields of fatigue life analysis. Generally, Level 1 damage identification falls into the category of forward problem. Changes in natural frequencies in vibration measurements indicate the change of structural rigidity. In case, if crack appears in an inaccessible location that are not possible to detect by visual means or traditional methods, the reduction of natural frequency if detected after vibration test or from ambient vibration data, raises an alarm about the state of the structure. This forms a theoretical basis in vibration based NDT. When Level 1 is positive, then one should further try for Level 2 and Level 3 for complete damage assessment. On obtaining information of Level 2 and Level 3, suitable repairing or rehabilitation of the structure can be planned. With assessment of damage, one can further attempt Level 4 to predict the remaining life of the structures.

The techniques, applicability and success for damage detection differ widely based on various conditions. Reviews of earlier studies and historical background of the research works in the arena of damage detection have been presented. Success, difficulties and limitations of the earlier studies have been pointed out. The study has enabled to establish the scope of the present work.

1.2 Literature review

There are plenty of studies available that deal with the identification of damages in different structural and mechanical systems. Numerous techniques have been suggested, out of which

some are carried out experimentally and some are theoretically. Since review of existing literatures is important to understand the problems in a particular area of the research work, some of the relevant literatures have been reviewed and presented in this section.

In general, different damage detection approaches may be classified into techniques based on non-destructive testing and vibratory information. The present literature review has been reported in three sections based on work done by previous authors. It is classified into the following sections-

- Traditional non-destructive tests
- Static based methods
- Vibration based methods
  - Damage detection based on free-vibration.
  - Damage detection based on forced-vibration.
  - Damage detection based on combination of free and forced vibration.

After discussing the works of previous authors on damage detection, a review of literature on thin walled beams and their practical application are presented, as we have focused our study on thin walled beams.

1.2.1 Traditional non-destructive tests

Non-destructive testing refers to the evaluation and inspection procedure of materials for finding defects without harming the object being tested [2, 3]. The traditional NDT methods have been classified as contact and non-contact methods. Non-contact methods are visual inspection, radiography testing, thermography and shearography testing. Contact methods are liquid penetrant testing, ultrasonic testing and eddy current testing. A brief description of contact and non-contact methods are given below:

Visual inspection testing

Visual Inspection means an inspection of equipment and structures using human senses such as vision, touch and hearing. Very common accessories such as measuring tape, small hammer, flashlight and magnifying glass etc. may be carried to aid visual detection. This technique is a category of non-contact non-destructive technique. It is not sufficient to identify damage location in a structure, particularly when damage lies in the inner part and is not visible to the naked eye. Visual inspections are time consuming, expensive and require the components to be readily accessible. Generally an inspection interval is decided.

However, if a crack develops in between an inspection interval, it may propagate and reach a critical size before it can be detected during next inspection. Visual inspection is very important which can guide to select the type of NDT. However, interpretation of inspection report requires sufficient experience.

Radiography testing

Radiography is the method of preparing a shadow image of a solid using penetrating radiation such as x-rays or γ-rays. For thinner dense materials (e.g., aluminum), electrically generated x-rays are commonly used. In case of thicker dense materials, γ-rays are generally used because γ-rays have shorter wavelengths. It can be observed from Figure 1.2 that the radiation passing through the specimen exposes the media, causing an end effect of having darker areas where more radiation has passed through the part and lighter areas where less radiation has penetrated. If there is a crack or discontinuity in the part, more radiation passes through, producing a darker image on the film. There are number of radiographic testing methods for different applications which are film radiography [4], computed radiography [5] and digital radiography [6].

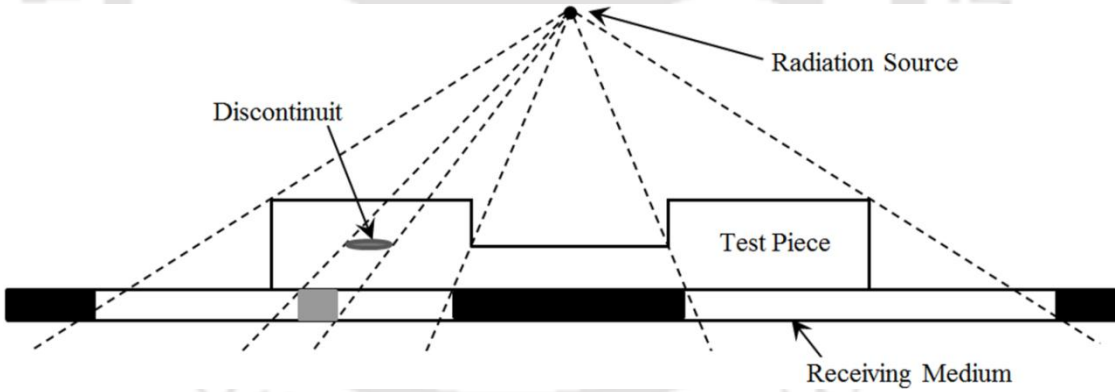

Figure 1.2: Schematic of a radiographic system

Thermography testing

Thermography inspection refers to the nondestructive testing method of an object or systems through the imaging or mapping of surface temperatures as heat flows. These mapping systems generate images of heat flow and allow thermal information to be rapidly collected over a wide range of area in a non-contact mode. A delamination or damage causes a change in the thermal radiation of the area [7]. This type of inspection requires sensitive and expensive instrumentation. Lack of clarity of defects, if they occur too deep under the surface of the object is the major disadvantage. Świątczak *et al*. [8] proposed the

application of active thermography for detection of defection of voids inside the wire joints. They have used a thermal camera to acquire sequences of thermo-grams showing the joints during transient heating. Li *et al*. [9] provide a novel method to report damage evolution of the impacted composite materials based on the active infrared thermography. The infrared thermography was applied to quantitatively evaluate the damage area in the specimen.

Shearography testing

Shearography uses coherent light or coherent sound waves to give information about the quality of different materials in nondestructive testing. It is extensively used in production and development in aerospace, wind rotor blades and in materials research areas. Advantages of shearography are the large area testing capabilities and non-contact properties. It is relatively insensitive to characterization of defect types other than delamination. Thus, it is sometimes paired with other types of non-destructive evaluation techniques that can help to identify certain defects. Hung and Ho [10] presented the shearography technique and its applications.

Liquid penetrant testing

Liquid penetrant testing (LPT) is a simple and inexpensive method of inspecting surface areas for cracks or discontinuities. This technique falls under the category of contact non-destructive technique. The visible dye penetrant process is demonstrated in Figure 1.3. Penetrant inspection extremely depends on the visual abilities of the operator. A test panel is considered to investigate the effectiveness of penetrant materials [11]. Liquid penetrant testing on nonmetallic test panel can be found in reference [12]. The basic concept of liquid penetrant testing is that when a very low viscosity or highly fluid liquid is used to the surface of a part, it will penetrate into cracks open to the surface. The penetrant trapped in those cracks will flow back out, when the excess penetrant is removed and developing an ‘indication’ as shown in Figure 1.3. Penetrant testing can be executed on magnetic and non-magnetic materials. This test does not work well on porous materials. It is essential that the surface being tested must be free of any foreign materials or liquids that may prevent penetrant from entering cracks open to the surface of the part. After applying the penetrant, it is left on the surface for a sufficient time to allow penetration into cracks. Then the part is carefully cleaned to remove excess penetrant from the surface area. The operator must be careful not to remove any penetrant that has flowed into the cracks. Thereafter, a coating of developer is applied to the surface and is given time to permit the penetrant from any cracks

to seep up into the developer, which creates a visible indication. Most developers are dry powder. This test depends heavily on the visual acuity and abilities of the operator.

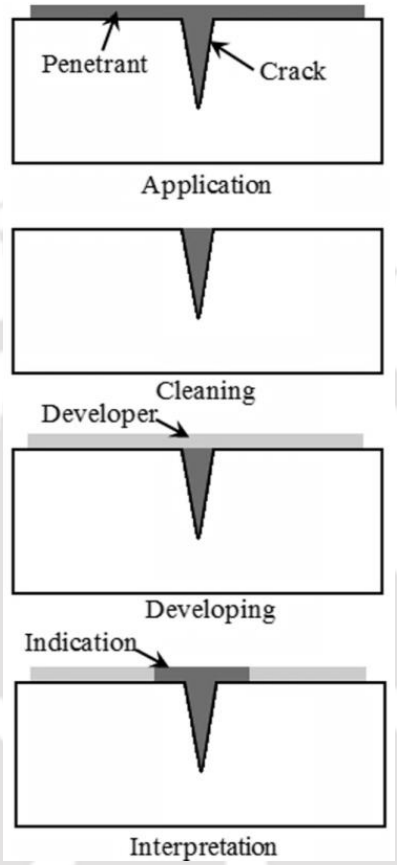

Figure 1.3: Action of penetrants and developers

Ultrasonic testing

Ultrasonic testing (UT) is a very flexible and robust technique based on the propagation of ultrasonic waves through the object tested. In ultrasonic tests, two types of transducers are used and these are transmitter and receiver. The transmitter initiates the wave pulse into the test object whereas the receiver senses the entry of wave by measuring the time taken by the pulse. A schematic diagram of pulse velocity test circuit is shown in Figure 1.4. Abnormal low velocity of the wave through the known medium provides evidence of damage or crack inside. Highly experienced technician is required for ultrasonic techniques. Due to available of portable ultrasonic testing device, its application in structural health monitoring is very common. Theoretically path length of the propagated wave should not affect its velocity. However, study conducted by Diederichs *et al*. [13] has revealed that shorter path lengths tend to give more variable results and higher velocity in concrete specimen. Temperature in

the range of 5° to 30° C does not cause any major variation of test result, however, at higher temperature difference is caused in pulse velocity and therefore, correction factor has been suggested by Malhotra and Carino [3].

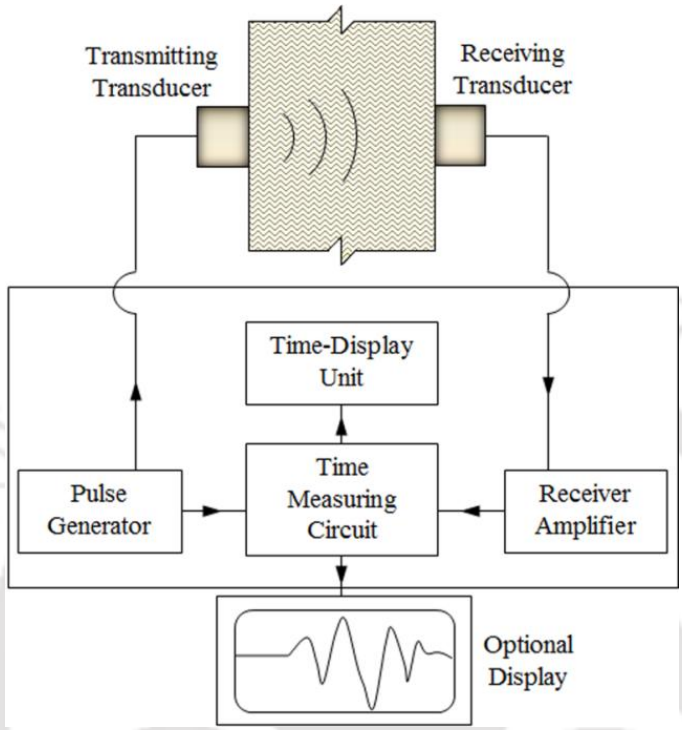

Figure 1.4: Pulse velocity test circuit

A brief review of the characteristic and application of ultrasonic fatigue testing technology have been presented by Peng *et al*. [14]. The very high frequency causes some problems such as thermal effect and frequency effect which are briefly discussed in their paper. Chaix *et al.* [15] investigated damage in concrete using backscattered ultrasonic waves. Rahani *et al.* [16] demonstrated that the ultrasonic waves are not very effective in detecting internal defects in some materials such as ceramic foam tiles.

Eddy current testing

Eddy-current testing (ECT) is one of the electromagnetic testing methods used in NDT making use of electromagnetic induction to detect and characterize surface cracks or discontinuity in conductive materials. Some of the damage detection studies based on ECT have been reported in the literatures [17-19]. The alternating electrical current is applied to an inspection excitation wire coil. This wire coil generates a magnetic field around itself in the direction ascertained by the right-hand rule. The magnetic field oscillates at the same frequency as the current flows through the coil. The magnetic field is brought close to a

conductive material like a metal test piece. When a crack in the surface immediately underneath the coil is encountered, it will reduce the eddy current flow, thus decreasing the loading on the coil and increasing its effective impedance. An eddy current testing has been shown in Figure 1.5 to detect the character of conductivity material.

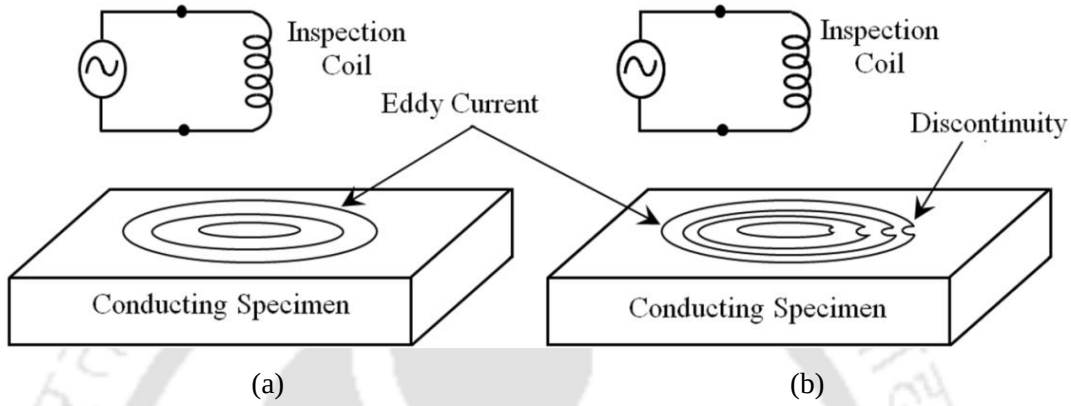

Figure 1.5: An eddy current probe used to detect the character of conductive materials: (a) in the absence of crack or discontinuity and (b) in the presence of discontinuity

Eddy current testing does not require surface preparation like penetrants and magnetic particle methods. The most inconvenience is that the interrogated material must be a conductor. Cracks parallel to the current path will not produce any significant interruption and may not be detected.

Apart from these methods, there are several other methods available such as Magnetic particle testing, Acoustic emission monitoring, Magnetic flux leakage, etc. Conventional NDTs are operated offline during maintenance whereas vibration based structural health monitoring techniques can be operated off-line as well as on-line. On-line indicates, monitoring of the structure or a system during operation. The health monitoring technique of a structure is part of the on-board systems. Sensors are permanently attached to the systems. Hence, continuous information on the system state is available. Furthermore, all these NDTs need the location of crack be known priori and these techniques are inconvenient for large-scale structures with inaccessible part. Moreover, most of the NDTs are highly expensive. These limitations led to the improvement of global monitoring procedures based on changes in the vibration characteristics of the structural or mechanical system.

1.2.2 Static based methods

Static based techniques permit damage detection by measuring changes in the response due to static loading. The measured responses are typically displacements or strains. The works based on the static analysis of cracked systems are described subsequently.

The influence of reduced rigidity on the load carrying capacity, deflection and fracture load of a single edge cracked slender column based on the column theory together with the relationship between the stress intensity factor and the compliance of a cracked member have been demonstrated in the literatures. [20-22].

Sanayei and Scampoli [23] studied the static parameter identification of structures for the systematic identification of plate-bending stiffness parameters for a one-third scale, reinforced-concrete pier-deck model based on finite element method. Numerous parameter identification examples are presented using simulated static force and displacement measurements. Their identification approach required displacement to be measured at the same position as the applied external force. This limitation was lifted in a work by Sanayei and Onipede [24] by minimizing a condensation procedure. The authors carried out an analytical study to identify the properties of structural elements from static test data such as a set of applied static forces and another set of measured displacements. This method is able to obtain changes in structural element stiffnesses including element failure.

Quek *et al*. [25] used finite element method to obtain the deflection profiles (treated as spatially distributed signals) of a beam under static load. Thereafter, they performed the wavelet transforms on these signals to achieve the wavelet coefficients along the span of the beam. A peak in the distribution of the wavelet coefficients showing a strong local perturbation in the signal is represented as crack. Two types of wavelets compared in this study are the Haar and Gabor wavelets. The authors show that the Haar wavelets reveal superior performance for detection of cracks compare to Gabor wavelets.

Rucka and Wilde [26] implemented an analysis of a curve resulting from static deflection of a cantilever damaged beam using wavelet transform. They computed static displacement of a crack beam with different locations and depths by commercial finite element software SOFiSTiK. They considered continuous wavelet of Gaussian and Coiflets wavelets group for analyzing curve of beam static deflection. The main drawback of this study is that it can only detect relatively large cracks.

Sain and Chandra Kishen [27] proposed an analytical model to detect damage based on static displacement measurements using the concepts of inverse method and fracture mechanics. An experimental study is carried out to validate the analytical model. Damage is identified in terms of alterations in structural properties due to the formation of discrete cracks. The compatibility equation established using Grobner bases serves as a means to identify damage from field data for displacements. However, this approach requires undamaged beam response as baseline reference for damage detection.

Buda and Caddemi [28] demonstrated an inverse identification procedure of concentrated damages in Euler-Bernoulli beams under static loads. The modeling of concentrated damages has been done by means of the well-known Dirac's delta distributions in the flexural stiffness. Closed form solutions for both statically determinate and indeterminate beams were found in terms of damage intensities and positions. They proposed a non-quadratic optimization procedure as an inverse damage identification problem. The presented procedure relies on the minimization of a residual function found as the difference between the theoretical model response and experimental data.

Caddemi and Morassi [29] have studied the identification of a single crack in an elastic straight beam in bending from the knowledge of static measurements in order to provide explicit expressions for the position and the severity, which represent the exact solutions of the inverse problem. They modeled the open crack as a linear elastic rotational spring. Later they have extended their study [30] to the identification of multiple open cracks in a beam by static test. Yang and Sun [31] investigated a static-based detection method to determine the location and extent of structural damage. First, they obtained the damage location by calculating a damage localization vector, which has been derived from the static response equation. Thereafter, the corresponding damage extent has been calculated using determined damage location based on simple arithmetic operations.

Abdo [32] presented an analytical study of the relationship between damage characteristics (location and severity) and changes in displacement curvatures. They carried out a parametric study using changes in displacement curvature in structural damage detection. The influence of many parameters such as: number of measurement data, cases of loading, intensity of loading and measurement noise were investigated. To demonstrate the results, they considered numerical analyses of two examples: an over-hanging beam (statically determinate structure) and a two-span continuous beam (statically indeterminate

structure) with different damage characteristics. However, no experimental results are used to validate the crack model and also compare the results with those from other crack models.

RaghuPrasad *et al*. [33] derived a simple method based on loss of symmetry due to damage and presented for identification of damage in a bridge girder modeled as a simply supported beam using changes in static deflections. They extended the methodology for a base-line-free as well as base-line-inclusive measurement. A laboratory-based experiment has been used by the authors to validate the approach.

Kaushik *et al*. [34] proposed a methodology combining Damage Locating Vector (DLV) method and deflection from static measurements for damage localization. Several structures including trusses and beams were modeled and analyzed by the authors for various damage scenarios using the proposed methodology.

Grandić and Grandić [35] presented an approach in damage severity estimation in beams based on curvature of displacement influence lines and grey coefficient using sparse static measurements. In their study they found damage location based on difference of curvature of static deflection pattern and also suggested an expression for reduction in bending stiffness in a segment based on curvature ratio of undamaged to the the damaged state. However, they did not find damage severity accurately with their proposed method.

Online damage detection of an in-service structure is more difficult and expensive in the case of static based damage detection method. Moreover, in these methods, a large number of measurements points are necessary to achieve the required degree of accuracy. Hence monitoring of defective structures by means of non-destructive vibration based damage detection tools are other alternative techniques to maintain safety and integrity of those structures. Therefore, vibration based damage detection technique has been adopted for the present study.

1.2.3 Vibration based methods

1.2.3.1 General concept

The basic idea of vibration-based damage detection is to obtain dynamic characteristics in a regular basis. The state and degradation of the structure is reflected in the changes of these characteristics. The revolution in the field of vibration based damage detection has occurred

in late 1960s and the study of Lifshitz and Rotem [36] is the evidence of it. In their study, they observed the change in the dynamic moduli, which can be connected to the frequency shift, as indicating damage in particle filled elastomers. This work may be the first journal article to propose damage detection based on vibration measurements.

Doebling *et al*. [37] gives an extensive literature review of vibration-based damage detection approaches, beginning in the 1970s with the investigation of their capability for assessing offshore structures and continuing to the more widespread implementations proposed through the 1980s and early 1990s. The authors have classified the vibration based methods into various categories by their damage-sensitive feature as: (a) Frequency, (b) Mode shape, (c) Strain mode shape (mode shape curvature), (d) Dynamic Flexibility and (e) Stiffness. Furthermore, to detect changes in these characteristics, other techniques based on matrix updating and neural networks have been used. Similarly, Sohn *et al*. [38], Thatoi *et al*. [39] and Fan and Qiao [40] presented comprehensive reviews on damage detection and health monitoring methods for structural and mechanical systems. A review paper addressed by Dimarogonas [41] produces a collection of research works that are carried out so far, in which analysis methods for open and breathing crack, effect of crack as discontinuity on dynamic characteristics of cracked beams and studies of vibration of cracked plates are provided. Jassim *et al*. [42] presented a review on the vibration analysis for a damage occurrence of a cantilever beam. Fasl *et al*. [43] investigated the development of a wireless system for both long- and short-term monitoring of steel bridges. A radio frequency (RF) study was carried out as a part of the investigation to understand multi-path effects of the radio signal and the potential benefit of using high-gain antennas in wireless bridge monitoring applications. Salawu [44] introduces an excellent review on utilizing changes in measured natural frequencies as a diagnostic parameter for structural damage identification. Relationship between frequency changes and structural damages were discussed. Various methods proposed for detecting damages using natural frequencies were reviewed. The studies based on the vibration analysis of cracked systems are described subsequently with the help of different subsections.

1.2.3.2 Damage detection based on free-vibration

The study of damage detection based on free vibration have been carried out by many researchers since modal parameters notably frequencies, mode shapes, and modal damping

are important for understanding the dynamic response behaviour of undamaged and damaged structure.

Vandiver [45] carried out damage detection on an offshore light station tower by examining the frequency changes in the first two bending modes and the first torsional mode. Wojnarowski *et al*. [46] studied the effects of eleven different parameters affecting the lower mode vibration characteristics of an offshore lighthouse platform structure using finite element method. Foundation modeling assumptions, leg height, entrained water, marine growth, corrosion, variation in deck loads and breakage of members are some of the parameters that were studied by the authors. The largest change in frequencies comes from alterations of soil foundation properties.

Adams *et al*. [47] investigated a method where the integrity of structures is described and applied to structures for one-dimensional analysis. They have identified the damage from changes in the resonant frequencies associated with two modes. Experimental results are obtained by the authors on a variety of components, including straight prismatic bars, a doubly-tapered bar and an automobile camshaft. Excellent agreement between the actual and predicted damage sites being found. In particular, they looked at longitudinal vibration modes. The method is dependent on the relationship between the receptance function on either side of the damage and also they have modeled the damage by a linear spring of infinitesimal length separating two sections of the bar. They also remarked that a need to correct frequency measurements due to changes in temperature, which is another possible source of error when frequency changes are considered to locate damage.

Cawley and Adams [48] presented a method to detect damage in composite materials based on measured frequency shifts. For each potential damage location, the frequency shift ratios between two significant modes are estimated from the analytic model by assuming a local stiffness reduction at that location. To obtain the damage location, an error term is utilized to correlate the measured frequency shifts to those predicted from the analytic model. Comparing the errors for all potential damage locations, the actual location of damage is indicated. However, this approach is only applicable for identification of a single damage location and the study is unable to show the way to handle multiple cracked system.

Yuen [49] demonstrated the changes in the mode shape and mode shape slope parameters. The changes in these parameters were found to occur for a reduction in stiffness

in each structural element. Thereafter predicted changes were computed to the measured changes to estimate the damage location. The author pointed out the need for some orthonormalization process in order to look at higher mode shapes. Moreover, no assessment of the extension of damage was carried out by the author.

Sato [50] has demonstrated the effects of the groove dimensions on the first natural frequency by the numerical calculations and experiments. The calculation of first natural frequencies of free-free square beams with a rectangular slot is presented as example. Nevertheless, the higher vibration modes were not considered in the analysis on the accuracy of predicted vibration characteristics of the damaged beam, from a damage detection viewpoint.

Narkis [51] obtained the natural frequencies of a cracked simply supported uniform beam by an approximate analytical solution and then applied to the non-iterative inverse problem to identify the crack location from frequency measurement. In this study crack was simulated by an equivalent spring. Author also confirmed the proposed method by comparing it with results of numerical finite element calculations. However, in this study, the case of identification of depth and locations of multiple cracks remain unsolved.

Shen and Taylor [52] developed an identification method to obtain the crack characteristics (location and size of the crack) from dynamic measurements. This method is based on minimization of either the mean-square or the maximum difference between measurement data (natural frequencies and mode shapes) and the corresponding predictions obtained from the computational model. Authors tested the method for simulated damage in the form of one side or symmetric cracks in a simply supported beam. However, the results of the study could not be supported by laboratory or field tests on the beam.

Armon *et al*. [53] presented a method for detection and localization of slots and cracks in a beam using rank ordering of the modes according to the reduction of natural frequencies. They have shown that the rank ordering of the eigenfrequency shifts is a function of the crack location but it does not depend on the damage magnitude for small cracks.

Liang *et al.* [54] and Nikolakopoulos *et al.* [55] suggested that the position and the size of a single crack could be identified by determining the intersection point of the lowest three natural frequencies. However, in many cases, the three curves of frequency contour

plot might not intersect because of inaccuracies in the modeling with respect to the measured results. To address this issue, a zero-setting procedure was proposed by Nandwana and Maiti [56] and Chinchalkar [57].

Chasalevris and Papadopoulos [58] presented the free bending vibration of a rotating shaft having a uniform circular cross-section with transverse crack and introduced results of the change of the local compliance matrix. They have shown that the change in the total stiffness in transfer directions rely on the change in the crack local compliance. The rotation of the transverse crack changes the shaft stiffness and the existence of the crack introduces the coupling between vibrations in the vertical and horizontal planes, which affects the response and amplified higher harmonics of vibration.

Kikidis and Papadopoulos [59] investigated the influence of the slenderness ratio on dynamic behaviour of a shaft with a cross-sectional open crack. Numerical results obtained from the Euler-Bernoulli theory are compared with those obtained from Timoshenko theory for different crack depths and different slenderness ratios of the shaft. Authors demonstrated that the Euler-Bernoulli theory and the Timoshenko theory provide the same results for large slenderness ratios, with or without a crack in the shaft and when the slenderness ratio decreases, the influence of the shearing deflection increases.

Narkis and Elmalah [60] showed the possibility of crack detection in cantilever beams under uncertain end conditions using free vibration analysis. Authors developed a method for characterizing the effect of clamp rigidity and for direct estimation of crack location based on variations of three natural frequencies. They also found that when clamp rigidity of an undamaged cantilever beam changes, the corresponding relative frequency changes are equal for all bending modes and unequal changes in relative frequencies indicate the presence of cracks.

Loya *et al*. [61] estimated the natural frequencies for bending vibrations of Timoshenko cracked beams with simple boundary conditions. They have modelled the beam as two segments connected by two massless springs (one extensional and another rotational). The differential equations for free bending vibrations are solved individually for each segment at the cracked section.

Labib *et al*. [62] presented a new method for estimating the natural frequencies of cracked beam and frames. In the proposed method the cracks are represented by a rotational

spring model. For beams, dynamic stiffness matrices are obtained in a recursive manner according to the number of cracks. On the other hand, global dynamic stiffness matrix of a frame structure with multiple cracked members is then assembled. Thereafter, Wittrick–Williams algorithm is applied to estimate the natural frequencies of the multiple cracked beams and frames but they have not validated the theoretical results with experimental results.

Elshafey *et al*. [63] executed an experimental program for testing the feasibility to detect the occurrence of structural damage using a modified mode shape difference technique. An experimental study was performed using a hinged-fixed beam to illustrate the use and the feasibility of the technique. Authors used the FRF function to identify the existence of damage and the modified mode shape difference technique was considered to locate the damage.

Öz [64] studied in-plane vibrations of slightly curved open cracked beams based on numerical and experimental methods. Curved beam specimens were made of steel with different lengths but with the same radius. They have shown that the decrease in the frequencies in all modes is very high, when the crack is adjacent to the fixed end. The consistency of the results and validity of the equations are discussed.

Cerri *et al*. [65] investigated the dynamic behaviour of a circular arch in undamaged and damaged configurations based on experimental and analytical results. Damage is represented by a notch and modeled as a torsion spring. They observed good agreement between analytical and experimental results.

Pandey and Biswas [66] introduced a damage detection method based on changes in the measured flexibility of the structure. The results of the numerical and experimental study showed that estimates of the damage condition and the location of the damage could be obtained from few of the lower modes of vibration. They also presented the experimental verification of flexibility difference method [67] for locating damage in structures. However, in their work, the study related to estimation of crack severity remains absent.

Sinha *et al*. [68] models beam structures with cracks at different positions by using Euler-Bernoulli beam elements with some modification to the local flexibility in the vicinity of the crack. Later they used the crack model to estimate the crack locations and sizes, by minimizing the difference between the measured and predicted natural frequencies via

model updating. This procedure of crack detection works well only at the lower modes of vibration.

Zheng and Kessissoglou [69] obtained the natural frequencies and mode shapes of a cracked beam using the finite element method. They have introduced the overall additional flexibility matrix instead of the local additional flexibility matrix to produce the total flexibility matrix of a cracked beam. Authors also developed a shape function that can satisfy the local flexibility conditions at the crack locations.

Weng *et al*. [70] presented a substructuring method for damage detection of a structure. The global flexibility matrix from the experimental modal data is disassembled for obtaining the independent substructural flexibility matrices. They have used the substructural flexibility matrix and its eigenparameters as indicators for damage detection. The substructuring method was verified by applying on a laboratory tested portal frame structure. They have found that the substructural eigenparameters are more sensitive to the local damage than the global eigenparameters.

Tsai and Wang [71] investigated the free vibrational analysis of multi-step and multi-cracked rotor having cracks of the first mode or opening mode of fracture. They used transfer matrix method for modeling of the rotor along with the Timoshenko beam theory. The authors obtained the results only by computer simulation without validation of experimental studies.

Xiaoqing *et al*. [72] presented an analytical approach for the identification of a beam with multiple cracks. The approach is based on the bending vibration theory of Euler-Bernoulli beam and the cracks are represented as massless rotational springs, by which the cracked beam is separated into a number of segments of perfect beams. They established a relation correlating the positions and depths of the cracks to the vibration frequency of the beam by considering the boundary conditions, continuity conditions at cracks and the condition for a nontrivial solution of the vibration modes of the beam elements. Authors also used the transfer matrix method to detect the presence of more than two cracks the beams.

Attar [73] introduced a transfer matrix method to explore the free vibration analysis of stepped Euler Bernoulli beams with multiple cracks. The proposed method is used to derive the general form of characteristic equation for the cracked beam which is a function of

frequency, crack parameters, boundary conditions, geometrical and physical parameters of the beam. However, structures with simple geometries can be solved using their approach.

Pandey *et al*. [74] introduced the absolute difference between curvature mode shapes of undamaged and damaged structure to identify and locate the damage in a structure. They obtained the curvature mode shapes from displacement mode shapes using a central finite difference approximation. They also demonstrated that the MAC and COMAC are insensitive to detect damage in the structure.

Abdel Wahab and De Roeck [75] proposed a damage parameter called "Curvature Damage Factor" (CDF) which averages the difference in curvature mode shapes of intact and damaged structure for first few modes into a single index at each measurement point. To establish the method, simply supported and continuous beams containing damaged parts at different locations are tested by the authors. Later, the technique was applied to a real pre-stressed concrete bridge. The results showed that the application of the parameter to detect damage in civil engineering structures seems to be promising. However, the method was silent about the detection of severity of crack.

Ratcliffe [76] used finite difference approximation of Laplace's differential operator to the mode shape successfully to identify the location of damage. However, author found that the mode shapes associated with higher natural frequencies can be used to verify the location of damage, but they are not as sensitive in the lower modes.

Dutta and Talukdar [77] carried out a eigenvalue analysis using Lanczos algorithm in an adaptive h-version finite element environment in order to control the discretization error for accurate evaluation of modal parameters. They used Ahmed Shell elements for the discretization of bridge deck. They also conducted numerical experiments to show the necessity of adaptive eigenfrequency analysis by considering simply supported and continuous bridges with damaged parts at different positions.

Kisa [78] investigated the effects of cracks on the dynamical characteristics of a cantilever composite beam, which is made of graphite fibre-reinforced polyamide. The finite element and the component mode synthesis methods are used to model the problem. This method has been extended by Kisa and Arif Gurel [79] for free vibration analysis of stepped cracked beams with circular cross sections. However, only uniform beams can be solved using their approach.

Lee and Eun [80] studied a damage detection method that uses the response data transformed to the frequency-domain from the time-domain. Welch method has been applied to find the power spectral density estimation (PSE) of a signal. They have evaluated the damages using the curvature of the PSE. This method bypasses the baseline data and has a promising sign for on line health monitoring.

Nanda *et al*. [81] presented a two-step procedure to detect damages in a beam like structures from changes in curvature mode shapes. The particle swarm optimization technique has been applied in their studies to obtain the damage location and severity. The merit of the approach was to reduce the search space which results in computational cost while increasing the accuracy of prediction.

Nguyen [82] studied the mode shapes of a three dimensional cracked beam with rectangular cross section using finite element method but no laboratory experiments were conducted to verify the theoretical approach. They have shown the influence of the coupling mechanism between horizontal bending and vertical bending vibrations due to the crack on the mode shapes. They also established the relationships between the maximum inclines of the projections of the mode shapes and the crack depth, which is represented by a second-order polynomials.

Wang *et al*. [83] suggest a method for blade damage detection and diagnosis. This method includes finite element method (FEM) for dynamics analysis (modal analysis and response analysis) and the mode shape difference curvature (MSDC) information for damage detection or diagnosis. Finite element models of wind turbine blades have been established by the authors and modified via frequency comparison with measured data using the model updating technique.

Çam *et al*. [84] used impact shocks to obtain the information about the location and depth of cracked cantilever beam. Frequency domain is chosen to compare the responses of intact and damaged beams. Hsiao *et al*. [85] studied the feasibility of applying the impact-echo method for detection of flaws in concrete blocks.

Rezaee and Hassannejad [86] proposed an analytical method as an alternative to the numerical methods for vibration analysis of the breathing cracked beam. They have shown that the damping factor is sensitive to the crack depth and location. They also validated the

free vibration response of the cracked beam with a given crack depth and location obtained by the analytical method with that obtained by the numerical method.

Aydin [87] investigated the free vibration of functionally graded (FG) beams with open edge cracks. The investigation is based on Euler-Bernoulli beam and massless rotational springs connecting two uncracked segments of the beam. Authors also examined the influences of crack depth, crack location, total number of cracks, material property distribution, and boundary conditions on the natural frequencies of the damaged FG beams. More advanced model for study of the vibration of functionally graded material (FGM) plate has been reported by Gupta *et al*. [88]. They investigated the effects of volume fraction indices, geometric configurations and boundary conditions on the natural frequency of plates using higher-order deformation theory.

Rucevskis *et al*. [89] studied the detection and localization of damage in plate like structures by using two dimensional mode shape curvature. To calculate mode shape curvatures from mode shapes they have proposed three approaches and these are central difference approximation, the other two are classical approaches based on Tikhonov's regularization technique with smoothing functional. The efficiency of the proposed damage detection approaches are presented experimentally on an aluminium plate, which contain mill-cut damage.

Bikri *et al*. [90] investigated the geometrically non-linear free vibrations of a clamped–clamped beam containing an open crack without experimental validation. Authors used a semi-analytical model based on an extension of the Rayleigh–Ritz method to non-linear vibrations. They introduced an admissible function, called as cracked beam functions designated as CBF, which satisfy the natural and geometrical end conditions, as well as the inner boundary conditions at the crack location. The proposed research work is restricted to the fundamental mode in order to focus on the study of the influence of the crack on the non-linear dynamic response near to the fundamental resonance.

Carrera *et al*. [91] studied the free vibration analyses of damaged metallic aircraft structures employing natural frequency tracking and mode shape changes by considering the component-wise (CW) models. Use of Lagrange polynomials was made to expand the generalized displacement field in CW analysis. The authors concluded that some form of damage changes natural frequencies but mode shape may remain unaffected. The main aim

of using CW models was to create a data base of possible damage scenarios to be compared to experimental data in a trained neural network.

Moore *et al*. [92] presented a model-based approach to identify the size, location and orientation of a single crack in a real clamped thin plate undergoing free vibration. An impact test was carried out where strains are measured only at three locations. They have shown that even with limited, noisy vibration data valuable information concerning the damage state can be successfully calculated.

Wei *et al*. [93] suggested an analytical approach for free vibration analysis of beams of functionally graded materials (FGM) with edge cracks. Rotational spring model is used to represent the crack. In this study, the equations of motions of cracked Timoshenko beam are developed based on Hamilton's principle and solved analytically. The influence of the location and number of cracks, axial load, rotary inertia, shear deformation, material properties and various boundary conditions on the frequencies and vibration mode shapes are studied by the authors.

Viola *et al*. [94] used two different approaches to study in-plane free vibration of circular arches, in case of intact and damaged system. These two different approaches are: (a) first approach solves the fundamental system in closed form by means of a characteristic polynomial and (b) second approach is based on differential quadrature and domain decomposition technique. Domain decomposition technique [95] was used to impose jump conditions across the crack. The mode shapes of damaged arch did not reveal symmetry and skew symmetry. However, for the lightest damage case studied, mode shapes are found insensitive in damage identification. This work did not report the comparison of theoretical results with experimental ones. The drawback of such method is that one has to know the frequency and mode shapes of undamaged state to predict the damage.

Ricci and Viola [96] and Viola et al. [97] conducted a study on cracked T-section beams by excluding warping effects. The authors have used the simple beam theory to calculate approximate stress intensity factors of cracked beams suggested by Kienzler and Herrmann [98] by applying to cracked T-beams subjected to bending moment, shear force and torsion. They have modeled the crack as a line spring element [99-101].

Öz and Daş [102] studied the in plane vibrations of a circular curved beams with Mode I open transverse crack. FEM have been used to estimate the natural frequencies of the

curved beam with a crack in different positions and depths. Comparisons of natural frequencies are also shown for different angles. The other two modes of fracture have not been considered in their study.

Krawczuk and Ostachowicz [103] investigated a finite element model of transverse cracked arch. The crack in the arch is considered as nonpropagating and open. The influences of the crack position and its depth on the changes of the in-plane natural frequencies and mode shapes of the clamped-clamped arch are explored by the authors. However, their study was limited to identification of single crack problem without any experimental evidence.

Wolff and Richardson [104] proposed that the modal assurance criterion (MAC) can be used to compare the overall differences between two sets of mode shapes. Ko *et al*. [105] established a method that uses a combination of sensitivity analysis, MAC and COMAC to detect the damage in a steel portal frame structure. After numerical and experimental investigation of a beam, Fox [106] revealed that the MAC value is insensitive to damage detection and recommended that graphical comparison of the mode shapes might be a good way to locate damage. A contradictory statement has been given about the utility of MAC values in the paper published by Carrera *et al*. [91]. Therefore, studies using MAC numbers are necessary in other cases too to verify the opinions of different authors

Ndambi *et al*. [107] showed that the MAC factors are less sensitive to damage detection compared to eigenfrequencies, but it gives an indication of the symmetrical or asymmetrical nature of the induced crack damage. Authors also studied the COMAC factors, the strain energy evolution and the changes in flexibility matrices and their capability for detection and localization of damage in the RC beams. They have found that the strain energy method appears to be more precise than the others.

Alnefaie [108] demonstrated that the strain energy damage index (SEDI) and a similar parameter called SEDI2 are insensitive to the magnitude of the underlying damage in beams, although they do help to locate the damage itself. Author developed a new damage sensitive parameter, which is called as modal moment index (MMI). They have demonstrated that the MMI also jumps sharply at the location of damage in the beam and the magnitude of the MMI is closely related to the decrease in relative modulus.

Samali *et al*. [109] presented a method of damage evaluation for identifying single and multiple damage in timber bridges, numerically and experimentally. A finite element model of a laboratory timber bridge was developed by the authors to investigate the capabilities and limitations of the method to detect damage. The damage index (DI) method for plate-like structures (DI-P) was considered for damage detection, where the method utilizes changes in modal strain energy between the undamaged and damaged states. Patil and Maiti [110] introduced a method for prediction of position and size of multiple cracks based on measurement of natural frequencies. Experimental validation for slender cantilever beams with two and three normal edge cracks have been presented. Their proposed method is based on energy principle where a crack is represented by a rotational spring. They have divided the beam into a number of segments and each segment is considered to be associated with a damage index. The damage index is the mark of the extent of strain energy stored in the rotational spring. Eraky *et al*. [111] suggested a damage index method (DIM) may be a tool for determining local damages occurred in flexural structural elements. The method was based on the comparison of modal strain energy for different structural degradation stages from which they have calculated the damage index (DI). Free vibration responses of undamaged and damaged finite element models were used to locate the location of damage throughout the beams and plates. Rezaei *et al*. [112] considered the modal based indices to detect damage for the nonlinear model of modern wind turbine blade. The various modal-based damage indices including the frequency, mode shape, curvature of mode shape, modal assurance, modal strain energy (MSE) and the difference of indices (between the intact and damaged blades) are explored by the authors to check the accuracy and efficiency of each indices. Moreover, they showed the enough sensitivity of the mode shape curvature and MSE indices to the local damages. These damage index based approaches required the information of undamaged beam for identification of damage. This stands as an obstacle in real life application as the information of modal features of undamaged structures may not be available.

Hosseini-Hashemi *et al*. [113] constructed a set of exact closed-form characteristic equations incorporating shear deformation and rotary inertia, based on the Mindlin plate theory to analyze free vibration problem of moderately thick rectangular cracked plates for different boundary conditions. They have assumed that, the crack is open and non-propagating. The accuracy of the proposed approach is inspected through comparing the exact natural frequencies obtained from this approach with finite element method obtained

by ABAQUS software package. The study revealed that significant reduction of natural frequencies occurs when the crack is present near the clamped edge.

Sokolinsky *et al*. [114] investigated the free vibration of sandwich beams with a locally damaged core. They have used the higher-order theory in the approach to derive the free vibration equations. The proposed approach of damage detection based on the derived equations has been verified with the commercial finite element software ABAQUS.

Xiang *et al*. [115] proposed a method, based on the conjunction with the natural frequencies and support vector regression to detect the multi-damage in beam like structures. They have considered the wavelet finite element method for numerical simulation to determinate the relationship among multi-damage locations, depths and natural frequencies of a beam.

Solís *et al*. [116] suggested a methodology for beams based on wavelet analysis to locate the damage from changes in the mode shapes (geometric based analysis). The proposed methodology requires the mode shapes information of a reference undamaged state as well as the damaged one. Thus, the use of undamaged beam information is the serious drawback of the study.

Kao and Hung [117] demonstrated a two-step approach for detection of cracks using artificial neural networks (ANN). The first step relates to the system identification based on neural system identification networks (NSINs) for identification of the undamaged and damaged states of a structural system. The second step is structural damage detection, using trained NSINs to generate free vibration responses with the same initial condition or impulsive force. Sahin and Shenoi [118] also studied the damage detection in a beam structures based on artificial neural networks.

Few studies on damage detection using statistical tool have been reported in the literatures. The study using second order moment of nodal displacement and velocity of discretized structures have been conducted by Imollonia *et al*. [119] to predict change of structural stiffness and modal damping ratio. Response Surface Methodology (RSM) is another combined mathematical and statistical techniques useful for modeling and analysis of problems in which a response of interest is influenced by several variables [120-122]. RSM has been employed in various fields such as in biotechnology, chemical engineering and process industries with wide range of applicability [123-125]. Recently the application

of this methodology has been found in structural, Mechanical and Electrical engineering [126-131]. Mukhopadhyay et al. [132] demonstrated the damage detection using Response surface method (RSM) where they considered only bending behavior of the structure. No physical tests were conducted to verify the theoretical approach. Response surface based model updating has been used in damage identification of girder with symmetrical cross section [133], where flexural behavior of the structure was only considered. It may be mentioned that the study incorporating model updating suffers from serious drawbacks [134] in damage identification problem as this may cause errors due to contamination of actual cracked stiffness matrix in updating process. In structural reliability problem, RSM has been applied by Faravelli [135], Rajasekhar and Elligwood [136] and Guan and Melchers [137]. Those studies mainly focused on the probability of failure of the structure. It may be noted that although RSM has been applied to some specific cases of system identification and model updating, studies on detection of crack location and depth using this method has not been attempted for structural health monitoring.

Moradi *et al*. [138] demonstrated the application of "bees algorithm" to identify the location and depth of the cracked cantilever beams. The efficiency of the algorithm has been verified through both numerical and experimental studies. An objective function based on weighted sum of the squared residuals between the measured and calculated natural frequencies is used to obtain the crack parameters.

Cerri and Ruta [139] studied two different procedures to identify the damage parameters in a plane doubly hinged circular arch by means of measured natural frequencies. First procedure is based on the search of a crossing point of curves indicating the amount of the damage obtained by the modal equation. Second one is the minimization of an objective function obtained by a response comparison.

Vakil-Baghmisheh *et al*. [140] implemented the genetic algorithm approach to detect crack location and depth in the cantilever beam. Authors uses the binary and continuous genetic algorithm to obtain the optimal crack by minimizing the cost function parameters which is based on the difference of estimated natural frequencies and measured one. They observed that the prediction error rates of crack parameters in case of continuous GAs are less than those of binary GAs.

Moezi *et al*. [141] illustrates the open edge-crack detection in an Euler–Bernoulli cantilever beam through the application of modified cuckoo optimization algorithm. They have modeled the crack as torsional spring. Optimizing the cost function the authors have been able to obtain the location and depth of the crack.

Ding *et al*. [142] studied an improved artificial bee colony algorithm (I-ABC) for open crack identification in beam structures. The differential evolution mechanism is incorporated to apply bee phase, tournament selection approach is chosen instead of roulette selection approach and a new formula is utilized to simulate onlooker bee's behaviour. The authors found that the I-ABC can obtain more precise damage identification results compared to original artificial bee colony algorithm (ABC).

The free vibration based analyses of the structural system with damage are available in the literature since the beginning of 1970. The FEM was utilized in most of the subsequent studies. The component mode synthesis, transfer matrix, integration methods, wavelet analysis, statistical tools and optimization techniques etc., were also adopted in some of them. Reviews on the damage detection based on forced vibration are presented in the next subsection.

1.2.3.3 Damage detection based on forced-vibration

When a system is excited by an external agency then the produced response is called forced response. In this section previous works of the various authors on the damage detection has been discussed.

Khiem and Lien [143] investigated the dynamic behaviour of a beam with multiple transverse crack based on forced vibration analysis. Authors observed that the solution for static response of a beam with an arbitrary number of cracks has been achieved exactly in an analytical form, when the forcing frequency is close to zero. The authors also computed the displacement, slope, bending moment and shear force depending on the number and depth of cracks. However, proposed method requires the response of the uncracked beam as a baseline for the crack detection.

Loutridis *et al*. [144] demonstrated a method for crack detection in double-cracked cantilever beams based on wavelet analysis. The locations of the cracks were detected by the sudden changes in the spatial variation of the continuous wavelet transform (CWT). To calculate the relative depth of the cracks, an intensity factor is formed which connects the

size of the cracks to the coefficients of the wavelet transform. The formulation of the study is limited up to the double cracked beam scenario. The calculation of the crack depths had encountered difficulties when the values of the intensity factor were high.

Dharmaraju *et al*. [145] presented a general identification algorithm to obtain the crack flexibility coefficients and the crack depth using forced vibration analysis. The authors included the static reduction technique in the identification algorithm for eliminating some of the response measurements. They constructed an error function based on theoretically derived and estimated flexibility coefficients. With the help of least squares technique in conjunction with the root searching method, they obtained crack depth. However, the identification algorithm depends on the measurement of the beam response for a known sinusoidal force. In practical cases, excitation type and magnitude may remain unknown. This suggests that there is a necessity to develop method which can detect the excitation parameters also along with crack information.

Loutridis *et al*. [146] presented an approach for crack detection in beams based on the instantaneous frequency (IF) and empirical mode decomposition (EMD). They have studied dynamic responses of a cantilever beam with a breathing crack subjected to harmonic excitation both theoretically and experimentally. They suggested that the time–frequency approach is superior compared to Fourier analysis and intended to improve the usefulness of vibration-based crack identification techniques. However, sometimes noise will increase the EMD error so greatly that the intrinsic mode functions (IMFs) are distorted seriously and fail to represent the actual modes involved in the signal [147].

Behzad *et al*. [148] established the equation of motion and corresponding boundary conditions for forced vibration analysis of a beam with crack using variational principle. Using developed model in conjunction with the Galerkin projection method, the authors obtained the natural frequencies and the forced response of this beam specimen for damage detection. Lin and Chang [149] presented an analytical method to demonstrate the dynamic response of a cracked cantilever beam subjected to a concentrated moving load. They modeled the cracked beam system as a two span Euler–Bernoulli beam. They have shown the effects of crack through numerical example considering load moving at different speeds. Both the studies only can detect the single crack at a time which is the major drawback of the works.

Joglekar and Mitra [150] presented an approach based on the use of wavelet spectral finite elements (WSFE) for studying the non-linear interaction of flexural waves with a breathing crack present in a slender beam. The authors obtained the crack location with reasonable accuracy.

Karthikeyan *et al*. [151] presented an algorithm for crack detection, localization and sizing in a Timoshenko beam based on forced vibration analysis. They have considered an open transverse surface crack for crack modeling. The proposed algorithm is iterative in nature and begins with an assumption that a crack exists in the beam. They have used the Tikhonov regularization technique to estimate the crack flexibility coefficients. Thereafter, the crack flexibility coefficients are utilized to achieve the crack size by minimizing an objective function. Lastly, they have updated the crack location, with the help of achieved crack size and measured natural frequency.

Yang *et al*. [152] introduced the inner product vector (IPV) based damage detection method in composite structures. The IPV is connected to the mode shapes and can be directly estimated from the time domain vibration responses to white noise excitation. However, in practice band pass white noise excitation can only be measured, which is the limitation of the study. Based on the proposed method the difference of IPVs between the undamaged and damaged structure is considered as the damage index, and the abrupt change in the difference of IPV indicate the damage location. This method cannot be used to localize the damage if the influence of the damage on the structure's dynamics is too small when the measurement noise is too high.

Karthikeyan and Tiwari [153] reported an experimental investigation to detect location and size of the crack present in a circular beam based on forced response measurement. The support condition was rolling bearings at both ends. Harmonic force of continuously varying frequency was used by the authors to excite the specimen. Resonant frequencies, phase information and amplitude of responses were considered in the proposed experimental identification approach for subsequent calculation of crack parameters.

Huh *et al*. [154] suggested a local damage detection method based on the vibratory power estimated from the accelerations measured on cracked beam structures. Changes in the vibratory power of the damaged beam are used to evaluate the damage index. Thereafter, damage index is applied to identify the structural damage. Numerical simulation

and experiment are carried out by the authors to confirm the validity of the proposed approach. The formulation was limited to single crack.

Merrimi *et al*. [155] presents a semi-analytical method for determination of the steady state periodic forced vibration responses of clamped–clamped beams with an edge open crack. The proposed method is formed using Hamilton's principle and spectral analysis to find the effect of the excitation frequency and level of the executed harmonic force, concentrated at the cracked beam middle span. The formulation also used admissible functions also known as cracked beam functions (CBF), which satisfy the natural and geometrical end conditions, as well as the inner boundary conditions at the crack location.

Andreaus and Baragatti [156] reported a study of a cantilever beam subjected to harmonic force. Based on tip response, they formed a relation to calculate the location and size of the crack, which is known as nonlinear damage indicators (NDIs). Nonlinear Damage Indicators (NDIs), namely excursion and eccentricity of the orbit in the phase portrait and the amplitude of the super- or sub- harmonics are used to obtain the location and depth of the crack. The identification procedure was performed based on the intersection of constructed surfaces which allowed to identify the structural crack.

Heydari *et al*. [157] investigated the forced vibration analysis of a Timoshenko beam with an open edge crack using a continuous bilinear model for the displacement field. The governing equation of motion for a general force distribution has been established based on the Hamilton principle and the proposed displacement field. The results obtained using this proposed model are also compared to results of a similar model with Euler-Bernoulli assumptions to ensure the advantages of the proposed model in the case of short beams.

Chen and Maung [158] obtained the position and size of the damage in structures directly form measured dynamic response such as accelerations. Based on the governing equations of motion for undamaged and damaged structural systems, the relationship between the change in stiffness due to structural damage development and the related dynamic response measurements of the monitored structural system is suggested by the authors. The Tikhonov regularisation algorithm including the L-curve criterion is proposed to decrease the effect of noise in vibration measurements and then to provide stable solutions for structural damage parameters. However, there are some limitations of the

proposed approach for practical applications, such as requirement of complete dynamic output measurements and use of the known excitation forces.

Rangaraj *et al*. [159] identify the crack parameters in cantilever beam from forced vibration measurements based on the principles of dynamic state calculation. The crack parameters namely, position and size of the crack are considered as the variables in the particle filter algorithm. The damage detection approach bypasses the demand for baseline measurements of the vibration response of the intact beam.

Wang *et al*. [160] studied the effect of multiple cracks on the force response of centrifugal impellers using finite-element based hybrid interface component mode synthesis (CMS) method. The shift of natural frequencies, nonlinear forced response and vibration localization due to double cracks are investigated using proposed approach. However, the study was only theoretical. No experimental validation of the proposed crack detection approach is included in their study.

Wu [161] investigated the forced vibration characteristics of a beam structure with a breathing edge crack under various dynamic excitations. The author applied an iterative numerical method to solve the forced vibration of the cracked beam considering its multiple vibration modes and the bi-linearity. The study showed a non-linear variation of the crack breathing frequency when the excitation frequency increases from the first to the second resonant frequencies of the beam.

Zhao *et al*. [162] established the Green's functions for the steady state response of a cracked Euler Bernoulli beam subjected to harmonic force. They obtained dynamic response of a single cracked beam by means of Green's functions method. On the other hand, the transfer matrix method has been implemented to produce the steady state outputs of a multiple cracked beam, which can be easily reduced to those for a single cracked beam.

Hu *et al*. [163] proposed a crack parameter identification approach based on homotopy continuation [164]. A fully opened cracked Euler Bernoulli beam has been considered in the proposed approach. The homotopy equation is derived from minimizing the error between the calculated and the simulated measured acceleration responses. Newton's iterative method is implemented to calculate the more accurate value in the homotopy path. Numerical simulations of simply supported beam and two-span beam are presented through the proposed method for both single and multiple crack scenarios. The simulated

acceleration responses are adopted in the present study instead of physically measured responses, which is the shortfall of the study.

Cacciola *et al*. [165] studied the dynamic response of a cantilever beam with an edge non-propagating crack subjected to white noise excitation. It has been observed that the higher order statistical moments of the response are used to locate the crack in the structures. Variation of skewness coefficients are used to indicate the presence of crack and location. The study remained silent about the depth of the crack. Wang *et al*. [166] demonstrated the damage identification method based on statistical moment of beam-type structures under white noise excitation. At first they introduced the difference curves of forth strains statistical moment (FSSM) before and after damage to locate damage elements. Thereafter they utilized the model updating method based on the least square algorithm to assess the damage severity. The experimental study on this topic has been presented in another publication by the authors [167]. These studies cannot identify the damage in the structure without using the response of the undamaged beam, which is the basic limitation of these studies. Moreover, the usefulness of the study was shown only for the beams with bending vibrations.

Zheng *et al*. [168] investigated the structural responses and power spectral density under stationary and random excitations using pseudo excitation method. They studied the sensitivities of power spectral density with respect to the structural damage parameters. Later, finite element model updating method has been considered to identify the damages from the calculated and the simulated measured power spectral density. The conclusions were drawn for plane frames by means of theoretical calculations without utilizing any measured data.

From the discussions in this section, it has been realized that the damage detection study based on forced vibration analysis is limited when compared to free vibration analysis. However, the interest of the researchers in this area using forced vibration analysis is growing day by day. Damage detection based on the combination of free and forced vibration analysis are presented in the next subsection.

1.2.3.4 Damage detection based on free and forced-vibration

In this section, literature focusing on crack detection based on combination of free and forced vibration analysis is reviewed.

Orhan [169] presents the free and forced vibration analysis of a cracked cantilever beam to identify the cracks. It has been found that free vibration analysis is an effective method compared to forced vibration analysis in the case of two cracks present on the top and bottom surfaces of the beam to detect the cracks and on the other hand harmonic response analysis is better than the free vibration for single crack exists on top and bottom faces of the beam.

Karthikeyan *et al*. [170] introduced a finite element method for simply supported and cantilever beam with open transverse surface crack using free and forced vibration analysis. The FEM is based on Timoshenko beam theory. The localization and sizing of crack are iterative in nature. The detection approach algorithm uses both fundamental natural frequency and force-response measurements. However, the study could not identify forcing parameters.

Mei *et al*. [171] investigated the free and forced vibrations of cracked Timoshenko beams under axial loading from wave propagation analysis. They derived the transmission and reflection matrices for different discontinuities on an axially loaded cracked beam.

Shafiei and Khaji [172] studied free and forced vibrations of Timoshenko beam with an arbitrary number of cracks subjected to a moving load. In their study, they utilized eigen-functions to detect crack location. In addition, they have obtained the forced vibration response by the modal superposition method. The authors carried out some parametric study to show the influences of crack parameters and moving load velocity on beam. The results show that the response of the beam is insensitive to the crack depth ratios, especially for practical length-to-height ratios.

Collins *et al*. [173] investigated the free and forced longitudinal vibrations of a cantilevered bar with a crack without conducting any experimental study. First of all, they have studied the influences of crack position and compliance on the fundamental natural frequency. Then they computed the steady-state amplitude of motion of the bar at free end, which is happened due to harmonic excitation. The variation of the motion as a function of the forcing frequency, crack location, and crack compliance were studied.

Yang *et al*. [174] investigated the free and forced vibration analysis of inhomogeneous Euler–Bernoulli beams with open edge cracks. An axial compressive force and a concentrated moving load along the longitudinal direction have been considered in the

study. Crack has been modeled as rotational spring model. Using modal series expansion technique, the authors obtained the forced response. Analytical solutions of natural frequencies and dynamic deflections are presented for different support conditions. It has been observed from their study that the dynamic deflection is not very sensitive to the presence and the location of the crack.

The survey shows that the damage detection study based on free and forced vibration is scanty and therefore, research is necessary to further enrich the knowledge in the area of vibration based damage detection.

1.2.4 Vibration of thin walled beams

Thin-walled beams are widely used in aerospace engineering, civil and mechanical engineering as principal load carrying members. Self-weight of thin walled structures are low while they possess satisfactory strength and ductility. They are often curved for architectural reason or due to space constraints. The mechanics of thin walled beams are complex due to coupling of axial, bending and non-uniform torsional deformation. The development and improvement of thin-walled structures have been reported by Vlasov. According to Vlasov [175] and Megson [176] if the ratio of thickness of the beam to any characteristic dimension of the cross-section is less than or equal to 0.1, then such type of beams come under thin-walled beam categories. Several theoretical studies on uncracked thin-walled straight and curved beams for different configurations are available. Some of them are discussed here.

Dokumaci [177] carried out analytical investigation for the bending-torsion vibrations of uniform asymmetrical beams to determine the natural frequencies of the beam by ignoring the warping effects.

Banerjee and Williams [178] presented an analytical expression for the exact dynamic stiffness matrix elements of a uniform bending-torsion coupled Timoshenko beam. The equations have been derived including the effects of shear deformation and rotatory inertia but the influence of warping was not included in their study. Later, Banerjee *et al*. [179] developed an exact dynamic stiffness matrix for a bending-torsion coupled beam including warping stiffness. Authors demonstrated that the large errors may be produced in the estimation of natural frequencies of thin-walled open section beams, when the effect of warping is neglected.

Noor *et al*. [180] introduced the mixed finite element models for free vibration analysis of thin-walled beams with arbitray open cross-section. Vlasov's type thin-walled beam theory has been considered in the proposed approach including the effects of flexural-torsional coupling and the additional effects of transverse shear deformation and rotary inertia.

Ohga *et al*. [181] developed an analytical approach to calculate both the natural frequencies and mode shapes of thin-walled members using the transfer matrix method. They derived the transfer matrix from the differential equations of the plate panel of thin-walled members.

Mei [182] developed the stiffness and consistent mass matrices based on finite element method for a thin walled beam element with open cross-section. Tanaka and Bercin [183] investigated the coupled bending and torsional natural frequencies of uniform beams with arbitrary cross-section using the finite element method.

Jun *et al*. [184] studied the bending–torsion coupled random response of a monosymmetric thin-walled Timoshenko beam subjected to various kinds of random excitations. The effects of warping stiffness, shear deformation and rotary inertia are included in their work. Lue *et al*. [185] proposed a reliable and useful procedure for computing the warping constant for an arbitrary cold formed steel open section.

Chen and Hsiao [186] studied the coupled axial–torsional free vibration of thin-walled Z-section beam. The effect of boundary conditions and the value of warping function at centroid on the coupled axial and torsional natural frequency of Z-section beam has been studied through numerical examples.

Vo *et al*. [187] investigated the vibration analysis of thin-walled composite I-beams with arbitrary lay-ups. The influences of fiber orientation, location of applied load, and types of loads on the natural frequencies and load–frequency interaction curves as well as vibration mode shapes are studied.

Obst *et al*. [188] studied the thin-walled cold formed steel beams with open section subjected to pure bending. The authors explained the factors which are responsible for the torsion moment in the examined thin-walled steel beams with open sections subjected to pure bending.

Culver [189] presented an exact solution for the free vibrations of simply supported horizontally curved beams. The author introduced an expression for the calculation of natural frequencies of doubly symmetric curved beams. Chaudhuri and Shore [190] reported the results of the dynamic analysis of a horizontally curved I-girder bridge subjected to highway loadings incorporating the centrifugal forces.

Yang and Kuo [191] derived the differential equations for curved I-beams from the principal of virtual displacements. The authors have shown through two examples that the effect of curvature is significant, especially when the subtended angle is large.

Snyder and Wilson [192] introduced a closed form solution for the out-of-plane free vibration frequencies of a horizontally curved thin walled continuous beam. Several range of significant parameters representing variations in warping stiffness, torsional stiffness, radius of curvature, included angle of the curve and polar mass moment of inertia have been considered to study first six free vibration frequencies and the associated mode shapes for prismatic beams with three equal spans. Kang *et al*. [193] used the differential quadrature method (DQM) to compute the eigenvalues of free vibration for horizontally curved beams incorporating a warping contribution.

Yoon *et al*. [194] studied free vibration analysis of horizontally curved steel I-girder bridges using finite element method. The authors investigate the free vibration characteristics of the bridges considering effects of the initial curvature, boundary condition, modeling method, and degrees of freedom of cross frame.

Nam-ll and Moon-young [195] developed a curved beam theory based on centroid-shear center formulation using free vibration and elastic analysis. In order to show the efficiency of the study, example based on channel section and angle cross-section horizontally curved beams are illustrated. Duan [196] investigated the nonlinear finite element method for free vibrations of thin-walled curved beams with open non-symmetric cross-section. The author shows that nonlinear natural frequencies tend to increase as the curvature increases. Peres *et al*. [197] introduced a first-order generalized beam theory formulation for naturally curved thin-walled members with deformable cross-section. The authors demonstrated that the proposed formulation gives accurate results with a reduced number of degree of freedom. Ricci and Viola [96] and Viola et al. [97] studied the modal characteristics of cracked T-section beams ignoring warping effects. However, study did not consider the case where

bending-torsion coupled vibration takes place due to the fact that shear loading does not pass through shear center.

The literature shows that the vibration of cracked thin walled beams are limited and even in some isolated case, complex mechanics arising due to coupling of bending torsion vibration was not reflected.

1.3 Outcome of the literature survey

Considering the detail literature survey, it has been realized that the traditional non-destructive testing methods usually require that the structural component for assessment be accessible. Moreover, it is time consuming and expensive. On the other hand, online damage detection of an in-service structure is very difficult and costly in the case of traditional non-destructive testing and static based damage detection method. Thus, monitoring of defective structures by means of vibration based methods are other alternatives to maintain safety and integrity of those structures. The major disadvantage of most of the vibration based damage detection techniques discussed in the literature is that these techniques rely on mode shape vectors, which are too difficult to measure physically, whereas natural frequencies can be conveniently acquired using either free vibration or forced vibration experiments. The limitation of vibration based method studied so far was seen that it requires the vibration characteristics of undamaged structure to detect damage location and severity. However, most of the earlier studies did not report noticeable success in detection of damage severity by using vibration data.

Damage detection using vibration techniques comes under the group of “inverse problem”. Response Surface Method (RSM) can be regarded as a powerful and user friendly tool for solving inverse problem in various fields of science and engineering. Recently, vibration based techniques for structural health monitoring has entered from research stage to real life application due to development of sophisticated measuring instruments and signal processing software. Application of combined RSM and GA has not been addressed by the past researchers for crack detection study. Therefore, further research is required to prove its effectiveness for structures involving complex deformation pattern commonly encountered in thin walled structural components. The present study adopted RSM tool to solve diagnostic problems in structural health monitoring. The present approach has become more efficient in search operation with the

use of GA. Moreover, in vibration study of cracked thin walled beam, earlier works did not consider the effect of warping in calculating cracked stiffness which has a serious drawback if natural frequency is used as an indicator of damage.

Literature survey shows that the most of the researchers have studied damage detection techniques based on vibration responses to diagnose the cracks in solid beams of doubly symmetrical cross-section such as circular, square, rectangular and I-section using the knowledge of modal parameters. To the best of the authors' knowledge, modal features in thin-walled curved and straight beams considering warping effects with one axis of symmetry and with no axis of symmetry have not been studied prior to the work presented in this thesis. In fact, damage detection studies in thin walled structures are inadequate. Considering the significant role played by the thin walled elements in various structures for its superior strength and low weight, research is necessary in structural health monitoring of such structures. Furthermore, damage detection based on free and forced vibration analysis is very limited.

Usually, damage identification focuses on the determination of location of crack and severity. However, past literatures showed that the reported works for determining severity of damage did not lead to a very good prediction. The most of the past works in the area of structural damage detection using vibration data requires prior knowledge of natural frequencies, which in most cases becomes unavailable. Therefore, the research in the said area needs to be directed towards an approach that can use only the vibration data of the structures in the current state during assessment.

1.4 Objectives of the thesis

Since very limited number of works has been carried out by the previous researchers on damage detection in thin-walled beam, especially in case of un-symmetrical cross-section, the present study aims to fulfill the following objectives.

- To develop a FE model of cracked thin walled beams (i) with one axis of symmetry and (ii) with no axis of symmetry having straight and horizontally curved profile using linear fracture mechanics approach incorporating the effects of warping.

- To develop a method for detecting crack parameters (crack location and crack-depth ratio) based on vibration measurements that can be used without prior knowledge of undamaged structures.
- To conduct vibration experiments on thin walled straight and curved beam specimen to extract natural frequency and steady state amplitude.
- To use experimental data in the present approach for detecting crack parameters in straight and curved beam of unsymmetrical cross-sections.
- To compare the efficiency of methods in detecting crack parameters using natural frequencies, steady state acceleration amplitude and combination of these two parameters.

1.5 Organization of the thesis

The content of the thesis is organized in eight major chapters in addition to abstract, appendices and references:

- **Chapter-1** gives introduction, literature review, research scope and objectives of the present work.
- **Chapter-2** outlines a generalized finite element model for cracked and uncracked thin-walled beams with arbitrary cross-section.
- **Chapter-3** presents a method for detecting crack parameters using response surface methodology (RSM) and genetic algorithm (GA).
- **Chapter-4** describes the test specimen, experimental setup and procedure for conducting vibration experiment.
- **Chapter-5** presents the results of the crack identification in straight and horizontally curved thin-walled steel beam with single and double crack scenario using free vibration response. First, the FEM models are validated with published theoretical results and results from experiments carried out in the present study. Modal features of cracked and uncracked beams are described. RSM and GA based techniques developed in the study has been applied with measured natural frequencies in several cases and accuracies have been commented.

- **Chapter-6** gives a detailed study of the application of forced vibration data for determination of the crack parameters and forcing parameters using the present hybrid approach.
- **Chapter-7** demonstrates the heterogeneous data utilization for detecting crack and forcing parameter. Heterogeneous data represents the combination of free vibration (natural frequencies) and forced vibration (steady state acceleration) responses.
- **Chapter-8** provides a summary of the outcomes of the work performed in this study, followed by some suggestions for future work.

1.6 Closure

In this chapter, introduction to various traditional nondestructive tests has been given. The vibration based techniques which have drawn the attention of large number of researchers worldwide have been critically discussed with reference to the works of the past authors. Literature review presented in this chapter on damage detection using vibration techniques are grouped in to three heads-(i) using free vibration data (ii) using forced vibration data and (iii) using heterogeneous data (combination of free and forced vibration data). Considering the thin walled structures as complex and important structural system, the literatures related to vibrations of thin walled structures are presented in separate section. Outcome of the literature review has been given and objectives of the thesis have been stated. The thesis comprises of eight chapters. Finally, organization of thesis has been provided.

Chapter 2

Finite Element Formulation

2.1 Overview

The finite element method (FEM) is an effective numerical technique to obtain an approximate solution to a class of problems governed by partial differential equations. Such problems are known as boundary value problems as the boundary conditions are to be prescribed for solving the partial differential equation. The FEM converts the partial differential equation into a set of algebraic equations which are not difficult to solve. In the present day, this technique is used not only for the analysis in solid mechanics, but even in the analysis of heat transfer, fluid flow, magnetic and electric fields and many other applications. In FEM, a continuum domain is discretized into number of pieces or elements by a certain numbers of nodes. These nodes are connected by lines. The present chapter deals with the FE analysis of uncracked and cracked arbitrary cross-sectional thin-walled straight and curved beam. According to Megson [176], thin walled sections are defined as those sections in which ratio of maximum thickness of an element to the typical cross-sectional dimension is less than 0.10. These beams respond to a very complicated manner to the external load. In general combination of bending, axial and non-uniform torsion is common. Due to non-uniform torsion, bi-moment effect is one of the characteristics of its response. Thin walled beams can be broadly classified into two categories, depending upon the location of shear center and centroid of the cross-section:

(a) Symmetric: A cross-section possessing two axes of symmetry is called double cross-sectional symmetry or symmetric section. Example includes beam of 'I' cross-section (Figure 2.1(a)).

(b) Un-symmetric: In this category, the section may have – (i) one axis of symmetry (channel cross-section), also known as mono-symmetric and (ii) with no axis of symmetry (Angle cross-section). The cross-section of one axis and no axis of symmetry have been shown in Figure 2.1(b) and Figure 2.1(c) respectively. Because of cross-sectional un-symmetry the elastic axis and mass axis of this type of cross-section are not coincident. Consequently, the bending and torsional vibrations are coupled.

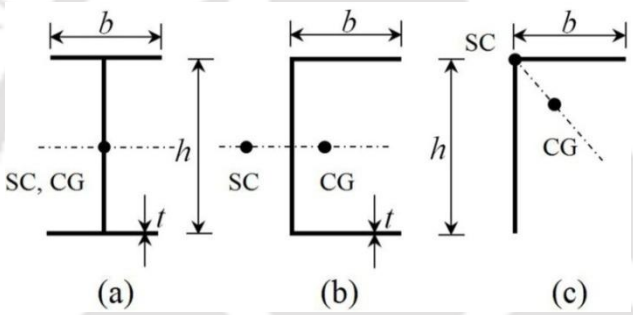

Figure 2.1: Thin-walled members of variable cross-section: (a) I section; (b) Channel section and (c) Angle section. (SC = shear center; CG = mass center)

The present work focuses on un-symmetrical sectional beam for damage identification. Finite element formulation has been developed in generalized form and used to illustrate damage detection procedure for straight and curved thin-walled beams.

2.2 FEM for uncracked beam model

An arbitrary cross-sectional thin-walled uncracked horizontally curved beam is shown in Figure 2.2. L is measured along the x-axis of beam. Radius of the centroidal axis of a curved beam and subtended angle are represented by R and θ_s respectively. CG and SC are the mass and shear center respectively. The offset distance between centroid and shear center are denoted by e_y in y- direction and e_z in z- direction respectively. The signs of radius of curvature and curvatures are illustrated in Figure 2.3.

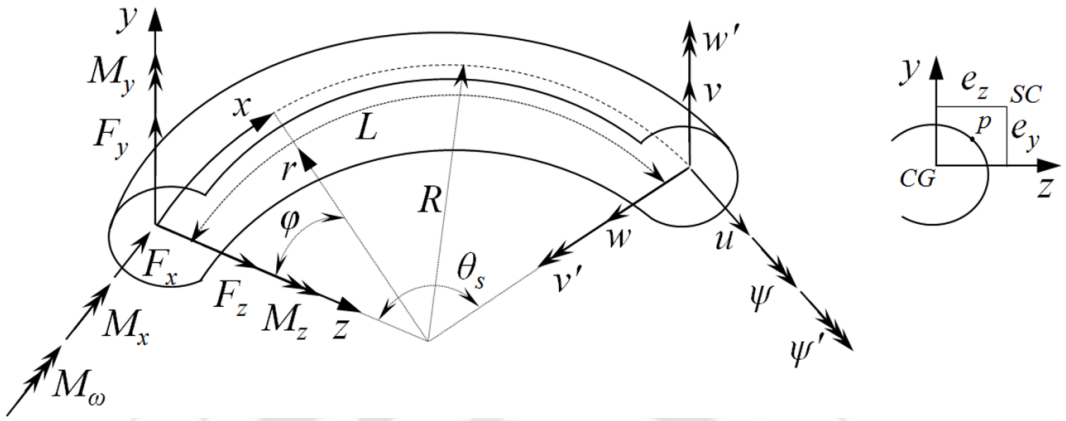

Figure 2.2: Horizontally curved beam of arbitrary cross-section

Let the two noded beam element of length l_e connects the nodes as *i* and *j* of the finite element mesh. It can be observed from the Figure 2.4 that all of the forces and couples are assumed to be in *x*-*y* and *x*-*z* plane. Seven reaction components exist at each node of the element involving axial forces (F_{xi}, F_{xj}) in *x*-direction, vertical shear forces (F_{yi}, F_{yj}) in *y*-direction, transverse shear forces (F_{zi}, F_{zj}) in *z*-direction. The bending moment about *y*-axis and *z*-axis are (M_{yi}, M_{yj}) and (M_{zi}, M_{zj}) respectively. The torsion about *x*-axis and bimoment are denoted by (M_{xi}, M_{xj}) and ($M_{\omega i}$, $M_{\omega j}$) respectively.

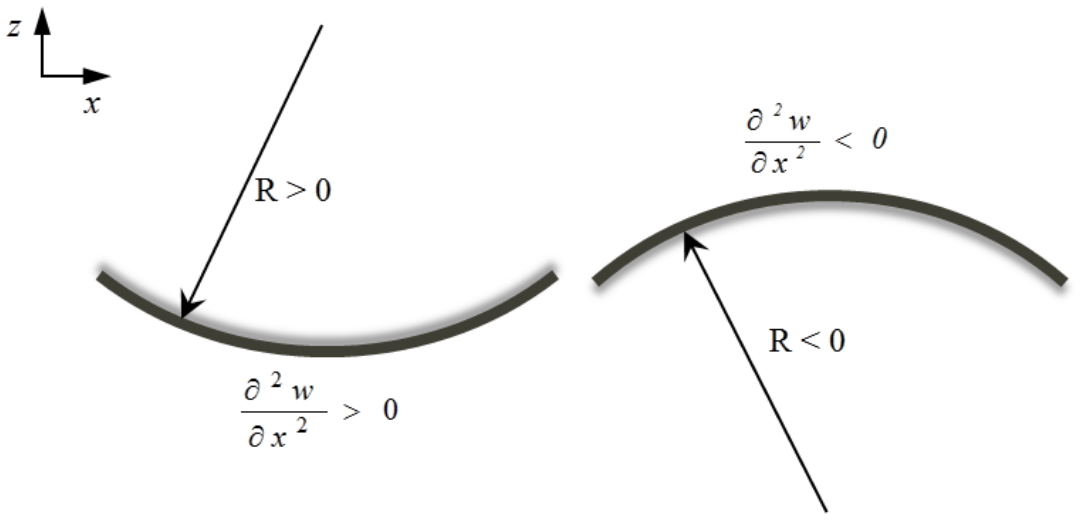

Figure 2.3: Sign of radius of curvature and curvature

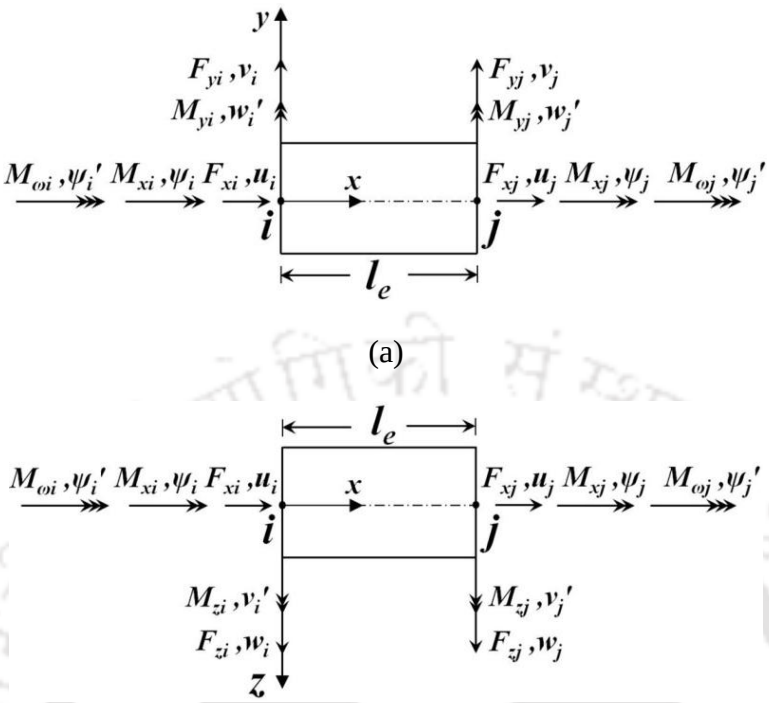

Figure 2.4: View of two noded beam element on (a) *x*-*y* plane (b) *x*-*z* plane

The corresponding motion components are axial displacement (u_i, u_j) in *x*-direction, flexural translation (w_i, w_j) in *z*-direction and (v_i, v_j) in *y*-direction whereas torsional rotation and their first derivatives are (ψ_i, ψ_j) and (w_i', w_j', v_i', v_j', ψ_i', ψ_j') respectively in which ($'$) denotes space derivative. The bending rigidities of the section about *z*-axis and *y*-axis are represented by EI_{zz} and EI_{yy} respectively. GJ and $E\Gamma_\omega$ are Saint-Venant torsional rigidity and warping rigidity respectively. The polar moment of inertia of the cross-section about shear center is I_s. Density of material and cross-sectional area of the curved beam have been represented by ρ and A respectively.

Let u_x, u_y and u_z represent the displacements, at an arbitrary point $p(x, y, z)$ of cross-section in the *x*, *y* and *z* direction, respectively. Then,

$$u_x = u - v'y - \left(w' - \frac{u}{R}\right)z - \left(\psi' - \frac{v'}{R}\right)\varpi \tag{2.1}$$

$$u_y = v - \psi\left(z - e_z\right) \tag{2.2}$$

$$u_z = w + \psi\left(y - e_y\right) \tag{2.3}$$

where *u*, *v* and *w* are the displacement components of the centroid from original position; ψ is angle of twist of the cross-section around the shear center. ϖ is sectorial area.

For thin-walled curved beam, the cylindrical co-ordinate is used to express linear strain-displacement relationship. A cylindrical co-ordinate system has been shown in Figure 2.5. Cylindrical coordinates are the combination of polar coordinates in the *x*-*z* plane with the usual *y* coordinate of Cartesian system. To obtain the cylindrical coordinates of an arbitrary point *p*, it can be projected down to a point Q_p in the *x*-*z* plane. Thereafter, the polar coordinates (r, φ) of the point Q_p has been calculated by estimating the distance *r* from origin to Q_p and φ is the angle between the *x*-axis and the line segment from the origin to Q_p. The cylindrical coordinate is similar to *y*-coordinate of Cartesian coordinates.

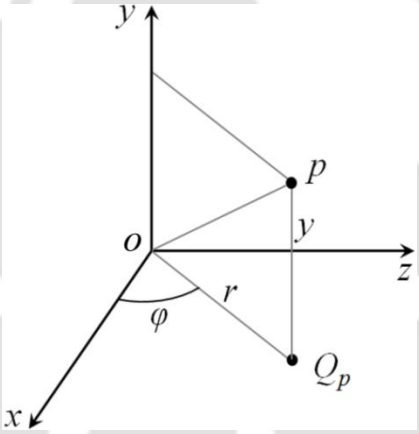

Figure 2.5: Cylindrical co-ordinate system

The expressions of linear strain-displacement relations in cylindrical co-ordinate for thin-walled curved beam can be written as [191, 196].

$$e_{xx} = \left(\frac{\partial u_x}{r\,\partial \varphi} + \frac{u_z}{r} \right) \tag{2.4}$$

$$e_{yy} = \frac{\partial u_y}{\partial y} \tag{2.5}$$

$$e_{zz} = \frac{\partial u_z}{\partial z} \tag{2.6}$$

$$e_{xy} = \frac{\partial u_x}{\partial y} + \frac{\partial u_y}{r\,\partial \varphi} \tag{2.7}$$

$$e_{xz} = \frac{\partial u_x}{\partial z} + \left(\frac{\partial u_z}{r\,\partial \varphi} - \frac{u_x}{R} \right) \tag{2.8}$$

$$e_{yz} = \frac{\partial u_y}{\partial z} + \frac{\partial u_z}{\partial y} \tag{2.9}$$

where the center of the curvature have been considered as a origin of the cylindrical coordinates (r, φ, y). Using $\varphi = x/R$ and $r = R + z$ (Figure 2.2) in the above equations, one may obtain the strain-displacement relationship as

$$e_{xx} = \left(\frac{\partial u_x}{\partial x} + \frac{u_z}{R}\right)\left(1 + \frac{z}{R}\right)^{-1} \tag{2.10}$$

$$e_{xy} = \frac{\partial u_x}{\partial y} + \frac{\partial u_y}{\partial x}\left(1 + \frac{z}{R}\right)^{-1} \tag{2.11}$$

$$e_{xz} = \frac{\partial u_x}{\partial z} + \left(\frac{\partial u_z}{\partial x} - \frac{u_x}{R}\right)\left(1 + \frac{z}{R}\right)^{-1} \tag{2.12}$$

$$e_{yy} = e_{zz} = e_{yz} = 0 \tag{2.13}$$

The in-plane strains e_{yy}, e_{zz} and e_{yz} are negligible according to the assumption of an undistorted cross-section with respect to the plane. The elastic strain energy (U) and kinetic energy (T) for thin-walled curved beam now can be expressed as follows:

$$U = \frac{1}{2}\int_V \sigma_{ij}\, e_{ij}\, dV \tag{2.14}$$

$$T = \frac{1}{2}\int_V \rho\left(\dot{u}_x^2 + \dot{u}_y^2 + \dot{u}_z^2\right) dV \tag{2.15}$$

In Equation (2.14), σ_{ij} and e_{ij} represent the components of the stress and strain tensor respectively. The differential volume is represented by dV and ($\dot{}$) denotes the time derivative. The differential volume element of an arbitrary cross-sectional curved beam has been presented in Figure 2.6.

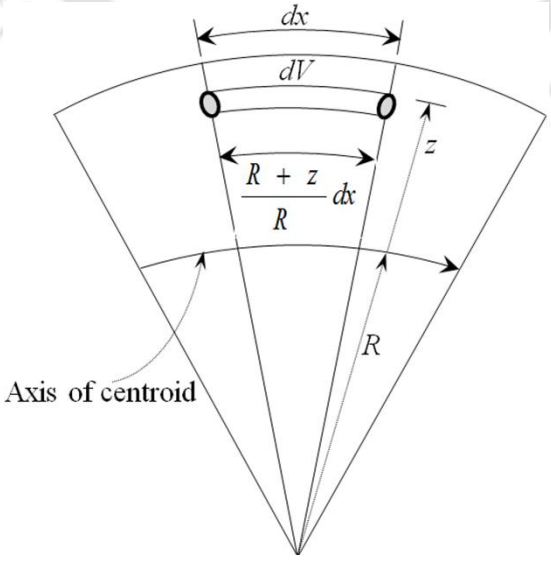

Figure 2.6: Differential volume element of an arbitrary cross-sectional curved beam

The differential volume (*dV*) can be expressed by differential length *dx*, differential cross-sectional area *dA*, and radius of curvature *R* in the longitudinal direction depicted in Figure 2.6 as following

$$dV = \frac{R+z}{R}\, dA\, dx \tag{2.16}$$

Further, substitution of Equation (2.16) into Equation (2.14) and Equation (2.15) give following equations

$$U = \frac{1}{2}\int_L\int_A \sigma_{ij}\, e_{ij}\left(1+\frac{z}{R}\right) dA\, dx \tag{2.17}$$

$$T = \frac{1}{2}\int_L\int_A \rho\left(\dot{u}_x^2+\dot{u}_y^2+\dot{u}_z^2\right)\left(1+\frac{z}{R}\right) dA\, dx \tag{2.18}$$

Here, z ≪ *R* because the in-plane displacement components in z-direction are very small compared to *R*. Thus, neglecting *z/R* in Equations (2.10 - 2.12) and Equation (2.17 and 2.18) leads to [196]

$$e_{xx} = \frac{\partial u_x}{\partial x} + \frac{u_z}{R} \tag{2.19}$$

$$e_{xy} = \frac{\partial u_x}{\partial y} + \frac{\partial u_y}{\partial x} \tag{2.20}$$

$$e_{xz} = \frac{\partial u_x}{\partial z} + \frac{\partial u_z}{\partial x} - \frac{u_x}{R} \tag{2.21}$$

$$U = \frac{1}{2}\int_L\int_A \sigma_{ij}\, e_{ij}\, dA\, dx \tag{2.22}$$

$$T = \frac{1}{2}\int_L\int_A \rho\left(\dot{u}_x^2+\dot{u}_y^2+\dot{u}_z^2\right) dA\, dx \tag{2.23}$$

Substituting the displacement Equations (2.1 - 2.3) and strain Equations (2.19 – 2.21) into Equation (2.22 and 2.23) and integrating over the cross-section, the following equations for strain energy and kinetic energy are obtained

$$U = \frac{1}{2}\int_0^L \left[\begin{array}{l} EA\left(u' + \frac{w}{R}\right)^2 + EI_{yy}\left(w'' + \frac{w}{R^2}\right)^2 + EI_{zz}\left(v'' - \frac{\psi}{R}\right)^2 + E\Gamma_\omega\left(\psi'' + \frac{v''}{R}\right)^2 + GJ\left(\psi' + \frac{v'}{R}\right)^2 \\ + 2EI_{\omega y}\left(w'' + \frac{w}{R^2}\right)\left(\psi'' + \frac{v''}{R}\right) + 2EI_{\omega z}\left(v'' - \frac{\psi}{R}\right)\left(\psi'' + \frac{v''}{R}\right) + 2EI_{yz}\left(v'' - \frac{\psi}{R}\right)\left(w'' + \frac{w}{R^2}\right) \end{array}\right] dx \tag{2.24}$$

$$T = \frac{1}{2}\rho \int_0^L \left[\begin{array}{l} A\left(\dot{u}^2+\dot{v}^2+\dot{w}^2\right) + I_s\dot{\psi}^2 + I_{yy}\left(\dot{w}'-\frac{\dot{u}}{R}\right)^2 + I_{zz}\dot{v}'^2 + \Gamma_\omega\left(\dot{\psi}'+\frac{\dot{v}'}{R}\right)^2 + 2I_{yz}\dot{v}'\left(\dot{w}'-\frac{\dot{u}}{R}\right) \\ + 2I_{\omega y}\dot{v}'\left(\dot{\psi}'+\frac{\dot{v}'}{R}\right) + 2I_{\omega z}\left(\dot{w}'-\frac{\dot{u}}{R}\right)\left(\dot{\psi}'+\frac{\dot{v}'}{R}\right) + 2S_z\left(\dot{w}\dot{\psi}-\dot{u}\dot{v}'\right) - 2S_y\left(\dot{v}\dot{\psi}+\dot{u}\dot{w}'-\frac{\dot{u}^2}{R}\right) \\ - 2S_\omega\dot{u}\left(\dot{\psi}'+\frac{\dot{v}'}{R}\right) + 2e_z A\dot{v}\dot{\psi} - 2e_y A\dot{w}\dot{\psi} \end{array} \right] dx \tag{2.25}$$

Further, integrating Equation (2.24 and 2.25) over the cross-sectional area in local co-ordinate system, one obtains

$$U = \frac{1}{2}\int_{-1}^{1} \left[\begin{array}{l} EA\left(\sqrt{\frac{2}{l_e}}u' + \sqrt{\frac{l_e}{2}}\frac{w}{R}\right)^2 + EI_{yy}\left(\sqrt{\frac{8}{l_e^3}}w'' + \sqrt{\frac{l_e}{2}}\frac{w}{R^2}\right)^2 + EI_{zz}\left(\sqrt{\frac{8}{l_e^3}}v'' - \sqrt{\frac{l_e}{2}}\frac{\psi}{R}\right)^2 + E\Gamma_\omega\left(\sqrt{\frac{8}{l_e^3}}\psi'' + \sqrt{\frac{8}{l_e^3}}\frac{v''}{R}\right)^2 \\ + GJ\left(\sqrt{\frac{2}{l_e}}\psi' + \sqrt{\frac{2}{l_e}}\frac{v'}{R}\right) + 2EI_{\omega y}\left(\sqrt{\frac{8}{l_e^3}}w'' + \sqrt{\frac{l_e}{2}}\frac{w}{R^2}\right)\left(\sqrt{\frac{8}{l_e^3}}\psi'' + \sqrt{\frac{8}{l_e^3}}\frac{v''}{R}\right) + 2EI_{\omega z}\left(\sqrt{\frac{8}{l_e^3}}v'' - \sqrt{\frac{l_e}{2}}\frac{\psi}{R}\right) \\ \left(\sqrt{\frac{8}{l_e^3}}\psi'' + \sqrt{\frac{8}{l_e^3}}\frac{v''}{R}\right) + 2EI_{yz}\left(\sqrt{\frac{8}{l_e^3}}v'' - \sqrt{\frac{l_e}{2}}\frac{\psi}{R}\right)\left(\sqrt{\frac{8}{l_e^3}}w'' + \sqrt{\frac{l_e}{2}}\frac{w}{R^2}\right) \end{array} \right] d\xi \tag{2.26}$$

$$T = \frac{1}{2}\rho \int_{-1}^{1} \left[\begin{array}{l} A\left(\dot{u}^2+\dot{v}^2+\dot{w}^2\right) + I_s\dot{\psi}^2 + I_{yy}\left(\frac{2\dot{w}'}{l_e}-\frac{\dot{u}}{R}\right)^2 + \frac{4I_{zz}\dot{v}'^2}{l_e^2} + \frac{4\Gamma_\omega}{l_e^2}\left(\dot{\psi}'+\frac{\dot{v}'}{R}\right)^2 + \frac{4I_{yz}\dot{v}'}{l_e}\left(\frac{2\dot{w}'}{l_e}-\frac{\dot{u}}{R}\right) \\ + \frac{8I_{\omega y}\dot{v}'}{l_e^2}\left(\dot{\psi}'+\frac{\dot{v}'}{R}\right) + \frac{4I_{\omega z}}{l_e^2}\left(2\dot{w}'-\frac{\dot{u}l_e}{R}\right)\left(\dot{\psi}'+\frac{\dot{v}'}{R}\right) + 2S_z\left(\dot{w}\dot{\psi}-\frac{2\dot{u}\dot{v}'}{l_e}\right) - 2S_y\left(\dot{v}\dot{\psi}+\frac{2\dot{u}\dot{w}'}{l_e}-\frac{\dot{u}^2}{R}\right) \\ - \frac{4S_\omega\dot{u}}{l_e}\left(\dot{\psi}'+\frac{\dot{v}'}{R}\right) + 2e_z A\dot{v}\dot{\psi} - 2e_y A\dot{w}\dot{\psi} \end{array} \right] \frac{l_e}{2} d\xi \tag{2.27}$$

where ($'$) denotes space derivative, ($\dot{}$) indicates time derivative. A, I_{yy}, I_{zz}, I_{yz}, I_s, Γ_ω, S_z, S_y, S_ω, $I_{\omega y}$, $I_{\omega z}$ are the geometrical properties of the cross-section. These can be defined as

$$A = \int_A dA \tag{2.28}$$

$$I_{yy} = \int_A z^2 dA \tag{2.29}$$

$$I_{zz} = \int_A y^2 dA \tag{2.30}$$

$$I_{yz} = \int_A yz\, dA \tag{2.31}$$

$$I_s = \int_A \left[(y-e_y)^2 + (z-e_z)^2 \right] dA \tag{2.32}$$

$$\Gamma_\omega = \int_A \varpi^2 dA \tag{2.33}$$

$$I_{\omega y} = \int_A y\varpi\, dA \tag{2.34}$$

$$I_{\omega z} = \int_A z\varpi\, dA \tag{2.35}$$

$$S_y = \int_A z\, dA \tag{2.36}$$

$$S_z = \int_A y\, dA \tag{2.37}$$

$$S_\omega = \int_A \varpi\, dA \tag{2.38}$$

Let us take ξ as the local non-dimensional spatial coordinate as

$$\xi = \frac{2x}{l_e} - 1, \; -1 \le \xi \le 1 \tag{2.39}$$

Using Hermite shape functions [198], the flexural displacements and torsional rotation can be presented in the following form

$$\begin{bmatrix} u(\xi,t) \\ w(\xi,t) \\ v(\xi,t) \\ \psi(\xi,t) \end{bmatrix} = \begin{bmatrix} H_{ai}(\xi)u_i(t) + H_{aj}(\xi)u_j(t) \\ H_i^{(0)}(\xi)w_i(t) + H_i^{(1)}(\xi)w_i'(t) + H_j^{(0)}(\xi)w_j(t) + H_j^{(1)}(\xi)w_j'(t) \\ H_i^{(0)}(\xi)v_i(t) + H_i^{(1)}(\xi)v_i'(t) + H_j^{(0)}(\xi)v_j(t) + H_j^{(1)}(\xi)v_j'(t) \\ H_i^{(0)}(\xi)\psi_i(t) + H_i^{(1)}(\xi)\psi_i'(t) + H_j^{(0)}(\xi)\psi_j(t) + H_j^{(1)}(\xi)\psi_j'(t) \end{bmatrix} \tag{2.40}$$

where $H_i^{(0)}$, $H_j^{(0)}$, $H_i^{(1)}$ and $H_j^{(1)}$ are Hermite polynomials, the superscript (*0*) is referred to the displacement function whereas superscript (*1*) corresponds to their first derivative. Thus, the Hermite polynomials are given as

$$H_{ai}(\xi) = \frac{1-\xi}{2}; \; H_{aj}(\xi) = \frac{1+\xi}{2} \tag{2.41}$$

$$H_n^{(0)}(\xi) = \frac{1}{4}\begin{cases} \left(2 - 3\xi + \xi^3\right); n = i; \\ \left(2 + 3\xi - \xi^3\right); n = j; \end{cases} \tag{2.42}$$

$$H_n^{(1)}(\xi) = \frac{l_e}{8}\begin{cases} \left(1 - \xi - \xi^2 + \xi^3\right); n = i; \\ \left(-1 - \xi + \xi^2 + \xi^3\right); n = j; \end{cases} \tag{2.43}$$

Substituting Equation (2.40) into strain energy (U) and kinetic energy (T) in Equation (2.26 and 2.27) and then performing the integration, following matrix-relations have been obtained

$$U = \frac{1}{2}\boldsymbol{Q}^T \boldsymbol{k}^e \boldsymbol{Q} \tag{2.44}$$

$$T = \frac{1}{2}\dot{\boldsymbol{Q}}^T \boldsymbol{m}^e \dot{\boldsymbol{Q}} \tag{2.45}$$

where $\boldsymbol{k}^e$ and $\boldsymbol{m}^e$ are the element stiffness and mass matrix for uncracked curved beam respectively. These matrices are shown in Appendix A. The vector $\boldsymbol{Q}$ containing fourteen nodal displacements and slopes, as given below

$$\boldsymbol{Q}^T = \begin{bmatrix} u_1 & u_2 & w_1 & w_1' & w_2 & w_2' & v_1 & v_1' & v_2 & v_2' & \psi_1 & \psi_1' & \psi_2 & \psi_2' \end{bmatrix} \tag{2.46}$$

The coupled bending and torsional vibrations are considered for the beam element in the present study by neglecting translation along longitudinal direction due to axil load. In case

of one axis of symmetry (for an example about *z*-axis), the size of stiffness and mass matrix can be reduced by neglecting the sub-matrices related to *W* displacement components. The theory of curved members developed herein can be reduced to that of straight beam simply by letting the radius of curvature approach to infinity.

2.3 FEM for multiple cracked beam model

An arbitrary cross-sectional thin-walled horizontally curved beam with *n* number of cracks has been shown in Figure 2.7, where *L* is total span of the beam and *R* is radius of the curvature. Let the cracks be located at the distance L_1, L_2,…, L_n from one end along the axis of the curved beam respectively. The corresponding angular distance (in degrees) of the cracks from one end of the beam are indicated by θ_{S1}, θ_{S2},…, θ_{Sn}. The depth of 'n^{th}' crack is a_n which is shown in Figure 2.7. It is assumed that the sufficient preload is presents such that the cracks remain always open. The present crack identification study mainly focused on one axis of symmetry (channel cross-section) and with no axis of symmetrical (Angle cross-section) cross-sectional thin-walled beam. The configurations of cracked channel and angle cross-sectional horizontally curved beam have been presented in Figure 2.8(a) and Figure 2.9(a) respectively. The corresponding crack beam portion for both the beam is shown in Figure 2.8(b) and Figure 2.9(b).

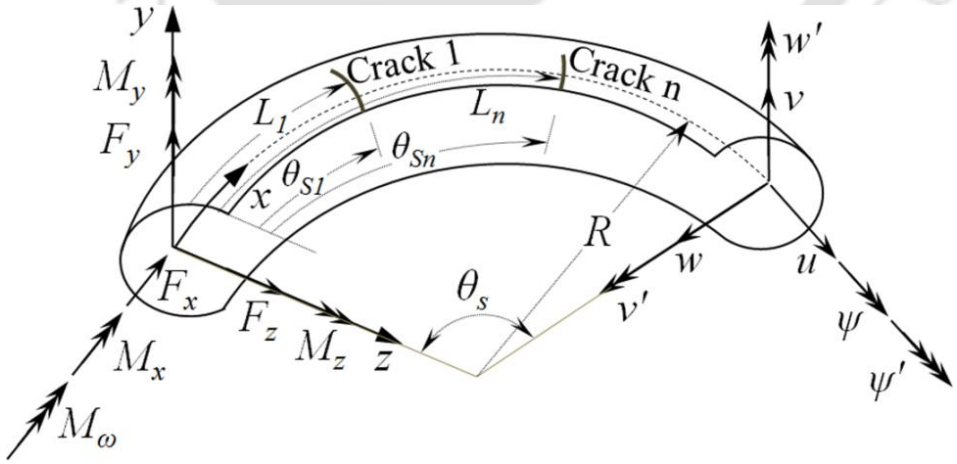

Figure 2.7: An arbitrary cross-sectional curved beam with *n* numbers of cracks

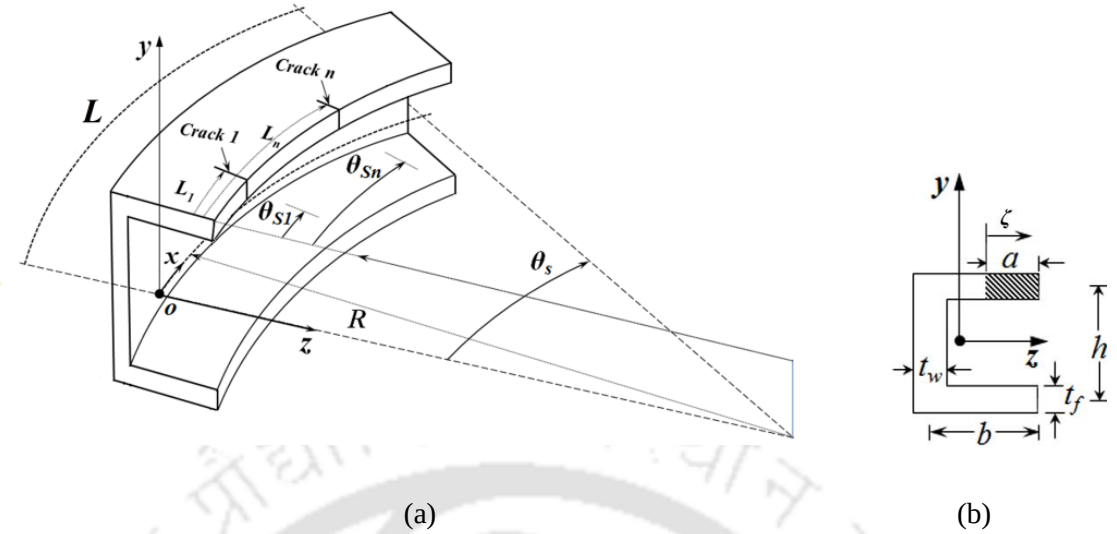

(a) (b)

Figure 2.8: (a) Configuration of cracked channel cross-sectional horizontally curved beam, (b) cross-section of the cracked beam portion

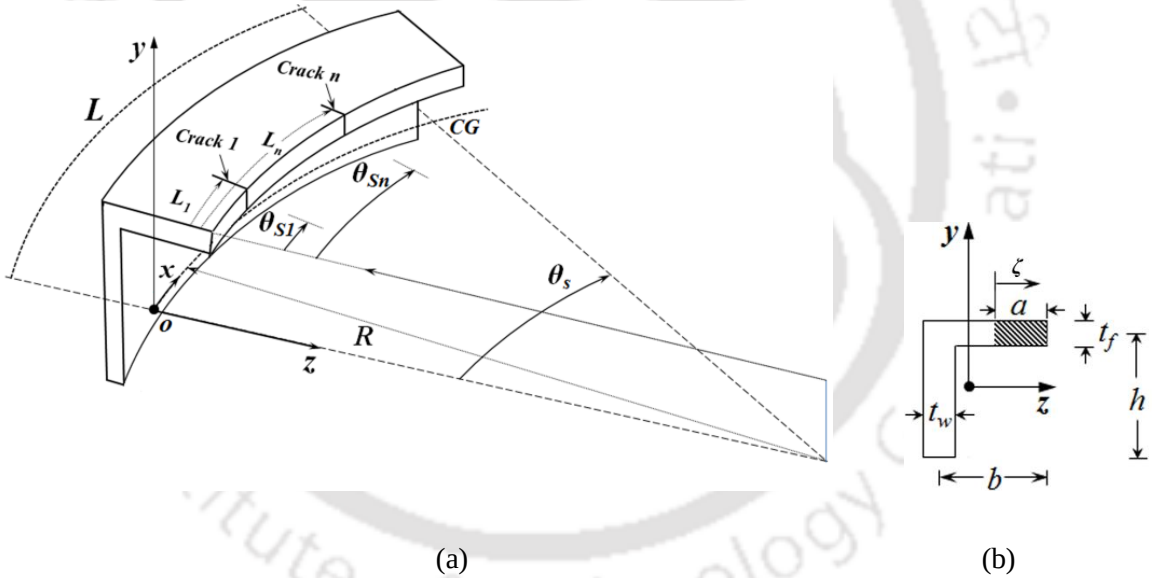

(a) (b)

Figure 2.9: (a) Configuration of cracked angle cross-sectional horizontally curved beam, (b) cross-section of the cracked beam portion

Let u_i and P_i be the additional displacement and loading respectively along the i^{th} co-ordinate and U_S be the strain energy due to crack. Using Castigliano's theorem, additional displacement is given by

$$u_i = \frac{\partial U_S}{\partial P_i} \tag{2.47}$$

where, $U_S = \int_0^{a_n} J(\zeta_n) d\zeta$

$J(\zeta_n)$ = Strain energy release rate, ζ_n = length of the crack.

Considering Paris equation [199] u_i can be expressed as

$$u_i = \frac{\partial}{\partial P_i}\left[\int_0^{a_n} J(\zeta_n) d\zeta\right] \tag{2.48}$$

The local flexibility matrix, $$C_{ij} = \frac{\partial u_i}{\partial P_j} = \frac{\partial^2}{\partial P_i \partial P_j}\int_0^{a_n} J(\zeta_n) d\zeta \tag{2.49}$$

The strain energy release rate $J(\zeta_n)$ is given by

$$J(\zeta_n) = \frac{1}{E^*}\left[\left(\sum_{i=1}^{6} K_{Iin}\right)^2 + \left(\sum_{i=1}^{6} K_{IIin}\right)^2 + k\left(\sum_{i=1}^{6} K_{IIIin}\right)^2\right] \tag{2.50}$$

where $E^* = E$ for plane stress condition and $k = 1+ \mu$. E and v are Young's modulus and Poisson's ratio respectively. K_{Ii}, K_{IIi} and K_{IIIi} are the stress intensity factors (SIFs) of the fracture mode for opening type, in-plane shear type and out-of-plane shear type of cracks respectively. The subscripts *I*, *II* and *III* of SIFs in Equation (2.50) represent the first, second and third mode of fracture. The associated subscripts *i* and *n* represents the number of force components and number of cracks respectively. The modes of fractures are shown in Figure 2.10.

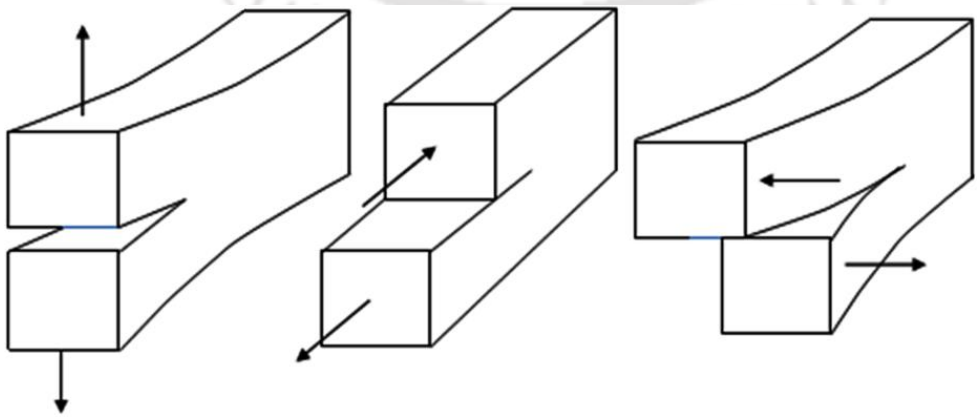

Figure 2.10: Three modes of fracture: (a) Mode *I*, (b) Mode *II* and (c) Mode *III*

Now, substituting the Equation (2.50) into Equation (2.49), the local flexibility matrix can be obtained as

$$C_{ij} = \frac{1}{E^*} \int_0^{a_n} \frac{\partial^2}{\partial P_i \partial P_j} \left[\int_{-t_f/2}^{t_f/2} \left(\left(\sum_{i=1}^{6} K_{Iin} \right)^2 + \left(\sum_{i=1}^{6} K_{IIin} \right)^2 + k \left(\sum_{i=1}^{6} K_{IIIin} \right)^2 \right) dy \right] d\zeta \tag{2.51}$$

Here, for arbitrary cross-sectional beam $K_{IFy} = K_{IFz} = K_{IMx} = 0$, $K_{IIFy} = K_{IIM\,y} = K_{IIMz} = K_{IIMx} = K_{IIM\omega} = 0$, $K_{IIIFz} = K_{IIIMy} = K_{IIIMz} = K_{IIIM\omega} = 0$. Thus, local flexibility coefficients can be stated as follows

$$C^z_{qqn} = \frac{1}{E^*} \int_0^{a_n} \frac{\partial^2}{\partial F_z^2} \left[\int_0^{t_f} \left(K_{IIF_z n} \right)^2 \, dy \right] d\zeta \tag{2.52}$$

$$C^y_{mmn} = \frac{1}{E^*} \int_0^{a_n} \frac{\partial^2}{\partial M_y^2} \left[\int_0^{t_f} \left(K_{IM_y n} \right)^2 dy \right] d\zeta \tag{2.53}$$

$$C^y_{qqn} = \frac{1}{E^*} \int_0^{a_n} \frac{\partial^2}{\partial F_y^2} \left[\int_0^{t_f} k \left(K_{IIIF_y n} \right)^2 dy \right] d\zeta \tag{2.54}$$

$$C^z_{mmn} = \frac{1}{E^*} \int_0^{a_n} \frac{\partial^2}{\partial M_z^2} \left[\int_0^{t_f} \left(K_{IM_z n} \right)^2 dy \right] d\zeta \tag{2.55}$$

$$C_{ttn} = \frac{1}{E^*} \int_0^{a_n} \frac{\partial^2}{\partial M_x^2} \left[\int_0^{t_f} k \left(K_{IIIM_x n} \right)^2 \, dy \right] d\zeta \tag{2.56}$$

$$C_{bbn} = \frac{1}{E^*} \int_0^{a_n} \frac{\partial^2}{\partial M_\omega^2} \left[\int_0^{t_f} \left(K_{IM_\omega n} \right)^2 dy \right] d\zeta \tag{2.57}$$

where $C_{qq}{}^y$ and $C_{qq}{}^z$ are compliances due to shear force in y and z direction respectively. $C_{mm}{}^y$, $C_{mm}{}^z$, C_{tt} and C_{bb} are for flexural moments, twisting moment and bi-moment respectively and associated n in subscript represents the n^{th} crack. The expression for stress intensity factors from previous studies are given as follows [96, 98, 100, 200]:

$$K_{IM\,y} = M_y \sqrt{\frac{\beta_{M_y}}{t_f I_{yy}} \left(\frac{I_{yy}}{I^C_{yy}} - 1 \right)} \tag{2.58}$$

$$K_{IM_z} = M_z \sqrt{\frac{\beta_{M_z}}{t_f I_{zz}} \left(\frac{I_{zz}}{I_{zz}^C} - 1 \right)} \tag{2.59}$$

$$K_{IIF_z} = F_z \sqrt{\frac{2\kappa_z \beta_{F_z} (1+\mu)}{t_f A} \left(\frac{A}{A^C} - 1 \right)} \tag{2.60}$$

$$K_{IIIF_y} = \frac{F_y \kappa_y}{t_f b} \sqrt{\pi a} \sqrt{\frac{2b}{\pi a} \tan\left(\frac{\pi a}{2b} \right)} \tag{2.61}$$

$$K_{IIIM_x} = M_x \sqrt{\frac{\beta_{M_x}}{t_f J} \left(\frac{J}{J^C} - 1 \right)} \tag{2.62}$$

where I_{yy} and I_{zz} are the moment of inertia of the cross-section about y-axis and z-axis respectively. κ_y and κ_z are the shearing factor along y and z direction respectively, J is torsional constant and their super script 'C' indicates the cracked beam portion.

In the present study, stress intensity factor due to bi-moment in Equation (2.57) arising out of the warping effect has been incorporated to obtain the crack stiffness matrix of the line spring element. This is expressed by the equation

$$K_{IM_\omega} = M_\omega \sqrt{\frac{\beta_{M_\omega}}{t_f \Gamma_\omega} \left(\frac{\Gamma_\omega}{\Gamma_\omega^C} - 1 \right)} \tag{2.63}$$

where Γ_ω and Γ_ω^C are the warping constants of uncracked and cracked section respectively. The slope factor $\beta = \beta_{My} = \beta_{Mz} = \beta_{Fy} = \beta_{Fz} = \beta_{Mx} = \beta_{M\omega}$ for plane stress and $\beta_{My} = \beta_{Mz} = \beta_{Fy} = \beta_{Fz} = \beta_{Mx} = \beta_{M\omega} = \beta / (1- \mu^2)$ for plane strain conditions. This study examines the plane stress condition for small thickness t_f of the beam and considers β=1 as researchers [96, 98, 99] found very good results in several applications by assuming β=1. The expression of $K_{IM\omega}$ has been derived based on linear fracture mechanics principle which has been given in Appendix-B.

Figure 2.11 shows the 'N' number of equal finite beam elements connected with line-spring elements (L_S). These are placed where cracks exist. Figure 2.12 shows the reactions and corresponding degree of freedom (dof) at each node of the line spring element, which is same as healthy beam element. In the same figure, *lt* and *rt* indicate the left and right node of the line spring element.

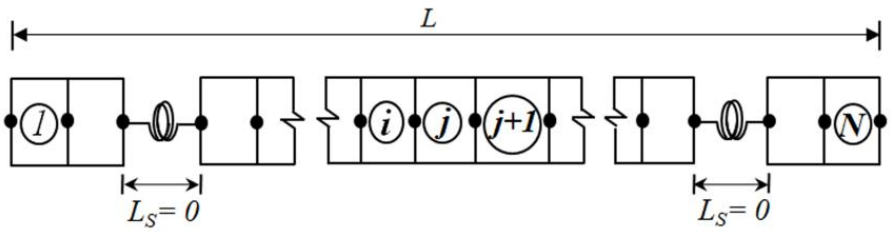

Figure 2.11: Configuration of cracked finite element beam

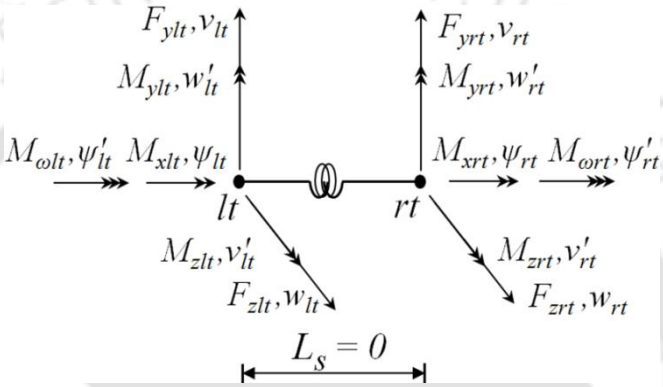

Figure 2.12: Force components and degree of freedom at each node of the line spring

The length of the line-spring is always zero and therefore, both the nodes fall in the same coordinate. Thus, static equilibrium requires

$$F_{zlt} = F_{zrt} = F_z \tag{2.64}$$

$$M_{ylt} = M_{yrt} = M_y \tag{2.65}$$

$$F_{ylt} = F_{yrt} = F_y \tag{2.66}$$

$$M_{zlt} = M_{zrt} = M_z \tag{2.67}$$

$$M_{xlt} = M_{xrt} = M_x \tag{2.68}$$

$$M_{\omega lt} = M_{\omega rt} = M_\omega \tag{2.69}$$

where subscript *lt* and *rt* indicate the left and right nodes of line spring element. The compatibility conditions due to the local flexibility of the crack can be defined as

$$w = C^z_{qq} F_z \tag{2.70}$$

$$w' = C^y_{mm} M_y \tag{2.71}$$

$$v = C_{qq}^{y} F_y \tag{2.72}$$

$$v' = C_{mm}^{z} M_z \tag{2.73}$$

$$\psi = C_{tt} M_x \tag{2.74}$$

$$\psi' = C_{bb} M_\omega \tag{2.75}$$

Strain energy U_S in the line spring is presented by the following relation,

$$U_S = \frac{1}{2}\left(F_z w + M_y w' + F_y v + M_z v' + M_x \psi + M_\omega \psi'\right) \tag{2.76}$$

Using the relationship, $w = w_{rt} - w_{lt}$, $w' = w'_{rt} - w'_{lt}$, $v = v_{rt} - v_{lt}$, $v' = v'_{rt} - v'_{lt}$, $\psi = \psi_{rt} - \psi_{lt}$, $\psi' = \psi'_{rt} - \psi'_{lt}$ and Equations (2.70) to (2.75) in Equation (2.76) can be express the strain energy (U_S) in terms of nodal variables

$$\begin{aligned} U_S = {} & \frac{1}{2C_{qq}^{z}}\left(w_{rt} - w_{lt}\right)^2 + \frac{1}{2C_{mm}^{y}}\left(w'_{rt} - w'_{lt}\right)^2 + \frac{1}{2C_{qq}^{y}}\left(v_{rt} - v_{lt}\right)^2 \\ & + \frac{1}{2C_{mm}^{z}}\left(v'_{rt} - v'_{lt}\right)^2 + \frac{1}{2C_{tt}}\left(\psi_{rt} - \psi_{lt}\right)^2 + \frac{1}{2C_{bb}}\left(\psi'_{rt} - \psi'_{lt}\right)^2 \end{aligned} \tag{2.77}$$

The stiffness matrix $\boldsymbol{K_C}$ obtained by partial differentiation of Equation (2.77) with respect to each of the nodal displacements are given as below:

$$F_{zlt} = \frac{\partial U_S}{\partial w_{lt}} = \frac{1}{C_{qq}^{z}} w_{lt} - \frac{1}{C_{qq}^{z}} w_{rt} \tag{2.78}$$

$$M_{ylt} = \frac{\partial U_S}{\partial w'_{lt}} = \frac{1}{C_{mm}^{y}} w'_{lt} - \frac{1}{C_{mm}^{y}} w'_{rt} \tag{2.79}$$

$$F_{ylt} = \frac{\partial U_S}{\partial v_{lt}} = \frac{1}{C_{qq}^{y}} v_{lt} - \frac{1}{C_{qq}^{y}} v_{rt} \tag{2.80}$$

$$M_{zlt} = \frac{\partial U_S}{\partial v'_{lt}} = \frac{1}{C_{mm}^{z}} v'_{lt} - \frac{1}{C_{mm}^{z}} v'_{rt} \tag{2.81}$$

$$M_{xlt} = \frac{\partial U_S}{\partial \psi_{lt}} = \frac{1}{C_{tt}} \psi_{lt} - \frac{1}{C_{tt}} \psi_{rt} \tag{2.82}$$

$$M_{\omega lt} = \frac{\partial U_S}{\partial \psi'_{lt}} = \frac{1}{C_{bb}} \psi'_{lt} - \frac{1}{C_{bb}} \psi'_{rt} \tag{2.83}$$

$$F_{zrt} = \frac{\partial U_S}{\partial w_{rt}} = \frac{1}{C_{qq}^{z}} w_{rt} - \frac{1}{C_{qq}^{z}} w_{lt} \tag{2.84}$$

$$M_{yrt} = \frac{\partial U_S}{\partial w'_{rt}} = \frac{1}{C_{mm}^{y}} w'_{rt} - \frac{1}{C_{mm}^{y}} w'_{lt} \tag{2.85}$$

$$F_{yrt} = \frac{\partial U_S}{\partial v_{rt}} = \frac{1}{C_{qq}^{y}} v_{rt} - \frac{1}{C_{qq}^{y}} v_{lt} \tag{2.86}$$

$$M_{zrt} = \frac{\partial U_S}{\partial v'_{rt}} = \frac{1}{C_{mm}^{z}} v'_{rt} - \frac{1}{C_{mm}^{z}} v'_{lt} \tag{2.87}$$

$$M_{xrt} = \frac{\partial U_S}{\partial \psi_{rt}} = \frac{1}{C_{tt}} \psi_{rt} - \frac{1}{C_{tt}} \psi_{lt} \tag{2.88}$$

$$M_{\omega rt} = \frac{\partial U_S}{\partial \psi'_{rt}} = \frac{1}{C_{bb}} \psi'_{rt} - \frac{1}{C_{bb}} \psi'_{lt} \tag{2.89}$$

Equation (2.78) to Equation (2.89) can be rearranged in matrix form as,

$$\boldsymbol{P_C} = \boldsymbol{K_C}\, \boldsymbol{Q_C} \tag{2.90}$$

where

$$\boldsymbol{P_C}^T = \begin{bmatrix} F_{zlt} & M_{ylt} & F_{ylt} & M_{zlt} & M_{xlt} & M_{\omega lt} & F_{zrt} & M_{yrt} & F_{yrt} & M_{zrt} & M_{xrt} & M_{\omega rt} \end{bmatrix} \tag{2.91}$$

$$\boldsymbol{Q_C}^T = \begin{bmatrix} w_{lt} & w'_{lt} & v_{lt} & v'_{lt} & \psi_{lt} & \psi'_{lt} & w_{rt} & w'_{rt} & v_{rt} & v'_{rt} & \psi_{rt} & \psi'_{rt} \end{bmatrix} \tag{2.92}$$

$$\boldsymbol{K_{Cn}} = \begin{bmatrix}
\frac{1}{C_{qqn}^{z}} & 0 & 0 & 0 & 0 & 0 & -\frac{1}{C_{qqn}^{z}} & 0 & 0 & 0 & 0 & 0 \\
0 & \frac{1}{C_{mmn}^{y}} & 0 & 0 & 0 & 0 & 0 & -\frac{1}{C_{mmn}^{y}} & 0 & 0 & 0 & 0 \\
0 & 0 & \frac{1}{C_{qqn}^{y}} & 0 & 0 & 0 & 0 & 0 & -\frac{1}{C_{qqn}^{y}} & 0 & 0 & 0 \\
0 & 0 & 0 & \frac{1}{C_{mmn}^{z}} & 0 & 0 & 0 & 0 & 0 & -\frac{1}{C_{mmn}^{z}} & 0 & 0 \\
0 & 0 & 0 & 0 & \frac{1}{C_{ttn}} & 0 & 0 & 0 & 0 & 0 & -\frac{1}{C_{ttn}} & 0 \\
0 & 0 & 0 & 0 & 0 & \frac{1}{C_{bbn}} & 0 & 0 & 0 & 0 & 0 & -\frac{1}{C_{bbn}} \\
-\frac{1}{C_{qqn}^{z}} & 0 & 0 & 0 & 0 & 0 & \frac{1}{C_{qqn}^{z}} & 0 & 0 & 0 & 0 & 0 \\
0 & -\frac{1}{C_{mmn}^{y}} & 0 & 0 & 0 & 0 & 0 & \frac{1}{C_{mmn}^{y}} & 0 & 0 & 0 & 0 \\
0 & 0 & -\frac{1}{C_{qqn}^{y}} & 0 & 0 & 0 & 0 & 0 & \frac{1}{C_{qqn}^{y}} & 0 & 0 & 0 \\
0 & 0 & 0 & -\frac{1}{C_{mmn}^{z}} & 0 & 0 & 0 & 0 & 0 & \frac{1}{C_{mmn}^{z}} & 0 & 0 \\
0 & 0 & 0 & 0 & -\frac{1}{C_{ttn}} & 0 & 0 & 0 & 0 & 0 & \frac{1}{C_{ttn}} & 0 \\
0 & 0 & 0 & 0 & 0 & -\frac{1}{C_{bbn}} & 0 & 0 & 0 & 0 & 0 & \frac{1}{C_{bbn}}
\end{bmatrix} \tag{2.93}$$

The $\boldsymbol{P_C}$ and $\boldsymbol{Q_C}$ represent the reaction vector and corresponding displacement vector of the line-spring element respectively. In Equation (2.93), $\boldsymbol{K_{Cn}}$ represents the crack or line spring stiffness matrix where subscript n indicates the n^{th} crack.

2.4 System equation of motion

A beam is discretized into finite elements as demonstrated in Figure 2.11. The equation of motion of a complete system can be obtained after generation of structural mass and stiffness matrix by the assembly of element matrix. After assembly, let the global mass matrix be $\boldsymbol{M} = \Sigma_e \boldsymbol{m^e}$ and stiffness matrix be $\boldsymbol{K} = \Sigma_e \boldsymbol{k^e}$. $\boldsymbol{D}$ is system damping matrix assumed to be proportional to mass and stiffness matrix [204]. It is given by

$$\boldsymbol{D} = a_0 \boldsymbol{M} + a_1 \boldsymbol{K} \tag{2.94}$$

where a_0 and a_1 are the constants of proportionality called as Rayleigh's damping factors.

The relationship between damping ratio ς_i and natural frequency ω_i is presented as [204]

$$\varsigma_i = \frac{a_0}{2\omega_i} + \frac{a_1 \omega_i}{2} \tag{2.95}$$

The Rayleigh damping factors can be obtained by the solution of a pair of simultaneous equations, if the damping ratios ς_k and ς_i corresponding with two specific known frequencies ω_k and ω_i are known. Writing Equation (2.95) for each of the modes and then presenting them in the matrix form leads to

$$\begin{Bmatrix} \varsigma_k \\ \varsigma_i \end{Bmatrix} = \frac{1}{2}\begin{bmatrix} 1/\omega_k & \omega_k \\ 1/\omega_i & \omega_i \end{bmatrix}\begin{Bmatrix} a_0 \\ a_1 \end{Bmatrix} \tag{2.96}$$

From Equation (2.96), one can obtain a_0 and a_1 as,

$$\begin{Bmatrix} a_0 \\ a_1 \end{Bmatrix} = 2\frac{\omega_k \omega_i}{\omega_i^2 - \omega_k^2}\begin{bmatrix} \omega_i & -\omega_k \\ -1/\omega_i & 1/\omega_k \end{bmatrix}\begin{Bmatrix} \varsigma_k \\ \varsigma_i \end{Bmatrix} \tag{2.97}$$

where ω_k and ω_i are the system natural frequencies of interest ($\omega_k \neq \omega_i$).

The generalized second order differential system equation of motion for an uncracked beam can be written as

$$\boldsymbol{M}\ddot{\boldsymbol{d}}(t) + \boldsymbol{D}\dot{\boldsymbol{d}}(t) + \boldsymbol{K}\boldsymbol{d}(t) = \boldsymbol{F}(t) \tag{2.98}$$

The vector ***d(t)*** contains nodal degree of freedoms. ***F(t)*** is the effective external force vector acting on the system. The size of the global stiffness, mass and damping matrices are

$n \times n$, n is the number of degrees of freedom. In the above equation (˙) indicates time derivative.

In case of free vibration analysis of a uncracked beam, the solution of Equation (2.98) is to be obtained considering the homogeneous form as

$$\boldsymbol{M}\,\ddot{\boldsymbol{d}}(t)+\boldsymbol{D}\,\dot{\boldsymbol{d}}(t)+\boldsymbol{K}\,\boldsymbol{d}(t)=\boldsymbol{0} \tag{2.99}$$

with given initial conditions.

2.4.1 Eigenvalue problem for undamped system

Uncracked beam

For obtaining the eigenvalues (natural frequencies) and eigenmodes (mode shapes), let us consider undamped free vibration. Let $\boldsymbol{d} = \boldsymbol{\chi}\, e^{i\omega t}$, where, ω is the natural frequency and $\boldsymbol{\chi}$ is the corresponding mode shape. Thus taking $\boldsymbol{D} = \boldsymbol{0}$ in Equation in (2.99) and substituting $\boldsymbol{d}$, one obtains

$$\left(\boldsymbol{K}-\lambda_i\,\boldsymbol{M}\right)\boldsymbol{\chi_i}=\boldsymbol{0} \tag{2.100}$$

where $\lambda_i = \omega_i^2$. Equation (2.100) is a generalized eigenvalue problem, which has been solved by finding the roots of the characteristic equation given below

$$\boldsymbol{det}\left[\boldsymbol{K}-\lambda_i\,\boldsymbol{M}\right]=\boldsymbol{0} \tag{2.101}$$

Solving the Equation (2.101) one can obtain the multiple roots λ_i (i = 1, 2, 3,… n) which are then used to find the natural frequencies of the beam. On substitution λ_i in Equation (2.100), one can obtain the corresponding eigenvector $\boldsymbol{\chi_i}$.

Cracked beam

Similarly, the eigenvalue problem for undamped free vibration of a cracked beam can be stated as

$$\left(\boldsymbol{K_{cr}}-\lambda_{cri}\,\boldsymbol{M_{cr}}\right)\boldsymbol{\chi_{cri}}=\boldsymbol{0} \tag{2.102}$$

where $\boldsymbol{M_{cr}}$ and $\boldsymbol{K_{cr}}$ are global mass and stiffness matrices of the cracked beam structure. Subscript '*cr*' refers to the crack. It is also assumed that the crack affects only stiffness of the beam whereas the mass remains unchanged. Here, in case of cracked beam the size of the stiffness and mass matrices are ($n_{cr} \times n_{cr}$}. n_{cr} is the number of degrees of freedom. The

modal characteristics of cracked beam structures are found after obtaining ω_{cri} and $\boldsymbol{\chi_{cri}}$. Where ω_{cri} is the i^{th} eigenvalue and $\boldsymbol{\chi_{cri}}$ is the corresponding eigenvectors.

2.4.2 Forced vibration analysis of cracked and uncracked beam

The system equation of motion for damped forced vibration of uncracked beam model has been given in Equation (2.98) of subsection 2.4 is used in the present section also. The damped forced vibration of cracked beam model can be expressed as

$$\boldsymbol{M_{cr}}\,\ddot{\boldsymbol{d}}_{\boldsymbol{cr}}(\boldsymbol{t})+\boldsymbol{D_{cr}}\,\dot{\boldsymbol{d}}_{\boldsymbol{cr}}(\boldsymbol{t})+\boldsymbol{K_{cr}}\,\boldsymbol{d_{cr}}(\boldsymbol{t})=\boldsymbol{F_{cr}}(\boldsymbol{t}) \tag{2.103}$$

In the present work, the excitation force has been considered as harmonic excitation. Forced vibration response can be obtained by implementing any suitable numerical method in Equation (2.103) with known initial conditions. For the present work, Newmark-β algorithm has been considered to find out the response time history of the system. Appendix-C illustrates the Newmark-β algorithm.

2.5 Closure

In the present study, a generalized finite element model for multiple cracked and uncracked thin-walled curved beams with arbitrary cross-section has been developed. The formulations of curved members developed herein can be reduced to that of straight beam simply by considering the radius of curvature as infinity. The cracks or damages in the beam are represented by line-spring element. The length of the line-spring is always zero, i.e., both the nodes fall on the same coordinate. Thus, mesh refinement is not required in the vicinity of the crack. The improvement of the crack stiffness matrix of the beam has been achieved based on linear fracture mechanics theory by consideration of warping effects in first mode stress intensity factor due to bi-moment Rayleigh damping has been assumed in the formulation. Eigen value analysis and numerical integration with the help of Newmark – β method have been explained to obtain dynamic response for extracting crack parameters in the present study.

Chapter 3

Methodology for Crack Detection

3.1 Overview

Different approaches have been introduced for damage detection, since last couple of decades. Among these approaches, most of the damage detection methodologies depend on baseline measurement. Baseline data relates to the static or dynamic properties of the structures before any damage occurs. In vibration based damage detection, generally natural frequencies, mode shapes or ambient response of the undamaged structures are considered as baseline data which are then compared with the currently measured response to interpret the state of the structures. In most of the cases, baseline data is not available and as such the application of the method does not predict the damage state properly. To overcome such difficulties, the present study outlines an integrated hybrid approach based on Response surface method (RSM) and Genetic algorithm (GA) to predict the crack parameters. In the present report, crack parameters are understood as crack location and crack depth ratio. Finite element (FE) analysis presented in the previous chapter is carried out for combination of process parameters selected for design of experiments (DOE) to obtain the coefficients of a polynomial model for the Response surface function (RSF). These models are trained and tested based on analysis of variance (ANOVA). An objective function is formed by finding root mean square between theoretical and experimental results. The final task involves the minimization of objective function using GA to estimate the crack parameters. The present approach can also be used to estimate the externally applied forcing parameters (peak value of the force time history and excitation frequency). At the end of this present chapter a flowchart based on the above mentioned combined approach has been provided. The

practical application of the approach has been demonstrated through experimental data in Chapter 5, Chapter 6 and Chapter 7 respectively.

3.2 Theory of response surface methodology (RSM)

Response surface methodology (RSM) is a combination of mathematical and statistical techniques convenient for modeling and analysis of problems in which a response of interest is influenced by several variables. RSM has been employed in various fields such as in biotechnology, chemical engineering, and process industries with a wide range of applicability. Recently, the application of this methodology has been found in structural engineering problem. For an example, the growth rate of a plant y is affected by two environmental factors, such as amount of water X_1 and sunshine X_2. Water is the key factor for growth of the plant. It transports the nutrient throughout the plant. It also assists the plant's temperature to be stabilized by the process of evaporation. On the other hand, sunlight is necessary for photosynthesis, i.e. production of food; higher the quantity of sunlight, more would be the food production and higher would be the plant growth rate. The response surface for the plant growth can be mathematically expressed as

$$y = f(X_1, X_2) + \varepsilon \tag{3.1}$$

where X_1 and X_2 are independent variables or factors; y is the response or state variable. The experimental error term is designated as ε. The above expression is applicable for other engineering problems also.

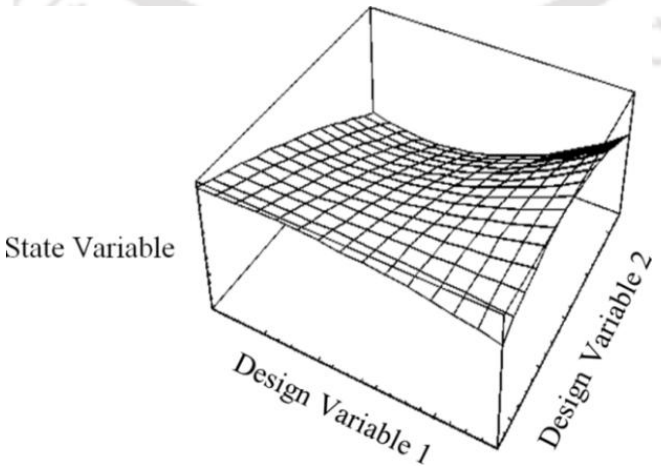

Figure 3.1: Response surface plot

A three-dimensional graph as shown in Figure 3.1 illustrates a typical response surface plot. In order to understand the surface, graphs are useful tools. It is less complicated to judge the response surface in the case of two-dimensional plots. But, when there are more than two independent variables or design variables, plots cannot be used to illustrate the response surface. For this reason, response surface models in mathematical form are mandatory for analyzing the unknown function *f*.

3.2.1 Construction of response surface function (RSF)

Regression model is a general tool to represent response surface function. "Regression model" is a relationship between a set of independent variables and dependent variable in a physical system. When there are more than two independent variables the regression model is known as multiple-regression model. In terms of the second-order RSF, the $f(X_1, X_2,\ldots, X_p)$ is expressed as

$$f(\boldsymbol{X},\boldsymbol{c}) = c_0 + \sum_{i=1}^{p} c_i X_i + \sum_{i=1}^{p} c_{ii} X_i^2 + \sum_{i=1}^{p-1} \sum_{j=i+1}^{p} c_{ij} X_i X_j \tag{3.2}$$

where p is number of parameters in the fitted model, c_0 is the model constant; c_i represents the linear coefficient; c_{ii} denotes the quadratic coefficient; c_{ij} is the interaction coefficient; X_i (i=1,2,..p) are the independent variables.

To obtain the unknown parameters vector $\boldsymbol{c}$, a series of experiments are conducted and the corresponding responses y are calculated at specified variables or factors ranges. At the n^{th} experimental run, the i^{th} variable is set to $X_i^{(n)}$ (i = 1, 2, …, p; n =1, 2,…, m) whereas $y^{(n)}$ indicates the corresponding response value. The mathematical form of the statement is given below

$$\begin{aligned} y^{(n)} &= f(X_1^n, X_2^n, \ldots, X_p^n) + \varepsilon^{(n)} \\ &= c_0 + \sum_{i=1}^{p} c_i X_i^{(n)} + \sum_{i=1}^{p} c_{ii} \left(X_i^{(n)}\right)^2 + \sum_{i=1}^{p-1} \sum_{j=i+1}^{p} c_{ij} X_i^{(n)} X_j^{(n)} + \varepsilon^{(n)} \end{aligned} \tag{3.3}$$

The response $y^{(n)}$ presented in Equation (3.3), can be expressed in matrix notation as follows:

$$\boldsymbol{Y} = \boldsymbol{X}\,\boldsymbol{c} + \boldsymbol{\varepsilon} \tag{3.4}$$

The matrix $\boldsymbol{X}$ is given as

$$\boldsymbol{X}=\begin{bmatrix} 1 & X_1^{(1)} & \cdots & X_p^{(1)} & \left(X_1^{(1)}\right)^2 & \cdots & \left(X_p^{(1)}\right)^2 & X_1^{(1)}X_2^{(1)} & \cdots & X_{p-1}^{(1)}X_p^{(1)} \\ \vdots & \vdots & \vdots & \vdots & \vdots & \vdots & \vdots & \vdots & \vdots & \vdots \\ 1 & X_1^{(n)} & \cdots & X_p^{(n)} & \left(X_1^{(n)}\right)^2 & \cdots & \left(X_p^{(n)}\right)^2 & X_1^{(n)}X_2^{(n)} & \cdots & X_{p-1}^{(n)}X_p^{(n)} \\ \vdots & \vdots & \vdots & \vdots & \vdots & \vdots & \vdots & \vdots & \vdots & \vdots \\ 1 & X_1^{(m)} & \cdots & X_p^{(m)} & \left(X_1^{(m)}\right)^2 & \cdots & \left(X_p^{(m)}\right)^2 & X_1^{(m)}X_2^{(m)} & \cdots & X_{p-1}^{(m)}X_p^{(m)} \end{bmatrix} \tag{3.5}$$

where $\boldsymbol{X}$ is the design matrix of independent variables of order $m \times q$ in which $q = (p+1)(p+2)/2$ and m is the number of response parameters; $\boldsymbol{Y} = (y_1, y_2, \ldots, y_m)^T$, $\boldsymbol{\varepsilon} = (\varepsilon_1, \varepsilon_2, \ldots, \varepsilon_m)^T$ and $\boldsymbol{c} = (c_0, c_1, \ldots, c_{ij})^T$. From Equations (3.4) and (3.5), it is to be noted that the number of unknown coefficients $\boldsymbol{c}$ is $(p+1)(p+2)/2$. Therefore, to calculate these parameters, an equal or more number of experimental runs (i.e. $m \geq q$) is required.

The least-squares method is used to minimize the sum of squares of the random error, which is used to calculate the unknown vector $\boldsymbol{c}$. Thus, the least-squares function $\boldsymbol{L_f}$ is expressed as

$$\boldsymbol{L_f} = \sum_{i=1}^{n} (\varepsilon^{(n)})^2 = \boldsymbol{\varepsilon}^T \boldsymbol{\varepsilon} = (\boldsymbol{Y} - \boldsymbol{Xc})^T (\boldsymbol{Y} - \boldsymbol{Xc}) \tag{3.6}$$

where $\boldsymbol{\varepsilon^T}$ is the transpose of the matrix $\boldsymbol{\varepsilon}$.

Now, $\boldsymbol{L_f}$ can be expanded as

$$\begin{aligned} \boldsymbol{L_f} &= \boldsymbol{Y}^T\boldsymbol{Y} - \boldsymbol{c}^T\boldsymbol{X}^T\boldsymbol{Y} - \boldsymbol{Y}^T\boldsymbol{Xc} + \boldsymbol{c}^T\boldsymbol{X}^T\boldsymbol{Xc} \\ &= \boldsymbol{Y}^T\boldsymbol{Y} - 2\boldsymbol{c}^T\boldsymbol{X}^T\boldsymbol{Y} + \boldsymbol{c}^T\boldsymbol{X}^T\boldsymbol{Xc} \end{aligned} \tag{3.7}$$

since $\boldsymbol{c}^T\boldsymbol{X}^T\boldsymbol{Y}$ is a scalar quantity and its transpose $(\boldsymbol{c}^T\boldsymbol{X}^T\boldsymbol{Y})^T = \boldsymbol{Y}^T\boldsymbol{Xc}$ is the same scalar. The calculated vector $\hat{\boldsymbol{c}}$ of unknown vector $\boldsymbol{c}$ must satisfy the following equation

$$\left.\frac{\partial \boldsymbol{L_f}}{\partial \boldsymbol{c}}\right|_{\hat{\boldsymbol{c}}} = -2\boldsymbol{X}^T\boldsymbol{Y} + 2\boldsymbol{X}^T\boldsymbol{X}\hat{\boldsymbol{c}} = 0. \tag{3.8}$$

From Equation (3.8), $\hat{\boldsymbol{c}} = \left(\boldsymbol{X}^T\boldsymbol{X}\right)^{-1}\boldsymbol{X}^T\boldsymbol{Y}$ (3.9)

After rearranging the Equation (3.9) the fitted response vector $\hat{\boldsymbol{Y}}$ is given as

$$\hat{\boldsymbol{Y}} = \boldsymbol{X}\hat{\boldsymbol{c}} \tag{3.10}$$

Again Equation (3.10) can be written as

$$\hat{\boldsymbol{Y}} = \boldsymbol{H}\boldsymbol{Y} \tag{3.11}$$

where

$$\boldsymbol{H} = \boldsymbol{X}\left(\boldsymbol{X}^{T}\boldsymbol{X}\right)^{-1}\boldsymbol{X}^{T} \tag{3.12}$$

where the matrix $\boldsymbol{H}$ is usually called as hat matrix. It transforms the vector of the observed response values $\boldsymbol{Y}$ to the vector of fitted values $\hat{\boldsymbol{Y}}$. This $\boldsymbol{H}$ matrix and its properties play an important role in regression analysis.

3.2.2 Experimental design

Design of experiments (DOE) is a powerful tool for planning experiments so that the data obtained can be analyzed to yield valid and objective conclusions. Generally, DOE is used when more than one input variable is suspected to influence an output. For example, it may be desirable to understand the effect of water and sunshine on the growth rate of a plant.

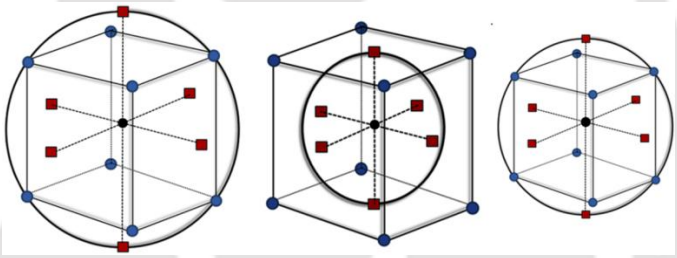

CCC CCF CCI

(a)

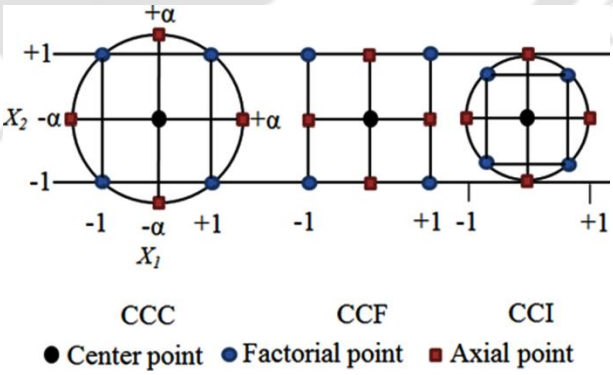

(b)

Figure 3.2: Central composite design (CCD)

In the present work, the central composite design (CCD) of experiment has been considered to obtain interactions of design variables and curvature properties of response

surface. The CCD is also known as Box-Wilson Central Composite Design. CCD has been extensively applied for building a second order response surface [120-122]. A central composite design has been shown in Figure 3.2, where (a) represents the three-factors design and (b) illustrates the two-factors design. The CCD has been classified into three categories-(i) circumscribed (CCC) (ii) faced centered (CCF) and (iii) inscribed (CCI) which are illustrated in Figure 3.2.

CCD consists of center, factorial and axial points. CCD holds a fractional factorial design with center points augmenting with a group of 'star points' or 'axial points' that permit estimate of curvature. If the distance from the center of the design space to a factorial point is ±1 unit for each factor, then the distance from the center of the design space to a star point is ±α with $|\alpha| > 1$. The precise value of α rely on certain properties required for the design and on the number of factors involved.

CCC – CCC is a central composite design where the axial points are at a distance 'α' from the center points. CCC requires five levels for each factor. The actual value of α depends of the number of factors in the factorial design. Thus,

$$\begin{aligned} \alpha &= [\text{number of factorial runs}]^{1/4} \\ &= [2^p]^{1/4} \end{aligned} \tag{3.13}$$

Thus for two factors, p=2 and Equation (3.13) gives α = 1.414.

CCF – In this work, central composite face-centered (CCF) design (a category of CCD) has been chosen to design the experiments and evaluate the interactive effects of the variables on output responses. In this design experiment method, the star or axial points are at center of each face of the factorial space, thus α = ±1. This variety needs 3 levels of each factor.

CCI – This design is a scaled down CCC design with each factor level of the CCC design divided by α to generate the CCI design. This design also requires 5 levels for each factor. For example, CCD for two variables, the factorial points would range between -1 and +1 and the axial points would range between -1.414 and +1.414. In the corresponding inscribed design, the factorial points would range between -0.707 and +0.707 and the axial points would range between -1 and +1.

The total number of experimental run can be obtained using following formula:

$$N_{ET} = 2^p + 2p + n_{cr} \tag{3.14}$$

where N_{ET} is the total number of experimental trials required; p is the number of factors or variables and n_{cr} is the total number of center points.

Before organizing any design experiments coding scheme is necessary, because coded values ensures the orthogonality which is a desired statistical property. Coded values were adopted for the factor levels; –1, 0 and +1 corresponding to the minimum, central point and maximum levels of the factors respectively. Hence, the test factors were coded according to the equation as follows:

$$X_i = \frac{\eta_i - (\eta_{i,high} + \eta_{i,low})/2}{(\eta_{i,high} - \eta_{i,low})/2} \tag{3.15}$$

Here, X_i is the coded value of the natural or original predictor variable η_i . $\eta_{i,low}$ and $\eta_{i,high}$ are the natural values of the variable at low and high levels, respectively.

3.2.3 Analysis of variance (ANOVA)

It is always important to inspect the fitted model to judge whether the model gives an adequate approximation of the true response surface. In order to check the significance level of the RSM, analysis of variance (ANOVA) is used. The total variation in a set of data is known as the total sum of squares (SS_T).

$$SS_T = \sum_{i=1}^{N_{ET}} \left(Y_i - \bar{Y}\right)^2 \tag{3.16}$$

where $\bar{Y}$ is the average response value and N_{ET} is the experimental run number. SS_T can be divided into two parts, namely the sum of the squares due to regression (SS_R) and the sum of squares of residuals (SS_E). Thus,

$$SS_T = SS_R + SS_E \tag{3.17}$$

These two parts are computed as

$$SS_R = \sum_{i=1}^{N_{ET}} \left(\hat{Y}_i - \bar{Y}\right)^2 \tag{3.18}$$

$$SS_E = \sum_{i=1}^{N_{ET}} \left(Y_i - \hat{Y}_i\right)^2 \tag{3.19}$$

where $\hat{Y}_i$ indicates the i^{th} response value predicted by the fitted model. The number of degrees of freedom (df) associated with SS_R, df (SS_R) and SS_E, df (SS_E) are (q-1) and (N_{ET} – q) respectively.

Therefore, the total mean square (MSS_T), regression mean square (MSS_R) and error mean square (MSS_E) can be expressed as follows

$$MSS_T = \frac{SS_T}{df\,(SS_T)} = \frac{SS_T}{(N_{ET}-1)} \tag{3.20}$$

$$MSS_R = \frac{SS_R}{df\,(SS_R)} = \frac{SS_R}{(q-1)} \tag{3.21}$$

$$MSS_E = \frac{SS_E}{df\,(SS_E)} = \frac{SS_E}{(N_{ET}-q)} \tag{3.22}$$

The statistical significance of the fitted models and model terms are tested by using ANOVA. The F-values and the degrees of freedom are used to determine the p-values. In addition, the model is highly significant when p-value is less than 0.0001. Similarly, if the p-value lies in between 0.0001 and 0.05, the model is significant [120-122]. When the p-value exceeds 0.05, the model becomes insignificant.

A hypothesis tests in multiple regression model has been performed in this section. These tests can only be carried out if it can be assumed that the random error terms (ε_i) are normally distributed with a zero mean and variance σ^2, abbreviated as $\varepsilon \sim N\ (0,\ \sigma^2)$. Generally, F test can be performed simultaneously to verify the significance of a number of regression coefficients and also be used to test the individual coefficients too. To conduct a hypothesis test an example has been presented based on generalized polynomial model given in Equation (3.3). To explore how the given factors affect the response, the following hypothesis assessments are required to be carried out

$$\begin{aligned} H_0 &: \ c_i = 0 \\ H_1 &: \ c_i \neq 0 \end{aligned} \tag{3.23}$$

where H_0 is null hypothesis and H_1 is the alternative hypothesis being valid.
This test inspects the effect of the factor X_i by obtaining $(F_0)_{Xi}$

$$(F_0)_{X_i} = \frac{(MSS_R)_{X_i}}{MSS_E} \tag{3.24}$$

Hypotheses for other two factor interaction effects X_i and X_j associated with interaction coefficient c_{ij} can be stated as

$$\begin{aligned} H_0 &: \quad c_{ij} = 0 \\ H_1 &: \quad c_{ij} \neq 0 \end{aligned} \tag{3.25}$$

Statistics for the test is,

$$(F_0)_{X_i X_j} = \frac{(MSS_R)_{X_i X_j}}{MSS_E} \tag{3.26}$$

Similarly, this test can be performed on c_{ii} to find the significance level of the model.
If the null hypothesis, H_0, is true then the statistics F_0 follows the F distribution with m *df* in the numerator and $(N_{ET} - q)$ *df* in the denominator.

$$F_0 = \frac{MSS_R}{MSS_E} = \frac{SS_R / df_R}{SS_E / (df_T - df_R)} \tag{3.27}$$

where total degree of freedom df_T is $N_{ET} - 1$; the degree of freedom for regression df_R is $(q-1)$ or $[2p+\{p(p-1)\}/2]$.
H_0, is rejected if the estimated statistics, F_0, is such that:

$$F_0 > F_{\delta, m, N_{ET} - q} \tag{3.28}$$

where $F_{(\delta,\ m,\ N_{ET}\ -\ q)}$ is the percentile of the F distribution corresponding to a cumulative probability of $(1 - \delta)$ and δ is the significant level. Thus,

$$p\ value = 1 - P(F \leq F_0) \tag{3.29}$$

For an example, if p value < δ, then $H_0 : c_i = 0$ and is rejected but the alternative hypothesis is valid. If $c_i \neq 0$ then, X_i contributes significantly to the model.

The fitness and adequacy of the models are also decided by using the coefficient of determination (R^2), adjusted coefficient of determination (R_{adj}^2), and standard deviation value (Std. Dev.). Closeness of the value of R_{adj}^2 to 1 represents better empirical model fitting to the actual data. But the adjusted R-squared values must be lower than the R-squared value. On the other hand, small value of Std. Dev. shows that the experimental results are precise and reliable. The R^2, R_{adj}^2 and Std. Dev. can be expressed as follows [120-122]:

$$R^2 = \frac{SS_R}{SS_T} \tag{3.30}$$

$$R^2_{adj} = 1 - \frac{SS_E/(N_{ET}-q)}{SS_T/(N_{ET}-1)} = 1 - \left(\frac{N_{ET}-1}{N_{ET}-q}\right)(1-R^2) \tag{3.31}$$

$$\text{Std.Dev.} = \sqrt{\frac{SS_E}{(N_{ET}-q)}} \tag{3.32}$$

Finally, residual analysis can be performed to assess the quality of the regression using residual plots. The difference between the observed value of the state variable (Y) and the predicted value ($\hat{Y}$) is known as residual or error (ε). Thus,

$$\varepsilon_i = Y_i - \hat{Y}_i \tag{3.33}$$

Plots of statistical assumptions about residuals are used to check for the following:

1. Residuals follow the normal distribution.
2. Residuals have a constant variance.
3. There are no outliers.

A normal probability plot can be obtained by plotting the residuals of the observed sample verses the corresponding residuals of a standard normal distribution. If the plot demonstrates a straight line, it is rational to assume that the observed sample comes from a normal distribution [121].

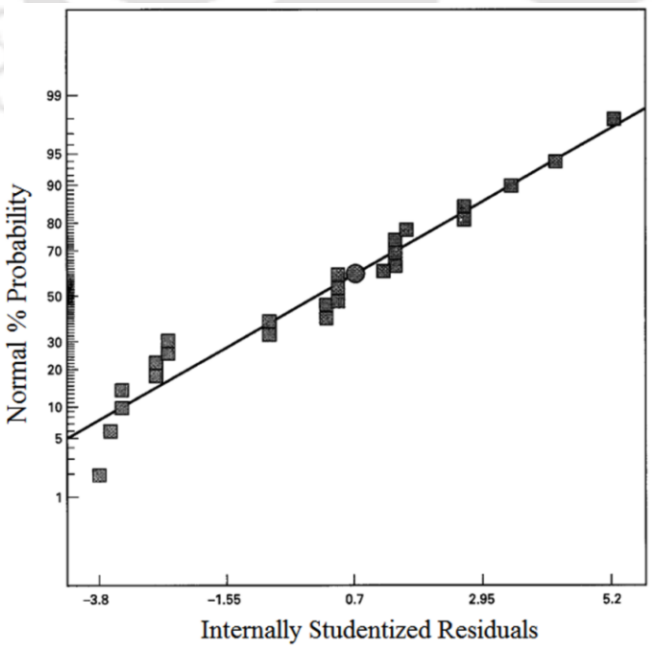

Figure 3.3: Normal probability plot of residuals

A normal probability plot of residuals has been shown in Figure 3.3. If the points diverge a lot from a straight line, there is confirmation for the assumption that the random errors are an independent sample from a normal distribution.

A possible residuals plot between residuals versus order has been presented in Figure 3.4. In Figure 3.4, the "internally studentized residuals" are also known as standardized residuals. Standardized residuals allow the residuals to be compared on the standard scale. Thus, internally studentized residuals can be expressed as [120-122]

$$r_i = \frac{\varepsilon_i}{\sqrt{MSS_E\,(1-h_{ii})}} \tag{3.34}$$

where h_{ii} is the i^{th} diagonal element of the hat (***H***) matrix.

The residuals falling in a funnel shape can be observed from Figure 3.4(a) and Figure 3.4(b). Figure 3.4(a) represents the increasing trend and figure 3.4(b) illustrates a decreasing trend of residuals. It indicates that the assumption of constant variance is not likely to be true and the regression is not a good one. On the other hand, in figure 3.4 (c), a horizontal-band pattern suggests that the variance of the residuals is constant. Most of the residuals should lie within the horizontal lines at point of ±3 [121].

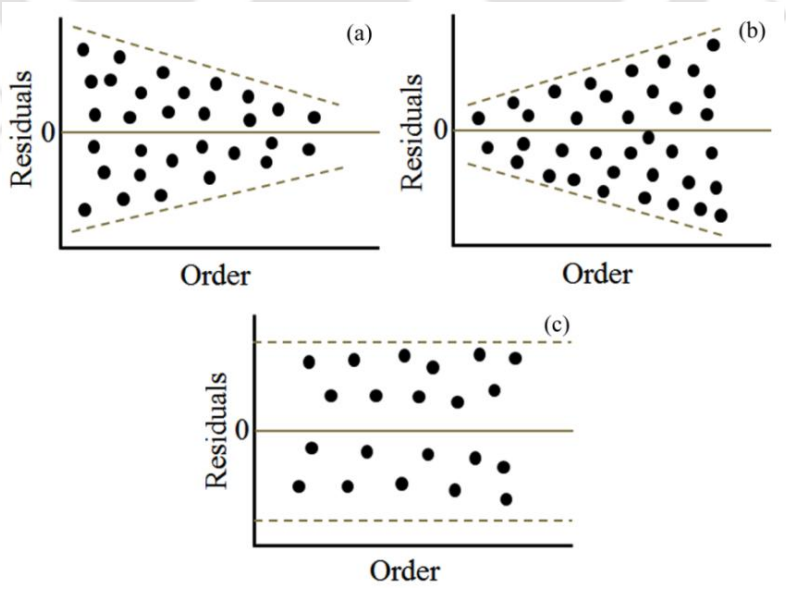

Figure 3.4: Possible residual plots

3.3 Theory of genetic algorithm (GA)

Genetic algorithm (GA) is a heuristic search and optimization technique based on natural evolution, as Darwin's theory explains. Concept on survival of the fittest and reproduction are followed by this algorithm to search new solutions in each generation. Holland [205] made the first presentation of the GA techniques in the early 70's and further improvement is credited to Goldberg [206]. GA is different from more traditional optimization and search techniques in three ways: (a) This algorithm performs with a coding of the parameter set, not the parameters themselves (b) It searches from a population of points, not from a single point and (c) GA uses objective function information, not derivatives or other auxiliary information.

The key steps of the GA to optimize an objective function are as follows:

(1) Initial population: In GA, a population of candidate solutions (known as individuals or phenotypes) to an optimization problem is evolved towards improved solutions. The first step when applying the algorithms is to choose randomly an initial population consisting of members called solutions or chromosomes or genotype and each chromosome (solution) is the collection of several genes (variables). A structure of population has been depicted in Figure 3.5.

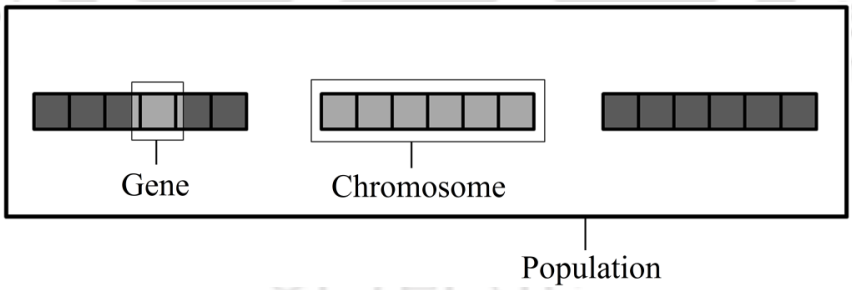

Figure 3.5: Structure of population

(2) Evaluation: Once the random population is initiated, the solution or chromosome represented by each string is evaluated by an iterative process. The population in each iteration is known as generation. The fitness function is the function responsible for evaluation of the quality of each chromosome at each step. The fitness of every individual in the population has been evaluated in each generation. The fitness is usually the value of the objective or fitness function in the

optimization problem. The “more fit” individuals are stochastically selected from the current population and each individual's genome is modified to form a new generation. The new generation of candidate solutions is then considered in the next iteration of the algorithm.

(3) Selection: Selection is considered to obtain two individuals that will be mated to contribute for the next generation. The selection is done on the basis of qualified fitness. There are several types of selection operator namely, the *roulette* selection and the *tournament* selection etc. A more common selection operator is roulette wheel selection, also known as Fitness-proportional selection in genetic algorithms for selecting potentially capable solutions for recombination. In this approach, the probability of the selection is proportional to an individual’s fitness. The analogy with a roulette wheel appears because one can visualize the whole population organizing a roulette wheel with the size of any individuals slot proportional to its fitness. The circumference of the wheel is segmented in proportion to the fitness of each string. Thereafter, the roulette wheel is spun for the same number of times as the number of strings required in the mating pool. Each time selecting one string to the mating pool using a figurative ball thrown in the wheel. By this way many copies of better strings are copied to the mating pool. This approach has been illustrated in Figure 3.6.

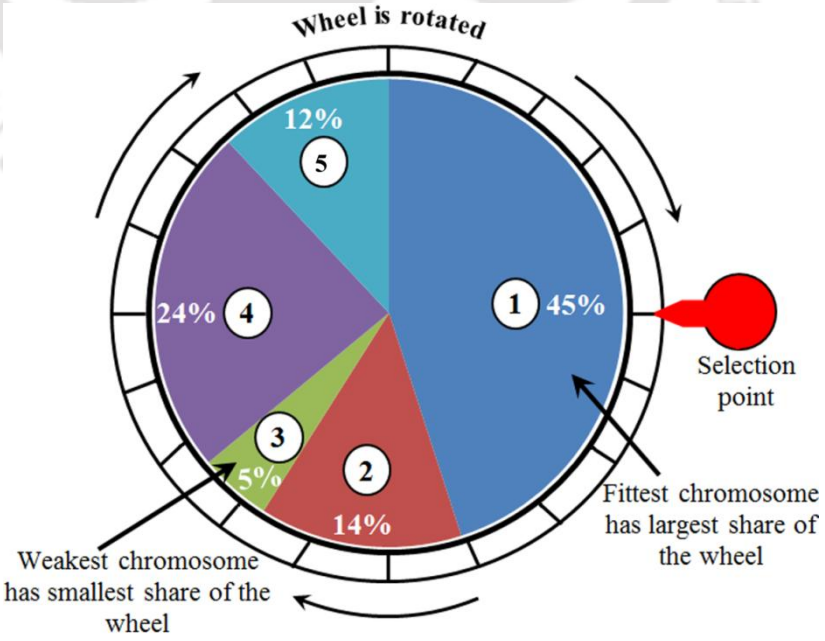

Figure 3.6: Roulette wheel selection

Tournament selection is a technique of selecting an individual from a population of individuals or chromosomes. This selection involves running several tournaments among a few chromosomes considered at random from the population. The winner (based upon the fitness value of the string) of each tournament is selected for crossover or mating pool. If size of the tournament is larger, weak individuals have a lesser chance to be selected. Tournament selection procedure has been illustrated through Figure 3.7.

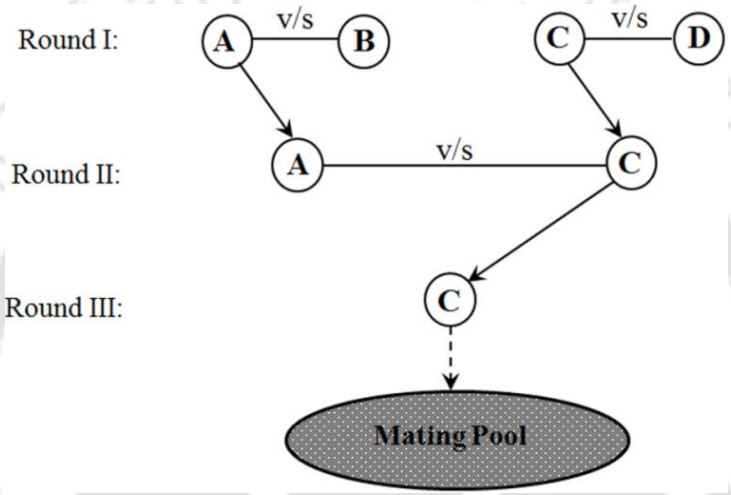

Figure 3.7: Tournament selection

(4) Crossover: The third important step is crossover where two qualified individuals or parents are going to exchange their information to form a new solution or child or offspring. This is the way similar to that used by living beings for the reproduction involving exchange their genes. This new offspring carries the information from both parents. There are many ways to perform crossover such as single point, two-point and uniform crossover. A single crossover point on two parent's organism strings is specified. All information or gene beyond that point in either organism string is swapped between the two parent organisms and resulting organisms are the children or new offspring. In single point crossover, a crossover point is selected at random at some point S_p in the individual or chromosome length L_C shown in Figure 3.8.

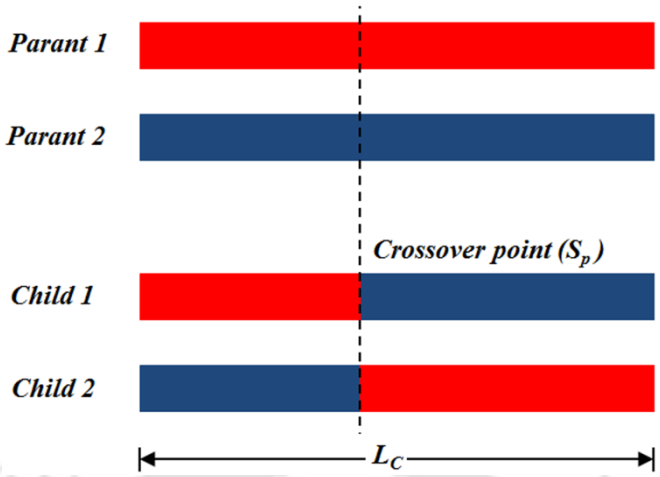

Figure 3.8: Single-point crossover

Figure 3.9 represent the two point crossover method. In this method two points are to be selected on the parent organism strings. Therefore, it is known as two-point crossover. All the information between the two points is swapped between the parent organisms, producing two child organisms.

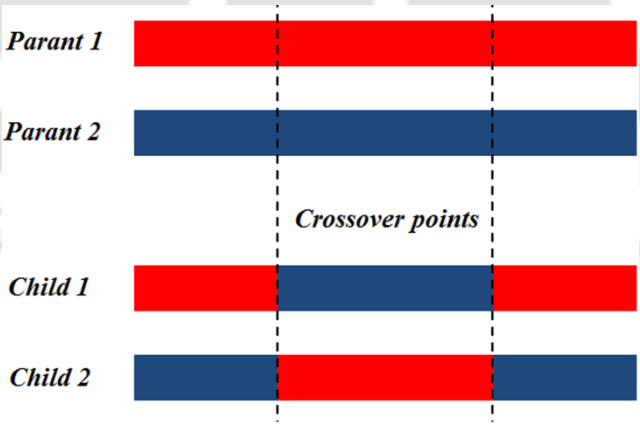

Figure 3.9: Two-point crossover

Fixed mixing ratios between two parents are used in uniform crossover. For example, if the mixing ratio is 0.5, the child has approximately half of the genes or information from parent one and the other half from parent two, although cross over points can be randomly chosen as illustrated in Figure 3.10.

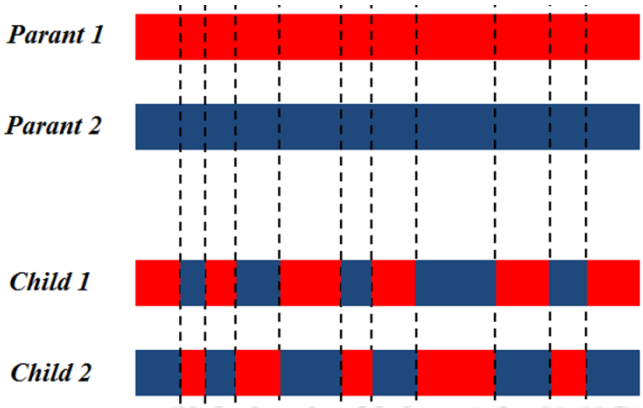

Figure 3.10: Uniform crossover

(5) Mutation: After crossover, mutation takes place. This operator is used to keep genetic diversity from one generation of a population to the next generation. It is generally applied with a low probability. This probability is used to decide whether a selected string will go through mutation. But in case of higher probability the GA gets reduced to a random search.

(6) Stopping criterion: The fitness value is examined in every generation and if this value gains a certain level, or if the maximum number of iterations is attained, the algorithm is stopped. If stopping criteria have not been met, return to Step 2.

Steps involved in hybrid approach for crack parameters detection:

The localization and quantification of the crack has been described in the present sub-section based on a hybrid approach built by a combination of RSM and GA. Various steps involved in proposed approach are given as follows:

1. *Selection of design variables and their levels*: For example, let us consider the crack parameter identification using free vibration parameters or steady state amplitude of motion at different sensor location. For double crack problems, let the design variables be first crack location (X_1), first crack depth ratio (X_2), second crack location (X_3) and second crack depth ratio (X_4). The responses variables are first n number of natural frequencies or other response such as peak acceleration/ strain at n number of sensor locations (y_i, i=1, 2, 3,…, n). The appropriate levels for design variables are then selected.

2. *Selection of the experimental design:* FE simulation is to be used as numerical experiments and thereafter regression analysis is to be carried out to provide the RSF. Here, CCF design experiment has been considered.

3. *Analysis of variance (ANOVA):* It is to be performed to justify the significance and adequacy of the developed regression polynomial model.

4. *Obtain Measured Data:* Laboratory experiments are to be carried out and response quantities selected as output are to be collected.

5. *Application of GA*: Once, the RSF is constructed, the GA has been utilized to minimize the objective function formed based on the root mean square (RMS) of the residuals between the computed RSF (y_i, i =1, 2, 3,…, n) and measured output of the experiment (y_i *, i=1, 2, 3,…, n). Thus, an objective function is expressed as

$$F_{Obj} = \left(\sum_{i=1}^{n} (y_i - y_i^*)^2 \right)^{1/2} \tag{3.35}$$

where, F_{Obj} is objective function, y_i is predicted responses and y_i^* is laboratory measured output (i = 1, 2, 3,…, n).

The optimization problem can be stated as:

Find: X_p that minimizes: $F_{Obj}(X_p)$

subject to $-1 \leq X_p \leq 1$;

6. *Stopping criterion:* When the maximum number of iterations is achieved, the algorithm is stopped and provides the predicted optimal crack parameters known as crack location and crack depth ratio.

Figure 3.11 illustrates a flow chart for more clarity of the identification approach discussed above. The first phase of the approach contains the establishment of RSF using CCF experimental design and regression analysis. Second phase represents the crack parameters searching using GA. After finding optimum crack parameters, the absolute error between predicted and actual crack parameters are calculated based on the following expression,

$$\text{Error (\%)} = \frac{\left| \text{Predicted value} - \text{Actual value} \right|}{\text{Actual value}} \times 100 \tag{3.36}$$

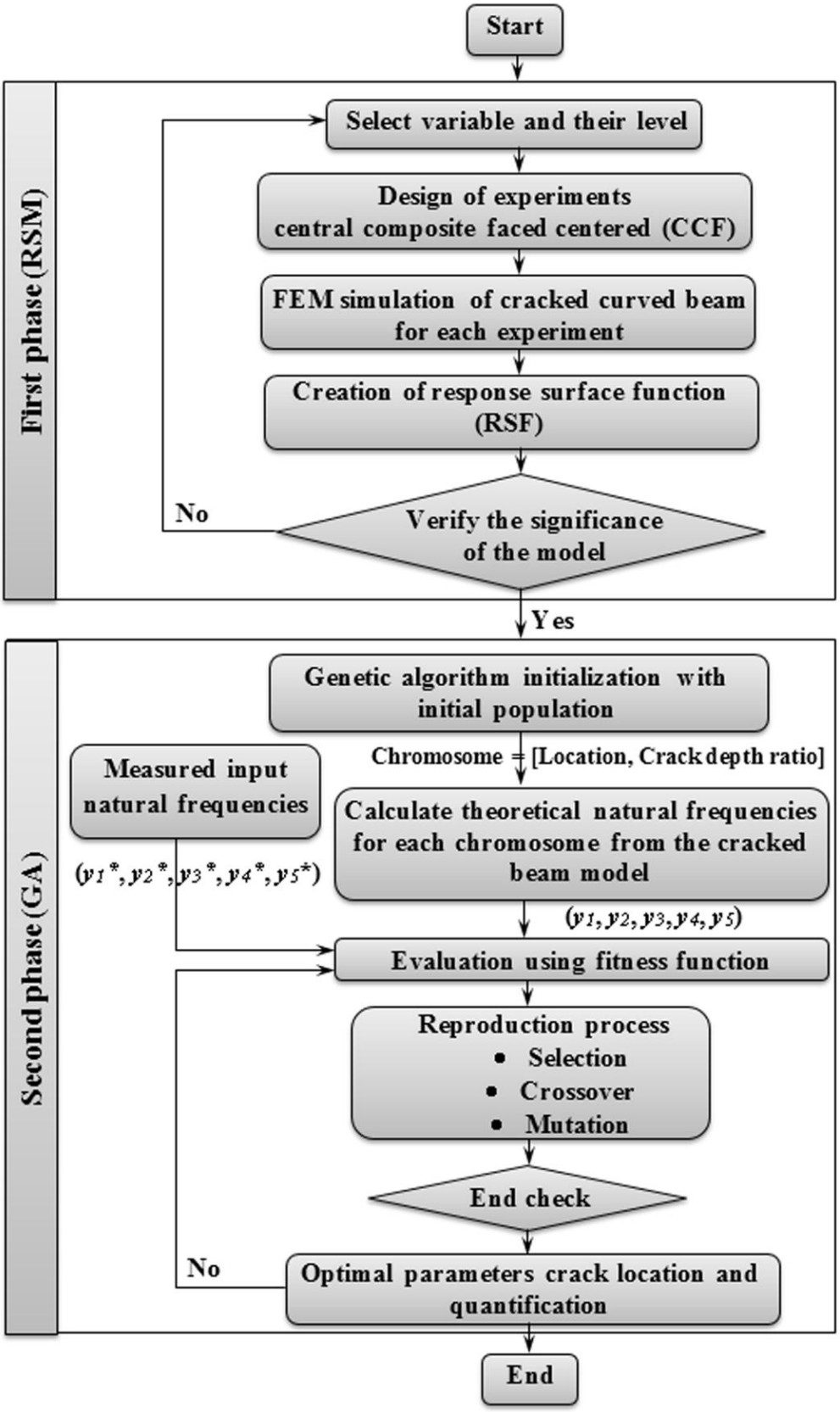

Figure 3.11: The flow chart for the proposed approach

3.4 Closure

In the present chapter, the theory of Response surface methodology (RSM) and Genetic algorithm (GA) has been discussed. Step by step procedure for a particular case and its general application has been stated. At the end of the chapter the crack parameter identification has been presented in the form of flow chart. The novelty of the proposed approach is that the baseline measurement can be avoided. This makes it suitable for application in aged structures where records of physical properties may not be available. The present approach is applicable for free vibration or forced vibration measurements. The acceptability of the response surface model is to be judged by statistical analysis. In the present chapter, statistical parameters used to examine the adequacy of the models are explained.

Chapter 4

Experimental Programme

4.1 Overview

In this chapter, the experimental programme undertaken in the research has been discussed in detail. Tests are conducted in laboratory with steel thin-walled straight and curved beams. Both uncracked and cracked beams have been considered in the experiment. The aim was to utilize experimentally measured responses in the proposed hybrid approach (presented in previous chapter) to detect crack location and crack depth. The cracks in the model of beams were introduced artificially using saw cut.

4.2 Experimental model

A typical schematic diagram of a model consisting of specimen and rigid support (concrete post) is demonstrated in Figure 4.1. Thin-walled beam shown in the same figure is the test specimen for present investigation.

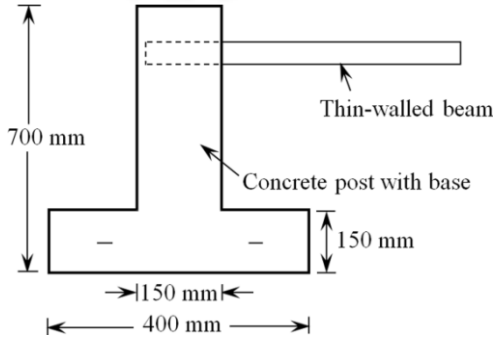

Figure 4.1: Schematic diagram of the model

4.2.1 Beam specimens

In the present work, different types of open cross-sectional (channel and angle) thin-walled straight and curved steel beam specimens have been considered. Mild steel plate of 2 mm thick has been used to make the beam specimen. A laser cutting machine (Type: LVD Orion 3015) as shown in Figure 4.2 has been used to cut the plate into appropriate sizes. The cut pieces of plates are then folded using plate bending machine as shown in Figure 4.3(a) to give the shape of the straight channel and angle section beam forming flange and web in channel beam; and upper and lower legs in case of angle section beam. Further, for a curved beam a pipe bending tool with hinged frame as shown in Figure 4.3(b) has been used to induce the required curvature of corresponding central subtended angle.

Figure 4.2: Laser cutting machine

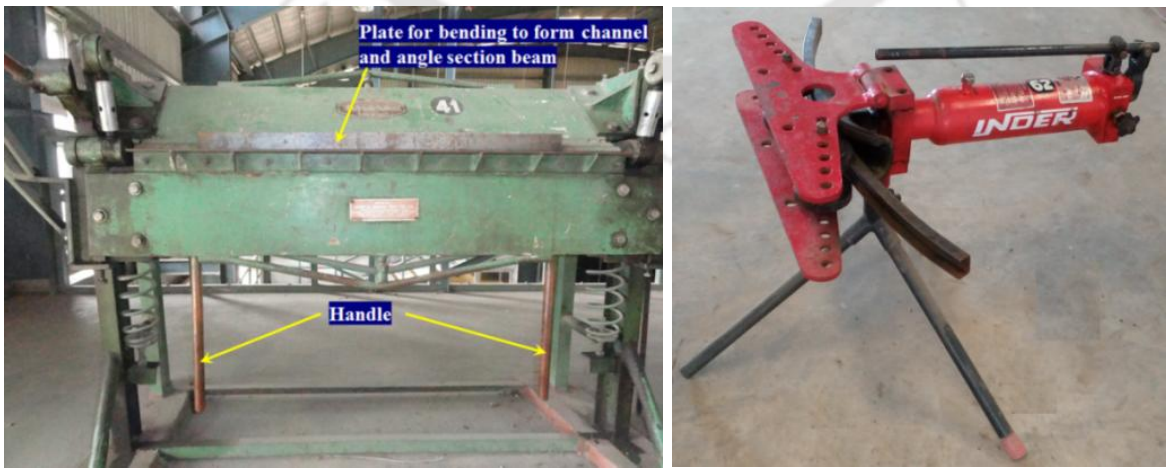

(a) (b)

Figure 4.3: (a) Plate bending machine and (b) pipe bending machine

The fabricated beam specimen- both straight and curved types are used in the experiments. The length of all specimens was kept same. Top view of a channel section beam is shown in Figure 4.4 (a) while top view of curved beam specimen in Figure 4.4 (b) and (c) respectively. Figure 4.4 (b) shows a curved beam of subtended angle θ_s = 25° and radius of curvature R=1833.50 mm while 4.4 (c) shows the curved specimen having θ_s = 50° and R= 916.70 mm. Figure 4.5 represents the end view of channel and angle section beam with dimensions.

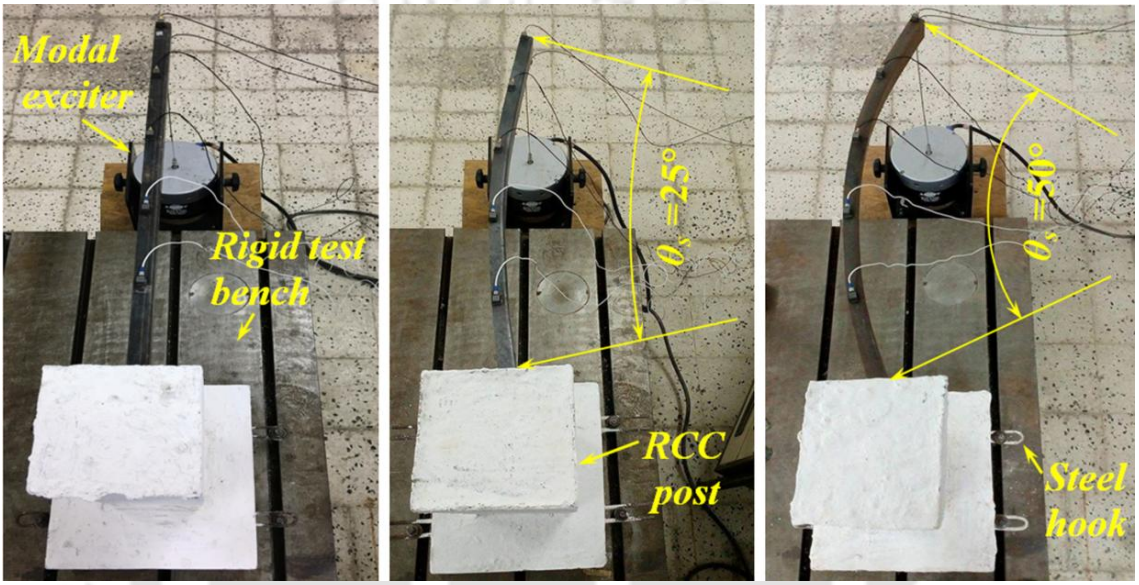

(a) (b) (c)

Figure 4.4: Top view of thin-walled beams (a) straight (b) curved (θ_s=25°) and (c) curved (θ_s=50°)

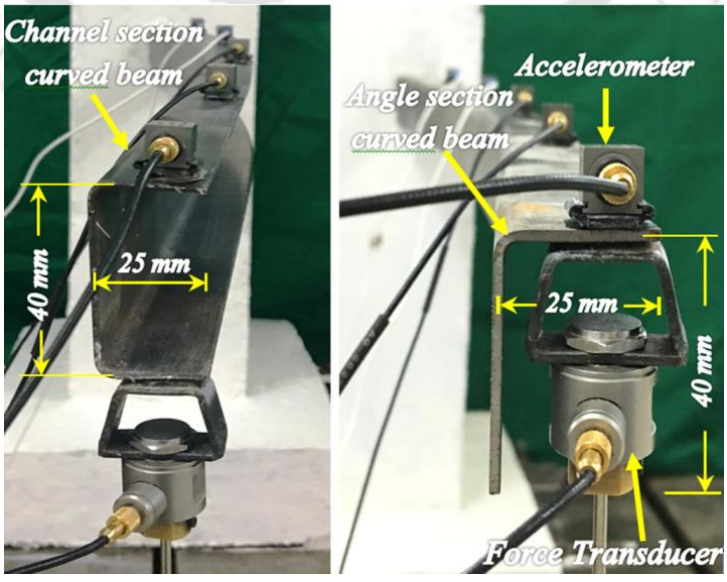

Figure 4.5: End view of channel and angle section beam specimen

The total length of the straight and curved beam (along mass axis) specimen was 925 mm out of which 125 mm is embedded in concrete post. Other physical dimensions of the beam are given as h = 40 mm, b = 25 mm, $t_w = t_f$ = 2 mm. The symbols h, b, t_w and t_f are explained in chapter 2 with reference to Figure 2.8 and 2.9.

4.2.2 Support detail

The support conditions are very essential that controls the deflected shape in natural mode of vibration. In the present study, the experimental work has been carried out with beam having clamped-free boundary conditions. For the purpose of ensuring fixed condition in one end, a short concrete post was cast during which a part of steel beam specimen measuring 125 mm was embedded inside the concrete. The other end remains free, making the span of the cantilever as 800 mm. The size of the concrete pillar is 150 × 150 mm cross-section and height 550 mm. The pillar had a base of size 400 × 400 mm with side hooks. The reinforcement detailing of the post or support has been presented in Figure 4.6(a) and 4.6(b). After 28 days of casting of the concrete post, the same with the base was lifted and anchored to the rigid test bench by means of bolt.

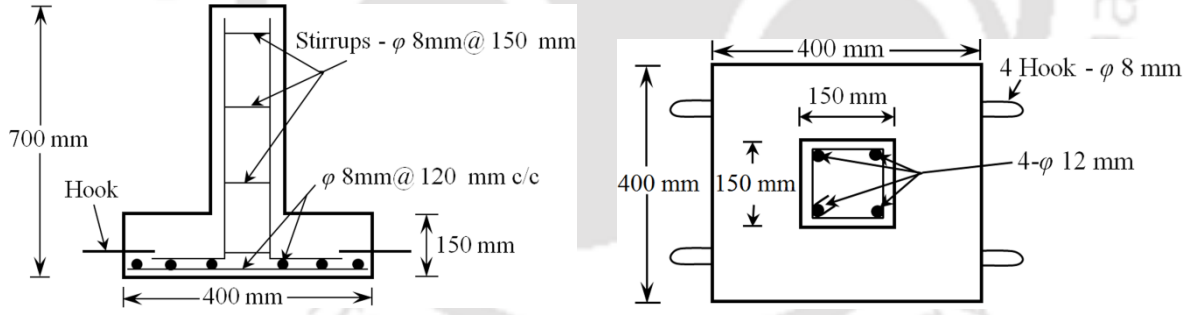

(a) (b)

Figure 4.6: Reinforcement detailing of the RCC post

4.2.3 Material properties

Mild steel plates of 2 mm thickness have been used to make the test specimen of channel and angle section beam. It was essential to determine the material properties of which the specimen has been made so as to give realistic input to the finite element analysis. The tensile strength test has been carried out on a specimen from the same mild steel sheet (as per IS 1608: 2005). Figure 4.7 shows the detail of specimen used in tensile testing.

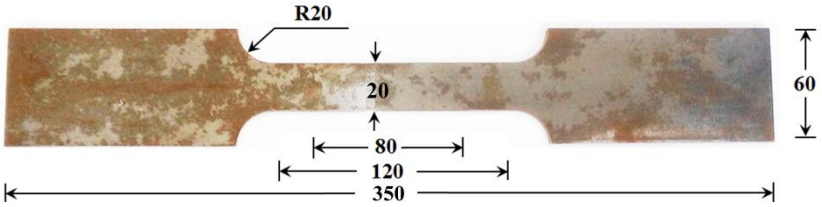

Figure 4.7: Specimen for tensile testing (All dimensions are in mm)

The uniaxial tensile testing has been carried out in a universal testing machine (INSTRON, Model: 8801, Capacity: 1000 KN). The tensile load was applied gradually till failure. The stress vs. strain plot for mild steel specimen obtained during experiment has been presented in the Figure 4.8.

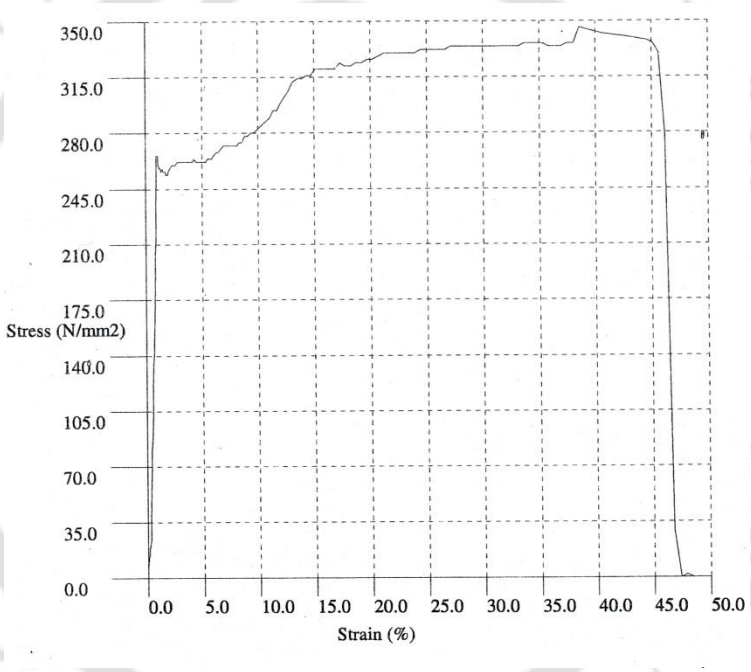

Figure 4.8: Experimental stress-strain curve for mild steel

The slope of the initial linear portion of the stress-strain curve was considered as the modulus of elasticity (E). The linear relationship between stress-strain in the elastic region of stress-strain curve is illustrated by Hook's law as

$$\text{Modulus of Elasticity}\,(E)=\frac{\text{Tensile stress}}{\text{Tensile strain}}$$

The average value of modulus of elasticity (E) has been found as 2×10^5 N/mm^2.

Finding the density of material used to make the specimens is also an important task to precede the theoretical study. Two different bunch of mild steel plate ($2.4 \times 1.2 \times 0.002$ m) has been taken to fabricate channel and angle section thin walled beams. First bunch

(channel beam) of mild steel plate consisted of three numbers of trials to obtain the density of the material. Similarly, second bunch included three numbers of trials. Out of three trials from first bunch one trial has been demonstrated through Figure 4.9 to avoid the repetition. Figure 4.9(a) represents the steel plate considered to obtain the density of the material. Figure 4.9(b) and (c) represent the electronic balance without and with steel plate respectively.

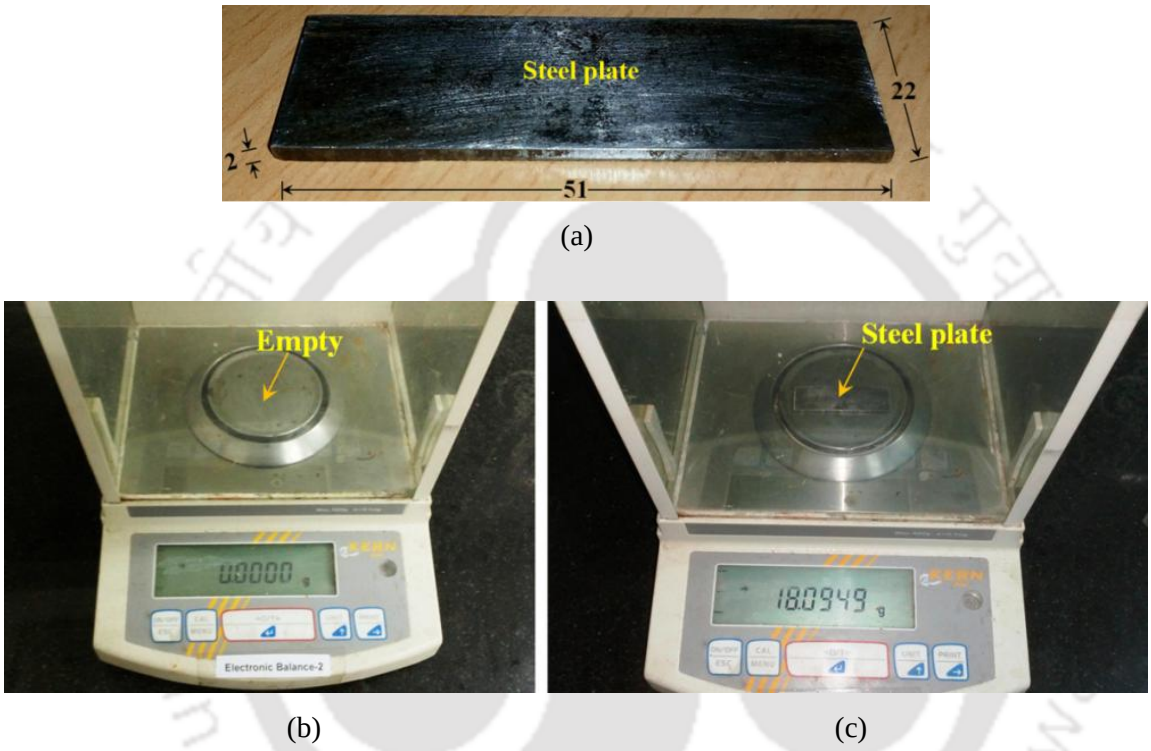

(a)

(b) (c)

Figure 4.9: (a) Plate for density calculation (plate dimensions in mm), (b) empty and (c) electronic balance with steel plate

The average densities of the channel and angle section beam specimens have been measured as 8000 kg/m^3 and 7880 kg/m^3 respectively.

Support of the beam specimens are very important that leads to the mode of vibration. Thus, it is also necessary to obtain the strength of the support material (concrete) experimentally. The Portland cement concrete mix with locally available course and fine aggregates has been used. Detail of mix proportion is given in Table 4.1. The grading of the fine aggregate was conforming to IS zone III. The nominal maximum size of the aggregate was 20 mm. Ordinary Portland cement of 43 grade was used for the required mix of concrete. The water cement ratio of the mix was considered as 0.5.

Table 4.1: Detail of mix proportion

Item	Quantity (Kg/m^3)
Cement	380
Water	191
Fine aggregate	662
Course aggregate	1142

Three cubes of sizes 150 mm × 150 mm were cast from the same mix on the same day for compressive strength test. Extensive care has been taken for the compaction of the concrete cubes. The concrete cubes were removed from the mould after 24 hours and was kept for curing. The average compressive strength of the cubes was found to be 29.2 N/mm^2 after 28 days.

4.3 Test procedure

4.3.1 Instrumentations

Health monitoring of a structural system based on experiment involves the use of several instruments. Appropriate functioning and calibration of the instruments are very important to acquire reliable results. Some of the instruments used in this experimental study are:

1. A signal generator
2. Excitation unit
3. Power amplifier
4. Accelerometers
5. Force transducers
6. Data acquisition system

These are described in detail in the subsequent subsections.

4.3.1.1 A signal generator

A signal generator is an electronic device. It generates repeating or non-repeating electronic signals in either the analog or the digital domain. There are several types of signal generators with different purposes and applications. These types cover function generators, microwave signal generators, arbitrary waveform generators, digital pattern generators and frequency generators. Front, rear and side view of the signal generator module (B&K, Type 3107) has been shown in Figure 4.10. Following types of excitation functions are available that can be utilized to generate excitations on the model:

a) Sinusoidal b) Sine sweep c) Transient d) Periodic and e) Random excitation.

Figure 4.10: A signal generator module

The frequency range covers 0 to 102.4 kHz. Output levels are modifiable from 1 mV to 5 V. In the present experiment, sinusoidal excitation has been used. The sinusoidal signals of various frequencies are generated within the specified frequency range.

4.3.1.2 Excitation unit

Modal testing demands an exciter in combination with the generator to generate forces that move the structural system to respond dynamically. There are several types of exciters present with different capabilities and modes of operations. Three primary types of exciters are easily available for practical applications: (a) Inertial exciters, (b) Hydraulic exciters and (c) Electromagnetic exciters.

Figure 4.11: An electromagnetic exciter

An electromagnetic exciter (B&K, Type 4824) shown in Figure 4.11 is the most common type of exciter. This type of exciter has been used during the present experiment. It provides sufficient force output to generate measurable and controllable responses. In this type of exciters, the supplied input electrical signal is converted to an alternating magnetic field by means of a coil attached to the driving part of the device. The driving head is connected to the structural system through a rod or stringer. A force sensor is connected at the other end of the stringer to measure the applied force. The exciter has a force rating of 100 N (sine) with wide frequency range.

4.3.1.3 Power amplifier

Magnitude of an electrical signal can be represented by variables such as current, voltage, charge and power. This signal magnitude must be appropriately adjusted for adequate performance of the components and the overall system. For an example, force input to an exciter must have sufficient power to drive it. This can be fulfilled by signal amplification, which has been done with appropriate guideline of the signal level in order to execute a specific function. Generally, amplifiers are employed to carry out the amplification of a signal. The analog power amplifier type 2732 has been used in the present laboratory experiment for the control of vibration test systems with a maximum AC output of 120 VA. The RMS output power is estimated at a load impedance of 4Ω. The usable frequency of the power amplifier ranges from 40 Hz to 15 kHz at full capacity or with DC to 150 kHz with reduced capacity. The maximum voltage gain is 17 dB. The instrument is highly reliable because it can tolerate temperature and supply line variations while maintaining excellent stability. This power amplifier can be utilized as a voltage generator with low output impedance and a flat voltage frequency response, or as a current generator with high output impedance and a flat current frequency response. Its RMS output current limit is adjustable. A power amplifier (B&K, Type 2732) is shown in Figure 4.12. The dimensions (W × H × D) of the instrument are (482 × 88 × 450) in mm and its weight is 14 kg.

Figure 4.12: Power amplifier

4.3.1.4 Accelerometers

In the present work, piezoelectric transducers are used to measure the acceleration of the test specimens at various locations. Piezoelectric transducers are mostly used in accelerometers. Piezoelectric accelerometers are frequently used because of small size, high stiffness and high range of sensitivity. A view of an accelerometer (B&K, Type 4507) has been shown in Figure 4.13.

Figure 4.13: View of an accelerometer

These piezoelectric accelerometers are generally used to measure all type of vibrations regardless of the nature of the vibration in real time. The characteristics of accelerometers include the frequency range: 0.3 - 6000 Hz; sensitivity: 100 mV/g and weight: 4.8 gram. Maximum operational level (peak) of the accelerometer is 70g, whereas maximum shock Level (±peak) is 5000g. The piezoelectric elements working as the heart of the accelerometer are usually made from an artificially polarized ferroelectric ceramic. These elements have the property of producing an electric charge, which is directly proportional to strain and thus the applied force, when loaded either in tension, compression or shear.

4.3.1.5 Force transducers

The force transducer is inserted directly between the exciter and the test specimen being excited. It is the simplest type of the piezoelectric transducer and suited for measuring tensile and compressive forces. The transmitted force is applied directly across the crystal which generates the corresponding charge, proportional to the force. A view of B&K, Type 8230-001 force transducer is shown in Figure 4.14.

Figure 4.14: View of a force transducer

The main features of the transducer include the sensitivity: 22 mV/N; maximum compression: 2200 N; maximum tension: 2.2 N and weight: 30.2 grams. Force transducers are mainly designed for the modal exciter and to measure the compressive and tensile forces. This type of transducer has low impedance output.

4.3.1.6 Data acquisition system

Pulse analyzer® (B&K, 3560C) with data acquisition system is a PC based sound and vibration analysis equipment. It has been used for picking up the responses from the specimens subjected to vibration. The system consists of a PC with LAN interface, PULSE software, Microsoft® Windows® operating system and data acquisition front-end hardware. Pulse software has real time measurements capabilities, real time DSP resources to conduct FFT analysis on 16 channels up to 25.6 kHz bandwidth and 1/3 octave analysis on 6 channels up to 25.6 kHz bandwidth. A Pentium III 1 GHz computer or faster configuration is required for this performance.

4.3.2 Experimental set up and conduct of vibration test

The experimental setups for both straight and horizontally curved channel and angle cross-sectional steel beam specimens are same. Figure 4.15 shows the experimental setup of channel section curved beam with close-up view of tip of the beam.

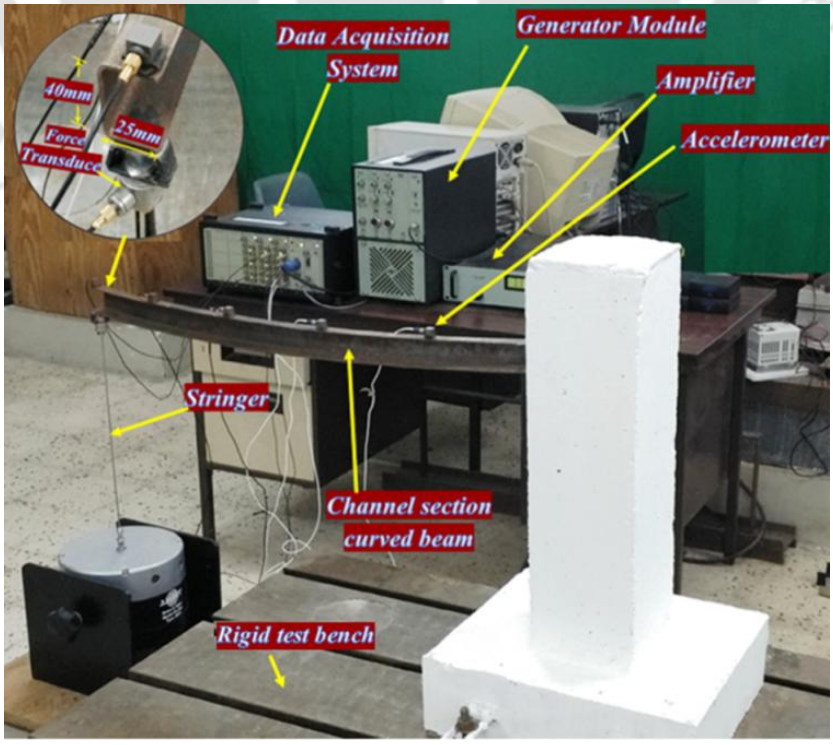

Figure 4.15: Experimental setup and close-up view of tip of the beam

The cracks are introduced by means of saw cut (width=2mm) on the top flange of the channel and horizontal leg of angle section beam perpendicular to the longitudinal axis. The crack depth ratio has been maintained in the range of 0.08 to 0.8 of the flange or leg width in different specimen for the experimental study. Cracks in the specimen are introduced in single location as well as two locations in the beam specimen for experimental purpose. The single crack cases are studied considering location at 0.02 m and 0.5 m in case of straight beams. Double crack cases are considered in two combinations of location such as 0.02 m, 0.1 m and 0.5 m, 0.6 m for straight beams. In case of curved beams two different locations-at 0.625° and 15.625° are considered for testing purpose in single crack cases, when the subtended angle (θ_s) of the beam is 25°. Two different crack locations-at 1.250° and 31.250° are considered in case of single cracked curved beams with subtended angle 50°. The double cracks in curved beams are introduced in two combinations of location such as-0.625°, 3.125° and 15.625°, 18.750° for curved beams with subtended angle 25°, whereas 1.250°, 6.250° and 31.250°, 37.500° for curved beams with subtended angle 50°. The physical and material properties of channel and angle section straight and curved beam with different subtended angle have been summarized in Table 4.2.

Table 4.2: Details of beam properties and applied frequency ranges

Specimen	L (mm)	h (mm)	b (mm)	t_w (mm)	t_f (mm)	θ_s (deg)	ρ (Kg/m^3)	E (N/mm^2)	Forcing freq. range (Hz)
Thin-walled straight beam									
Channel	800	40	25	2	2	-	8000	2×10^5	5 to 750
Angle	800	40	25	2	2	-	7880	2×10^5	2 to 250
Thin-walled curved beam									
Channel	800	40	25	2	2	25°	8000	2×10^5	5 to 850
	800	40	25	2	2	50°	8000	2×10^5	5 to 850
Angle	800	40	25	2	2	25°	7880	2×10^5	2 to 250
	800	40	25	2	2	50°	7880	2×10^5	2 to 250

The beam assembly was attached to an electromagnetic modal exciter at the free end of the cantilever beam. The modal exciter was connected with a signal generator module and a power amplifier. Generator module can be used for generating various types of signals but

in the present study sinusoidal vibration signals were used. The accelerometers have been mounted on the upper surface of the top flange in case of channel and the horizontal leg in case of angle section beam. Five accelerometers were located at 160 mm, 320 mm, 480 mm, 640 mm and 800 mm from the fixed end. Each accelerometer was connected to data acquisition system. A force transducer has been connected at the tip of the beam to measure the exciting force.

During vibration test, the beam was subjected to dynamic loading with an electromagnetic shaker attached through a stringer at the tip of the cantilever beam. The force transducer was set to the position at the point of excitation to measure the force generated in the beam. The operating frequency range was varied manually from 2 to 850 Hz for the beam specimen. The incremental step was lowered suitably on approaching towards resonance so as to distinctly identify each natural frequency. When operating frequency coincides with the natural frequency, the amplitude of response was large. This has been observed in Pulse analyzer software to identify the resonance point. The output signals (acceleration responses) of the accelerometers were acquired using a data acquisition system which processes the accelerometer responses utilizing the Pulse analyzer software to produce the frequency response function (FRF).

4.4 Closure

The present chapter provides the detail of fabrication of beam specimen and procedure for conducting vibration test with the help of electromagnetic shaker imposing harmonic excitation. Material characteristics and physical dimensions of test specimen are given. Description of the experimental setup, necessary signal recording and processing instruments are also given in this chapter. Data acquisition is an important part of this study. Method of acquisition of the experimental data (natural frequencies and peak acceleration of steady state motion) in several experimental trials on uncracked and cracked specimen has been discussed.

Chapter 5

Identification using Free Vibration Response

5.1 Overview

The free vibration response has been studied theoretically and experimentally for identification of crack parameters in straight and horizontally curved thin-walled steel beams with different subtended angle. Before presenting results of the analysis, convergence test of the FE model was carried out. After that, the present model and computer programme have been validated by comparing FE results with published analytical results and then with experimental ones. The effects of characteristic dimensions of the cross-section (i.e., flange thickness and web height) of beam and crack depth ratio on stress intensity factor (SIF) have also been studied. The vibration based conventional methods of damage identification have been first used and drawbacks are pointed. Thereafter, the proposed hybrid approach (based on RSM and GA) has been utilized for predicting single and multiple damage scenarios using first five measured natural frequencies of the cracked beams. An improved Finite Element (FE) simulation of cracked beam has been utilized based on Design of Experiment (DOE) approach to construct the Response Surface Function (RSF). Regression analysis has been performed to construct the RSF by means of the least-squares method (LSM). The crack parameters (namely crack location and crack depth ratio) are then obtained using GA by minimizing an objective function which has been formed as the root mean square (RMS) of the residuals between the computed natural frequencies from RSFs and actual measured frequencies.

5.2 Convergence study of FE model

A simple convergence test is carried out for deciding appropriate number of elements to be used in subsequent calculations. Figure 5.1(a and b) shows the plot of convergence test between natural frequencies vs. number of elements for first two frequencies for channel section straight beam. Figure 5.2(a and b) presents the plot of convergence test of angle section straight beam for first and second natural frequencies respectively. It can be seen that from the results of the frequency converge consistently after 30 numbers of finite elements.

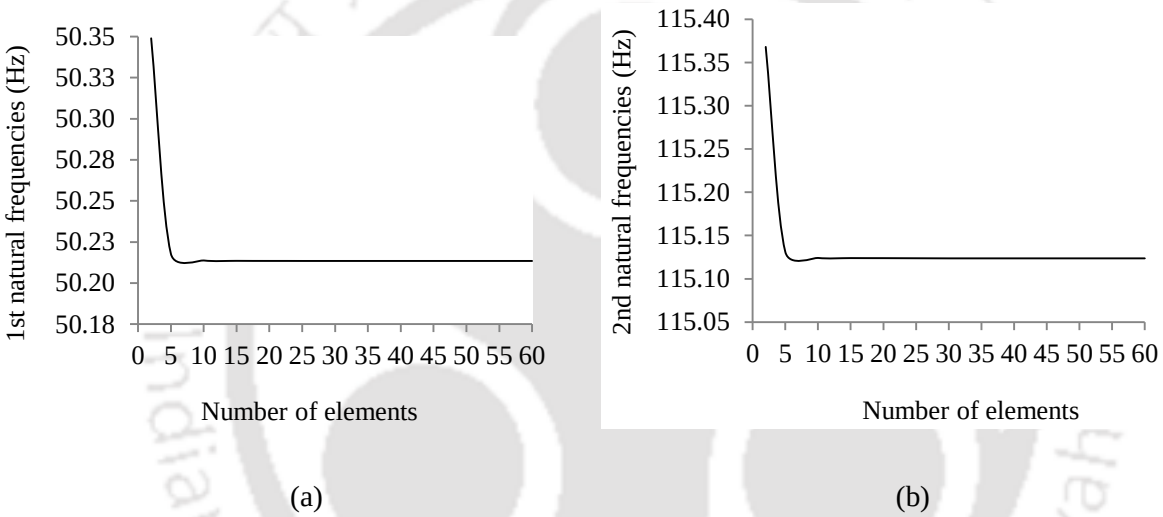

(a) (b)

Figure 5.1: Convergence test of first two natural frequencies for channel section straight beam

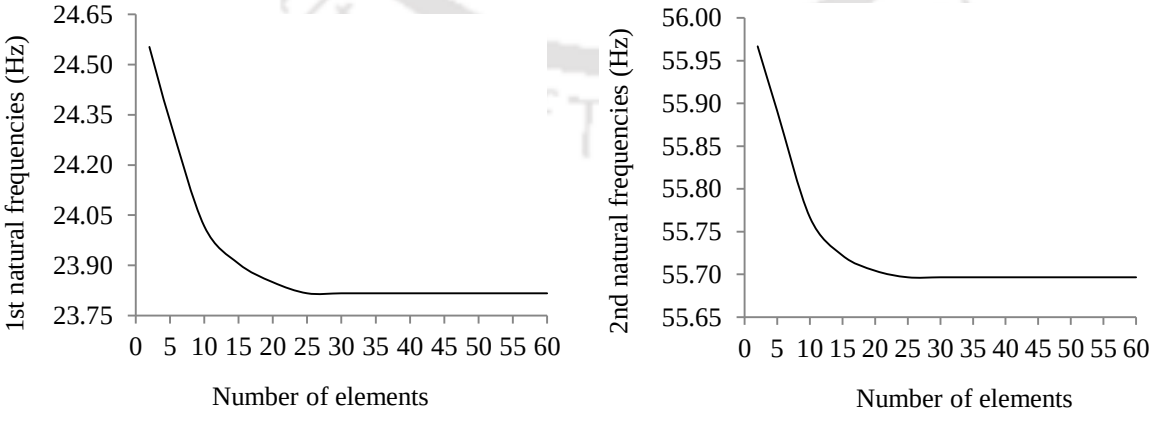

(a) (b)

Figure 5.2: Convergence test of first two natural frequencies for angle section straight beam

Similarly, Figure 5.3(a and b) and Figure 5.4(a and b) show the plot of convergence test of channel and angle cross-sectional curved beam (for θ_s = 25°) for first two natural frequencies respectively. The results obtained from 25 to 60 elements shows no significant difference of frequencies. It can be argued that the use of greater number of elements will provide the more accurate results. However, using higher number of elements will take a longer computational time. Therefore, it is general practice in FE analysis that minimum number of elements which give the results of desired accuracy should be used. In the present study, 40 numbers of elements are considered to be appropriate.

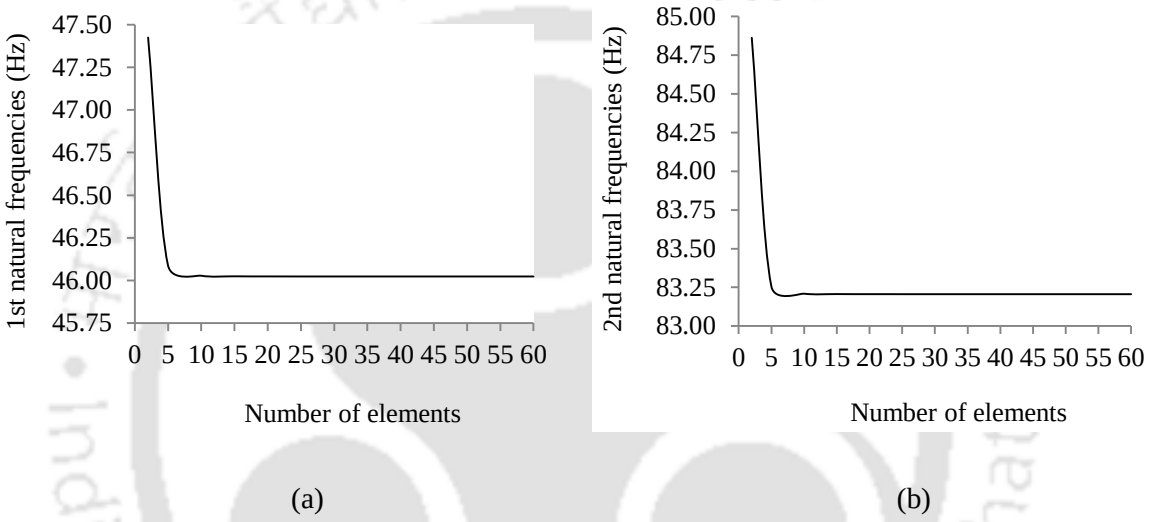

Figure 5.3: Convergence test of first two natural frequencies for channel section curved beam with subtended angle (θ_s = 25°, R = 1833.50 mm)

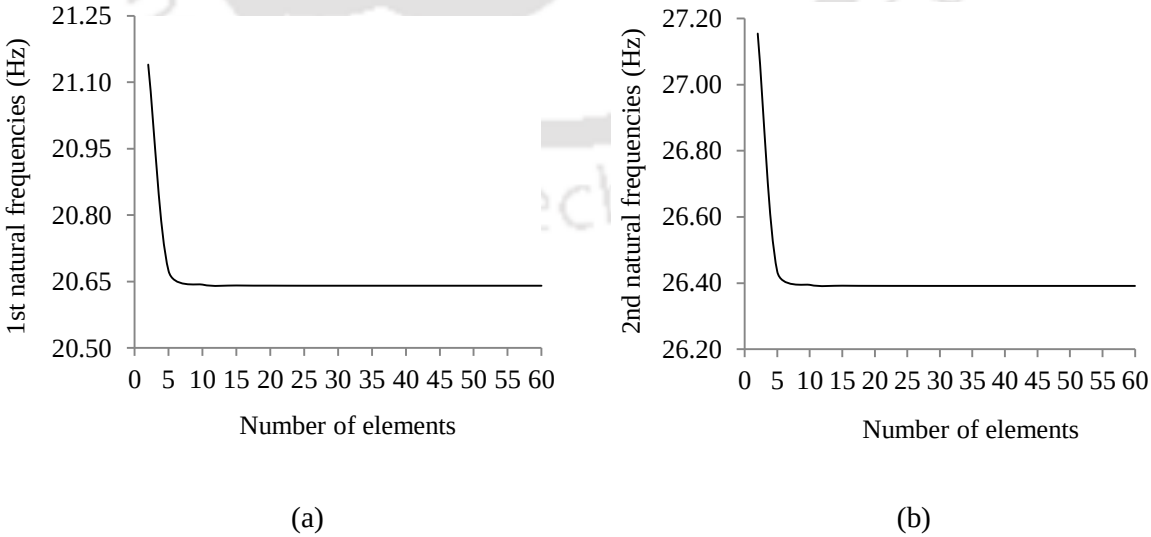

Figure 5.4: Convergence test of first two natural frequencies for angle section curved beam with subtended angle (θ_s = 25°, R = 1833.50 mm)

5.3 Validation of FE results with published results

In this study, the work of Banerjee *et al*. [179] based on exact dynamic stiffness method has been referred to verify the accuracy and effectiveness of the FE model for straight beam. The physical properties of the beam are b= 0.057375 m, h = 0.09875 m, L = 1.28 m, $t_w = t_f$ = 0.00125 m, EI_{zz} = 0.974 × 10^5 N-m^2, GJ = 11.21 N-m^2, $EI\Gamma_\omega$ = 35.40 N-m^4. Comparisons of the results for uncracked straight beam for Clamped free (C-F) and simply supported (S-S) condition is given in Table 5.1. There is very good agreement between the natural frequencies obtained by the present FE formulation and the exact method in reference [179].

Table 5.1: Comparison of natural frequency of uncracked channel section straight beam with published result

Support condition	Mode	Natural frequencies of uncracked beam (Hz)	
		Present Method	Banerjee *et al.* [179]
C-F[a]	1	25.41	25.37
	2	99.11	98.57
	3	148.19	149.40
S-S[b]	1	66.96	67.13
	2	262.66	263.67
	3	277.25	275.80

[a]Clamped-Free; [b]Simply supported

Next, the curved beam model has been validated with the result reported by Nam-ll and Moon-young [195] which was based on centroid-shear center formulation. They reported the results of beams with two kinds of cross sections-channel and angle. The physical properties of the channel section thin-walled curved beam are b = 0.10 m, h = 0.05 m, L = 2.00 m, θ_s = 90°, $t_w = t_f$ = 0.005 m, E = 2×10^{11} N/m^2, G = 7.69×10^{10} N/m^2, Γ_ω = 641.02 × 10^{-12} m^6, J = 1.04 × 10^{-8} m^4. On the other hand, the physical properties of the angle section thin-walled curved beam are b = 0.0635 m, h = 0.1270 m, L = 6.096 m, R = 9.144 m, $t_w = t_f$ = 0.00127 m, E = 2.068×10^{11} N/m^2, G = 7.955×10^{10} N/m^2, J = 13.007 × 10^{-8} m^4.

As reported in the referred paper, the boundary conditions for channel beam was taken simply supported whereas for angle section beam end condition was clamped-clamped. The results for two different sections of curved beam are shown in Table 5.2and 5.3.

The excellent agreement is found between the results obtained by present method and the published results. However, the referred works were limited to only uncracked beam without any experimental validation.

Table 5.2: Comparison of natural frequency of uncracked channel section curved beam with published result

Support condition	Mode	Natural frequencies of uncracked beam (rad/sec)	
		Present Method	Nam-ll and Moon-young [195]
Simply supported (S-S)	1	1.659	1.657
	2	32.770	33.049
	3	38.473	37.792

Table 5.3: Comparison of natural frequency of uncracked angle section curved beam with published result

Support condition	Mode	Natural frequencies of uncracked beam (rad/sec)	
		Present Method	Nam-ll and Moon-young [195]
Clamped- Clamped (C-C)	1	2.364	2.372
	2	2.400	2.456
	3	3.217	3.285

The present theory which relies on beam elements is again compared with the result reported by Noor *et al*. [180] in which the authors modelled the uncracked channel beam using finite element method. They considered two dimensional shell elements to model flange and web plates. However, no curvature effect was considered in the model. The physical properties of the aluminium beam from the referred paper are as follows $E = 6.895 \times 10^{10}$ N/m^2, $\mu = 0.32$, $\rho = 2600$ Kg/m^3, $L = 1.016$ m, $b = 2.54 \times 10^{-2}$ m and $t_w = t_f = 6.35 \times 10^{-4}$ m.

The comparison of the results of the present finite element model using beam theory with that of FE results using shell elements has been presented in Table 5.4. The results show that the predicted natural frequencies using present beam model are in close agreement with that obtained using shell elements [180].

Table 5.4: Comparison of natural frequencies of uncracked channel straight beam using beam and shell elements in Finite element method

Support condition	Mode number	Natural frequencies of uncracked beam in Hz	
		Present Method with beam elements	Noor *et al.*[180] with shell elements
Clamped-Free (C-F)	1	11.42	11.38
	2	23.16	23.15
	3	42.69	42.57
	4	58.20	57.67
	5	107.36	106.5
	6	145.14	144.5

5.4 Validation of FE results with experimental values in present study

In this section, the comparison of first five natural frequencies between experimental values and FE results with warping and without warping of uncracked and cracked (single and double) specimen have been presented. The physical and material properties of the beams are presented in Table 4.2 of Chapter 4.

Frequency response function (FRF) curve obtained from experimentally measured tip acceleration in vertical direction for uncracked, single and double cracked channel and angle section straight beam has been presented in Figure 5.5 and Figure 5.6 respectively.

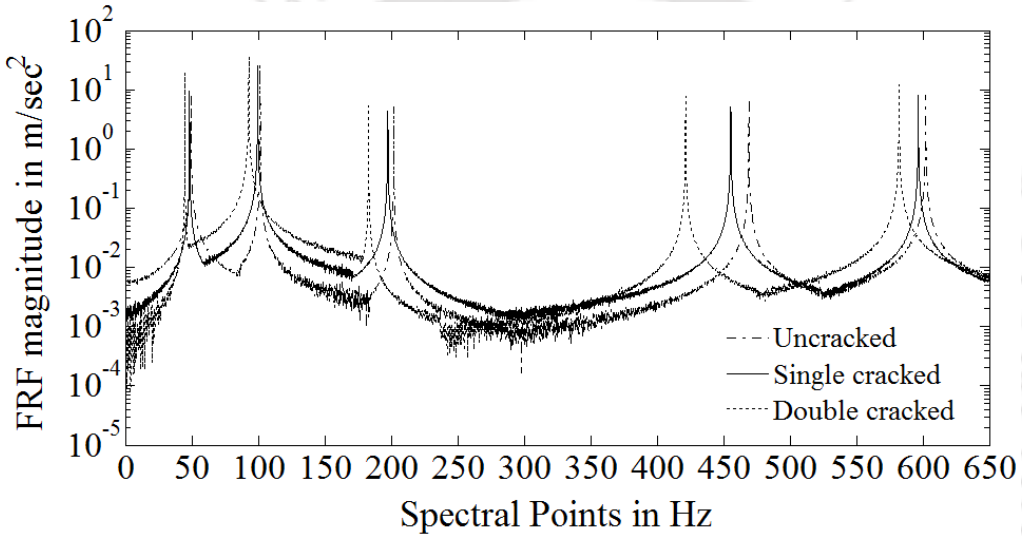

Figure 5.5: FRF of tip acceleration response in vertical direction for channel section beam

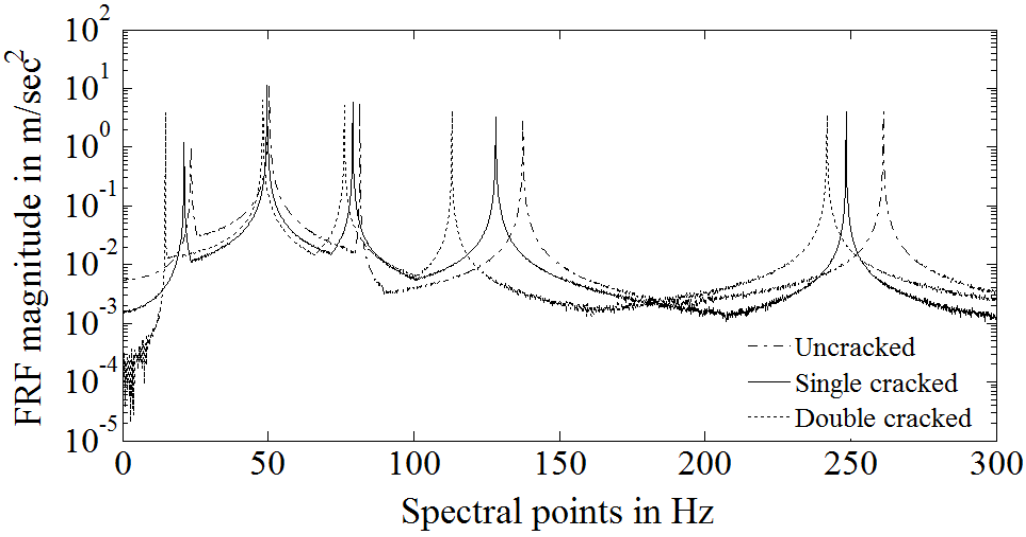

Figure 5.6: FRF of tip acceleration response in vertical direction for angle section beam

In case of single cracked channel section beam a crack has been considered at a distance of 20 mm from the fixed end of the cantilever beam with 0.5 crack depth ratio. For double cracked channel section beam, first crack location (L_1) and second crack location (L_2) are at 20 mm and 100 mm from the fixed end of the beam respectively where corresponding crack depth ratios are 0.8 and 0.08 respectively. It can be observed from the figure that the peak of FRF shifts towards left in case of cracked beam and shifting of peak is more prominent when two cracks are present in the structure.

The FRF-curve obtained from physically measured tip acceleration responses in vertical direction for uncracked, single and double cracked channel and angle section curved beam with 25° subtended angle has been illustrated in Figure 5.7 and Figure 5.8 respectively. For single cracked curved beam the crack has been selected at an angular distance (θ_{S1}) = 0.625° from the fixed end of the cantilever steel beam and corresponding crack depth ratio (ζ_1/b) = 0.5. In case of double cracked beam, first crack position (θ_{S1}) and second crack position (θ_{S2}) are at an angle 0.625° and 3.125° from the fixed end of the beam respectively. The corresponding crack depth ratios are 0.8 and 0.08 respectively. It can be distinguished from the figures that the peak of FRF shifts towards the left when crack exist in the beam. This reduction of natural frequency is caused by the increase of flexibility of cracked beam.

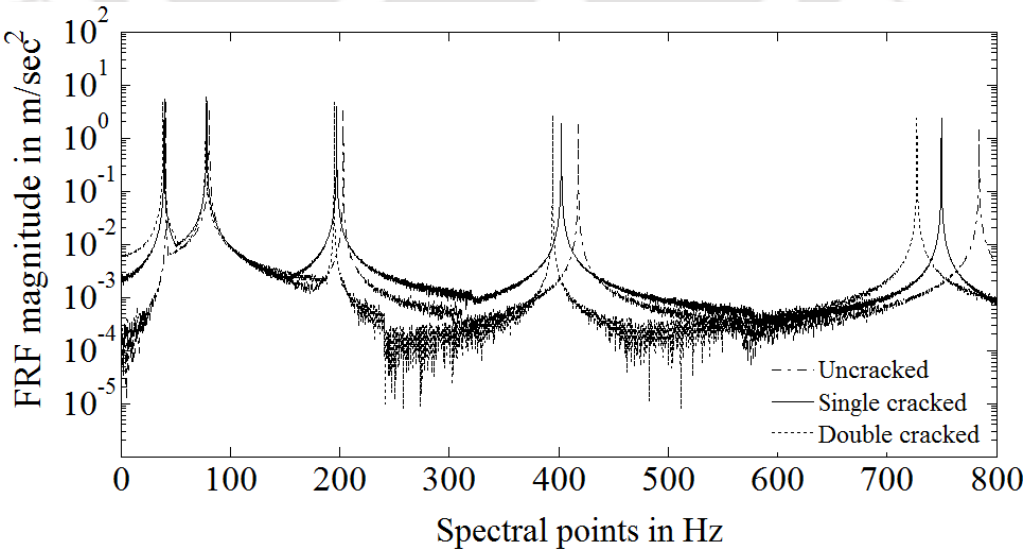

Figure 5.7: FRF of tip acceleration response in vertical direction for channel section curved beam (θ_s = 25°, R = 1833.50 mm)

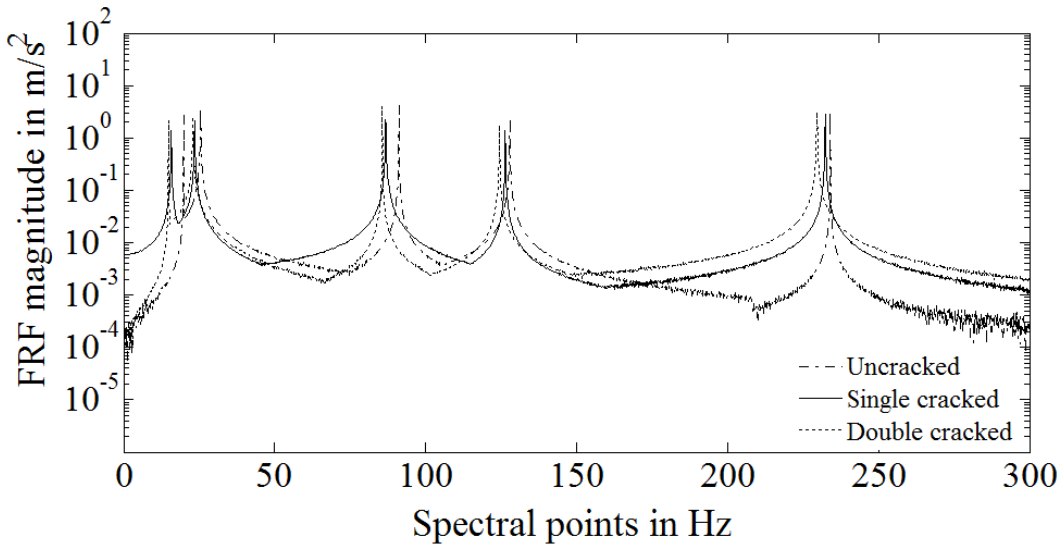

Figure 5.8: FRF of tip acceleration response in vertical direction for angle section curved beam (θ_s = 25°, R = 1833.50 mm)

Figure 5.9, Figure 5.10 and Figure 5.11 show the comparison between finite element results and experimentally obtained frequencies for channel section uncracked and cracked (single and double) straight beam respectively in the form of bar diagrams. Figures 5.12, 5.13 and 5.14 represent the same for angle section straight beam. Finite element results have been presented without warping and with warping in the beam.

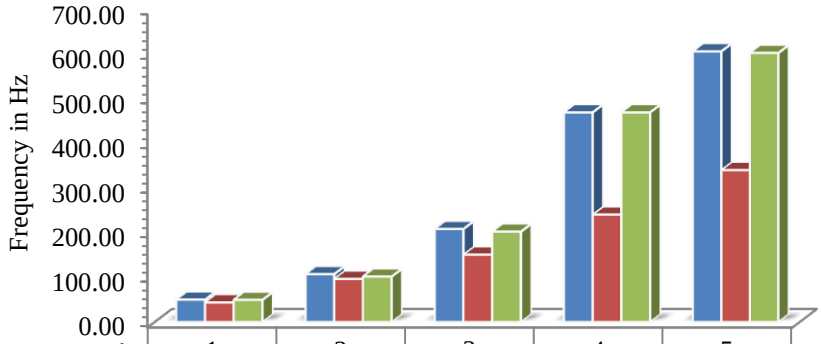

Mode Number	1	2	3	4	5
FE results with warping	49.80	106.98	207.99	469.07	605.67
FE results without warping	43.78	96.43	150.66	240.18	340.03
Measured values	49.40	101.50	202.00	469.00	602.00

Figure 5.9: Comparison between FE and experimental natural frequencies for channel section uncracked straight beam

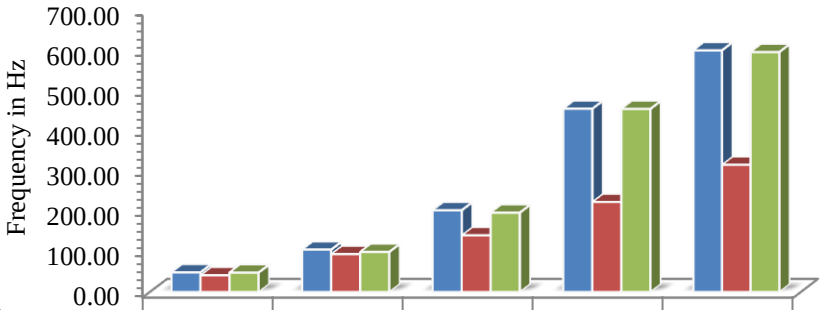

Mode Number	1	2	3	4	5
FE results with warping	48.95	105.40	203.54	455.83	600.81
FE results without warping	41.38	94.37	141.06	224.07	316.73
Measured values	48.36	99.60	197.45	455.40	596.50

Figure 5.10: Comparison between FE and experimental natural frequencies for single cracked channel section straight beam

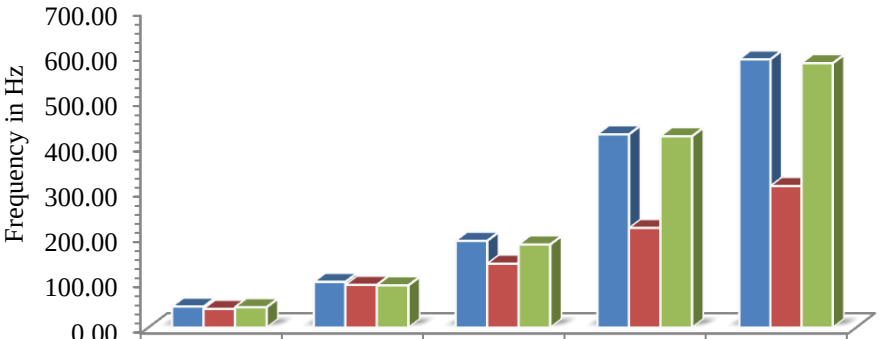

Mode Number	1	2	3	4	5
FE results with warping	45.93	100.47	191.08	425.77	590.41
FE results without warping	40.94	93.96	140.66	219.43	311.97
Measured values	44.75	92.90	183.00	421.50	582.00

Figure 5.11: Comparison between FE and experimental natural frequencies for double cracked channel section straight beam

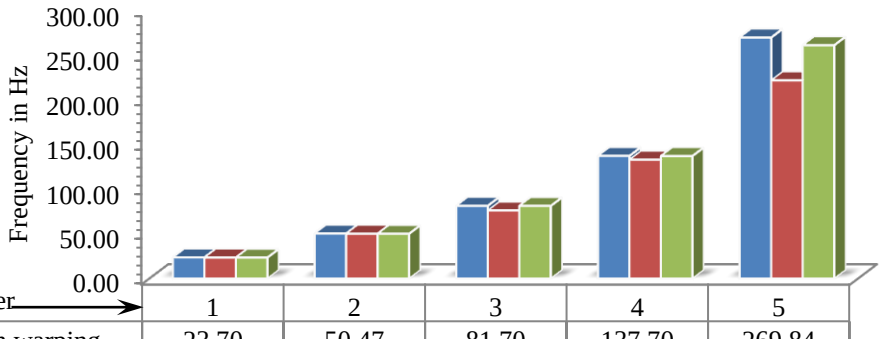

Mode Number	1	2	3	4	5
FE results with warping	23.70	50.47	81.70	137.70	269.84
FE results without warping	23.63	50.38	76.45	133.45	222.11
Measured values	23.50	50.26	81.51	137.50	261.30

Figure 5.12: Comparison between FE and experimental natural frequencies for angle section uncracked straight beam

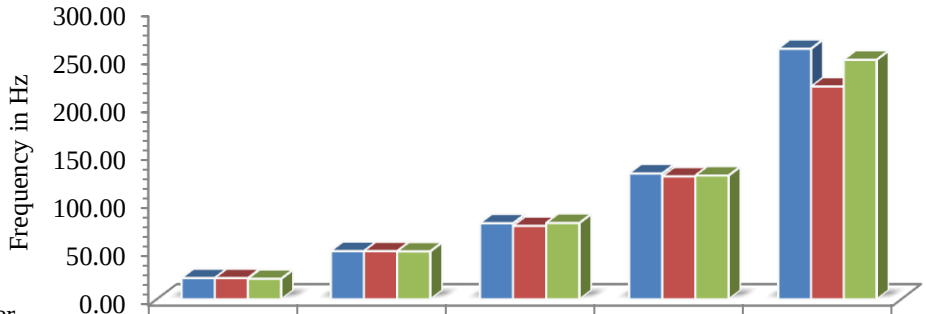

Mode Number	1	2	3	4	5
FE results with warping	21.93	49.91	78.81	130.48	259.95
FE results without warping	21.91	49.87	75.97	127.42	220.72
Measured values	21.13	49.63	79.13	128.30	248.50

Figure 5.13: Comparison between FE and experimental natural frequencies for single cracked angle section straight beam

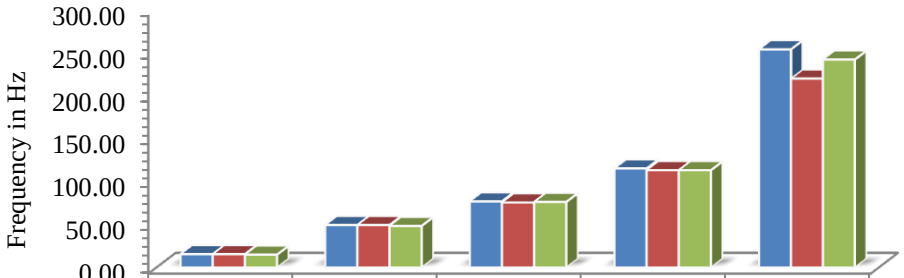

Mode Number	1	2	3	4	5
FE results with warping	15.42	49.32	76.87	115.17	253.82
FE results without warping	15.42	49.32	75.50	113.10	219.75
Measured values	14.75	48.26	76.13	113.10	241.90

Figure 5.14: Comparison between FE and experimental natural frequencies for double cracked angle section straight beam

Single crack has been considered at a distance 0.02 m from the fixed end of the cantilever beam with corresponding crack depth ratio 0.5. On the other hand, the double cracks are present at 0.02 m and 0.1 m from the fixed end of the cantilever beam. The corresponding crack depth ratios are 0.8 and 0.08 respectively. It can be noticed that the FE results are in good agreement with the experimental measurements, only when warping is considered in the model. The result indicates that consideration of warping in the theoretical model predicts a realistic behavior of the steel beam. The effect of warping is negligible in lower modes in case of angle section beams. However, such effect needs to be accounted while considering the higher modes. This statement is supported by the results in Figures 5.12, 5.13 and 5.14 where difference of FE results without considering warping and the measured values is noticeable in case of fifth mode. On the contrary, when warping is

considered FE results are in good agreement with experimentally measured values. The reduction of natural frequencies has been observed in all modes in both FE and experimental results, when crack is present. Comparison of natural frequencies of uncracked and cracked channel and angle section curved beam with 25° subtended angle for all configurations, as adopted in case of straight beams has been presented in Figures (5.15-5.20) respectively. Figure 5.15 and Figure 5.16 illustrate the comparison between finite element results and experimentally obtained first five natural frequencies for uncracked channel and angle section curved beam. Figure 5.17 and Figure 5.18 describe the single cracked scenario where crack located is at an angular distance (θ_{S1}) 0.625° from the fixed end of the beam with corresponding crack depth ratio 0.5. The double crack scenario for channel and angle section beam (i.e., θ_{S1} = 0.625°; θ_{S2} = 3.125° and corresponding ζ_1 /b = 0.8 and ζ_2 /b = 0.08) are presented in Figure 5.19 and Figure 5.20 respectively.

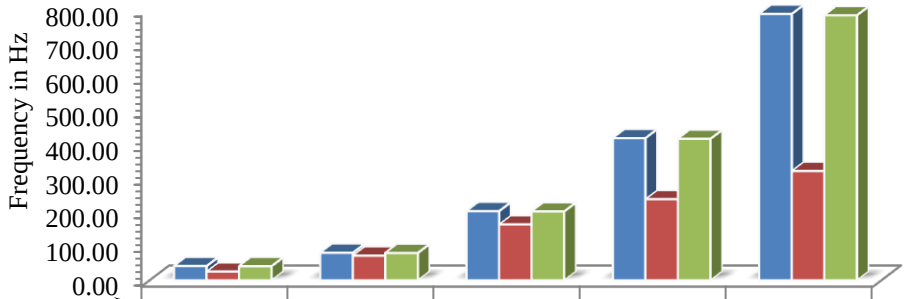

Mode Number	1	2	3	4	5
FE results with warping	41.85	81.21	204.29	419.97	787.98
FE results without warping	25.61	72.86	164.88	239.57	323.06
Measured values	41.50	80.80	203.25	417.87	784.00

Figure 5.15: Comparison between FE and experimental natural frequencies for curved channel section uncracked beam (θ_s = 25°, R = 1833.50 mm)

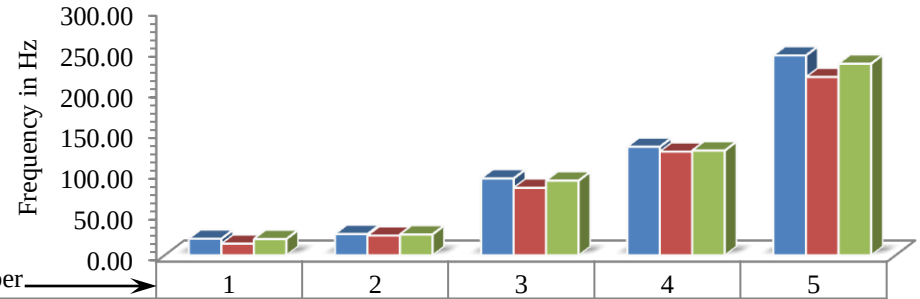

Mode Number	1	2	3	4	5
FE results with warping	20.23	25.92	93.80	132.42	244.17
FE results without warping	14.14	24.06	82.44	126.53	217.71
Measured values	19.87	25.46	91.13	127.83	233.99

Figure 5.16: Comparison between FE and experimental natural frequencies for curved angle section uncracked beam (θ_s = 25°, R = 1833.50 mm)

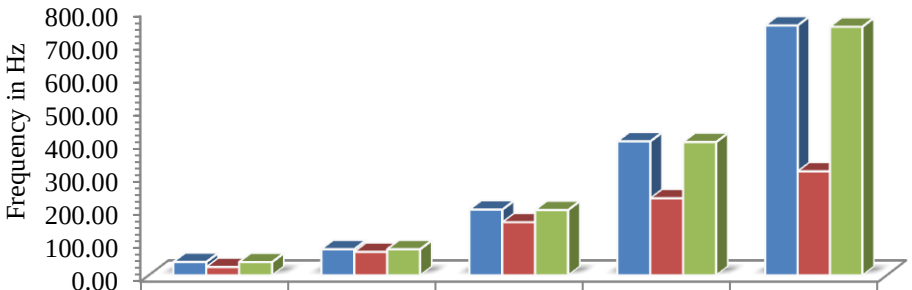

Mode Number	1	2	3	4	5
FE results with warping	39.94	78.86	198.19	404.53	753.54
FE results without warping	24.88	70.89	160.34	232.89	314.12
Measured values	39.73	78.45	197.14	402.39	749.56

Figure 5.17: Comparison between FE and experimental natural frequencies for curved single cracked channel section beam (θ_s = 25°, R = 1833.50 mm)

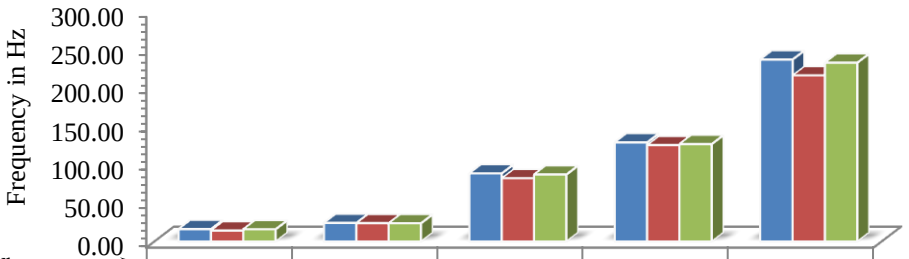

Mode Number	1	2	3	4	5
FE results with warping	15.99	23.96	88.32	128.61	236.40
FE results without warping	14.05	23.61	82.03	125.00	215.79
Measured values	15.71	23.55	86.80	126.40	232.33

Figure 5.18: Comparison between FE and experimental natural frequencies for curved single cracked angle section beam (θ_s = 25°, R = 1833.50 mm)

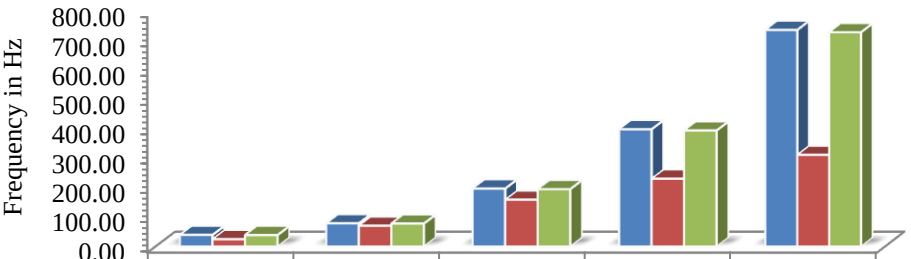

Mode Number	1	2	3	4	5
FE results with warping	39.00	78.48	196.95	398.69	735.01
FE results without warping	24.68	70.44	159.01	230.54	311.57
Measured values	38.59	77.65	194.86	394.47	727.23

Figure 5.19: Comparison between FE and experimental natural frequencies for curved double cracked channel section beam (θ_s = 25°, R = 1833.50 mm)

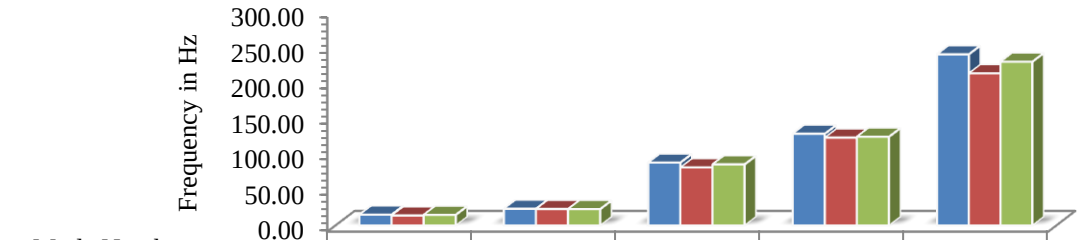

Mode Number →	1	2	3	4	5
FE results with warping	15.13	23.37	88.15	128.62	239.93
FE results without warping	13.96	23.08	81.39	123.19	213.36
Measured values	14.87	22.94	85.61	124.40	229.56

Figure 5.20: Comparison between FE and experimental natural frequencies for curved double cracked angle section beam (θ_s = 25°, R = 1833.50 mm)

Finite element results have been provided with and without warping effect in the curved beam. Like straight beams, natural frequencies of curved beam are also significantly affected by warping.

Figure 5.21 and Figure 5.22 show the comparison of the theoretical values with the experimentally measured results for the fundamental natural frequencies of the cantilever channel section straight and curved beam for uncracked and double cracked cases. Double crack in a beam has been considered at L_1 = 20 mm and L_2 = 100 mm in case of straight beam. For curved beam, keeping the peripheral location same as that for straight beam, the angular position of first crack θ_{S1} is 0.625° and second crack position θ_{S2} is 3.125° in a beam of subtended angle θ_s = 25°. In the beam of higher subtended angle θ_s =50°, the crack positions are at θ_{S1} = 1.250° and θ_{S2} = 6.250°. The angular distances are measured from the fixed end of the curved beam. The crack depth ratios for double cracked beams are ζ_1/b = 0.8 at first location and ζ_2/b = 0.5 for second location respectively.

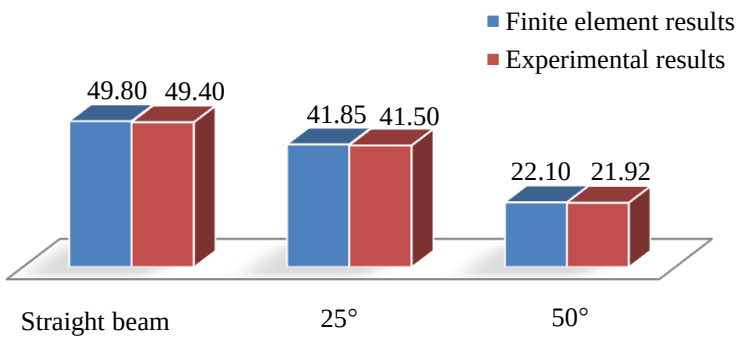

Figure 5.21: Comparison of theoretical values with experimental results for fundamental frequency (in Hz) of uncracked beam

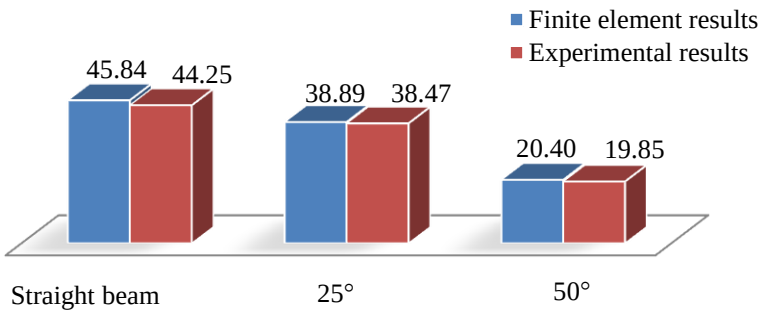

Figure 5.22: Comparison of theoretical values with experimental results for fundamental frequency (in Hz) of double cracked beam

In the bar plots, it can be observed that the numerical results are close to the experimental values. Also the results indicate that, as the subtended angle (θ_s) increases, the fundamental natural frequencies decreases in both uncracked and cracked beams.

5.5 Stress intensity factor

One of the relevant fracture parameter is the stress intensity factor (SIF), which represents intensification of the stress near the tip of a crack caused by a remote load. The normalized first mode stress intensity factor verses crack depth ratio for cracked channel section beam has been shown in Figure 5.23(a) under moment and bi-moment. Figure 5.23(b) describes the normalized first mode stress intensity factor due to moment. Similarly, the normalized first mode stress intensity factor verses crack depth ratio for cracked angle section beam has been presented in Figure 5.24(a) under moment and bi-moment. Figure 5.24(b) describes the normalized first mode stress intensity factor in angle section due to moment.

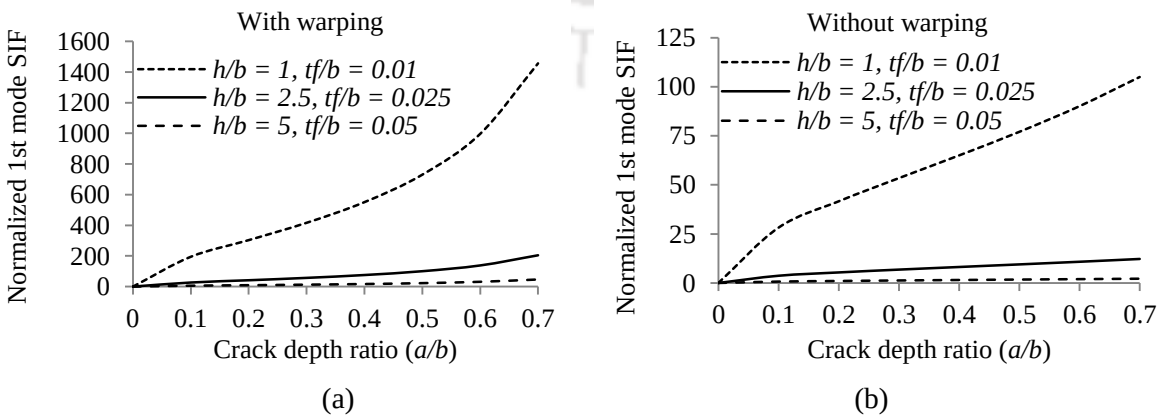

Figure 5.23: Normalized 1st mode SIF for channel section cracked beam under: (a) Moment and bimoment, (b) Moment

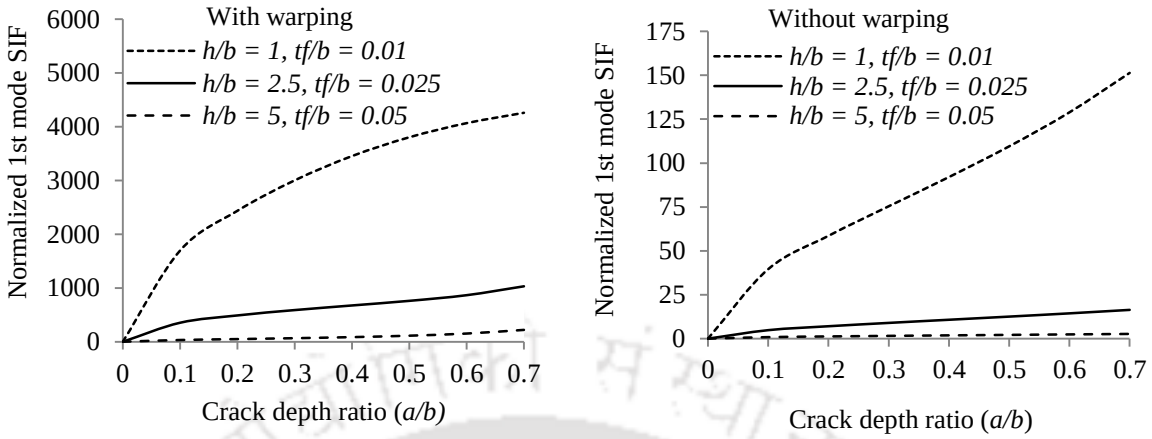

Figure 5.24: Normalized 1st mode SIF for angle section cracked beam under: (a) Moment and bimoment, (b) Moment

From the figures it can observed that the normalized stress intensity factor increases with the increase of crack depth ratio and decreases with the increase of non-dimensional flange thickness (t_f / b) and non-dimensional web height (h / b). It is found that the warping condition yields higher value of normalized first mode stress intensity factor compared to that of the condition where warping is not considered. It may also be noted that angle section shows higher values of SIF compared to channel section. It may also be worth to note that for wide flange of channel or outstand leg of angle section SIF values are significantly higher. SIF for different modes of fracture is used to develop the line spring element stiffness matrix representing a crack.

5.6 Bandwidth of frequency response curve

It has been found in the previous section that the peak of frequency response curves (FRC) shifts towards left in case of cracked beam and this shifting of peak tells about the existence of crack. Based on this observation, further insight is given to obtain the difference in modal features of cracked and uncracked beam by finding the bandwidth of the FRC obtained experimentally. The bandwidth is calculated as the difference of the upper and lower cutoff frequencies obtained at 0.707 of the resonance peaks termed as half power points [207]. The bandwidth of channel and angle beam with crack depth ratio varying from 0.08 to 0.8 has been compared with that of an uncracked beam in Table 5.5 to Table 5.8.

Table 5.5: Bandwidth of FRC for uncracked and cracked channel section straight beam

Mode No.	Crack Location	Crack depth ratio	Bandwidth (Δf) in Hz	
			Uncracked	Cracked
		Straight beam		
1	Uncracked	-	0.09	
2	beam	-	0.08	
1	L_1 = 0.02	ζ_1/b = 0.08		0.18
		ζ_1/b = 0.50		0.10
		ζ_1/b = 0.80		0.20
2	L_1 = 0.02	ζ_1/b = 0.08		0.14
		ζ_1/b = 0.50		0.09
		ζ_1/b = 0.80		0.09
1	L_1 = 0.50	ζ_1/b = 0.08		0.10
		ζ_1/b = 0.50		0.10
		ζ_1/b = 0.80		0.10
2	L_1 = 0.50	ζ_1/b = 0.08		0.09
		ζ_1/b = 0.50		0.25
		ζ_1/b = 0.80		0.10
1	L_1 = 0.02, L_2 =0.10	ζ_1/b = 0.50, ζ_2/b =0.80		0.18
		ζ_1/b = 0.80, ζ_2/b =0.08		0.10
2	L_1 = 0.02, L_2 =0.10	ζ_1/b = 0.50, ζ_2/b =0.80		0.14
		ζ_1/b = 0.80, ζ_2/b =0.08		0.11
1	L_1 = 0.50, L_2 =0.60	ζ_1/b = 0.50, ζ_2/b =0.80		0.10
		ζ_1/b = 0.80, ζ_2/b =0.08		0.10
2	L_1 = 0.50, L_2 =0.60	ζ_1/b = 0.50, ζ_2/b =0.80		0.11
		ζ_1/b = 0.80, ζ_2/b =0.08		0.11

Table 5.6: Bandwidth of FRC for uncracked and cracked channel section curved beam (θ_s = 25°)

Mode No.	Crack Location	Crack depth ratio	Bandwidth (Δf) in Hz	
			Uncracked	Cracked
1	Uncracked	-	0.15	
2	beam	-	0.13	
1	θ_{S1} = 0.625°	ζ_1/b = 0.08		0.18
		ζ_1/b = 0.50		0.21
		ζ_1/b = 0.80		0.18
2	θ_{S1} = 0.625°	ζ_1/b = 0.08		0.17
		ζ_1/b = 0.50		0.16
		ζ_1/b = 0.80		0.23
1	θ_{S1} =15.625°	ζ_1/b = 0.08		0.18
		ζ_1/b = 0.50		0.20
		ζ_1/b = 0.80		0.16
2	θ_{S1} =15.625°	ζ_1/b = 0.08		0.18
		ζ_1/b = 0.50		0.27
		ζ_1/b = 0.80		0.20
1	θ_{S1} = 0.625°, θ_{S2} = 3.125°	ζ_1/b = 0.50, ζ_2/b =0.80		0.20
		ζ_1/b = 0.80, ζ_2/b =0.08		0.19
2	θ_{S1} = 0.625°, θ_{S2} = 3.125°	ζ_1/b = 0.50, ζ_2/b =0.80		0.16
		ζ_1/b = 0.80, ζ_2/b =0.08		0.18
1	θ_{S1} = 15.625°, θ_{S2} = 18.750°	ζ_1/b = 0.50, ζ_2/b =0.80		0.19
		ζ_1/b = 0.80, ζ_2/b =0.08		0.21
2	θ_{S1} = 15.625°, θ_{S2} = 18.750°	ζ_1/b = 0.50, ζ_2/b =0.80		0.23
		ζ_1/b = 0.80, ζ_2/b =0.08		0.15

Table 5.7: Bandwidth of FRC for uncracked and cracked angle section straight beam

Mode No.	Crack Location	Crack depth ratio	Bandwidth (Δf) in Hz	
			Uncracked	Cracked
		Straight beam		
1	Uncracked	-	0.22	
2	beam	-	0.18	
1	$L_1 = 0.02$	$\zeta_1/b = 0.08$		0.25
		$\zeta_1/b = 0.50$		0.24
		$\zeta_1/b = 0.80$		0.23
2	$L_1 = 0.02$	$\zeta_1/b = 0.08$		0.19
		$\zeta_1/b = 0.50$		0.22
		$\zeta_1/b = 0.80$		0.20
1	$L_1 = 0.50$	$\zeta_1/b = 0.08$		0.23
		$\zeta_1/b = 0.50$		0.25
		$\zeta_1/b = 0.80$		0.24
2	$L_1 = 0.50$	$\zeta_1/b = 0.08$		0.20
		$\zeta_1/b = 0.50$		0.19
		$\zeta_1/b = 0.80$		0.21
1	$L_1 = 0.02$, $L_2 = 0.10$	$\zeta_1/b = 0.50$, $\zeta_2/b = 0.80$		0.24
		$\zeta_1/b = 0.80$, $\zeta_2/b = 0.08$		0.23
2	$L_1 = 0.02$, $L_2 = 0.10$	$\zeta_1/b = 0.50$, $\zeta_2/b = 0.80$		0.20
		$\zeta_1/b = 0.80$, $\zeta_2/b = 0.08$		0.26
1	$L_1 = 0.50$, $L_2 = 0.60$	$\zeta_1/b = 0.50$, $\zeta_2/b = 0.80$		0.23
		$\zeta_1/b = 0.80$, $\zeta_2/b = 0.08$		0.24
2	$L_1 = 0.50$, $L_2 = 0.60$	$\zeta_1/b = 0.50$, $\zeta_2/b = 0.80$		0.20
		$\zeta_1/b = 0.80$, $\zeta_2/b = 0.08$		0.19

Table 5.8: Bandwidth of FRC for uncracked and cracked angle section curved beam ($\theta_s = 25°$)

Mode No.	Crack Location	Crack depth ratio	Bandwidth (Δf) in Hz	
			Uncracked	Cracked
1	Uncracked	-	0.20	
2	beam	-	0.11	
1	$\theta_{S1} = 0.625°$	$\zeta_1/b = 0.08$		0.21
		$\zeta_1/b = 0.50$		0.25
		$\zeta_1/b = 0.80$		0.22
2	$\theta_{S1} = 0.625°$	$\zeta_1/b = 0.08$		0.14
		$\zeta_1/b = 0.50$		0.18
		$\zeta_1/b = 0.80$		0.19
1	$\theta_{S1} = 15.625°$	$\zeta_1/b = 0.08$		0.22
		$\zeta_1/b = 0.50$		0.21
		$\zeta_1/b = 0.80$		0.23
2	$\theta_{S1} = 15.625°$	$\zeta_1/b = 0.08$		0.15
		$\zeta_1/b = 0.50$		0.25
		$\zeta_1/b = 0.80$		0.22
1	$\theta_{S1} = 0.625°$, $\theta_{S2} = 3.125°$	$\zeta_1/b = 0.50$, $\zeta_2/b = 0.80$		0.21
		$\zeta_1/b = 0.80$, $\zeta_2/b = 0.08$		0.22
2	$\theta_{S1} = 0.625°$, $\theta_{S2} = 3.125°$	$\zeta_1/b = 0.50$, $\zeta_2/b = 0.80$		0.14
		$\zeta_1/b = 0.80$, $\zeta_2/b = 0.08$		0.20
1	$\theta_{S1} = 15.625°$, $\theta_{S2} = 18.750°$	$\zeta_1/b = 0.50$, $\zeta_2/b = 0.80$		0.22
		$\zeta_1/b = 0.80$, $\zeta_2/b = 0.08$		0.23
2	$\theta_{S1} = 15.625°$, $\theta_{S2} = 18.750°$	$\zeta_1/b = 0.50$, $\zeta_2/b = 0.80$		0.14
		$\zeta_1/b = 0.80$, $\zeta_2/b = 0.08$		0.16

The results are given for straight and curved beam. The results obtained from curved beams with subtended angle θ_s = 25° are only presented here. The results show that the bandwidth increases in case of single and multiple cracked beam. This can be attributed to the fact that there is increased dissipation of vibration energy in presence of crack.

5.7 Effect of crack on mode shape vectors

Mode shape of a vibrating system is a specific pattern of motion in which all parts of the system exhibit harmonic motion with same frequency. In discrete model of beam consisting of *n* degrees of freedom, there will have *n* number of corresponding mode shapes. Each mode shape of cracked and uncracked beam is an independent and normalized displacement pattern. Two different examples (straight and curved beam) are used to show the effect of crack on mode shape vectors. Mode shapes of cracked beams (single and double) are shown along with mode shapes of uncracked beams in the following cases:

Channel section straight beams with single crack: Figure 5.25(a-e) and Figure 5.26(a-e) represent the first five bending and torsional mode shapes of uncracked and single cracked channel section straight beam respectively. In case of single crack, the crack was introduced at a distance (L_1) = 0.02 m from the fixed end while crack depth ratio (ζ_1 /b) = 0.5 has been considered. Coupling of bending and torsion are weak in lower modes, however, significant coupling occurs in higher modes. Location of crack is apparent from a discontinuity in fourth and fifth bending mode shape at crack location. No difference can be noticed in the position of nodes in bending mode shapes. However, there is a slight shift of one of the nodes in fourth torsional mode shape of cracked beam.

Channel section straight beams with double cracks: Figure 5.27 (a-e) and Figure 5.28 (a-e) shows the first five bending and torsional modes of uncracked and double cracked channel beam respectively. It is to be noted that the double cracks were considered at L_1 = 0.50 m and L_2 = 0.60 m from the fixed end of the cantilever beam where corresponding first crack depth ratio (ζ_1 /b) is 0.5 and second crack depth ratio (ζ_2 /b) is 0.8 respectively. Presence of crack results in discontinuity of mode shape. However, this is only visible in third and fifth bending mode. Discontinuity of mode shape in double cracked beam is more clearly visible compared to single cracked channel beam in third, fourth and fifth bending as well as torsional mode shapes.

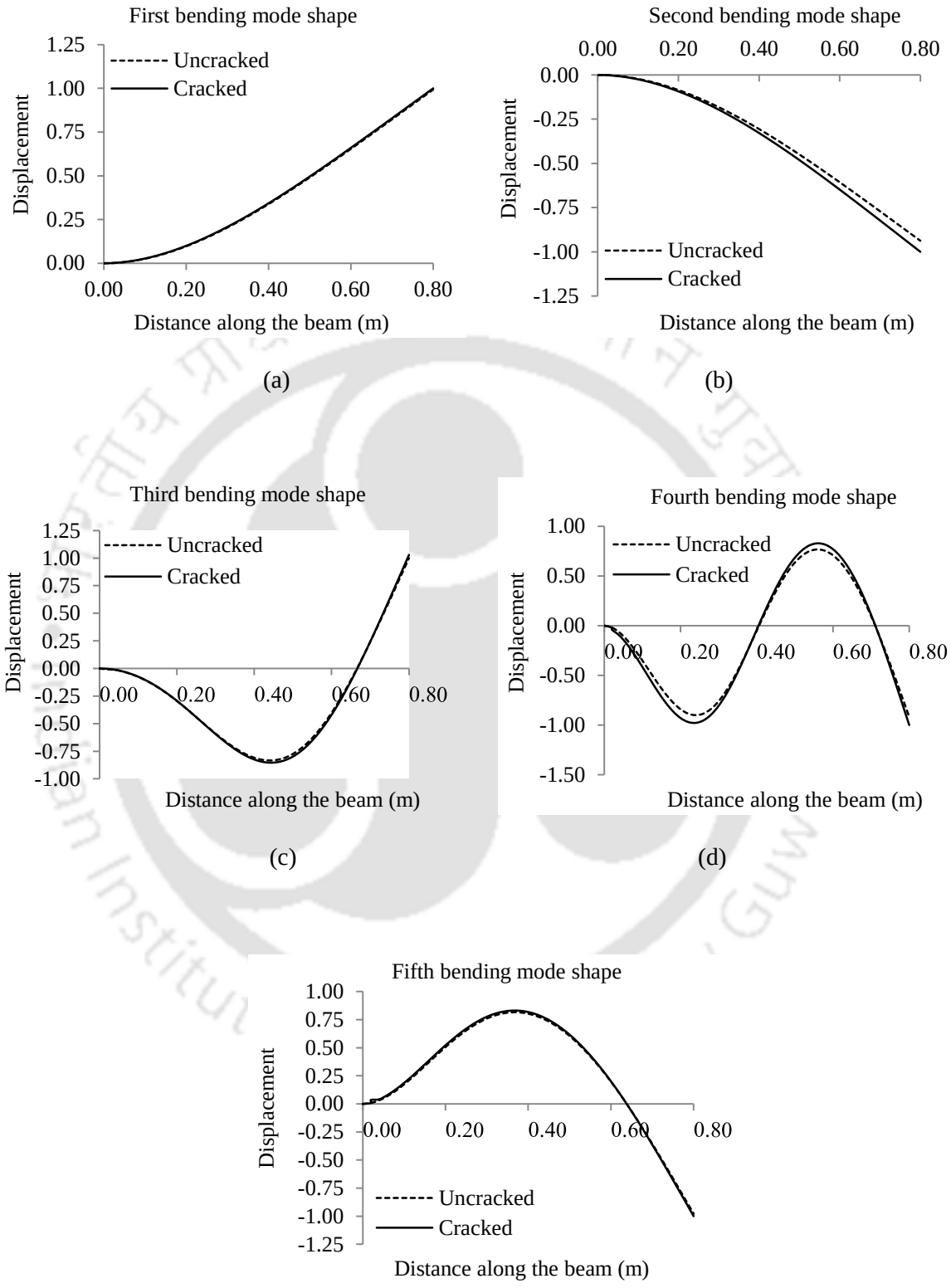

Figure 5.25: First five bending modes for uncracked and single cracked channel section cantilever straight beam

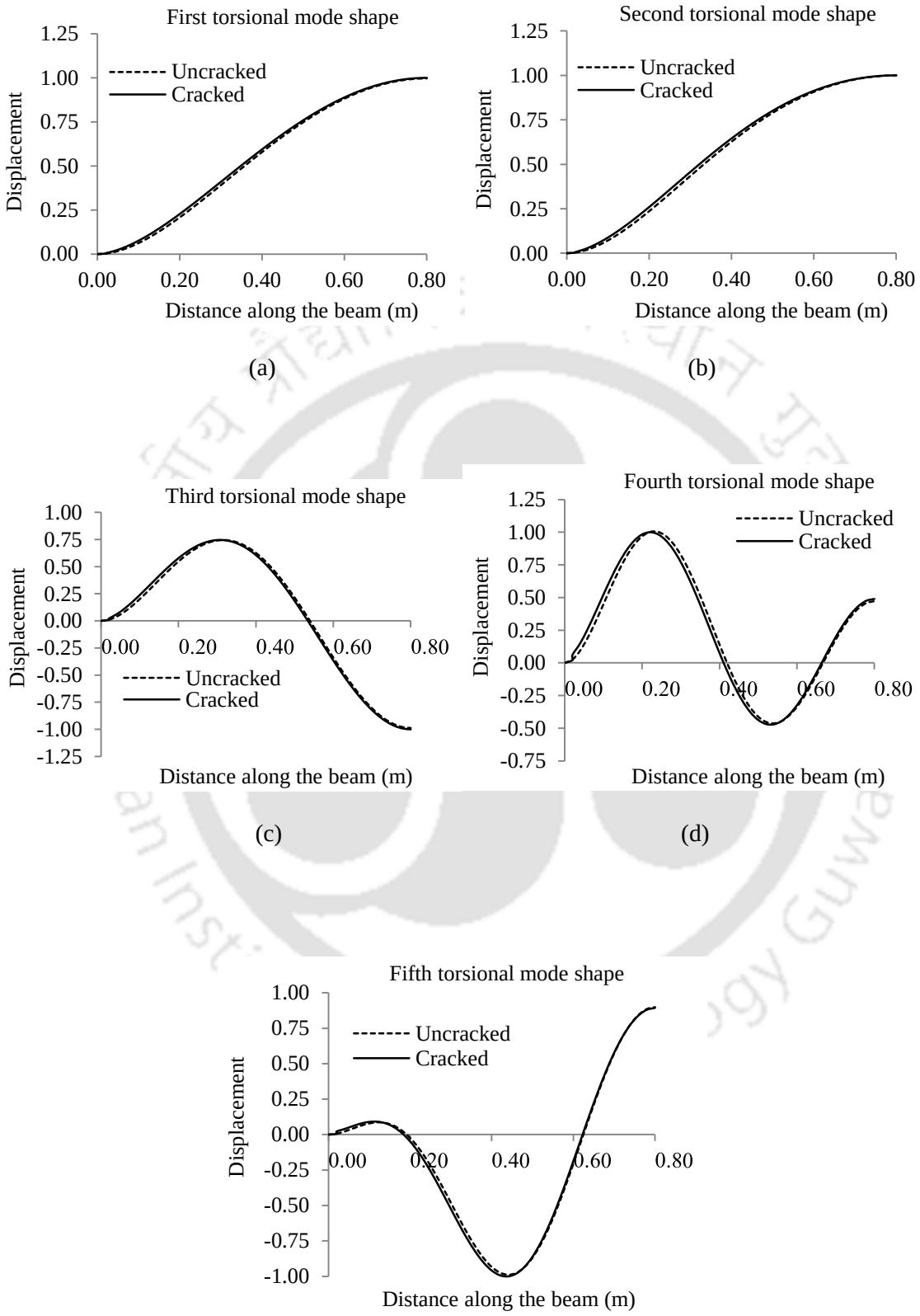

Figure 5.26: First five torsional modes for uncracked and single cracked channel section cantilever straight beam

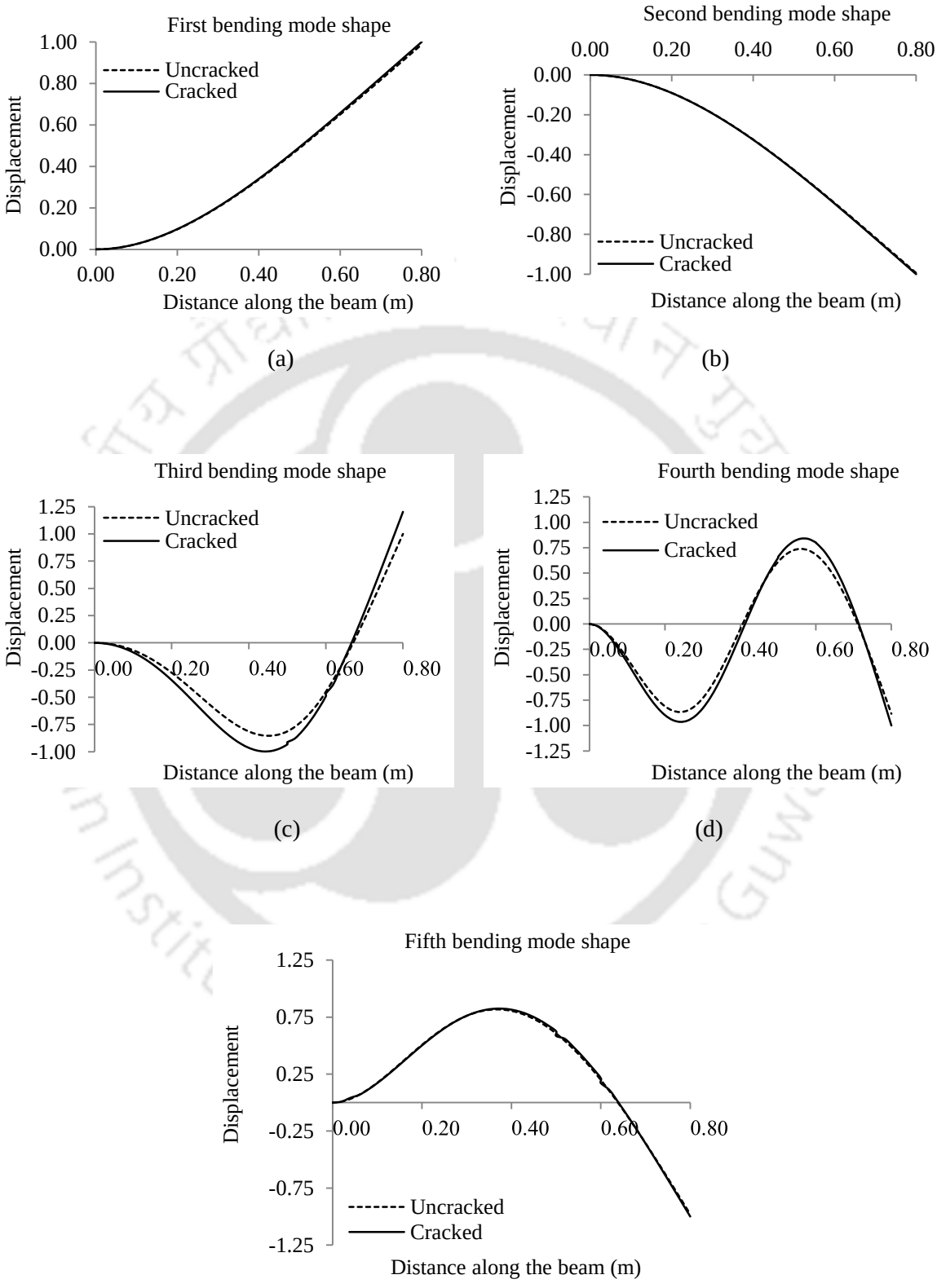

Figure 5.27: First five bending modes for uncracked and double cracked channel section cantilever straight beam

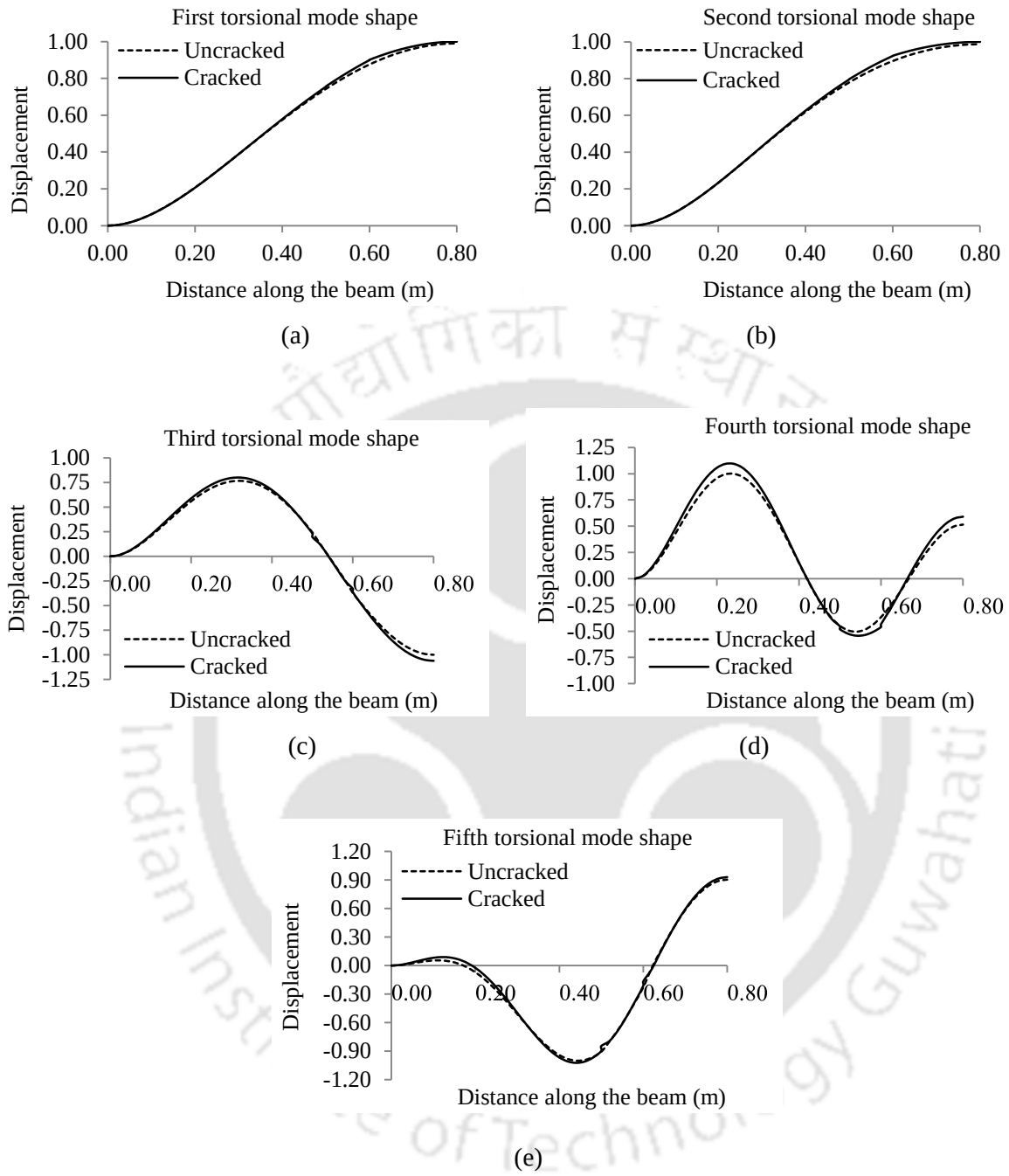

Figure 5.28: First five torsional modes for uncracked and double cracked channel section cantilever straight beam

Angle section straight beams with single crack: First five bending and torsional modes of an angle section cantilever beam with single crack are shown in Figure 5.29 (a-e) and 5.30 (a-e). Same crack parameters as in channel straight beam have been taken. There is strong coupling between bending and torsional modes as usual feature of mode shape in independent bending and torsion is not seen. In this case, although difference in magnitude of displacement of cracked and uncracked beam are observed clearly compared to channel

beam from second mode onward, but crack location cannot be ascertained clearly from mode shape plot.

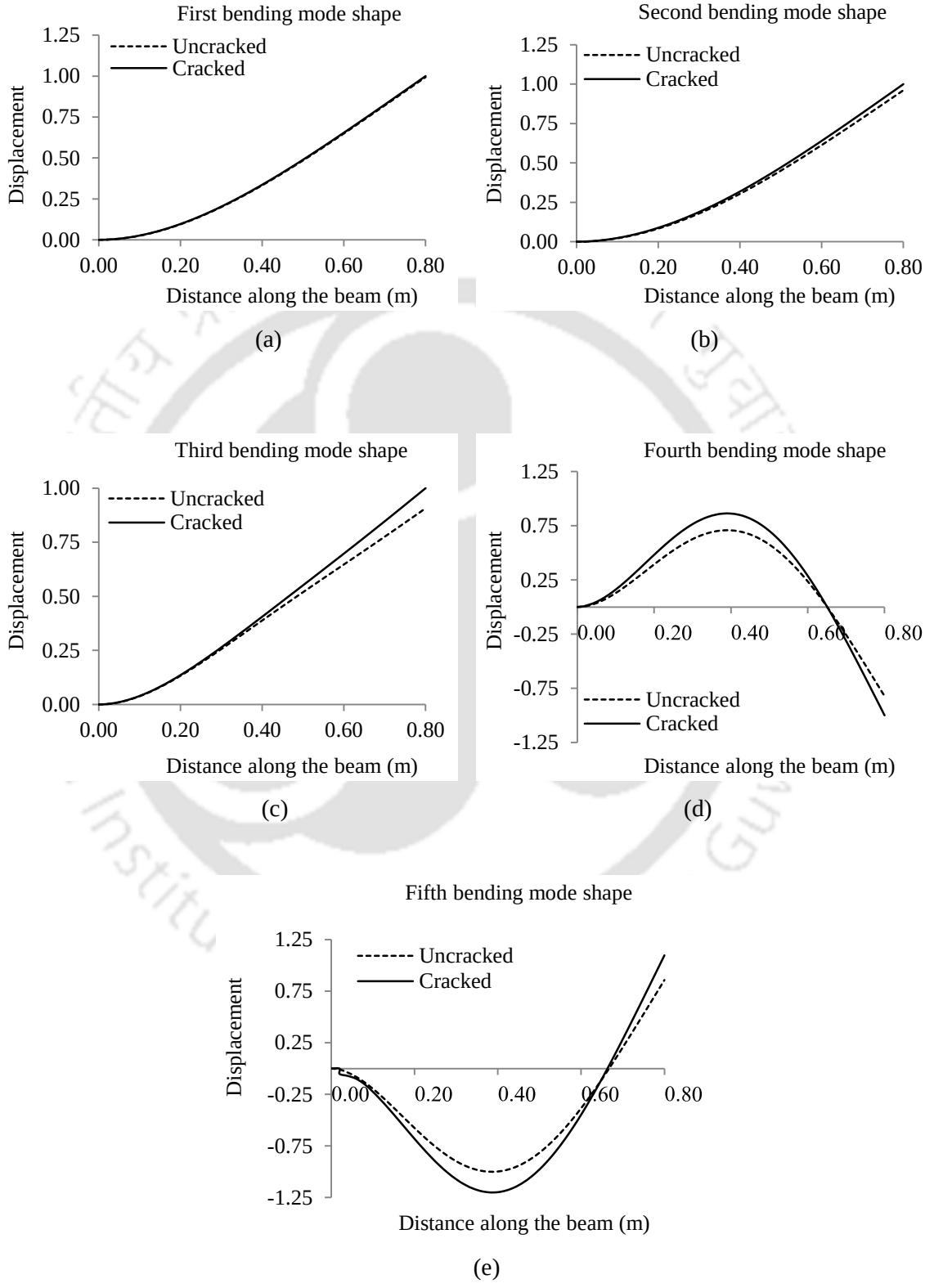

Figure 5.29: First five bending modes for uncracked and single cracked angle section cantilever straight beam

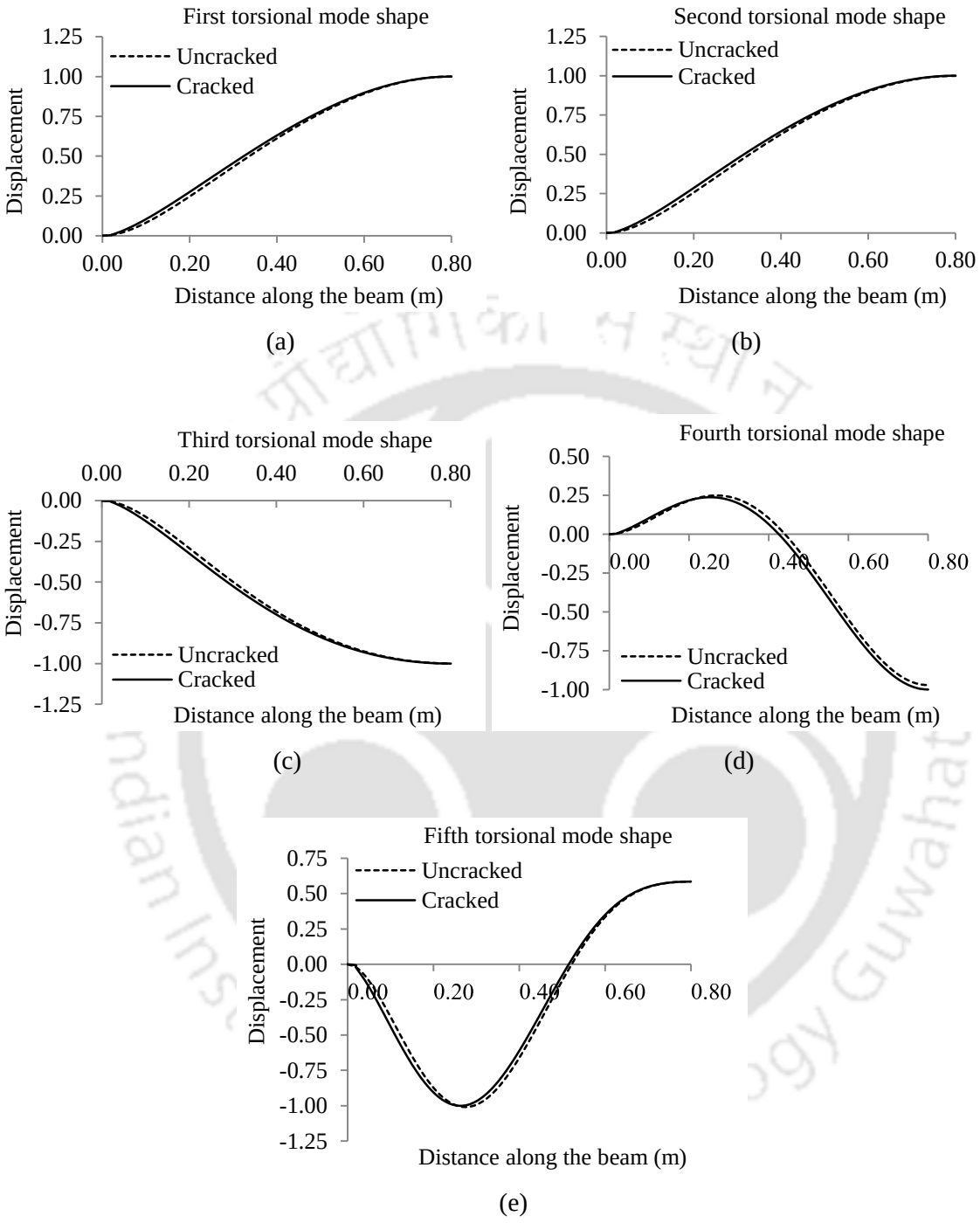

Figure 5.30: First five torsional modes for uncracked and single cracked angle section cantilever straight beam

Angle section straight beams with double crack: Figure 5.31 (a-e) and Figure 5.32 (a-e) show the first five bending and torsional modes of uncracked and double cracked angle beam respectively. Same locations of crack and same depth as in channel beam were considered here also. In the fifth mode of bending and torsion, discontinuity in mode shape

of the cracked beam appears at crack location. No specific inference can be drawn about the crack severity.

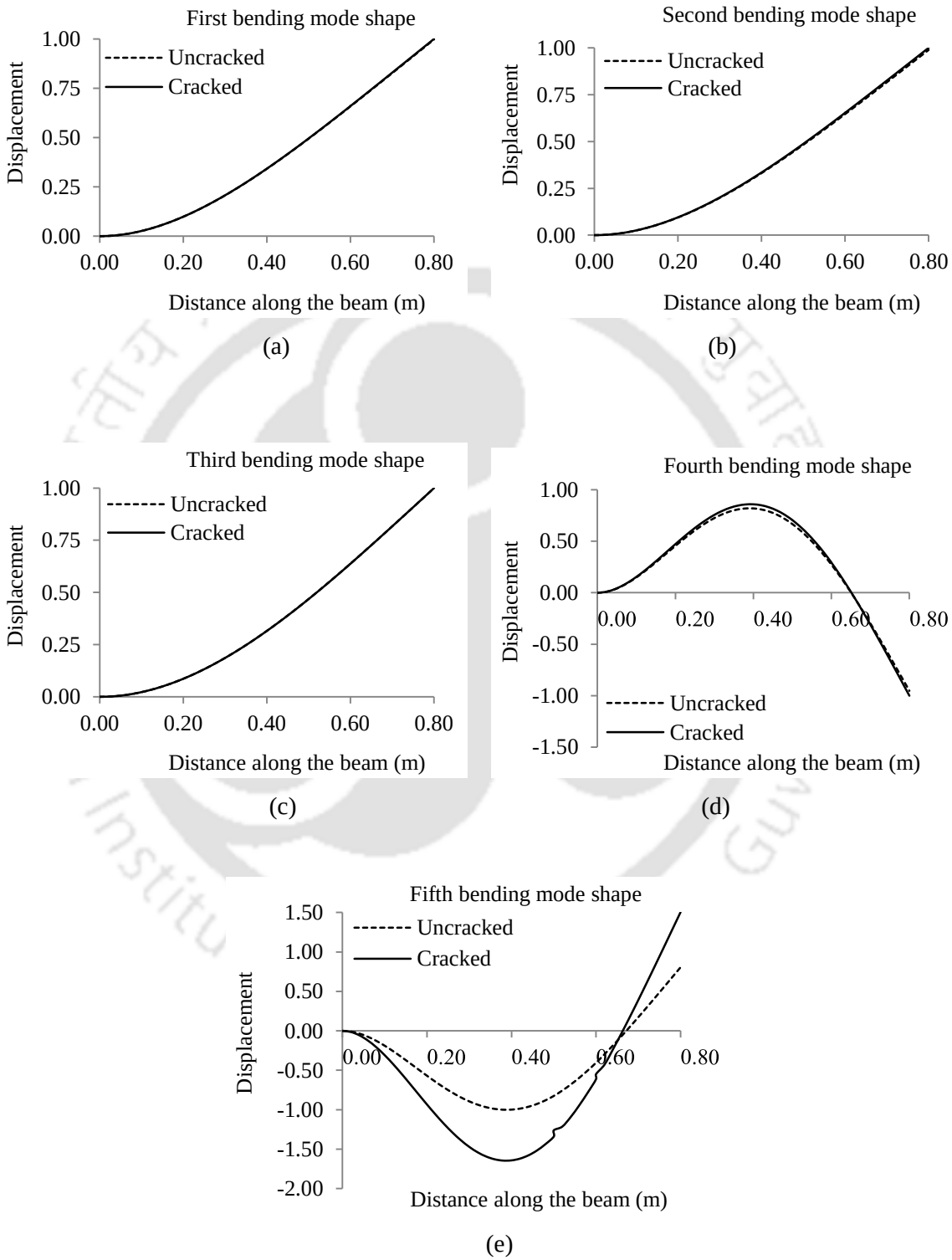

Figure 5.31: First five bending modes for uncracked and double cracked angle section cantilever straight beam

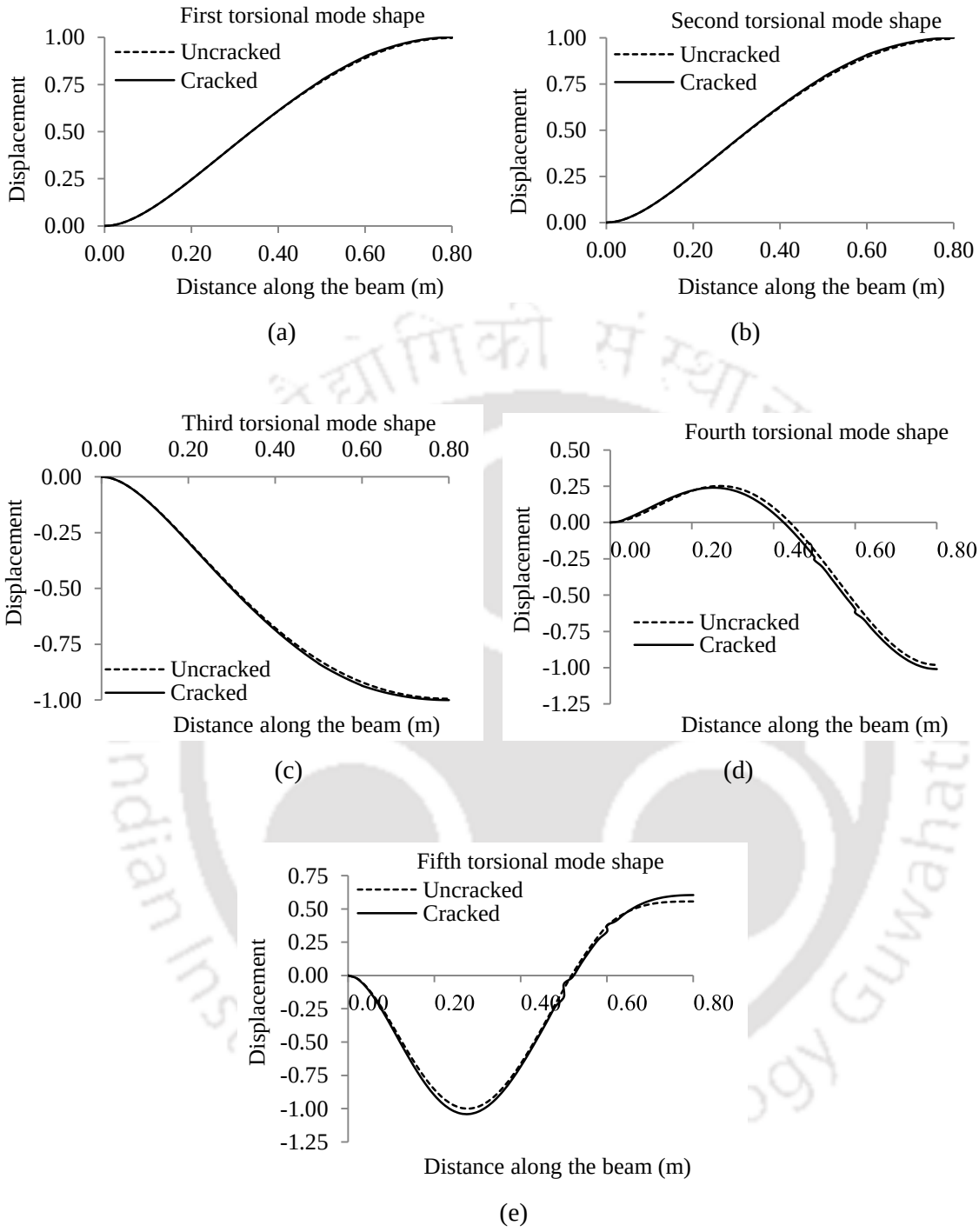

Figure 5.32: First five torsional modes for uncracked and double cracked angle section cantilever straight beam

Channel section curved beams with single crack: Bending and torsional mode shapes of first five modes are presented in Figure 5.33 (a-e) and 5.34 (a-e) respectively. The channel beam has curvature with subtended angle θ_s = 25°. The crack location is at angular distance of θ_{S1} = 0.625° and crack depth ratio is 0.5. The fundamental mode shape in both straight and curved beams is similar and reflects independent motions. However, second mode onwards

strong coupling of bending and torsion is apparent. Slight discontinuity is noted in fourth and fifth mode shape very near to support indicating the location of the crack in this particular case.

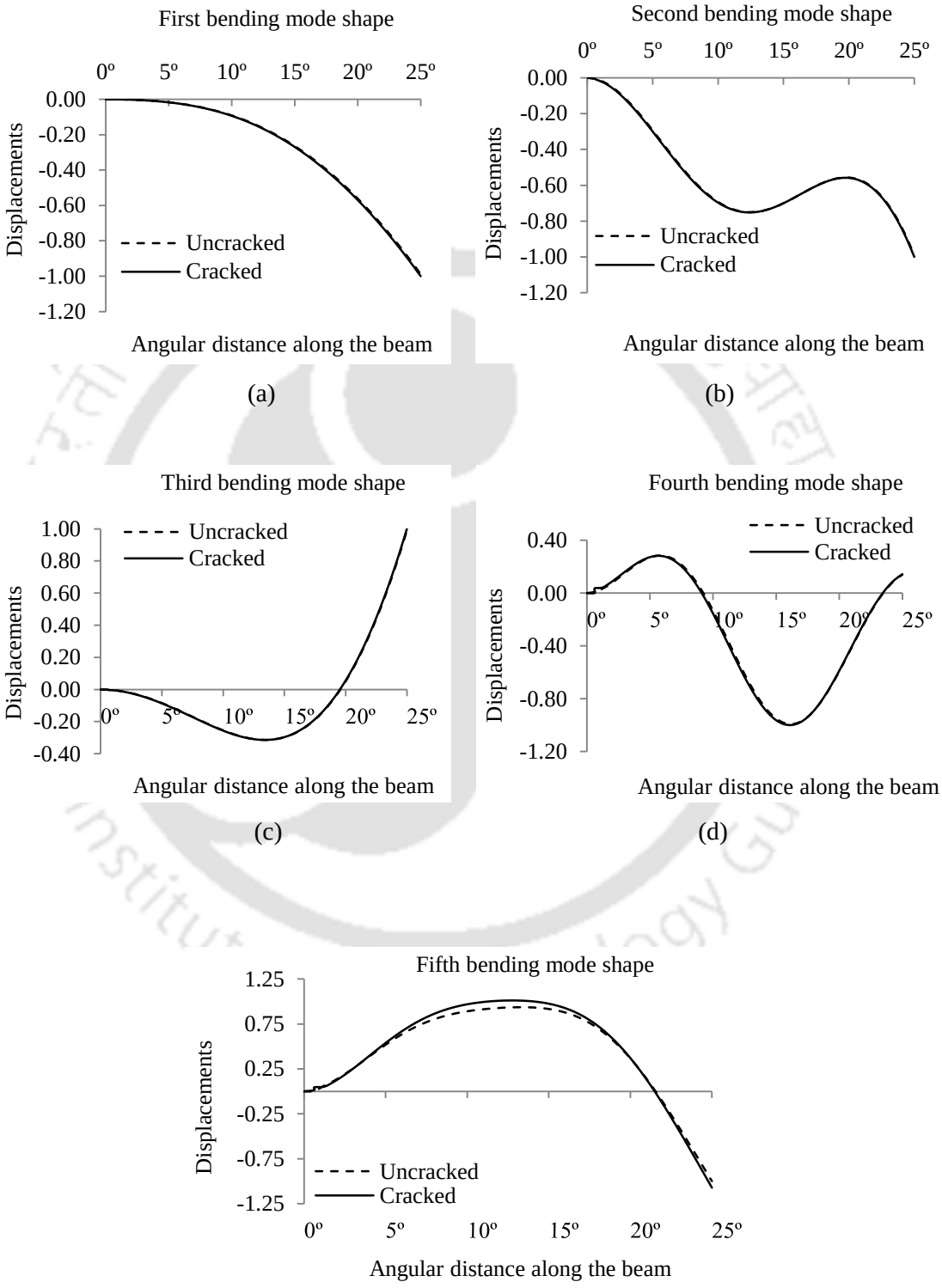

Figure 5.33: First five bending modes for uncracked and single cracked channel section curved beam (θ_s = 25°, R = 1833.50 mm)

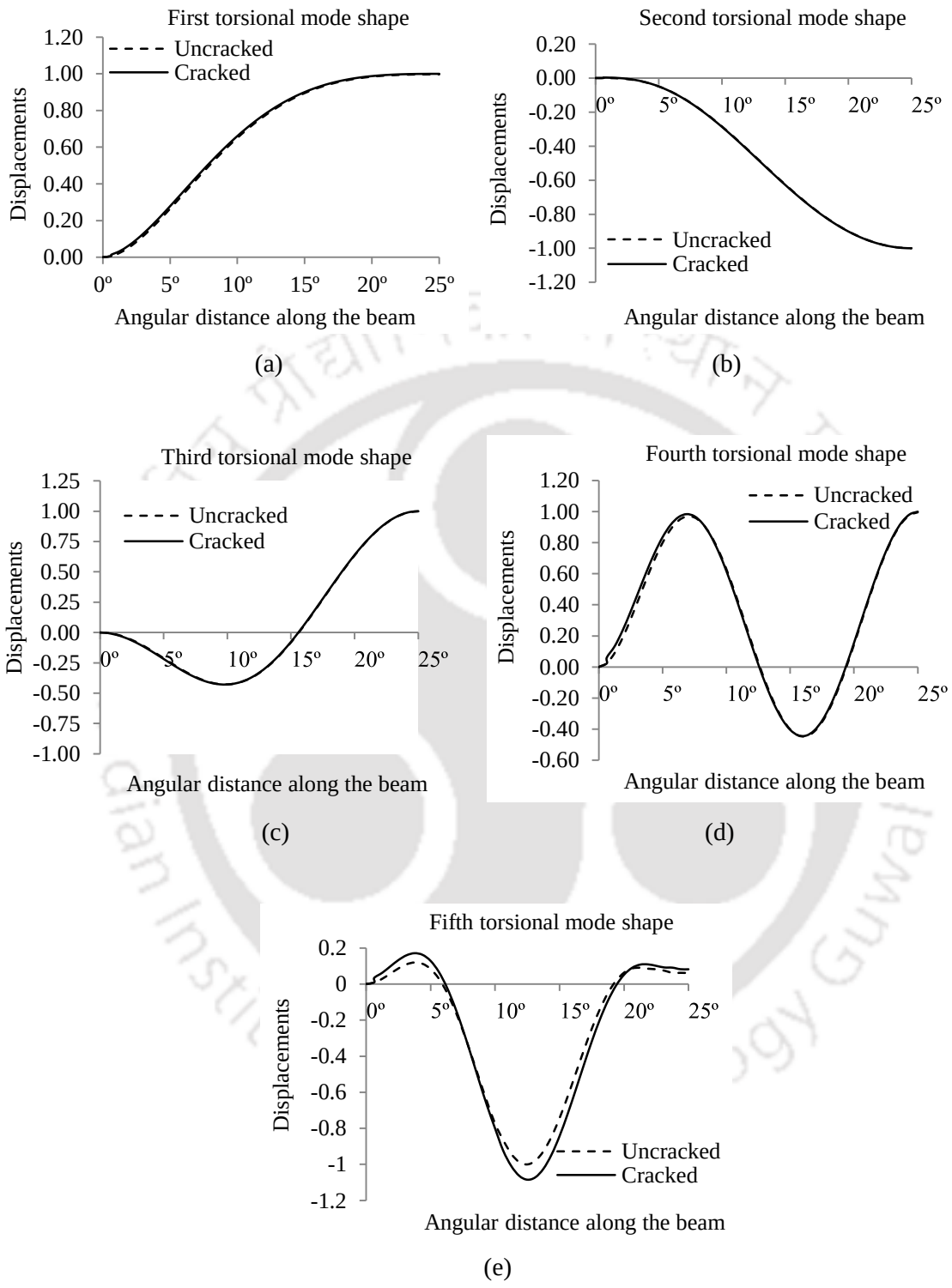

Figure 5.34: First five torsional modes for uncracked and single cracked channel section curved beam (θ_s = 25°, R = 1833.50 mm)

Channel section curved beams with double cracks: Figure 5.35 (a-e) and 5.36 (a-e) present the bending and torsional mode shape respectively for the channel section curved beams with double cracks. The subtended angle is θ_s = 25° where as two cracks are located at θ_{S1} =

15.625° and θ_{S2} = 18.750° with corresponding crack depth ratio 0.5 and 0.8 respectively. Here, strong coupling of bending and torsion is evident from second and other higher modes as the mode shape does not appear in the manner as found in the independent bending and torsional mode. Discontinuity of the mode shape of the cracked beam is visible at crack location more clearly in higher bending modes.

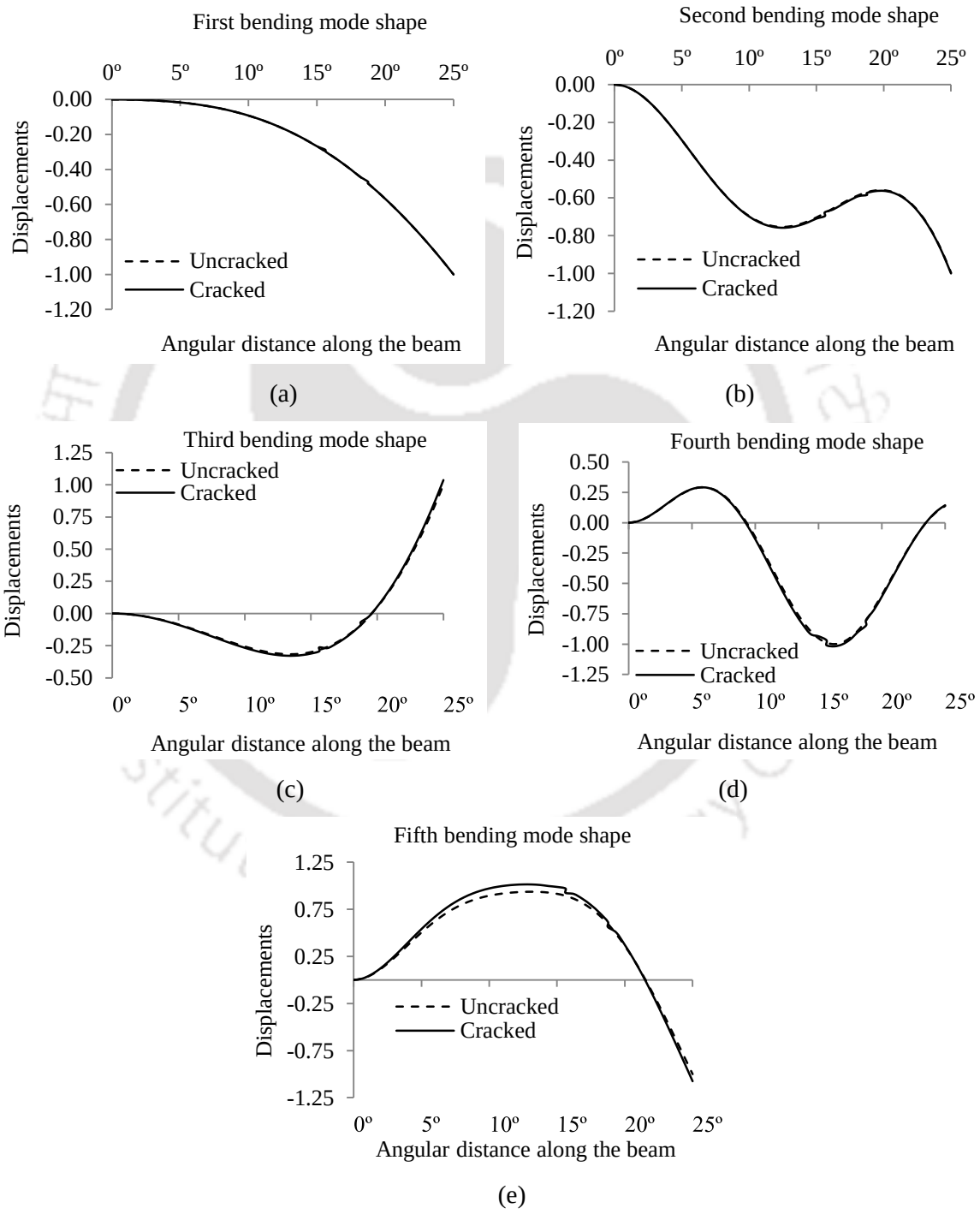

Figure 5.35: First five bending modes for uncracked and double cracked channel section curved beam (θ_s = 25°, R = 1833.50 mm)

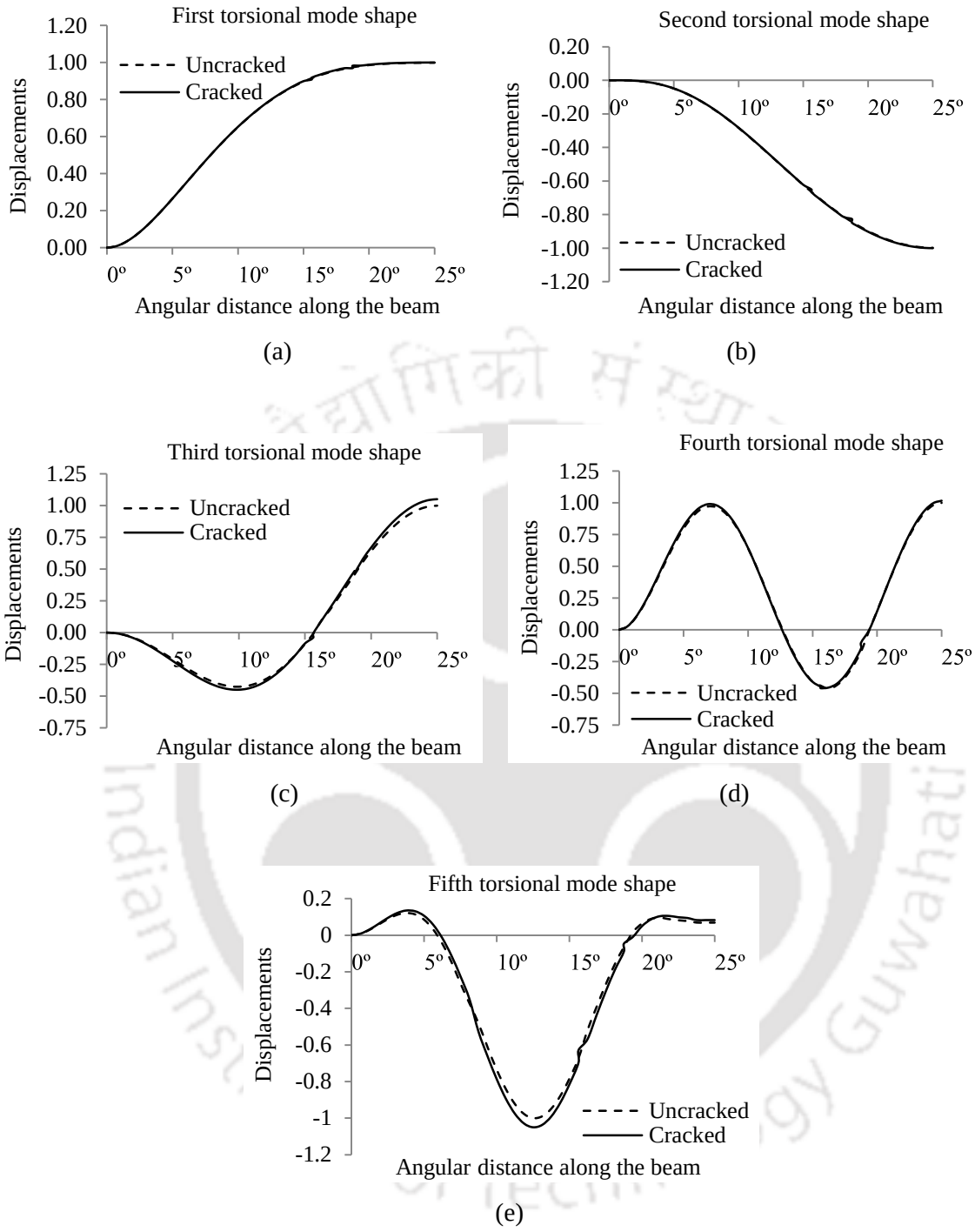

Figure 5.36: First five torsional modes for uncracked and double cracked channel section curved beam (θ_s = 25°, R = 1833.50 mm)

Angle section curved beam with single crack: Figure 5.37 (a-e) and 5.38 (a-e) show the bending and torsional mode shape for the angle section curved beams with single crack respectively. A single crack very near to support as in the case of channel section curved beam has been considered. There is considerable difference in the appearance of mode shape of angle curved beam as compared to channel curved beam suggestive of stronger

coupling as the section is unsymmetrical about both the centroidal axis. There is considerable shifting of node in fourth bending modes.

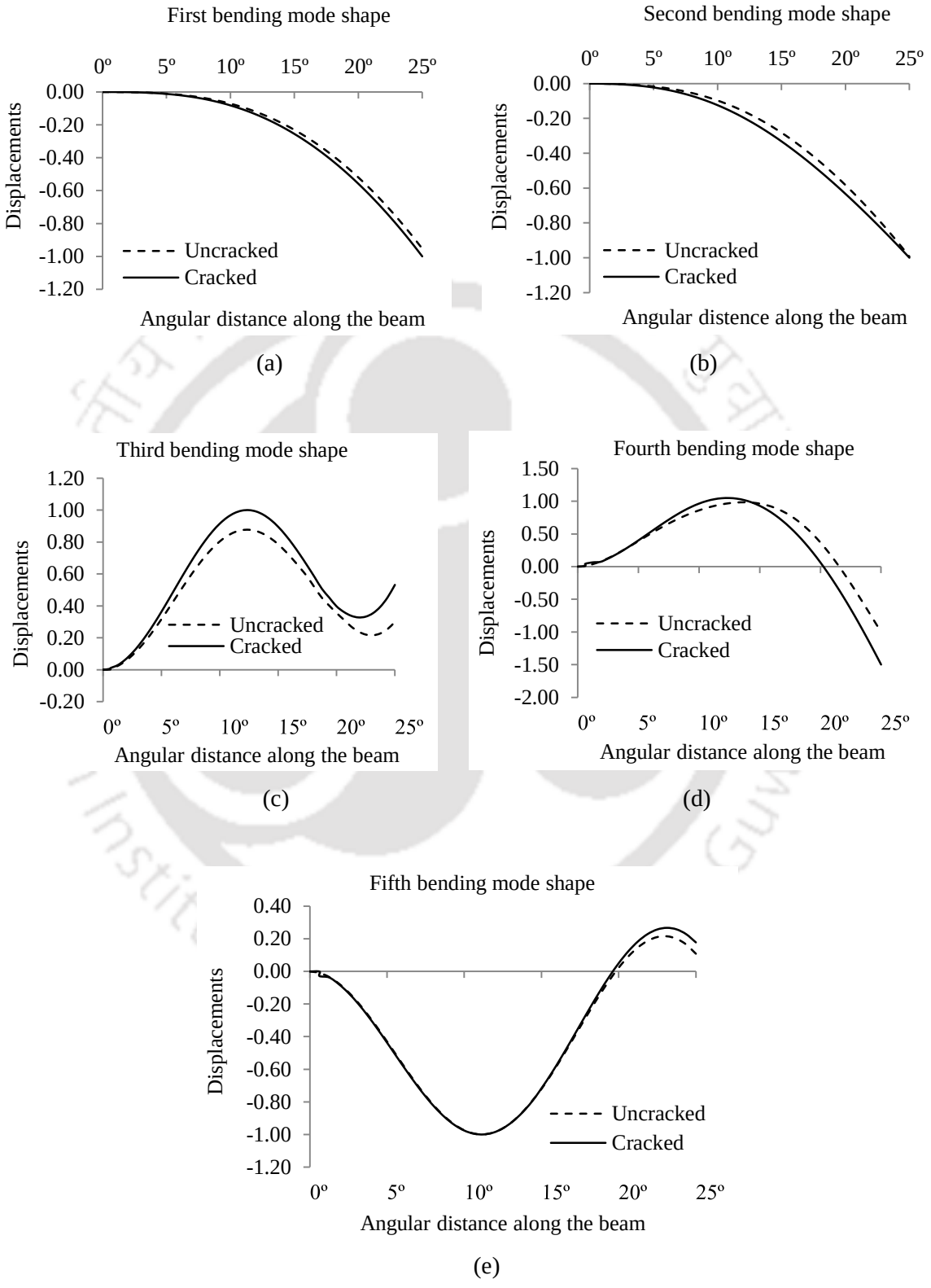

Figure 5.37: First five bending modes for uncracked and single cracked angle section curved beam (θ_s = 25°, R = 1833.50 mm)

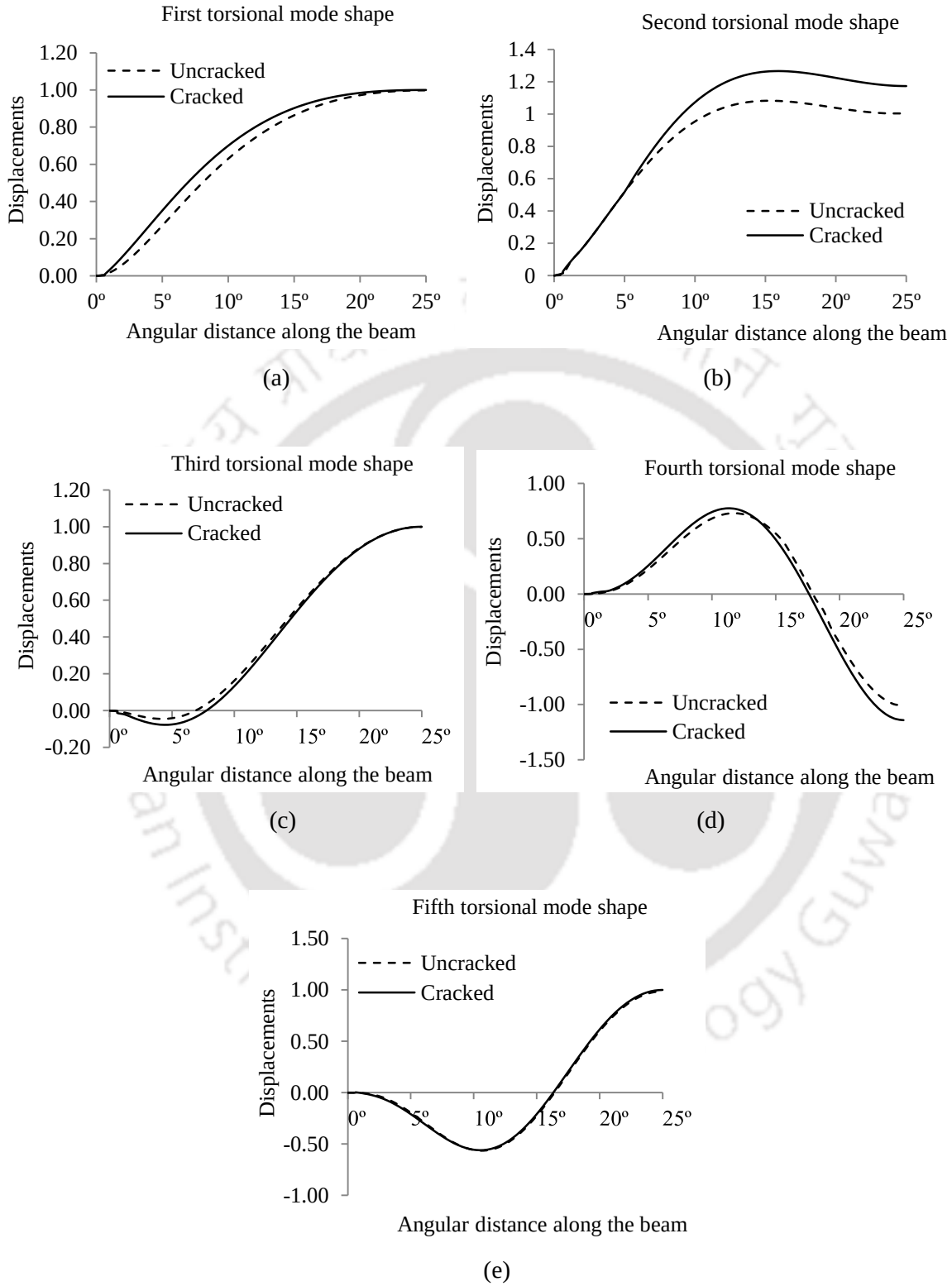

Figure 5.38: First five torsional modes for uncracked and single cracked angle section curved beam (θ_s = 25°, R = 1833.50 mm)

Angle section curved beam with double cracks: Bending and torsional modes of angle section beam with two cracks are shown in Figure 5.39(a-e) and 5.40 (a-e) respectively. Two cracks are considered at the locations same as that for the channel beam. In this case, discontinuity in cracked beam mode shape is visible more clearly at crack locations compared to channel curved beam.

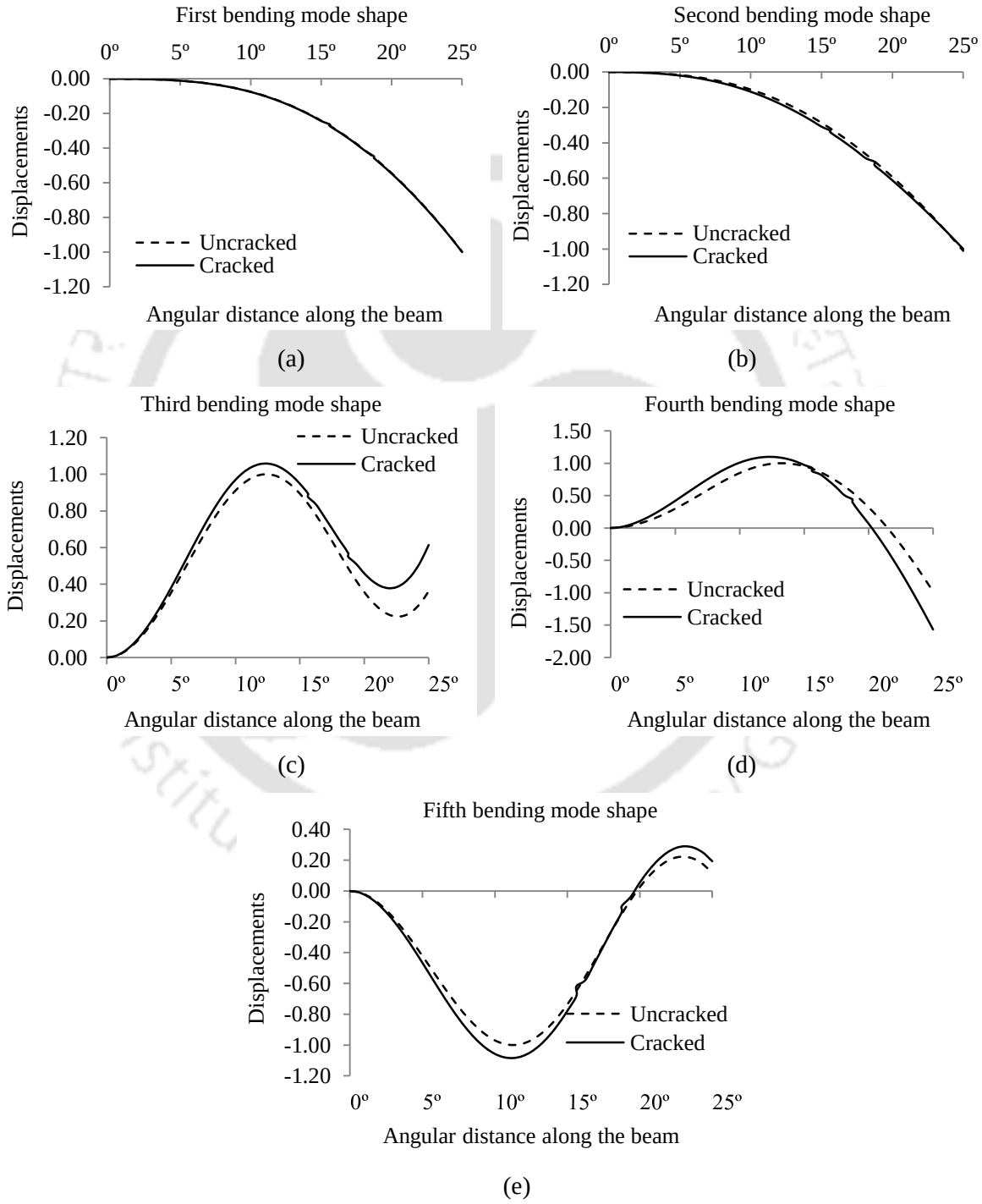

Figure 5.39: First five bending modes for uncracked and double cracked angle section curved beam (θ_s = 25°, R = 1833.50 mm)

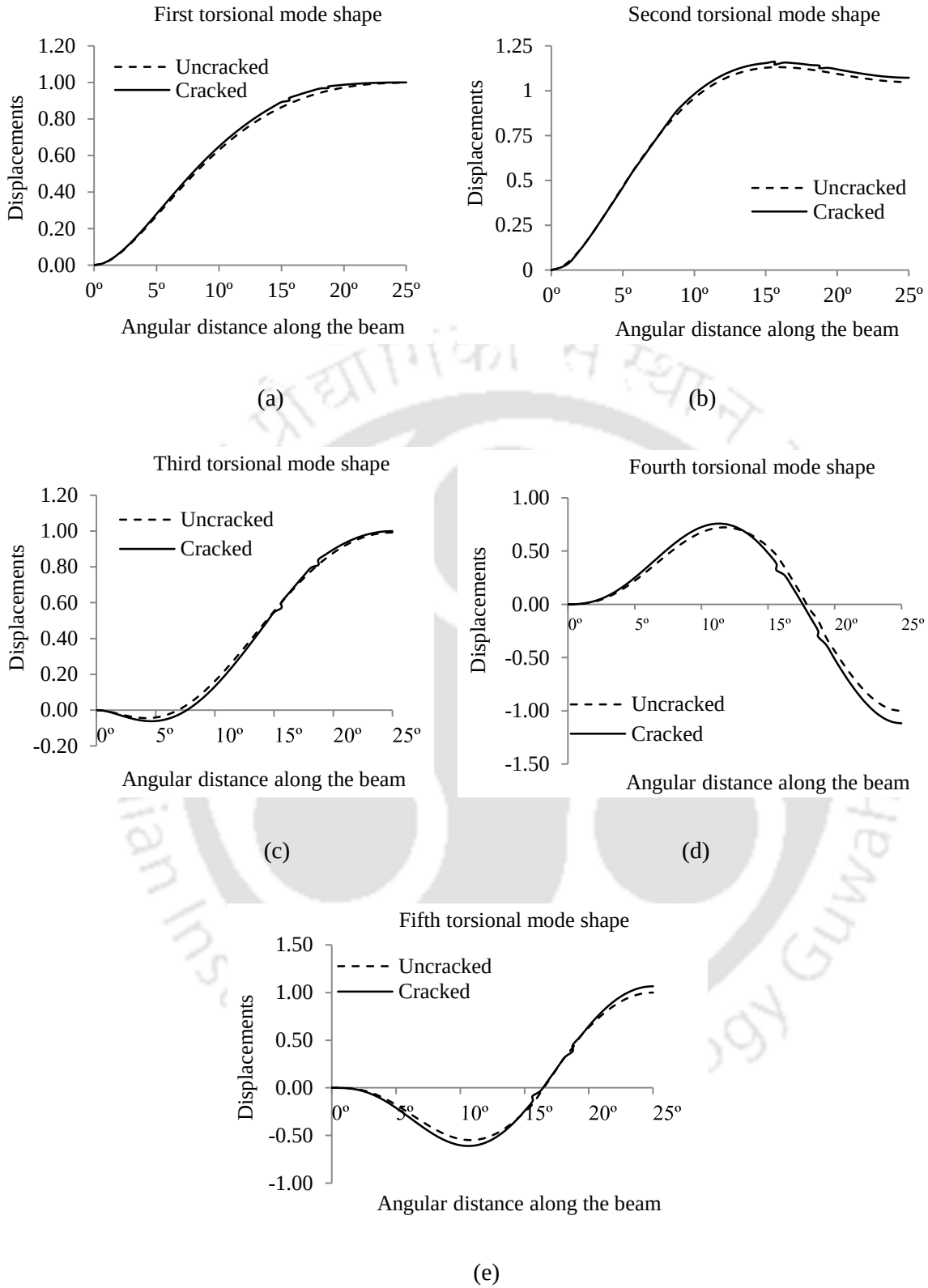

Figure 5.40: First five torsional modes for uncracked and double cracked angle section curved beam (θ_s = 25°, R = 1833.50 mm)

It has been found from the study of mode shape in various cases that it does not assist to locate or quantify damage. In higher modes, in some cases discontinuity appears indicate the crack.

5.8 Damage detection using modal assurance criterion (MAC)

MAC is a well-known statistical tool for the quantitative comparison of modal vectors to determine the level of correlation between the modal vectors formed by uncracked and cracked beam. MAC matrix can be calculated using following expression [208]:

$$MAC(i,j)=\frac{\left|\{\phi_o\}_i^T\{\phi_d\}_j\right|^2}{\left(\{\phi_o\}_i^T\{\phi_d\}_i\right)\left(\{\phi_o\}_j^T\{\phi_d\}_j\right)} \tag{5.1}$$

where, ϕ_o is the theoretical modal vector for uncracked beam and ϕ_d is the theoretical modal vector for cracked or damaged beam. The MAC value lies between 0 and 1. The number '0' describes no consistent correspondence between two modes, whereas the number '1' illustrates a consistent correspondence. Therefore, if the diagonal elements in the matrix are close to 1, then it indicates no difference between the modal vectors and if such things are not happened then there may have some deviation. Table 5.9 displays MAC numbers for channel beam for different cases considered in the study. It is evident from the table that diagonal elements are very close to 1. As such, no useful inference can be drawn that uncracked and cracked modes are different.

MAC values of angle section beams are shown in Table 5.10. Here also the values do not indicate difference between two displacement shapes in the same mode.

For visualization purpose a 3D plot for MAC values are presented in Figure 5.41(a) and Figure 5.41(b) for Case No. (1) of Table 5.9 and Table 5.10 respectively. For a particular crack depth ratio at a fixed crack position, the entire diagonal elements in both the table are close to 1, which explains that the mode shapes are almost identical. Thus, MAC values are not sensitive to damage detection. Similar observations were made by Pandey *et al*. [74] and Fox [106].

Table 5.9: MAC values for the uncracked and damaged displacement mode shapes (*channel*)

Case No. and particulars	Intact beam mode no.	Cracked beam mode no.					
		1	2	3	4	5	6
(1) Straight channel beam	1	**0.9999**	0.9998	0.0242	0.0017	0.0040	0.0035
ζ_1/b = 0.5	2	0.9997	**0.9999**	0.0203	0.0008	0.0040	0.0036
L_1 = 0.02	3	0.0258	0.0216	**0.9999**	0.9271	0.0292	0.0041
(For translation)	4	0.0020	0.0009	0.9343	**0.9999**	0.0059	0.0015
	5	0.0035	0.0036	0.0246	0.0068	**0.9993**	0.0019
	6	0.0059	0.0062	0.0297	0.0097	0.0686	**0.8831**
(2) Straight channel beam	1	**0.9998**	0.9976	0.0686	0.0260	0.0243	0.0013
ζ_1/b = 0.5	2	0.9996	**0.9997**	0.0536	0.0295	0.0334	0.0009
L_1 = 0.02	3	0.0522	0.0380	**0.9984**	0.1104	0.5975	0.0326
(For rotation)	4	0.0339	0.0393	0.1533	**0.9937**	0.0062	0.0005
	5	0.0261	0.0359	0.5411	0.0255	**0.9988**	0.0120
	6	0.0006	0.0003	0.0432	0.0117	0.0077	**0.9903**
(3) Straight channel beam	1	**0.9999**	0.9998	0.0344	0.0020	0.0042	0.0049
ζ_1/b = 0.5	2	0.9998	**0.9999**	0.0297	0.0010	0.0043	0.0052
ζ_2/b = 0.8	3	0.0248	0.0208	**0.9987**	0.9357	0.0205	0.0451
L_1 = 0.5	4	0.0017	0.0008	0.9109	**0.9998**	0.0108	0.0132
L_2 = 0.6	5	0.0036	0.0036	0.0367	0.0043	**0.9980**	0.1332
(For translation)	6	0.0059	0.0062	0.0301	0.0114	0.0460	**0.9812**
(4) Straight channel beam	1	**0.9999**	0.9991	0.0554	0.0299	0.0259	0.0009
ζ_1/b = 0.5	2	0.9988	**0.9999**	0.0420	0.0335	0.0353	0.0005
ζ_2/b = 0.8	3	0.0597	0.0458	**0.9998**	0.1012	0.5962	0.0404
L_1 = 0.5	4	0.0282	0.0323	0.1388	**0.9920**	0.0062	0.0098
L_2 = 0.6	5	0.0235	0.0324	0.5829	0.0263	**0.9987**	0.0076
(For rotation)	6	0.0007	0.0004	0.0348	0.0000	0.0141	**0.9846**
(5) Curved (θ_s = 25°)	1	**0.9999**	0.6584	0.2585	0.2510	0.0103	0.0181
channel beam	2	0.6601	**0.9999**	0.0001	0.4000	0.3731	0.0123
ζ_1/b = 0.5	3	0.2500	0.0000	**0.9999**	0.1353	0.6090	0.0125
θ_{S1} = 0.625°	4	0.2567	0.3874	0.1227	**0.9995**	0.3824	0.4047
(For translation)	5	0.0089	0.3669	0.6113	0.3908	**0.9996**	0.0013
	6	0.0162	0.0147	0.0126	0.3866	0.0007	**0.9991**
(6) Curved (θ_s = 25°)	1	**0.9999**	0.9334	0.1807	0.1838	0.3567	0.0783
channel beam	2	0.9291	**0.9999**	0.4105	0.1322	0.1836	0.0118
ζ_1/b = 0.5	3	0.1747	0.4060	**0.9999**	0.0294	0.1150	0.1981
θ_{S1} = 0.625°	4	0.1885	0.1324	0.0270	**0.9989**	0.0037	0.0000
(For rotation)	5	0.3623	0.1828	0.1251	0.0014	**0.9957**	0.1399
	6	0.0652	0.0075	0.1869	0.0010	0.0659	**0.9929**
(7) Curved channel beam	1	**0.9999**	0.6587	0.2543	0.2561	0.0096	0.0177
ζ_1/b = 0.5	2	0.6577	**0.9999**	0.0000	0.3837	0.3710	0.0150
ζ_2/b = 0.8	3	0.2529	0.0000	**0.9999**	0.1234	0.6131	0.0100
θ_{S1} = 15.625°	4	0.2541	0.3943	0.1262	**0.9997**	0.3832	0.3873
θ_{S2} = 18.750°	5	0.0083	0.3685	0.6143	0.3653	**0.9998**	0.0024
(For translation)	6	0.0160	0.0132	0.0134	0.4140	0.0007	**0.9991**
(8) Curved channel beam	1	**0.9999**	0.9317	0.1780	0.1842	0.3576	0.0746
ζ_1/b = 0.5	2	0.9327	**0.9999**	0.4063	0.1319	0.1839	0.0108
ζ_2/b = 0.8	3	0.1790	0.4096	**0.9999**	0.0278	0.1171	0.1933
θ_{S1} = 15.625°	4	0.1840	0.1325	0.0299	**0.9998**	0.0019	0.0004
θ_{S2} = 18.750°	5	0.3605	0.1800	0.1300	0.0026	**0.9983**	0.1234
(For rotation)	6	0.0626	0.0072	0.1870	0.0001	0.0776	**0.9982**

Table 5.10: MAC values for the uncracked and damaged displacement mode shapes (*angle*)

Case No. and particulars	Intact beam mode no.	Cracked beam mode no.					
		1	2	3	4	5	6
(1) Straight angle beam	1	**0.9999**	0.9998	0.9956	0.0097	0.0519	0.0190
$\zeta_1/b = 0.5$	2	0.9996	**0.9999**	0.9929	0.0064	0.0442	0.0228
$L_1 = 0.02$	3	0.9931	0.9900	**0.9997**	0.0330	0.0957	0.0069
(For translation)	4	0.0098	0.0067	0.0264	**0.9999**	0.9802	0.4738
	5	0.0413	0.0347	0.0707	0.9879	**0.9990**	0.4127
	6	0.0047	0.0066	0.0006	0.5541	0.4812	**0.9893**
(2) Straight angle beam	1	**0.9995**	0.9990	0.9957	0.5750	0.0006	0.0373
$\zeta_1/b = 0.5$	2	0.9998	**0.9995**	0.9970	0.5641	0.0002	0.0353
$L_1 = 0.02$	3	0.9992	0.9996	**0.9995**	0.5300	0.0003	0.0296
(For rotation)	4	0.5113	0.5007	0.4661	**0.9975**	0.4419	0.2019
	5	0.0003	0.0008	0.0039	0.3973	**0.9965**	0.0316
	6	0.0523	0.0515	0.0489	0.0728	0.0184	**0.9188**
(3) Straight angle beam	1	**0.9999**	0.9999	0.9993	0.0111	0.0688	0.0003
$\zeta_1/b = 0.5$	2	0.9999	**0.9999**	0.9996	0.0096	0.0651	0.0001
$\zeta_2/b = 0.8$	3	0.9994	0.9997	**0.9999**	0.0064	0.0565	0.0000
$L_1 = 0.5$	4	0.0107	0.0092	0.0061	**0.9999**	0.9721	0.4866
$L_2 = 0.6$	5	0.0432	0.0402	0.0334	0.9874	**0.9968**	0.4401
(For translation)	6	0.0042	0.0050	0.0071	0.5606	0.4725	**0.9623**
(4) Straight angle beam	1	**0.9607**	0.9565	0.9420	0.7118	0.0292	0.0855
$\zeta_1/b = 0.5$	2	0.9578	**0.9535**	0.9385	0.7178	0.0313	0.0872
$\zeta_2/b = 0.8$	3	0.9503	0.9455	**0.9295**	0.7327	0.0367	0.0912
$L_1 = 0.5$	4	0.0894	0.0955	0.1157	**0.1667**	0.6434	0.1070
$L_2 = 0.6$	5	0.1583	0.1662	0.1916	0.1016	**0.6228**	0.0690
(For rotation)	6	0.0066	0.0077	0.0115	0.1118	0.0992	**0.7317**
(5) Curved ($\theta_s = 25°$)	1	**0.9998**	0.9903	0.2395	0.0062	0.0144	0.0079
angle beam	2	0.9989	**0.9975**	0.2753	0.0157	0.0247	0.0034
$\zeta_1/b = 0.5$	3	0.3486	0.4133	**0.9867**	0.6494	0.7664	0.0590
$\theta_{S1} = 0.625°$	4	0.0320	0.0102	0.5391	**0.9233**	0.7813	0.2480
(For translation)	5	0.0084	0.0241	0.8136	0.8340	**0.9982**	0.0846
	6	0.0260	0.0116	0.0562	0.2293	0.0605	**0.9898**
(6) Curved ($\theta_s = 25°$)	1	**0.9972**	0.8254	0.8443	0.0022	0.0900	0.2257
angle beam	2	0.9908	**0.9179**	0.7299	0.0320	0.0278	0.2322
$\zeta_1/b = 0.5$	3	0.8332	0.4843	**0.9987**	0.0821	0.3662	0.1488
$\theta_{S1} = 0.625°$	4	0.0021	0.0902	0.1873	**0.9827**	0.9431	0.0611
(For rotation)	5	0.0603	0.0129	0.3759	0.8838	**0.9995**	0.0716
	6	0.2092	0.2088	0.1164	0.0398	0.0677	**0.9927**
(7) Curved angle beam	1	**0.9999**	0.0842	0.0273	0.2416	0.0137	0.0026
$\zeta_1/b = 0.5$	2	0.9978	**0.1131**	0.0416	0.2769	0.0238	0.0007
$\zeta_2/b = 0.8$	3	0.3378	0.6807	**0.5806**	0.9883	0.7650	0.0094
$\theta_{S1} = 15.625°$	4	0.0369	0.7186	0.6670	**0.5292**	0.7870	0.0992
$\theta_{S2} = 18.750°$	5	0.0065	0.6247	0.6785	0.8145	**0.9985**	0.0071
(For translation)	6	0.0293	0.2985	0.0124	0.0547	0.0677	**0.9464**
(8) Curved angle beam	1	**0.9999**	0.9227	0.8482	0.0004	0.0907	0.1995
$\zeta_1/b = 0.5$	2	0.9827	**0.9805**	0.7346	0.0125	0.0287	0.2040
$\zeta_2/b = 0.8$	3	0.8626	0.6327	**0.9990**	0.1167	0.3617	0.1330
$\theta_{S1} = 15.625°$	4	0.0055	0.0330	0.1851	**0.9933**	0.9462	0.0636
$\theta_{S2} = 18.750°$	5	0.0757	0.0002	0.3738	0.9129	**0.9988**	0.0682
(For rotation)	6	0.1900	0.1899	0.1180	0.0701	0.0846	**0.9952**

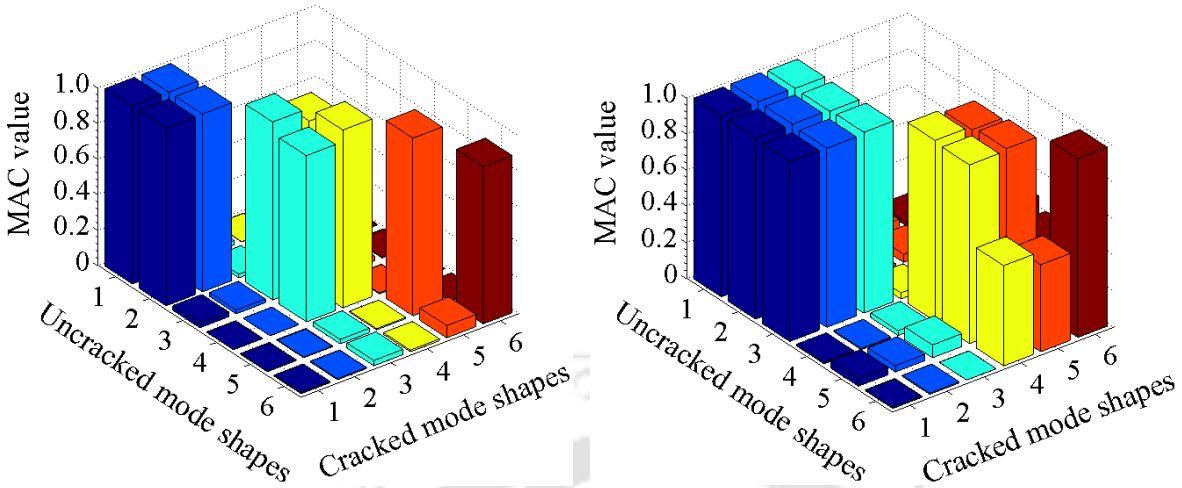

(a) (b)

Figure 5.41: 3D MAC plot for: (a) Case No. (1) of Table 5.9 and (b) Case No. (1) of Table 5.10

5.9 Effect of crack on absolute difference between curvature mode shapes and curvature damage factor (CDF)

The alterations of mode shapes due to presence of crack are too small to make the existence of crack detectable compared to the mode shapes of healthy beam. However, the alterations in mode shape vectors due to existence of crack in the structure may be distinguished by using its derivatives. The second derivatives of mode shape vectors are implemented here to observe their capability to magnify the crack effect in the mode shape data. In the present section, the absolute difference between curvature mode shapes of uncracked and cracked beams has been presented in the following form

$$Absolute\ Difference = |\phi_o'' - \phi_d''| \tag{5.2}$$

where ϕ indicate mode shape in bending or torsion. Subscript 'o' and 'd' expresses the curvature mode shape of the uncracked and cracked structures respectively. The use of absolute difference of modal curvature had remarkable success in localizing cracks in past studies [74, 75].

Figure 5.42(a and b) and Figure 5.43(a and b) represent the absolute difference between the curvature mode shapes of uncracked and single cracked cantilever channel and angle section beam respectively in bending and torsional mode separately. On the other hand,

Figure 5.44(a and b) and Figure 5.45(a and b) display the double cracked scenario for both cross-sectional configuration. In case of single crack, the crack was considered at a distance (L_1) = 0.02 m from the fixed end for which crack depth ratio (ζ_1 /b) was 0.5. Furthermore, the double cracks were introduced at L_1 = 0.50 m and L_2 = 0.60 m from the fixed end of the cantilever beam and the associated crack depth ratio (ζ_1 /b) at first crack location is 0.5 and at second crack location ζ_2 /b is 0.8 respectively. It can be noticed from the figures that the crack location is identified by sharp peaks where crack exists. It has been found that the discontinuity in absolute difference between curvature mode shapes for all cases are clearly visible at crack locations compared to only mode shape vector.

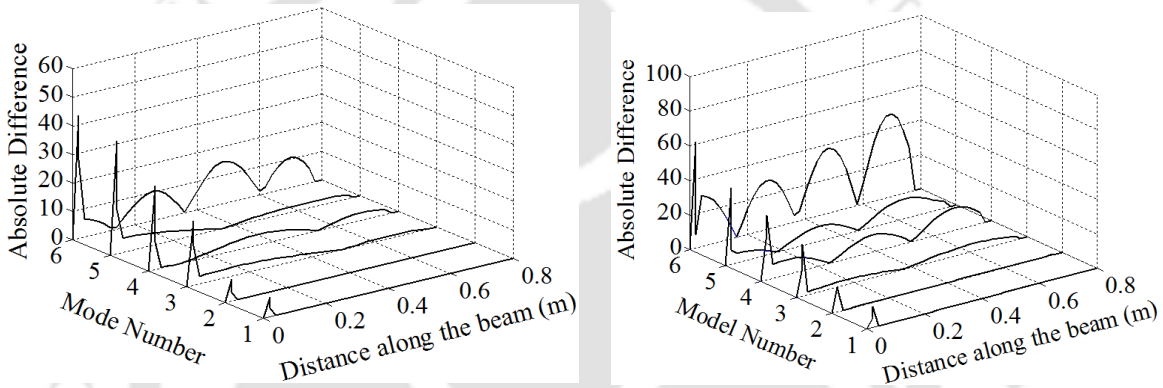

(a) (b)

Figure 5.42: Absolute difference between the curvature mode shapes for single cracked cantilever channel section straight beam in (a) Bending and (b) Torsional mode

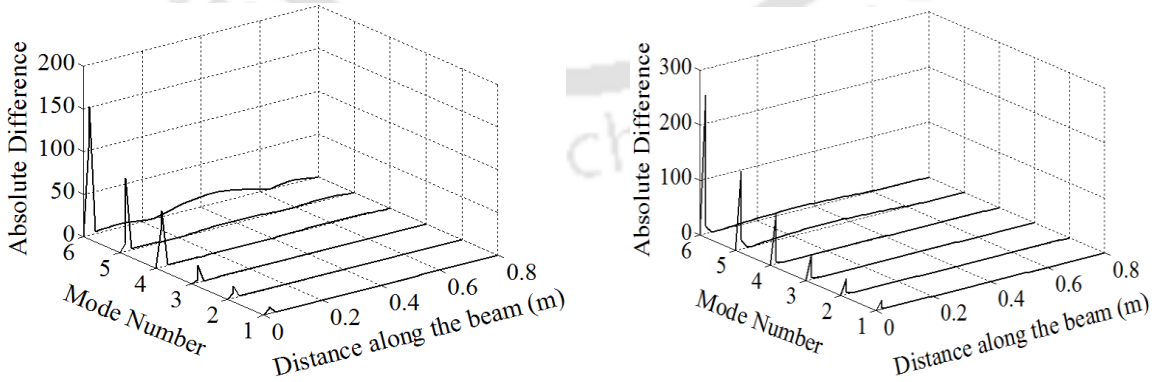

(a) (b)

Figure 5.43: Absolute difference between the curvature mode shapes for single cracked cantilever angle section straight beam in (a) Bending and (b) Torsional mode

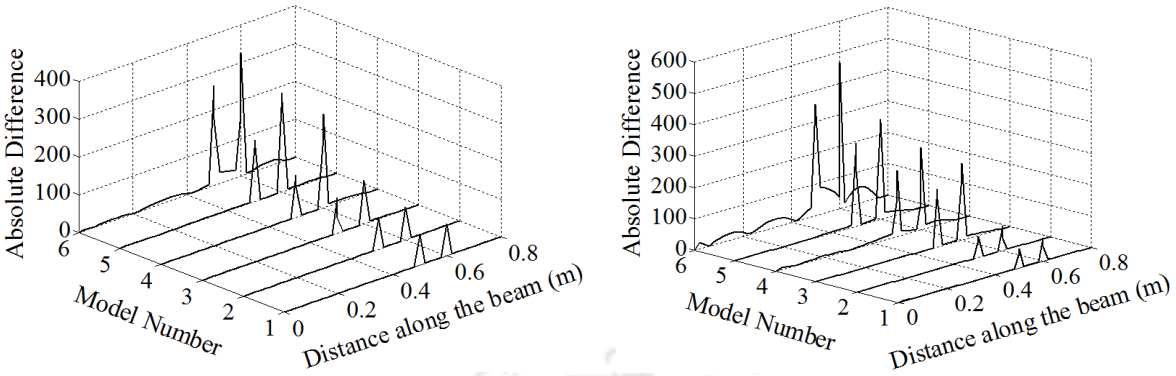

(a) (b)

Figure 5.44: Absolute difference between the curvature mode shapes for double cracked cantilever channel section straight beam in (a) Bending and (b) Torsional mode

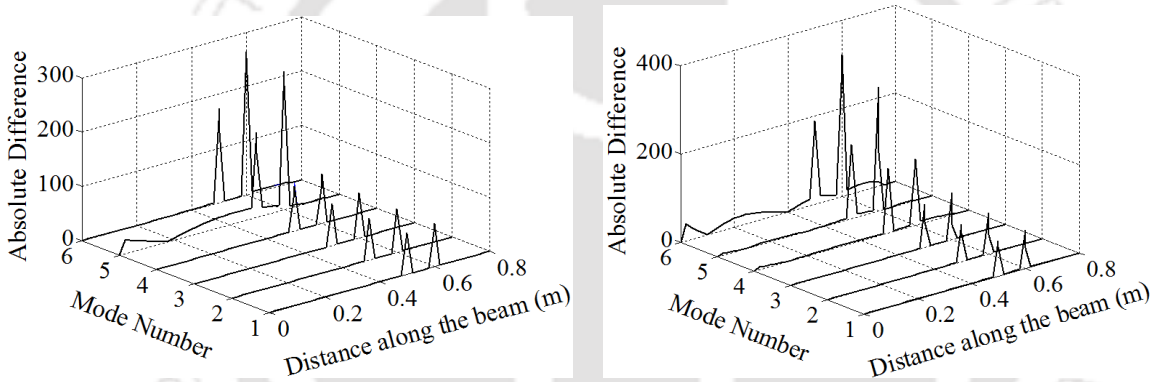

(a) (b)

Figure 5.45: Absolute difference between the curvature mode shapes for double cracked cantilever angle section straight beam in (a) Bending and (b) Torsional mode

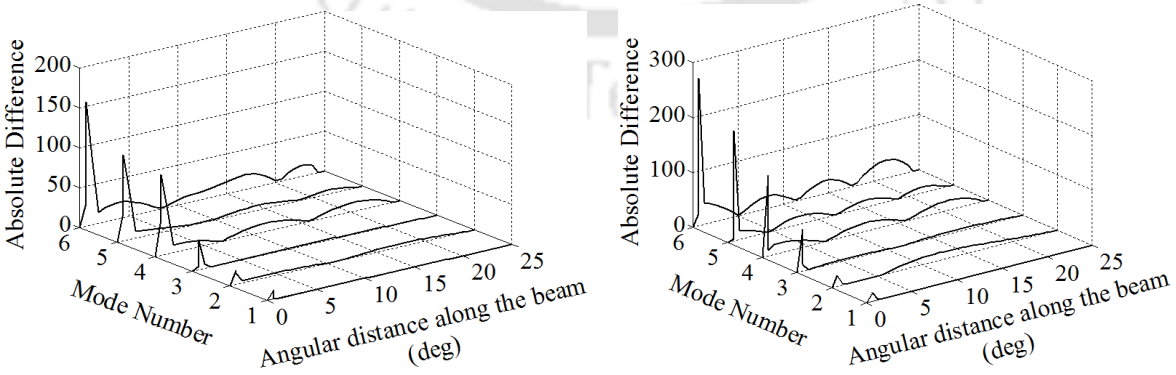

(a) (b)

Figure 5.46: Absolute difference between the curvature mode shapes for single cracked cantilever channel section curved beam (θ_s = 25°, R = 1833.50 mm) in (a) Bending and (b) Torsional mode

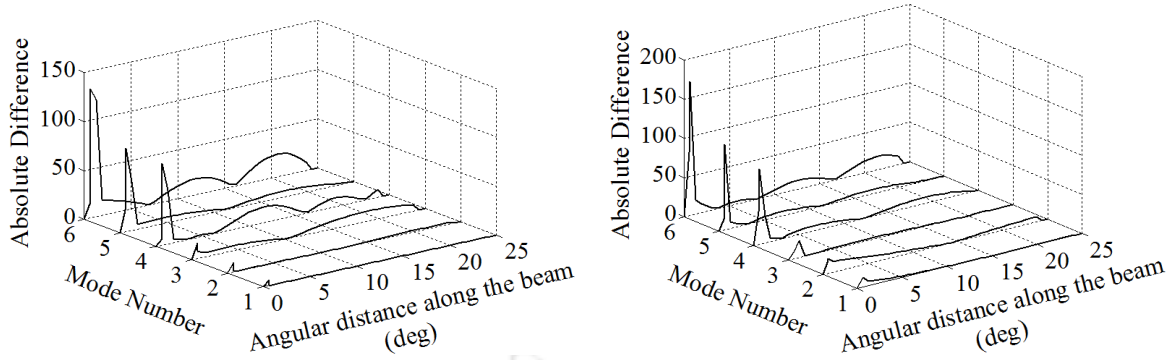

(a) (b)

Figure 5.47: Absolute difference between the curvature mode shapes for single cracked cantilever angle section curved beam (θ_s = 25°, R = 1833.50 mm) in (a) Bending and (b) Torsional mode

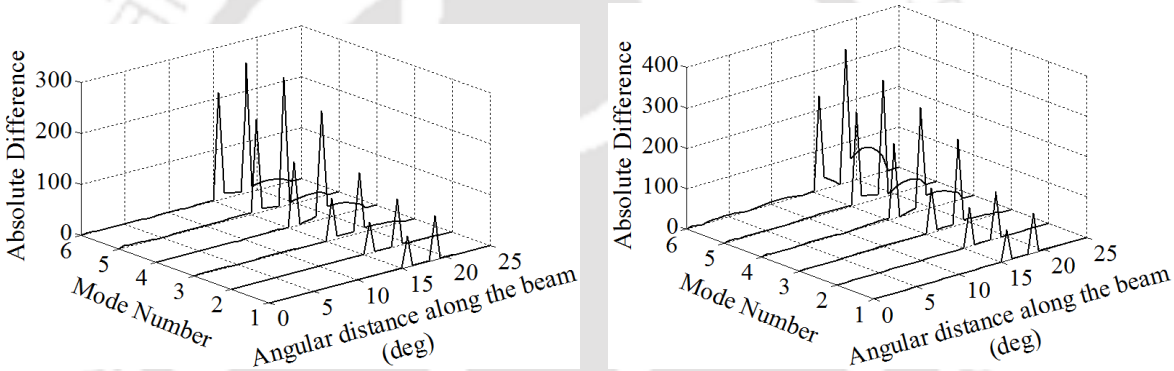

(a) (b)

Figure 5.48: Absolute difference between the curvature mode shapes for double cracked cantilever channel section curved beam (θ_s = 25°, R = 1833.50 mm) in (a) Bending and (b) Torsional mode

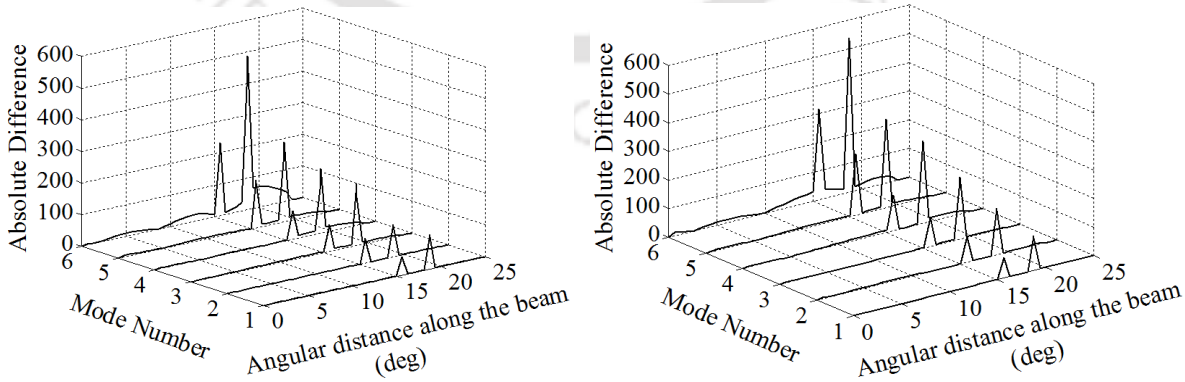

(a) (b)

Figure 5.49: Absolute difference between the curvature mode shapes for double cracked cantilever angle section curved beam (θ_s = 25°, R = 1833.50 mm) in (a) Bending and (b) Torsional mode

The absolute difference between curvature mode shapes for the curved beams having single and double crack has been given in Figure 5.46(a and b) to Figure 5.49(a and b) respectively. The crack location and crack depth for the single crack case are: location (θ_{S1}) = 0.625° and crack depth ratio (ζ_1 /b) = 0.5, whereas for double crack case locations are θ_{S1} = 15.625°; θ_{S2} = 18.750° and corresponding crack depth ratios are ζ_1 /b = 0.5; ζ_2 /b = 0.8.

Curvature damage factor (CDF) is another single parameter which includes contribution of all significant modes. These are often used in crack localization. Abdel Wahab and De Roeck [75] defined the curvature damage factor (CDF) as

$$CDF = \frac{1}{N}\sum_{N} Abs\left(\phi_o'' - \phi''\right) \tag{5.3}$$

where N is number of first significant modes, ϕ represent mode in bending or torsion.

Figure 5.50(a and b) to Figure 5.57(a and b) represent the plot of CDF against distance along the beam for channel and angle section straight and curved beam for bending and torsional mode separately.

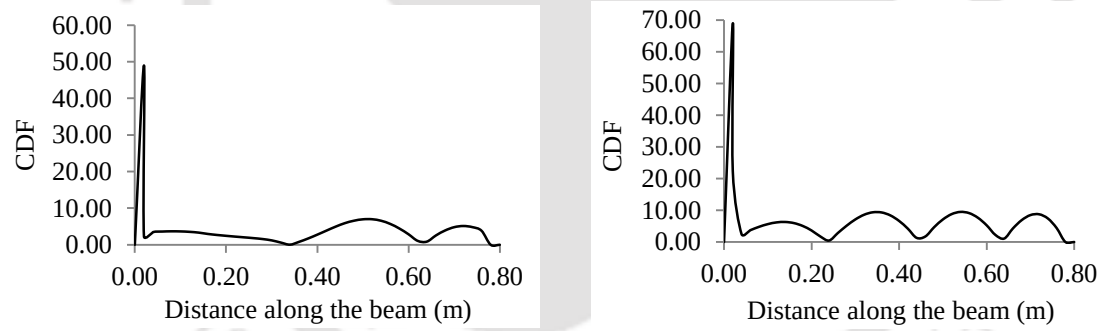

(a) (b)

Figure 5.50: CDF for single cracked cantilever channel section straight beam in (a) Bending and (b) Torsional mode

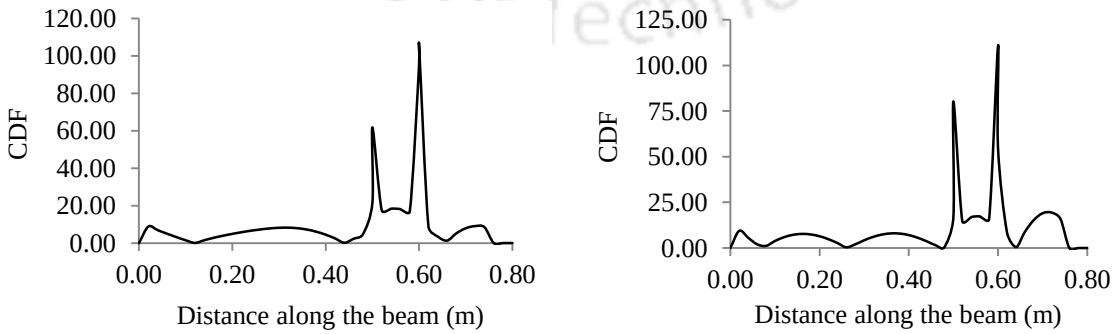

(a) (b)

Figure 5.51: CDF for double cracked cantilever channel section straight beam in (a) Bending and (b) Torsional mode

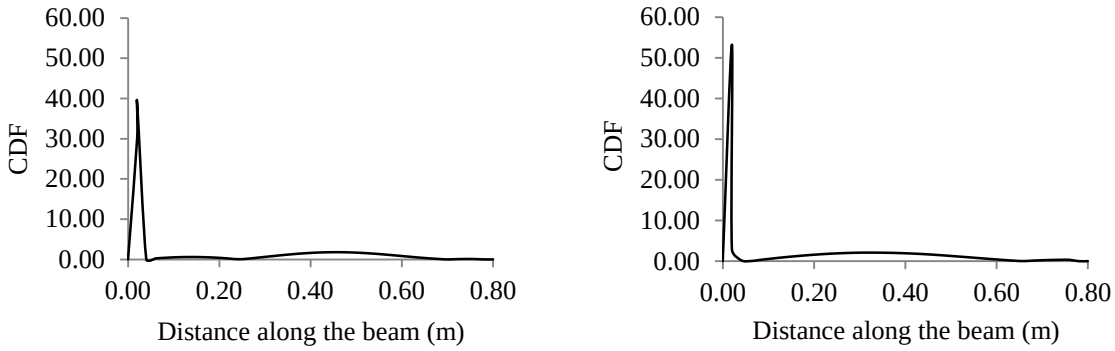

(a) (b)

Figure 5.52: CDF for single cracked cantilever angle section straight beam in (a) Bending and (b) Torsional mode

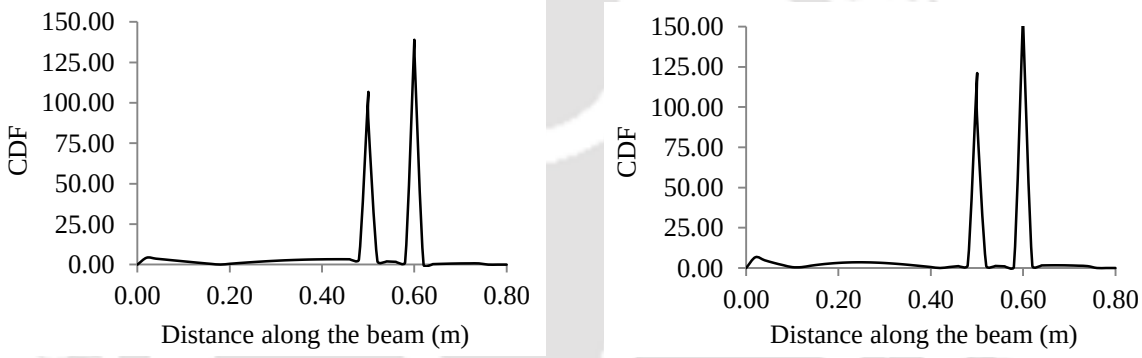

(a) (b)

Figure 5.53: CDF for double cracked cantilever angle section straight beam in (a) Bending and (b) Torsional mode

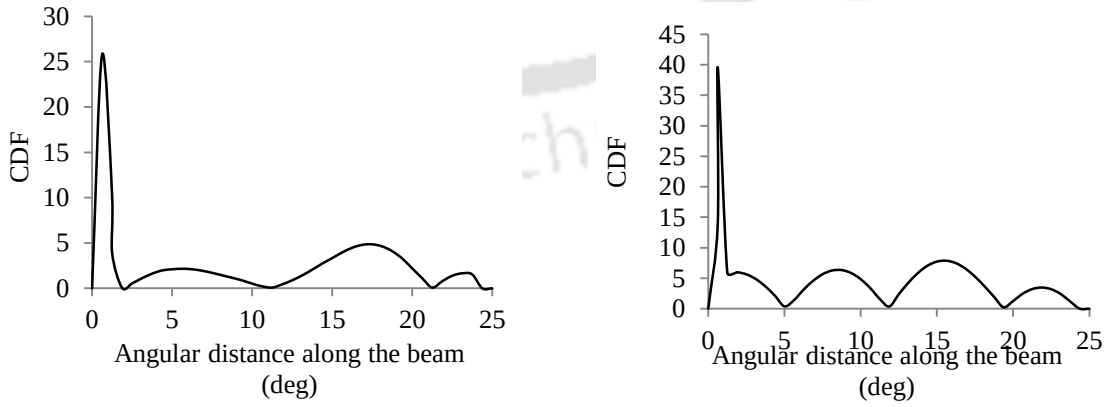

(a) (b)

Figure 5.54: CDF for single cracked cantilever channel section curved beam (θ_s = 25°, R = 1833.50 mm) in (a) Bending and (b) Torsional mode

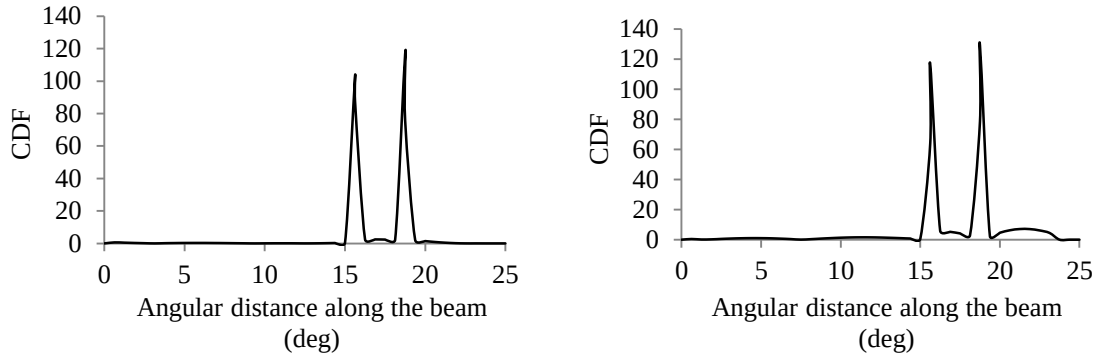

(a) (b)

Figure 5.55: CDF for double cracked cantilever channel section curved beam (θ_s = 25°, R = 1833.50 mm) in (a) Bending and (b) Torsional mode

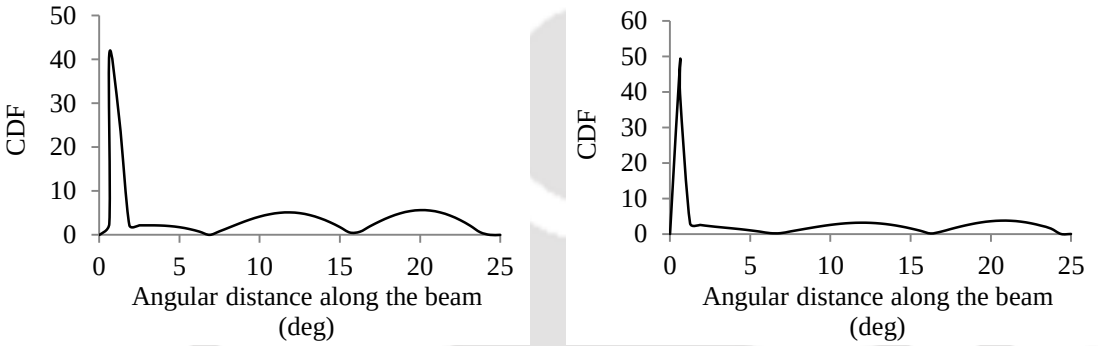

(a) (b)

Figure 5.56: CDF for single cracked cantilever angle section curved beam (θ_s = 25°, R = 1833.50 mm) in (a) Bending and (b) Torsional mode

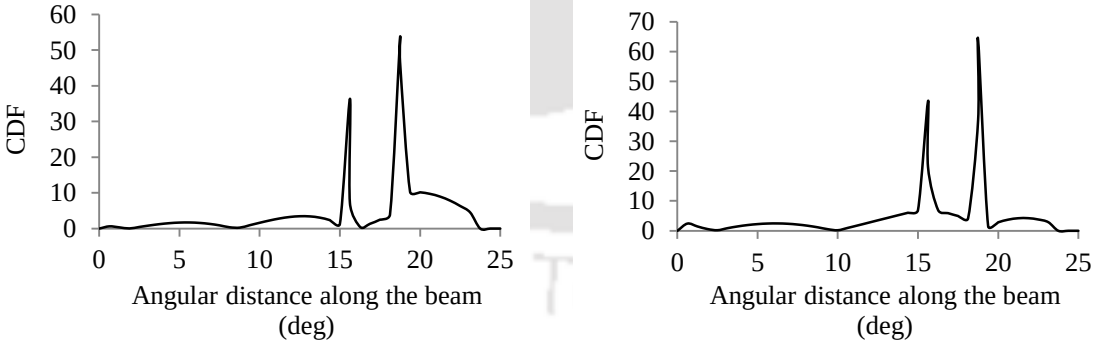

(a) (b)

Figure 5.57: CDF for double cracked cantilever angle section curved beam (θ_s = 25°, R = 1833.50 mm) in (a) Bending and (b) Torsional mode

It can be observed from these figures that the crack position is identified by sharp peak. The magnitude of CDF is larger in case of torsional mode compared to bending mode, reason being that the discontinuity of the torsional mode shape is more prominent.

5.10 Damage identification in thin-walled steel beam based on a hybrid approach using free vibration response

From the discussions in the preceding sections, it has been realized that modal parameters – frequency, mode shapes and curvature mode shapes can give an indication of crack and its location, but cannot evaluate the extent of cracks. Moreover, the information of undamaged beams are necessary.

To overcome these difficulties, present study outlines a hybrid approach using Response Surface Method (RSM) – Genetic Algorithm (GA) to predict the crack parameters, namely crack position and crack depth ratio using measured free vibration responses (natural frequencies) of cracked thin walled beams. The identification of crack parameters in cantilever thin-walled beam using a hybrid approach was applied on two different cases with several number of laboratory experiments to show the practicability of the present approach. First case consists of identification of single and multiple cracks in channel and angle cross-sectional straight steel beam and second case relates to identification of single and multiple crack scenarios in horizontally curved beams.

5.10.1 Case I – Identification of single and multiple cracks in channel and angle cross-sectional straight beam using free vibration response

Central composite face-centered (CCF) design of experiment has been employed in the present approach. Single crack identification problem (p = 2 and n_{cr} = 5) required 13 experiments with the crack location (X_1) and crack depth ratio (X_2) as the independent variables. The double crack identification problem (p = 4 and n_{cr} = 6) required 30 experimental trials with first crack parameters- location (X_1) and crack depth ratio (X_2) and second crack parameters: location (X_3) and crack depth ratio (X_4) as independent variables. The locations are measured from fixed end of the cantilever. Here p is the number of factors or variables and n_{cr} is the number of center points present in DOE, which are already described in the Chapter 3. The independent factors for CCF design along with their low, medium and high levels for thin walled single and double cracked channel and angle section beams has been given in Table 5.11. The variables are coded to the levels -1, 0, +1 as discussed previously. From Table 5.11 it can be realized that the cracks can be present anywhere in the range of 0 to 0.8 m length of the beam with the range of crack depth ratio 0 to 0.9.

Table 5.11: Independent variables and their levels of channel and angle section beam for CCF

Crack identification problem	Factors	Coded Symbol	Real values of coded Levels		
			Low level (-1)	Medium level (0)	High level (1)
Single	Crack location (m)	X_1	0.00	0.40	0.80
	Crack depth ratio	X_2	0.00	0.45	0.90
Multiple (Double crack)	First crack location (m)	X_1	0.00	0.40	0.80
	First crack depth ratio	X_2	0.00	0.45	0.90
	Second crack location (m)	X_3	0.04	0.42	0.80
	Second crack depth ratio	X_4	0.00	0.45	0.90

Table 5.12: CCF design with coded variables and calculated responses for single crack

Expt. trial no.	Coded levels of variables		Output frequency responses in Hz				
	X_1	X_2	y_1	y_2	y_3	y_4	y_5
Channel cross-sectional beam							
1	1	-1	49.8014	106.9762	207.9897	469.0712	605.6716
2	-1	0	49.0319	105.5555	203.4930	454.3590	601.0374
3	-1	1	42.9853	96.2408	179.9399	396.8157	580.5699
4	0	0	49.7612	106.8641	206.3584	467.5004	603.3037
5	-1	-1	49.8014	106.9762	207.9897	469.0712	605.6716
6	0	0	49.7612	106.8641	206.3584	467.5004	603.3037
7	0	1	49.5613	106.1120	183.7684	461.4356	581.9404
8	0	-1	49.8014	106.9762	207.9897	469.0712	605.6716
9	0	0	49.7612	106.8641	206.3584	467.5004	603.3037
10	0	0	49.7612	106.8641	206.3584	467.5004	603.3037
11	1	0	49.8014	106.9762	207.9897	469.0712	605.6716
12	0	0	49.7612	106.8641	206.3584	467.5004	603.3037
13	1	1	49.8014	106.9762	207.9897	469.0712	605.6716
Angle cross-sectional beam							
1	0	-1	23.7030	50.4680	81.6992	137.6978	269.8373
2	-1	0	22.2683	49.9378	78.2037	130.6256	256.7604
3	0	0	23.4297	50.1851	81.0400	134.1580	266.0422
4	1	1	23.7030	50.4680	81.6992	137.6978	269.8373
5	0	0	23.4297	50.1851	81.0400	134.1580	266.0422
6	0	0	23.4297	50.1851	81.0400	134.1580	266.0422
7	0	1	20.0518	49.9914	75.1341	105.3379	248.3697
8	0	0	23.4297	50.1851	81.0400	134.1580	266.0422
9	0	0	23.4297	50.1851	81.0400	134.1580	266.0422
10	1	-1	23.7030	50.4680	81.6992	137.6978	269.8373
11	-1	-1	23.7030	50.4680	81.6992	137.6978	269.8373
12	-1	1	11.3212	48.9003	74.7570	105.3145	245.4715
13	1	0	23.7030	50.4680	81.6992	137.6978	269.8373

The values of first five natural frequencies (y_1, y_2, y_3, y_4 and y_5) for each experimental run were extracted using FE simulation for single cracked channel and angle section beam (see, Table 5.12). For example, when coded value X_1 is 0 the corresponding natural value of crack location (η_1) is 0.4 m and similarly, when X_2 value is 0 the corresponding natural

value of crack depth ratio (η_2) is 0.45 for single cracked problem. Therefore, when the crack is located at a distance 0.4 m from fixed end of the cantilever channel section beam with 0.45 crack depth ratio, the corresponding first five natural frequencies are obtained using FE simulation which appears as 49.7612, 106.8641, 206.3584, 467.5004 and 603.3037 Hz against experimental trial no.4 (Table 5.12). In this approach, the value of simulated output frequency responses are considered up to four decimal places for more accuracy of estimation as desired in thin element.

Table 5.13: Independent variables and calculated responses for double cracked channel beam

Run	Coded levels of variables				Response (Hz)				
	X_1	X_2	X_3	X_4	y_1	y_2	y_3	y_4	y_5
1	-1	1	1	-1	42.9853	96.2408	179.9399	396.8157	580.5699
2	0	0	0	0	49.7420	106.8117	205.6182	466.5632	602.0767
3	-1	1	1	1	42.9853	96.2408	179.9399	396.8157	580.5699
4	1	-1	1	1	49.8014	106.9762	207.9897	469.0712	605.6716
5	1	1	1	-1	49.8014	106.9762	207.9897	469.0712	605.6716
6	0	1	0	0	49.5439	106.0679	183.6363	460.5923	581.1498
7	1	1	-1	1	44.5730	98.5983	189.6189	429.6170	587.6299
8	0	0	0	0	49.7420	106.8117	205.6182	466.5632	602.0767
9	1	1	1	1	49.8014	106.9762	207.9897	469.0712	605.6716
10	-1	-1	-1	-1	49.8014	106.9762	207.9897	469.0712	605.6716
11	1	0	0	0	49.7627	106.8706	206.4179	467.1891	603.1693
12	0	0	0	0	49.7420	106.8117	205.6182	466.5632	602.0767
13	-1	1	-1	-1	49.8014	106.9762	207.9897	469.0712	605.6716
14	1	-1	1	-1	49.8014	106.9762	207.9897	469.0712	605.6716
15	0	0	0	1	49.6120	106.3306	189.911	458.9950	587.5554
16	-1	-1	-1	1	44.5730	98.5983	189.6189	429.6170	587.6299
17	1	-1	-1	1	44.5730	98.5983	189.6189	429.6170	587.6299
18	1	-1	-1	-1	49.8014	106.9762	207.9897	469.0712	605.6716
19	0	0	1	0	49.7612	106.8641	206.3584	467.5004	603.3037
20	0	0	0	0	49.7420	106.8117	205.6182	466.5632	602.0767
21	0	0	0	0	49.7420	106.8117	205.6182	466.5632	602.0767
22	-1	-1	1	-1	49.8014	106.9762	207.9897	469.0712	605.6716
23	-1	1	-1	1	42.5657	95.1259	179.0418	389.9201	573.3590
24	0	-1	0	0	49.7627	106.8706	206.4179	467.1891	603.1693
25	0	0	0	-1	49.7612	106.8641	206.3584	467.5004	603.3037
26	-1	-1	1	1	49.8014	106.9762	207.9897	469.0712	605.6716
27	-1	0	0	0	49.0129	105.5026	202.7470	453.4020	599.7961
28	0	0	0	0	49.7420	106.8117	205.6182	466.5632	602.0767
29	1	1	-1	-1	49.8014	106.9762	207.9897	469.0712	605.6716
30	0	0	-1	0	49.2493	105.9115	204.6906	461.4814	601.3623

Similarly the independent coded variables and FE simulated responses for double cracked channel and angle section steel beam have been presented in Table 5.13 and Table 5.14 respectively. The main goal of the experiment is to establish a relationship between independent design variables and output responses. From Table 5.13 (experimental run no.

15) and Table 5.14 (experimental run no. 29) it can be observed that the first crack is located at a distance 0.4 m (X_1 = 0) and second crack located at a distance 0.42 m (X_3 = 0) from the fixed end of the cantilever channel and angle section beam with first crack depth ratio 0.45 (X_2 = 0) and second crack depth ratio 0.9 (X_4 = 1). The obtained corresponding simulated first five natural frequencies are tabulated in respective experimental run numbers. Thereafter, RSFs have been developed using regression analysis. Before confirming the RSFs of each output responses for further analysis, statistical significances are studied through analysis of variance (ANOVA).

Table 5.14: Independent variables and calculated responses for double cracked angle section beam

Run	Coded levels of variables				Response (Hz)				
	X_1	X_2	X_3	X_4	y_1	y_2	y_3	y_4	y_5
1	0	0	0	0	23.3690	50.1753	80.9360	133.3747	264.8121
2	0	0	1	0	23.4297	50.1852	81.0401	134.1580	266.0422
3	1	-1	-1	1	11.9975	49.1110	77.3046	114.5218	256.8939
4	-1	1	1	1	11.3213	48.9003	74.7571	105.3145	245.4715
5	1	1	-1	1	11.9975	49.1110	77.3046	114.5218	256.8939
6	-1	-1	1	1	23.7030	50.4680	81.6992	137.6978	269.8373
7	0	0	-1	0	22.3931	49.9891	79.7102	132.3367	262.7917
8	0	-1	0	0	23.4544	50.1894	81.0511	134.1443	265.7655
9	0	0	0	0	23.3690	50.1753	80.9360	133.3747	264.8121
10	0	1	0	0	20.0112	49.9821	75.0136	105.3649	248.3958
11	1	-1	-1	-1	23.7030	50.4680	81.6992	137.6978	269.8373
12	1	0	0	0	23.4544	50.1894	81.0511	134.1443	265.7655
13	-1	0	0	0	22.2169	49.9281	78.0996	129.7542	255.3577
14	-1	-1	1	-1	23.7030	50.4680	81.6992	137.6978	269.8373
15	0	0	0	0	23.3690	50.1753	80.9360	133.3747	264.8121
16	1	-1	1	1	23.7030	50.4680	81.6992	137.6978	269.8373
17	1	1	1	-1	23.7030	50.4680	81.6992	137.6978	269.8373
18	1	1	1	1	23.7030	50.4680	81.6992	137.6978	269.8373
19	-1	1	-1	-1	11.3213	48.9003	74.7571	105.3145	245.4715
20	-1	1	-1	1	9.8125	48.4293	74.1152	105.4979	243.7971
21	0	0	0	0	23.3690	50.1753	80.9360	133.3747	264.8121
22	1	-1	1	-1	23.7030	50.4680	81.6992	137.6978	269.8373
23	-1	1	1	-1	11.3213	48.9003	74.7571	105.3145	245.4715
24	0	0	0	-1	23.4297	50.1852	81.0401	134.1580	266.0422
25	-1	-1	-1	-1	23.7030	50.4680	81.6992	137.6978	269.8373
26	1	1	-1	-1	23.7030	50.4680	81.6992	137.6978	269.8373
27	-1	-1	-1	1	11.9975	49.1110	77.3046	114.5218	256.8939
28	0	0	0	0	23.3690	50.1753	80.9360	133.3747	264.8121
29	0	0	0	1	21.7897	50.0881	77.9348	112.5336	249.9042
30	0	0	0	0	23.3690	50.1753	80.9360	133.3747	264.8121

In order to check the adequacy of RSFs, ANOVA test has been carried out and results of the statistical test for single cracked channel and angle section beams are presented in Table

5.15 and Table 5.16 respectively. Theoretical background of the above statistical estimators is well known and can be found elsewhere [120-122]. Model-I, Model-II, Model-III, Model-IV and Model-V are the RSFs for first, second, third, fourth and fifth natural frequencies (y_1, y_2, y_3, y_4 and y_5) respectively for single cracked beam. P-values obtained are less than 0.05 which clearly shows that polynomial terms are significant for all the models. The calculated R^2 values are 0.7000, 0.7303, 0.9075, 0.8758, 0.8861 for y_1, y_2, y_3, y_4 and y_5 respectively in channel and 0.9145, 0.9544, 0.8192, 0.8731, 0.8812 for y_1, y_2, y_3, y_4 and y_5 respectively in angle section beams. The high values ensure a satisfactory adjustment of the model to the experimental data.

Table 5.15: ANOVA for output response surfaces for single cracked channel section beam

SD	SS	Df	MS	F-value	P-value	R^2	R^2_{adj}	Std. Dev	Comment
Model-I	29.50	3	9.83	6.99	0.0100	0.7000	0.6000	1.19	Significant
X_1	9.59	1	9.59	6.82	0.0282				
X_2	8.30	1	8.30	5.90	0.0380				
X_1X_2	11.62	1	11.62	8.26	0.0184				
Residual	12.66	9	1.41						
Total	42.17	12							
Model-II	75.87	3	25.29	8.12	0.0063	0.7303	0.6403	1.76	Significant
X_1	24.63	1	24.63	7.91	0.0203				
X_2	22.43	1	22.43	7.20	0.0251				
X_1X_2	28.81	1	28.81	9.25	0.0140				
Residual	28.02	9	3.11						
Total	103.89	12							
Model-III	982.63	4	245.66	19.63	0.0003	0.9075	0.8613	3.54	Significant
X_1	176.55	1	176.55	14.11	0.0056				
X_2	455.38	1	455.38	36.39	0.0003				
X_1X_2	196.70	1	196.70	15.72	0.0042				
X_2^2	154.01	1	154.01	12.31	0.0080				
Residual	100.12	8	12.51						
Total	1082.75	12							
Model-IV	4116.88	4	1029.22	14.11	0.0011	0.8758	0.8138	8.54	Significant
X_1	1260.56	1	1260.56	17.28	0.0032				
X_2	1063.77	1	1063.77	14.58	0.0051				
X_1X_2	1305.21	1	1305.21	17.89	0.0029				
X_1^2	487.34	1	487.34	6.68	0.0324				
Residual	583.56	8	72.95						
Total	4700.44	12							
Model-V	810.48	4	202.62	15.55	0.0008	0.8861	0.8291	3.61	Significant
X_1	147.37	1	147.37	11.31	0.0099				
X_2	397.44	1	397.44	30.51	0.0006				
X_1X_2	157.52	1	157.52	12.09	0.0084				
X_2^2	108.14	1	108.14	8.30	0.0205				
Residual	104.23	8	13.03						
Total	914.71	12							

SD = Source of data; SS = Sum of squares; Df = Degrees of freedom; MS = Mean square.

Table 5.16: ANOVA for output response surfaces for single cracked angle section beam

SD	SS	Df	MS	F value	P-value	R^2	R^2_{adj}	Std. Dev.	Comment
Model-I	129.66	4	32.42	21.39	0.0002	0.9145	0.8718	1.23	Significant
X_1	31.82	1	31.82	21.00	0.0018				
X_2	42.84	1	42.84	28.27	0.0007				
X_1X_2	38.33	1	38.33	25.29	0.0010				
X_2^2	16.68	1	16.68	11.01	0.0106				
Residual	12.12	8	1.52						
Total	141.78	12							
Model-II	2.04	3	0.68	62.82	<0.0001	0.9544	0.9392	0.10	Significant
X_1	0.73	1	0.73	67.62	<0.0001				
X_2	0.70	1	0.70	64.21	<0.0001				
X_1X_2	0.61	1	0.61	56.64	<0.0001				
Residual	0.098	9	0.011						
Total	2.14	12							
Model-III	60.61	3	20.20	13.59	0.0011	0.8192	0.7589	1.22	Significant
X_1	18.16	1	18.16	12.22	0.0068				
X_2	30.41	1	30.41	20.46	0.0014				
X_1X_2	12.05	1	12.05	8.11	0.0192				
Residual	13.38	9	1.49						
Total	73.99	12							
Model-IV	1390.14	4	347.54	13.76	0.0012	0.8731	0.8097	5.02	Significant
X_1	259.46	1	259.46	10.28	0.0125				
X_2	698.61	1	698.61	27.67	0.0008				
X_1X_2	262.17	1	262.17	10.38	0.0122				
X_2^2	169.90	1	169.90	6.73	0.0319				
Residual	202.00	8	25.25						
Total	1592.14	12							
Model-V	732.20	3	244.07	22.25	0.0002	0.8812	0.8416	3.31	Significant
X_1	233.66	1	233.66	21.30	0.0013				
X_2	350.12	1	350.12	31.91	0.0003				
X_1X_2	148.42	1	148.42	13.53	0.0051				
Residual	98.74	9	10.97						
Total	830.94	12							

SD = Source of data; SS = Sum of squares; Df = Degrees of freedom; MS = Mean square.

In case of fitted model, the low standard deviation (Std. Dev.) values in Table 5.15 and Table 5.16 also indicate that variations between predicted and experimental values are very low and also show a high degree of precision in conducting experiments. Similarly, the analysis of variance (ANOVA) and statistical results of the fitted models for double cracked scenario are presented in Table 5.17 and Table 5.18. Model-I to Model-V are the RSFs for first to fifth natural frequencies respectively of the double crack problem. One can observe from ANOVA that all the models are highly significant as p-value becomes less than 0.0001. Since, R^2 values are fairly close to 1, there is an indication of high correlation between the predicted and observed data.

Table 5.17: ANOVA for output response surfaces for double cracked channel section beam

SD	SS	Df	MS	Fvalue	P-value	R^2	R^2_{adj}	Std.Dev.	Remark
Model-I	162.49	14	11.61	11.21	<0.0001	0.9128	0.8314	1.02	Highly
Residual	15.53	15	1.04						significant
Total	178.02	29							
Model-II	413.98	14	29.57	12.37	<0.0001	0.9203	0.8459	1.55	Highly
Residual	35.86	15	2.39						significant
Total	449.85	29							
Model-III	2608.27	14	186.31	8.65	<0.0001	0.8898	0.7869	4.64	Highly
Residual	323.18	15	21.55						significant
Total	2931.46	29							
Model-IV	15053.05	14	1075.22	11.85	<0.0001	0.9171	0.8397	9.52	Highly
Residual	1360.84	15	90.72						significant
Total	16413.89	29							
Model-V	2458.04	14	175.57	9.34	<0.0001	0.8971	0.8011	4.34	Highly
Residual	281.96	15	18.80						significant
Total	2739.99	29							

Table 5.18: ANOVA for output response surfaces for double cracked angle section beam

SD	SS	Df	MS	Fvalue	P-value	R^2	R^2_{adj}	Std. Dev.	Remark
Model-I	718.89	14	51.35	15.51	<0.0001	0.9354	0.8751	1.82	Highly
Residual	49.66	15	3.31						significant
Total	768.55	29							
Model-II	10.12	14	0.72	18.77	<0.0001	0.9460	0.8956	0.02	Highly
Residual	0.58	15	0.04						significant
Total	10.70	29							
Model-III	186.00	14	13.29	13.34	<0.0001	0.9257	0.8563	1.00	Highly
Residual	14.94	15	1.00						significant
Total	200.94	29							
Model-IV	4037.96	14	288.43	8.83	<0.0001	0.8918	0.7908	5.72	Highly
Residual	489.94	15	32.66						significant
Total	4527.90	29							
Model-V	2078.52	14	148.47	12.13	<0.0001	0.9189	0.8431	3.50	Highly
Residual	183.52	15	12.23						significant
Total	2262.04	29							

In case of these fitted models, the low standard deviation (Std. Dev.) values (1.02, 1.55, 4.64, 9.52 and 4.34) for double cracked channel beam and (1.82, 0.02, 1.00, 5.72 and 3.50) for angle section beams are obtained for output responses y_1, y_2, y_3, y_4 and y_5 respectively, which are very small compared to magnitude of frequencies and thus shows high precision and reliability of conducted experiments. The quadratic models come out appropriate for all the first five natural frequencies. Final generalized model equation for natural frequency in coded terms using ANOVA for single and multiple cracked channel and angle beam problem is obtained in the form as given in Equation (3.2) of Chapter 3. The estimated regression coefficients for these equations have been given in Table (D.1 to D.4) of Appendix-D. Generally, adequacy of the models is investigated via residual analysis. Two

plots needed for this are (i) normal probability plot of residuals and (ii) plot of residuals vs experimental run number. These are also known as diagnostic plot to determine the residual analysis of response surface design. To avoid repetition of similar plots only the diagnostic plot for Model-I has been presented in Figure 5.58 and Figure 5.59. Figure 5.58(a) and Figure 5.59(a) depict the normal probability plot of residuals for single and double cracked channel section beam respectively and Figure 5.60(a) and Figure 5.61(a) for single and double cracked angle section beam respectively. From these figures it can be noticed that all the residuals fall on a straight line. This indicates that the data are almost normally distributed with small deviation in an acceptable range of error. Similar observations are recorded by previous researchers too [120-122].

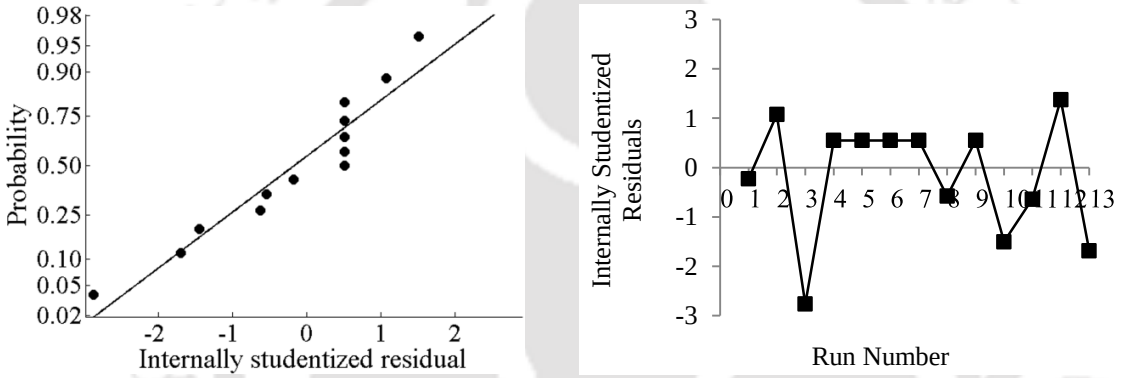

(a) (b)

Figure 5.58: Diagnostic plot for Model-I (Single cracked channel section beam): (a) Normal Probability plot and (b) Plot of residuals vs experimental run number

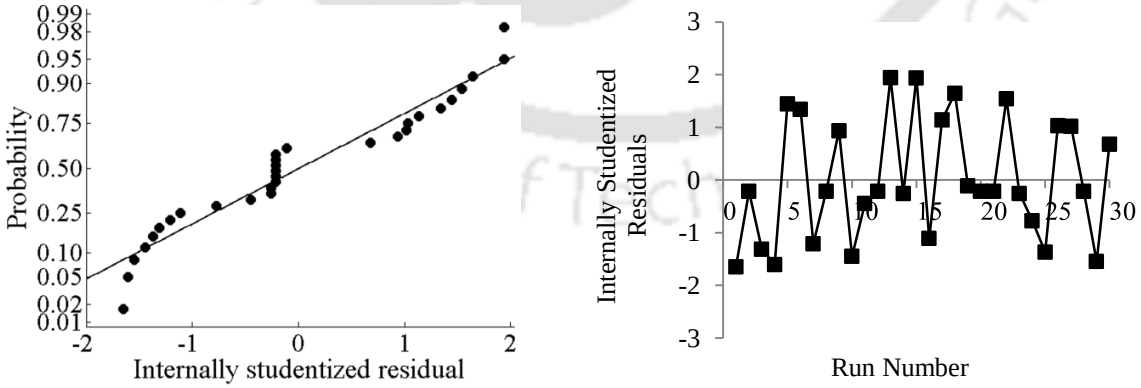

(a) (b)

Figure 5.59: Diagnostic plot for Model-I (Double cracked channel section beam): (a) Normal Probability plot and (b) Plot of residuals vs experimental run number

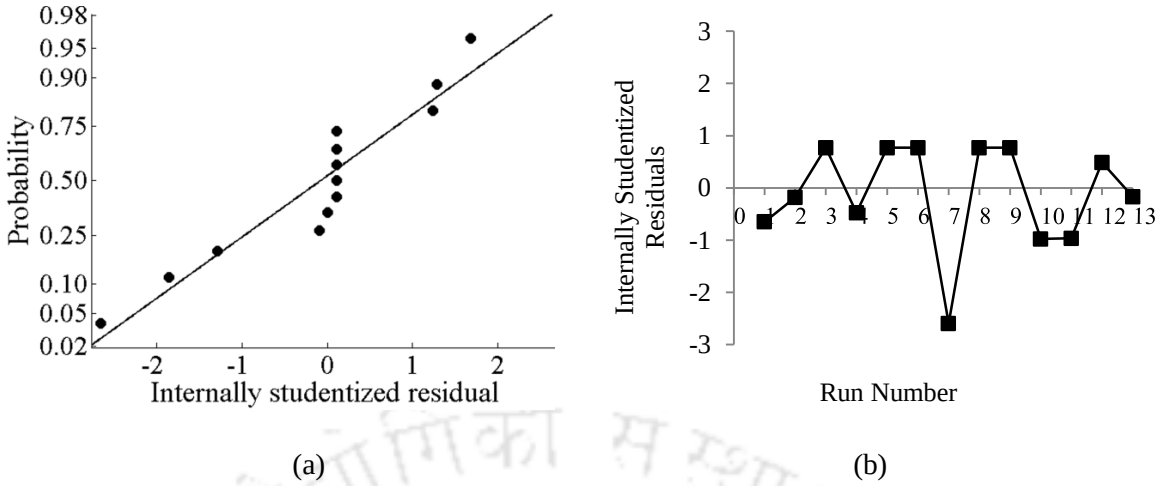

(a) (b)

Figure 5.60: Diagnostic plot for Model-I (Single cracked angle section beam): (a) Normal Probability plot and (b) Plot of residuals vs experimental run number

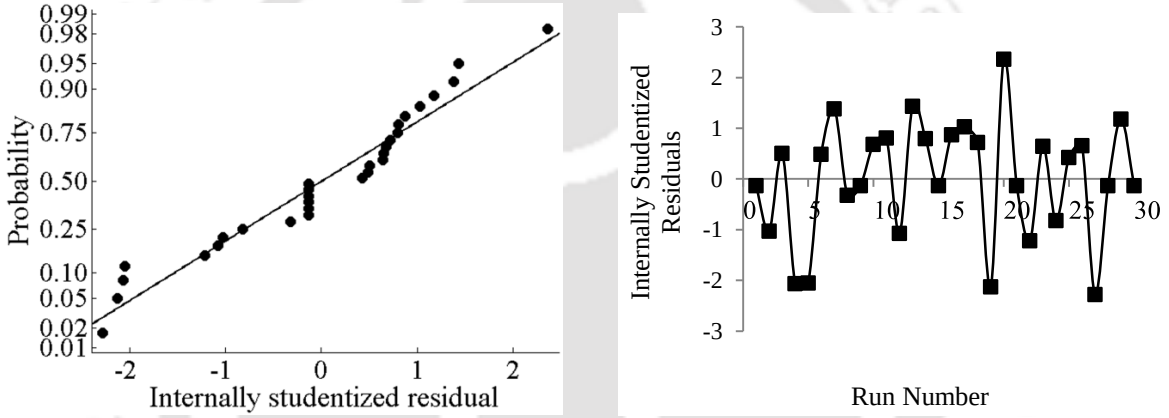

(a) (b)

Figure 5.61: Diagnostic plot for Model-I (Double cracked angle section beam): (a) Normal Probability plot and (b) Plot of residuals vs experimental run number

Figure 5.58(b), Figure 5.59(b), Figure 5.60(b) and Figure 5.61(b) represent the corresponding single and double cracked channel and angle section straight beam for residual vs experimental run number plot where residuals are randomly scattered around the horizontal axis without making systematic patterns within the constant range of residuals across the graph, i.e. within the horizontal lines at point of ±3. This shows that the models proposed are adequate and constant variance assumption was confirmed [121].

Finally, obtained response surface equations from statistical analysis are used in optimization technique. To calculate the optimum crack parameters (known as crack location and crack depth ratio) by minimizing an objective function a searching tool GA has been used. The objective function has been formed by root mean square (RMS) of the errors

between the computed responses from RSFs and measured responses, which is presented in Equation (3.35) of Chapter 3. In order to evaluate the optimum crack parameters the GA parameters like population size 20, elite count 2, crossover fraction 0.8, mutation rate 0.01 are kept same for single and multi-cracked channel and angle section beam. The number of variables for single cracked problem = 2 and for double cracked problem = 4. The number of generation has been required for single and double cracked optimization problem are 100 and 250.

Four different crack depth ratios at two different locations along the longitudinal axis of the single cracked cantilever beam have been considered to generate the test points. Therefore, in total eight numbers of test points are used to examine the feasibility and applicability of the proposed approach for single crack identification problem for each cross-sectional beam. Table 5.19 represents the actual crack parameters and corresponding physically measured first five natural frequencies of the single cracked channel and angle section cantilever beam obtained in laboratory. Similarly, the physical experimental tests have been performed for double crack scenario.

Table 5.19: Actual single crack parameters and measured first five natural frequencies

Test point	Crack parameters		Measured natural frequencies (Hz)				
	L_1 (m)	ζ_1/b	1st	2nd	3rd	4th	5th
Channel cross-sectional beam							
1	0.02	0.08	49.32	101.41	201.85	468.50	601.70
2	0.02	0.30	49.05	101.10	201.20	465.25	599.20
3	0.02	0.50	48.36	99.60	197.45	455.40	596.50
4	0.02	0.80	44.95	93.88	183.51	422.10	583.94
5	0.50	0.08	49.38	101.48	201.95	468.90	601.90
6	0.50	0.30	49.30	101.30	201.88	467.50	601.65
7	0.50	0.50	49.10	101.05	201.00	464.70	600.70
8	0.50	0.80	48.35	99.50	199.55	448.30	598.00
Angle cross-sectional beam							
1	0.02	0.08	23.45	50.13	80.20	136.00	254.20
2	0.02	0.30	23.25	49.80	79.95	133.65	253.85
3	0.02	0.50	21.13	49.63	79.13	128.30	248.50
4	0.02	0.80	14.80	48.78	76.40	113.25	242.00
5	0.50	0.08	23.50	50.18	80.75	136.55	257.40
6	0.50	0.30	23.47	50.15	80.35	136.10	256.95
7	0.50	0.50	23.40	50.00	79.86	133.28	256.35
8	0.50	0.80	22.88	49.50	79.25	115.86	235.00

The actual crack parameters and corresponding measured first five natural frequencies in laboratory for the double cracked channel and angle section beam has been tabulated in

Table 5.20 and Table 5.21 respectively. Total eighteen numbers of test points are considered for each sectional beam to examine the feasibility and practicability of the proposed approach for double crack identification problem.

Table 5.20: Actual crack position and crack depth ratio and corresponding natural frequency for channel beam

Test point	L_1 (m)	ζ_1/b	L_2 (m)	ζ_2/b	Measured natural frequencies (Hz)				
					1st	2nd	3rd	4th	5th
1	0.02	0.08	0.10	0.30	48.95	101.15	201.50	465.31	599.95
2	0.02	0.08	0.10	0.50	48.83	101.00	200.90	463.42	598.25
3	0.02	0.08	0.10	0.80	48.45	100.25	200.20	461.00	597.35
4	0.02	0.50	0.10	0.08	48.20	99.00	198.50	453.50	591.70
5	0.02	0.50	0.10	0.30	48.10	98.95	198.25	451.20	591.30
6	0.02	0.50	0.10	0.80	47.80	98.45	197.00	449.00	589.00
7	0.02	0.80	0.10	0.08	44.75	92.90	183.00	421.50	582.00
8	0.02	0.80	0.10	0.30	44.50	92.25	182.70	421.00	581.65
9	0.02	0.80	0.10	0.50	44.25	92.00	182.30	420.75	579.85
10	0.50	0.08	0.60	0.30	49.30	101.35	201.75	468.20	601.35
11	0.50	0.08	0.60	0.50	49.10	101.10	201.20	467.50	600.80
12	0.50	0.08	0.60	0.80	48.85	99.90	199.85	465.00	599.50
13	0.50	0.50	0.60	0.08	48.90	100.85	200.90	464.25	600.35
14	0.50	0.50	0.60	0.30	48.50	100.25	200.25	463.90	600.15
15	0.50	0.50	0.60	0.80	48.00	99.15	198.75	463.00	598.50
16	0.50	0.80	0.60	0.08	47.85	98.75	199.00	445.00	596.00
17	0.50	0.80	0.60	0.30	47.20	98.35	198.50	444.25	595.10
18	0.50	0.80	0.60	0.50	46.80	97.85	198.00	443.80	594.00

Table 5.21: Actual crack position and crack depth ratio and corresponding natural frequency for angle section beam

Test point	L_1 (m)	ζ_1/b	L_2 (m)	ζ_2/b	Measured natural frequencies (Hz)				
					1st	2nd	3rd	4th	5th
1	0.02	0.08	0.10	0.30	23.38	50.10	80.15	135.96	254.05
2	0.02	0.08	0.10	0.50	22.85	49.85	80.00	135.45	253.80
3	0.02	0.08	0.10	0.80	19.20	49.35	79.80	131.90	251.20
4	0.02	0.50	0.10	0.08	21.00	49.05	78.75	127.96	248.25
5	0.02	0.50	0.10	0.30	20.85	48.90	78.55	127.60	248.00
6	0.02	0.50	0.10	0.80	18.35	48.45	77.80	127.10	247.40
7	0.02	0.80	0.10	0.08	14.75	48.26	76.13	113.10	241.90
8	0.02	0.80	0.10	0.30	14.45	48.05	76.00	112.90	241.30
9	0.02	0.80	0.10	0.50	14.20	47.85	75.95	112.55	240.80
10	0.50	0.08	0.60	0.30	23.45	50.15	80.70	136.40	257.15
11	0.50	0.08	0.60	0.50	23.35	50.10	80.55	136.20	256.95
12	0.50	0.08	0.60	0.80	23.20	49.80	80.35	132.10	252.20
13	0.50	0.50	0.60	0.08	23.30	49.25	79.60	132.95	256.10
14	0.50	0.50	0.60	0.30	23.15	49.10	79.35	132.40	253.65
15	0.50	0.50	0.60	0.80	22.90	49.00	78.85	130.90	250.70
16	0.50	0.80	0.60	0.08	22.75	48.85	78.20	114.95	234.80
17	0.50	0.80	0.60	0.30	22.55	48.40	78.05	114.20	234.15
18	0.50	0.80	0.60	0.50	22.30	48.15	77.45	113.75	233.50

The GA results for first test points of single cracked channel and angle sectional beam are demonstrated in Figure 5.62 and Figure 5.63 respectively. Figure 5.62(a) and Figure 5.63(a) represent the optimization history for objective function. Plot between objective function versus the number of generations have been presented during GA implementation. The corresponding current best individuals are illustrated in Figure 5.62(b) and Figure 5.63(b) respectively. For an example (see first test point of Table 5.18), the optimal crack parameters are acquired after 52 iterations which predicts the current best individual coded values X_1 = -0.94980 and X_2 = -0.82550. After the conversion of the coded value into natural value one can obtain η_1 = 0.02010 and η_2 = 0.07850. The absolute percentage error has been obtained for crack location and crack depth ratio by comparing actual and predicted natural variables.

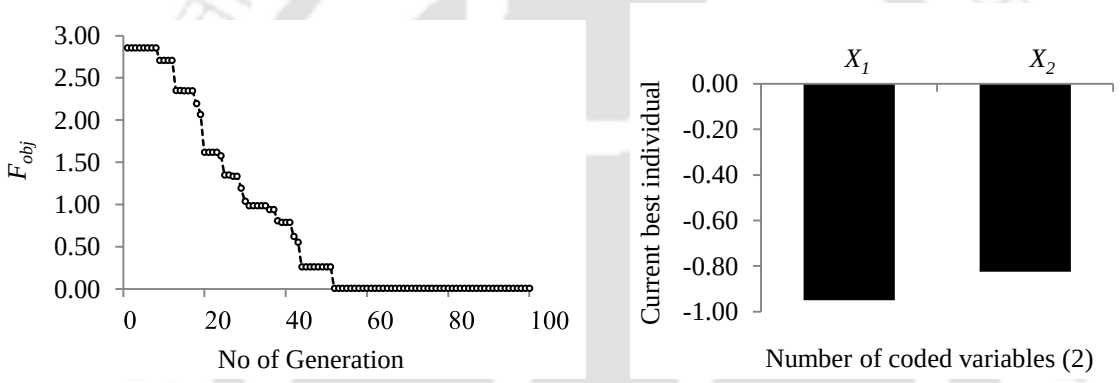

(a) (b)

Figure 5.62: GA results for first test point of single cracked channel section beam (a) Optimization history for objective Function and (b) Current best individual variables

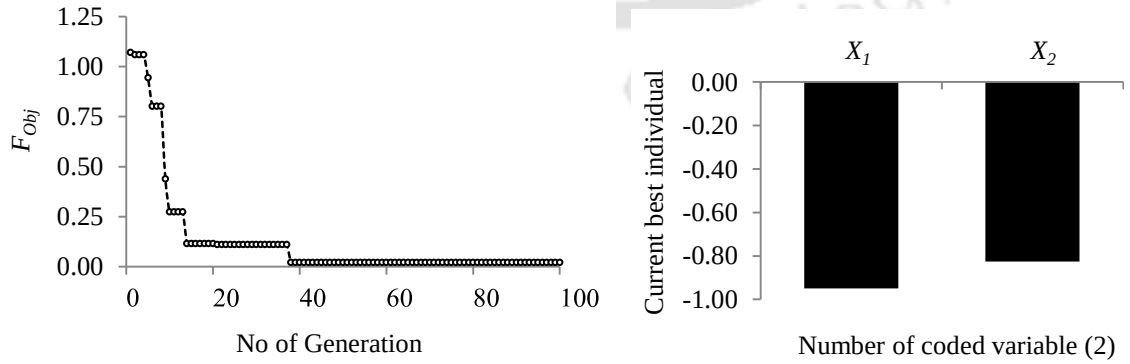

(a) (b)

Figure 5.63: GA results for first test point of single cracked angle section beam (a) Optimization history for objective Function and (b) Current best individual variables

The absolute error (%) between actual and predicted natural crack parameters for single cracked channel and angle section beams are estimated using Equation (3.36) and estimated values are presented in Table 5.22. It can be observed from Table 5.22 that the absolute errors for single cracked channel section beams range from 0.42-1.00% and 1.17-8.00% whereas, the absolute errors for single cracked angle section beam specimens lie in the range of 0.42-1.45% and 0.9-7.20% for crack localization and crack depth ratio respectively.

Table 5.22: Actual and predicted crack parameters for single cracked beam

Test point	Actual variables		Predicted variables				Abs error (%) in	
	L_1 (m)	ζ_1/b	Coded variable (X)		Natural variable (η)		L_1	ζ_1/b
			X_1	X_2	η_1	η_2		
Channel cross-sectional beam								
1	0.02	0.08	-0.94980	-0.82550	0.02010	0.07850	0.50	1.86
2	0.02	0.30	-0.95020	-0.32000	0.01990	0.30600	0.50	2.00
3	0.02	0.50	-0.95020	0.08640	0.01990	0.48890	0.50	2.22
4	0.02	0.80	-0.95040	0.85150	0.01980	0.83320	1.00	4.15
5	0.50	0.08	0.25900	-0.83650	0.50360	0.07360	0.72	8.00
6	0.50	0.30	0.25520	-0.34100	0.50210	0.29650	0.42	1.17
7	0.50	0.50	0.26000	0.07100	0.50400	0.48200	0.80	3.60
8	0.50	0.80	0.26200	0.69840	0.50480	0.76430	0.96	4.46
Angle cross-sectional beam								
1	0.02	0.08	-0.94967	-0.82640	0.02013	0.07812	0.65	2.35
2	0.02	0.30	-0.95022	-0.32733	0.01991	0.30270	0.45	0.90
3	0.02	0.50	-0.95027	0.06933	0.01989	0.48120	0.55	3.76
4	0.02	0.80	-0.94965	0.83502	0.02014	0.82576	0.70	3.22
5	0.50	0.08	0.25525	-0.83377	0.50210	0.07480	0.42	6.50
6	0.50	0.30	0.23187	-0.31733	0.49275	0.30720	1.45	2.40
7	0.50	0.50	0.24000	0.03111	0.49600	0.46400	0.80	7.20
8	0.50	0.80	0.24225	0.67964	0.49690	0.75584	0.62	5.52

The objective function v/s the number of generation for double cracked channel and angle section beam has been depicted in Figure 5.64(a) and Figure 5.65(a) respectively. It can be noticed that the results converge consistently towards the best fitness value obtaining the final output variables namely, crack location and crack depth ratio. Figure 5.64(b) and Figure 5.65(b) represent the corresponding current best individual, where one can find the identified coded values for double cracked channel beam are X_1 = -0.94970, X_2 = -0.81688, X_3 = -0.84092 and X_4 = -0.31866 and that for angle beam are X_1 = -0.95020, X_2 = -0.82698, X_3 = -0.84303 and X_4 = -0.32433 of crack parameters in case of first test points. Predicted coded crack parameters for double cracked channel beam model have been tabulated in Table 5.23.

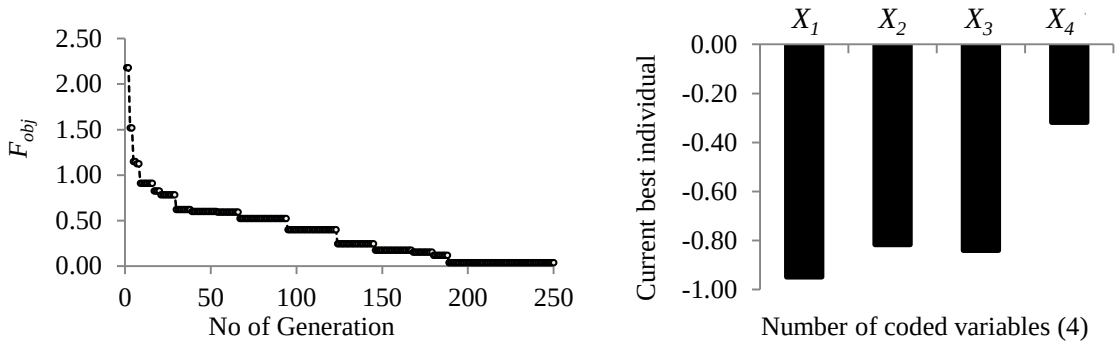

(a) (b)

Figure 5.64: GA results for first test point of double cracked channel section beam (a) Optimization history for objective function and (b) Current best individual variables

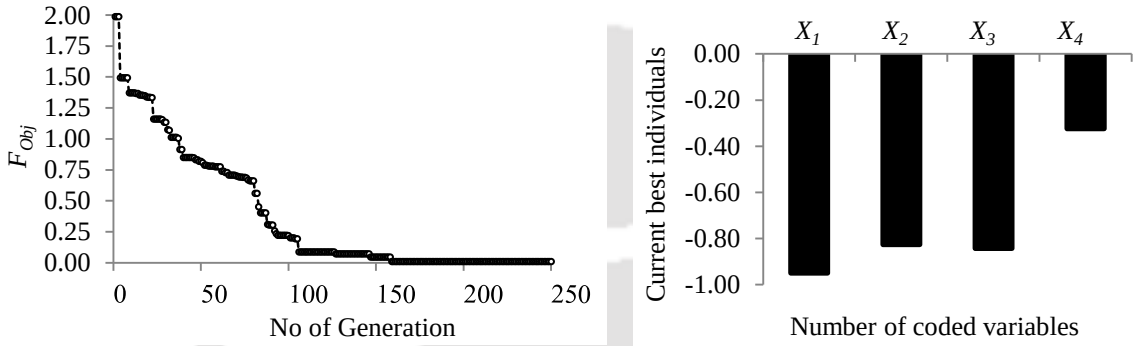

(a) (b)

Figure 5.65: GA results for first test point of double cracked angle section beam (a) Optimization history for objective function and (b) Current best individual variables

Table 5.23: Actual and predicted coded crack parameters for double cracked channel beam

Test point	L_1 (m)	ζ_1/b	L_2 (m)	ζ_2/b	Predicted coded variables			
					X_1	X_2	X_3	X_4
1	0.02	0.08	0.10	0.30	-0.94970	-0.81688	-0.84092	-0.31866
2	0.02	0.08	0.10	0.50	-0.94977	-0.81226	-0.84034	0.14666
3	0.02	0.08	0.10	0.80	-0.94972	-0.81733	-0.84171	0.85955
4	0.02	0.50	0.10	0.08	-0.94977	0.07111	-0.84302	-0.80933
5	0.02	0.50	0.10	0.30	-0.95032	0.13555	-0.84400	-0.35133
6	0.02	0.50	0.10	0.80	-0.95000	0.10000	-0.84078	0.71377
7	0.02	0.80	0.10	0.08	-0.94970	0.73333	-0.84434	-0.81133
8	0.02	0.80	0.10	0.30	-0.95012	0.69066	-0.84078	-0.31166
9	0.02	0.80	0.10	0.50	-0.95035	0.84000	-0.84236	0.05277
10	0.50	0.08	0.60	0.30	0.25313	-0.81960	0.47921	-0.36000
11	0.50	0.08	0.60	0.50	0.25775	-0.82800	0.46579	0.15000
12	0.50	0.08	0.60	0.80	0.24313	-0.82600	0.48663	0.80444
13	0.50	0.50	0.60	0.08	0.24250	0.16111	0.46105	-0.81910
14	0.50	0.50	0.60	0.30	0.25125	0.08167	0.47763	-0.31600
15	0.50	0.50	0.60	0.80	0.25450	0.05000	0.48158	0.88267
16	0.50	0.80	0.60	0.08	0.25875	0.88089	0.47605	-0.80980
17	0.50	0.80	0.60	0.30	0.24375	0.83733	0.46816	-0.35700
18	0.50	0.80	0.60	0.50	0.25813	0.84000	0.48553	0.16278

Table 5.24: Predicted natural crack parameters and percentage error for double cracked channel section beam

Test point	Predicted natural values				Abs error (%) in			
	η_1	η_2	η_3	η_4	L_1	ζ_1/b	L_2	ζ_2/b
1	0.02012	0.08240	0.10045	0.30660	0.60	3.00	0.45	2.20
2	0.02009	0.08448	0.10067	0.51599	0.45	5.60	0.67	3.19
3	0.02011	0.08220	0.10015	0.83679	0.55	2.75	0.15	4.60
4	0.02009	0.48199	0.09965	0.08580	0.45	3.60	0.35	7.25
5	0.01987	0.51099	0.09928	0.29190	0.65	2.19	0.72	2.70
6	0.02000	0.49500	0.10050	0.77119	0.00	1.00	0.50	3.60
7	0.02012	0.77999	0.09915	0.08490	0.60	2.50	0.85	6.12
8	0.01995	0.76079	0.10050	0.30975	0.25	4.90	0.50	3.25
9	0.01986	0.82800	0.09990	0.47374	0.70	3.50	0.10	5.25
10	0.50125	0.08118	0.60209	0.28800	0.25	1.48	0.35	4.00
11	0.50310	0.07740	0.59700	0.51750	0.62	3.25	0.50	3.50
12	0.49725	0.07830	0.60492	0.81199	0.55	2.12	0.82	1.50
13	0.49700	0.52249	0.59519	0.08140	0.60	4.49	0.80	1.75
14	0.50050	0.48675	0.60149	0.30780	0.10	2.65	0.25	2.60
15	0.50180	0.47250	0.60300	0.84720	0.36	5.50	0.50	5.90
16	0.50350	0.84640	0.60089	0.08559	0.70	5.80	0.15	6.99
17	0.49750	0.82679	0.59790	0.28935	0.50	3.35	0.35	3.55
18	0.50325	0.82800	0.60450	0.52325	0.65	3.50	0.75	4.65

Table 5.25: Actual and predicted coded crack parameters for double cracked angle section beam

Test point	L_1 (m)	ζ_1/b	L_2 (m)	ζ_2/b	Predicted coded variables			
					X_1	X_2	X_3	X_4
1	0.02	0.08	0.10	0.30	-0.95020	-0.82698	-0.84303	-0.32433
2	0.02	0.08	0.10	0.50	-0.94983	-0.82502	-0.84447	0.07111
3	0.02	0.08	0.10	0.80	-0.95008	-0.81556	-0.84039	0.83929
4	0.02	0.50	0.10	0.08	-0.95033	0.06889	-0.84321	-0.82449
5	0.02	0.50	0.10	0.30	-0.95020	0.13722	-0.84211	-0.36967
6	0.02	0.50	0.10	0.80	-0.94970	0.08667	-0.84276	0.71378
7	0.02	0.80	0.10	0.08	-0.95008	0.66311	-0.84171	-0.82978
8	0.02	0.80	0.10	0.30	-0.95043	0.73156	-0.84084	-0.31493
9	0.02	0.80	0.10	0.50	-0.95015	0.85778	-0.84350	0.06811
10	0.50	0.08	0.60	0.30	0.25938	-0.81731	0.46958	-0.31687
11	0.50	0.08	0.60	0.50	0.24475	-0.83093	0.46658	0.07267
12	0.50	0.08	0.60	0.80	0.24850	-0.81929	0.47811	0.75520
13	0.50	0.50	0.60	0.08	0.23163	0.09056	0.46642	-0.80996
14	0.50	0.50	0.60	0.30	0.24050	0.05933	0.47116	-0.35607
15	0.50	0.50	0.60	0.80	0.23838	0.16944	0.48505	0.80836
16	0.50	0.80	0.60	0.08	0.25800	0.67200	0.46279	-0.83253
17	0.50	0.80	0.60	0.30	0.24313	0.83378	0.46974	-0.35293
18	0.50	0.80	0.60	0.50	0.25488	0.72996	0.48284	0.14733

The predicted natural crack parameters and absolute percentage error between predicted and actual crack parameters for double cracked channel beam model have been presented in Table 5.24. The absolute error for double cracked channel section straight beam lies within

0.85 % and 7.25% for crack localization and crack depth ratio respectively. The actual and predicted coded crack parameters for double cracked angle section beam model have been shown in Table 5.25. Table 5.26 lists the predicted crack parameters and corresponding absolute percentage error obtained by comparing it with actual crack parameters. It has been found that the prediction of percentage error for crack positions and crack depth ratios for double cracked angle section beam specimens lies within the range of 0.12-1.47% and 1.27-6.90% respectively.

Table 5.26: Predicted natural crack parameters and percentage error with actual parameters

Test point	Predicted natural values				Abs error (%) in			
	η_1	η_2	η_3	η_4	L_1	ζ_1/b	L_2	ζ_2/b
1	0.01992	0.07786	0.09965	0.30405	0.40	2.68	0.35	1.35
2	0.02007	0.07874	0.09910	0.48200	0.35	1.58	0.90	3.60
3	0.01997	0.08300	0.10065	0.82768	0.15	3.75	0.65	3.46
4	0.01987	0.48100	0.09958	0.07898	0.65	3.80	0.42	1.28
5	0.01992	0.51175	0.10000	0.28365	0.40	2.35	0.00	5.45
6	0.02012	0.48900	0.09975	0.77120	0.60	2.20	0.25	3.60
7	0.01997	0.74840	0.10015	0.07660	0.15	6.45	0.15	4.25
8	0.01983	0.77920	0.10048	0.30828	0.85	2.60	0.48	2.76
9	0.01994	0.83600	0.09947	0.48065	0.30	4.50	0.53	3.87
10	0.50375	0.08221	0.59844	0.30741	0.75	2.76	0.26	2.47
11	0.49790	0.07608	0.59730	0.48270	0.42	4.90	0.45	3.46
12	0.49940	0.08132	0.60168	0.78984	0.12	1.65	0.28	1.27
13	0.49265	0.49075	0.59724	0.08552	1.47	1.85	0.46	6.90
14	0.49620	0.47670	0.59904	0.28977	0.76	4.66	0.16	3.41
15	0.49535	0.52625	0.60432	0.81376	0.93	5.25	0.72	1.72
16	0.50320	0.75240	0.59586	0.07536	0.64	5.95	0.69	5.80
17	0.49725	0.82520	0.59850	0.29118	0.55	3.15	0.25	2.94
18	0.50195	0.77848	0.60348	0.51630	0.39	2.69	0.58	3.26

5.10.2 Case II – Identification of cracks in channel and angle sectional horizontally curved beam using free vibration response

In this section, the proposed approach has been applied to horizontally curved channel and angle section beams of low and high curvature. In order to perform this procedure, two different examples based on two different subtended angles (θ_s) 25° and 50° with single and multiple cracks have been studied for channel and angle section beam using free vibration response respectively. The beam length is kept 800 mm in both the cases. The beam with subtended angles 25° has radius of curvature 1833.50 mm whereas radius of curvature of the beam with subtended angle 50° is 916.70 mm. The design experiment range and levels of the independent variables for both the subtended angles for channel and angle section beam have been presented in Table 5.27.

Table 5.27: Real and coded levels of the independent variables for two cases of subtended angles

No. of crack	Factors	Real Symbol	θ_s	Real values of coded Levels		
				(-1)	(0)	(1)
Single	Crack location (degree)	η_1	25°	0.000	12.500	25.000
			50°	0.000	25.000	50.000
	Crack depth ratio	η_2	25°	0.000	0.450	0.900
			50°	0.000	0.450	0.900
Double	First crack location (degree)	η_1	25°	0.000	12.500	25.000
			50°	0.000	25.000	50.000
	First crack depth ratio	η_2	25°	0.000	0.450	0.900
			50°	0.000	0.450	0.900
	Second crack location (degree)	η_3	25°	1.250	13.125	25.000
			50°	2.500	26.250	50.000
	Second crack depth ratio	η_4	25°	0.000	0.450	0.900
			50°	0.000	0.450	0.900

5.10.2.1 Example – I : Curved beam with subtended angle (θ_s) = 25°

The FE based numerical experiments were planned according to CCF design. As per Equation (3.14) of Chapter 3, $p = 2$, $n_{cr} = 5$ for single cracked and $p = 4$, $n_c = 6$ for double cracked curved channel and angle section beam. Hence, 13 and 30 number of experimental trials was carried out randomly to obtain the RSFs for single and double cracked scenario respectively. Independent coded variables (X_1, X_2) and FE simulated responses (y_1, y_2, y_3, y_4 and y_5) for single cracked channel and angle section beam for 25° subtended angle have been presented in Table 5.28 and Table 5.29 respectively.

Table 5.28: Independent variables and calculated responses for single cracked channel section curved beam

Expt. trial no.	Coded levels of variables		First five natural frequencies (Hz)				
	X_1	X_2	y_1	y_2	y_3	y_4	y_5
1	0	1	40.6610	78.8373	197.6437	404.3725	757.4698
2	0	0	40.7513	79.0655	198.6179	408.0264	764.3796
3	0	0	40.7513	79.0655	198.6179	408.0264	764.3796
4	1	0	41.8526	81.2055	204.2942	419.9720	787.9753
5	0	0	40.7513	79.0655	198.6179	408.0264	764.3796
6	-1	0	39.8600	78.8715	198.2730	404.3980	752.4752
7	0	0	40.7513	79.0655	198.6179	408.0264	764.3796
8	0	-1	41.8526	81.2055	204.2942	419.9720	787.9753
9	-1	-1	41.8526	81.2055	204.2942	419.9720	787.9753
10	0	0	40.7513	79.0655	198.6179	408.0264	764.3796
11	-1	1	38.0881	78.1942	196.1175	393.9526	717.8893
12	1	-1	41.8526	81.2055	204.2942	419.9720	787.9753
13	1	1	41.8526	81.2055	204.2942	419.9720	787.9753

Table 5.29: Independent variables and calculated responses for single cracked curved beam (*angle*)

Expt. trial no.	Coded levels of variables		First five natural frequencies (Hz)				
	X_1	X_2	y_1	y_2	y_3	y_4	y_5
1	0	0	17.5720	24.5576	89.4715	128.5791	234.0962
2	0	0	17.5720	24.5576	89.4715	128.5791	234.0962
3	1	1	20.2211	25.9025	92.7269	130.0748	238.0878
4	1	-1	20.2211	25.9025	92.7269	130.0748	238.0878
5	-1	1	14.2119	23.1330	85.7738	125.9784	232.6813
6	0	0	17.5720	24.5576	89.4715	128.5791	234.0962
7	0	0	17.5720	24.5576	89.4715	128.5791	234.0962
8	0	1	17.4786	24.4495	89.2321	126.3612	229.0816
9	0	0	17.5720	24.5576	89.4715	128.5791	234.0962
10	-1	-1	20.2211	25.9025	92.7269	130.0748	238.0878
11	-1	0	15.5345	23.9159	87.3356	128.5439	235.9676
12	1	0	20.2211	25.9025	92.7269	130.0748	238.0878
13	0	-1	20.2211	25.9025	92.7269	130.0748	238.0878

Table 5.30: Independent variables and calculated responses for double cracked curved beam (*channel*)

Run	Coded levels of variables				Response (Hz)				
	X_1	X_2	X_3	X_4	y_1	y_2	y_3	y_4	y_5
1	1	0	0	0	40.7546	79.0721	198.6082	407.9671	764.3114
2	1	1	-1	-1	41.8526	81.2055	204.2942	419.9720	787.9753
3	0	0	0	-1	40.7513	79.0655	198.6179	408.0264	764.3796
4	1	1	-1	1	39.1266	78.4172	196.6316	398.3216	734.9180
5	0	0	0	0	40.7324	79.0270	198.3669	407.3446	762.5748
6	1	-1	-1	1	39.1266	78.4172	196.6316	398.3216	734.9180
7	0	0	0	1	40.6912	78.9204	197.8682	405.4943	758.8155
8	0	1	0	0	40.6428	78.7991	197.4069	403.7036	755.7940
9	-1	-1	1	1	41.8526	81.2055	204.2942	419.9720	787.9753
10	0	0	-1	0	40.2313	78.8984	198.1707	405.4546	756.8790
11	0	0	0	0	40.7324	79.0270	198.3669	407.3446	762.5748
12	-1	1	1	1	38.0881	78.1942	196.1175	393.9526	717.8893
13	0	0	0	0	40.7324	79.0270	198.3669	407.3446	762.5748
14	-1	0	0	0	39.8417	78.8333	198.0170	403.7314	750.7024
15	-1	1	-1	1	37.4287	77.8532	194.9453	389.2933	705.2706
16	1	-1	-1	-1	41.8526	81.2055	204.2942	419.9720	787.9753
17	1	-1	1	-1	41.8526	81.2055	204.2942	419.9720	787.9753
18	-1	-1	1	-1	41.8526	81.2055	204.2942	419.9720	787.9753
19	-1	1	1	-1	38.0881	78.1942	196.1175	393.9526	717.8893
20	1	1	1	-1	41.8526	81.2055	204.2942	419.9720	787.9753
21	-1	-1	-1	1	39.1266	78.4172	196.6316	398.3216	734.9180
22	1	-1	1	1	41.8526	81.2055	204.2942	419.9720	787.9753
23	0	0	0	0	40.7324	79.0270	198.3669	407.3446	762.5748
24	1	1	1	1	41.8526	81.2055	204.2942	419.9720	787.9753
25	0	0	0	0	40.7324	79.0270	198.3669	407.3446	762.5748
26	0	-1	0	0	40.7546	79.0721	198.6082	407.9671	764.3114
27	0	0	1	0	40.7513	79.0655	198.6179	408.0264	764.3796
28	-1	-1	-1	-1	41.8526	81.2055	204.2942	419.9720	787.9753
29	0	0	0	0	40.7324	79.0270	198.3669	407.3446	762.5748
30	-1	1	-1	-1	38.0881	78.1942	196.1175	393.9526	717.8893

Similarly, the FE simulated responses (y_1, y_2, y_3, y_4 and y_5) and the corresponding independent variables (X_1, X_2, X_3, X_4) for double cracked channel and angle section curved beam (for θ_s = 25°, R = 1833.50 mm) are tabulated in Table 5.30 and Table 5.31 respectively.

Table 5.31: Independent variables and calculated responses for double cracked angle section curved beam

Run	Coded levels of variables				Response (Hz)				
	X_1	X_2	X_3	X_4	y_1	y_2	y_3	y_4	y_5
1	-1	-1	-1	-1	20.2211	25.9025	92.7269	130.0748	238.0878
2	0	0	0	0	17.4643	24.4140	89.0008	127.3238	231.5606
3	1	-1	-1	1	15.7858	23.4896	88.4267	127.3530	234.6267
4	-1	1	1	-1	14.2119	23.1330	85.7738	125.9784	232.6813
5	0	0	0	0	17.4643	24.4140	89.0008	127.3238	231.5606
6	-1	-1	1	1	20.2211	25.9025	92.7269	130.0748	238.0878
7	0	0	0	0	17.4643	24.4140	89.0008	127.3238	231.5606
8	1	-1	1	1	20.2211	25.9025	92.7269	130.0748	238.0878
9	0	0	1	0	17.5720	24.5576	89.4715	128.5791	234.0962
10	-1	1	-1	1	14.0817	22.6189	84.6551	124.1410	229.2252
11	-1	0	0	0	15.4304	23.7765	86.8763	127.1274	232.5790
12	0	0	0	1	17.4169	24.3680	88.9185	126.1224	228.7904
13	0	1	0	0	17.3841	24.3104	88.7685	125.2989	227.2582
14	1	0	0	0	17.5762	24.5677	89.5208	128.5340	234.0731
15	0	0	0	-1	17.5720	24.5576	89.4715	128.5791	234.0962
16	1	-1	-1	-1	20.2211	25.9025	92.7269	130.0748	238.0878
17	-1	-1	-1	1	15.7858	23.4896	88.4267	127.3530	234.6267
18	-1	1	1	1	14.2119	23.1330	85.7738	125.9784	232.6813
19	1	1	-1	-1	20.2211	25.9025	92.7269	130.0748	238.0878
20	0	0	0	0	17.4643	24.4140	89.0008	127.3238	231.5606
21	1	1	1	1	20.2211	25.9025	92.7269	130.0748	238.0878
22	-1	-1	1	-1	20.2211	25.9025	92.7269	130.0748	238.0878
23	-1	1	-1	-1	14.2119	23.1330	85.7738	125.9784	232.6813
24	1	1	-1	1	15.7858	23.4896	88.4267	127.3530	234.6267
25	0	0	-1	0	16.5568	24.0130	88.6360	127.6260	233.4935
26	1	1	1	-1	20.2211	25.9025	92.7269	130.0748	238.0878
27	1	-1	1	-1	20.2211	25.9025	92.7269	130.0748	238.0878
28	0	-1	0	0	17.5762	24.5677	89.5208	128.5340	234.0731
29	0	0	0	0	17.4643	24.4140	89.0008	127.3238	231.5606
30	0	0	0	0	17.4643	24.4140	89.0008	127.3238	231.5606

After regression analysis, ANOVA was carried out to predict the response values accurately and detail analyses for these free vibration responses are reported in Table 5.32 and Table 5.33 for single cracked channel and angle section curved beam.

Table 5.32: ANOVA for output response surfaces for single cracked channel section curved beam (θ_s = 25°, R = 1833.50 mm)

SD	SS	Df	MS	F value	P-value	R^2	R^2_{adj}	Std.Dev	Comment
Model-I	13.39	5	2.68	61.89	< 0.0001	0.9779	0.9621	0.21	Highly
Residual	0.30	7	0.043						significant
Total	13.69	12							
Model-II	16.26	5	3.25	33.52	< 0.0001	0.9599	0.9313	0.31	Highly
Residual	0.68	7	0.097						significant
Total	16.94	12							
Model-III	117.26	5	23.45	34.52	< 0.0001	0.9610	0.9332	0.82	Highly
Residual	4.76	7	0.68						significant
Total	122.01	12							
Model-IV	814.73	5	162.95	113.12	< 0.0001	0.9878	0.9790	1.20	Highly
Residual	10.08	7	1.44						significant
Total	824.81	12							
Model-V	4868.83	5	973.77	130.23	< 0.0001	0.9894	0.9818	2.73	Highly
Residual	52.34	7	7.48						significant
Total	4921.17	12							

Table 5.33: ANOVA for output response surfaces for single cracked angle section curved beam (θ_s = 25°, R = 1833.50 mm)

SD	SS	Df	MS	F value	P-value	R^2	R^2_{adj}	Std. Dev	Comment
Model-I	44.82	5	8.96	57.17	<0.0001	0.9761	0.9590	0.40	Highly
Residual	1.10	7	0.16						significant
Total	45.91	12							
Model-II	9.71	5	1.94	70.89	<0.0001	0.9806	0.9668	0.17	Highly
Residual	0.19	7	0.027						significant
Total	9.90	12							
Model-III	61.84	5	12.37	60.49	<0.0001	0.9774	0.9612	0.45	Highly
Residual	1.43	7	0.20						significant
Total	63.27	12							
Model-IV	21.05	4	5.26	32.66	<0.0001	0.9423	0.9134	0.40	Highly
X_1	5.28	1	5.28	32.75	0.0004				significant
X_2	10.17	1	10.17	63.09	< 0.0001				
X_1X_2	4.20	1	4.20	26.03	0.0009				
X_1^2	1.41	1	1.41	8.76	0.0182				
Residual	1.29	8	0.16						
Total	22.34	12							
Model-V	78.23	4	19.56	11.30	0.0022	0.8497	0.7745	1.32	Significant
X_1	9.44	1	9.44	5.46	0.0477				
X_2	34.62	1	34.62	20.01	0.0021				
X_1X_2	7.31	1	7.31	4.22	0.0039				
X_1^2	26.86	1	26.86	15.52	0.0043				
Residual	13.84	8	1.73						
Total	92.07	12							

Model-I to Model-V are the RSFs or polynomial models for first five natural frequencies respectively for single cracked scenario. Sequential F-tests and P-value test were performed for each model and corresponding probability was evaluated to judge the

significance of the model. It can be noted from both the table that, when the model is highly significant the P-value becomes less than 0.0001 and for significant model the value becomes less than 0.05.

Table 5.34: ANOVA for output response surfaces for double cracked channel section curved beam

SD	SS	Df	MS	F value	P-value	R^2	R^2_{adj}	Std. Dev	Comment
Model-I	46.90	14	3.35	15.48	< 0.0001	0.9353	0.8748	0.47	Highy
Residual	3.25	15	0.22						significant
Total	50.15	29							
Model-II	37.44	14	2.67	10.58	< 0.0001	0.9080	0.8222	0.50	Highy
Residual	3.79	15	0.25						significant
Total	41.23	29							
Model-III	282.33	14	20.17	11.70	< 0.0001	0.9161	0.8378	1.31	Highy
Residual	25.85	15	1.72						significant
Total	308.18	29							
Model-IV	2391.95	14	170.85	14.82	< 0.0001	0.9326	0.8696	3.40	Highy
Residual	172.96	15	11.53						significant
Total	2564.91	29							
Model-V	16422.20	14	1173.01	16.74	< 0.0001	0.9399	0.8837	8.37	Highy
Residual	1050.87	15	70.06						significant
Total	17473.07	29							

Table 5.35: ANOVA for output response surfaces for double cracked angle section curved beam

SD	SS	df	MS	Fvalue	p-value	R^2	R^2_{adj}	Std.dev.	Remark
Model-I	114.31	14	8.16	12.00	<0.0001	0.9180	0.8415	0.82	Highly
Residual	10.21	15	0.68						significant
Total	124.51	29							
Model-II	28.68	14	2.05	15.45	<0.0001	0.9352	0.8746	0.36	Highly
Residual	1.99	15	0.13						significant
Total	30.67	29							
Model-III	164.85	14	11.78	24.14	<0.0001	0.9575	0.9178	0.70	Highly
Residual	7.32	15	0.49						significant
Total	172.17	29							
Model-IV	81.02	14	5.79	47.83	<0.0001	0.9781	0.9576	0.35	Highly
Residual	1.81	15	0.12						significant
Total	82.83	29							
Model-V	275.18	14	19.66	19.78	<0.0001	0.9486	0.9007	1.00	Highly
Residual	14.90	15	0.99						significant
Total	290.08	29							

Similarly, ANOVA for double cracked channel and angle section curved beam have been presented in Table 5.34 and Table 5.35. P-values are found highly significant for all five polynomial models for double cracked channel and angle section beam scenario. Low values of Std. Dev. in Table 5.32, Table 5.33, Table 5.34 and Table 5.35 ensures the high degree of precision and good authenticity of the experimental data. The final empirical model equations for first natural frequency generated in coded terms using ANOVA for

single and double cracked channel and angle section curved beam problem is obtained in the form as given in Equation (3.2). The calculated regression coefficients for these equations can be found in Table (D.5 to D.8) of Appendix-D.

Residuals were examined to check the capability of the model and it was carried out by major diagnostic plot such as (a) normal probability vs. residuals and (b) residuals vs. run number. Figure 5.66 and Figure 5.67 represent the diagnostic plot of Model-I for single cracked channel and angle section curved beam (θ_s = 25°), whereas, Figure 5.68 and Figure 5.69 represent the diagnostic plot of Model-I for double cracked channel and angle section curved beam.

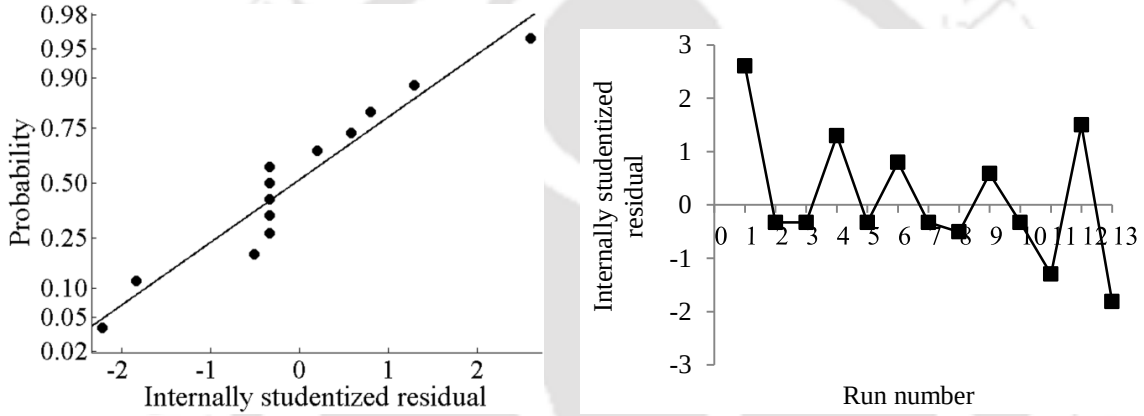

(a) (b)

Figure 5.66: Diagnostic plot for Model-I (Single cracked channel section curved beam, θ_s = 25°): (a) Normal Probability plot and (b) Plot of residuals vs experimental run number

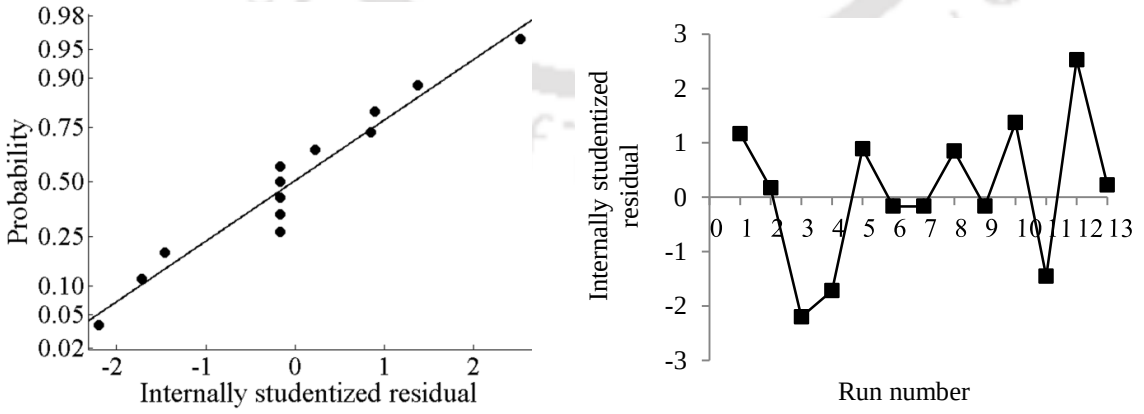

(a) (b)

Figure 5.67: Diagnostic plot for Model-I (Single cracked angle section curved beam, θ_s = 25°): (a) Normal Probability plot and (b) Plot of residuals vs experimental run number

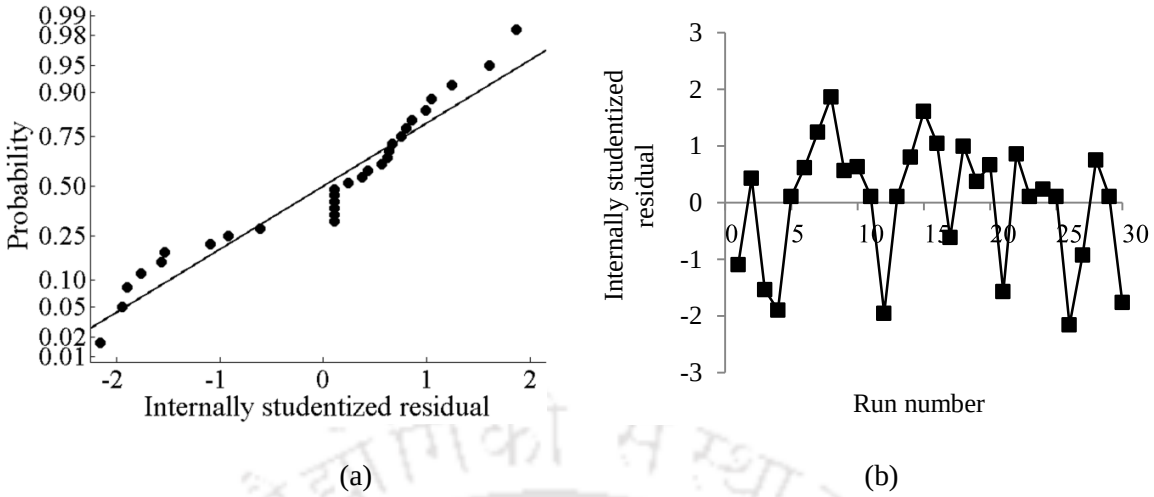

(a) (b)

Figure 5.68: Diagnostic plot for Model-I (Double cracked channel section curved beam, θ_s = 25°): (a) Normal Probability plot and (b) Plot of residuals vs experimental run number

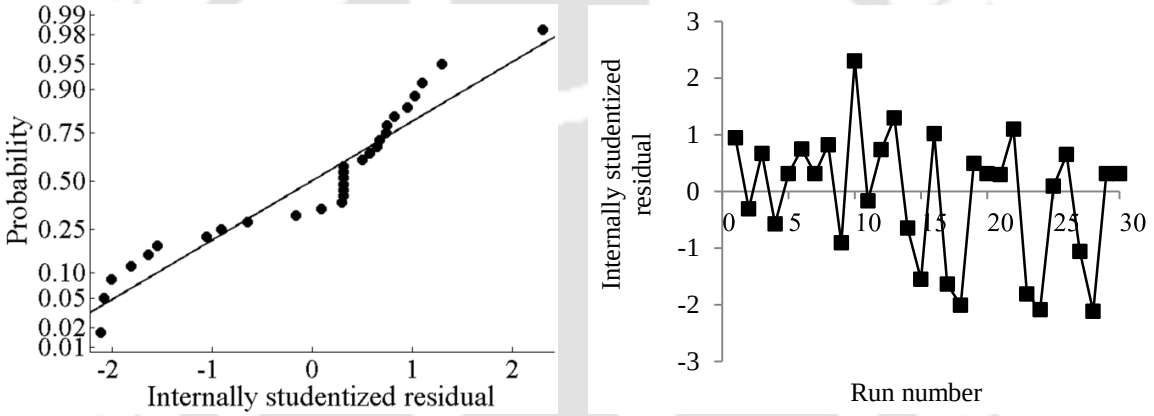

(a) (b)

Figure 5.69: Diagnostic plot for Model-I (Double cracked angle section curved beam, θ_s = 25°): (a) Normal Probability plot and (b) Plot of residuals vs experimental run number

The normal plot of residuals shows that all the residuals fall on a straight line. The first test of the adequacy of model is judged from this observation, which is known as Normality test or Normal probability plot of residual. In contrast, the residuals vs. run number plot is scattered and it is bounded in a narrow range. This proposes that the model is satisfactory and does not exhibit any violation of independence or constant variance assumption [121].

After carrying out statistical tests, the task remains to optimize the design variables by using genetic algorithm. The objective function has been established by root mean square (RMS) of the residuals between the computed polynomial responses from RSFs and measured responses. In order to estimate the optimum crack parameters using GAs,

population size = 20, elite count = 2, crossover fraction = 0.8, mutation rate = 0.01 are kept same for single and double cracked beam problem. Number of variables and generation used for single crack: 2 and 100; for double crack: 4 and 250 respectively. The actual crack parameters and measured first five natural frequencies for single cracked channel and angle section curved beam with 25° subtended angle have been listed in Table 5.36. Four different damage intensities at two different locations along the longitudinal axis of the single cracked cantilever curved beam have been considered to generate the test points. Thus, in total eight numbers of test points (laboratory tests) are used to examine the single crack identification problem for each cross-sectional beam individually. For example, in the first test point (see Table 5.36) the crack is located at angular distance θ_{S1} = 0.625° from the fixed end of the cantilever beam with corresponding crack depth ratio 0.08. It is assumed that cracks are present at the top flange of the beam in case of channel section while cracks are present at upper leg of the angle section curved beam.

Table 5.36: Actual single crack parameters and measured first five natural frequencies for single cracked channel and angle section curved beam (θ_s = 25°, R = 1833.50 mm)

Test point	Actual crack parameters		Measured natural frequencies (Hz)				
	θ_{S1} (deg)	ζ_1/b	1st	2nd	3rd	4th	5th
Curved channel beam							
1	0.625	0.08	40.55	78.72	198.04	407.02	763.51
2	0.625	0.30	40.23	78.62	197.71	405.23	758.27
3	0.625	0.50	39.73	78.45	197.14	402.39	749.56
4	0.625	0.80	38.80	78.07	195.92	396.61	731.20
5	15.625	0.08	40.58	78.73	198.05	407.10	763.82
6	15.625	0.30	40.56	78.70	197.84	406.29	761.98
7	15.625	0.50	40.53	78.66	197.51	405.05	758.58
8	15.625	0.80	40.51	78.56	196.86	402.63	750.52
Curved angle beam							
1	0.625	0.08	17.27	24.17	88.00	127.74	233.69
2	0.625	0.30	16.51	23.88	87.43	127.18	233.15
3	0.625	0.50	15.71	23.55	86.80	126.40	232.33
4	0.625	0.80	14.94	23.07	86.06	125.04	230.76
5	15.625	0.08	17.34	24.20	88.05	127.75	233.65
6	15.625	0.30	17.32	24.18	88.01	127.21	232.58
7	15.625	0.50	17.29	24.16	87.94	126.43	230.93
8	15.625	0.80	17.24	24.14	87.82	125.17	228.40

Total eight numbers of test points are used for single cracked curved beam of both type of cross-section to show the applicability of the proposed approach. Among them optimization history for first test point of single cracked channel and angle section curved beam has been shown in Figure 5.70(a) and Figure 5.71(a) respectively to avoid the

repetition. The corresponding current best individual bar plot of the variables are presented in Figure 5.70(b) and Figure 5.71(b).

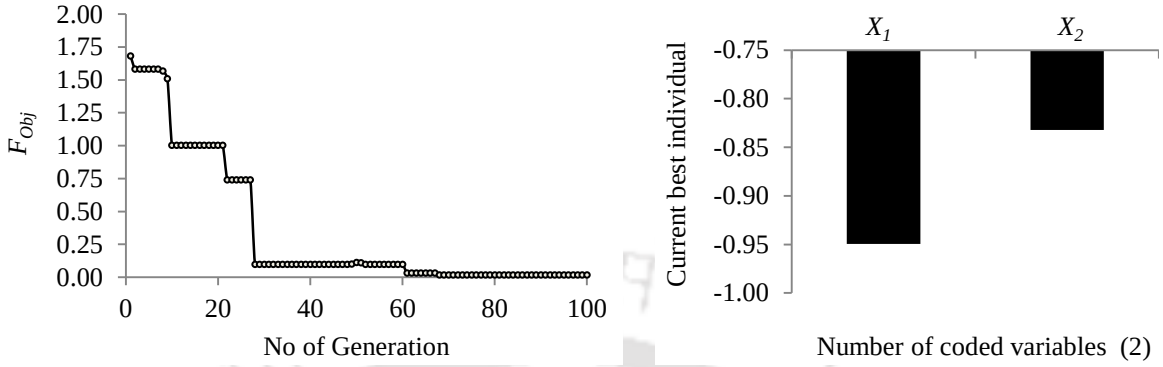

(a) (b)

Figure 5.70: GA results for first test point of single cracked channel section curved beam, θ_s = 25°: (a) Optimization history for objective function and (b) Current best individuals

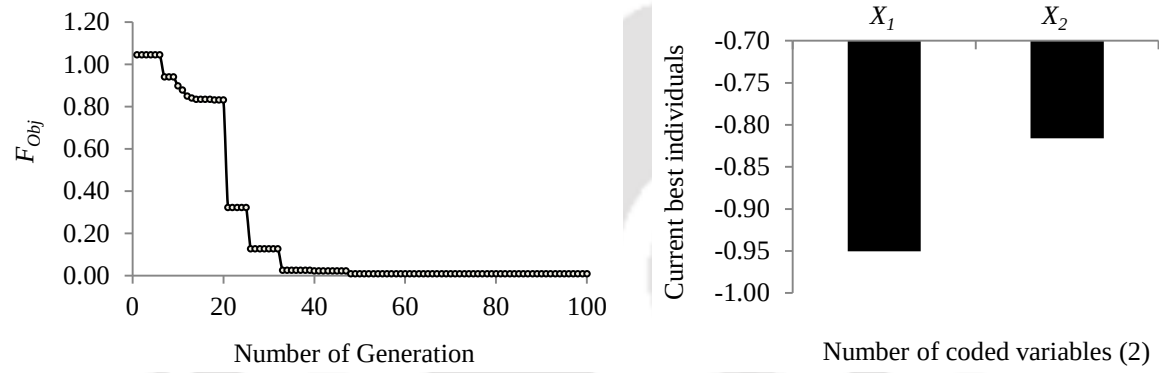

(a) (b)

Figure 5.71: GA results for first test point of single cracked angle section curved beam, θ_s = 25°: (a) Optimization history for objective function and (b) Current best individuals

As seen in the Figure 5.70(a) and Figure 5.71(a), value of the fitness decreases with increasing number of iteration. The optimal crack parameters are obtained at the end of 67 and 47 iterations, predicting the current best individual coded variables for single cracked channel and angle section curved beam (X_1 = -0.94952, X_2 = -0.83204); and (X_1 = -0.95045, X_2 = -0.81609) respectively. Table 5.37 illustrates the predicted coded and natural values for crack parameters and corresponding absolute error (%) between actual and predicted natural parameters. It can be noticed from the same table that the errors in crack localization lie within 1.16% and 1.52% in case of single cracked channel and angle section curved beam

respectively, whereas errors related to crack depth ratio remains maximum upto 8.25% and 7.80% in the said beams.

Table 5.37: Actual and predicted crack parameters for single cracked channel and angle section curved beam (θ_s = 25°, R = 1833.50 mm)

Test point	Actual crack parameters		Predicted coded value		Predicted natural value		Abs error (%) in	
	θ_{S1} (deg)	ζ_1/b	X_1	X_2	η_1	η_2	θ_{S1}	ζ_1/b
Curved channel beam								
1	0.625	0.08	-0.94952	-0.83204	0.63106	0.07558	0.97	5.52
2	0.625	0.30	-0.94985	-0.29313	0.62688	0.31809	0.30	6.03
3	0.625	0.50	-0.95015	0.04511	0.62319	0.47030	0.29	5.94
4	0.625	0.80	-0.95054	0.92444	0.61831	0.86600	1.07	8.25
5	15.625	0.08	0.23550	-0.81705	15.44375	0.08233	1.16	2.91
6	15.625	0.30	0.25725	-0.32387	15.71563	0.30426	0.58	1.42
7	15.625	0.50	0.24600	0.09167	15.57500	0.49125	0.32	1.75
8	15.625	0.80	0.26025	0.89262	15.75313	0.85168	0.82	6.46
Curved angle beam								
1	0.625	0.08	-0.95045	-0.81609	0.61944	0.08276	0.89	3.45
2	0.625	0.30	-0.94968	-0.36640	0.62900	0.28512	0.64	4.96
3	0.625	0.50	-0.95076	0.17878	0.61550	0.53045	1.52	6.09
4	0.625	0.80	-0.94946	0.68658	0.63175	0.75896	1.08	5.13
5	15.625	0.08	0.26650	-0.81538	15.83125	0.08308	1.32	3.85
6	15.625	0.30	0.24075	-0.28133	15.50938	0.32340	0.74	7.80
7	15.625	0.50	0.25150	0.03633	15.64375	0.46635	0.12	6.73
8	15.625	0.80	0.24488	0.69156	15.56094	0.76120	0.41	4.85

Table 5.38: Actual crack parameters and corresponding natural frequencies for double cracked channel section curved beam (θ_s = 25°, R = 1833.50 mm)

Test point	θ_{S1} (deg)	ζ_1/b	θ_{S2} (deg)	ζ_2/b	Measured natural frequencies (Hz)				
					1st	2nd	3rd	4th	5th
1	0.625	0.08	3.125	0.30	40.28	78.26	196.87	404.44	758.34
2	0.625	0.08	3.125	0.50	40.19	78.19	196.68	403.76	756.53
3	0.625	0.08	3.125	0.80	40.00	78.05	196.26	402.14	752.40
4	0.625	0.50	3.125	0.08	39.52	78.03	196.08	400.22	745.49
5	0.625	0.50	3.125	0.30	39.47	77.99	195.98	399.86	744.57
6	0.625	0.50	3.125	0.80	39.22	77.78	195.38	397.70	739.30
7	0.625	0.80	3.125	0.08	38.59	77.65	194.86	394.47	727.23
8	0.625	0.80	3.125	0.30	38.55	77.61	194.76	394.14	726.43
9	0.625	0.80	3.125	0.50	38.47	77.55	194.59	393.54	725.03
10	15.625	0.08	18.750	0.30	40.55	78.46	196.92	404.47	758.70
11	15.625	0.08	18.750	0.50	40.50	78.42	196.81	403.82	757.23
12	15.625	0.08	18.750	0.80	40.47	78.38	196.55	402.55	754.37
13	15.625	0.50	18.750	0.08	40.35	78.25	196.45	402.85	754.45
14	15.625	0.50	18.750	0.30	40.33	78.23	196.39	402.44	753.51
15	15.625	0.50	18.750	0.80	40.32	78.18	196.02	400.87	749.29
16	15.625	0.80	18.750	0.08	39.65	78.14	195.80	400.45	746.43
17	15.625	0.80	18.750	0.30	39.20	78.13	195.25	399.15	744.53
18	15.625	0.80	18.750	0.50	38.85	78.11	194.74	396.44	740.15

The experimentally measured natural frequencies for double cracked channel and angle section curved beam with subtended angle (θ_s) 25° have been presented for various combinations of crack parameters in Table 5.38 and Table 5.39 respectively. Total 18 number of laboratory experiments was carried out for each cross sectional beam to form 18 test points which are then utilized to evaluate the objective function.

Table 5.39: Actual crack parameters and corresponding natural frequencies for double cracked angle section curved beam (θ_s = 25°, R = 1833.50 mm)

Test point	θ_{S1} (deg)	ζ_1/b	θ_{S2} (deg)	ζ_2/b	Experimentally measured natural frequencies (Hz)				
					1st	2nd	3rd	4th	5th
1	0.625	0.08	3.125	0.30	17.13	23.98	87.43	126.95	232.15
2	0.625	0.08	3.125	0.50	17.05	23.90	87.24	126.73	231.60
3	0.625	0.08	3.125	0.80	16.93	23.74	86.92	126.37	230.67
4	0.625	0.50	3.125	0.08	15.63	23.42	86.35	125.75	231.13
5	0.625	0.50	3.125	0.30	15.61	23.37	86.16	125.63	230.80
6	0.625	0.50	3.125	0.80	15.58	23.14	85.28	125.13	229.26
7	0.625	0.80	3.125	0.08	14.87	22.94	85.61	124.40	229.56
8	0.625	0.80	3.125	0.30	14.85	22.89	85.38	124.30	229.23
9	0.625	0.80	3.125	0.50	14.80	22.81	85.00	124.14	228.70
10	15.625	0.08	18.75	0.30	17.26	24.15	87.53	127.02	232.38
11	15.625	0.08	18.75	0.50	17.24	24.12	87.41	126.90	232.25
12	15.625	0.08	18.75	0.80	17.22	24.10	87.20	126.67	231.99
13	15.625	0.50	18.75	0.08	17.18	24.00	87.49	125.78	229.76
14	15.625	0.50	18.75	0.30	17.16	23.95	87.43	125.71	229.69
15	15.625	0.50	18.75	0.80	17.15	23.90	87.13	125.41	229.34
16	15.625	0.80	18.75	0.08	17.12	23.85	87.37	124.53	227.24
17	15.625	0.80	18.75	0.30	17.10	23.80	87.32	124.47	227.17
18	15.625	0.80	18.75	0.50	17.05	23.77	87.22	124.38	227.06

GA results for first test point of double cracked channel and angle section curved beam have been presented in Figure 5.72 and Figure 5.73 respectively. The predicted current best individual coded variables for double cracked channel beam are X_1 = -0.94965, X_2 = -0.81018, X_3 = -0.84350, X_4 = -0.36900 with corresponding natural values η_1 = 0.62938, η_2 = 0.08542, η_3 = 3.10844, η_4 = 0.28395. For angle section coded parameters are found as X_1 = -0.94928, X_2 = -0.83268, X_3 = -0.83897, X_4 = -0.36840 with corresponding natural values η_1 = 0.63400, η_2 = 0.07530, η_3 = 3.16219, η_4 = 0.28422. The number of iterations required for convergence is 174 and 146 for channel and angle section curved beam for double crack scenario.

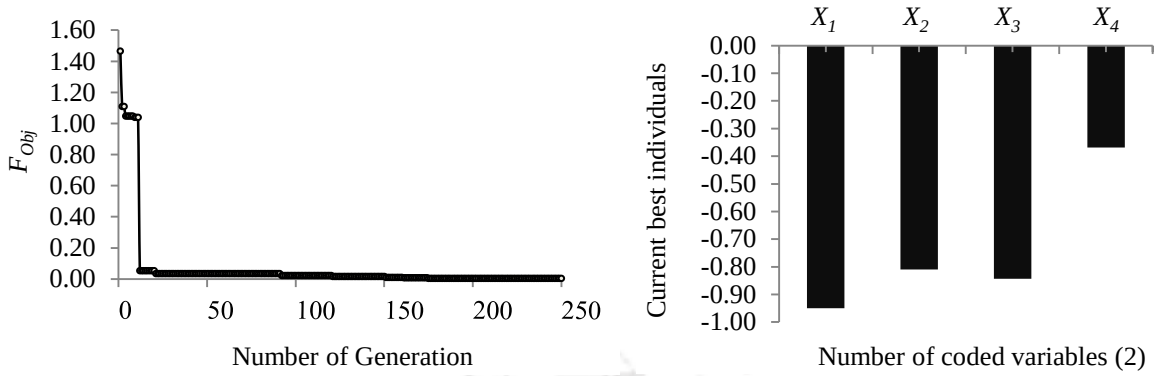

(a) (b)

Figure 5.72: GA results for first test point of double cracked channel section curved beam, θ_s = 25°: (a) Optimization history for objective function and (b) Current best individuals

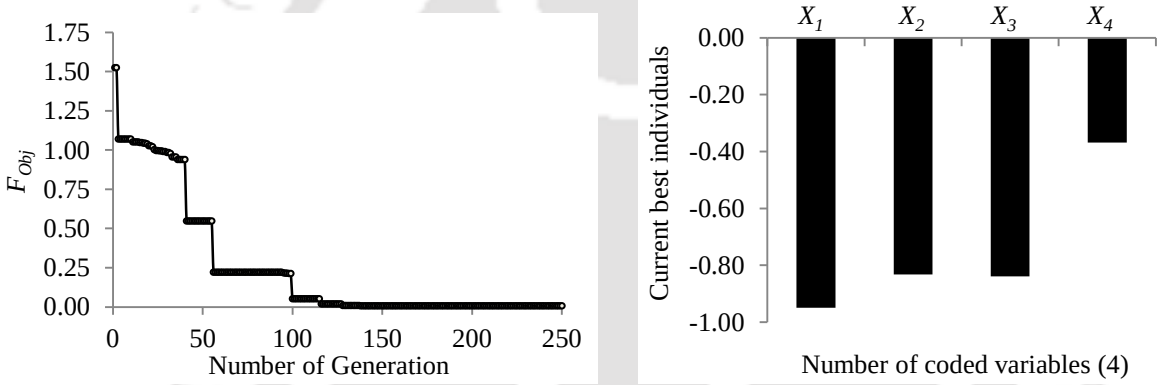

(a) (b)

Figure 5.73: GA results for first test point of double cracked angle section curved beam, θ_s = 25°: (a) Optimization history for objective function and (b) Current best individuals

The predicted crack parameters and their deviation from the actual parameters for double cracked channel and angle section curved beam have been presented in Table 5.40 and Table 5.41 respectively. The absolute errors between actual and predicted crack parameters are calculated using Equation (3.36), given in Chapter 3. The proposed approach detects the crack parameters with an error range of 0.10-1.22% and 0.51-1.58% in case of crack localization for double cracked channel and angle section beams respectively whereas, the prediction errors for crack depth ratio fall within the range of 1.18-7.36% and 1.81-7.95% in for double cracked channel and angle section curved beam respectively.

Table 5.40: Predicted crack parameters and absolute percentage error for double cracked channel section curved beam (θ_s = 25°, R = 1833.50 mm)

Test point	Predicted natural values				Abs. percentage error in			
	η_1	η_2	η_3	η_4	θ_{S1}	ζ_1/b	θ_{S2}	ζ_2/b
1	0.62938	0.08542	3.10844	0.28395	0.70	6.78	0.53	5.35
2	0.62194	0.08225	3.13813	0.52295	0.49	2.81	0.42	4.59
3	0.62694	0.07538	3.14750	0.83072	0.31	5.77	0.72	3.84
4	0.62656	0.48515	3.15188	0.08158	0.25	2.97	0.86	1.97
5	0.61738	0.50675	3.11625	0.31299	1.22	1.35	0.28	4.33
6	0.62713	0.52175	3.13406	0.76480	0.34	4.35	0.29	4.40
7	0.63094	0.75272	3.13813	0.07411	0.95	5.91	0.42	7.36
8	0.62094	0.85504	3.14938	0.30450	0.65	6.88	0.78	1.50
9	0.61944	0.78536	3.11188	0.48105	0.89	1.83	0.42	3.79
10	15.53750	0.08377	18.71063	0.28752	0.56	4.71	0.21	4.16
11	15.59531	0.07881	18.52313	0.48790	0.19	1.49	1.21	2.42
12	15.68438	0.07793	18.76875	0.83128	0.38	2.59	0.10	3.91
13	15.53438	0.49305	18.78563	0.08586	0.58	1.39	0.19	7.32
14	15.65000	0.51085	18.64688	0.28176	0.16	2.17	0.55	6.08
15	15.80313	0.51710	18.82313	0.84112	1.14	3.42	0.39	5.14
16	15.81094	0.75448	18.59625	0.07722	1.19	5.69	0.82	3.48
17	15.52188	0.85536	18.86063	0.30354	0.66	6.92	0.59	1.18
18	15.54844	0.83144	18.62063	0.47780	0.49	3.93	0.69	4.44

Table 5.41: Predicted crack parameters and absolute percentage error for double cracked angle section curved beam (θ_s = 25°, R = 1833.50 mm)

Test point	Predicted natural values				Abs. percentage error in			
	η_1	η_2	η_3	η_4	θ_{S1}	ζ_1/b	θ_{S2}	ζ_2/b
1	0.63400	0.07530	3.16219	0.28422	1.44	5.88	1.19	5.26
2	0.61888	0.07720	3.07563	0.47250	0.98	3.50	1.58	5.50
3	0.62863	0.08636	3.14625	0.77632	0.58	7.95	0.68	2.96
4	0.61700	0.53160	3.08688	0.08170	1.28	6.32	1.22	2.13
5	0.62063	0.51255	3.14156	0.28758	0.70	2.51	0.53	4.14
6	0.63213	0.51340	3.14938	0.85272	1.14	2.68	0.78	6.59
7	0.62163	0.76328	3.10781	0.07736	0.54	4.59	0.55	3.30
8	0.63331	0.77352	3.14375	0.31380	1.33	3.31	0.60	4.60
9	0.61731	0.75544	3.16688	0.48655	1.23	5.57	1.34	2.69
10	15.79219	0.07562	18.97313	0.32091	1.07	5.48	1.19	6.97
11	15.77656	0.07772	18.98438	0.48420	0.97	2.85	1.25	3.16
12	15.54531	0.08334	18.92813	0.84712	0.51	4.18	0.95	5.89
13	15.49844	0.52200	18.87188	0.08155	0.81	4.40	0.65	1.94
14	15.78594	0.48885	18.50063	0.29457	1.03	2.23	1.33	1.81
15	15.52031	0.51145	18.94500	0.76336	0.67	2.29	1.04	4.58
16	15.79688	0.77712	18.87375	0.08482	1.10	2.86	0.66	6.02
17	15.50625	0.75232	18.85875	0.27954	0.76	5.96	0.58	6.82
18	15.80469	0.77720	18.57375	0.51125	1.15	2.85	0.94	2.25

5.10.2.2 Example – II: Curved beam with subtended angle (θs)=50°

Here, the evaluation of crack parameters has been studied on a channel and angle section curved beam with subtended angle 50°. This example is taken to understand the difference in accuracy of prediction since dynamic behavior is different with change of curvature. FE simulation for each experimental trial was performed based on CCF design. Thereafter regression analysis was carried out to obtain the polynomial model. Before finalizing the RSFs or polynomial model, ANOVA has been performed to study the level of significance of proposed models. Final generalized model equations for first five natural frequencies in coded terms for single and double cracked channel and angle beam are obtained in the form of Equation (3.2) as expressed in Chapter 3. The estimated regression coefficients for these polynomial models have been given in Table (D.9 to D.12) of Appendix-D. The empirical polynomial equations obtained have been further utilized in genetic algorithm. The optimum crack parameters are obtained by evaluating the fitness function, which is based on RMS of the residuals between the computed RSFs and measured natural frequency responses. The actual single crack parameters and corresponding measured first five natural frequencies for channel and angle section cantilever curved beam with 50° subtended angle have been obtained in laboratory is presented in Table 5.42. Total eight numbers of physical experiments were conducted for each cross-sectional curved beam.

Table 5.42: Actual single crack parameters and measured first five natural frequencies for single cracked channel and angle section curved beam (θ_s = 50°, R = 916.70 mm)

Test point	Actual crack parameters		Measured natural frequencies (Hz)				
	θ_{S1} (deg)	ζ_1/b	1st	2nd	3rd	4th	5th
Curved channel beam							
1	1.250	0.08	21.41	88.85	207.45	406.60	734.97
2	1.250	0.30	21.21	88.51	206.91	405.62	731.11
3	1.250	0.50	20.92	87.90	205.97	404.00	724.66
4	1.250	0.80	20.36	86.65	204.00	400.45	710.57
5	31.250	0.08	21.45	88.91	207.47	406.62	735.15
6	31.250	0.30	21.43	88.87	207.20	405.85	733.42
7	31.250	0.50	21.41	88.79	206.80	404.67	730.18
8	31.250	0.80	21.38	88.65	206.02	402.36	722.55
Curved angle beam							
1	1.250	0.08	9.10	24.35	71.01	129.55	217.05
2	1.250	0.30	8.52	24.32	68.94	128.75	213.65
3	1.250	0.50	8.03	24.28	66.85	127.79	209.58
4	1.250	0.80	7.57	24.24	64.44	126.26	203.21
5	31.250	0.08	9.23	24.37	71.41	129.62	217.56
6	31.250	0.30	9.04	24.33	69.95	129.27	216.00
7	31.250	0.50	8.90	24.29	69.25	128.65	214.50
8	31.250	0.80	8.48	24.10	68.91	127.75	209.35

The θ_{S1} in Table 5.42 represents angular distance of the single crack position from the fixed end of the cantilever channel and angle section curved beams, where ζ_1/b represents the corresponding crack depth ratio. When the angular distance (θ_{S1}) of the single crack is 1.25°, the distance (L_1) along the longitudinal axis from the fixed end of the cantilever curve beam becomes 20 mm. It is considered that the cracks are present at the top flange of the beam in case of channel section and cracks are present at upper leg of the angle section curved beam. The actual and predicted crack parameters for single cracked channel and angle section curved have been shown in Table 5.43. From Table 5.43 it has been observed that the maximum absolute error (%) for channel and angle section curved beam specimens are 1.25% and 1.75% respectively. The corresponding prediction errors related to crack depth ratios goes up to 8.60% and 8.10% for channel and angle section curved beam specimens.

Table 5.43: Actual and predicted crack parameters for single cracked channel and angle section curved beam (θ_s = 50°, R = 916.70 mm)

Test point	Actual crack parameters		Predicted coded value		Predicted natural value		Abs error (%) in	
	θ_{S1} (deg)	ζ_1/b	X_1	X_2	η_1	η_2	θ_{S1}	ζ_1/b
Curved channel beam								
1	1.250	0.08	-0.94967	-0.82843	1.25825	0.07721	0.66	3.49
2	1.250	0.30	-0.95021	-0.34527	1.24475	0.29463	0.42	1.79
3	1.250	0.50	-0.95013	0.20667	1.24675	0.54300	0.26	8.60
4	1.250	0.80	-0.94971	0.85280	1.25738	0.83376	0.59	4.22
5	31.250	0.08	0.23813	-0.83028	30.95313	0.07638	0.95	4.53
6	31.250	0.30	0.26213	-0.29687	31.55313	0.31641	0.97	5.47
7	31.250	0.50	0.26563	0.07489	31.64063	0.48370	1.25	3.26
8	31.250	0.80	0.23900	0.88178	30.97500	0.84680	0.88	5.85
Curved angle beam								
1	1.250	0.08	-0.94940	-0.81543	1.26513	0.08306	1.21	3.82
2	1.250	0.30	-0.95088	-0.37800	1.22813	0.27990	1.75	6.70
3	1.250	0.50	-0.94967	0.16422	1.25825	0.52390	0.66	4.78
4	1.250	0.80	-0.95013	0.92178	1.24688	0.86480	0.25	8.10
5	31.250	0.08	0.24225	-0.81897	31.05625	0.08146	0.62	1.83
6	31.250	0.30	0.26975	-0.31507	31.74375	0.30822	1.58	2.74
7	31.250	0.50	0.27163	0.03200	31.79063	0.46440	1.73	7.12
8	31.250	0.80	0.23988	0.67716	30.99688	0.75472	0.81	5.66

The actual crack parameters and corresponding first five natural frequencies for double cracked channel and angle section curved beam (θ_s = 50°) have been shown in Table 5.44 and Table 5.45 respectively. The first crack and second crack position on the beams are represented by θ_{S1} and θ_{S2} respectively. The corresponding first and second damage intensity of the double crack problems are ζ_1/b and ζ_2/b respectively.

Table 5.44: Actual crack parameters and corresponding natural frequencies for double cracked channel section curved beam (θ_s = 50°, R = 916.70 mm)

Test point	θ_{S1} (deg)	ζ_1/b	θ_{S2} (deg)	ζ_2/b	Experimentally measured natural frequencies (Hz)				
					1st	2nd	3rd	4th	5th
1	1.250	0.08	6.250	0.30	21.27	88.35	206.22	404.09	730.03
2	1.250	0.08	6.250	0.50	21.21	88.24	206.03	403.50	728.26
3	1.250	0.08	6.250	0.80	21.11	88.01	205.59	402.07	724.12
4	1.250	0.50	6.250	0.08	20.80	87.42	204.87	401.82	720.72
5	1.250	0.50	6.250	0.30	20.78	87.36	204.76	401.51	719.82
6	1.250	0.50	6.250	0.80	20.63	87.05	204.15	399.55	714.38
7	1.250	0.80	6.250	0.08	20.25	86.18	202.90	398.28	706.70
8	1.250	0.80	6.250	0.30	20.23	86.13	202.79	397.99	705.89
9	1.250	0.80	6.250	0.50	19.85	85.92	202.62	397.45	704.43
10	31.250	0.08	37.500	0.30	21.40	88.66	206.83	405.08	732.24
11	31.250	0.08	37.500	0.50	21.37	88.55	206.69	404.44	730.84
12	31.250	0.08	37.500	0.80	21.34	88.36	205.81	402.11	726.17
13	31.250	0.50	37.500	0.08	21.24	88.34	205.70	402.47	726.20
14	31.250	0.50	37.500	0.30	21.15	88.30	205.62	402.07	725.31
15	31.250	0.50	37.500	0.80	21.05	87.90	205.16	400.23	721.31
16	31.250	0.80	37.500	0.08	20.75	87.55	204.91	400.18	718.62
17	31.250	0.80	37.500	0.30	20.40	87.17	204.65	399.78	717.77
18	31.250	0.80	37.500	0.50	20.10	86.85	203.75	398.18	716.47

Table 5.45: Actual crack parameters and corresponding natural frequencies for double cracked angle section curved beam (θ_s = 50°, R = 916.70 mm)

Test point	θ_{S1} (deg)	ζ_1/b	θ_{S2} (deg)	ζ_2/b	Experimentally measured natural frequencies (Hz)				
					1st	2nd	3rd	4th	5th
1	1.250	0.08	6.250	0.30	8.94	24.15	70.60	128.70	215.60
2	1.250	0.08	6.250	0.50	8.50	24.06	68.90	128.42	213.25
3	1.250	0.08	6.250	0.80	8.00	23.90	66.75	127.65	209.39
4	1.250	0.50	6.250	0.08	8.01	23.78	66.72	127.20	209.35
5	1.250	0.50	6.250	0.30	8.00	23.72	66.48	126.88	209.15
6	1.250	0.50	6.250	0.80	7.99	23.48	66.40	125.96	209.00
7	1.250	0.80	6.250	0.08	7.56	23.85	64.25	126.00	203.15
8	1.250	0.80	6.250	0.30	7.55	23.30	64.10	125.50	203.10
9	1.250	0.80	6.250	0.50	7.53	23.10	63.95	124.95	202.90
10	31.250	0.08	37.500	0.30	9.18	24.32	71.30	129.50	217.15
11	31.250	0.08	37.500	0.50	9.00	24.23	70.90	129.10	216.95
12	31.250	0.08	37.500	0.80	8.85	24.00	70.58	128.75	216.15
13	31.250	0.50	37.500	0.08	8.98	24.21	70.70	127.26	212.64
14	31.250	0.50	37.500	0.30	8.90	24.15	70.63	127.18	212.58
15	31.250	0.50	37.500	0.80	8.80	23.87	70.29	126.81	212.27
16	31.250	0.80	37.500	0.08	8.40	23.95	68.90	127.35	209.15
17	31.250	0.80	37.500	0.30	8.35	23.55	68.67	127.00	208.90
18	31.250	0.80	37.500	0.50	8.10	23.20	68.15	126.57	208.45

After the application of GA, the predicted crack location, crack depth ratio and corresponding absolute percentage error with respect to actual crack parameters are presented in Table 5.46 and Table 5.47 for double cracked channel and angle section curved

beam respectively. In this case it is observed that crack location can be estimated with maximum 1.42% and 1.82% error for double cracked channel and angle section curved beam respectively, whereas, the maximum error rises to 7.50% and 8.40% in case of crack depth ratio prediction in channel and angle specimen.

Table 5.46: Predicted crack parameters and absolute percentage error for double cracked channel section curved beam ($\theta_s = 50°$, $R = 916.70$ mm)

Test point	Predicted natural values				Percentage error in			
	η_1	η_2	η_3	η_4	θ_{S1}	ζ_1/b	θ_{S2}	ζ_2/b
1	1.24538	0.08326	6.21625	0.28266	0.37	4.07	0.54	5.78
2	1.26500	0.08102	6.31875	0.51980	1.20	1.27	1.10	3.96
3	1.24225	0.07739	6.18125	0.81368	0.62	3.26	1.10	1.71
4	1.25288	0.52215	6.26000	0.08500	0.23	4.43	0.16	6.25
5	1.24225	0.51105	6.19813	0.28653	0.62	2.21	0.83	4.49
6	1.26488	0.47560	6.32063	0.74000	1.19	4.88	1.13	7.50
7	1.23875	0.82248	6.33688	0.08134	0.90	2.81	1.39	1.68
8	1.23938	0.75840	6.22813	0.28827	0.85	5.20	0.35	3.91
9	1.26613	0.84336	6.30500	0.50925	1.29	5.42	0.88	1.85
10	31.39063	0.07455	37.57500	0.30546	0.45	6.81	0.20	1.82
11	31.34063	0.07708	37.34250	0.51425	0.29	3.65	0.42	2.85
12	31.33750	0.08170	37.40250	0.77152	0.28	2.12	0.26	3.56
13	31.34063	0.51930	37.43625	0.08197	0.29	3.86	0.17	2.46
14	30.86563	0.51015	38.03250	0.28404	1.23	2.03	1.42	5.32
15	31.53750	0.48880	38.00625	0.83048	0.92	2.24	1.35	3.81
16	31.42500	0.85920	37.78125	0.07575	0.56	7.40	0.75	5.31
17	31.00625	0.74288	37.21875	0.30642	0.78	7.14	0.75	2.14
18	31.05313	0.83904	37.70625	0.47645	0.63	4.88	0.55	4.71

Table 5.47: Predicted crack parameters and absolute percentage error for double cracked angle section curved beam ($\theta_s = 50°$, $R = 916.70$ mm)

Test point	Predicted natural values				Percentage error in			
	η_1	η_2	η_3	η_4	θ_{S1}	ζ_1/b	θ_{S2}	ζ_2/b
1	1.25500	0.08431	6.33875	0.27996	0.40	5.39	1.42	6.68
2	1.26875	0.07463	6.19250	0.51630	1.50	6.71	0.92	3.26
3	1.35438	0.08272	6.36375	0.79352	8.35	3.40	1.82	0.81
4	1.25400	0.51160	6.28188	0.08422	0.32	2.32	0.51	5.28
5	1.24325	0.52470	6.28438	0.30738	0.54	4.94	0.55	2.46
6	1.26088	0.54060	6.20313	0.77976	0.87	8.12	0.75	2.53
7	1.24300	0.83080	6.32188	0.08262	0.56	3.85	1.15	3.28
8	1.24213	0.75568	6.18188	0.32190	0.63	5.54	1.09	7.30
9	1.23013	0.82432	6.22813	0.48375	1.59	3.04	0.35	3.25
10	31.31563	0.08550	38.01000	0.27735	0.21	6.87	1.36	7.55
11	31.59063	0.07751	37.33500	0.48305	1.09	3.11	0.44	3.39
12	31.09063	0.08610	38.17125	0.86720	0.51	7.63	1.79	8.40
13	30.97188	0.52785	37.75875	0.08160	0.89	5.57	0.69	2.00
14	31.61250	0.52310	37.69875	0.30558	1.16	4.62	0.53	1.86
15	31.02813	0.48090	37.06125	0.76000	0.71	3.82	1.17	5.00
16	30.85938	0.85584	37.21875	0.08531	1.25	6.98	0.75	6.64
17	31.50938	0.84288	37.27500	0.27702	0.83	5.36	0.60	7.66
18	30.83750	0.75896	37.10625	0.48820	1.32	5.13	1.05	2.36

Furthermore, the mean errors between actual and predicted crack parameters are calculated based on three cases presented in this section for all configurations of thin walled beams using measured natural frequencies, which are summarized in the Table 5.48. The mean error provides an overall representation of the present method to accept its applicability in different problems of structural health monitoring or system identification.

Table 5.48: Mean error between actual and predicted crack parameters using measured natural frequencies

Sl. No.	Configuration of thin-walled beams	Abs error (%) for	
		Crack location	Crack depth ratio
Channel section configurations			
1	Single cracked straight beam	0.68	3.43
2	Double cracked straight beam	0.48	3.72
3	Single cracked curved beam (θ_s = 25°)	0.69	4.79
4	Double cracked curved beam (θ_s = 25°)	0.57	4.06
5	Single cracked curved beam (θ_s = 50°)	0.75	4.65
6	Double cracked curved beam (θ_s = 50°)	0.72	3.97
Angle section configurations			
1	Single cracked straight beam	0.71	3.98
2	Double cracked straight beam	0.49	3.43
3	Single cracked curved beam (θ_s = 25°)	0.84	5.36
4	Double cracked curved beam (θ_s = 25°)	0.88	4.22
5	Single cracked curved beam (θ_s = 50°)	1.08	5.09
6	Double cracked curved beam (θ_s = 50°)	1.10	4.78

In case of utilization of free vibration responses (with first five natural frequencies), it has been observed from above table that the mean error for single and double cracked channel section straight beams lies within 0.68% and 3.72% for crack localization and crack depth ratio respectively, whereas these percentage lies within 0.71% and 3.98% for angle cross-sectional straight beams. The mean error (%) between actual and predicted single and double crack parameters (position and severity of crack) for curved channel and angle section beam with θ_s = 25° has been found in the range of 0.69% and 4.79%; and 0.88% and 5.36% respectively. Besides that, this mean error (%) ranges for curved channel and angle section beam with θ_s = 50° has been obtained as 0.75% and 4.65%; and 1.10% and 5.09% respectively. From Table 5.48, it can be observed that, the accuracy of crack localization is higher compared to crack depth ratio in case of single and multiple crack models for both type of cross-section. Moreover, the result reveals that in case of single and double crack

scenario, almost same accuracy is maintained in crack localization and quantification, showing that the present method is a promising approach for damage detection.

5.11 Closure

A detailed study of free vibration response for the crack parameter identification in thin walled unsymmetrical section beams has been carried out on straight and curved beams and results are discussed with different illustrations in this chapter. The utilization of line spring elements as single or multiple cracks is found suitable for practical application in damage detection study as confirmed by the excellent agreement between theoretical and experimental results. The effect of warping is found to increase natural frequencies of the thin-wall beams, the ignorance of which in structural health monitoring of thin walled components may provide misleading judgment. From half power bandwidth study it has been observed that the presence of crack causes increased release of vibrational energy as reflected by the increased bandwidth. Absolute difference between the curvature mode shapes and curvature damage factor (CDF) are found to be a good indicator of the localization of crack. However, determination of crack severity required a different approach (combined RSM and GA) that has been illustrated with results of single and double cracked cases by conducting sufficient number of experiments. Based on case studies on different beam specimen, it has been revealed that crack location can be detected with more precision than that of crack depth. Measurement of natural frequency is comparatively easier than mode shape, and hence, the proposed approach for crack detection is the best suited for practical application.

Chapter 6

Identification using Forced Vibration Response

6.1 Overview

It is established in the preceding chapter that damage in a structure usually reduces its structural stiffness, thereby altering the vibration characteristics. These alterations in vibration signals give useful information about the position and intensity of crack. A hybrid technique (based on RSM and GA) for detecting damage to structural members is the theme of the present research. In this chapter, the method has been illustrated using peak acceleration response obtained in harmonically excited beams. The additional features in this approach are that it can predict the external excitation parameters (peak magnitude of the time varying force and excitation frequency). The technique requires measurement of peak acceleration at specified locations and to feed the data to response surface and GA based approach to proceed further for identification of crack parameters. The method has been illustrated from experimentally measured data of several thin walled beam specimens of straight and curved profiles. The present approach seems to be promising in structural health monitoring as many low cost spectrum analyzers do not give higher mode frequency accurately whereas the acceleration can be more easily recorded by simple device such as smart phone [209, 210].

6.2 Comparison of FE results with experimental forced responses based on the present study

In this section, the comparisons between experimentally obtained acceleration responses and theoretically calculated responses have been presented for channel and angle section beams of straight and curved profile.

It is considered that a harmonic force $F(t) = A_f \sin(\Omega t)$ N is applied at the tip of the uncracked and cracked channel section cantilever straight steel beam and the output is recorded in the form of acceleration response. In all the cases, the excitation frequency (Ω) is chosen as 50 Hz whereas peak value of force time history (A_f) was measured using a force transducer in each experimental trial. This is done in order to take one additional hidden parameter during identification process. Theoretical acceleration responses are obtained by implementing Newmark β algorithm. The experimental and theoretical tip acceleration responses of uncracked channel section straight beam in vertical direction have been presented in Figure 6.1. Figure 6.2(a) presents the experimental and theoretical tip acceleration (in vertical direction) of single cracked channel beam, where the crack parameters are : location (L_1): 0.50 m, crack depth ratio (ζ_1/b): 0.50. The measured peak magnitude of harmonic force (A_f): 0.87 N. Figure 6.2(b) shows the experimental and theoretical tip acceleration response of double cracked channel beam, where the crack parameters are - First crack: $L_1 = 0.50$ m, $\zeta_1/b = 0.50$, Second crack: $L_2 = 0.6$ m, $\zeta_2/b = 0.80$. The peak amplitude of the force (A_f) has been obtained as 0.80 N. The experimental and theoretical average peak accelerations at the tip of uncracked channel section straight beams were found to be 7.84 m/s^2 and 7.08 m/s^2 respectively. The average peak value of acceleration responses for single cracked channel section straight beam was found experimentally as 8.21 m/s^2 whereas the theoretical value is 7.50 m/s^2. On the other hand, the experimentally and theoretically obtained values are 14.32 m/s^2 and 13.06 m/s^2 for double cracked channel beam respectively.

The tip acceleration response (in vertical direction) plots obtained theoretically and experimentally for uncracked, single and double cracked channel section curved beams with subtended angle 25° have been presented in Figure 6.3 to Figure 6.4 (a and b) respectively. In case of single cracked beam, the crack location is at angular distance $\theta_{S1} = 15.625°$ in which crack depth ratio is 0.5. The corresponding peak magnitude of harmonic force (A_f) is 0.52 N. For double cracked beam problem, the crack parameters are - First crack: θ_{S1} =

15.625°, ζ_1/b = 0.50, Second crack θ_{S2} = 18.75°, ζ_2/b = 0.80. The value of corresponding peak amplitude of the excitation (A_f) is 0.63 N. The experimental and theoretical average peak accelerations at the tip of uncracked channel beam was 5.46 m/s^2 and 4.95 m/s^2 whereas those for single cracked channel beam was 5.74 m/s^2 and 5.14 m/s^2; respectively. The measured acceleration for double cracked beam is 6.74 m/s^2 and 6.09 m/s^2 respectively. Again, as expected the same trend as observed for straight beam has been found. However, as compared to straight beam the magnitude of acceleration is less in curved beam. This is expected as horizontally curved beam provides more resistance to flexure.

The acceleration time history plot obtained from experimental and theoretical studies for angle beam specimen (uncracked, single and double cracked) are presented in Figure 6.5 to Figure 6.8. It may be noted that only a part of steady state motions are presented in these figures.

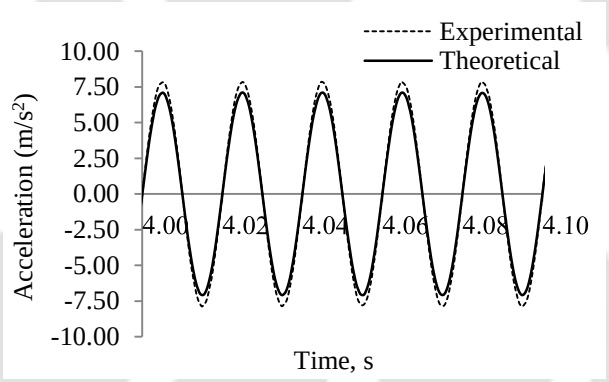

Figure 6.1: Experimental and theoretical tip acceleration response of uncracked channel section straight beam in vertical direction

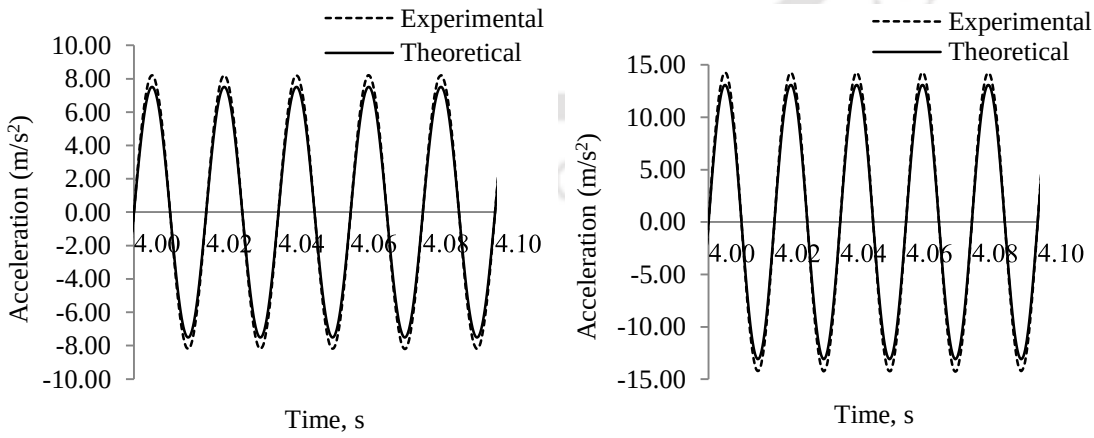

Figure 6.2: Experimental and theoretical tip acceleration response of (a) single cracked and (b) double cracked channel section straight beam in vertical direction

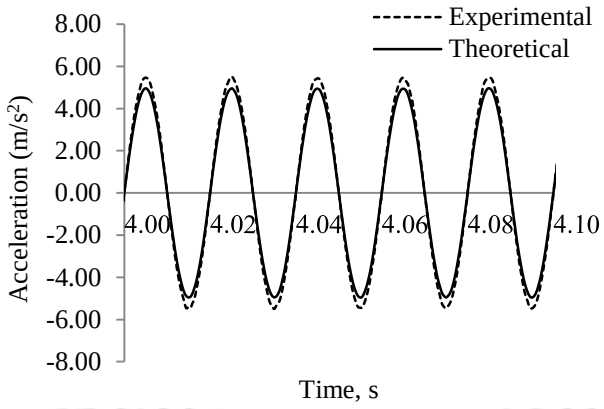

Figure 6.3: Experimental and theoretical tip acceleration response of uncracked channel section curved beam (θ_s=25°, R = 1833.50 mm) in vertical direction

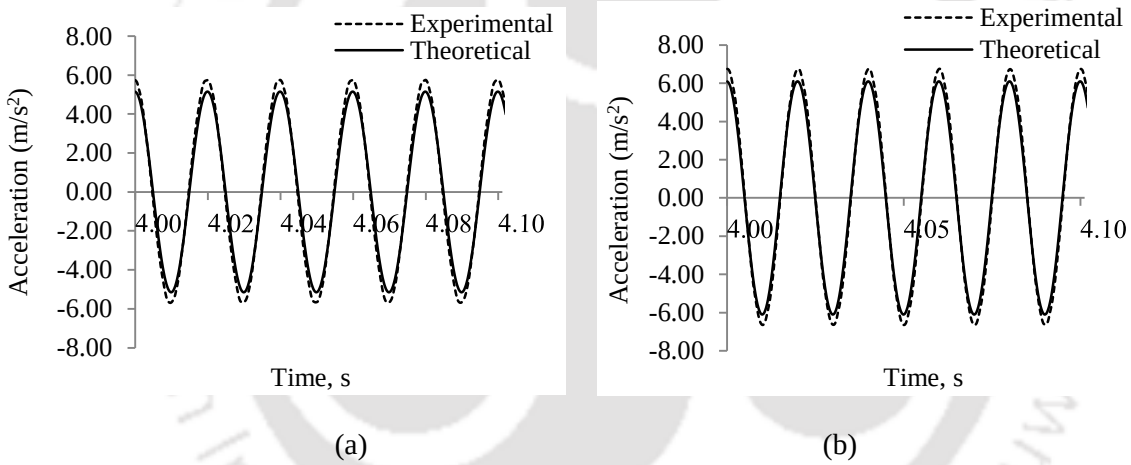

Figure 6.4: Experimental and theoretical tip acceleration response of (a) single cracked and (b) double cracked channel section curved beam (θ_s=25°, R = 1833.50 mm) in vertical direction

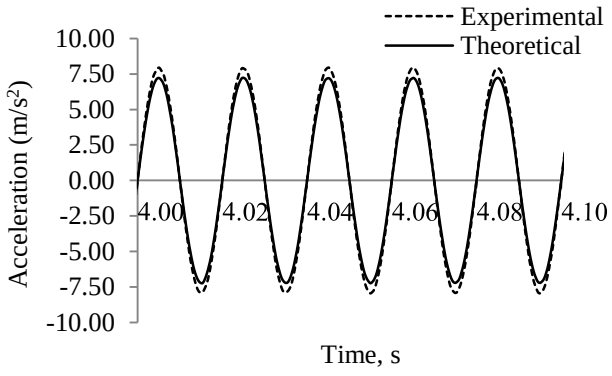

Figure 6.5: Experimental and theoretical tip acceleration response of uncracked angle section straight beam in vertical direction

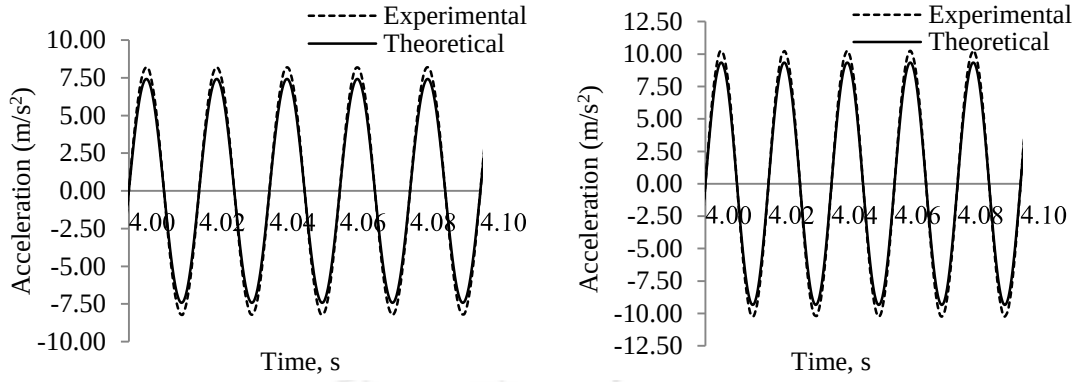

Figure 6.6: Experimental and theoretical tip acceleration response of (a) single cracked and (b) double cracked angle section straight beam in vertical direction

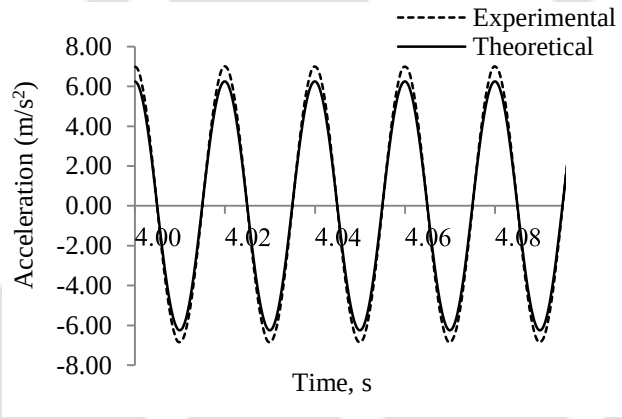

Figure 6.7: Experimental and theoretical tip acceleration response of uncracked angle section curved beam (θ_s =25°, R = 1833.50 mm) in vertical direction

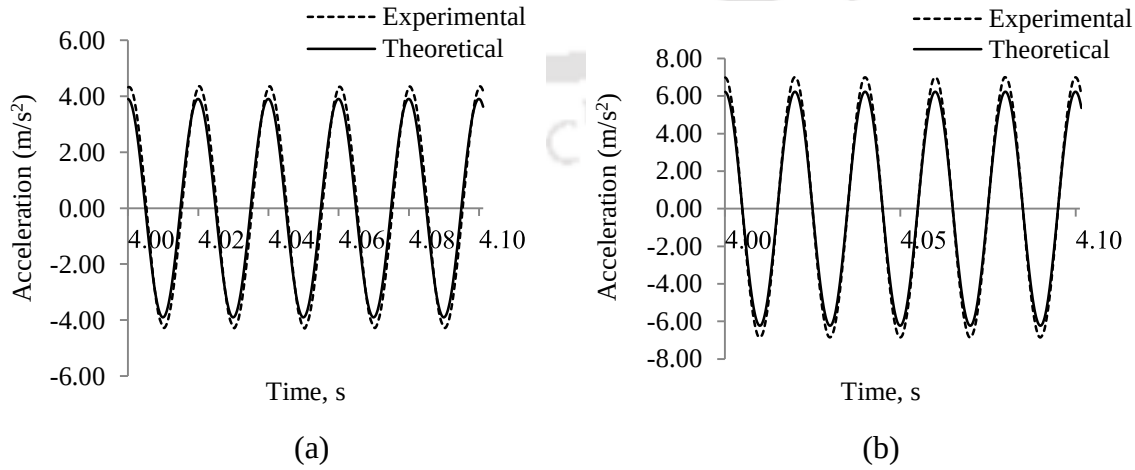

Figure 6.8: Experimental and theoretical tip acceleration response of (a) single cracked and (b) double cracked angle section curved beam (θ_s =25°, R = 1833.50 mm) in vertical direction

Table 6.1 represents peak magnitude of acceleration at the tip of cantilever beam from experimental and theoretical results for different beam specimen. The results serves as the validation of numerical integration scheme used to find the forced response of uncracked and cracked beam. The agreement between theoretical and experimental result is satisfactory.

Table 6.1: Peak magnitude of acceleration at the tip of cantilever beam from experimental and theoretical results

	Beam condition	Position and size of the crack	A_f (N)	Experimental (m/s^2)	Theoretical (m/s^2)
		Channel configuration			
Straight	Intact		0.82	7.84	7.08
	Single	L_1 = 0.50 m, ζ_1/b = 0.50	0.87	8.21	7.50
	Double	L_1 = 0.50 m, ζ_1/b =0.50	0.80	14.32	13.06
		L_2 = 0.6 m, ζ_1/b = 0.80			
Curved (θ_s =25°)	Intact		0.60	5.46	4.95
	Single	θ_{S1} = 15.625°, ζ_1/b = 0.50	0.52	5.74	5.14
	Double	θ_{S1} = 15.625°, ζ_1/b =0.50	0.63	6.74	6.09
		θ_{S2} = 18.750°, ζ_1/b = 0.80			
		Angle configuration			
Straight	Intact		0.46	7.93	7.21
	Single	L_1 = 0.50 m, ζ_1/b = 0.50	0.49	8.23	7.41
	Double	L_1 = 0.50 m, ζ_1/b =0.50	0.46	10.27	9.33
		L_2 = 0.6 m, ζ_1/b = 0.80			
Curved (θ_s =25°)	Intact		1.38	6.99	6.24
	Single	θ_{S1} = 15.625°, ζ_1/b = 0.50	1.04	4.34	3.89
	Double	θ_{S1} = 15.625°, ζ_1/b =0.50	1.64	6.95	6.22
		θ_{S2} = 18.750°, ζ_1/b = 0.80			

6.3 Damage identification in thin-walled steel beam using forced vibration response

In the previous chapter, measured natural frequencies have been utilized to find the crack parameters. However, when frequency measurement is not possible, one may utilize other response data. The dynamic response that can be easily recorded is the acceleration. In this chapter, the hybrid approach developed has been tested with measured acceleration at different sensor location for crack parameters identification. As in the previous case, here also we first apply the method to thin walled channel and angle beam of straight profile. Both single crack and double crack cases have been studied. Next horizontally curved channel and angle beams are investigated with single and double cracked specimen.

6.3.1 Case I – Identification of single and multiple cracks in channel and angle cross-sectional straight beam using forced vibration response

In the present study, the peak acceleration responses (y_1, y_2, y_3, y_4 and y_5) have been received by five sensors located at five different locations from the fixed end of the cantilever beam. Four factors (p = 4) have been selected to describe the single cracked polynomial model and these are crack location (X_1), crack depth ratio (X_2), peak value of force time history (X_3) and excitation frequency (X_4). In single crack identification problem 30 numbers of experimental trials are required. The factors involved in double cracked scenario (p = 6) are first crack location and depth ratio: X_1, X_2; second crack location and depth ratio: X_3, X_4, peak value of force time history X_5 and excitation frequency X_6. The first and second crack locations are considered from the fixed end of the cantilever beam respectively. The cracks are considered at top flange in case of channel beam and cracks are present at upper leg in case of angle section beam. The independent variables for CCF design along with their low, medium and high levels have been given in Table 6.2 for single and multiple cracked channel and angle section beam. In the same table peak value of the force time history and excitation frequency have been presented by A_f and Ω respectively. The coded levels of variables and corresponding simulated responses for single crack channel and angle section straight beams are summarized in the Table 6.3 and Table 6.4 respectively.

Table 6.2: Independent variables and their levels of channel and angle section straight beam for CCF design in case of forced vibration data

Crack identification problem	Factors	Coded symbol	Real values of coded Levels		
			Low (-1)	Medium (0)	High (1)
Single	Crack location (m)	X_1	0.00	0.40	0.80
	Crack depth ratio	X_2	0.00	0.45	0.90
	A_f (N)	X_3	0.10	5.05	10.00
	Ω (Hz)	X_4	5.00	352.50	700.00
Multiple (Double crack)	First crack location (m)	X_1	0.00	0.40	0.80
	First crack depth ratio	X_2	0.00	0.45	0.90
	Second crack location (m)	X_3	0.04	0.42	0.80
	Second crack depth ratio	X_4	0.00	0.45	0.90
	A_f (N)	X_5	0.10	5.05	10.00
	Ω (Hz)	X_6	5.00	352.50	700.00

Table 6.3: CCF design with coded variables and simulated responses for single cracked channel section straight beam in case of forced vibration data

Expt. trial no.	Coded levels of variables				Peak value of the acceleration response (m/s^2)				
	X_1	X_2	X_3	X_4	y_1	y_2	y_3	y_4	y_5
1	1	-1	1	-1	0.0094	0.0347	0.0722	0.1175	0.1669
2	-1	1	1	1	19.1700	30.3200	20.1100	44.9600	100.1000
3	0	0	0	0	5.6220	16.1000	23.0200	22.0900	17.3000
4	1	1	1	1	17.7100	32.7700	21.3100	45.0100	102.2000
5	-1	-1	1	1	17.7100	32.7700	21.3100	45.0100	102.2000
6	0	0	0	0	5.6220	16.1000	23.0200	22.0900	17.3000
7	1	0	0	0	5.5160	15.8100	22.6900	22.0500	17.7500
8	0	0	0	1	9.2310	16.9200	10.5600	23.0400	51.4000
9	0	0	0	0	5.6220	16.1000	23.0200	22.0900	17.3000
10	-1	1	-1	-1	0.0001	0.0004	0.0008	0.0012	0.0018
11	-1	1	1	-1	0.0113	0.0384	0.0776	0.1248	0.1760
12	0	0	0	0	5.6220	16.1000	23.0200	22.0900	17.3000
13	1	-1	-1	-1	0.0001	0.0003	0.0007	0.0012	0.0017
14	0	0	0	-1	0.0047	0.0175	0.0365	0.0595	0.0845
15	-1	-1	1	-1	0.0094	0.0347	0.0722	0.1175	0.1669
16	-1	0	0	0	5.8430	16.3600	23.1300	21.9700	17.2600
17	-1	-1	-1	-1	0.0001	0.0003	0.0007	0.0012	0.0017
18	0	0	-1	0	0.1113	0.3189	0.4558	0.4374	0.3426
19	0	-1	0	0	5.5160	15.8100	22.6900	22.0500	17.7500
20	0	0	0	0	5.6220	16.1000	23.0200	22.0900	17.3000
21	1	1	1	-1	0.0094	0.0347	0.0722	0.1175	0.1669
22	-1	-1	-1	1	0.1771	0.3277	0.2113	0.4501	1.0220
23	0	0	0	0	5.6220	16.1000	23.0200	22.0900	17.3000
24	1	1	-1	-1	0.0001	0.0003	0.0007	0.0012	0.0017
25	1	-1	1	1	17.7100	32.7700	21.3100	45.0100	102.2000
26	1	1	-1	1	0.1771	0.3277	0.2113	0.4501	1.0220
27	0	0	1	0	11.1300	31.8900	45.5800	43.7300	34.2600
28	0	1	0	0	5.8330	16.5700	23.4500	22.1500	17.9300
29	1	-1	-1	1	0.1771	0.3277	0.2113	0.4501	1.0220
30	-1	1	-1	1	0.1917	0.3032	0.2011	0.4496	1.0010

For example, it can be noticed from Table 6.3 (experimental trial no. 16) for channel beam that when the single crack of crack-depth ratio 0.45 is located at the fixed end (0 m) then X_1 = -1 and X_2 = 0. The corresponding forcing parameters are-peak value of the force time history: 0.10 N (X_3 = 0) and excitation frequency: 5.00 Hz (X_4 = 0). Harmonic excitation has been imposed at the tip of the cantilever beam for which peak acceleration is treated as output response as y_1 = 5.8430 m/s^2, y_2 = 16.3600 m/s^2, y_3 = 23.1300 m/s^2, y_4 = 21.9700 m/s^2 and y_5 = 17.2600 m/s^2 at their respective measured location. Similarly in Table 6.4 (experimental trial no. 5) for the angle beam, with the same crack parameters and excitation characteristics as in case of channel beam, output response at corresponding locations are y_1 = 7.9060 m/s^2, y_2 = 18.1300 m/s^2, y_3 = 17.6000 m/s^2, y_4 = 15.7500 m/s^2 and

y_5 = 38.8200 m/s^2. In the physical experiment these accelerations are recorded by the accelerometers at the specified sensor locations.

Table 6.4: CCF design with coded variables and simulated responses for single cracked angle section straight beam in case of forced vibration data

Trial no.	Coded levels of variables				Peak value of the acceleration response (m/s^2)				
	X_1	X_2	X_3	X_4	y_1	y_2	y_3	y_4	y_5
1	1	1	1	-1	0.0220	0.0810	0.1690	0.2740	0.3900
2	0	-1	0	0	8.8150	20.3300	19.2300	15.7500	41.3600
3	1	0	0	0	8.8150	20.3300	19.2300	15.7500	41.3600
4	-1	1	-1	1	0.0708	0.1343	0.1199	0.2808	0.7369
5	-1	0	0	0	7.9060	18.1300	17.6000	15.7500	38.8200
6	0	0	0	0	8.0700	18.7400	18.0900	15.7600	39.5800
7	0	0	0	0	8.0700	18.7400	18.0900	15.7600	39.5800
8	0	0	0	0	8.0700	18.7400	18.0900	15.7600	39.5800
9	-1	-1	-1	-1	0.0002	0.0008	0.0017	0.0027	0.0039
10	1	-1	-1	-1	0.0002	0.0008	0.0017	0.0027	0.0039
11	0	1	0	0	7.1020	16.7800	16.7700	15.7700	37.3000
12	0	0	0	0	8.0700	18.7400	18.0900	15.7600	39.5800
13	-1	1	1	1	7.0800	13.4300	11.9900	28.0800	73.6900
14	0	0	0	-1	0.0110	0.0410	0.0860	0.1400	0.2000
15	0	0	0	0	8.0700	18.7400	18.0900	15.7600	39.5800
16	1	-1	1	-1	0.0220	0.0810	0.1690	0.2740	0.3900
17	1	1	-1	1	0.0992	0.1633	0.1515	0.2996	0.8190
18	1	-1	1	1	9.9200	16.3300	15.1500	29.9600	81.9000
19	0	0	-1	0	0.1598	0.3711	0.3582	0.3120	0.7837
20	-1	1	1	-1	0.0251	0.0878	0.1789	0.2888	0.4082
21	0	0	0	1	4.6250	7.9400	7.2760	14.8900	40.7200
22	1	-1	-1	1	0.0992	0.1633	0.1515	0.2996	0.8190
23	0	0	0	0	8.0700	18.7400	18.0900	15.7600	39.5800
24	0	0	1	0	15.9800	37.1100	35.8200	31.2000	78.3700
25	1	1	1	1	9.9200	16.3300	15.1500	29.9600	81.9000
26	-1	-1	1	1	9.9200	16.3300	15.1500	29.9600	81.9000
27	-1	1	-1	-1	0.0003	0.0009	0.0018	0.0029	0.0041
28	-1	-1	-1	1	0.0992	0.1633	0.1515	0.2996	0.8190
29	-1	-1	1	-1	0.0220	0.0810	0.1690	0.2740	0.3900
30	1	1	-1	-1	0.0002	0.0008	0.0017	0.0027	0.0039

Table 6.5 and Table 6.6 summarize the DOE with coded variables and FE simulated responses for double cracked channel and angle section thin-walled straight beam. Here, 86 number of experimental trials have been conducted for each cross-sectional double cracked beam, where 10 number of center points (n_{cr}) are present in DOE.

Table 6.5: CCF design with coded variables and simulated responses for double cracked channel section straight beam in case of forced vibration data

Expt. trial no.	Coded levels of variables						Peak value of the acceleration response (m/s^2)				
	X_1	X_2	X_3	X_4	X_5	X_6	y_1	y_2	y_3	y_4	y_5
1	-1	-1	-1	1	1	1	19.0100	31.4700	20.2300	45.2500	100.6000
2	0	0	0	0	0	0	6.2120	17.7700	25.0000	22.3800	12.9500
3	0	0	0	0	-1	0	0.1230	0.3518	0.4952	0.4432	0.2564
4	1	-1	1	-1	-1	1	0.1771	0.3277	0.2113	0.4501	1.0220
5	-1	-1	-1	-1	1	-1	0.0094	0.0347	0.0722	0.1176	0.1670
6	0	0	0	0	0	0	6.2120	17.7700	25.0000	22.3800	12.9500
7	0	0	0	0	0	0	6.2120	17.7700	25.0000	22.3800	12.9500
8	-1	-1	1	-1	-1	-1	0.0001	0.0003	0.0007	0.0012	0.0017
9	1	1	1	-1	1	-1	0.0094	0.0347	0.0722	0.1176	0.1670
10	-1	-1	-1	1	-1	1	0.1901	0.3147	0.2023	0.4526	1.0060
11	0	-1	0	0	0	0	5.6230	16.1000	23.0200	22.0900	17.2900
12	0	1	0	0	0	0	6.6520	18.8400	26.1200	22.5200	12.2600
13	-1	1	-1	-1	-1	-1	0.0001	0.0004	0.0008	0.0012	0.0018
14	1	-1	-1	1	-1	1	0.1901	0.3147	0.2023	0.4526	1.0060
15	-1	1	-1	-1	1	1	19.1700	30.3200	20.1100	44.9500	100.1000
16	0	0	0	0	0	0	6.2120	17.7700	25.0000	22.3800	12.9500
17	1	1	-1	-1	1	1	17.7100	32.7600	21.1300	45.0100	102.2000
18	-1	1	1	1	-1	-1	0.0001	0.0004	0.0008	0.0012	0.0018
19	1	-1	-1	-1	-1	1	0.1771	0.3277	0.2113	0.4501	1.0220
20	0	0	1	0	0	0	5.6220	16.1000	23.0200	22.0900	17.3000
21	-1	1	1	1	1	1	19.1700	30.3200	20.1100	44.9500	100.1000
22	-1	1	-1	1	1	1	32.3700	40.8800	19.1800	54.3400	91.2900
23	0	0	0	0	0	0	6.2120	17.7700	25.0000	22.3800	12.9500
24	-1	-1	1	-1	1	-1	0.0094	0.0347	0.0722	0.1176	0.1670
25	-1	1	-1	1	-1	1	0.3237	0.4089	0.1918	0.5434	0.9129
26	-1	-1	1	1	1	1	17.7100	32.7600	21.1300	45.0100	102.2000
27	1	-1	1	1	-1	1	0.1771	0.3277	0.2113	0.4501	1.0220
28	-1	1	1	-1	-1	-1	0.0001	0.0004	0.0008	0.0012	0.0018
29	0	0	0	0	0	0	6.2120	17.7700	25.0000	22.3800	12.9500
30	1	1	-1	1	-1	-1	0.0001	0.0004	0.0008	0.0012	0.0018
31	1	-1	-1	-1	-1	-1	0.0001	0.0003	0.0007	0.0012	0.0017
32	1	-1	-1	-1	1	1	17.7100	32.7600	21.1300	45.0100	102.2000
33	1	1	-1	1	1	-1	0.0107	0.0378	0.0769	0.1240	0.1751
34	-1	1	-1	1	1	-1	0.0119	0.0399	0.0800	0.1280	0.1801
35	0	0	0	-1	0	0	5.6220	16.1000	23.0200	22.0900	17.3000
36	1	-1	1	-1	-1	-1	0.0001	0.0003	0.0007	0.0012	0.0017
37	-1	-1	1	1	1	-1	0.0094	0.0347	0.0722	0.1176	0.1670
38	-1	-1	1	1	-1	-1	0.0001	0.0003	0.0007	0.0012	0.0017
39	-1	-1	1	1	-1	1	0.1771	0.3277	0.2113	0.4501	1.0220
40	-1	-1	-1	-1	-1	1	0.1771	0.3277	0.2113	0.4501	1.0220
41	0	0	0	0	0	0	6.2120	17.7700	25.0000	22.3800	12.9500
42	1	-1	-1	1	1	1	19.0100	31.4700	20.2300	45.2500	100.6000
43	1	1	1	1	-1	1	0.1771	0.3277	0.2113	0.4501	1.0220
44	-1	1	-1	1	-1	-1	0.0001	0.0004	0.0008	0.0013	0.0018
45	1	1	-1	1	1	1	19.0100	31.4700	20.2300	45.2500	100.6000
46	1	-1	1	-1	1	1	17.7100	32.7600	21.1300	45.0100	102.2000
47	1	-1	-1	-1	1	-1	0.0094	0.0347	0.0722	0.1176	0.1670

Table 6.5 contd.

Expt. trial no.	Coded levels of variables						Peak value of the acceleration response (m/s^2)				
	X_1	X_2	X_3	X_4	X_5	X_6	y_1	y_2	y_3	y_4	y_5
48	-1	-1	1	-1	-1	1	0.1771	0.3277	0.2113	0.4501	1.0220
49	-1	1	1	-1	-1	1	0.1917	0.3032	0.2011	0.4496	1.0010
50	1	1	1	-1	-1	-1	0.0001	0.0003	0.0007	0.0012	0.0017
51	0	0	0	0	0	-1	0.0047	0.0176	0.0365	0.0596	0.0846
52	0	0	-1	0	0	0	6.3620	17.9700	25.1200	22.3000	12.7200
53	1	1	-1	1	-1	1	0.1901	0.3147	0.2023	0.4526	1.0060
54	1	1	-1	-1	-1	-1	0.0001	0.0003	0.0007	0.0012	0.0017
55	-1	-1	-1	1	1	-1	0.0107	0.0378	0.0769	0.1240	0.1751
56	0	0	0	0	0	1	14.4300	23.1200	8.7220	27.6700	46.1000
57	0	0	0	1	0	0	6.4900	18.4000	25.6200	22.4400	12.5300
58	-1	-1	-1	1	-1	-1	0.0001	0.0004	0.0008	0.0012	0.0018
59	-1	0	0	0	0	0	6.4820	18.1800	24.9300	23.3100	13.7500
60	0	0	0	0	0	0	6.2120	17.7700	25.0000	22.3800	12.9500
61	1	1	1	1	-1	-1	0.0001	0.0003	0.0007	0.0012	0.0017
62	-1	1	1	-1	1	-1	0.0113	0.0384	0.0776	0.1248	0.1760
63	1	-1	1	-1	1	-1	0.0094	0.0347	0.0722	0.1176	0.1670
64	1	-1	1	1	-1	-1	0.0001	0.0003	0.0007	0.0012	0.0017
65	1	-1	-1	1	-1	-1	0.0001	0.0004	0.0008	0.0012	0.0018
66	-1	1	1	1	1	-1	0.0113	0.0384	0.0776	0.1248	0.1760
67	-1	-1	-1	-1	1	1	17.7100	32.7600	21.1300	45.0100	102.2000
68	1	-1	1	1	1	-1	0.0094	0.0347	0.0722	0.1176	0.1670
69	1	1	1	1	1	1	17.7100	32.7600	21.1300	45.0100	102.2000
70	-1	1	1	-1	1	1	19.1700	30.3200	20.1100	44.9500	100.1000
71	-1	1	-1	-1	-1	1	0.1917	0.3032	0.2011	0.4496	1.0010
72	0	0	0	0	1	0	12.3000	35.1900	49.5100	44.3200	25.6400
73	0	0	0	0	0	0	6.2120	17.7700	25.0000	22.3800	12.9500
74	-1	1	-1	-1	1	-1	0.0113	0.0384	0.0776	0.1248	0.1760
75	-1	1	1	1	-1	1	0.1917	0.3032	0.2011	0.4496	1.0010
76	1	-1	1	1	1	1	17.7100	32.7600	21.1300	45.0100	102.2000
77	0	0	0	0	0	0	6.2120	17.7700	25.0000	22.3800	12.9500
78	-1	-1	-1	-1	-1	-1	0.0001	0.0003	0.0007	0.0012	0.0017
79	-1	-1	1	-1	1	1	17.7100	32.7600	21.1300	45.0100	102.2000
80	1	-1	-1	1	1	-1	0.0107	0.0378	0.0769	0.1240	0.1751
81	1	1	-1	-1	-1	1	0.1771	0.3277	0.2113	0.4501	1.0220
82	1	1	1	1	1	-1	0.0094	0.0347	0.0722	0.1176	0.1670
83	1	1	1	-1	1	1	17.7100	32.7600	21.1300	45.0100	102.2000
84	1	0	0	0	0	0	5.6230	16.1000	23.0200	22.0900	17.2900
85	1	1	-1	-1	1	-1	0.0094	0.0347	0.0722	0.1176	0.1670
86	1	1	1	-1	-1	1	0.1771	0.3277	0.2113	0.4501	1.0220

Table 6.6: CCF design with coded variables and simulated responses for double cracked angle section straight beam in case of forced vibration data

Expt. trial no.	Coded levels of variables						Peak value of the acceleration response (m/s^2)				
	X_1	X_2	X_3	X_4	X_5	X_6	y_1	y_2	y_3	y_4	y_5
1	1	-1	1	-1	1	1	9.9200	16.3300	15.1500	29.9600	81.9000
2	0	0	-1	0	0	0	4.1800	10.4700	12.8800	15.6000	28.9700
3	-1	-1	-1	-1	1	-1	0.0220	0.0810	0.1690	0.2740	0.3900
4	-1	-1	1	1	-1	1	0.0992	0.1633	0.1515	0.2996	0.8190
5	0	0	0	0	0	0	4.1400	10.4800	12.9100	15.6200	29.0100
6	-1	-1	1	1	1	1	9.9200	16.3300	15.1500	29.9600	81.9000
7	-1	1	1	-1	1	-1	0.0251	0.0878	0.1789	0.2888	0.4082
8	1	-1	1	-1	1	-1	0.0220	0.0810	0.1690	0.2740	0.3900
9	0	0	1	0	0	0	8.0700	18.7400	18.0900	15.7600	39.5800
10	-1	-1	1	1	1	-1	0.0220	0.0810	0.1690	0.2740	0.3900
11	-1	1	1	1	1	-1	0.0251	0.0878	0.1789	0.2888	0.4082
12	-1	1	-1	1	-1	1	0.0720	0.1340	0.1200	0.2810	0.7340
13	1	1	-1	-1	1	-1	0.0220	0.0810	0.1690	0.2740	0.3900
14	0	-1	0	0	0	0	4.1400	10.4700	12.9200	15.6200	28.9900
15	-1	-1	-1	-1	1	1	9.9200	16.3300	15.1500	29.9600	81.9000
16	-1	1	1	-1	1	1	7.0800	13.4300	11.9900	28.0800	73.6900
17	-1	1	1	-1	-1	1	0.0708	0.1343	0.1199	0.2808	0.7369
18	1	-1	1	1	-1	-1	0.0002	0.0008	0.0017	0.0027	0.0039
19	-1	-1	-1	1	1	1	6.8600	13.5100	12.1000	28.0300	73.7100
20	0	0	0	-1	0	0	8.0700	18.7400	18.0900	15.7600	39.5800
21	-1	-1	-1	-1	-1	-1	0.0002	0.0008	0.0017	0.0027	0.0039
22	1	1	1	1	-1	-1	0.0002	0.0008	0.0017	0.0027	0.0039
23	-1	1	-1	1	-1	-1	0.0003	0.0009	0.0018	0.0029	0.0042
24	0	0	0	0	0	0	4.1400	10.4800	12.9100	15.6200	29.0100
25	0	0	0	1	0	0	4.1500	10.5100	12.9300	15.6200	29.1200
26	-1	1	-1	1	1	-1	0.0262	0.0903	0.1828	0.2941	0.4148
27	1	-1	-1	-1	1	1	9.9200	16.3300	15.1500	29.9600	81.9000
28	1	-1	-1	-1	-1	1	0.0992	0.1633	0.1515	0.2996	0.8190
29	-1	1	-1	-1	-1	-1	0.0003	0.0009	0.0018	0.0029	0.0041
30	1	1	1	-1	1	-1	0.0220	0.0810	0.1690	0.2740	0.3900
31	-1	1	1	1	-1	-1	0.0003	0.0009	0.0018	0.0029	0.0041
32	1	-1	-1	-1	-1	-1	0.0002	0.0008	0.0017	0.0027	0.0039
33	1	-1	-1	1	1	-1	0.0243	0.0869	0.1778	0.2876	0.4068
34	1	1	-1	-1	1	1	9.9200	16.3300	15.1500	29.9600	81.9000
35	1	0	0	0	0	0	4.1400	10.4700	12.9200	15.6200	28.9900
36	0	0	0	0	0	0	4.1400	10.4800	12.9100	15.6200	29.0100
37	0	0	0	0	0	0	4.1400	10.4800	12.9100	15.6200	29.0100
38	-1	1	1	1	-1	1	0.0708	0.1343	0.1199	0.2808	0.7369
39	0	0	0	0	0	-1	0.0110	0.0410	0.0860	0.1400	0.1990
40	1	1	1	-1	1	1	9.9200	16.3300	15.1500	29.9600	81.9000
41	1	-1	1	1	-1	1	0.0992	0.1633	0.1515	0.2996	0.8190
42	1	1	-1	-1	-1	1	0.0992	0.1633	0.1515	0.2996	0.8190
43	-1	-1	1	1	-1	-1	0.0002	0.0008	0.0017	0.0027	0.0039
44	-1	-1	1	-1	1	-1	0.0220	0.0810	0.1690	0.2740	0.3900
45	1	1	-1	1	1	-1	0.0243	0.0869	0.1778	0.2876	0.4068

Table 6.6 contd.

Expt. trial no.	Coded levels of variables						Peak value of the acceleration response (m/s^2)				
	X_1	X_2	X_3	X_4	X_5	X_6	y_1	y_2	y_3	y_4	y_5
46	0	0	0	0	0	0	4.1400	10.4800	12.9100	15.6200	29.0100
47	1	-1	1	-1	-1	1	0.0992	0.1633	0.1515	0.2996	0.8190
48	1	-1	-1	1	1	1	6.8600	13.5100	12.1000	28.0300	73.7100
49	-1	1	1	1	1	1	7.0800	13.4300	11.9900	28.0800	73.6900
50	1	1	-1	1	-1	1	0.0686	0.1351	0.1210	0.2803	0.7371
51	1	1	1	1	1	1	9.9200	16.3300	15.1500	29.9600	81.9000
52	0	0	0	0	1	0	8.2100	20.7400	25.5700	30.9400	57.4500
53	-1	-1	1	-1	-1	-1	0.0002	0.0008	0.0017	0.0027	0.0039
54	1	-1	-1	1	-1	1	0.0686	0.1351	0.1210	0.2803	0.7371
55	0	0	0	0	0	0	4.1400	10.4800	12.9100	15.6200	29.0100
56	0	0	0	0	0	0	4.1400	10.4800	12.9100	15.6200	29.0100
57	-1	1	-1	1	1	1	7.1700	13.4000	11.9700	28.1200	73.4300
58	-1	-1	-1	1	1	-1	0.0243	0.0869	0.1778	0.2876	0.4068
59	1	1	1	-1	-1	1	0.0992	0.1633	0.1515	0.2996	0.8190
60	0	0	0	0	0	0	4.1400	10.4800	12.9100	15.6200	29.0100
61	1	1	1	1	-1	1	0.0992	0.1633	0.1515	0.2996	0.8190
62	-1	1	-1	-1	1	1	7.0800	13.4300	11.9900	28.0800	73.6900
63	1	-1	-1	1	-1	-1	0.0002	0.0009	0.0018	0.0029	0.0041
64	-1	-1	1	-1	-1	1	0.0992	0.1633	0.1515	0.2996	0.8190
65	-1	-1	1	-1	1	1	9.9200	16.3300	15.1500	29.9600	81.9000
66	0	0	0	0	0	0	4.1400	10.4800	12.9100	15.6200	29.0100
67	-1	-1	-1	1	-1	1	0.0686	0.1351	0.1210	0.2803	0.7371
68	-1	-1	-1	1	-1	-1	0.0002	0.0009	0.0018	0.0029	0.0041
69	0	1	0	0	0	0	4.1500	10.5200	12.9100	15.6200	29.2100
70	-1	-1	-1	-1	-1	1	0.0992	0.1633	0.1515	0.2996	0.8190
71	-1	1	1	-1	-1	-1	0.0003	0.0009	0.0018	0.0029	0.0041
72	-1	1	-1	-1	-1	1	0.0708	0.1343	0.1199	0.2808	0.7369
73	0	0	0	0	0	1	3.3100	6.8700	6.1900	14.1300	37.4000
74	1	1	1	1	1	-1	0.0220	0.0810	0.1690	0.2740	0.3900
75	1	1	-1	1	1	1	6.8600	13.5100	12.1000	28.0300	73.7100
76	1	1	1	-1	-1	-1	0.0002	0.0008	0.0017	0.0027	0.0039
77	1	1	-1	-1	-1	-1	0.0002	0.0008	0.0017	0.0027	0.0039
78	0	0	0	0	-1	0	0.0820	0.2070	0.2560	0.3090	0.5750
79	1	-1	1	-1	-1	-1	0.0002	0.0008	0.0017	0.0027	0.0039
80	1	-1	1	1	1	-1	0.0220	0.0810	0.1690	0.2740	0.3900
81	1	1	-1	1	-1	-1	0.0002	0.0009	0.0018	0.0029	0.0041
82	0	0	0	0	0	0	4.1400	10.4800	12.9100	15.6200	29.0100
83	-1	0	0	0	0	0	4.2100	10.5000	12.8800	15.5900	28.9900
84	1	-1	1	1	1	1	9.9200	16.3300	15.1500	29.9600	81.9000
85	-1	1	-1	-1	1	-1	0.0251	0.0878	0.1789	0.2888	0.4082
86	1	-1	-1	-1	1	-1	0.0220	0.0810	0.1690	0.2740	0.3900

The numerical values of output peak acceleration responses are kept up to four decimal places so that effect of rounding off error on crack parameter estimation is minimized. Result presented in Table 6.3, Table 6.4, Table 6.5 and Table 6.6 are now can be used to develop the response surface (RS) model for five peak acceleration responses. The

generated RS or polynomial models for forced vibration responses are for the cases illustrated in the thesis.

The adequacies of RSFs have been tested by means of analysis of variance (ANOVA). The results of the statistical test are represented in Table 6.7 for single cracked channel and angle section beams, whereas double cracked beam scenario has been presented in Table 6.8. Model-I, Model-II, Model-III, Model-IV and Model-V are the RSFs for first, second, third, fourth and fifth peak acceleration output responses respectively for single crack and double cracked beam problem. P-values obtained is less than 0.0001, which indicate that polynomial models are highly significant.

Table 6.7: ANOVA for output response surfaces for single cracked straight beam in case of forced vibration data

SD	SS	Df	MS	F-value	P-value	R^2	R^2_{adj}	Std. Dev.	Comment
Channel section beam									
Model-I	1083.93	14	77.42	449.39	<0.0001	0.9976	0.9954	0.42	Highly significant
Residual	2.58	15	0.17						
Total	1086.51	29							
Model-II	4069.06	14	290.65	39.07	<0.0001	0.9733	0.9484	2.73	Highly significant
Residual	111.60	15	7.44						
Total	4180.66	29							
Model-III	4104.65	14	293.19	8.21	<0.0001	0.8846	0.7768	5.98	Highly significant
Residual	535.73	15	35.72						
Total	4640.38	29							
Model-IV	7848.83	14	560.63	43.06	<0.0001	0.9757	0.9531	3.61	Highly significant
Residual	195.30	15	13.02						
Total	8044.13	29							
Model-V	33043.25	14	2360.23	288.82	<0.0001	0.9963	0.9929	2.86	Highly significant
Residual	122.58	15	8.17						
Total	33165.83	29							
Angle section beam									
Model-I	576.28	14	41.16	10.34	<0.0001	0.9061	0.8185	2.00	Highly significant
Residual	59.70	15	3.98						
Total	635.98	29							
Model-II	2645.77	14	188.98	7.43	<0.0001	0.8739	0.7562	5.04	Highly significant
Residual	381.74	15	25.45						
Total	3027.50	29							
Model-III	2420.61	14	172.90	7.19	<0.0001	0.8703	0.7492	4.90	Highly significant
Residual	360.84	15	24.06						
Total	2781.45	29							
Model-IV	3535.75	14	252.55	32.35	<0.0001	0.9679	0.9380	2.79	Highly significant
Residual	117.12	15	7.81						
Total	3652.87	29							
Model-V	24860.52	14	1775.75	40.15	<0.0001	0.9740	0.9498	6.65	Highly significant
Residual	663.35	15	44.22						
Total	25523.87	29							

Table 6.8: ANOVA for output response surfaces for double cracked straight beam in case of forced vibration data

SD	SS	Df	MS	F-value	P-value	R^2	R^2_{adj}	Std. Dev.	Comment
Channel section beam									
Model-I	4642.61	27	171.95	75.10	<0.0001	0.9722	0.9592	1.51	Highly significant
Residual	132.80	58	2.29						
Total	4775.40	85							
Model-II	14660.51	27	542.98	114.91	<0.0001	0.9816	0.9731	2.17	Highly significant
Residual	274.07	58	4.73						
Total	14934.58	85							
Model-III	11412.37	27	422.68	32.78	<0.0001	0.9385	0.9099	3.59	Highly significant
Residual	747.84	58	12.89						
Total	12160.21	85							
Model-IV	27698.15	27	1025.86	207.99	<0.0001	0.9898	0.9850	2.22	Highly significant
Residual	286.07	58	4.98						
Total	27984.22	85							
Model-V	124300.00	27	4603.17	663.29	<0.0001	0.9968	0.9953	2.63	Highly significant
Residual	402.52	58	6.94						
Total	124702.52	85							
Angle section beam									
Model-I	1035.96	27	38.37	56.77	<0.0001	0.9635	0.9466	0.82	Highly significant
Residual	39.20	58	0.68						
Total	1075.16	85							
Model-II	3778.54	27	139.95	47.39	<0.0001	0.9566	0.9364	1.72	Highly significant
Residual	171.29	58	2.95						
Total	3949.83	85							
Model-III	3971.07	27	147.08	40.57	<0.0001	0.9497	0.9263	1.90	Highly significant
Residual	210.24	58	3.62						
Total	4181.31	85							
Model-IV	11535.18	27	427.23	187.21	<0.0001	0.9887	0.9834	1.51	Highly significant
Residual	132.36	58	2.28						
Total	11667.54	85							
Model-V	76821.13	27	2845.23	417.94	<0.0001	0.9949	0.9925	2.61	Highly significant
Residual	394.85	58	6.81						
Total	77215.99	85							

The obtained R^2 values for single and double cracked channel and angle section beam scenario were high i.e., close to unity which confirms a satisfactory adjustment of the model to the experimental data. The low standard deviation values clearly indicate that, the variations between predicted and experimental values are very low which represent a high degree of precision in conducted experiments. Final model equations of five peak acceleration responses for single and double cracked channel and angle beams are generated based on generalized equation, which is given in Equation (3.2) of Chapter-3. The calculated regression coefficients for these polynomial equations have been given in Table D.13 to D.16 of Appendix-D.

Figure 6.9(a) and Figure 6.10(a) display the normal probability plot of residuals for single cracked channel and angle section thin walled straight beam respectively, whereas Figure 6.11(a) and Figure 6.12(a) for double cracked beams. Use the normal plot of residuals to verify the assumption that the residuals are normally distributed. It can be seen from the figures that, the points on this plot form a nearly linear pattern, which indicates that the normal distribution is a good model for this data set.

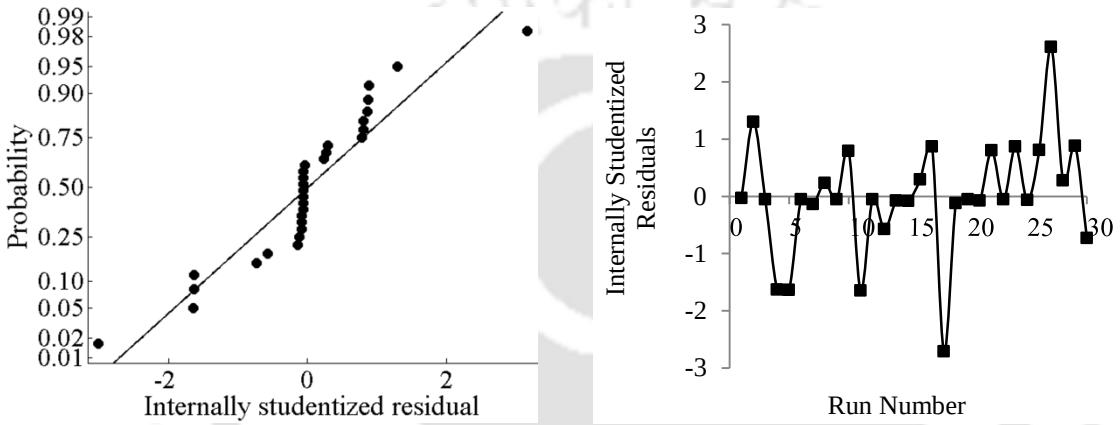

(a) (b)

Figure 6.9: Diagnostic plot for Model-I (Single cracked channel section straight beam): (a) Normal Probability plot and (b) Plot of residuals vs experimental run number in case of forced vibration data

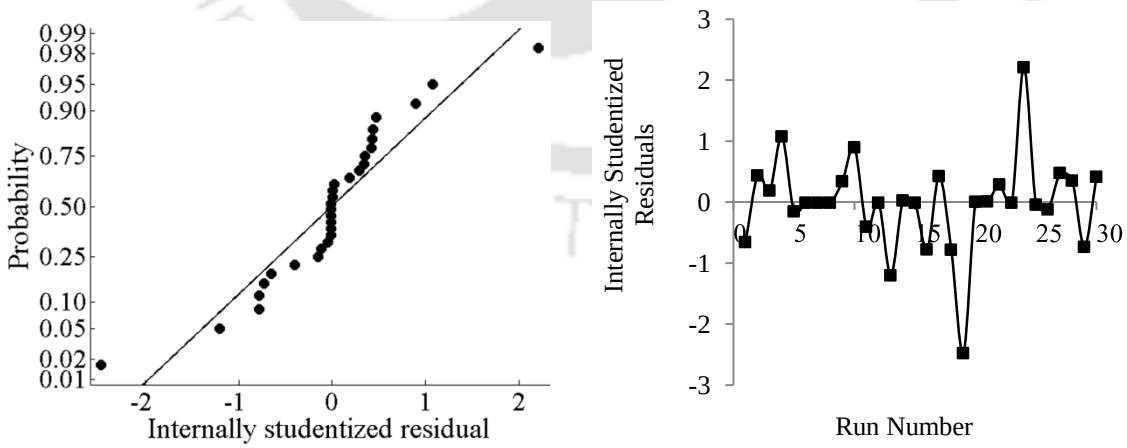

(a) (b)

Figure 6.10: Diagnostic plot for Model-I (Single cracked angle section straight beam): (a) Normal Probability plot and (b) Plot of residuals vs experimental run number in case of forced vibration data

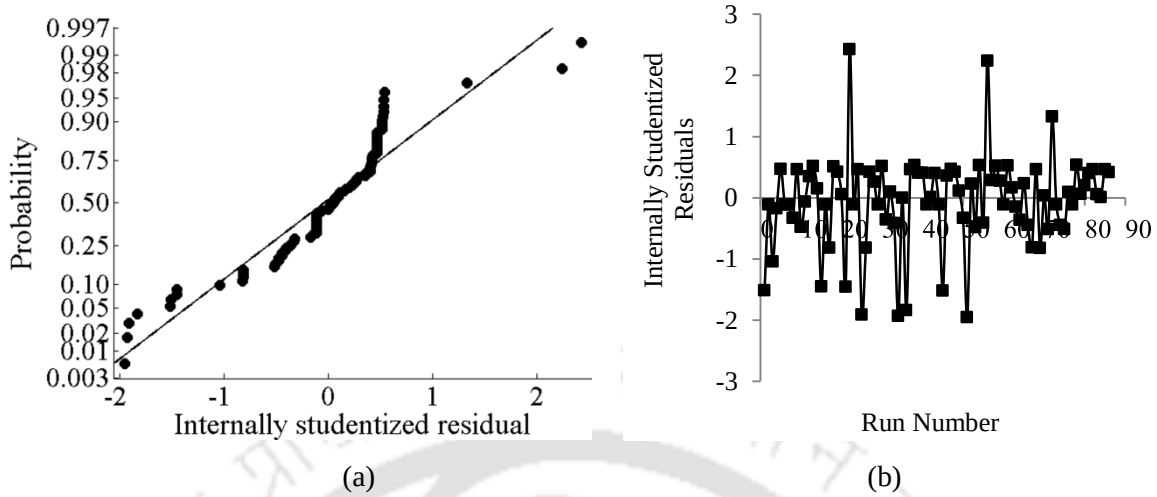

Figure 6.11: Diagnostic plot for Model-I (Double cracked channel section straight beam): (a) Normal Probability plot and (b) Plot of residuals vs experimental run number in case of forced vibration data

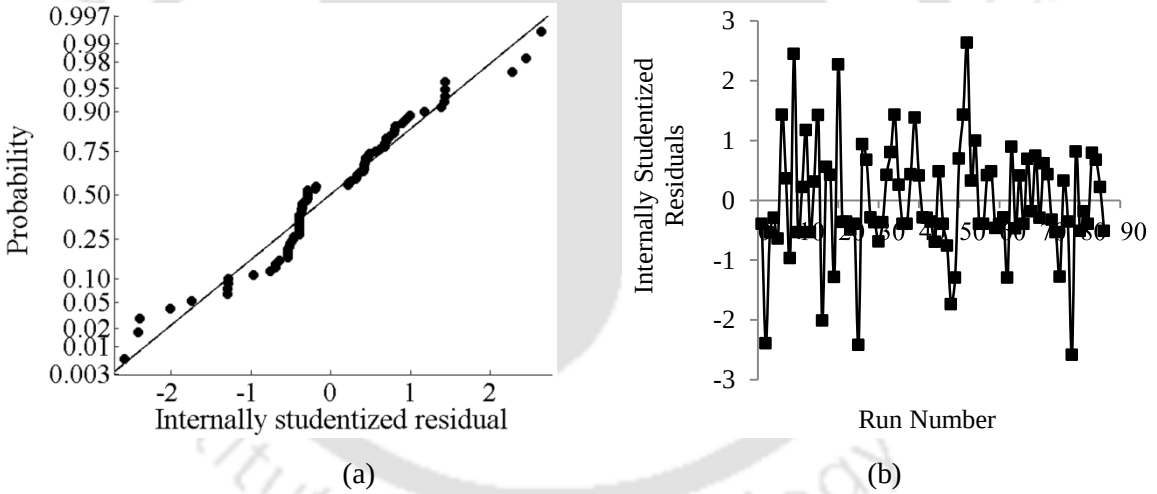

Figure 6.12: Diagnostic plot for Model-I (Double cracked angle section straight beam): (a) Normal Probability plot and (b) Plot of residuals vs experimental run number in case of forced vibration data

Figure 6.9(b), Figure 6.10(b), Figure 6.11(b) and Figure 6.12(b) demonstrate the residuals versus experimental run number plot for single and double cracked channel and angle section beam. These plots show a random pattern of residuals on both sides of zero. The residuals versus experimental run number plot verify the assumption that the residuals have a constant variance.

Finally, GA is implemented through computer simulations to calculate the crack and external excitation parameters for single and double cracked beam problem. The procedure

of optimization through GA is illustrated by a flow chart in Figure 3.11 of chapter 3. For single and double cracked optimization problem, the population size is set to 20 members (that is, 20 different possible solutions), elite count as 2, crossover fraction as 0.8 and mutation rate as 0.01. The lower and upper bound of control factors are -1 and +1 respectively. The maximum number of generations, which denote the number of total iterations, is set to 150 and 300 for single and double cracked straight beam respectively.

During vibration test, a harmonic force was applied to excite the channel and angle beam by a modal exciter near the free end of the cantilever beam. Five accelerometers were mounted on each beam to record acceleration response at a distance 0.16 m, 0.32 m, 0.48 m, 0.64 m and 0.80 m from the fixed end. The measured peak acceleration response and corresponding actual parameters for single and double cracked channel and angle section beam have been illustrated in Table 6.9 and Table 6.10. All total forty eight number of laboratory experiments are conducted for single and double crack scenario.

Table 6.9: Measured peak force, driving frequency and peak acceleration response for single cracked straight beams for various combination of crack parameters in steady state condition

Test point	Actual parameters				Measured peak acceleration response (m/s^2)				
	L_1	ζ_1/b	A_f	Ω	y_1*	y_2*	y_3*	y_4*	y_5*
Channel section beam									
1	0.02	0.08	0.65	50	0.4	1.43	2.86	4.49	6.16
2	0.02	0.08	0.78	300	0.65	1.95	3.06	3.5	3.26
3	0.02	0.50	0.85	50	0.33	1.16	2.30	3.57	4.88
4	0.02	0.50	1.20	300	1.04	3.06	4.74	5.3	4.93
5	0.02	0.80	0.45	50	0.03	0.11	0.21	0.31	0.40
6	0.02	0.80	0.56	300	0.53	1.50	2.25	2.44	2.21
7	0.50	0.08	0.65	50	0.41	1.47	2.93	4.60	6.31
8	0.50	0.08	0.94	300	0.79	2.38	3.73	4.25	3.99
9	0.50	0.50	0.87	50	0.53	1.91	3.82	5.96	8.21
10	0.50	0.50	0.68	300	0.58	1.73	2.72	3.06	2.89
11	0.50	0.80	0.57	50	0.32	1.13	2.24	3.50	4.83
12	0.50	0.80	0.79	300	0.68	2.03	3.19	3.57	3.32
Angle section beam									
1	0.02	0.08	1.52	50	4.10	8.58	13.32	17.44	21.07
2	0.02	0.08	2.42	300	15.87	16.03	17.40	16.16	21.64
3	0.02	0.50	2.99	50	7.70	16.08	24.91	32.37	40.18
4	0.02	0.50	5.76	300	17.65	34.17	28.70	34.01	45.67
5	0.02	0.80	0.33	50	1.00	2.03	3.15	4.20	5.05
6	0.02	0.80	0.64	300	0.82	2.84	1.78	4.23	3.48
7	0.50	0.08	0.48	50	1.52	3.46	5.26	6.84	8.28
8	0.50	0.08	0.91	300	1.98	4.80	6.72	5.45	7.05
9	0.50	0.50	0.49	50	1.53	3.48	5.32	6.84	8.23

Table 6.9 contd.

Test point	Actual parameters				Measured peak acceleration response (m/s^2)				
	L_1	ζ_1/b	A_f	Ω	y_1*	y_2*	y_3*	y_4*	y_5*
Angle section beam									
10	0.50	0.50	0.99	300	2.50	5.89	8.02	6.51	7.41
11	0.50	0.80	0.49	50	1.48	3.36	5.20	6.77	8.30
12	0.50	0.80	1.01	300	2.52	5.91	8.30	7.21	7.44

Table 6.10: Measured peak force, driving frequency and peak acceleration response for double cracked straight beams for various combination of crack parameters in steady state condition

Test point	Actual parameters						Measured peak acceleration response (m/s^2)				
	L_1	ζ_1/b	L_2	ζ_2/b	A_f	Ω	y_1*	y_2*	y_3*	y_4*	y_5*
Channel section beam											
1	0.02	0.08	0.10	0.50	0.65	50	0.75	2.68	5.35	8.37	11.52
2	0.02	0.08	0.10	0.50	0.82	300	0.72	2.16	3.34	3.71	3.33
3	0.02	0.50	0.10	0.80	0.60	50	0.21	0.71	1.38	2.15	2.92
4	0.02	0.50	0.10	0.80	0.72	300	0.67	1.95	2.97	3.25	2.84
5	0.02	0.80	0.10	0.50	0.45	50	0.04	0.15	0.27	0.39	0.51
6	0.02	0.80	0.10	0.50	0.76	300	0.76	2.16	3.22	3.40	2.83
7	0.50	0.08	0.60	0.50	0.88	50	1.18	4.25	8.49	13.41	18.36
8	0.50	0.08	0.60	0.50	0.96	300	0.83	2.50	3.92	4.38	3.88
9	0.50	0.50	0.60	0.80	0.80	50	0.93	3.30	6.64	10.40	14.32
10	0.50	0.50	0.60	0.80	1.12	300	0.98	2.93	4.60	5.10	4.56
11	0.50	0.80	0.60	0.50	0.38	50	0.42	1.50	2.99	4.70	6.50
12	0.50	0.80	0.60	0.50	0.48	300	0.44	1.28	1.98	2.19	1.93
Angle section beam											
1	0.02	0.08	0.10	0.50	0.55	50	0.77	2.76	5.56	8.77	12.17
2	0.02	0.08	0.10	0.50	0.74	300	0.61	1.62	2.37	2.13	3.70
3	0.02	0.50	0.10	0.80	0.63	50	0.88	3.15	6.26	9.94	13.67
4	0.02	0.50	0.10	0.80	0.81	300	0.68	1.77	2.60	2.32	4.07
5	0.02	0.80	0.10	0.50	0.79	50	1.12	3.90	7.77	12.18	16.82
6	0.02	0.80	0.10	0.50	0.97	300	0.85	2.14	3.08	2.76	4.87
7	0.50	0.08	0.60	0.50	0.39	50	0.54	1.97	3.95	6.30	8.68
8	0.50	0.08	0.60	0.50	0.46	300	0.39	1.02	1.51	1.35	2.31
9	0.50	0.50	0.60	0.80	0.46	50	0.64	2.31	4.68	7.40	10.27
10	0.50	0.50	0.60	0.80	0.61	300	0.51	1.35	1.98	1.78	3.09
11	0.50	0.80	0.60	0.50	0.83	50	1.15	4.15	8.41	13.37	18.58
12	0.50	0.80	0.60	0.50	0.92	300	0.76	2.04	2.97	2.71	4.67

GA results for first test point of single and double cracked channel and angle section beam have been demonstrated in Figure 6.13, Figure 6.14, Figure 6.15 and Figure 6.16 respectively. It can be observed from the respective optimization history v/s objective function plot that the results converge consistently towards the best individuals from where one can obtain the identified coded values of crack and forcing or excitation parameter.

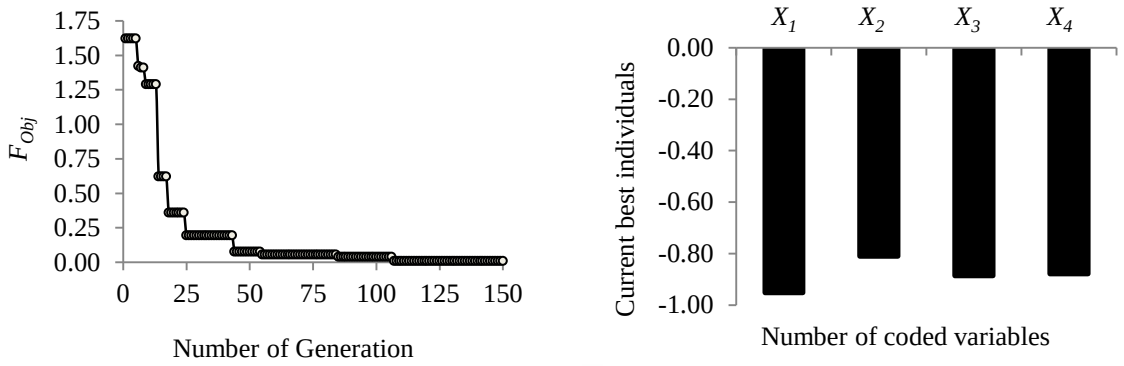

(a) (b)

Figure 6.13: GA results for first test point of single cracked channel section straight beam in case of forced vibration data: (a) Optimization history for objective function and (b) Current best individual variables

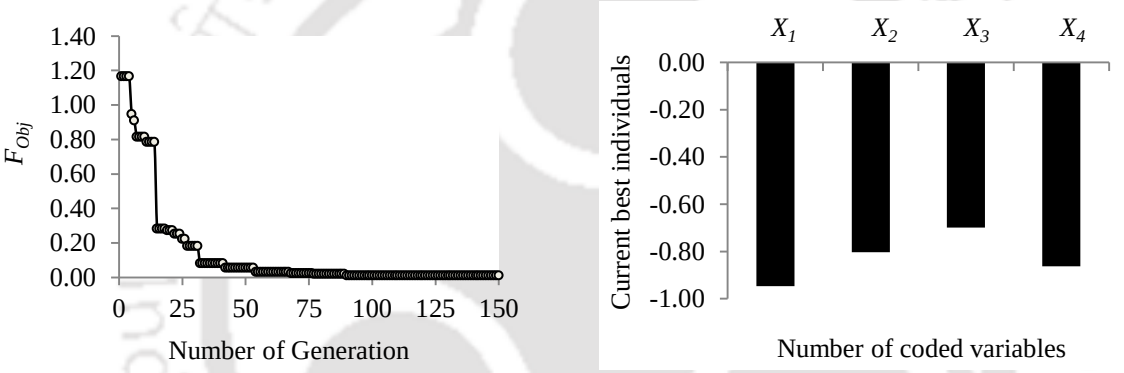

(a) (b)

Figure 6.14: GA results for first test point of single cracked angle section straight beam in case of forced vibration data: (a) Optimization history for objective function and (b) Current best individual variables

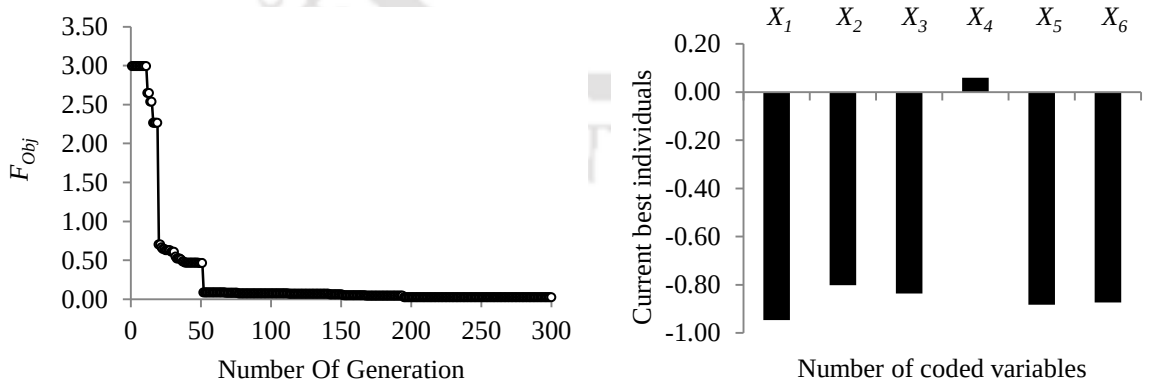

(a) (b)

Figure 6.15: GA results for first test point of double cracked channel section straight beam in case of forced vibration data: (a) Optimization history for objective function and (b) Current best individual variables

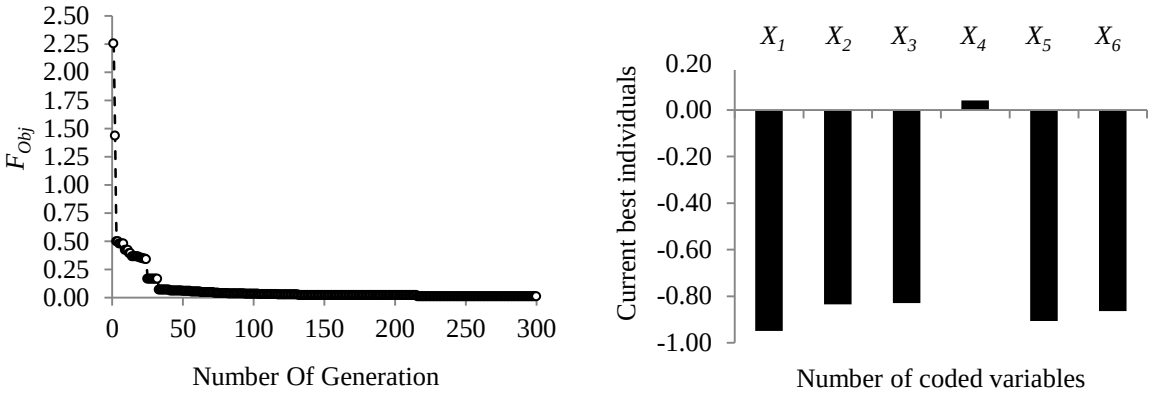

(a) (b)

Figure 6.16: GA results for first test point of double cracked angle section straight beam in case of forced vibration data: (a) Optimization history for objective function and (b) Current best individual variables

For the purpose of illustration, GA results for first test point of single cracked channel section straight beam have been considered as an example where optimization results start converging after 106 iteration and display the current best coded individuals as X_1 = -0.95138, X_2 = -0.81022, X_3 = -0.88502 and X_4 = -0.87845. The conversion of these coded predicted values (X) into natural predicted values (η) and absolute (Abs.) error in percentage with actual parameters are presented in Table 6.11 and Table 6.12. Absolute error can be evaluated using Equation (3.36) of Chapter 3. In the same table L_1 and ζ_1/b are crack location and crack depth ratio for single crack scenario, known as crack parameters. A_f and Ω represents peak value of the force time history and excitation frequency also known as forcing parameters.

Table 6.11: Predicted parameters and percentage error in estimation for single cracked straight beams in case of forced vibration data

Test point	Predicted parameters				Abs. error in percentage			
	η_1	η_2	η_3	η_4	L_1	ζ_1/b	A_f	Ω
Channel section beam								
1	0.01945	0.08540	0.66918	47.24000	2.75	6.75	2.95	5.52
2	0.02089	0.07704	0.75543	285.15000	4.45	3.70	3.15	4.95
3	0.02038	0.45075	0.89803	48.60000	1.90	9.85	5.65	2.80
4	0.02124	0.51350	1.15620	312.75000	6.20	2.70	3.65	4.25
5	0.01929	0.76080	0.45855	53.41500	3.55	4.90	1.90	6.83
6	0.02064	0.84440	0.54544	289.65000	3.20	5.55	2.60	3.45
7	0.51430	0.08300	0.67743	52.77000	2.86	3.75	4.22	5.54
8	0.53250	0.08960	0.96613	310.92000	6.50	12.00	2.78	3.64
9	0.51710	0.52560	0.91507	52.15000	3.42	5.12	5.18	4.30

Table 6.11 contd.

Test point	Predicted parameters				Abs. error in percentage			
	η_1	η_2	η_3	η_4	L_1	ζ_1/b	A_f	Ω
				Channel section beam				
10	0.51900	0.53380	0.70353	307.41000	3.80	6.76	3.46	2.47
11	0.52960	0.82288	0.59668	51.83500	5.92	2.86	4.68	3.67
12	0.52260	0.86520	0.82342	309.63000	4.52	8.15	4.23	3.21
				Angle section beam				
1	0.02102	0.08834	1.59402	52.80000	5.12	10.42	4.87	5.60
2	0.02090	0.08572	2.47397	321.75000	4.50	7.15	2.23	7.25
3	0.02045	0.53245	3.03336	53.46500	2.23	6.49	1.45	6.93
4	0.02118	0.51790	6.08256	312.36000	5.90	3.58	5.60	4.12
5	0.02087	0.90000	0.34673	52.74000	4.36	12.50	5.07	5.48
6	0.02042	0.89296	0.66157	308.94000	2.11	11.62	3.37	2.98
7	0.48685	0.08581	0.46685	47.42500	2.63	7.26	2.74	5.15
8	0.51780	0.07310	0.94340	311.49000	3.56	8.62	3.67	3.83
9	0.52925	0.52130	0.48290	52.27500	5.85	4.26	1.45	4.55
10	0.47715	0.51225	0.94793	291.45000	4.57	2.45	4.25	2.85
11	0.47270	0.70960	0.47697	53.13500	5.46	11.30	2.66	6.27
12	0.51130	0.82568	1.03929	282.66000	2.26	3.21	2.90	5.78

It has been found that the percentage error in prediction of crack position is within 6.50% and 5.90% for single cracked channel and angle section straight beam respectively. For double cracked beam scenario these are found within 6.12% and 6.15%. On the other hand, the prediction errors of crack depth ratios using present approach yielded maximum error 12.00% and 12.50% in case of single cracked channel and angle section straight beam respectively, whereas the maximum errors lies within 12.50% and 12.66% in case of double cracked beam specimens.

In the present study, external forcing parameters (force amplitude and frequency) are also taken as the hidden parameters. It has been found that the error related to peak values of the force time history are within 5.65% and 5.60% for single cracked channel and angle section straight beam respectively, whereas the values are 6.15% and 5.97% for double cracked channel and angle section straight beams respectively. The absolute error in prediction of excitation frequencies lies within 6.83% and 7.25% for single cracked beam while for double cracked beam these errors are within 6.50% and 7.50% respectively.

Table 6.12: Predicted parameters and percentage error in estimation for double cracked straight beams in case of forced vibration data

Test point	Predicted natural parameters						Abs. error in percentage					
	η_1	η_2	η_3	η_4	η_5	η_6	L_1	ζ_1/b	L_2	ζ_2/b	A_f	Ω
Channel section beam												
1	0.02117	0.08944	0.10234	0.47665	0.67828	48.90000	5.86	11.80	2.34	4.67	4.35	2.20
2	0.01905	0.08336	0.10315	0.46415	0.79991	280.50000	4.73	4.20	3.15	7.17	2.45	6.50
3	0.02089	0.48125	0.09735	0.84448	0.58398	51.58500	4.45	3.75	2.65	5.56	2.67	3.17
4	0.01926	0.47750	0.10147	0.78184	0.75787	289.29000	3.68	4.50	1.47	2.27	5.26	3.57
5	0.02045	0.84448	0.10495	0.51875	0.47187	52.79000	2.25	5.56	4.95	3.75	4.86	5.58
6	0.01881	0.74592	0.09478	0.55635	0.71326	314.28000	5.95	6.76	5.22	11.27	6.15	4.76
7	0.51640	0.09000	0.62328	0.52930	0.92374	46.92500	3.28	12.50	3.88	5.86	4.97	6.15
8	0.47225	0.08652	0.60930	0.53360	0.99072	287.25000	5.55	8.15	1.55	6.72	3.20	4.25
9	0.47870	0.55115	0.56328	0.73048	0.76600	48.77500	4.26	10.23	6.12	8.69	4.25	2.45
10	0.49255	0.47405	0.57270	0.83640	1.15192	309.99000	1.49	5.19	4.55	4.55	2.85	3.33
11	0.51175	0.74208	0.63570	0.48275	0.36423	47.04000	2.35	7.24	5.95	3.45	4.15	5.92
12	0.51910	0.82768	0.61926	0.52740	0.50688	313.05000	3.82	3.46	3.21	5.48	5.60	4.35
Angle section beam												
1	0.02045	0.07423	0.10489	0.46860	0.56573	52.26500	2.25	7.21	4.89	6.28	2.86	4.53
2	0.01931	0.07444	0.09480	0.51890	0.69582	289.32000	3.46	6.95	5.20	3.78	5.97	3.56
3	0.02098	0.51635	0.10365	0.77664	0.65205	47.25000	4.88	3.27	3.65	2.92	3.50	5.50
4	0.02079	0.47230	0.09744	0.78040	0.78189	307.14000	3.96	5.54	2.56	2.45	3.47	2.38
5	0.01934	0.88120	0.10420	0.54850	0.82689	48.89000	3.29	10.15	4.20	9.70	4.67	2.22
6	0.01948	0.86824	0.09613	0.45685	0.93848	289.59000	2.58	8.53	3.87	8.63	3.25	3.47
7	0.52775	0.08580	0.61896	0.56330	0.38275	52.42500	5.55	7.25	3.16	12.66	1.86	4.85
8	0.52950	0.08280	0.56310	0.47220	0.47334	277.50000	5.90	3.50	6.15	5.56	2.90	7.50
9	0.48695	0.44270	0.61722	0.75800	0.44040	53.08000	2.61	11.46	2.87	5.25	4.26	6.16
10	0.52260	0.53125	0.59244	0.82952	0.57486	291.66000	4.52	6.25	1.26	3.69	5.76	2.78
11	0.47125	0.77632	0.57426	0.47565	0.80286	51.90500	5.75	2.96	4.29	4.87	3.27	3.81
12	0.48300	0.83720	0.61704	0.46900	0.96756	280.02000	3.40	4.65	2.84	6.20	5.17	6.66

6.3.2 Case II – Identification of single and multiple cracks in channel and angle cross-sectional horizontally curved beam using forced vibration response

The dynamic quantities measured on the curved beam specimen are the input external forcing parameters and output peak acceleration responses. The theoretical and laboratory experiments are performed on uncracked and several cracked specimen. Two different examples based on two different subtended angles (θ_s) 25° and 50° with single and multiple cracks have been demonstrated for channel and angle section beam using forced vibration response respectively. The design experiment range and levels of the independent factors for both the subtended angles for channel and angle section beam have been listed in Table 6.13. The range of force amplitudes for simulation purpose are taken as 0.1-10 N for both the case of channel and angle section in two cases of subtended angle. In table 6.13, this information is written in symbolic form as BS in 4th column against 3rd row. In the same Table, frequency range for channel section beam with both subtended angle is written symbolically as CBS which is meant to represent frequency range 5 to 800 Hz. Similarly, ABS represents the frequency range (5-700 Hz) for angle section beams in case of two different subtended angles.

Table 6.13: Real and coded levels of the independent variables for two cases of subtended angles in case of forced vibration data

No. of crack	Factors	Coded Symb.	θ_s	Real values of coded Levels		
				(-1)	(0)	(1)
Single	Crack location (degree)	X_1	25°	0.000	12.500	25.000
			50°	0.000	25.000	50.000
	Crack depth ratio	X_2	25°	0.000	0.450	0.900
			50°	0.000	0.450	0.900
	Peak value of the force time history (N)	X_3	BS	0.100	5.050	10.000
	Excitation frequency (Hz)	X_4	CBS	5.000	402.500	800.000
			ABS	5.000	352.500	700.000
Double	First crack location (degree)	X_1	25°	0.000	12.500	25.000
			50°	0.000	25.000	50.000
	First crack depth ratio	X_2	25°	0.000	0.450	0.900
			50°	0.000	0.450	0.900
	Second crack location (degree)	X_3	25°	1.250	13.125	25.000
			50°	2.500	26.250	50.000
	Second crack depth ratio	X_4	25°	0.000	0.450	0.900
			50°	0.000	0.450	0.900
	Peak value of the force time history (N)	X_5	BS	0.100	5.050	10.000
	Excitation frequency (Hz)	X_6	CBS	5.000	402.500	800.000
			ABS	5.000	352.500	700.000

6.3.2.1 Example - I: Curved beam with subtended angle (θ_s)=25°

In this example, thirty numbers of simulated experiments were carried out for forced vibration data using FE model of single cracked channel and angle beam. Here, position of the crack (θ_{S1}) is denoted by coded values (X_1) in the Table 6.14 which correspond to actual position (θ_{S1}) given in Table 6.13. The results in the form of peak acceleration at different sensor locations are presented in Table 6.14 and Table 6.15 for single cracked channel and angle section curved beam.

Table 6.14: Coded values of the independent variables and finite element simulated responses for single cracked channel section curved beam (θ_s = 25°, R = 1833.50 mm) in case of forced vibration data

Expt. trial no.	Coded levels of variables				Peak value of the acceleration response (m/s^2) at specified sensor locations				
	X_1	X_2	X_3	X_4	y_1	y_2	y_3	y_4	y_5
1	1	-1	-1	-1	0.0001	0.0008	0.0025	0.0056	0.0104
2	-1	-1	-1	-1	0.0001	0.0008	0.0025	0.0056	0.0104
3	-1	-1	1	1	15.4500	26.5500	19.4500	42.1100	105.1000
4	1	1	1	1	15.4500	26.5500	19.4500	42.1100	105.1000
5	1	-1	1	-1	0.0133	0.0798	0.2493	0.5624	1.0430
6	0	0	0	0	8.9480	21.6600	21.1400	17.4900	38.8900
7	1	1	1	-1	0.0133	0.0798	0.2493	0.5624	1.0430
8	-1	0	0	0	9.1880	21.7400	20.9000	17.5700	39.3100
9	0	0	0	0	8.9480	21.6600	21.1400	17.4900	38.8900
10	0	0	1	0	17.7200	42.8900	41.8700	34.6400	77.0100
11	-1	-1	-1	1	0.1545	0.2655	0.1945	0.4211	1.0500
12	-1	1	-1	1	0.1448	0.2422	0.1796	0.4052	1.0180
13	0	0	0	1	6.8160	12.5100	8.9780	20.5600	51.4300
14	-1	1	1	1	14.4800	24.2200	17.9600	40.5200	101.8000
15	0	0	-1	0	0.1772	0.4289	0.4187	0.3464	0.7701
16	1	1	-1	1	0.1545	0.2655	0.1945	0.4211	1.0500
17	1	-1	-1	1	0.1545	0.2655	0.1945	0.4211	1.0500
18	0	0	0	0	8.9480	21.6600	21.1400	17.4900	38.8900
19	0	0	0	0	8.9480	21.6600	21.1400	17.4900	38.8900
20	-1	-1	1	-1	0.0133	0.0798	0.2493	0.5624	1.0430
21	0	-1	0	0	10.8100	26.1600	25.1000	17.3700	42.4000
22	0	0	0	0	8.9480	21.6600	21.1400	17.4900	38.8900
23	1	0	0	0	10.8100	26.1600	25.1000	17.3700	42.4000
24	0	1	0	0	8.9430	21.6900	21.2000	17.6400	39.2600
25	0	0	0	-1	0.0071	0.0426	0.1330	0.3001	0.5565
26	1	-1	1	1	15.4500	26.5500	19.4500	42.1100	105.1000
27	-1	1	-1	-1	0.0002	0.0010	0.0031	0.0068	0.0124
28	-1	1	1	-1	0.0179	0.1012	0.3060	0.6760	1.2370
29	1	1	-1	-1	0.0001	0.0008	0.0025	0.0056	0.0104
30	0	0	0	0	8.9480	21.6600	21.1400	17.4900	38.8900

Table 6.15: Coded values of the independent variables and simulated responses for single cracked angle section curved beam (θ_s=25°, R = 1833.50 mm) in case of forced vibration data

Expt. trial no.	Coded levels of variables				Peak value of the acceleration response (m/s^2) at specified sensor locations				
	X_1	X_2	X_3	X_4	y_1	y_2	y_3	y_4	y_5
1	1	1	-1	1	0.0629	0.1416	0.1151	0.3312	0.8477
2	0	0	0	0	4.4140	10.1700	8.2490	13.6400	29.4700
3	0	-1	0	0	1.8830	4.8130	6.5830	14.9200	32.6400
4	1	-1	1	-1	0.0318	0.1982	0.6061	1.3190	2.3600
5	1	1	1	-1	0.0318	0.1982	0.6061	1.3190	2.3600
6	0	0	0	1	4.1480	7.4490	6.3990	13.8600	38.7900
7	-1	1	1	-1	0.0550	0.3279	0.9477	1.9830	3.4550
8	0	0	0	-1	0.0163	0.1019	0.3122	0.6802	1.2160
9	-1	-1	1	1	6.2850	14.1600	11.5100	33.1200	84.7700
10	0	0	-1	0	0.0874	0.2014	0.1633	0.2701	0.5836
11	-1	1	1	1	8.2050	14.2100	12.3000	27.1600	75.9900
12	0	1	0	0	4.3000	9.9500	8.0690	13.6600	29.3600
13	1	1	1	1	6.2850	14.1600	11.5100	33.1200	84.7700
14	1	0	0	0	1.8830	4.8130	6.5830	14.9200	32.6400
15	1	-1	-1	-1	0.0003	0.0020	0.0061	0.0132	0.0236
16	0	0	0	0	4.4140	10.1700	8.2490	13.6400	29.4700
17	1	-1	1	1	6.2850	14.1600	11.5100	33.1200	84.7700
18	-1	-1	-1	1	0.0629	0.1416	0.1151	0.3312	0.8477
19	0	0	0	0	4.4140	10.1700	8.2490	13.6400	29.4700
20	0	0	0	0	4.4140	10.1700	8.2490	13.6400	29.4700
21	-1	1	-1	1	0.0821	0.1421	0.1230	0.2716	0.7599
22	-1	0	0	0	4.4060	10.0500	8.0880	13.5900	29.4800
23	-1	1	-1	-1	0.0006	0.0033	0.0095	0.0198	0.0346
24	0	0	0	0	4.4140	10.1700	8.2490	13.6400	29.4700
25	1	1	-1	-1	0.0003	0.0020	0.0061	0.0132	0.0236
26	-1	-1	-1	-1	0.0003	0.0020	0.0061	0.0132	0.0236
27	0	0	0	0	4.4140	10.1700	8.2490	13.6400	29.4700
28	-1	-1	1	-1	0.0318	0.1982	0.6061	1.3190	2.3600
29	1	-1	-1	1	0.0629	0.1416	0.1151	0.3312	0.8477
30	0	0	1	0	8.7410	20.1400	16.3400	27.0100	58.3600

The peak value of acceleration output responses (y_1, y_2, y_3, y_4 and y_5) have been recorded at five sensors located at five different locations serially from the fixed end of the cantilever curved beam. For knowing the exact position of the accelerometer, Figure (4.15) of Chapter 4 may be referred. The first and second crack locations θ_{S1} and θ_{S2} are the angular distance from the fixed end of the cantilever curved beam. The single cracked polynomial model consists of crack location (X_1), crack depth ratio (X_2), peak value of force time history (X_3) and excitation frequency (X_4). On the other hand, double crack (p = 6) model includes the first crack location (X_1), first crack depth ratio (X_2), second crack location (X_3), second crack depth ratio (X_4), peak value of force time history (X_5) and excitation frequency (X_6). Coded

values of the independent factors and simulated output for double cracked channel and angle section curved beam (θ_s =25°) have been presented in Table 6.16 and Table 6.17.

Table 6.16: Coded values of the independent variables and simulated responses for double cracked channel section curved beam (θ_s =25°, R = 1833.50 mm) in case of forced vibration data

Trial no.	Coded levels of variables						Peak value of the acceleration response (m/s^2) at specified sensor locations				
	X_1	X_2	X_3	X_4	X_5	X_6	y_1	y_2	y_3	y_4	y_5
1	-1	1	1	1	1	1	14.4800	24.2200	17.9600	40.5200	101.8000
2	0	0	0	0	0	0	12.9100	30.8400	28.2200	18.6500	50.6600
3	-1	-1	1	1	1	1	15.4500	26.5500	19.4500	42.1100	105.1000
4	-1	0	0	0	0	0	13.1200	30.6400	27.6100	18.8700	50.9000
5	-1	1	1	1	-1	1	0.1448	0.2422	0.1796	0.4052	1.0180
6	1	0	0	0	0	0	8.9470	21.6600	21.1500	17.4900	38.9100
7	-1	-1	1	1	-1	-1	0.0001	0.0008	0.0025	0.0056	0.0104
8	-1	-1	-1	-1	-1	1	0.1545	0.2655	0.1945	0.4211	1.0510
9	-1	-1	1	-1	1	-1	0.0133	0.0799	0.2494	0.5624	1.0430
10	1	-1	1	1	-1	-1	0.0001	0.0008	0.0025	0.0056	0.0104
11	-1	1	-1	-1	-1	1	0.1448	0.2422	0.1796	0.4052	1.0180
12	1	-1	-1	-1	-1	-1	0.0001	0.0008	0.0025	0.0056	0.0104
13	0	0	0	0	0	0	12.9100	30.8400	28.2200	18.6500	50.6600
14	1	1	-1	1	1	1	14.2900	24.3900	17.8700	40.5700	101.8000
15	1	-1	-1	1	1	1	14.2900	24.3900	17.8700	40.5700	101.8000
16	0	0	0	0	0	0	12.9100	30.8400	28.2200	18.6500	50.6600
17	1	-1	-1	-1	1	1	15.4500	26.5500	19.4500	42.1100	105.1000
18	0	0	0	-1	0	0	8.9480	21.6600	21.1400	17.4900	38.8900
19	0	0	0	0	0	0	12.9100	30.8400	28.2200	18.6500	50.6600
20	1	-1	-1	-1	-1	1	0.1545	0.2655	0.1945	0.4211	1.0510
21	1	-1	1	1	1	-1	0.0133	0.0799	0.2494	0.5624	1.0430
22	1	-1	1	1	1	1	15.4500	26.5500	19.4500	42.1100	105.1000
23	0	0	0	0	0	0	12.9100	30.8400	28.2200	18.6500	50.6600
24	-1	1	1	1	1	-1	0.0179	0.1012	0.3060	0.6760	1.2370
25	-1	1	1	-1	-1	1	0.1448	0.2422	0.1796	0.4052	1.0180
26	1	1	-1	-1	1	-1	0.0133	0.0799	0.2494	0.5624	1.0430
27	0	0	1	0	0	0	8.9480	21.6600	21.1400	17.4900	38.8900
28	0	0	0	0	0	0	12.9100	30.8400	28.2200	18.6500	50.6600
29	1	1	1	-1	-1	1	0.1545	0.2655	0.1945	0.4211	1.0510
30	1	1	1	1	-1	1	0.1545	0.2655	0.1945	0.4211	1.0510
31	0	1	0	0	0	0	12.9200	30.8900	28.2800	18.8900	51.1700
32	1	-1	-1	1	-1	-1	0.0002	0.0009	0.0029	0.0064	0.0118
33	-1	-1	-1	1	1	1	14.2900	24.3900	17.8700	40.5700	101.8000
34	-1	-1	-1	1	1	-1	0.0159	0.0936	0.2879	0.6428	1.1840
35	1	1	1	1	1	-1	0.0133	0.0799	0.2494	0.5624	1.0430
36	1	-1	1	-1	1	-1	0.0133	0.0799	0.2494	0.5624	1.0430
37	1	1	1	-1	1	-1	0.0133	0.0799	0.2494	0.5624	1.0430
38	-1	-1	1	-1	1	1	15.4500	26.5500	19.4500	42.1100	105.1000
39	1	1	-1	1	-1	1	0.1429	0.2439	0.1787	0.4057	1.0180
40	-1	-1	-1	1	-1	1	0.1429	0.2439	0.1787	0.4057	1.0180

Table 6.16 contd.

Expt. trial no.	Coded levels of variables						Peak value of the acceleration response (m/s^2) at specified sensor locations				
	X_1	X_2	X_3	X_4	X_5	X_6	y_1	y_2	y_3	y_4	y_5
41	1	1	1	-1	-1	-1	0.0001	0.0008	0.0025	0.0056	0.0104
42	-1	1	1	-1	-1	-1	0.0002	0.0010	0.0031	0.0068	0.0124
43	0	0	0	0	0	0	12.9100	30.8400	28.2200	18.6500	50.6600
44	-1	1	-1	1	1	1	17.5900	25.6400	21.4200	41.7000	108.7000
45	-1	1	-1	1	-1	-1	0.0002	0.0011	0.0032	0.0070	0.0128
46	0	0	0	0	1	0	25.5700	61.0700	55.8800	36.9300	100.3000
47	-1	-1	1	1	-1	1	0.1545	0.2655	0.1945	0.4211	1.0510
48	1	-1	-1	1	-1	1	0.1429	0.2439	0.1787	0.4057	1.0180
49	1	-1	1	-1	-1	-1	0.0001	0.0008	0.0025	0.0056	0.0104
50	1	1	1	1	-1	-1	0.0001	0.0008	0.0025	0.0056	0.0104
51	0	0	0	0	0	0	12.9100	30.8400	28.2200	18.6500	50.6600
52	1	-1	1	-1	-1	1	0.1545	0.2655	0.1945	0.4211	1.0510
53	-1	-1	1	-1	-1	-1	0.0001	0.0008	0.0025	0.0056	0.0104
54	1	1	-1	-1	1	1	15.4500	26.5500	19.4500	42.1100	105.1000
55	0	0	0	0	0	0	12.9100	30.8400	28.2200	18.6500	50.6600
56	-1	-1	-1	1	-1	-1	0.0002	0.0009	0.0029	0.0064	0.0118
57	-1	-1	-1	-1	-1	-1	0.0001	0.0008	0.0025	0.0056	0.0104
58	1	-1	1	1	-1	1	0.1545	0.2655	0.1945	0.4211	1.0510
59	-1	1	1	-1	1	-1	0.0179	0.1012	0.3060	0.6760	1.2370
60	1	1	1	1	1	1	15.4500	26.5500	19.4500	42.1100	105.1000
61	1	1	-1	1	1	-1	0.0159	0.0936	0.2879	0.6428	1.1840
62	1	-1	1	-1	1	1	15.4500	26.5500	19.4500	42.1100	105.1000
63	0	0	0	0	0	1	8.3960	13.7300	10.7600	21.4900	55.0300
64	-1	-1	1	1	1	-1	0.0133	0.0799	0.2494	0.5624	1.0430
65	1	1	-1	-1	-1	-1	0.0001	0.0008	0.0025	0.0056	0.0104
66	-1	1	-1	-1	-1	-1	0.0002	0.0010	0.0031	0.0068	0.0124
67	-1	1	-1	-1	1	-1	0.0179	0.1012	0.3060	0.6760	1.2370
68	-1	1	1	-1	1	1	14.4800	24.2200	17.9600	40.5200	101.8000
69	1	-1	-1	-1	1	-1	0.0133	0.0799	0.2494	0.5624	1.0430
70	-1	1	-1	-1	1	1	14.4800	24.2200	17.9600	40.5200	101.8000
71	-1	1	1	1	-1	-1	0.0002	0.0010	0.0031	0.0068	0.0124
72	0	0	0	1	0	0	12.9100	30.8700	28.2600	18.7700	50.9300
73	0	-1	0	0	0	0	8.9470	21.6600	21.1500	17.4900	38.9100
74	0	0	0	0	0	0	12.9100	30.8400	28.2200	18.6500	50.6600
75	1	1	1	-1	1	1	15.4500	26.5500	19.4500	42.1100	105.1000
76	0	0	0	0	-1	0	0.2557	0.6107	0.5588	0.3693	1.0030
77	-1	-1	-1	-1	1	1	15.4500	26.5500	19.4500	42.1100	105.1000
78	-1	1	-1	1	1	-1	0.0188	0.1057	0.3176	0.6992	1.2770
79	0	0	0	0	0	-1	0.0071	0.0426	0.1331	0.3003	0.5570
80	1	-1	-1	1	1	-1	0.0159	0.0936	0.2879	0.6428	1.1840
81	1	1	-1	1	-1	-1	0.0002	0.0009	0.0029	0.0064	0.0118
82	-1	-1	1	-1	-1	1	0.1545	0.2655	0.1945	0.4211	1.0510
83	-1	-1	-1	-1	1	-1	0.0133	0.0799	0.2494	0.5624	1.0430
84	-1	1	-1	1	-1	1	0.1759	0.2564	0.2142	0.4170	1.0870
85	0	0	-1	0	0	0	13.0800	30.7900	27.9000	18.7100	50.7800
86	1	1	-1	-1	-1	1	0.1545	0.2655	0.1945	0.4211	1.0510

Table 6.17: Coded values of the independent variables and observed responses for double cracked angle section curved beam (θ_s=25°, R = 1833.50 mm) in case of forced vibration data

Expt. trial no.	Coded levels of variables						Peak value of the acceleration response (m/s^2) at specified sensor locations				
	X_1	X_2	X_3	X_4	X_5	X_6	y_1	y_2	y_3	y_4	y_5
1	1	-1	1	1	-1	-1	0.0003	0.0020	0.0061	0.0132	0.0236
2	0	0	0	0	0	0	4.3840	10.1100	8.1990	13.6500	29.4500
3	-1	1	-1	-1	1	1	8.2050	14.2100	12.3000	27.1600	75.9900
4	-1	1	-1	-1	-1	-1	0.0006	0.0033	0.0095	0.0198	0.0346
5	-1	-1	1	1	1	1	6.2850	14.1600	11.5100	33.1200	84.7700
6	0	0	0	0	0	0	4.3840	10.1100	8.1990	13.6500	29.4500
7	-1	0	0	0	0	0	4.3660	9.9760	8.0170	13.6000	29.4500
8	1	1	-1	1	-1	1	0.0823	0.1438	0.1242	0.2724	0.7627
9	0	0	0	0	0	0	4.3840	10.1100	8.1990	13.6500	29.4500
10	1	-1	1	1	1	-1	0.0318	0.1982	0.6061	1.3190	2.3600
11	1	1	-1	1	1	-1	0.0374	0.2438	0.7425	1.6010	2.8420
12	0	-1	0	0	0	0	4.4150	10.1700	8.2490	13.6400	29.4700
13	1	1	1	1	-1	-1	0.0003	0.0020	0.0061	0.0132	0.0236
14	1	-1	-1	-1	-1	-1	0.0003	0.0020	0.0061	0.0132	0.0236
15	-1	1	-1	1	1	-1	0.0554	0.3310	0.9571	2.0030	3.4890
16	-1	1	-1	-1	-1	1	0.0821	0.1421	0.1230	0.2716	0.7599
17	1	1	1	-1	1	-1	0.0318	0.1982	0.6061	1.3190	2.3600
18	1	-1	1	-1	1	1	6.2850	14.1600	11.5100	33.1200	84.7700
19	-1	-1	-1	1	1	1	8.2260	14.3800	12.4200	27.2400	76.2700
20	0	0	0	0	0	0	4.3840	10.1100	8.1990	13.6500	29.4500
21	1	-1	-1	-1	1	-1	0.0318	0.1982	0.6061	1.3190	2.3600
22	0	0	0	0	0	0	4.3840	10.1100	8.1990	13.6500	29.4500
23	1	-1	1	-1	-1	1	0.0629	0.1416	0.1151	0.3312	0.8477
24	-1	1	1	-1	1	-1	0.0550	0.3279	0.9477	1.9830	3.4550
25	1	-1	1	1	1	1	6.2850	14.1600	11.5100	33.1200	84.7700
26	0	0	0	0	0	0	4.3840	10.1100	8.1990	13.6500	29.4500
27	-1	-1	-1	-1	-1	1	0.0629	0.1416	0.1151	0.3312	0.8477
28	-1	1	-1	-1	1	-1	0.0550	0.3279	0.9477	1.9830	3.4550
29	-1	-1	1	1	1	-1	0.0318	0.1982	0.6061	1.3190	2.3600
30	1	1	-1	1	-1	-1	0.0004	0.0024	0.0074	0.0160	0.0284
31	1	-1	-1	-1	-1	1	0.0629	0.1416	0.1151	0.3312	0.8477
32	-1	1	1	-1	1	1	8.2050	14.2100	12.3000	27.1600	75.9900
33	-1	-1	-1	1	-1	-1	0.0004	0.0024	0.0074	0.0160	0.0284
34	1	0	0	0	0	0	4.4150	10.1700	8.2490	13.6400	29.4700
35	1	1	-1	-1	1	1	6.2850	14.1600	11.5100	33.1200	84.7700
36	0	0	0	0	0	0	4.3840	10.1100	8.1990	13.6500	29.4500
37	-1	-1	-1	1	-1	1	0.0823	0.1438	0.1242	0.2724	0.7627
38	1	-1	-1	1	1	-1	0.0374	0.2438	0.7425	1.6010	2.8420
39	1	1	1	1	1	1	6.2850	14.1600	11.5100	33.1200	84.7700
40	1	-1	-1	1	-1	1	0.0823	0.1438	0.1242	0.2724	0.7627
41	1	1	1	-1	1	1	6.2850	14.1600	11.5100	33.1200	84.7700
42	0	1	0	0	0	0	4.2870	9.9240	8.0470	13.6700	29.3600
43	1	1	-1	-1	-1	1	0.0629	0.1416	0.1151	0.3312	0.8477
44	-1	1	1	1	1	-1	0.0550	0.3279	0.9477	1.9830	3.4550
45	0	0	0	0	0	0	4.3840	10.1100	8.1990	13.6500	29.4500
46	0	0	0	0	0	1	4.1430	7.4460	6.4040	13.8600	38.8000
47	0	0	0	0	1	0	8.6840	20.0300	16.2400	27.0300	58.3100
48	1	1	-1	-1	1	-1	0.0318	0.1982	0.6061	1.3190	2.3600

Table 6.17 contd.

Expt. trial no.	Coded levels of variables						Peak value of the acceleration response (m/s^2) at specified sensor locations				
	X_1	X_2	X_3	X_4	X_5	X_6	y_1	y_2	y_3	y_4	y_5
49	1	-1	1	-1	-1	-1	0.0003	0.0020	0.0061	0.0132	0.0236
50	-1	1	-1	1	1	1	8.2350	14.0500	12.2400	27.0900	75.8300
51	-1	-1	-1	-1	-1	-1	0.0003	0.0020	0.0061	0.0132	0.0236
52	1	1	-1	1	1	1	8.2260	14.3800	12.4200	27.2400	76.2700
53	-1	1	1	-1	-1	-1	0.0006	0.0033	0.0095	0.0198	0.0346
54	-1	1	-1	1	-1	1	0.0824	0.1405	0.1224	0.2709	0.7583
55	-1	-1	1	-1	-1	1	0.0629	0.1416	0.1151	0.3312	0.8477
56	0	0	1	0	0	0	4.4140	10.1700	8.2490	13.6400	29.4700
57	1	-1	1	1	-1	1	0.0629	0.1416	0.1151	0.3312	0.8477
58	-1	-1	1	-1	-1	-1	0.0003	0.0020	0.0061	0.0132	0.0236
59	-1	-1	-1	-1	1	-1	0.0318	0.1982	0.6061	1.3190	2.3600
60	0	0	0	0	0	0	4.3840	10.1100	8.1990	13.6500	29.4500
61	0	0	0	0	0	0	4.3840	10.1100	8.1990	13.6500	29.4500
62	0	0	0	0	0	-1	0.0163	0.1019	0.3126	0.6815	1.2190
63	-1	1	-1	1	-1	-1	0.0006	0.0033	0.0096	0.0200	0.0349
64	-1	1	1	1	1	1	8.2050	14.2100	12.3000	27.1600	75.9900
65	-1	-1	-1	1	1	-1	0.0374	0.2438	0.7425	1.6010	2.8420
66	1	-1	-1	-1	1	1	6.2850	14.1600	11.5100	33.1200	84.7700
67	-1	1	1	1	-1	-1	0.0006	0.0033	0.0095	0.0198	0.0346
68	0	0	0	0	-1	0	0.0868	0.2003	0.1624	0.2703	0.5831
69	1	-1	1	-1	1	-1	0.0318	0.1982	0.6061	1.3190	2.3600
70	1	-1	-1	1	-1	-1	0.0004	0.0024	0.0074	0.0160	0.0284
71	-1	1	1	1	-1	1	0.0821	0.1421	0.1230	0.2716	0.7599
72	0	0	0	1	0	0	4.3220	9.9850	8.0970	13.6600	29.3800
73	-1	-1	1	1	-1	-1	0.0003	0.0020	0.0061	0.0132	0.0236
74	-1	-1	-1	-1	1	1	6.2850	14.1600	11.5100	33.1200	84.7700
75	1	1	1	-1	-1	1	0.0629	0.1416	0.1151	0.3312	0.8477
76	1	1	1	1	-1	1	0.0629	0.1416	0.1151	0.3312	0.8477
77	1	1	-1	-1	-1	-1	0.0003	0.0020	0.0061	0.0132	0.0236
78	0	0	0	-1	0	0	4.4140	10.1700	8.2490	13.6400	29.4700
79	1	1	1	1	1	-1	0.0318	0.1982	0.6061	1.3190	2.3600
80	-1	1	1	-1	-1	1	0.0821	0.1421	0.1230	0.2716	0.7599
81	-1	-1	1	-1	1	1	6.2850	14.1600	11.5100	33.1200	84.7700
82	0	0	-1	0	0	0	4.3910	10.0500	8.1750	13.5900	29.4100
83	-1	-1	1	1	-1	1	0.0629	0.1416	0.1151	0.3312	0.8477
84	1	1	1	-1	-1	-1	0.0003	0.0020	0.0061	0.0132	0.0236
85	-1	-1	1	-1	1	-1	0.0318	0.1982	0.6061	1.3190	2.3600
86	1	-1	-1	1	1	1	8.2260	14.3800	12.4200	27.2400	76.2700

A combination of variables or factors of experimental trials are illustrated from Table 6.16 (experimental trial no. 79) and Table 6.17 (experimental trial no. 62), where first crack location (η_1) = 12.500° (X_1 = 0) and second crack location (η_3) = 13.125° (X_3 = 0) are calculated in angular direction from the fixed end of the cantilever beam. The corresponding first crack depth ratio (η_2) = 0.450 (X_2 = 0) and second crack depth ratio (η_4) = 0.450 (X_4 = 0). The peak value of the force time history 5.050 N (X_5 = 0) and excitation frequency 5.000

Hz (X_6 = -1) have been applied at the tip of the cantilever beam which produces the peak acceleration output responses (y_1, y_2, y_3, y_4 and y_5) in their respective measured location. These design experiments are conducted to obtain the polynomial models using regression analysis, which are next verified based on ANOVA.

Table 6.18: ANOVA for output response surfaces for single cracked channel section curved beam (θ_s=25°, R = 1833.50 mm) in case of forced vibration data

SD	SS	Df	MS	F-value	P-value	R^2	R^2_{adj}	Std. Dev.	Comment
Channel section beam									
Model-I	1040.83	14	74.34	23.15	< 0.0001	0.9558	0.9145	1.79	Highy significant
Residual	48.17	15	3.21						
Total	1088.99	29							
Model-II	4425.79	14	316.13	11.54	< 0.0001	0.9151	0.8358	5.23	Highy significant
Residual	410.75	15	27.38						
Total	4836.54	29							
Model-III	3597.53	14	256.97	8.21	< 0.0001	0.8846	0.7769	5.59	Highy significant
Residual	469.40	15	31.29						
Total	4066.93	29							
Model-IV	6187.69	14	441.98	82.46	< 0.0001	0.9872	0.9752	2.32	Highy significant
Residual	80.39	15	5.36						
Total	6268.09	29							
Model-V	37352.00	14	2668.00	147.29	< 0.0001	0.9928	0.9860	4.26	Highy significant
Residual	271.70	15	18.11						
Total	37623.71	29							
Angle section beam									
Model-I	211.48	14	15.11	11.57	< 0.0001	0.9153	0.8362	1.14	Highy significant
Residual	19.58	15	1.31						
Total	231.05	29							
Model-II	985.91	14	70.42	10.08	< 0.0001	0.9039	0.8142	2.64	Highy significant
Residual	104.82	15	6.99						
Total	1090.73	29							
Model-III	665.54	14	47.54	15.04	< 0.0001	0.9335	0.8715	1.78	Highy significant
Residual	47.40	15	3.16						
Total	712.94	29							
Model-IV	3532.87	14	252.35	60.68	< 0.0001	0.9826	0.9665	2.04	Highy significant
Residual	62.38	15	4.16						
Total	3595.25	29							
Model-V	22746.41	14	1624.74	168.55	< 0.0001	0.9937	0.9878	3.10	Highy significant
Residual	144.59	15	9.64						
Total	22891.00	29							

The statistical significance of these polynomial models are determined by applying the analysis of variance (ANOVA) method before using them in objective functions. ANOVA for output response surfaces for single cracked channel and angle section beam have been presented in Table 6.18. Similarly, ANOVA results for double cracked curved beam are summarized in Table 6.19. It can be noticed from all two tables that the p-values are less

than 0.0001 for all the models in single and double cracked beam scenario, which implies that selected models for crack identifications are highly significant. Calculated R^2 values for all models in single and double cracked scenario are close to unity which indicates a satisfactory performance of the model to the observed data.

Table 6.19: ANOVA for output response surfaces for double cracked channel section curved beam (θ_s =25°, R = 1833.50 mm) in case of forced vibration data

SD	SS	Df	MS	F-value	P-value	R^2	R^2_{adj}	Std. Dev.	Comment
Channel section beam									
Model-I	4013.65	27	148.65	42.13	< 0.0001	0.9515	0.9289	1.88	Highy significant
Residual	204.64	58	3.53						
Total	4218.29	85							
Model-II	16451.92	27	609.33	26.33	< 0.0001	0.9246	0.8894	4.81	Highy significant
Residual	1342.38	58	23.14						
Total	17794.30	85							
Model-III	12212.15	27	452.30	22.66	< 0.0001	0.9134	0.8731	4.47	Highy significant
Residual	1157.73	58	19.96						
Total	13369.88	85							
Model-IV	22040.17	27	816.30	363.36	< 0.0001	0.9941	0.9914	1.50	Highy significant
Residual	130.30	58	2.25						
Total	22170.47	85							
Model-V	140900.00	27	5218.79	200.67	< 0.0001	0.9894	0.9845	5.10	Highy significant
Residual	1508.41	58	26.01						
Total	142400.00	85							
Angle section beam									
Model-I	745.52	27	27.61	81.62	< 0.0001	0.9744	0.9624	0.58	Highy significant
Residual	19.62	58	0.34						
Total	765.14	85							
Model-II	3161.54	27	117.09	86.85	< 0.0001	0.9759	0.9646	1.16	Highy significant
Residual	78.20	58	1.35						
Total	3239.73	85							
Model-III	2104.05	27	77.93	93.39	< 0.0001	0.9775	0.9670	0.91	Highy significant
Residual	48.40	58	0.83						
Total	0.91	85							
Model-IV	11682.88	27	432.7	190.89	< 0.0001	0.9889	0.9837	1.51	Highy significant
Residual	131.47	58	2.27						
Total	11814.35	85							
Model-V	79902.71	27	2959.36	596.23	< 0.0001	0.9964	0.9947	2.23	Highy significant
Residual	287.88	58	4.96						
Total	80190.58	85							

The low Std. Dev. values clearly indicate that, the deviation of predicted values from the observed values are very low which represents a high degree of precision in experiments. Final model equations for peak acceleration response at any sensor in coded terms can be generated using ANOVA. The regression coefficients of these equations are listed in Table (D.17 to D.20) of Appendix-D.

Next, the residuals were predicted by the best-fit normal distribution and plotted against the residuals obtained from experiments, as shown in Figure 6.17(a), Figure 6.18(a), Figure 6.19(a) and Figure 6.20(a) for single and double cracked channel and angle section curved beam respectively. It can be seen that the residuals follow a normal distribution, as evidenced from the straight line in these figures. Hence, it can be deduced that the quadratic regression model gives an adequate description of peak value of acceleration responses.

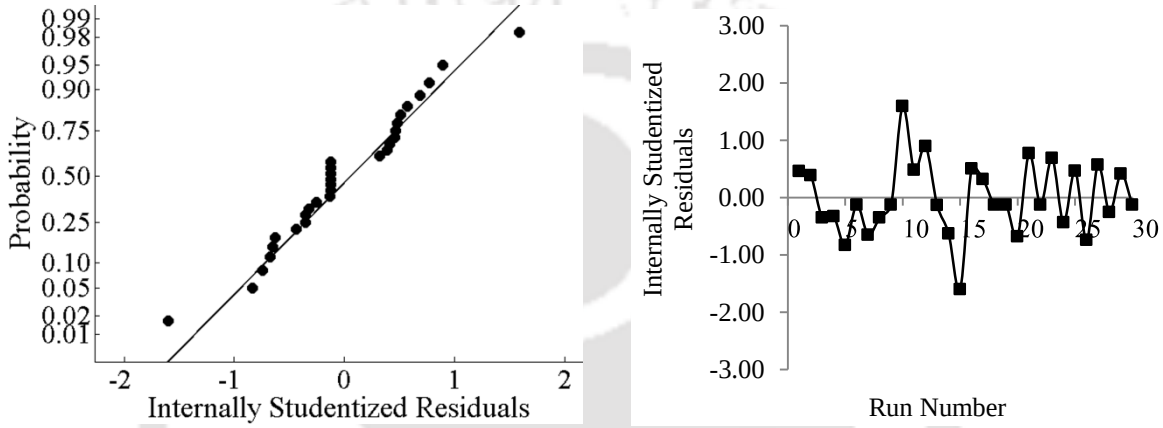

(a) (b)

Figure 6.17: Diagnostic plot for Model-I (Single cracked channel section beam, for θ_s =25° in case of forced vibration data): (a) Normal Probability plot and (b) Plot of residuals vs experimental run number

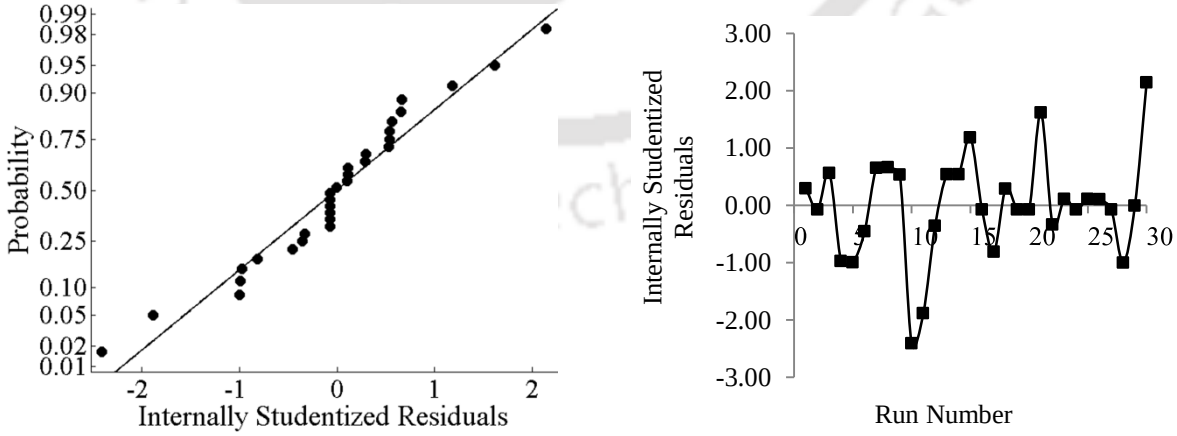

(a) (b)

Figure 6.18: Diagnostic plot for Model-I (Single cracked angle section beam, for θ_s =25° in case of forced vibration data): (a) Normal Probability plot and (b) Plot of residuals vs experimental run number

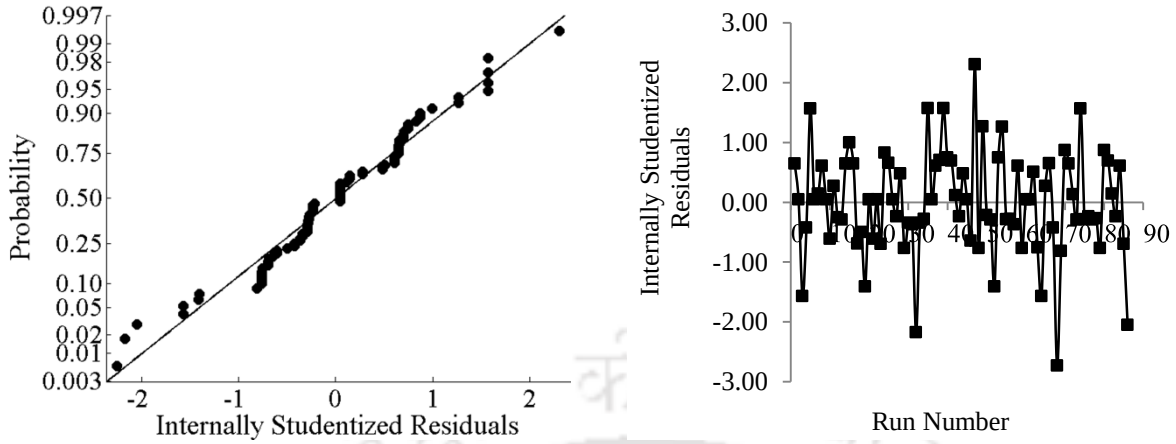

(a) (b)

Figure 6.19: Diagnostic plot for Model-I (Double cracked channel section beam, for θ_s =25° in case of forced vibration data): (a) Normal Probability plot and (b) Plot of residuals vs experimental run number

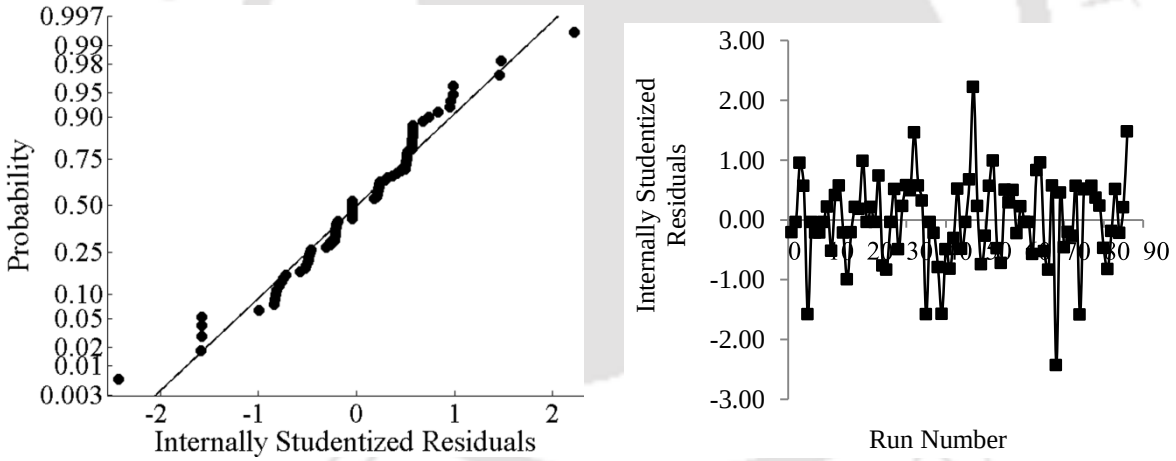

(a) (b)

Figure 6.20: Diagnostic plot for Model-I (Double cracked angle section beam, for θ_s =25° in case of forced vibration data): (a) Normal Probability plot and (b) Plot of residuals vs experimental run number

Again, the residuals were plotted against the experimental run number as shown in Figure 6.17(b), Figure 6.18(b), Figure 6.19(b) and Figure 6.20(b) respectively. It can be observed from these figures (residuals vs run number) that the data points are scattered randomly in the plot and all of the residuals lie well within the ±3.00 units, indicating that there is good approximation of the fitted model to the response surface [120].

Table 6.20: Actual parameters and five peak acceleration response for single cracked curved beam (θ_s =25°) in case of forced vibration data

Test point	Actual parameters				Measured peak acceleration response (m/s^2)				
	θ_{S1}	ζ_1/b	A_f	Ω	y_1*	y_2*	y_3*	y_4*	y_5*
				Channel section beam					
1	0.625°	0.08	0.63	50	0.68	1.43	0.72	1.28	5.19
2	0.625°	0.08	1.14	300	3.65	5.03	0.56	4.79	7.33
3	0.625°	0.50	1.02	50	0.76	1.53	0.83	1.28	5.54
4	0.625°	0.50	1.13	300	2.98	4.26	0.5	4.35	6.34
5	0.625°	0.80	1.75	50	0.86	1.7	0.83	1.5	6.37
6	0.625°	0.80	1.27	300	2.28	3.22	0.47	3.72	5.45
7	15.625°	0.08	0.81	50	2.01	3.06	2.43	2.79	6.57
8	15.625°	0.08	0.72	300	4.14	3.02	2.87	3.17	8.93
9	15.625°	0.50	0.52	50	0.7	1.4	0.59	2.18	5.74
10	15.625°	0.50	0.9	300	1.15	1.64	0.12	2.21	3.41
11	15.625°	0.80	0.56	50	0.76	1.57	0.66	2.24	6.03
12	15.625°	0.80	0.94	300	1.06	1.58	0.12	2.34	3.56
				Angle section beam					
1	0.625°	0.08	1.08	50	0.71	0.75	0.54	2.27	4.95
2	0.625°	0.08	0.43	300	2.16	1.47	1.83	3.40	3.20
3	0.625°	0.50	1.09	50	0.69	0.66	0.54	2.27	4.87
4	0.625°	0.50	0.47	300	2.57	2.07	1.93	4.11	3.33
5	0.625°	0.80	1.11	50	0.65	0.53	0.42	2.26	4.78
6	0.625°	0.80	0.56	300	3.56	3.61	2.29	5.75	3.13
7	15.625°	0.08	1.2	50	0.80	1.38	1.87	3.17	5.00
8	15.625°	0.08	0.53	300	2.77	1.91	1.97	4.19	4.24
9	15.625°	0.50	1.04	50	0.68	0.86	1.09	2.31	4.34
10	15.625°	0.50	0.47	300	2.39	1.73	1.71	3.78	3.65
11	15.625°	0.80	1.29	50	0.83	0.86	1.08	2.72	5.46
12	15.625°	0.80	0.64	300	2.70	3.18	2.29	5.97	5.25

The actual crack and forcing parameters for single and double cracked channel and angle section beam have been tabulated in Table 6.20 and Table 6.21 respectively. Each table is formed from the results of laboratory vibration test conducted on twenty four number of specimen. In the laboratory five accelerometers were mounted on each beam specimen to record acceleration responses at an angular distance of 5° (1^{st}), 10° (2^{nd}), 15° (3^{rd}), 20° (4^{th}) and 25° (5^{th} at tip) from the fixed end of the cantilever beam. Simultaneously, external forcing parameters are measured with the help of force transducer. Measured peak accelerations are used in the optimization technique to obtain the optimum crack parameters and external excitation parameters.

Table 6.21: Actual parameters and five peak acceleration response for double cracked curved beam (θ_s =25°) in case of forced vibration data

Test point	Actual parameters						Measured peak acceleration response (m/s^2)				
	θ_{S1}	ζ_1/b	θ_{S2}	ζ_2/b	A_f	Ω	y_1*	y_2*	y_3*	y_4*	y_5*
Channel section beam											
1	0.625°	0.08	3.125°	0.50	1.14	50	0.53	1.11	0.54	0.97	4.11
2	0.625°	0.08	3.125°	0.50	0.85	300	1.56	2.21	0.30	2.55	3.72
3	0.625°	0.50	3.125°	0.80	3.25	50	5.91	5.50	3.40	5.39	9.87
4	0.625°	0.50	3.125°	0.80	0.41	300	1.31	1.85	0.11	1.95	2.81
5	0.625°	0.80	3.125°	0.50	0.35	50	0.36	0.46	0.93	2.62	4.27
6	0.625°	0.80	3.125°	0.50	0.18	300	0.06	0.13	0.05	0.14	0.15
7	15.625°	0.08	18.750°	0.50	0.66	50	0.83	1.74	0.80	2.41	6.69
8	15.625°	0.08	18.750°	0.50	1.03	300	1.04	1.56	0.16	2.42	3.73
9	15.625°	0.50	18.750°	0.80	0.63	50	0.86	1.82	0.76	2.51	6.74
10	15.625°	0.50	18.750°	0.80	1.03	300	1.02	1.60	0.17	2.40	3.69
11	15.625°	0.80	18.750°	0.50	0.56	50	0.81	1.65	0.62	2.44	6.38
12	15.625°	0.80	18.750°	0.50	0.97	300	0.92	1.38	0.16	2.22	3.42
Angle section beam											
1	0.625°	0.08	3.125°	0.50	1.23	50	0.68	0.54	0.46	2.58	5.40
2	0.625°	0.08	3.125°	0.50	0.66	300	4.34	4.38	2.72	6.94	3.62
3	0.625°	0.50	3.125°	0.80	1.21	50	0.66	0.52	0.44	2.50	5.18
4	0.625°	0.50	3.125°	0.80	0.63	300	4.18	4.24	2.59	6.69	3.40
5	0.625°	0.80	3.125°	0.50	1.27	50	0.72	0.56	0.49	2.68	5.54
6	0.625°	0.80	3.125°	0.50	0.71	300	4.59	4.92	2.79	7.59	3.58
7	15.625°	0.08	18.750°	0.50	1.19	50	0.73	0.76	1.03	2.58	5.14
8	15.625°	0.08	18.750°	0.50	0.62	300	2.57	3.10	2.17	5.80	4.22
9	15.625°	0.50	18.750°	0.80	1.64	50	1.02	1.06	1.27	3.31	6.95
10	15.625°	0.50	18.750°	0.80	0.81	300	3.40	4.00	2.99	7.61	5.74
11	15.625°	0.80	18.750°	0.50	1.57	50	0.98	1.00	1.23	3.27	6.70
12	15.625°	0.80	18.750°	0.50	0.81	300	3.16	4.09	2.87	7.73	5.55

The result of optimization problem defined by Equation (3.35) in Chapter 3 is presented in Figure 6.21, Figure 6.22, Figure 6.23 and Figure 6.24 for single and double cracked channel and angle section beams with subtended angle (θ_s) equal to twenty five degree. It has been observed from the optimization history for objective function plot that the improvement of the best fitness value in each iteration or generation progressively increased and provide the final best individual variables or factors. These final optimum coded variables are presented in Figure 6.21(b), Figure 6.22(b), Figure 6.23(b) and Figure 6.24(b) for single and double cracked channel and angle section beams respectively. Then coded parameters are converted into natural parameters.

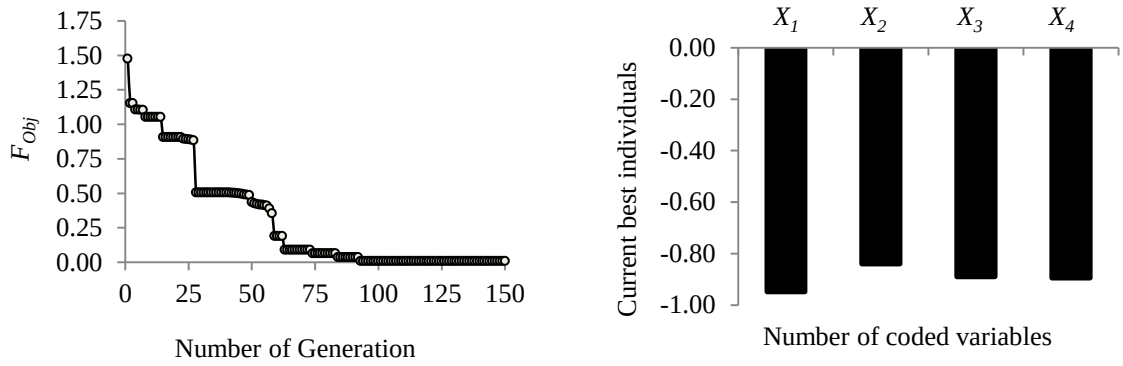

(a) (b)

Figure 6.21: GA results for first test point of single cracked channel beam, for θ_s =25° in case of forced vibration data: (a) Optimization history for objective function and (b) Current best individual variables

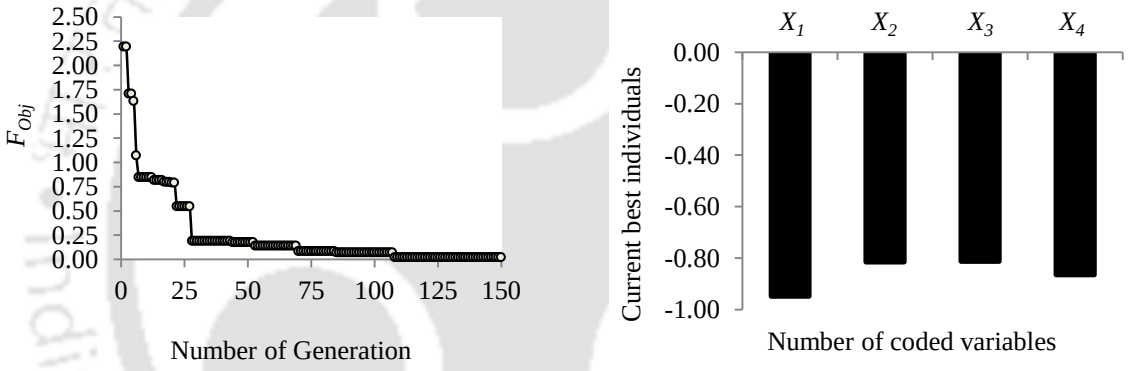

(a) (b)

Figure 6.22: GA results for first test point of single cracked angle beam, for θ_s =25° in case of forced vibration data: (a) Optimization history for objective function and (b) Current best individual variables

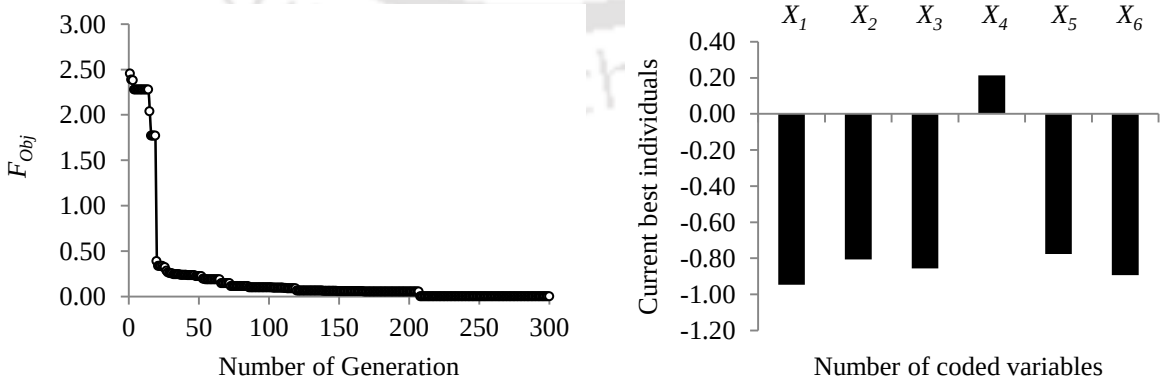

(a) (b)

Figure 6.23: GA results for first test point of double cracked channel beam, for θ_s =25° in case of forced vibration data: (a) Optimization history for objective function and (b) Current best individual variables

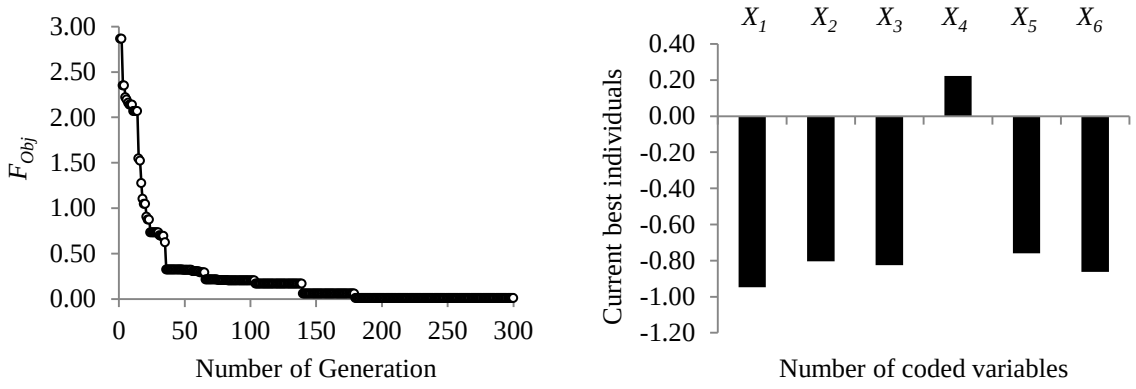

(a) (b)

Figure 6.24: GA results for first test point of double cracked angle beam, for θ_s =25° in case of forced vibration data: (a) Optimization history for objective function and (b) Current best individual variables

The predicted natural crack and forcing parameters are obtained following optimization process, which are tabulated in Table 6.22 for single cracked channel and angle section curved beam. It can be seen from this table that, the absolute errors in prediction of crack locations for single cracked channel and angle section curved beams lie within 6.75% and 6.55% respectively, whereas the corresponding prediction error of the crack depth ratios falls within a range of 12.21% to 12.92%. Table 6.23 represents the prediction of crack and forcing parameters for double cracked curved beams for both cross-sections. The absolute error between actual and predicted values of crack position for double cracked channel and angle section curved beams differs in the range of 2.62-6.45% and 2.42-6.82% respectively whereas corresponding crack depth ratios lie in the range of 3.78-12.67% and 3.80-13.15%.

Table 6.22: Predicted parameters and percentage error for single cracked channel and angle section curved beam (θ_s =25°) in case of forced vibration data

Test point	Predicted parameters				Abs. error in percentage			
	η_1	η_2	η_3	η_4	L_1	ζ_1/b	A_f	Ω
				Channel section beam				
1	0.65544	0.07226	0.64890	47.09500	4.87	9.68	3.00	5.81
2	0.58450	0.08806	1.20749	288.90000	6.48	10.07	5.92	3.70
3	0.58981	0.53605	0.99368	51.06000	5.63	7.21	2.58	2.12
4	0.64763	0.52960	1.09587	293.07000	3.62	5.92	3.02	2.31
5	0.65163	0.76368	1.79183	53.34500	4.26	4.54	2.39	6.69
6	0.66719	0.86272	1.24041	279.72000	6.75	7.84	2.33	6.76
7	14.73281	0.07051	0.86095	47.64500	5.71	11.86	6.29	4.71
8	16.40000	0.08517	0.75406	305.76000	4.96	6.46	4.73	1.92

Table 6.22 contd.

Test point	Predicted parameters				Abs. error in percentage			
	η_1	η_2	η_3	η_4	L_1	ζ_1/b	A_f	Ω
Channel section beam								
9	16.50469	0.56105	0.48771	46.40000	5.63	12.21	6.21	7.20
10	15.30313	0.52860	0.85536	305.04000	2.06	5.72	4.96	1.68
11	16.52969	0.86328	0.57960	49.08500	5.79	7.91	3.50	1.83
12	16.18750	0.72328	0.89892	292.47000	3.60	9.59	4.37	2.51
Angle section beam								
1	0.65613	0.08360	1.03075	52.20000	4.98	4.50	4.56	4.40
2	0.65800	0.09034	0.44591	317.67000	5.28	12.92	3.70	5.89
3	0.64163	0.55600	1.13349	52.78500	2.66	11.20	3.99	5.57
4	0.66319	0.44160	0.48946	286.41000	6.11	11.68	4.14	4.53
5	0.63919	0.83440	1.05883	51.12500	2.27	4.30	4.61	2.25
6	0.58956	0.85816	0.58033	313.71000	5.67	7.27	3.63	4.57
7	14.96563	0.07524	1.27104	48.12000	4.22	5.95	5.92	3.76
8	16.64844	0.07117	0.49820	288.45000	6.55	11.04	6.00	3.85
9	16.42969	0.54475	1.01223	47.18000	5.15	8.95	2.67	5.64
10	14.91406	0.55110	0.48687	280.98000	4.55	10.22	3.59	6.34
11	16.03438	0.74000	1.22202	51.97500	2.62	7.50	5.27	3.95
12	14.79688	0.87320	0.66765	287.52000	5.30	9.15	4.32	4.16

Moreover, the present approach could detect the external forcing parameters. The absolute error associated with the prediction of peak value of force time history lies within a range of 4.13-6.47% and 2.58-5.52% for double cracked channel and angle section curved beam with θ_s = 25° and for excitation frequencies these error lies within a range of 3.94-6.57% and 3.92-6.38%.

6.3.2.2 Example – II : Curved beam with subtended angle (θs)=50°

Here, the crack parameters have been identified for horizontally curved beam of θ_s =50° and radius of curvature R=916.70 mm. To avoid repetitions of some intermediate results, the present sub-section directly provides the results of predicted crack and forcing parameters that are obtained by a sequentially integrated FEM - RSM - GA approach. Final generalized polynomial model equations for five peak acceleration output responses in coded terms for single and double cracked channel and angle beam are obtained using FEM and RSM in the form as given in Equation (3.2). The calculated regression coefficients for these polynomial models are presented in Table (D.21 to D.24) of Appendix-D.

Table 6.23: Predicted parameters and percentage error for double cracked angle beam (θ_s=25°) in case of forced vibration data

Test point	Predicted natural parameters						Abs. error in percentage					
	η_1	η_2	η_3	η_4	η_5	η_6	θ_{S1}	ζ_1/b	θ_{S2}	ζ_2/b	A_f	Ω
						Channel section beam						
1	0.66188	0.08731	2.95531	0.54625	1.20965	47.29500	5.90	9.14	5.43	9.25	6.11	5.41
2	0.66356	0.07514	3.30188	0.55310	0.81362	312.96000	6.17	6.07	5.66	10.62	4.28	4.32
3	0.60081	0.44395	3.04313	0.84592	3.03973	52.56000	3.87	11.21	2.62	5.74	6.47	5.12
4	0.66531	0.51890	3.26938	0.72792	0.42894	282.78000	6.45	3.78	4.62	9.01	4.62	5.74
5	0.65856	0.74352	3.29281	0.54405	0.36446	53.17500	5.37	7.06	5.37	8.81	4.13	6.35
6	0.64869	0.85272	3.00031	0.47590	0.17226	319.71000	3.79	6.59	3.99	4.82	4.30	6.57
7	16.30000	0.07223	19.78313	0.52235	0.62390	47.37500	4.32	9.71	5.51	4.47	5.47	5.25
8	16.42344	0.08919	19.42313	0.53770	1.08160	311.82000	5.11	11.49	3.59	7.54	5.01	3.94
9	16.61250	0.52510	19.55438	0.69864	0.60083	51.99000	6.32	5.02	4.29	12.67	4.63	3.98
10	16.30469	0.55235	19.43063	0.85008	1.09345	312.96000	4.35	10.47	3.63	6.26	6.16	4.32
11	16.24531	0.85688	19.45875	0.54125	0.59007	46.90500	3.97	7.11	3.78	8.25	5.37	6.19
12	14.63125	0.86992	17.65313	0.47340	1.02102	287.07000	6.36	8.74	5.85	5.32	5.26	4.31
						Angle section beam						
1	0.66163	0.08791	3.32469	0.55025	1.28744	52.87500	5.86	9.89	6.39	10.05	4.67	5.75
2	0.66375	0.08851	3.26938	0.53245	0.67815	312.81000	6.20	10.64	4.62	6.49	2.75	4.27
3	0.64550	0.54250	3.30625	0.89960	1.25792	52.51000	3.28	8.50	5.80	12.45	3.96	5.02
4	0.58238	0.53595	3.22906	0.83056	0.65911	316.80000	6.82	7.19	3.33	3.82	4.62	5.60
5	0.65731	0.87736	3.26188	0.56575	1.30277	53.08500	5.17	9.67	4.38	13.15	2.58	6.17
6	0.64481	0.84088	3.31969	0.53545	0.73251	319.14000	3.17	5.11	6.23	7.09	3.17	6.38
7	16.22500	0.08892	19.83188	0.55355	1.23403	52.57000	3.84	11.15	5.77	10.71	3.70	5.14
8	16.38281	0.08304	19.95000	0.53815	0.64678	311.76000	4.85	3.80	6.40	7.63	4.32	3.92
9	16.62344	0.53055	19.73625	0.84208	1.73053	51.97500	6.39	6.11	5.26	5.26	5.52	3.95
10	16.00313	0.51965	19.29938	0.86488	0.84289	312.81000	2.42	3.93	2.93	8.11	4.06	4.27
11	16.15469	0.83536	19.87125	0.53850	1.64018	53.01000	3.39	4.42	5.98	7.70	4.47	6.02
12	16.47500	0.89008	19.93125	0.54795	0.84135	312.78000	5.44	11.26	6.30	9.59	3.87	4.26

Further, these empirical polynomial equations are used in genetic programming to obtain the optimum crack and external forcing parameters by evaluating the objective function, which is based on root mean square (RMS) of residuals between the computed polynomial models and measured peak acceleration responses. Measured peak acceleration responses have been presented in Table 6.24 and Table 6.25 for single cracked channel and angle section beam respectively.

Table 6.24: Actual crack and forcing parameters and measured five peak acceleration responses for single cracked channel curved beam (θ_s = 50°, R=916.70 mm) in case of forced vibration data

Test point	Actual crack parameters				Measured peak acceleration response (m/s^2)				
	θ_{S1}	ζ_1/b	A_f	Ω	y_1*	y_2*	y_3*	y_4*	y_5*
1	1.250°	0.08	1.19	50	0.13	0.15	0.62	2.49	6.44
2	1.250°	0.08	3.52	300	18.02	33.33	6.83	24.84	14.21
3	1.250°	0.50	1.00	50	0.10	0.08	0.60	2.14	5.26
4	1.250°	0.50	3.01	300	15.81	28.86	5.66	21.81	12.31
5	1.250°	0.80	0.72	50	0.06	0.12	0.65	1.74	3.65
6	1.250°	0.80	1.52	300	7.25	12.66	1.99	10.05	5.46
7	31.250°	0.08	0.24	50	0.08	0.05	0.30	0.70	1.24
8	31.250°	0.08	0.33	300	1.73	2.78	0.39	2.32	1.28
9	31.250°	0.50	0.86	50	0.24	0.06	0.91	2.32	4.79
10	31.250°	0.50	2.41	300	14.35	23.05	2.95	18.72	10.28
11	31.250°	0.80	0.67	50	0.18	0.05	0.67	1.76	3.68
12	31.250°	0.80	1.89	300	11.63	18.59	2.39	15.03	8.03

Table 6.25: Actual crack and forcing parameters and measured five peak acceleration responses for single cracked angle curved beam (θ_s = 50°, R=916.70 mm) in case of forced vibration data

Test point	Actual crack parameters				Measured peak acceleration response (m/s^2)				
	θ_{S1}	ζ_1/b	A_f	Ω	y_1*	y_2*	y_3*	y_4*	y_5*
1	1.250°	0.08	0.85	50	0.15	0.11	0.85	2.02	3.82
2	1.250°	0.08	0.33	300	6.07	0.24	2.05	7.47	3.20
3	1.250°	0.50	1.08	50	0.18	0.15	1.13	2.62	4.92
4	1.250°	0.50	0.07	300	4.17	0.52	1.07	5.00	3.96
5	1.250°	0.80	1.14	50	0.17	0.17	1.19	2.75	5.12
6	1.250°	0.80	0.12	300	3.17	0.64	0.63	3.58	4.07
7	31.250°	0.08	1.17	50	0.07	1.19	2.70	3.87	4.30
8	31.250°	0.08	0.69	300	1.61	1.45	2.12	3.13	4.00
9	31.250°	0.50	1.24	50	0.08	1.20	2.68	3.91	4.47
10	31.250°	0.50	0.73	300	1.72	1.53	2.16	3.64	3.91
11	31.250°	0.80	1.14	50	0.06	1.07	2.39	3.52	4.06
12	31.250°	0.80	2.18	300	8.27	3.88	7.85	31.57	6.49

The actual crack parameters and corresponding physically measured five peak acceleration response of the double cracked channel and angle section curved beam (θ_s = 50°) obtained in laboratory are presented in Table 6.26. Twelve numbers of physical experiments were conducted for single and double cracked beams for each cross-section. In Table 6.24 and Table 6.25, θ_{S1} (in degree) illustrates the angular distance of the single crack position from the fixed end of the cantilever curved beams, where ζ_1/b represents the corresponding crack depth ratio. In the same table, A_f (in N) and Ω (in Hz) representing peak value of the force time history and excitation frequency are also shown. In Table 6.26, θ_{S1} and θ_{S2} indicate the first and second angular position of the two cracks from fixed end of the cantilever beam with corresponding crack depth ratios ζ_1/b and ζ_2/b respectively.

Table 6.26: Actual crack and forcing parameters and measured five peak acceleration responses for double cracked curved beam (θ_s = 50°, R = 916.70 mm) in case of forced vibration data

Test point	Actual parameters						Measured peak acceleration response (m/s^2)				
	θ_{S1}	ζ_1/b	θ_{S2}	ζ_2/b	A_f	Ω	y_1*	y_2*	y_3*	y_4*	y_5*
Curved channel beam											
1	1.250°	0.08	6.250°	0.50	1.07	50	0.08	0.10	0.75	2.20	4.97
2	1.250°	0.08	6.250°	0.50	3.44	300	18.44	32.50	5.18	25.16	12.01
3	1.250°	0.50	6.250°	0.80	1.08	50	0.28	0.10	0.75	2.22	5.00
4	1.250°	0.50	6.250°	0.80	2.59	300	0.31	22.69	3.92	17.72	9.48
5	1.250°	0.80	6.250°	0.50	1.06	50	0.07	0.10	0.74	2.21	4.98
6	1.250°	0.80	6.250°	0.50	2.81	300	14.28	25.05	4.03	19.53	9.85
7	31.250°	0.08	37.500°	0.50	0.67	50	0.19	0.07	0.69	1.77	3.66
8	31.250°	0.08	37.500°	0.50	1.89	300	11.76	18.78	2.40	15.19	8.11
9	31.250°	0.50	37.500°	0.80	0.41	50	0.12	0.05	0.40	1.07	2.21
10	31.250°	0.50	37.500°	0.80	1.15	300	7.14	11.40	1.48	9.25	4.88
11	31.250°	0.80	37.500°	0.50	1.86	50	0.20	0.07	0.75	1.96	1.66
12	31.250°	0.80	37.500°	0.50	4.37	300	15.13	24.22	3.02	19.62	5.21
Curved angle beam											
1	1.250°	0.08	6.250°	0.50	1.16	50	0.18	0.17	1.20	2.78	5.22
2	1.250°	0.08	6.250°	0.50	0.13	300	3.20	0.63	0.63	3.58	4.11
3	1.250°	0.50	6.250°	0.80	1.13	50	0.17	0.16	1.15	2.70	5.09
4	1.250°	0.50	6.250°	0.80	0.12	300	3.08	0.67	0.55	3.51	4.06
5	1.250°	0.80	6.250°	0.50	1.11	50	0.19	0.16	1.12	2.62	4.94
6	1.250°	0.80	6.250°	0.50	0.15	300	2.81	0.63	0.43	3.15	4.00
7	31.250°	0.08	37.500°	0.50	1.25	50	0.75	0.23	1.70	3.92	4.69
8	31.250°	0.08	37.500°	0.50	0.86	300	1.86	1.71	1.52	3.41	4.32
9	31.250°	0.50	37.500°	0.80	1.36	50	0.84	0.38	1.79	3.97	4.72
10	31.250°	0.50	37.500°	0.80	0.90	300	1.88	1.76	1.57	3.51	4.38
11	31.250°	0.80	37.500°	0.50	1.20	50	0.73	0.21	1.64	3.84	4.63
12	31.250°	0.80	37.500°	0.50	2.20	300	6.14	2.92	2.32	5.21	9.16

The predicted natural values of crack and external forcing parameters for single cracked channel and angle section curved beams are presented in Table 6.27 and Table 6.28 separately where. Furthermore, these tables show the absolute errors between the actual and predicted parameters. From Table 6.27 and Table 6.28, it can be observed that the prediction percentage error associated with single crack localization covers the values in the range of 2.43-6.96% and 3.56-7.10% for channel and angle section beams respectively. The corresponding percentage error related to crack depth ratio lies in the range of 2.45-12.59% and 4.32-13.65%.

Table 6.27: Absolute error between actual and predicted crack and forcing parameters for single cracked channel section curved beam (θ_s = 50°, R = 916.70 mm) in case of forced vibration data

Test point	Predicted natural parameters				Abs error (%) in			
	η_1	η_2	η_3	η_4	θ_{S1}	ζ_1/b	A_f	Ω
1	1.31125	0.08196	1.13907	53.01500	4.90	2.45	4.28	6.03
2	1.30888	0.07647	3.72698	285.78000	4.71	4.41	5.88	4.74
3	1.16300	0.55905	1.06510	53.24000	6.96	11.81	6.51	6.48
4	1.28450	0.54805	2.90826	304.98000	2.76	9.61	3.38	1.66
5	1.32650	0.85536	0.75910	47.87500	6.12	6.92	5.43	4.25
6	1.21788	0.73664	1.55967	292.68000	2.57	7.92	2.61	2.44
7	33.04375	0.09007	0.24401	47.75000	5.74	12.59	1.67	4.50
8	30.49063	0.07473	0.31126	316.53000	2.43	6.59	5.68	5.51
9	30.25000	0.46360	0.80341	50.92000	3.20	7.28	6.58	1.84
10	29.20313	0.52035	2.29119	315.99000	6.55	4.07	4.93	5.33
11	30.04688	0.89752	0.71757	49.13000	3.85	12.19	7.10	1.74
12	32.03438	0.73256	1.77036	288.30000	2.51	8.43	6.33	3.90

Table 6.28: Absolute error between actual and predicted crack and forcing parameters for single cracked angle section curved beam (θ_s = 50°, R = 916.70 mm) in case of forced vibration data

Test point	Predicted natural parameters				Abs error (%) in			
	η_1	η_2	η_3	η_4	θ_{S1}	ζ_1/b	A_f	Ω
1	1.31963	0.08838	0.80053	51.15500	5.57	10.47	5.82	2.31
2	1.29650	0.08429	0.34274	287.67000	3.72	5.36	3.86	4.11
3	1.16925	0.55710	1.13141	52.31000	6.46	11.42	4.76	4.62
4	1.29450	0.52160	0.07482	279.54000	3.56	4.32	6.88	6.82
5	1.33875	0.90344	1.17021	52.52500	7.10	12.93	2.65	5.05
6	1.19863	0.70904	0.11342	312.51000	4.11	11.37	5.48	4.17
7	29.42500	0.08675	1.12624	46.62000	5.84	8.44	3.74	6.76
8	33.16563	0.08634	0.72871	278.91000	6.13	7.92	5.61	7.03
9	32.95938	0.54330	1.17552	51.71500	5.47	8.66	5.20	3.43
10	32.67813	0.45660	0.76161	285.09000	4.57	8.68	4.33	4.97
11	29.31875	0.90920	1.21456	52.82000	6.18	13.65	6.54	5.64
12	29.94375	0.70744	2.08844	313.32000	4.18	11.57	4.20	4.44

Table 6.29 is prepared for double cracked channel and angle beam respectively. In the case of double cracked channel and angle section curved beam, the crack position can be estimated with less than 6.86% and 7.36% error respectively, whereas, the estimation of crack depth shows an error between 12.88% and 13.80% for channel and angle beam respectively. Besides that, the absolute percentage error related to peak values of the force time history lies within a range of 1.67-7.10% and 2.65-6.88% for single cracked channel and angle section curved beam respectively, whereas the percentage errors for forcing frequencies lie in the range of 1.66-6.48% in case of channel and 2.31-7.03% in case of angle beam. In case of double cracked channel and angle section curved beams the prediction is related to peak values of the force time history cover the error range 2.93-6.80% and 3.68-6.54% respectively. The corresponding absolute error associated with excitation frequencies are found in the range of 2.72-6.75% and 3.54-6.08%.

Finally, a summary is given in Table 6.30 showing the mean error in all types of beam investigated for detection of crack parameters based on forced vibration response. It can be observed from the same table that the mean error for single and double cracked channel section straight beams lies within 4.09% and 6.37% for crack localization and crack depth ratio respectively, whereas these percentage lies within 4.05% and 7.41% for angle cross-sectional straight beams. The mean error between actual and predicted single and double crack parameters (position and crack depth ratio) for channel and angle section curved (θ_s = 25°) beam has been found as 4.95% and 8.25%; and 5.00% and 8.72% respectively. The mean error for curved channel and angle section beam for θ_s = 50° has been found as 5.01% and 7.86%; and 5.70% and 9.57% respectively. Moreover, the result reveals that in case of single and double crack scenarios, almost same accuracy is maintained to obtain the forcing parameters, showing that the present method is a promising approach for external force identification too. It may be noted that in earlier chapter, when natural frequencies are used in identification approach, higher accuracy was seen. It is also emphasized that natural frequencies were largely used instead of forced vibration response. However, since accelerometer is used in common application of vibration measurement and directly using acceleration output in the present work has also shown that combined RSM and GA based approach is not input specific.

Table 6.29: Predicted parameters and percentage error for double cracked channel and angle beam (θ_s=50°) in case of forced vibration data

Test point	Predicted natural parameters						Abs. error in percentage					
	η_1	η_2	η_3	η_4	η_5	η_6	θ_{S1}	ζ_1/b	θ_{S2}	ζ_2/b	A_f	Ω
Channel section beam												
1	1.33225	0.08354	6.61375	0.52540	1.11301	52.15500	6.58	4.43	5.82	5.08	4.02	4.31
2	1.19425	0.08948	5.87438	0.47105	3.21468	308.52000	4.46	11.85	6.01	5.79	6.55	2.84
3	1.32550	0.51770	6.56313	0.83808	1.03507	48.21000	6.04	3.54	5.01	4.76	4.16	3.58
4	1.32538	0.46885	6.48625	0.88472	2.66770	290.85000	6.03	6.23	3.78	10.59	3.00	3.05
5	1.30975	0.83744	5.98313	0.56440	1.12477	51.66500	4.78	4.68	4.27	12.88	6.11	3.33
6	1.31763	0.88832	6.66063	0.53765	2.69058	310.74000	5.41	11.04	6.57	7.53	4.25	3.58
7	32.42188	0.08338	35.99625	0.54135	0.69405	47.81000	3.75	4.23	4.01	8.27	3.59	4.38
8	30.41250	0.07442	39.85125	0.52380	1.97165	308.16000	2.68	6.97	6.27	4.76	4.32	2.72
9	32.90000	0.52880	39.49125	0.71280	0.42201	53.28000	5.28	5.76	5.31	10.90	2.93	6.56
10	33.16250	0.55220	40.07250	0.87120	1.18554	279.75000	6.12	10.44	6.86	8.90	3.09	6.75
11	30.42500	0.85792	38.91000	0.53275	1.73464	47.64500	2.64	7.24	3.76	6.55	6.74	4.71
12	32.48125	0.74880	39.37125	0.46020	4.07284	314.10000	3.94	6.40	4.99	7.96	6.80	4.70
Angle section beam												
1	1.33988	0.08951	6.63625	0.55620	1.23517	47.32500	7.19	11.89	6.18	11.24	6.48	5.35
2	1.18288	0.08481	5.95500	0.46935	0.13576	315.09000	5.37	6.01	4.72	6.13	4.43	5.03
3	1.33238	0.43130	6.71000	0.73032	1.06265	51.77000	6.59	13.74	7.36	8.71	5.96	3.54
4	1.30063	0.53550	6.02313	0.71440	0.11286	286.20000	4.05	7.10	3.63	10.70	5.95	4.60
5	1.31413	0.84416	5.92563	0.56340	1.05739	52.01500	5.13	5.52	5.19	12.68	4.74	4.03
6	1.19563	0.75128	6.56063	0.52520	0.15803	318.24000	4.35	6.09	4.97	5.04	5.35	6.08
7	33.30000	0.08788	39.91875	0.54570	1.29688	52.25500	6.56	9.85	6.45	9.14	3.75	4.51
8	33.50000	0.07330	39.96375	0.52465	0.82835	315.66000	7.20	8.37	6.57	4.93	3.68	5.22
9	33.13438	0.53560	35.91750	0.91040	1.43113	47.98000	6.03	7.12	4.22	13.80	5.23	4.04
10	30.11250	0.56030	40.12125	0.75080	0.84573	316.38000	3.64	12.06	6.99	6.15	6.03	5.46
11	29.13125	0.87624	35.54250	0.56080	1.27848	52.17500	6.78	9.53	5.22	12.16	6.54	4.35
12	33.47188	0.87328	39.52125	0.46940	2.28624	283.11000	7.11	9.16	5.39	6.12	3.92	5.63

Table 6.30: Mean error between actual and predicted crack parameters and excitation characteristics using measured steady state amplitude

Sl. No.	Configuration of thin-walled beams	Abs error (%) for			
		Crack location	Crack depth ratio	A_f	Ω
Channel section configurations					
1	Single cracked straight beam	4.09	6.01	3.70	4.22
2	Double cracked straight beam	3.86	6.37	4.23	4.35
3	Single cracked curved beam (θ_s = 25°)	4.95	8.25	4.11	3.94
4	Double cracked curved beam (θ_s = 25°)	4.85	7.88	5.15	5.12
5	Single cracked curved beam (θ_s = 50°)	4.36	7.86	5.03	4.04
6	Double cracked curved beam (θ_s = 50°)	5.01	7.37	4.63	4.21
Angle section configurations					
1	Single cracked straight beam	4.05	7.41	3.36	5.07
2	Double cracked straight beam	3.88	6.23	3.91	4.45
3	Single cracked curved beam (θ_s = 25°)	4.61	8.72	4.37	4.58
4	Double cracked curved beam (θ_s = 25°)	5.00	8.07	3.97	5.06
5	Single cracked curved beam (θ_s = 50°)	5.24	9.57	4.92	4.95
6	Double cracked curved beam (θ_s = 50°)	5.70	8.89	5.17	4.82

6.4 Closure

A detailed study of utilization of force vibration response for the crack and forcing parameter identification has been carried out in this chapter using the present hybrid approach. Crack parameters are identified using information of steady state amplitude when the beams are excited harmonically. The theoretical and experimental studies for straight and curved thin-walled beams with single and double cracks on channel and angle section configurations are provided in this chapter. In case of curved beam, two different types of subtended angle (25° and 50°) are chosen to examine the present approach. It was found that, the accuracy of the crack depth ratio (size of the crack) is lower compared to crack localization for single and multiple crack specimens. In addition to crack parameters, frequency and amplitude of harmonic force applied in the shaker has been identified by using acceleration amplitudes in RSM and GA based method. In this study, there is no necessity of knowing the vibration characteristics in the undamaged state of the structures. Since, usually resonance condition may not be obtained in ambient vibration, this method may prove useful in practical application when the structures are excited not in natural frequencies.

Chapter 7

Identification using Heterogeneous Response Data

7.1 Overview

To check the robustness of the present approach, measured heterogeneous output data have been utilized to estimate the crack location and its size. Here, heterogeneous data refers to combination of free vibration (natural frequencies) and forced vibration (peak value of acceleration) responses. The crack and forcing parameter identification algorithm developed in the present study have been applied on thin walled straight and curved steel beam for different cross-sectional configurations. The investigation has been carried out with two combinations of data. First one is with two natural frequencies and three steady state amplitude at three sensor locations. Second combination is with three natural frequencies and two steady state amplitudes at two sensor locations. The difference in accuracy of prediction of crack parameters and excitation features has been discussed.

7.2 Damage identification in thin-walled beam using heterogeneous response data

In this chapter, two different cases with several number of theoretical and experimental results have been discussed to justify the consistency of the present approach. First case stands for identification of single and multiple cracks in channel and angle cross-sectional straight beam and second case relates to the identification of single and multiple cracks in horizontally curved beams using heterogeneous output data. Also, two combinations of output responses are studied using the present approach for all cases, which are mentioned above. Here input y_i (i =1,2,…,5) required in the identification algorithm represent either

natural frequencies or peak accelerations measured at some sensor locations. Total five accelerometers are mounted at points 1, 2, …,5 on the beam as shown by a schematic sketch in Figure 7.1. The first combination (Case-I) of heterogeneous data contains first two natural frequencies (here denoted as y_1 and y_2) and three peak acceleration responses (y_3, y_4 and y_5) at sensor location 3, 4 and 5. Second combination (Case-II) consists of first three natural frequencies (here denoted as y_1, y_2 and y_3) and two peak acceleration responses y_4 and y_5 at sensor locations 4 and 5.

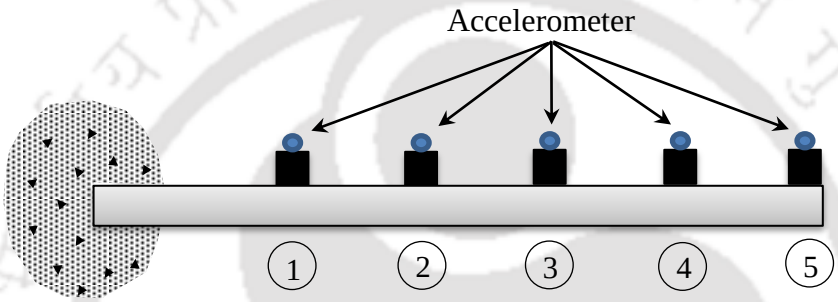

Figure 7.1: Schematic diagram of a cantilever beam with accelerometers

The crack and forcing parameters identification methodology has been presented in earlier Chapter 3. This methodology was successfully applied on several case studies based on free and forced vibration response separately on different configuration of thin-walled steel beam, which was presented in Chapter 5 and Chapter 6 respectively. Hence, to avoid repetition of discussing the approach in detail, the identified parameters which are outcome of the said methodology are directly presented here, rather than repeating the entire steps. The main task in this chapter is to show the utilization of mixed data in identification problem outlined in the present thesis.

7.2.1 Identification of single and double cracks in channel and angle cross-sectional straight beam using heterogeneous output (Data combination-Case-I)

The present parameter identification procedure begins with the RSM and ends with GA by optimizing the objective function constructed according to Equation (3.35) of Chapter 3. In the optimization procedure theoretically obtained RSFs and physically measured dynamic responses are required. The physically measured heterogeneous response obtained for different combination of crack parameters for the single and double cracked channel and

angle beam specimen have been presented in Table 7.1 and Table 7.2 respectively for Case-I. First two natural frequencies of the beam corresponding to different crack parameters and peak acceleration responses at sensor locations of 0.48 m, 0.64 m and 0.80 m from the fixed end of the cantilever beam have been utilized.

Table 7.1: Actual parameters and corresponding heterogeneous response for single cracked straight beams for Case-I

Test point	Actual parameters				Measured heterogeneous response				
	L_1 (m)	ζ_1/b	A_f (N)	Ω (Hz)	y_1* (Hz)	y_2* (Hz)	y_3* (m/s^2)	y_4* (m/s^2)	y_5* (m/s^2)
Channel section straight beam									
1	0.02	0.08	0.65	50	49.32	101.41	2.86	4.49	6.16
2	0.02	0.08	0.78	300	49.32	101.41	3.06	3.5	3.26
3	0.02	0.50	0.85	50	48.36	99.6	2.3	3.57	4.88
4	0.02	0.50	1.2	300	48.36	99.6	4.74	5.3	4.93
5	0.02	0.80	0.45	50	44.95	93.88	0.21	0.31	0.40
6	0.02	0.80	0.56	300	44.95	93.88	2.25	2.44	2.21
7	0.50	0.08	0.65	50	49.38	101.48	2.93	4.60	6.31
8	0.50	0.08	0.94	300	49.38	101.48	3.73	4.25	3.99
9	0.50	0.50	0.87	50	49.10	101.05	3.82	5.96	8.21
10	0.50	0.50	0.68	300	49.10	101.05	2.72	3.06	2.89
11	0.50	0.80	0.57	50	48.35	99.50	2.24	3.50	4.83
12	0.50	0.80	0.79	300	48.35	99.50	3.19	3.57	3.32
Angle section straight beam									
1	0.02	0.08	1.52	50	23.45	50.13	13.32	17.44	21.07
2	0.02	0.08	2.42	300	23.45	50.13	17.40	16.16	21.64
3	0.02	0.50	2.99	50	21.13	49.63	24.91	32.37	40.18
4	0.02	0.50	5.76	300	21.13	49.63	28.70	34.01	45.67
5	0.02	0.80	0.33	50	14.80	48.78	3.15	4.20	5.05
6	0.02	0.80	0.64	300	14.80	48.78	1.78	4.23	3.48
7	0.50	0.08	0.48	50	23.50	50.18	5.26	6.84	8.28
8	0.50	0.08	0.91	300	23.50	50.18	6.72	5.45	7.05
9	0.50	0.50	0.49	50	23.40	50.00	5.32	6.84	8.23
10	0.50	0.50	0.99	300	23.40	50.00	8.02	6.51	7.41
11	0.50	0.80	0.49	50	22.88	49.50	5.20	6.77	8.30
12	0.50	0.80	1.01	300	22.88	49.50	8.30	7.21	7.44

The predicted natural crack and external forcing parameters for single and double cracked channel and angle section straight beams have been presented in Table 7.3 and Table 7.4 respectively. It can be observed from Table 7.3 and Table 7.4 that the prediction errors associated with the localization of crack lies within 4.23% (single cracked channel), 4.65% (single cracked angle), 4.56% (double cracked channel) and 4.72% (double cracked

angle). The corresponding absolute percentage error related to crack depth ratio is found maximum up to 10.37%, 10.48%, 10.98% and 10.69% when two natural frequencies plus three steady state amplitudes are considered in the heterogeneous data. The maximum value of absolute error related to peak values of force time history (A_f) is found to be 6.37% and 5.89% for single cracked channel and angle straight beam respectively whereas the maximum error related to peak values of force time history (A_f) are 6.89% and 5.77% for double cracked channel and angle section beam respectively. The absolute error in prediction of forcing frequencies (Ω) applied during experiments with single cracked channel and angle beam are found to be 5.85% and 5.93% respectively while that for double cracked channel and angle beams are 4.53% and 6.46% respectively.

Table 7.2: Actual parameters and corresponding heterogeneous response for double cracked straight beam for Case-I

Test point	Actual parameters						Measured heterogeneous responses				
	L_1 (m)	ζ_1/b	L_2 (m)	ζ_2/b	A_f (N)	Ω (Hz)	y_1* (Hz)	y_2* (Hz)	y_3* (m/s^2)	y_4* (m/s^2)	y_5* (m/s^2)
Channel section straight beam											
1	0.02	0.08	0.10	0.50	0.65	50	48.83	101.00	5.35	8.37	11.52
2	0.02	0.08	0.10	0.50	0.82	300	48.83	101.00	3.34	3.71	3.33
3	0.02	0.50	0.10	0.80	0.60	50	47.80	98.45	1.38	2.15	2.92
4	0.02	0.50	0.10	0.80	0.72	300	47.80	98.45	2.97	3.25	2.84
5	0.02	0.80	0.10	0.50	0.45	50	44.25	92.00	0.27	0.39	0.51
6	0.02	0.80	0.10	0.50	0.76	300	44.25	92.00	3.22	3.40	2.83
7	0.50	0.08	0.60	0.50	0.88	50	49.10	101.10	8.49	13.41	18.36
8	0.50	0.08	0.60	0.50	0.96	300	49.10	101.10	3.92	4.38	3.88
9	0.50	0.50	0.60	0.80	0.80	50	48.00	99.15	6.64	10.40	14.32
10	0.50	0.50	0.60	0.80	1.12	300	48.00	99.15	4.60	5.10	4.56
11	0.50	0.80	0.60	0.50	0.38	50	46.80	97.85	2.99	4.70	6.50
12	0.50	0.80	0.60	0.50	0.48	300	46.80	97.85	1.98	2.19	1.93
Angle section straight beam											
1	0.02	0.08	0.10	0.50	0.55	50	22.85	49.85	5.56	8.77	12.17
2	0.02	0.08	0.10	0.50	0.74	300	22.85	49.85	2.37	2.13	3.70
3	0.02	0.50	0.10	0.80	0.63	50	18.35	48.45	6.26	9.94	13.67
4	0.02	0.50	0.10	0.80	0.81	300	18.35	48.45	2.60	2.32	4.07
5	0.02	0.80	0.10	0.50	0.79	50	14.20	47.85	7.77	12.18	16.82
6	0.02	0.80	0.10	0.50	0.97	300	14.20	47.85	3.08	2.76	4.87
7	0.50	0.08	0.60	0.50	0.39	50	23.35	50.10	3.95	6.30	8.68
8	0.50	0.08	0.60	0.50	0.46	300	23.35	50.10	1.51	1.35	2.31
9	0.50	0.50	0.60	0.80	0.46	50	22.90	49.00	4.68	7.40	10.27
10	0.50	0.50	0.60	0.80	0.61	300	22.90	49.00	1.98	1.78	3.09
11	0.50	0.80	0.60	0.50	0.83	50	22.30	48.15	8.41	13.37	18.58
12	0.50	0.80	0.60	0.50	0.92	300	22.30	48.15	2.97	2.71	4.67

Table 7.3: Predicted parameters and absolute percentage error for single cracked straight beams for Case-I

Test point	Predicted parameters				Abs. error in percentage			
	η_1	η_2	η_3	η_4	L_1	ζ_1/b	A_f	Ω
Channel section straight beam								
1	0.02082	0.08621	0.68179	52.47000	4.12	7.76	4.89	4.94
2	0.02057	0.08223	0.80831	315.30000	2.86	2.79	3.63	5.10
3	0.02074	0.52300	0.89888	51.74500	3.70	4.60	5.75	3.49
4	0.02039	0.54960	1.23216	314.52000	1.94	9.92	2.68	4.84
5	0.02054	0.82616	0.46814	52.38000	2.69	3.27	4.03	4.76
6	0.02085	0.86896	0.58150	309.33000	4.23	8.62	3.84	3.11
7	0.50975	0.08718	0.69141	51.83500	1.95	8.98	6.37	3.67
8	0.51435	0.08606	0.95852	307.59000	2.87	7.58	1.97	2.53
9	0.51600	0.51730	0.91211	52.64000	3.20	3.46	4.84	5.28
10	0.51570	0.55185	0.69374	308.28000	3.14	10.37	2.02	2.76
11	0.50830	0.81896	0.60392	51.94000	1.66	2.37	5.95	3.88
12	0.51385	0.83832	0.83803	317.55000	2.77	4.79	6.08	5.85
Angle section straight beam								
1	0.02090	0.07392	1.59174	47.61000	4.52	7.60	4.72	4.78
2	0.02066	0.08345	2.34788	314.97000	3.32	4.31	2.98	4.99
3	0.01915	0.55240	3.16611	48.60500	4.24	10.48	5.89	2.79
4	0.02039	0.52515	5.66323	313.95000	1.96	5.03	1.68	4.65
5	0.02057	0.74088	0.34168	47.73500	2.84	7.39	3.54	4.53
6	0.01912	0.82440	0.61901	293.19000	4.39	3.05	3.28	2.27
7	0.51980	0.07372	0.50419	51.03500	3.96	7.85	5.04	2.07
8	0.52325	0.08145	0.95714	311.43000	4.65	1.81	5.18	3.81
9	0.48215	0.52000	0.47834	52.96500	3.57	4.00	2.38	5.93
10	0.50815	0.44815	1.02732	309.27000	1.63	10.37	3.77	3.09
11	0.47910	0.81912	0.50749	47.89500	4.18	2.39	3.57	4.21
12	0.51220	0.87920	1.05535	292.38000	2.44	9.90	4.49	2.54

7.2.2 Identification of single and double cracks in channel and angle cross-sectional straight beam using heterogeneous output (Data combination-Case-II)

Now, the identification of crack parameters has been attempted using heterogeneous data which consists of three natural frequencies and two steady state amplitudes. Table 7.5 and Table 7.6 represent the predicted parameters and absolute percentage error with respect to actual parameters for single and double cracked channel and angle section straight beam respectively. From Table 7.5, it can be found that the prediction error associated with crack localization is found to lie in the range of 1.89-3.15% and 1.37-3.52% for single cracked channel and angle section beams respectively. The corresponding percentage error related to crack depth ratios lies in the range of 1.96-8.45% and 1.35-9.64%.

Table 7.4: Predicted parameters and percentage error for double cracked straight beam for Case-I

Test point	Predicted natural parameters						Abs. error in percentage					
	η_1	η_2	η_3	η_4	η_5	η_6	L_1	ζ_1/b	L_2	ζ_2/b	A_f	Ω
Channel section beam												
1	0.02043	0.07558	0.10387	0.51460	0.68133	48.60000	2.15	5.52	3.87	2.92	4.82	2.80
2	0.01909	0.08764	0.10308	0.51710	0.80221	313.11000	4.56	9.55	3.08	3.42	2.17	4.37
3	0.01963	0.47975	0.10263	0.76848	0.61842	51.44500	1.87	4.05	2.63	3.94	3.07	2.89
4	0.02079	0.51490	0.09690	0.75336	0.69350	306.51000	3.95	2.98	3.10	5.83	3.68	2.17
5	0.02081	0.77168	0.09777	0.52350	0.41900	47.98000	4.07	3.54	2.23	4.70	6.89	4.04
6	0.02084	0.88784	0.10324	0.55140	0.74526	308.85000	4.21	10.98	3.24	10.28	1.94	2.95
7	0.48955	0.08454	0.57384	0.52890	0.86170	48.73500	2.09	5.67	4.36	5.78	2.08	2.53
8	0.51470	0.08185	0.62406	0.48225	0.98621	291.00000	2.94	2.31	4.01	3.55	2.73	3.00
9	0.51280	0.51590	0.62160	0.71912	0.84160	47.75500	2.56	3.18	3.60	10.11	5.20	4.49
10	0.47940	0.55240	0.61728	0.88640	1.18294	306.69000	4.12	10.48	2.88	10.80	5.62	2.23
11	0.51510	0.85072	0.57570	0.52930	0.39972	49.07500	3.02	6.34	4.05	5.86	5.19	1.85
12	0.47840	0.83416	0.58020	0.51435	0.45994	286.41000	4.32	4.27	3.30	2.87	4.18	4.53
Angle section beam												
1	0.02042	0.08416	0.10327	0.51795	0.57470	48.36500	2.10	5.20	3.27	3.59	4.49	3.27
2	0.01953	0.08738	0.09753	0.45575	0.72646	281.49000	2.36	9.22	2.47	8.85	1.83	6.17
3	0.02071	0.48140	0.10390	0.82888	0.61280	51.71500	3.57	3.72	3.90	3.61	2.73	3.43
4	0.02039	0.48675	0.09788	0.84416	0.83714	293.73000	1.96	2.65	2.12	5.52	3.35	2.09
5	0.01914	0.88168	0.10372	0.47815	0.83558	47.22500	4.30	10.21	3.72	4.37	5.77	5.55
6	0.02048	0.77024	0.10211	0.44940	0.98552	310.59000	2.38	3.72	2.11	10.12	1.60	3.53
7	0.48360	0.08428	0.58380	0.47265	0.39679	51.38500	3.28	5.35	2.70	5.47	1.74	2.77
8	0.50990	0.07842	0.62112	0.51605	0.47099	310.83000	1.98	1.98	3.52	3.21	2.39	3.61
9	0.52125	0.54900	0.62832	0.87856	0.48245	48.99000	4.25	9.80	4.72	9.82	4.88	2.02
10	0.48245	0.55345	0.61068	0.71600	0.64233	306.60000	3.51	10.69	1.78	10.50	5.30	2.20
11	0.51320	0.75032	0.62694	0.52770	0.87042	46.80500	2.64	6.21	4.49	5.54	4.87	6.39
12	0.48420	0.76800	0.61872	0.48730	0.95542	280.62000	3.16	4.00	3.12	2.54	3.85	6.46

Table 7.5: Predicted parameters and absolute percentage error for single cracked straight beams for case-II

Test point	Predicted parameters				Abs. error in percentage			
	η_1	η_2	η_3	η_4	L_1	ζ_1/b	A_f	Ω
Channel section straight beam								
1	0.02058	0.08565	0.66502	52.16000	2.89	7.06	2.31	4.32
2	0.02060	0.08676	0.81190	308.76000	3.02	8.45	4.09	2.92
3	0.02039	0.53070	0.90321	52.63500	1.93	6.14	6.26	5.27
4	0.02062	0.50995	1.24020	305.64000	3.11	1.99	3.35	1.88
5	0.02053	0.85952	0.47025	51.68500	2.64	7.44	4.50	3.37
6	0.02038	0.86408	0.57568	309.48000	1.89	8.01	2.80	3.16
7	0.51575	0.08518	0.67808	52.18500	3.15	6.48	4.32	4.37
8	0.51215	0.08157	0.96256	313.62000	2.43	1.96	2.40	4.54
9	0.51435	0.51805	0.89132	51.38500	2.87	3.61	2.45	2.77
10	0.50975	0.54080	0.70013	312.78000	1.95	8.16	2.96	4.26
11	0.51170	0.81920	0.60249	52.08500	2.34	2.40	5.70	4.17
12	0.51515	0.85816	0.81331	307.05000	3.03	7.27	2.95	2.35
Angle section straight beam								
1	0.01933	0.08482	1.59539	49.09000	3.33	6.02	4.96	1.82
2	0.01962	0.08415	2.29222	280.71000	1.90	5.19	5.28	6.43
3	0.02059	0.49325	3.10003	50.64000	2.97	1.35	3.68	1.28
4	0.02062	0.54820	5.66208	316.29000	3.11	9.64	1.70	5.43
5	0.01941	0.82088	0.33818	47.17000	2.96	2.61	2.48	5.66
6	0.01949	0.86328	0.67949	317.79000	2.54	7.91	6.17	5.93
7	0.49290	0.07691	0.47006	49.14500	1.42	3.86	2.07	1.71
8	0.51225	0.08454	0.96187	310.20000	2.45	5.68	5.70	3.40
9	0.51760	0.48680	0.46967	48.67500	3.52	2.64	4.15	2.65
10	0.49315	0.54650	1.05554	316.68000	1.37	9.30	6.62	5.56
11	0.51685	0.82768	0.48182	51.79000	3.37	3.46	1.67	3.58
12	0.49230	0.85392	1.04676	281.52000	1.54	6.74	3.64	6.16

The absolute errors related to peak values of force time history (A_f) remain within a range of 2.31-6.26% and 1.67-6.62% for single cracked channel and angle section beams respectively. The error of prediction in forcing frequencies (Ω) is found in the range of 1.88-5.27% and 1.28-6.43% for single cracked channel and angle section beams respectively. In the case of double cracked channel and angle section straight beam (see, Table 7.6) the crack position can be calculated within an error of 1.35-3.20% and 1.31-3.41% respectively, whereas, the errors are found within the range of 2.21-8.50% and 2.53-9.70% in case of prediction of crack depth ratio. The absolute percentage error related to peak values of the force time history fall within a range of 1.97-6.58% and 2.37-5.87% for double cracked channel and angle section beam respectively, whereas the percentage errors for forcing frequencies lies in the span of 2.02-5.22% and 2.36-5.80%.

Table 7.6: Predicted parameters and percentage error with actual parameters for double cracked straight beams (Case-II)

Test point	Predicted natural parameters						Abs. error in percentage					
	η_1	η_2	η_3	η_4	η_5	η_6	L_1	ζ_1/b	L_2	ζ_2/b	A_f	Ω
Channel section beam												
1	0.02039	0.08346	0.09810	0.51565	0.68783	48.05000	1.94	4.33	1.90	3.13	5.82	3.90
2	0.02048	0.07746	0.09739	0.52350	0.87396	310.08000	2.40	3.18	2.61	4.70	6.58	3.36
3	0.01943	0.52555	0.10304	0.86800	0.56778	51.32000	2.87	5.11	3.04	8.50	5.37	2.64
4	0.02064	0.52055	0.10276	0.82128	0.74527	308.16000	3.19	4.11	2.76	2.66	3.51	2.72
5	0.01965	0.73456	0.10212	0.52885	0.42903	48.05500	1.74	8.18	2.12	5.77	4.66	3.89
6	0.02054	0.86376	0.10135	0.53680	0.77809	306.93000	2.70	7.97	1.35	7.36	2.38	2.31
7	0.48875	0.08177	0.58512	0.47795	0.93465	47.63500	2.25	2.21	2.48	4.41	6.21	4.73
8	0.51220	0.08541	0.61908	0.47135	1.01837	312.36000	2.44	6.76	3.18	5.73	6.08	4.12
9	0.50940	0.48175	0.61242	0.82824	0.84632	52.60000	1.88	3.65	2.07	3.53	5.79	5.20
10	0.51600	0.52335	0.61806	0.73400	1.15483	284.34000	3.20	4.67	3.01	8.25	3.11	5.22
11	0.48580	0.84400	0.58368	0.52980	0.36210	52.46000	2.84	5.50	2.72	5.96	4.71	4.92
12	0.51000	0.86496	0.61416	0.51810	0.48946	293.94000	2.00	8.12	2.36	3.62	1.97	2.02
Angle section beam												
1	0.01964	0.08490	0.10143	0.48505	0.58196	47.26500	1.81	6.13	1.43	2.99	5.81	5.47
2	0.02066	0.07682	0.10182	0.47900	0.76657	313.68000	3.28	3.98	1.82	4.20	3.59	4.56
3	0.01949	0.52945	0.10298	0.87760	0.59819	48.51000	2.54	4.89	2.98	9.70	5.05	2.98
4	0.02036	0.53450	0.09869	0.85848	0.78473	309.63000	1.82	5.9	1.31	4.31	3.12	3.21
5	0.01949	0.74152	0.10326	0.48365	0.80872	52.90000	2.55	3.31	3.26	3.27	2.37	5.80
6	0.02056	0.84160	0.09717	0.53810	0.91927	292.92000	2.79	5.2	2.83	7.62	5.23	2.36
7	0.49135	0.08399	0.61386	0.51525	0.40658	47.89500	1.73	4.99	2.31	2.05	4.25	4.21
8	0.51705	0.07231	0.58500	0.53560	0.44082	308.76000	3.41	9.61	2.50	7.12	4.17	2.92
9	0.50945	0.51265	0.61056	0.75256	0.48700	46.92000	1.89	2.53	1.76	4.93	5.87	6.16
10	0.49030	0.45580	0.58656	0.86712	0.58139	315.30000	1.94	3.84	2.24	4.39	4.69	5.10
11	0.48915	0.87320	0.61998	0.53790	0.79082	47.87500	2.17	9.15	3.33	6.58	4.72	4.25
12	0.51675	0.73456	0.61458	0.45510	0.86765	312.39000	3.35	4.18	2.43	3.98	5.69	4.13

7.2.3 Identification of single and multiple cracks in channel and angle cross-sectional horizontally curved beam using heterogeneous output (Data combination-Case-I)

In this section the identification of crack parameters in horizontally curved beam of different cross-section with single and double crack are presented using data combination-I. Here, Table 7.7 represents the actual parameters (crack and forcing parameters) and corresponding heterogeneous responses for single cracked channel section curved beam for different subtended angles (θ_s = 25° and 50°).

Table 7.7: Actual parameters and corresponding heterogeneous response for single cracked channel section curved beam for Case-I

Test point	Actual parameters				Measured heterogeneous responses				
	θ_{S1} (deg)	ζ_1/b	A_f (N)	Ω (Hz)	y_1* (Hz)	y_2* (Hz)	y_3* (m/s^2)	y_4* (m/s^2)	y_5* (m/s^2)
For subtended angle, θ_s = 25°									
1	0.625	0.08	0.63	50	40.55	78.72	0.72	1.28	5.19
2	0.625	0.08	1.14	300	40.55	78.72	0.56	4.79	7.33
3	0.625	0.5	1.02	50	39.73	78.45	0.83	1.28	5.54
4	0.625	0.5	1.13	300	39.73	78.45	0.5	4.35	6.34
5	0.625	0.8	1.75	50	38.80	78.07	0.83	1.5	6.37
6	0.625	0.8	1.27	300	38.80	78.07	0.47	3.72	5.45
7	15.625	0.08	0.81	50	40.58	78.73	2.43	2.79	6.57
8	15.625	0.08	0.72	300	40.58	78.73	2.87	3.17	8.93
9	15.625	0.5	0.52	50	40.53	78.66	0.59	2.18	5.74
10	15.625	0.5	0.90	300	40.53	78.66	0.12	2.21	3.41
11	15.625	0.8	0.56	50	40.51	78.56	0.66	2.24	6.03
12	15.625	0.8	0.94	300	40.51	78.56	0.12	2.34	3.56
For subtended angle, θs = 50°									
1	1.250	0.08	1.19	50	21.41	88.85	0.62	2.49	6.44
2	1.250	0.08	3.52	300	21.41	88.85	6.83	24.84	14.21
3	1.250	0.5	1.00	50	20.92	87.9	0.60	2.14	5.26
4	1.250	0.5	3.01	300	20.92	87.9	5.66	21.81	12.31
5	1.250	0.8	0.72	50	20.36	86.65	0.65	1.74	3.65
6	1.250	0.8	1.52	300	20.36	86.65	1.99	10.05	5.46
7	31.250	0.08	0.24	50	21.45	88.91	0.30	0.70	1.24
8	31.250	0.08	0.33	300	21.45	88.91	0.39	2.32	1.28
9	31.250	0.5	0.86	50	21.41	88.79	0.91	2.32	4.79
10	31.250	0.5	2.41	300	21.41	88.79	2.95	18.72	10.28
11	31.250	0.8	0.67	50	21.38	88.65	0.67	1.76	3.68
12	31.250	0.8	1.89	300	21.38	88.65	2.39	15.03	8.03

Here, the heterogeneous data contains first two measured natural frequencies (y_1* and y_2*) of the beam and three peak acceleration responses (y_3*, y_4* and y_5*) which are presented in the same table. The absolute percentage error between predicted natural and

actual parameters for single cracked channel section curved beam for different subtended angles are presented in Table 7.8. It can be seen from Table 7.8 that the localization errors associated with the angular position (θ_{S1}) lies within 4.62% and 4.90% in case of specimen of subtended angle 25° and 50° respectively. The corresponding maximum crack depth ratio can be predicted with an error of 11.21% and 11.65%.

Table 7.8: Predicted parameters and absolute percentage error for single cracked channel section curved beam for Case-I

Test point	Predicted parameters				Abs. error in percentage			
	η_1	η_2	η_3	η_4	θ_{S1}	ζ_1/b	A_f	Ω
				For subtended angle, θ_s = 25°				
1	0.60681	0.08345	0.67183	48.18500	2.91	4.31	6.64	3.63
2	0.65231	0.08169	1.05769	318.93000	4.37	2.11	7.22	6.31
3	0.60250	0.55605	1.04550	46.60500	3.60	11.21	2.50	6.79
4	0.63613	0.52350	1.16514	309.81000	1.78	4.70	3.11	3.27
5	0.65106	0.88592	1.63870	47.05000	4.17	10.74	6.36	5.90
6	0.65388	0.81600	1.30924	277.47000	4.62	2.00	3.09	7.51
7	15.05156	0.07531	0.75970	48.10500	3.67	5.86	6.21	3.79
8	16.07969	0.08745	0.74182	314.52000	2.91	9.31	3.03	4.84
9	16.34375	0.51725	0.53440	52.31500	4.60	3.45	2.77	4.63
10	15.96563	0.54670	0.92763	318.06000	2.18	9.34	3.07	6.02
11	15.03906	0.84736	0.53138	46.56000	3.75	5.92	5.11	6.88
12	15.90000	0.73728	0.98051	307.17000	1.76	7.84	4.31	2.39
				For subtended angle, θ_s = 50°				
1	1.28350	0.07611	1.15204	52.25000	2.68	4.86	3.19	4.50
2	1.22538	0.08465	3.68086	282.90000	1.97	5.81	4.57	5.70
3	1.27063	0.54920	0.96540	49.25000	1.65	9.84	3.46	1.50
4	1.19913	0.52930	2.93896	317.88000	4.07	5.86	2.36	5.96
5	1.27913	0.71592	0.77717	47.67500	2.33	10.51	7.94	4.65
6	1.31125	0.84376	1.54432	280.20000	4.90	5.47	1.60	6.60
7	30.05000	0.07255	0.24996	52.11000	3.84	9.31	4.15	4.22
8	32.10000	0.08442	0.34168	288.09000	2.72	5.53	3.54	3.97
9	32.30000	0.47335	0.92476	52.03500	3.36	5.33	7.53	4.07
10	30.00000	0.51845	2.49676	318.42000	4.00	3.69	3.60	6.14
11	30.31250	0.89320	0.65419	47.77000	3.00	11.65	2.36	4.46
12	30.75938	0.87616	1.81100	317.55000	1.57	9.52	4.18	5.85

The absolute error associated with peak values of force time history (A_f) is found to be less than 7.22% and 7.94% while corresponding error related to forcing frequencies (Ω) lies within 7.51% and 6.60% for 25° and 50° specimen respectively when two natural frequencies plus three steady state amplitudes are considered in the heterogeneous data.

Now, the actual parameters and corresponding heterogeneous response for double cracked channel section curved beam are presented in Table 7.9 for two types of specimen with different curvatures. In the same table the heterogeneous data consists of two natural frequencies and three peak acceleration responses. The angular distance of the first crack from the fixed end of the cantilever beam is represented by θ_{S1} and the second crack location from the fixed end is symbolized as θ_{S2}. The corresponding crack depth ratios are ζ_1/b and ζ_2/b.

Table 7.9: Actual parameters and corresponding heterogeneous response for double cracked channel section curved beam for Case-I

Test point	Actual parameters						Measured heterogeneous data				
	θ_{S1} (deg)	ζ_1/b	θ_{S2} (deg)	ζ_2/b	A_f (N)	Ω (Hz)	y_1* (Hz)	y_2* (Hz)	y_3* (m/s^2)	y_4* (m/s^2)	y_5* (m/s^2)
For subtended angle, θ_s = 25°											
1	0.625	0.08	3.125	0.5	1.14	50	40.19	78.19	0.54	0.97	4.11
2	0.625	0.08	3.125	0.5	0.85	300	40.19	78.19	0.30	2.55	3.72
3	0.625	0.5	3.125	0.8	3.25	50	39.22	77.78	3.40	5.39	9.87
4	0.625	0.5	3.125	0.8	0.41	300	39.22	77.78	0.11	1.95	2.81
5	0.625	0.8	3.125	0.5	0.35	50	38.47	77.55	0.93	2.62	4.27
6	0.625	0.8	3.125	0.5	0.18	300	38.47	77.55	0.05	0.14	0.15
7	15.625	0.08	18.750	0.5	0.66	50	40.50	78.42	0.80	2.41	6.69
8	15.625	0.08	18.750	0.5	1.03	300	40.50	78.42	0.16	2.42	3.73
9	15.625	0.5	18.750	0.8	0.63	50	40.32	78.18	0.76	2.51	6.74
10	15.625	0.5	18.750	0.8	1.03	300	40.32	78.18	0.17	2.40	3.69
11	15.625	0.8	18.750	0.5	0.56	50	38.85	78.11	0.62	2.44	6.38
12	15.625	0.8	18.750	0.5	0.97	300	38.85	78.11	0.16	2.22	3.42
For subtended angle, θ_s = 50°											
1	1.250	0.08	6.250	0.5	1.07	50	21.21	88.24	0.75	2.20	4.97
2	1.250	0.08	6.250	0.5	3.44	300	21.21	88.24	5.18	25.16	12.01
3	1.250	0.5	6.250	0.8	1.08	50	20.63	87.05	0.75	2.22	5.00
4	1.250	0.5	6.250	0.8	2.59	300	20.63	87.05	3.92	17.72	9.48
5	1.250	0.8	6.250	0.5	1.06	50	19.85	85.92	0.74	2.21	4.98
6	1.250	0.8	6.250	0.5	2.81	300	19.85	85.92	4.03	19.53	9.85
7	31.250	0.08	37.500	0.5	0.67	50	21.37	88.55	0.69	1.77	3.66
8	31.250	0.08	37.500	0.5	1.89	300	21.37	88.55	2.40	15.19	8.11
9	31.250	0.5	37.500	0.8	0.41	50	21.05	87.90	0.40	1.07	2.21
10	31.250	0.5	37.500	0.8	1.15	300	21.05	87.90	1.48	9.25	4.88
11	31.250	0.8	37.500	0.5	1.86	50	20.10	86.85	0.75	1.96	1.66
12	31.250	0.8	37.500	0.5	4.37	300	20.10	86.85	3.02	19.62	5.21

The absolute percentage differences between the predicted parameters and actual parameters for double cracked channel section curved beams are listed in Table 7.10. The final results in Table 7.10 are obtained from heterogeneous data based on two natural

frequencies and three peak acceleration responses. The proposed approach identifies the crack position with an error less than 4.82% and 5.10% whereas prediction error in case of crack depth ratio has risen up to 11.35% and 11.80% for double cracked channel section curved beams of subtended angle 25° and 50° respectively. The absolute errors in prediction of peak value of force time history are 1.95-7.27% and 2.19-7.44% % for double cracked channel section curved beams with subtended angle 25° and 50° respectively. The prediction error for excitation frequencies lies within a range of 1.83-6.63% and 2.60-7.16%.

Similarly, the present approach for crack identification has been applied for angle section curved beam. The actual parameters and corresponding measured heterogeneous responses for single cracked angle section curved beam for different subtended angles are shown in Table 7.11. Here also data combination –I (First two natural frequencies plus three peak acceleration) has been utilized. For example, if one considers the first test point in Table 7.11, then the angular crack position is 0.625° from the fixed end of the cantilever curved beam and the corresponding crack depth ratio is 0.08. The curved beam has been excited at the tip with excitation frequency 50Hz and the corresponding measured peak value of force time history was 1.08 N. The measured first two natural frequencies are 17.27 Hz and 24.17 Hz while peak accelerations at specified locations are 0.54 m/s^2, 2.27 m/s^2 and 4.95 m/s^2 as shown in table.

Table 7.10: Predicted parameters and absolute percentage error for double cracked channel section curved beam for Case-I

Test point	Predicted natural parameters						Abs. error in percentage					
	η_1	η_2	η_3	η_4	η_5	η_6	L_1	ζ_1/b	L_2	ζ_2/b	A_f	Ω
For subtended angle, $\theta_s = 25°$												
1	0.64675	0.07365	3.23875	0.46815	1.07844	51.22000	3.48	7.94	3.64	6.37	5.40	2.44
2	0.59488	0.08656	3.03531	0.54585	0.83037	289.17000	4.82	8.20	2.87	9.17	2.31	3.61
3	0.64350	0.55250	3.22375	0.86832	3.41445	53.00000	2.96	10.50	3.16	8.54	5.06	6.00
4	0.61331	0.45330	3.17813	0.71680	0.42763	282.48000	1.87	9.34	1.70	10.40	4.30	5.84
5	0.61031	0.81976	2.97656	0.51560	0.32638	50.91500	2.35	2.47	4.75	3.12	6.75	1.83
6	0.64913	0.83264	3.24250	0.47605	0.18900	310.98000	3.86	4.08	3.76	4.79	5.00	3.66
7	14.92188	0.07846	19.24500	0.46310	0.62159	47.82500	4.50	1.92	2.64	7.38	5.82	4.35
8	15.99531	0.08908	19.07625	0.51725	1.07069	311.25000	2.37	11.35	1.74	3.45	3.95	3.75
9	15.07813	0.48575	18.14438	0.81440	0.58420	53.31500	3.50	2.85	3.23	1.80	7.27	6.63
10	16.07188	0.54300	19.09125	0.72936	1.09139	314.67000	2.86	8.60	1.82	8.83	5.96	4.89
11	15.97500	0.77960	19.16625	0.44860	0.54908	48.46000	2.24	2.55	2.22	10.28	1.95	3.08
12	15.92031	0.76160	17.96063	0.46885	0.99153	288.51000	1.89	4.80	4.21	6.23	2.22	3.83
For subtended angle, $\theta_s = 50°$												
1	1.29075	0.08171	5.95375	0.44580	1.09921	51.30000	3.26	2.14	4.74	10.84	2.73	2.60
2	1.30363	0.08402	6.13000	0.53540	3.54217	290.97000	4.29	5.03	1.92	7.08	2.97	3.01
3	1.19400	0.44660	6.40625	0.82224	1.16035	47.94000	4.48	10.68	2.50	2.78	7.44	4.12
4	1.22500	0.48850	6.36563	0.71968	2.41932	308.37000	2.00	2.30	1.85	10.04	6.59	2.79
5	1.27850	0.83752	6.05063	0.52545	1.08862	48.57000	2.28	4.69	3.19	5.09	2.70	2.86
6	1.18625	0.81728	6.35750	0.47675	2.97186	321.48000	5.10	2.16	1.72	4.65	5.76	7.16
7	31.83125	0.07457	35.64375	0.54615	0.63576	52.50000	1.86	6.79	4.95	9.23	5.11	5.00
8	32.33125	0.08750	38.37750	0.50885	1.93139	318.87000	3.46	9.38	2.34	1.77	2.19	6.29
9	30.36875	0.45970	38.24625	0.89440	0.39602	48.37000	2.82	8.06	1.99	11.80	3.41	3.26
10	32.74063	0.51290	38.52000	0.86752	1.12045	321.30000	4.77	2.58	2.72	8.44	2.57	7.10
11	30.54063	0.71608	38.71125	0.53890	1.92994	48.41500	2.27	10.49	3.23	7.78	3.76	3.17
12	31.99688	0.72368	38.25750	0.53500	4.09819	312.15000	2.39	9.54	2.02	7.00	6.22	4.05

Table 7.11: Actual parameters and corresponding heterogeneous response for single cracked angle section curved beam for Case-I

Test point	Actual parameters				Measured heterogeneous responses				
	θ_{S1} (deg)	ζ_1/b	A_f (N)	Ω (Hz)	y_1* (Hz)	y_2* (Hz)	y_3* (m/s^2)	y_4* (m/s^2)	y_5* (m/s^2)
For subtended angle, θ_s = 25°									
1	0.625	0.08	1.08	50	17.27	24.17	0.54	2.27	4.95
2	0.625	0.08	0.43	300	17.27	24.17	1.83	3.40	3.20
3	0.625	0.5	1.09	50	15.71	23.55	0.54	2.27	4.87
4	0.625	0.5	0.47	300	15.71	23.55	1.93	4.11	3.33
5	0.625	0.8	1.11	50	14.94	23.07	0.42	2.26	4.78
6	0.625	0.8	0.56	300	14.94	23.07	2.29	5.75	3.13
7	15.625	0.08	1.2	50	17.34	24.20	1.87	3.17	5.00
8	15.625	0.08	0.53	300	17.34	24.20	1.97	4.19	4.24
9	15.625	0.5	1.04	50	17.29	24.16	1.09	2.31	4.34
10	15.625	0.5	0.47	300	17.29	24.16	1.71	3.78	3.65
11	15.625	0.8	1.29	50	17.24	24.14	1.08	2.72	5.46
12	15.625	0.8	0.64	300	17.24	24.14	2.29	5.97	5.25
For subtended angle, θ_s = 50°									
1	1.250	0.08	0.85	50	9.10	24.35	0.85	2.02	3.82
2	1.250	0.08	0.33	300	9.10	24.35	2.05	7.47	3.20
3	1.250	0.5	1.08	50	8.03	24.28	1.13	2.62	4.92
4	1.250	0.5	0.07	300	8.03	24.28	1.07	5.00	3.96
5	1.250	0.8	1.14	50	7.57	24.24	1.19	2.75	5.12
6	1.250	0.8	0.12	300	7.57	24.24	0.63	3.58	4.07
7	31.250	0.08	1.17	50	9.23	24.37	2.70	3.87	4.30
8	31.250	0.08	0.69	300	9.23	24.37	2.12	3.13	4.00
9	31.250	0.5	1.24	50	8.90	24.29	2.68	3.91	4.47
10	31.250	0.5	0.73	300	8.90	24.29	2.16	3.64	3.91
11	31.250	0.8	1.14	50	8.48	24.10	2.39	3.52	4.06
12	31.250	0.8	2.18	300	8.48	24.10	7.85	31.57	6.49

The predicted parameters and absolute percentage error for single cracked angle section curved beam for different subtended angle are presented in Table 7.12. Table 7.12 displays the absolute percentage error in prediction of crack locations which lies within a range of 1.77-4.91% and 2.23-5.25%, whereas percentage error in prediction of crack depth ratio lies within a range of 2.16-11.29% and 2.56-11.86% for two subtended angles respectively. The absolute errors related to peak values of force time history lie within a range of 1.64-6.22% and 2.26-6.23% in two types of specimen of different subtended angles. The corresponding absolute percentage error for forcing frequencies (Ω) are found in the range of 1.72-6.87% and 2.04-6.95%.

Table 7.12: Predicted parameters and absolute percentage error for single cracked angle section curved beam for Case-I

Test point	Predicted parameters				Abs. error in percentage			
	η_1	η_2	η_3	η_4	θ_{S1}	ζ_1/b	A_f	Ω
				For subtended angle, θ_s = 25°				
1	0.63606	0.07538	1.09771	51.77500	1.77	5.77	1.64	3.55
2	0.60094	0.08767	0.45675	292.62000	3.85	9.59	6.22	2.46
3	0.64569	0.55430	1.12630	48.14000	3.31	10.86	3.33	3.72
4	0.63681	0.47315	0.48180	312.36000	1.89	5.37	2.51	4.12
5	0.65569	0.87720	1.06682	53.43500	4.91	9.65	3.89	6.87
6	0.65188	0.87504	0.57781	285.84000	4.30	9.38	3.18	4.72
7	15.00313	0.07827	1.12716	51.20500	3.98	2.16	6.07	2.41
8	15.94844	0.08436	0.56138	306.54000	2.07	5.45	5.92	2.18
9	16.37813	0.55645	1.06954	49.14000	4.82	11.29	2.84	1.72
10	15.04063	0.53835	0.48678	312.66000	3.74	7.67	3.57	4.22
11	14.96250	0.83528	1.23634	47.13000	4.24	4.41	4.16	5.74
12	16.10781	0.75384	0.60141	314.22000	3.09	5.77	6.03	4.74
				For subtended angle, θ_s = 50°				
1	1.18475	0.08821	0.89930	48.36500	5.22	10.26	5.80	3.27
2	1.27900	0.07746	0.33759	306.60000	2.32	3.17	2.30	2.20
3	1.20600	0.54485	1.12190	47.66000	3.52	8.97	3.88	4.68
4	1.31563	0.55035	0.07180	307.14000	5.25	10.07	2.57	2.38
5	1.28525	0.83872	1.07377	48.83000	2.82	4.84	5.81	2.34
6	1.19075	0.72904	0.11659	315.90000	4.74	8.87	2.84	5.30
7	32.44375	0.08526	1.19808	46.52500	3.82	6.58	2.40	6.95
8	29.75625	0.07238	0.66716	312.81000	4.78	9.53	3.31	4.27
9	32.86875	0.51880	1.31725	48.28000	5.18	3.76	6.23	3.44
10	30.44375	0.55930	0.75489	290.25000	2.58	11.86	3.41	3.25
11	32.54688	0.77952	1.10284	52.58500	4.15	2.56	3.26	5.17
12	30.28750	0.74280	2.22927	306.12000	3.08	7.15	2.26	2.04

The results for double cracked angle section curved beams with data combination-Case-I are presented in Table 7.13. The absolute percentage errors between the calculated and actual parameters for double cracked angle section curved beams are illustrated in Table 7.14. The absolute percentage error have been found in the range of 2.17-4.96% and 2.31-5.36% in case of crack localization whereas the associated crack depth lies within 11.26% and 12.25% for specimens of subtended angle 25° and 50° respectively.

Table 7.13: Actual parameters and corresponding heterogeneous response for double cracked angle section curved beam for Case-I

Test point	Actual parameters						Measured peak acceleration response (m/s^2)				
	θ_{S1} (deg)	ζ_1/b	θ_{S2} (deg)	ζ_2/b	A_f (N)	Ω (Hz)	y_1* (Hz)	y_2* (Hz)	y_3* (m/s^2)	y_4* (m/s^2)	y_5* (m/s^2)
For subtended angle, $\theta_s = 25°$											
1	0.625	0.08	3.125	0.5	1.23	50	17.05	23.90	0.46	2.58	5.40
2	0.625	0.08	3.125	0.5	0.66	300	17.05	23.90	2.72	6.94	3.62
3	0.625	0.5	3.125	0.8	1.21	50	15.58	23.14	0.44	2.50	5.18
4	0.625	0.5	3.125	0.8	0.63	300	15.58	23.14	2.59	6.69	3.40
5	0.625	0.8	3.125	0.5	1.27	50	14.80	22.81	0.49	2.68	5.54
6	0.625	0.8	3.125	0.5	0.71	300	14.80	22.81	2.79	7.59	3.58
7	15.625	0.08	18.750	0.5	1.19	50	17.24	24.12	1.03	2.58	5.14
8	15.625	0.08	18.750	0.5	0.62	300	17.24	24.12	2.17	5.80	4.22
9	15.625	0.5	18.750	0.8	1.64	50	17.15	23.90	1.27	3.31	6.95
10	15.625	0.5	18.750	0.8	0.81	300	17.15	23.90	2.99	7.61	5.74
11	15.625	0.8	18.750	0.5	1.57	50	17.05	23.77	1.23	3.27	6.70
12	15.625	0.8	18.750	0.5	0.81	300	17.05	23.77	2.87	7.73	5.55
For subtended angle, $\theta_s = 50°$											
1	1.250	0.08	6.250	0.5	1.16	50	8.50	24.06	1.20	2.78	5.22
2	1.250	0.08	6.250	0.5	0.13	300	8.50	24.06	0.63	3.58	4.11
3	1.250	0.5	6.250	0.8	1.13	50	7.99	23.48	1.15	2.70	5.09
4	1.250	0.5	6.250	0.8	0.12	300	7.99	23.48	0.55	3.51	4.06
5	1.250	0.8	6.250	0.5	1.11	50	7.53	23.10	1.12	2.62	4.94
6	1.250	0.8	6.250	0.5	0.15	300	7.53	23.10	0.43	3.15	4.00
7	31.250	0.08	37.500	0.5	1.25	50	9.00	24.23	0.69	1.77	3.66
8	31.250	0.08	37.500	0.5	0.86	300	9.00	24.23	2.40	15.19	8.11
9	31.250	0.5	37.500	0.8	1.36	50	8.80	23.87	0.40	1.07	2.21
10	31.250	0.5	37.500	0.8	0.90	300	8.80	23.87	1.48	9.25	4.88
11	31.250	0.8	37.500	0.5	1.20	50	8.10	23.20	0.75	1.96	1.66
12	31.250	0.8	37.500	0.5	2.20	300	8.10	23.20	3.02	19.62	5.21

7.2.4 Identification of single and multiple cracks in channel and angle cross-sectional horizontally curved beam using heterogeneous output (Data combination-Case-II)

The predicted parameters and absolute percentage error for single cracked channel section curved beam are presented in Table 7.15. The prediction parameters present in the same table are obtained based on the heterogeneous data combination (Case-II) which includes first three measured natural frequencies (y_1*, y_2* and y_3*) of the beam and two peak acceleration responses (y_4* and y_5*). From the Table 7.15, it can be observed that the prediction related to crack positions can be obtained with less than 3.46% and 3.79% error for single cracked channel section curved beams.

Table 7.14: Predicted parameters and absolute percentage error for double cracked angle section curved beam for Case-I

Test point	Predicted natural parameters						Abs. error in percentage					
	η_1	η_2	η_3	η_4	η_5	η_6	L_1	ζ_1/b	L_2	ζ_2/b	A_f	Ω
For subtended angle, $\theta_s = 25°$												
1	0.61144	0.08747	2.98875	0.52370	1.19236	48.76500	2.17	9.34	4.36	4.74	3.06	2.47
2	0.65300	0.08397	3.22719	0.54035	0.67406	293.34000	4.48	4.96	3.27	8.07	2.13	2.22
3	0.60513	0.46010	2.98188	0.75344	1.13764	47.58000	3.18	7.98	4.58	5.82	5.98	4.84
4	0.59613	0.52800	3.21563	0.88512	0.60102	306.03000	4.62	5.60	2.90	10.64	4.60	2.01
5	0.64206	0.88896	3.25563	0.45490	1.31851	52.20500	2.73	11.12	4.18	9.02	3.82	4.41
6	0.64769	0.72288	3.20344	0.51595	0.74245	286.29000	3.63	9.64	2.51	3.19	4.57	4.57
7	15.97188	0.08324	17.94375	0.54960	1.14097	52.80500	2.22	4.05	4.30	9.92	4.12	5.61
8	14.85000	0.07399	17.97750	0.55630	0.63618	311.52000	4.96	7.51	4.12	11.26	2.61	3.84
9	15.99844	0.46395	19.28438	0.85240	1.70757	51.71000	2.39	7.21	2.85	6.55	4.12	3.42
10	14.89375	0.53405	18.31875	0.71888	0.83390	314.16000	4.68	6.81	2.30	10.14	2.95	4.72
11	15.23750	0.88000	19.35938	0.53635	1.51960	52.52500	2.48	10.00	3.25	7.27	3.21	5.05
12	14.97344	0.83312	19.64813	0.48465	0.86046	287.97000	4.17	4.14	4.79	3.07	6.23	4.01
For subtended angle, $\theta_s = 50°$												
1	1.29725	0.07580	6.46563	0.46140	1.12114	52.00500	3.78	5.25	3.45	7.72	3.35	4.01
2	1.22113	0.08579	5.98750	0.55105	0.13532	290.64000	2.31	7.24	4.20	10.21	4.09	3.12
3	1.31700	0.52115	6.10188	0.82960	1.10152	51.50000	5.36	4.23	2.37	3.70	2.52	3.00
4	1.22063	0.45715	6.57125	0.73296	0.12394	286.44000	2.35	8.57	5.14	8.38	3.28	4.52
5	1.28413	0.88920	6.41438	0.56125	1.08181	51.71000	2.73	11.15	2.63	12.25	2.54	3.42
6	1.19200	0.87368	6.06938	0.51875	0.16085	293.37000	4.64	9.21	2.89	3.75	7.23	2.21
7	32.18125	0.08616	39.25500	0.47680	1.31163	53.44000	2.98	7.70	4.68	4.64	4.93	6.88
8	29.91563	0.07689	36.13500	0.46965	0.83265	313.50000	4.27	3.89	3.64	6.07	3.18	4.50
9	32.88750	0.52085	39.21750	0.82208	1.30152	48.28500	5.24	4.17	4.58	2.76	4.30	3.43
10	30.17188	0.48605	36.25125	0.72792	0.92547	309.78000	3.45	2.79	3.33	9.01	2.83	3.26
11	32.60313	0.89096	38.59500	0.46940	1.24536	51.21000	4.33	11.37	2.92	6.12	3.78	2.42
12	29.83750	0.87392	35.53125	0.43930	2.30560	293.76000	4.52	9.24	5.25	12.14	4.80	2.08

The associated damage severity lies within 8.82% and 9.35% for subtended angle 25° and 50° respectively. It can be noted if number of frequency modes are more than number of acceleration input in mixed data, then accuracy of prediction improves.

Table 7.15: Predicted parameters and absolute percentage error for single cracked channel section curved beam for Case-II

Test point	Predicted parameters				Abs. error in percentage			
	η_1	η_2	η_3	η_4	θ_{S1}	ζ_1/b	A_f	Ω
				For subtended angle, θ_s = 25°				
1	0.63800	0.08282	0.66137	47.09500	2.08	3.53	4.98	5.81
2	0.64563	0.07409	1.21741	311.22000	3.30	7.39	6.79	3.74
3	0.64144	0.51485	1.06253	48.91000	2.63	2.97	4.17	2.18
4	0.64663	0.48220	1.09734	307.11000	3.46	3.56	2.89	2.37
5	0.63631	0.82168	1.64238	46.66500	1.81	2.71	6.15	6.67
6	0.60963	0.87056	1.31699	320.25000	2.46	8.82	3.70	6.75
7	15.91563	0.07369	0.83325	52.36000	1.86	7.89	2.87	4.72
8	15.09531	0.08465	0.66809	305.97000	3.39	5.81	7.21	1.99
9	16.11406	0.46115	0.53726	53.01500	3.13	7.77	3.32	6.03
10	16.12969	0.53060	0.84087	294.75000	3.23	6.12	6.57	1.75
11	15.90938	0.76656	0.53788	50.95000	1.82	4.18	3.95	1.90
12	15.99844	0.84272	0.91509	307.71000	2.39	5.34	2.65	2.57
				For subtended angle, θ_s = 50°				
1	1.29050	0.07840	1.24069	47.42500	3.24	2.00	4.26	5.15
2	1.21350	0.08524	3.41616	320.94000	2.92	6.55	2.95	6.98
3	1.22688	0.46445	0.97670	48.99500	1.85	7.11	2.33	2.01
4	1.28750	0.52750	3.08676	291.69000	3.00	5.50	2.55	2.77
5	1.20263	0.75368	0.70049	52.89500	3.79	5.79	2.71	5.79
6	1.27775	0.83408	1.43594	311.19000	2.22	4.26	5.53	3.73
7	31.73750	0.08210	0.25258	53.63000	1.56	2.62	5.24	7.26
8	30.07813	0.08748	0.33657	307.20000	3.75	9.35	1.99	2.40
9	32.38750	0.48125	0.80616	53.03500	3.64	3.75	6.26	6.07
10	30.34688	0.51635	2.36035	323.67000	2.89	3.27	2.06	7.89
11	31.78438	0.75192	0.71831	51.73000	1.71	6.01	7.22	3.46
12	31.85313	0.85272	1.78643	312.75000	1.93	6.59	5.48	4.25

Besides that, the absolute percentage error related to peak values of the force time history lies within a range of 2.65-7.21% and 1.99-7.22% for single cracked channel section curved beams for subtended angle 25° and 50° respectively, whereas the percentage errors for forcing frequencies remain in the range of 1.75-6.75% and 2.01-7.89% respectively for beams of two different curvature. It may be noted that accuracy of estimation decreases if the curvature of beam axis increases.

The absolute percentage deviation of predicted values from the actual values for double cracked channel section curved beams is listed in Table 7.16. The results in Table 7.16 are for the heterogeneous data consisting of three natural frequencies and two peak acceleration responses. The ranges of absolute percentage error in crack localization have been found as 1.53-3.51% and 1.90-4.17% for double cracked channel section curved beams with subtended angle 25° and 50° respectively while corresponding error in detection of crack depth lies within a range of 1.67-8.95% and 1.73-9.68%. The absolute error related to peak values of force time history is found in the range of 2.18-7.30% and 2.33-7.48% respectively while corresponding error in prediction of forcing frequencies fall within a range of 1.51-7.31% and 2.13-7.16% for double cracked channel section curved beams of subtended angle 25° and 50° respectively. It is worth mentioning that error in prediction decreases if number of frequency input is more than that of peak amplitudes.

Table 7.17 shows the predicted parameters and absolute percentage error with respect to actual parameters for single cracked angle section curved beam, where first three frequencies and two steady state amplitudes are considered in the heterogeneous data. It has been found that the percentage error of prediction of crack location lies within 3.78% and 4.26% for single cracked angle section curved beam for both the subtended angle 25° and 50° respectively. The corresponding percentage errors between predicted and actual crack depth ratio lie within 10.37% and 10.93% respectively. Simultaneously, the errors associated with peak value of the force time history are found within 6.17% and 6.13% for single cracked angle section curved beam with subtended angle 25° and 50° respectively, whereas the errors related to forcing frequencies lies within 5.97% and 6.73%.

Table 7.16: Predicted parameters and absolute percentage error for double cracked channel section curved beam for Case-II

Test point	Predicted natural parameters						Abs. error in percentage					
	η_1	η_2	η_3	η_4	η_5	η_6	L_1	ζ_1/b	L_2	ζ_2/b	A_f	Ω
For subtended angle, θ_s = 25°												
1	0.61544	0.08607	3.05656	0.46800	1.20224	48.30000	1.53	7.59	2.19	6.40	5.46	3.40
2	0.60325	0.08275	3.22719	0.46005	0.81668	309.51000	3.48	3.44	3.27	7.99	3.92	3.17
3	0.64275	0.47035	3.18406	0.75040	3.17558	53.24000	2.84	5.93	1.89	6.20	2.29	6.48
4	0.61431	0.50835	3.03188	0.87160	0.43481	321.51000	1.71	1.67	2.98	8.95	6.05	7.17
5	0.63906	0.86520	3.18750	0.51735	0.32445	52.03500	2.25	8.15	2.00	3.47	7.30	4.07
6	0.61313	0.76936	3.02063	0.48775	0.18837	278.07000	1.90	3.83	3.34	2.45	4.65	7.31
7	16.01250	0.08216	18.34875	0.51745	0.64561	46.73500	2.48	2.70	2.14	3.49	2.18	6.53
8	16.17344	0.08374	19.37063	0.51115	1.06595	304.65000	3.51	4.67	3.31	2.23	3.49	1.55
9	15.09844	0.48900	19.10250	0.75888	0.61337	47.00500	3.37	2.20	1.88	5.14	2.64	5.99
10	15.96563	0.52325	19.14000	0.84432	1.06698	313.14000	2.18	4.65	2.08	5.54	3.59	4.38
11	15.37344	0.84768	19.06500	0.47605	0.53323	48.84000	1.61	5.96	1.68	4.79	4.78	2.32
12	16.09063	0.75120	18.25125	0.54185	0.91733	295.47000	2.98	6.10	2.66	8.37	5.43	1.51
For subtended angle, θ_s = 50°												
1	1.29500	0.07589	6.06250	0.53530	1.02495	51.79000	3.60	5.14	3.00	7.06	4.21	3.58
2	1.30213	0.08554	6.36875	0.47445	3.24702	292.29000	4.17	6.92	1.90	5.11	5.61	2.57
3	1.28300	0.51275	6.08250	0.84232	1.14674	51.49000	2.64	2.55	2.68	5.29	6.18	2.98
4	1.28813	0.45160	6.12938	0.85248	2.71587	290.46000	3.05	9.68	1.93	6.56	4.86	3.18
5	1.22200	0.82536	6.37188	0.51075	1.03498	53.50000	2.24	3.17	1.95	2.15	2.36	7.00
6	1.20913	0.83040	6.02313	0.52100	2.96371	317.70000	3.27	3.80	3.63	4.20	5.47	5.90
7	32.15000	0.08645	38.40000	0.46070	0.68561	47.49500	2.88	8.06	2.40	7.86	2.33	5.01
8	30.60938	0.07554	36.30750	0.54625	1.74863	308.34000	2.05	5.58	3.18	9.25	7.48	2.78
9	32.38125	0.53915	35.97000	0.82136	0.42337	51.47000	3.62	7.83	4.08	2.67	3.26	2.94
10	31.85000	0.47580	36.46875	0.77032	1.17898	293.61000	1.92	4.84	2.75	3.71	2.52	2.13
11	30.01563	0.83088	38.77875	0.51205	1.77295	53.58000	3.95	3.86	3.41	2.41	4.68	7.16
12	31.95625	0.81576	38.83875	0.50865	4.49455	282.24000	2.26	1.97	3.57	1.73	2.85	5.92

Table 7.17: Predicted parameters and absolute percentage error for single cracked angle section curved beam for Case-II

Test point	Predicted parameters				Abs. error in percentage			
	η_1	η_2	η_3	η_4	θ_{S1}	ζ_1/b	A_f	Ω
				For subtended angle, θ_s = 25°				
1	0.63669	0.08413	1.03928	48.39000	1.87	5.16	3.77	3.22
2	0.61006	0.08703	0.40519	284.04000	2.39	8.79	5.77	5.32
3	0.61300	0.44955	1.14047	52.23000	1.92	10.09	4.63	4.46
4	0.64663	0.52215	0.44100	310.29000	3.46	4.43	6.17	3.43
5	0.60944	0.78000	1.14030	47.01500	2.49	2.50	2.73	5.97
6	0.61000	0.85560	0.53301	304.74000	2.40	6.95	4.82	1.58
7	15.81094	0.08830	1.23552	48.10500	1.19	10.37	2.96	3.79
8	15.03438	0.08424	0.50461	310.83000	3.78	5.30	4.79	3.61
9	15.11250	0.51460	1.06902	51.56000	3.28	2.92	2.79	3.12
10	15.30156	0.52020	0.45755	283.98000	2.07	4.04	2.65	5.34
11	15.84688	0.72448	1.22834	51.91500	1.42	9.44	4.78	3.83
12	15.17813	0.84968	0.60403	294.78000	2.86	6.21	5.62	1.74
				For subtended angle, θ_s = 50°				
1	1.27700	0.07365	0.82875	52.67500	2.16	7.94	2.50	5.35
2	1.19788	0.08251	0.31442	289.32000	4.17	3.14	4.72	3.56
3	1.27963	0.55210	1.13594	52.64000	2.37	10.42	5.18	5.28
4	1.30325	0.45435	0.06686	291.39000	4.26	9.13	4.48	2.87
5	1.29425	0.86848	1.19871	51.82500	3.54	8.56	5.15	3.65
6	1.28675	0.78032	0.11640	286.95000	2.94	2.46	3.00	4.35
7	29.92813	0.08852	1.22990	51.48500	4.23	10.65	5.12	2.97
8	30.68438	0.08223	0.64770	320.19000	1.81	2.79	6.13	6.73
9	30.18438	0.54055	1.19586	47.34000	3.41	8.11	3.56	5.32
10	32.21875	0.55465	0.75606	307.29000	3.10	10.93	3.57	2.43
11	30.31875	0.73240	1.19597	48.37500	2.98	8.45	4.91	3.25
12	32.54688	0.77960	2.08103	291.00000	4.15	2.55	4.54	3.00

The absolute percentage errors between the calculated and actual parameters for double cracked angle section curved beams are illustrated in 7.18. Here, three measured natural frequencies and two steady state amplitudes are considered data combination-Case-II for subtended. Angle beams having subtended 25° and 50° have been considered in the study. The absolute percentage error lies within a range of 1.57-3.82% and 1.55-4.09% in case of crack positioning while the corresponding error related to crack severity lies within 10.46% and 11.33%. The absolute errors related to peak value of force time history lies within 6.24% and 5.78% respectively, whereas the corresponding error associated with forcing frequencies are less than 6.42% and 7.08% for the beams with subtended angle 25° and 50° respectively

Finally, the crack parameter identification attempted in the different types of beam specimens based on heterogeneous data has been presented in Table 7.19 and Table 7.20. Table 7.19 is for channel beam while Table 7.20 is for angle cross section beam. Some observations need to be mentioned. First one is that mixed type of input data in detection algorithm increases accuracy of prediction in all hidden parameters compared to only forced vibration data. Second one is that when number of frequency input is taken more than peak acceleration input, improvement in prediction occurs. Further, it is seen from the results that higher degree of curvature in the beam induces slightly more error in prediction. In all cases, it is observed that crack location can be predicted more accurately than the crack depth.

Table 7.18: Predicted parameters and absolute percentage error for double cracked angle section curved beam for Case-II

Test point	Predicted natural parameters						Abs. error in percentage					
	η_1	η_2	η_3	η_4	η_5	η_6	L_1	ζ_1/b	L_2	ζ_2/b	A_f	Ω
For subtended angle, $\theta_s = 25°$												
1	0.63813	0.08651	3.07594	0.53875	1.18535	52.60500	2.10	8.14	1.57	7.75	3.63	5.21
2	0.64175	0.08542	3.23500	0.44945	0.64291	305.64000	2.68	6.78	3.52	10.11	2.59	1.88
3	0.60281	0.48120	3.21719	0.74936	1.28550	52.90500	3.55	3.76	2.95	6.33	6.24	5.81
4	0.63556	0.53745	3.24344	0.75576	0.64241	281.46000	1.69	7.49	3.79	5.53	1.97	6.18
5	0.60325	0.78152	3.03875	0.51335	1.24346	53.21000	3.48	2.31	2.76	2.67	2.09	6.42
6	0.64269	0.88368	3.20781	0.47035	0.72612	282.60000	2.83	10.46	2.65	5.93	2.27	5.80
7	15.05313	0.07404	18.11813	0.54575	1.21844	52.72000	3.66	7.45	3.37	9.15	2.39	5.44
8	15.13438	0.08645	19.46625	0.45330	0.59129	287.70000	3.14	8.06	3.82	9.34	4.63	4.10
9	15.17500	0.54745	19.25438	0.83176	1.71216	51.22500	2.88	9.49	2.69	3.97	4.40	2.45
10	16.15625	0.44850	19.42500	0.88256	0.79518	289.38000	3.40	10.30	3.60	10.32	1.83	3.54
11	15.32813	0.86728	19.28625	0.46705	1.47329	51.11500	1.90	8.41	2.86	6.59	6.16	2.23
12	16.21875	0.85392	18.09938	0.53630	0.76820	305.16000	3.80	6.74	3.47	7.26	5.16	1.72
For subtended angle, $\theta_s = 50°$												
1	1.20913	0.08711	6.12688	0.45370	1.09852	51.26500	3.27	8.89	1.97	9.26	5.30	2.53
2	1.28375	0.07700	6.38500	0.45060	0.13654	278.76000	2.70	3.75	2.16	9.88	5.03	7.08
3	1.22438	0.55075	6.34688	0.74824	1.17249	48.26500	2.05	10.15	1.55	6.77	3.76	3.47
4	1.27200	0.54520	6.00250	0.86200	0.11720	279.33000	1.76	9.04	3.96	7.75	2.33	6.89
5	1.20463	0.73520	6.44938	0.55425	1.12832	51.40000	3.63	8.1	3.19	3.85	1.65	2.80
6	1.27438	0.86824	6.00500	0.47070	0.14406	311.04000	1.95	4.73	3.92	5.86	3.96	3.68
7	32.52813	0.08625	38.19375	0.51045	1.28213	48.99500	4.09	7.81	1.85	2.09	2.57	2.01
8	32.25625	0.08850	38.95875	0.44990	0.81072	315.69000	3.22	6.82	3.89	10.12	5.73	5.23
9	30.05625	0.47330	36.54000	0.86160	1.31022	48.72500	3.82	5.84	2.56	7.7	3.66	2.55
10	30.36250	0.54760	39.00750	0.83992	0.96237	294.72000	2.84	3.52	4.02	4.99	6.93	1.76
11	32.28750	0.76304	38.49000	0.55665	1.26936	52.86000	3.32	4.62	2.64	11.33	5.78	5.72
12	30.65625	0.87608	36.68625	0.51850	2.09374	289.41000	1.90	9.51	2.17	3.7	4.83	3.53

Table 7.19: Mean error between actual and predicted crack parameters and excitation characteristics using heterogeneous data in channel beam

Sl. No.	Configuration of thin-walled beams	Abs error (%) for			
		Crack location	Crack depth ratio	A_f	Ω
	Case-I				
1	Single cracked straight beam	2.93	6.21	4.34	4.18
2	Double cracked straight beam	3.34	5.79	3.96	3.15
3	Single cracked curved beam (θ_s = 25°)	3.36	6.40	4.45	5.16
4	Double cracked curved beam (θ_s = 25°)	3.02	6.46	4.67	4.16
5	Single cracked curved beam (θ_s = 50°)	3.01	7.28	4.04	4.80
6	Double cracked curved beam (θ_s = 50°)	3.00	6.68	4.29	4.28
	Case-II				
1	Single cracked straight beam	2.60	5.75	3.67	3.62
2	Double cracked straight beam	2.46	5.31	4.68	3.75
3	Single cracked curved beam (θ_s = 25°)	2.63	5.51	4.60	3.87
4	Double cracked curved beam (θ_s = 25°)	2.47	5.08	4.32	4.49
5	Single cracked curved beam (θ_s = 50°)	2.71	5.23	4.05	4.81
6	Double cracked curved beam (θ_s = 50°)	2.92	5.06	4.32	4.26

Case-I: First two natural frequencies and three steady state amplitude; Case-II: First three natural frequencies and two steady state amplitude.

Table 7.20: Mean error between actual and predicted crack parameters and excitation characteristics using heterogeneous data in angle beam

Sl. No.	Configuration of thin-walled beams	Abs error (%) in			
		Crack location	Crack depth ratio	A_f	Ω
	Case-I				
1	Single cracked straight beam	3.48	6.18	3.88	3.81
2	Double cracked straight beam	3.06	6.08	3.57	3.96
3	Single cracked curved beam (θ_s = 25°)	3.50	7.28	4.11	3.87
4	Double cracked curved beam (θ_s = 25°)	3.55	7.42	3.95	3.93
5	Single cracked curved beam (θ_s = 50°)	3.96	7.30	3.67	3.77
6	Double cracked curved beam (θ_s = 50°)	3.79	7.15	3.90	3.57
	Case-II				
1	Single cracked straight beam	2.54	5.37	4.01	4.13
2	Double cracked straight beam	2.40	5.20	4.55	4.26
3	Single cracked curved beam (θ_s = 25°)	2.43	6.35	4.29	3.78
4	Double cracked curved beam (θ_s = 25°)	3.00	7.26	3.61	4.23
5	Single cracked curved beam (θ_s = 50°)	3.26	7.09	4.41	4.06
6	Double cracked curved beam (θ_s = 50°)	2.85	6.92	4.29	3.94

Case-I: Consideration of first two natural frequencies and three steady state amplitude; Case-II: Consideration of first three natural frequencies and two steady state amplitude.

7.3 Closure

A study of the crack and forcing parameter identification using heterogeneous data has been presented in this chapter. This study has been carried out for identification of single and multiple cracks in channel and angle cross-sectional straight and curved beam. For curved beam, two different subtended angles have been considered. The results are obtained using two combination of mixed data-Case-I: two natural frequencies and three steady state amplitudes and Case-II: three natural frequencies and two steady state amplitudes. It can be concluded from the study that the detection of position and size of the crack can be done more precisely when free vibration data dominates in heterogeneous input as seen in Case-II. The result also shows that the accuracy of the localization and sizing of cracks decrease when subtended angle of curved specimen increases. In all case studies, the location of crack can be found more accurately than the depth.

Chapter 8

Conclusions and Future Works

8.1 Overview

In this chapter, summary of works and conclusions are given. Moreover, scope of the future research is also stated.

8.2 Summary and conclusions

An integrated approach for health monitoring of straight and horizontally curved thin walled open section beam has been proposed based on the combined Finite element method (FEM), Response surface methodology (RSM) and Genetic algorithm (GA) by finding the location and the amount of the damage intensity. In fact, the method of detection of crack parameters is general and can be applied to any structural component with suitable change in Finite Element model. Two examples of beam cross section - one having single axis of symmetry and the other with no axis of symmetry are chosen to illustrate the method. The straight and horizontally curved beams with two different subtended angles are covered in the study. Laboratory tests were performed on thin walled channel and angle section beams with artificially induced cracks. Finite element (FE) simulations based on Central composite face-centered (CCF) design approach has been chosen in order to obtain the coefficients of a polynomial model for the Response surface functions (RSFs). These models are trained and tested by using analysis of variance (ANOVA). The development in FE model has been established by incorporating the warping stiffness in the cracked beam. To calculate the optimum crack and external forcing parameters, the searching tool GA has been used. The objective function has been formed by root mean square (RMS) of the errors between the

computed responses from RSFs and measured responses. Several examples are considered to illustrate the present integrated approach. Based on the studies carried out in this work, following major conclusions can be drawn

- The line spring elements used in the present study are the appropriate representation of cracks for practical implementation in crack identification study which can be confirmed from excellent agreement between FE results and measured values.
- The study reveals that the warping effects greatly alter the natural frequencies of uncracked and cracked thin-walled beams. The large errors can occur in the calculation of natural frequencies of thin-walled straight and curved beams, when the effect of warping stiffness is ignored. In higher modes, the effect becomes more prominent. Therefore, crack model including warping stiffness builds a strong base in structural health monitoring problems in thin walled beam.
- Warping condition in thin walled beam yields higher value of stress intensity factor compared to that of the condition where warping is neglected. It has been observed that the normalized stress intensity factor increases with the increase of crack depth ratio and decreases with the increase of non-dimensional flange thickness and non-dimensional web height.
- The bandwidth of different configurations of thin walled beams with various crack depth ratio has been compared with that of an uncracked beam. The results show that the bandwidth increases in case of cracked beam. This can be attributed to the fact that there is increased dissipation of vibration energy in presence of crack.
- The fundamental mode of cracked straight and curved beam of channel and angle section in bending and torsion follows the conventional pattern which exhibits weak coupling between bending and torsion. However, this fact is not true when higher mode is excited.
- In detection of crack parameters, it is found that mode shapes are of little help. Few cases in the present study show slight discontinuity in mode shapes of curved beam at crack location in higher modes.
- The absolute difference between curvature in each mode shapes has been proven to be a good indicator for the localization of crack. The discontinuity in absolute

difference between the curvature mode shapes is clearly visible at crack locations compared to only mode shape.

- Further, curvature damage factor (CDF) which includes the contribution of all significant modes has been found to be also a good indicator of the localization of crack compared to only mode shape vector.
- MAC factors have been found insensitive to damage detection.
- In case of horizontally curved beams, it has been observed that the fundamental natural frequencies of uncracked and cracked curved beams decrease when subtended angle (θ_s) increases.
- Combined application of RSM and GA can estimate the position and severity of cracks with high precision.
- Although free, force and heterogeneous response data can be used for damage detection, the first one proves to the best option for determining the location and extent of damage.
- Forced vibration data are found to have poor diagnostic use.
- Heterogeneous data (combined natural frequencies and steady state amplitude) when used in the identification algorithm yield better estimate compared to only force vibration data.
- Increase of number of natural frequency in the heterogeneous data further improves the accuracy of prediction.
- The present hybrid approach has also been utilized for the identification of external forcing parameters with reasonable accuracy. Thus the present method has promising application in structural health monitoring.
- The study with curved beam has shown that for the same curved length of the beam, radius of curvature has some influence on the accuracy of crack parameter identification.
- The study also reveals that crack location can be detected with more precision than that of crack depth for all configurations of open section thin-walled curved and straight beams.

- The present approach has been tested for small crack depth ratio up to 0.08. The output remains in the acceptable range of errors. Thus the method is capable of finding the crack in early stages also.
- In real applications, a structure oscillates in combined modes. Thus the study conducted with unsymmetrical thin walled structures proves its wider applicability in vibration based damage detection.
- In the present approach, information of undamaged state of the structure is not required. Only measured response in the current state of structure can be utilized in the presently developed method to detect crack parameters.
- The present approach offers a great advantage in structural health monitoring of aged structures as in most of the cases baseline information is not available.

8.3 Scope of future work

The scope of the future work has been listed as follows

- The finite element formulation can be extended for profile of varying curvature.
- Longitudinal crack can be considered as an extension of the present approach.
- Non-linear effects due to bilinear stiffness arising in case of breathing crack may be introduced in crack modeling.
- Random excitation can be incorporated for the study of damage parameters.
- Composite structures may be included to study crack detection using present hybrid approach.

Appendix A

Stiffness matrix k^e and Mass matrix m^e of Arbitrary Cross-Sectional Thin-Walled Beam

A1. Expression for Uncracked Elemental Stiffness and Mass Matrices

The uncracked element stiffness matrix $\boldsymbol{k^e}$ and consistent mass matrix $\boldsymbol{m^e}$, which have dimensions of 14 × 14, can be partitioned as follows:

$$\boldsymbol{k^e} = \begin{bmatrix} \boldsymbol{K_{AA}} & \boldsymbol{K_{AW}} & \boldsymbol{K_{AV}} & \boldsymbol{K_{A\Psi}} \\ \boldsymbol{K_{AW}^T} & \boldsymbol{K_{WW}} & \boldsymbol{K_{WV}} & \boldsymbol{K_{W\Psi}} \\ \boldsymbol{K_{AV}^T} & \boldsymbol{K_{WV}^T} & \boldsymbol{K_{VV}} & \boldsymbol{K_{V\Psi}} \\ \boldsymbol{K_{A\Psi}^T} & \boldsymbol{K_{W\Psi}^T} & \boldsymbol{K_{V\Psi}^T} & \boldsymbol{K_{\Psi\Psi}} \end{bmatrix} \tag{A.1}$$

$$\boldsymbol{m^e} = \begin{bmatrix} \boldsymbol{M_{AA}} & \boldsymbol{M_{AW}} & \boldsymbol{M_{AV}} & \boldsymbol{M_{A\Psi}} \\ \boldsymbol{M_{AW}^T} & \boldsymbol{M_{WW}} & \boldsymbol{M_{WV}} & \boldsymbol{M_{W\Psi}} \\ \boldsymbol{M_{AV}^T} & \boldsymbol{M_{WV}^T} & \boldsymbol{M_{VV}} & \boldsymbol{M_{V\Psi}} \\ \boldsymbol{M_{A\Psi}^T} & \boldsymbol{M_{W\Psi}^T} & \boldsymbol{M_{V\Psi}^T} & \boldsymbol{M_{\Psi\Psi}} \end{bmatrix} \tag{A.2}$$

The stiffness and mass sub-matrices given by Equations (A.1) and (A.2) are compiled in the present appendix. First of all the stiffness sub-matrices are expressed as follows:

$$\boldsymbol{K_{AA}} = \begin{bmatrix} \frac{EA}{l_e} & -\frac{EA}{l_e} \\ -\frac{EA}{l_e} & \frac{EA}{l_e} \end{bmatrix} \tag{A.3}$$

$$\boldsymbol{K}_{WW} = \begin{bmatrix} \left(\frac{12EI_{yy}}{l_e^3} - \frac{12EI_{yy}}{5R^2 l_e} + \frac{13EI_{yy}\,l_e}{35R^4} + \frac{13EAl_e}{35R^2}\right) & \left(\frac{6EI_{yy}}{l_e^2} - \frac{6EI_{yy}}{5R^2} + \frac{11EI_{yy}\,l_e^2}{210R^4} + \frac{11EAl_e^2}{210R^2}\right) & \left(-\frac{12EI_{yy}}{l_e^3} + \frac{12EI_{yy}}{5R^2 l_e} + \frac{9EI_{yy}\,l_e}{70R^4} + \frac{9EAl_e}{70R^2}\right) & \left(\frac{6EI_{yy}}{l_e^2} - \frac{EI_{yy}}{5R^2} - \frac{13EI_{yy}\,l_e^2}{420R^4} - \frac{13EAl_e^2}{420R^2}\right) \\ \left(\frac{6EI_{yy}}{l_e^2} - \frac{6EI_{yy}}{5R^2} + \frac{11EI_{yy}\,l_e^2}{210R^4} + \frac{11EAl_e^2}{210R^2}\right) & \left(\frac{4EI_{yy}}{l_e} - \frac{4EI_{yy}\,l_e}{15R^2} + \frac{EI_{yy}\,l_e^3}{105R^4} + \frac{EAl_e^3}{105R^2}\right) & \left(-\frac{6EI_{yy}}{l_e^2} + \frac{EI_{yy}}{5R^2} + \frac{13EI_{yy}\,l_e^2}{420R^4} + \frac{13EAl_e^2}{420R^2}\right) & \left(\frac{2EI_{yy}}{l_e} + \frac{EI_{yy}\,l_e}{15R^2} - \frac{EI_{yy}\,l_e^3}{140R^4} - \frac{EAl_e^3}{140R^2}\right) \\ \left(-\frac{12EI_{yy}}{l_e^3} + \frac{12EI_{yy}}{5R^2 l_e} + \frac{9EI_{yy}\,l_e}{70R^4} + \frac{9EAl_e}{70R^2}\right) & \left(-\frac{6EI_{yy}}{l_e^2} + \frac{EI_{yy}}{5R^2} + \frac{13EI_{yy}\,l_e^2}{420R^4} + \frac{13EAl_e^2}{420R^2}\right) & \left(\frac{12EI_{yy}}{l_e^3} - \frac{12EI_{yy}}{5R^2 l_e} + \frac{13EI_{yy}\,l_e}{35R^4} + \frac{13EAl_e}{35R^2}\right) & \left(-\frac{6EI_{yy}}{l_e^2} + \frac{6EI_{yy}}{5R^2} - \frac{11EI_{yy}\,l_e^2}{210R^4} - \frac{11EAl_e^2}{210R^2}\right) \\ \left(\frac{6EI_{yy}}{l_e^2} - \frac{EI_{yy}}{5R^2} - \frac{13EI_{yy}\,l_e^2}{420R^4} - \frac{13EAl_e^2}{420R^2}\right) & \left(\frac{2EI_{yy}}{l_e} + \frac{EI_{yy}\,l_e}{15R^2} - \frac{EI_{yy}\,l_e^3}{140R^4} - \frac{EAl_e^3}{140R^2}\right) & \left(-\frac{6EI_{yy}}{l_e^2} + \frac{6EI_{yy}}{5R^2} - \frac{11EI_{yy}\,l_e^2}{210R^4} - \frac{11EAl_e^2}{210R^2}\right) & \left(\frac{4EI_{yy}}{l_e} - \frac{4EI_{yy}\,l_e}{15R^2} + \frac{EI_{yy}\,l_e^3}{105R^4} + \frac{EAl_e^3}{105R^2}\right) \end{bmatrix} \tag{A.4}$$

$$\boldsymbol{K}_{VV} = \begin{bmatrix} \left(\frac{12EI_{zz}}{l_e^3} + \frac{12E\Gamma_\omega}{R^2 l_e^3} + \frac{6GJ}{5R^2\,l_e} + \frac{24EI_{\omega z}}{Rl_e^3}\right) & \left(\frac{6EI_{zz}}{l_e^2} + \frac{6E\Gamma_\omega}{R^2 l_e^2} + \frac{GJ}{10R^2} + \frac{12EI_{\omega z}}{Rl_e^2}\right) & \left(-\frac{12EI_{zz}}{l_e^3} - \frac{12E\Gamma_\omega}{R^2 l_e^3} - \frac{6GJ}{5R^2\,l_e} - \frac{24EI_{\omega z}}{Rl_e^3}\right) & \left(\frac{6EI_{zz}}{l_e^2} + \frac{6E\Gamma_\omega}{R^2 l_e^2} + \frac{GJ}{10R^2} + \frac{12EI_{\omega z}}{Rl_e^2}\right) \\ \left(\frac{6EI_{zz}}{l_e^2} + \frac{6E\Gamma_\omega}{R^2 l_e^2} + \frac{GJ}{10R^2} + \frac{12EI_{\omega z}}{Rl_e^2}\right) & \left(\frac{4EI_{zz}}{l_e} + \frac{4E\Gamma_\omega}{R^2 l_e} + \frac{2GJl_e}{15R^2} + \frac{8EI_{\omega z}}{Rl_e}\right) & \left(-\frac{6EI_{zz}}{l_e^2} - \frac{6E\Gamma_\omega}{R^2 l_e^2} - \frac{GJ}{10R^2} - \frac{12EI_{\omega z}}{Rl_e^2}\right) & \left(\frac{2EI_{zz}}{l_e} + \frac{2E\Gamma_\omega}{R^2 l_e} - \frac{GJl_e}{30R^2} + \frac{4EI_{\omega z}}{Rl_e}\right) \\ \left(-\frac{12EI_{zz}}{l_e^3} - \frac{12E\Gamma_\omega}{R^2 l_e^3} - \frac{6GJ}{5R^2\,l_e} - \frac{24EI_{\omega z}}{Rl_e^3}\right) & \left(-\frac{6EI_{zz}}{l_e^2} - \frac{6E\Gamma_\omega}{R^2 l_e^2} - \frac{GJ}{10R^2} - \frac{12EI_{\omega z}}{Rl_e^2}\right) & \left(\frac{12EI_{zz}}{l_e^3} + \frac{12E\Gamma_\omega}{R^2 l_e^3} + \frac{6GJ}{5R^2\,l_e} + \frac{24EI_{\omega z}}{Rl_e^3}\right) & \left(-\frac{6EI_{zz}}{l_e^2} - \frac{6E\Gamma_\omega}{R^2 l_e^2} - \frac{GJ}{10R^2} - \frac{12EI_{\omega z}}{Rl_e^2}\right) \\ \left(\frac{6EI_{zz}}{l_e^2} + \frac{6E\Gamma_\omega}{R^2 l_e^2} + \frac{GJ}{10R^2} + \frac{12EI_{\omega z}}{Rl_e^2}\right) & \left(\frac{2EI_{zz}}{l_e} + \frac{2E\Gamma_\omega}{R^2 l_e} - \frac{GJl_e}{30R^2} + \frac{4EI_{\omega z}}{Rl_e}\right) & \left(-\frac{6EI_{zz}}{l_e^2} - \frac{6E\Gamma_\omega}{R^2 l_e^2} - \frac{GJ}{10R^2} - \frac{12EI_{\omega z}}{Rl_e^2}\right) & \left(\frac{4EI_{zz}}{l_e} + \frac{4E\Gamma_\omega}{R^2 l_e} + \frac{2GJl_e}{15R^2} + \frac{8EI_{\omega z}}{Rl_e}\right) \end{bmatrix} \tag{A.5}$$

$$\boldsymbol{K}_{\psi\psi} = \begin{bmatrix} \left(\frac{12E\Gamma_\omega}{l_e^3} + \frac{6GJ}{5l_e} + \frac{13EI_{zz}\,l_e}{35R^2} + \frac{12EI_{\omega z}}{5Rl_e}\right) & \left(\frac{6E\Gamma_\omega}{l_e^2} + \frac{GJ}{10} + \frac{11EI_{zz}\,l_e^2}{210R^2} + \frac{6EI_{\omega z}}{5R}\right) & \left(-\frac{12E\Gamma_\omega}{l_e^3} - \frac{6GJ}{5l_e} + \frac{9EI_{zz}\,l_e}{70R^2} - \frac{12EI_{\omega z}}{5Rl_e}\right) & \left(\frac{6E\Gamma_\omega}{l_e^2} + \frac{GJ}{10} - \frac{13EI_{zz}\,l_e^2}{420R^2} + \frac{EI_{\omega z}}{5R}\right) \\ \left(\frac{6E\Gamma_\omega}{l_e^2} + \frac{GJ}{10} + \frac{11EI_{zz}\,l_e^2}{210R^2} + \frac{6EI_{\omega z}}{5R}\right) & \left(\frac{4E\Gamma_\omega}{l_e} + \frac{2GJl_e}{15} + \frac{EI_{zz}\,l_e^3}{105R^2} + \frac{4EI_{\omega z}\,l_e}{15R}\right) & \left(-\frac{6E\Gamma_\omega}{l_e^2} - \frac{GJ}{10} + \frac{13EI_{zz}\,l_e^2}{420R^2} - \frac{EI_{\omega z}}{5R}\right) & \left(\frac{2E\Gamma_\omega}{l_e} - \frac{GJl_e}{30} - \frac{EI_{zz}\,l_e^3}{140R^2} - \frac{EI_{\omega z}\,l_e}{15R}\right) \\ \left(-\frac{12E\Gamma_\omega}{l_e^3} - \frac{6GJ}{5l_e} + \frac{9EI_{zz}\,l_e}{70R^2} - \frac{12EI_{\omega z}}{5Rl_e}\right) & \left(-\frac{6E\Gamma_\omega}{l_e^2} - \frac{GJ}{10} + \frac{13EI_{zz}\,l_e^2}{420R^2} - \frac{EI_{\omega z}}{5R}\right) & \left(\frac{12E\Gamma_\omega}{l_e^3} + \frac{6GJ}{5l_e} + \frac{13EI_{zz}\,l_e}{35R^2} + \frac{12EI_{\omega z}}{5Rl_e}\right) & \left(-\frac{6E\Gamma_\omega}{l_e^2} - \frac{GJ}{10} - \frac{11EI_{zz}\,l_e^2}{210R^2} - \frac{6EI_{\omega z}}{5R}\right) \\ \left(\frac{6E\Gamma_\omega}{l_e^2} + \frac{GJ}{10} - \frac{13EI_{zz}\,l_e^2}{420R^2} + \frac{EI_{\omega z}}{5R}\right) & \left(\frac{2E\Gamma_\omega}{l_e} - \frac{GJl_e}{30} - \frac{EI_{zz}\,l_e^3}{140R^2} - \frac{EI_{\omega z}\,l_e}{15R}\right) & \left(-\frac{6E\Gamma_\omega}{l_e^2} - \frac{GJ}{10} - \frac{11EI_{zz}\,l_e^2}{210R^2} - \frac{6EI_{\omega z}}{5R}\right) & \left(\frac{4E\Gamma_\omega}{l_e} + \frac{2GJl_e}{15} + \frac{EI_{zz}\,l_e^3}{105R^2} + \frac{4EI_{\omega z}\,l_e}{15R}\right) \end{bmatrix} \tag{A.6}$$

$$\boldsymbol{K_{AW}} = \begin{bmatrix} -\frac{EA}{2R} & -\frac{EAl_e}{12R} & -\frac{EA}{2R} & \frac{EAl_e}{12R} \\ \frac{EA}{2R} & \frac{EAl_e}{12R} & \frac{EA}{2R} & -\frac{EAl_e}{12R} \end{bmatrix} \tag{A.7}$$

$$\boldsymbol{K_{AV}} = \begin{bmatrix} 0 & 0 & 0 & 0 \\ 0 & 0 & 0 & 0 \end{bmatrix} \tag{A.8}$$

$$\boldsymbol{K_{A\Psi}} = \begin{bmatrix} 0 & 0 & 0 & 0 \\ 0 & 0 & 0 & 0 \end{bmatrix} \tag{A.9}$$

$$\boldsymbol{K_{WV}} = \begin{bmatrix} \frac{E\left(I_{\omega y}+I_{yz}R\right)\left(60R^2-6l_e^2\right)}{5R^3l_e^3} & \frac{E\left(I_{\omega y}+I_{yz}R\right)\left(60R^2-11l_e^2\right)}{10R^3l_e^2} & \frac{E\left(I_{\omega y}+I_{yz}R\right)\left(6l_e^2-60R^2\right)}{5R^3l_e^3} & \frac{E\left(I_{\omega y}+I_{yz}R\right)\left(60R^2-l_e^2\right)}{10R^3l_e^2} \\ \frac{E\left(I_{\omega y}+I_{yz}R\right)\left(60R^2-l_e^2\right)}{10R^3l_e^2} & \frac{E\left(I_{\omega y}+I_{yz}R\right)\left(60R^2-2l_e^2\right)}{15R^3l_e} & \frac{E\left(I_{\omega y}+I_{yz}R\right)\left(l_e^2-60R^2\right)}{10R^3l_e^2} & \frac{E\left(I_{\omega y}+I_{yz}R\right)\left(l_e^2+60R^2\right)}{30R^3l_e} \\ \frac{E\left(I_{\omega y}+I_{yz}R\right)\left(6l_e^2-60R^2\right)}{5R^3l_e^3} & \frac{E\left(I_{\omega y}+I_{yz}R\right)\left(l_e^2-60R^2\right)}{10R^3l_e^2} & \frac{E\left(I_{\omega y}+I_{yz}R\right)\left(30R^2-6l_e^2\right)}{5R^3l_e^3} & \frac{E\left(I_{\omega y}+I_{yz}R\right)\left(11l_e^2-60R^2\right)}{10R^3l_e^2} \\ \frac{E\left(I_{\omega y}+I_{yz}R\right)\left(60R^2-l_e^2\right)}{10R^3l_e^2} & \frac{E\left(I_{\omega y}+I_{yz}R\right)\left(l_e^2+60R^2\right)}{30R^3l_e} & \frac{E\left(I_{\omega y}+I_{yz}R\right)\left(l_e^2-60R^2\right)}{10R^3l_e^2} & \frac{E\left(I_{\omega y}+I_{yz}R\right)\left(60R^2-2l_e^2\right)}{15R^3l_e^3} \end{bmatrix} \tag{A.10}$$

$$K_{W\Psi} = \begin{bmatrix} \left(\frac{12EI_{\omega y}}{l_e^3} - \frac{6EI_{\omega y}}{5l_e R^2} - \frac{13EI_{yz}l_e}{35R^3} + \frac{6EI_{yz}}{5Rl_e}\right) & \left(\frac{6EI_{\omega y}}{l_e^2} - \frac{11EI_{\omega y}}{10R^2} - \frac{11EI_{yz}l_e^2}{210R^3} + \frac{EI_{yz}}{10R}\right) & \left(-\frac{12EI_{\omega y}}{l_e^3} + \frac{6EI_{\omega y}}{5l_e R^2} - \frac{9EI_{yz}l_e}{70R^3} - \frac{6EI_{yz}}{5Rl_e}\right) & \left(\frac{6EI_{\omega y}}{l_e^2} - \frac{EI_{\omega y}}{10R^2} + \frac{13EI_{yz}l_e^2}{420R^3} + \frac{EI_{yz}}{10R}\right) \\ \left(\frac{6EI_{\omega y}}{l_e^2} - \frac{EI_{\omega y}}{10R^2} - \frac{11EI_{yz}l_e^2}{210R^3} + \frac{11EI_{yz}}{10R}\right) & \left(\frac{4EI_{\omega y}}{l_e} - \frac{2EI_{\omega y}l_e}{15R^2} - \frac{EI_{yz}l_e^3}{105R^3} + \frac{2EI_{yz}l_e}{15R}\right) & \left(-\frac{6EI_{\omega y}}{l_e^2} + \frac{EI_{\omega y}}{10R^2} - \frac{13EI_{yz}l_e^2}{420R^3} - \frac{EI_{yz}}{10R}\right) & \left(\frac{2EI_{\omega y}}{l_e} + \frac{EI_{\omega y}l_e}{30R^2} + \frac{EI_{yz}l_e^3}{140R^3} - \frac{EI_{yz}l_e}{30R}\right) \\ \left(-\frac{12EI_{\omega y}}{l_e^3} + \frac{6EI_{\omega y}}{5l_e R^2} - \frac{9EI_{yz}l_e}{70R^3} - \frac{6EI_{yz}}{5Rl_e}\right) & \left(-\frac{6EI_{\omega y}}{l_e^2} + \frac{EI_{\omega y}}{10R^2} - \frac{13EI_{yz}l_e^2}{420R^3} - \frac{EI_{yz}}{10R}\right) & \left(\frac{12EI_{\omega y}}{l_e^3} - \frac{6EI_{\omega y}}{5l_e R^2} - \frac{13EI_{yz}l_e}{35R^3} + \frac{6EI_{yz}}{5Rl_e}\right) & \left(-\frac{6EI_{\omega y}}{l_e^2} + \frac{11EI_{\omega y}}{10R^2} + \frac{11EI_{yz}l_e^2}{210R^3} - \frac{EI_{yz}}{10R}\right) \\ \left(\frac{6EI_{\omega y}}{l_e^2} - \frac{EI_{\omega y}}{10R^2} + \frac{13EI_{yz}l_e^2}{420R^3} + \frac{EI_{yz}}{10R}\right) & \left(\frac{2EI_{\omega y}}{l_e} + \frac{EI_{\omega y}l_e}{30R^2} + \frac{EI_{yz}l_e^3}{140R^3} - \frac{EI_{yz}l_e}{30R}\right) & \left(-\frac{6EI_{\omega y}}{l_e^2} + \frac{EI_{\omega y}}{10R^2} + \frac{11EI_{yz}l_e^2}{210R^3} - \frac{11EI_{yz}}{10R}\right) & \left(\frac{4EI_{\omega y}}{l_e} - \frac{2EI_{\omega y}l_e}{15R^2} - \frac{EI_{yz}l_e^3}{105R^3} + \frac{2EI_{yz}l_e}{15R}\right) \end{bmatrix} \quad \text{(A.11)}$$

$$K_{V\Psi} = \begin{bmatrix} K_{V\Psi}^{11} & K_{V\Psi}^{12} \\ K_{V\Psi}^{21} & K_{V\Psi}^{22} \end{bmatrix} \quad \text{(A.12)}$$

$$K_{V\Psi}^{11} = \begin{bmatrix} \left(\frac{12EI_{\omega z}}{l_e^3} + \frac{6EI_{\omega z}}{5R^2 l_e} + \frac{6EI_{zz}}{5Rl_e} + \frac{12E\Gamma_\omega}{Rl_e^3} + \frac{6GJ}{5Rl_e}\right) & \left(\frac{6EI_{\omega z}}{l_e^2} + \frac{EI_{\omega z}}{10R^2} + \frac{EI_{zz}}{10R} + \frac{6E\Gamma_\omega}{Rl_e^2} + \frac{GJ}{10R}\right) \\ \left(\frac{6EI_{\omega z}}{l_e^2} + \frac{11EI_{\omega z}}{10R^2} + \frac{11EI_{zz}}{10R} + \frac{6E\Gamma_\omega}{Rl_e^2} + \frac{GJ}{10R}\right) & \left(\frac{4EI_{\omega z}}{l_e} + \frac{2EI_{\omega z}l_e}{15R^2} + \frac{2EI_{zz}l_e}{15R} + \frac{4E\Gamma_\omega}{Rl_e} + \frac{2GJl_e}{15R}\right) \end{bmatrix} \quad \text{(A.13)}$$

$$K_{V\Psi}^{12} = \begin{bmatrix} \left(-\frac{12EI_{\omega z}}{l_e^3} - \frac{6EI_{\omega z}}{5Rl_e} - \frac{6EI_{zz}}{5l_e R} - \frac{12E\Gamma_\omega}{Rl_e^3} - \frac{6GJ}{5Rl_e}\right) & \left(\frac{6EI_{\omega z}}{l_e^2} + \frac{EI_{\omega z}}{10R^2} + \frac{EI_{zz}}{10R} + \frac{6E\Gamma_\omega}{Rl_e^2} + \frac{GJ}{10R}\right) \\ \left(-\frac{6EI_{\omega z}}{l_e^2} - \frac{EI_{\omega z}}{10R^2} - \frac{EI_{zz}}{10R} - \frac{6E\Gamma_\omega}{Rl_e^2} - \frac{GJ}{10R}\right) & \left(\frac{2EI_{\omega z}}{l_e} - \frac{EI_{\omega z}l_e}{30R^2} - \frac{EI_{zz}l_e}{10R} + \frac{2E\Gamma_\omega}{Rl_e} - \frac{GJl_e}{30R}\right) \end{bmatrix} \quad \text{(A.14)}$$

$$\boldsymbol{K}_{V\Psi}^{21} = \begin{bmatrix} \left(-\frac{12EI_{\omega z}}{l_e^3} - \frac{6EI_{\omega z}}{5R^2 l_e} - \frac{6EI_{zz}}{5Rl_e} - \frac{12E\Gamma_\omega}{Rl_e^3} - \frac{6GJ}{5Rl_e}\right) & \left(-\frac{6EI_{\omega z}}{l_e^2} - \frac{EI_{\omega z}}{10R^2} - \frac{EI_{zz}}{10R} - \frac{6E\Gamma_\omega}{Rl_e^2} - \frac{GJ}{10R}\right) \\ \left(\frac{6EI_{\omega z}}{l_e^2} + \frac{EI_{\omega z}}{10R^2} + \frac{EI_{zz}}{10R} + \frac{6E\Gamma_\omega}{Rl_e^2} + \frac{GJ}{10R}\right) & \left(\frac{2EI_{\omega z}}{l_e} - \frac{EI_{\omega z} l_e}{30R^2} - \frac{EI_{zz} l_e}{10R} + \frac{2E\Gamma_\omega}{Rl_e} - \frac{GJ l_e}{30R}\right) \end{bmatrix} \tag{A.15}$$

$$\boldsymbol{K}_{V\Psi}^{22} = \begin{bmatrix} \left(\frac{12EI_{\omega z}}{l_e^3} + \frac{6EI_{\omega z}}{5R^2 l_e} + \frac{6EI_{zz}}{5Rl_e} + \frac{12E\Gamma_\omega}{Rl_e^3} + \frac{6GJ}{5Rl_e}\right) & \left(-\frac{6EI_{\omega z}}{l_e^2} - \frac{EI_{\omega z}}{10R^2} - \frac{EI_{zz}}{10R} - \frac{6E\Gamma_\omega}{Rl_e^2} - \frac{GJ}{10R}\right) \\ \left(-\frac{6EI_{\omega z}}{l_e^2} - \frac{11EI_{\omega z}}{10R^2} - \frac{11EI_{zz}}{10R} - \frac{6E\Gamma_\omega}{Rl_e^2} - \frac{GJ}{10R}\right) & \left(\frac{4EI_{\omega z}}{l_e} + \frac{2EI_{\omega z} l_e}{15R^2} + \frac{2EI_{zz} l_e}{15R} + \frac{4E\Gamma_\omega}{Rl_e} + \frac{2GJl_e}{15R}\right) \end{bmatrix} \tag{A.16}$$

Similarly, the mass sub-matrices are given by

$$\boldsymbol{M}_{AA} = \begin{bmatrix} \left(\frac{Al_e\rho}{3} + \frac{I_{yy} l_e \rho}{3R^2} - \frac{2S_y l_e \rho}{3R}\right) & \left(\frac{Al_e\rho}{6} + \frac{I_{yy} l_e \rho}{6R^2} - \frac{S_y l_e \rho}{3R}\right) \\ \left(\frac{Al_e\rho}{6} + \frac{I_{yy} l_e \rho}{6R^2} - \frac{S_y l_e \rho}{3R}\right) & \left(\frac{Al_e\rho}{3} + \frac{I_{yy} l_e \rho}{3R^2} - \frac{2S_y l_e \rho}{3R}\right) \end{bmatrix} \tag{A.17}$$

$$\boldsymbol{M_{WW}} = \begin{bmatrix} \left(\frac{13Al_e\rho}{35}+\frac{6I_{yy}\rho}{5l_e}\right) & \left(\frac{11Al_e^2\rho}{210}+\frac{I_{yy}\rho}{10}\right) & \left(\frac{9Al_e\rho}{70}-\frac{6I_{yy}\rho}{5l_e}\right) & \left(-\frac{13Al_e^2\rho}{420}+\frac{I_{yy}\rho}{10}\right) \\ \left(\frac{11Al_e^2\rho}{210}+\frac{I_{yy}\rho}{10}\right) & \left(\frac{Al_e^3\rho}{105}+\frac{2I_{yy}l_e\rho}{15}\right) & \left(\frac{13Al_e^2\rho}{420}-\frac{I_{yy}\rho}{10}\right) & \left(-\frac{Al_e^3\rho}{140}-\frac{I_{yy}l_e\rho}{30}\right) \\ \left(\frac{9Al_e\rho}{70}-\frac{6I_{yy}\rho}{5l_e}\right) & \left(\frac{13Al_e^2\rho}{420}-\frac{I_{yy}\rho}{10}\right) & \left(\frac{13Al_e\rho}{35}+\frac{6I_{yy}\rho}{5l_e}\right) & \left(-\frac{11Al_e^2\rho}{210}-\frac{I_{yy}\rho}{10}\right) \\ \left(-\frac{13Al_e^2\rho}{420}+\frac{I_{yy}\rho}{10}\right) & \left(-\frac{Al_e^3\rho}{140}-\frac{I_{yy}l_e\rho}{30}\right) & \left(-\frac{11Al_e^2\rho}{210}-\frac{I_{yy}\rho}{10}\right) & \left(\frac{Al_e^3\rho}{105}+\frac{2I_{yy}l_e\rho}{15}\right) \end{bmatrix} \tag{A.18}$$

$$\boldsymbol{M_{VV}} = \begin{bmatrix} \left(\frac{13Al_e\rho}{35}+\frac{6I_{zz}\rho}{5l_e}+\frac{6\rho\Gamma_\omega}{5R^2l_e}+\frac{12I_{y\omega}\rho}{5Rl_e}\right) & \left(\frac{11Al_e^2\rho}{210}+\frac{I_{zz}\rho}{10}+\frac{\rho\Gamma_\omega}{10R^2}+\frac{I_{y\omega}\rho}{5R}\right) & \left(\frac{9Al_e\rho}{70}-\frac{6I_{zz}\rho}{5l_e}-\frac{6\rho\Gamma_\omega}{5R^2l_e}-\frac{12I_{y\omega}\rho}{5Rl_e}\right) & \left(-\frac{13Al_e^2\rho}{420}+\frac{I_{zz}\rho}{10}+\frac{\rho\Gamma_\omega}{10R^2}+\frac{I_{y\omega}\rho}{5R}\right) \\ \left(\frac{11Al_e^2\rho}{210}+\frac{I_{zz}\rho}{10}+\frac{\rho\Gamma_\omega}{10R^2}+\frac{I_{y\omega}\rho}{5R}\right) & \left(\frac{Al_e^3\rho}{105}+\frac{2I_{zz}l_e\rho}{15}+\frac{2l_e\Gamma_\omega\rho}{15R^2}+\frac{4I_{y\omega}l_e\rho}{15R}\right) & \left(\frac{13Al_e^2\rho}{420}-\frac{I_{zz}\rho}{10}-\frac{\rho\Gamma_\omega}{10R^2}-\frac{I_{y\omega}\rho}{5R}\right) & \left(-\frac{Al_e^3\rho}{140}-\frac{I_{zz}l_e\rho}{30}-\frac{\rho l_e\Gamma_\omega}{30R^2}-\frac{I_{y\omega}l_e\rho}{15R}\right) \\ \left(\frac{9Al_e\rho}{70}-\frac{6I_{zz}\rho}{5l_e}-\frac{6\rho\Gamma_\omega}{5R^2l_e}-\frac{12I_{y\omega}\rho}{5Rl_e}\right) & \left(\frac{13Al_e^2\rho}{420}-\frac{I_{zz}\rho}{10}-\frac{\rho\Gamma_\omega}{10R^2}-\frac{I_{y\omega}\rho}{5R}\right) & \left(\frac{13Al_e\rho}{35}+\frac{6I_{zz}\rho}{5l_e}+\frac{6\rho\Gamma_\omega}{5R^2l_e}+\frac{12I_{y\omega}\rho}{5Rl_e}\right) & \left(-\frac{11Al_e^2\rho}{210}-\frac{I_{zz}\rho}{10}-\frac{\rho\Gamma_\omega}{10R^2}-\frac{I_{y\omega}\rho}{5R}\right) \\ \left(-\frac{13Al_e^2\rho}{420}+\frac{I_{zz}\rho}{10}+\frac{\rho\Gamma_\omega}{10R^2}+\frac{I_{y\omega}\rho}{5R}\right) & \left(-\frac{Al_e^3\rho}{140}-\frac{I_{zz}l_e\rho}{30}-\frac{\rho l_e\Gamma_\omega}{30R^2}-\frac{I_{y\omega}l_e\rho}{15R}\right) & \left(-\frac{11Al_e^2\rho}{210}-\frac{I_{zz}\rho}{10}-\frac{\rho\Gamma_\omega}{10R^2}-\frac{I_{y\omega}\rho}{5R}\right) & \left(\frac{Al_e^3\rho}{105}+\frac{2I_{zz}l_e\rho}{15}+\frac{2l_e\Gamma_\omega\rho}{15R^2}+\frac{4I_{y\omega}l_e\rho}{15R}\right) \end{bmatrix} \tag{A.19}$$

$$\boldsymbol{M_{\Psi\Psi}} = \begin{bmatrix} \left(\frac{13I_sl_e\rho}{35}+\frac{6\Gamma_\omega\rho}{5l_e}\right) & \left(\frac{11I_sl_e^2\rho}{210}+\frac{\Gamma_\omega\rho}{10}\right) & \left(\frac{9I_sl_e\rho}{70}-\frac{6\Gamma_\omega\rho}{5l_e}\right) & \left(-\frac{13I_sl_e^2\rho}{420}+\frac{\Gamma_\omega\rho}{10}\right) \\ \left(\frac{11I_sl_e^2\rho}{210}+\frac{\Gamma_\omega\rho}{10}\right) & \left(\frac{I_sl_e^3\rho}{105}+\frac{2\Gamma_\omega l_e\rho}{15}\right) & \left(\frac{13I_sl_e^2\rho}{420}-\frac{\Gamma_\omega\rho}{10}\right) & \left(-\frac{I_sl_e^3\rho}{140}-\frac{\Gamma_\omega l_e\rho}{30}\right) \\ \left(\frac{9I_sl_e\rho}{70}-\frac{6\Gamma_\omega\rho}{5l_e}\right) & \left(\frac{13I_sl_e^2\rho}{420}-\frac{\Gamma_\omega\rho}{10}\right) & \left(\frac{13I_sl_e\rho}{35}+\frac{6\Gamma_\omega\rho}{5l_e}\right) & \left(-\frac{11I_sl_e^2\rho}{210}-\frac{\Gamma_\omega\rho}{10}\right) \\ \left(-\frac{13I_sl_e^2\rho}{420}+\frac{\Gamma_\omega\rho}{10}\right) & \left(-\frac{I_sl_e^3\rho}{140}-\frac{\Gamma_\omega l_e\rho}{30}\right) & \left(-\frac{11I_sl_e^2\rho}{210}-\frac{\Gamma_\omega\rho}{10}\right) & \left(\frac{I_sl_e^3\rho}{105}+\frac{2\Gamma_\omega l_e\rho}{15}\right) \end{bmatrix} \tag{A.20}$$

$$\boldsymbol{M_{AW}} = \begin{bmatrix} \left(\frac{\rho I_{yy}}{2R} + \frac{\rho S_y}{2}\right) & \left(-\frac{\rho l_e I_{yy}}{12R} - \frac{\rho l_e S_y}{12}\right) & \left(-\frac{\rho I_{yy}}{2R} - \frac{\rho S_y}{2}\right) & \left(\frac{\rho l_e I_{yy}}{12R} + \frac{\rho l_e S_y}{12}\right) \\ \left(\frac{\rho I_{yy}}{2R} + \frac{\rho S_y}{2}\right) & \left(\frac{\rho l_e I_{yy}}{12R} + \frac{\rho l_e S_y}{12}\right) & \left(-\frac{\rho I_{yy}}{2R} - \frac{\rho S_y}{2}\right) & \left(-\frac{\rho l_e I_{yy}}{12R} - \frac{\rho l_e S_y}{12}\right) \end{bmatrix} \tag{A.21}$$

$$\boldsymbol{M_{AV}} = \begin{bmatrix} \left(\frac{\rho S_z}{2} + \frac{\rho I_{z\omega}}{2R^2} + \frac{\rho I_{yz}}{2R} + \frac{\rho S_\omega}{2R}\right) & \left(-\frac{\rho l_e I_{z\omega}}{12R^2} - \frac{\rho l_e S_\omega}{12R} - \frac{\rho l_e S_z}{12} - \frac{\rho l_e I_{yz}}{12R}\right) & \left(-\frac{\rho S_z}{2} - \frac{\rho I_{z\omega}}{2R^2} - \frac{\rho I_{yz}}{2R} - \frac{\rho S_\omega}{2R}\right) & \left(\frac{\rho l_e I_{z\omega}}{12R^2} + \frac{\rho l_e S_\omega}{12R} + \frac{\rho l_e S_z}{12} + \frac{\rho l_e I_{yz}}{12R}\right) \\ \left(\frac{\rho S_z}{2} + \frac{\rho I_{z\omega}}{2R^2} + \frac{\rho I_{yz}}{2R} + \frac{\rho S_\omega}{2R}\right) & \left(\frac{\rho l_e I_{z\omega}}{12R^2} + \frac{\rho l_e S_\omega}{12R} + \frac{\rho l_e S_z}{12} + \frac{\rho l_e I_{yz}}{12R}\right) & \left(-\frac{\rho S_z}{2} - \frac{\rho I_{z\omega}}{2R^2} - \frac{\rho I_{yz}}{2R} - \frac{\rho S_\omega}{2R}\right) & \left(-\frac{\rho l_e I_{z\omega}}{12R^2} - \frac{\rho l_e S_\omega}{12R} - \frac{\rho l_e S_z}{12} - \frac{\rho l_e I_{yz}}{12R}\right) \end{bmatrix} \tag{A.22}$$

$$\boldsymbol{M_{A\Psi}} = \begin{bmatrix} \left(\frac{\rho I_{z\omega}}{2R} + \frac{\rho S_\omega}{2}\right) & \left(-\frac{\rho l_e I_{z\omega}}{12R} - \frac{\rho l_e S_\omega}{12}\right) & \left(-\frac{\rho I_{z\omega}}{2R} - \frac{\rho S_\omega}{2}\right) & \left(\frac{\rho l_e I_{z\omega}}{12R} + \frac{\rho l_e S_\omega}{12}\right) \\ \left(\frac{\rho I_{z\omega}}{2R} + \frac{\rho S_\omega}{2}\right) & \left(\frac{\rho l_e I_{z\omega}}{12R} + \frac{\rho l_e S_\omega}{12}\right) & \left(-\frac{\rho I_{z\omega}}{2R} - \frac{\rho S_\omega}{2}\right) & \left(-\frac{\rho l_e I_{z\omega}}{12R} - \frac{\rho l_e S_\omega}{12}\right) \end{bmatrix} \tag{A.23}$$

$$\boldsymbol{M_{WV}} = \begin{bmatrix} \left(\frac{6\rho I_{z\omega}}{5Rl_e} + \frac{6\rho I_{yz}}{5l_e}\right) & \left(\frac{\rho I_{z\omega}}{10R} + \frac{\rho I_{yz}}{10}\right) & \left(-\frac{6\rho I_{z\omega}}{5Rl_e} - \frac{6\rho I_{yz}}{5l_e}\right) & \left(\frac{\rho I_{z\omega}}{10R} + \frac{\rho I_{yz}}{10}\right) \\ \left(\frac{\rho I_{z\omega}}{10R} + \frac{\rho I_{yz}}{10}\right) & \left(\frac{2\rho l_e I_{z\omega}}{15R} + \frac{2\rho l_e I_{yz}}{15}\right) & \left(-\frac{\rho I_{z\omega}}{10R} - \frac{\rho I_{yz}}{10}\right) & \left(-\frac{\rho l_e I_{z\omega}}{30R} - \frac{\rho l_e I_{yz}}{30}\right) \\ \left(-\frac{6\rho I_{z\omega}}{5Rl_e} - \frac{6\rho I_{yz}}{5l_e}\right) & \left(-\frac{\rho I_{z\omega}}{10R} - \frac{\rho I_{yz}}{10}\right) & \left(\frac{6\rho I_{z\omega}}{5Rl_e} + \frac{6\rho I_{yz}}{5l_e}\right) & \left(-\frac{\rho I_{z\omega}}{10R} - \frac{\rho I_{yz}}{10}\right) \\ \left(\frac{\rho I_{z\omega}}{10R} + \frac{\rho I_{yz}}{10}\right) & \left(-\frac{\rho l_e I_{z\omega}}{30R} - \frac{\rho l_e I_{yz}}{30}\right) & \left(-\frac{\rho I_{z\omega}}{10R} - \frac{\rho I_{yz}}{10}\right) & \left(\frac{2\rho l_e I_{z\omega}}{15R} + \frac{2\rho l_e I_{yz}}{15}\right) \end{bmatrix} \tag{A.24}$$

$$\boldsymbol{M_{W\Psi}} = \begin{bmatrix} \left(-\frac{13Ae_y\, l_e\, \rho}{35}+\frac{13\rho\, S_z\, l_e}{35}+\frac{6\rho\, I_{z\omega}}{5l_e}\right) & \left(-\frac{11Ae_y\, l_e^2\, \rho}{210}+\frac{11\rho\, S_z\, l_e^2}{210}+\frac{\rho\, I_{z\omega}}{10}\right) & \left(-\frac{9Ae_y l_e\, \rho}{70}+\frac{9\rho\, S_z\, l_e^2}{70l_e}-\frac{6\rho I_{z\omega}}{5l_e}\right) & \left(\frac{13Ae_y l_e^2\, \rho}{420}-\frac{13\rho\, S_z\, l_e^2}{420}+\frac{\rho I_{z\omega}}{10}\right) \\ \left(-\frac{11Ae_y\, l_e^2\, \rho}{210}+\frac{11\rho\, S_z\, l_e^2}{210}+\frac{\rho\, I_{z\omega}}{10}\right) & \left(-\frac{Ae_y l_e^3\, \rho}{105}+\frac{\rho l_e^3\, S_z}{105}+\frac{14\rho\, l_e\, I_{z\omega}}{105}\right) & \left(-\frac{13Ae_y l_e^2\, \rho}{420}+\frac{13\rho\, S_z\, l_e^2}{420}-\frac{\rho I_{z\omega}}{10}\right) & \left(\frac{Ae_y l_e^3\, \rho}{140}-\frac{\backslash\rho\, S_z\, l_e^3}{140}-\frac{\rho\, l_e\, I_{z\omega}}{30}\right) \\ \left(-\frac{9Ae_y l_e\, \rho}{70}+\frac{9\rho\, S_z\, l_e^2}{70l_e}-\frac{6\rho I_{z\omega}}{5l_e}\right) & \left(-\frac{13Ae_y l_e^2\, \rho}{420}+\frac{13\rho\, S_z\, l_e^2}{420}-\frac{\rho I_{z\omega}}{10}\right) & \left(-\frac{13Ae_y\, l_e\, \rho}{35}+\frac{13\rho\, S_z\, l_e}{35}+\frac{6\rho\, I_{z\omega}}{5l_e}\right) & \left(\frac{11Ae_y l_e^2\, \rho}{210}-\frac{11\rho\, S_z\, l_e^2}{210}-\frac{\rho I_{z\omega}}{10}\right) \\ \left(\frac{13Ae_y l_e^2\, \rho}{420}-\frac{13\rho\, S_z\, l_e^2}{420}+\frac{\rho I_{z\omega}}{10}\right) & \left(\frac{Ae_y l_e^3\, \rho}{140}-\frac{\rho\, S_z\, l_e^3}{140}-\frac{\rho\, l_e\, I_{z\omega}}{30}\right) & \left(\frac{11Ae_y l_e^2\, \rho}{210}-\frac{11\rho\, S_z\, l_e^2}{210}-\frac{\rho I_{z\omega}}{10}\right) & \left(-\frac{Ae_y l_e^3\, \rho}{105}+\frac{\rho l_e^3\, S_z}{105}+\frac{14\rho\, l_e\, I_{z\omega}}{105}\right) \end{bmatrix} \quad \text{(A.25)}$$

$$\boldsymbol{M_{V\Psi}} = \begin{bmatrix} \left(\frac{13Ae_z\, l_e\, \rho}{35}+\frac{6\rho\Gamma_\omega}{5Rl_e}+\frac{6\rho I_{y\omega}}{5l_e}-\frac{13\rho\, S_y\, l_e}{35}\right) & \left(\frac{11Ae_z\, l_e^2\, \rho}{210}+\frac{\rho\Gamma_\omega}{10R}+\frac{\rho I_{y\omega}}{10}-\frac{11\rho\, S_y\, l_e^2}{210}\right) & \left(\frac{9Ae_z l_e\, \rho}{70}-\frac{6\rho\Gamma_\omega}{5Rl_e}-\frac{6\rho I_{y\omega}}{5l_e}-\frac{9\rho\, S_y\, l_e}{70}\right) & \left(-\frac{13Ae_z\, l_e^2\, \rho}{420}+\frac{\rho\Gamma_\omega}{10R}+\frac{\rho I_{y\omega}}{10}+\frac{13\rho\, S_y\, l_e^2}{420}\right) \\ \left(\frac{11Ae_z\, l_e^2\, \rho}{210}+\frac{\rho\Gamma_\omega}{10R}+\frac{\rho I_{y\omega}}{10}-\frac{11\rho\, S_y\, l_e^2}{210}\right) & \left(\frac{Ae_z l_e^3\, \rho}{105}+\frac{2\rho\Gamma_\omega\, l_e}{15R}+\frac{14l_e\, \rho I_{y\omega}}{105}-\frac{\rho\, S_y\, l_e^3}{105}\right) & \left(\frac{13Ae_z\, l_e^2\, \rho}{420}-\frac{\rho\Gamma_\omega}{10R}-\frac{\rho I_{y\omega}}{10}-\frac{13\rho\, S_y\, l_e^2}{420}\right) & \left(-\frac{Ae_z\, l_e^3\, \rho}{140}-\frac{\rho\Gamma_\omega\, l_e}{30R}-\frac{14l_e\, \rho I_{y\omega}}{420}+\frac{\rho\, S_y\, l_e^3}{140}\right) \\ \left(\frac{9Ae_z\, l_e\, \rho}{70}-\frac{6\rho\Gamma_\omega}{5Rl_e}-\frac{6\rho I_{y\omega}}{5l_e}-\frac{9\rho\, S_y\, l_e}{70}\right) & \left(\frac{13Ae_z\, l_e^2\, \rho}{420}-\frac{\rho\Gamma_\omega}{10R}-\frac{\rho I_{y\omega}}{10}-\frac{13\rho\, S_y\, l_e^2}{420}\right) & \left(\frac{13Ae_z\, l_e\, \rho}{35}+\frac{6\rho\Gamma_\omega}{5Rl_e}+\frac{6\rho I_{y\omega}}{5l_e}-\frac{13\rho\, S_y\, l_e}{35}\right) & \left(-\frac{11Ae_z l_e^2\, \rho}{210}-\frac{\rho\Gamma_\omega}{10R}-\frac{\rho I_{y\omega}}{10}+\frac{11\rho\, S_y\, l_e^2}{210}\right) \\ \left(-\frac{13Ae_z\, l_e^2\, \rho}{420}+\frac{\rho\Gamma_\omega}{10R}+\frac{\rho I_{y\omega}}{10}+\frac{13\rho\, S_y\, l_e^2}{420}\right) & \left(-\frac{Ae_z\, l_e^3\, \rho}{140}-\frac{\rho\Gamma_\omega\, l_e}{30R}-\frac{14l_e\, \rho I_{y\omega}}{420}+\frac{\rho\, S_y\, l_e^3}{140}\right) & \left(-\frac{11Ae_z l_e^2\, \rho}{210}-\frac{\rho\Gamma_\omega}{10R}-\frac{\rho I_{y\omega}}{10}+\frac{11\rho\, S_y\, l_e^2}{210}\right) & \left(\frac{Ae_z l_e^3\, \rho}{105}+\frac{2\rho\Gamma_\omega\, l_e}{15R}+\frac{14l_e\, \rho I_{y\omega}}{105}-\frac{\rho\, S_y\, l_e^3}{105}\right) \end{bmatrix} \quad \text{(A.26)}$$

Appendix B

Determination of $K_{IM\omega}$ for Warping Case of Cracked Section

B.1 Expression of $K_{IM\omega}$ for Local Flexibility Coefficient

Strain energy release rate for the cracked section is given by [199]

$$J = \lim_{\Delta a \to 0} \frac{(\gamma+1)\, K_{IM_\omega}(a)\, K_{IM_\omega}(a+\Delta a)}{4\pi G \Delta a} \int_0^{\Delta a} \sqrt{\frac{\Delta a - z}{z}}\, dz \tag{B.1}$$

where J is strain energy release rate, initial length of crack is a and Δa is crack extension. $K_{IM\omega}$ (Mode-I stress intensity factor) due to bi-moment, G is shear modulus, $\gamma = (3 - \mu)/ (1 + \mu)$ for plane stress condition and μ is Poisson's ratio. Evaluating the integral [201] in the Equation (B.1), following expression for J can be found

$$J = \lim_{\Delta a \to 0} \frac{(\gamma+1)\, K_{IM_\omega}(a)\, K_{IM_\omega}(a+\Delta a)}{8G} \tag{B.2}$$

Expanding $K_{IB}(a + \Delta a)$ about Δa using Taylor series [202], the Equation (B.2) can be written as

$$J = \lim_{\Delta a \to 0} \frac{(\gamma+1)\, K_{IM_\omega}(a) \left\{ K_{IM_\omega}(a) + \Delta a \frac{dK_{IM_\omega}(a)}{da} + \frac{1}{2!}(\Delta a)^2 \frac{dK_{IM_\omega}(a)}{da} + \ldots \right\}}{8G} \tag{B.3}$$

$$= \frac{(\gamma+1)\, K_{IM_\omega}^2}{8G} = \frac{K_{IM_\omega}^2}{E^*} \tag{B.4}$$

In which

$$E^* = \frac{8G}{\gamma+1} \tag{B.5}$$

Substituting the expression of γ and $G = E/2(1+ \mu)$ in Equation (B.5), it can be shown that for plane stress condition

$$E^* = E \tag{B.6}$$

where, E is Young's modulus.

Assume that the beam has warping stiffness EI_ω at the uncracked cross-sections and EI_ω^C at the cracked cross-section. Let the crack of initial width h_w be extended by an amount Δh_w. The change in strain energy of the beam due to bi-moment can be written following Kienzler and Herrmann's [98] expression as

$$\Delta U_S = \left(\frac{M_\omega^2}{2EI_\omega} - \frac{M_\omega^2}{2EI_\omega^C} \right) \Delta h_w \tag{B.7}$$

As $\Delta h_w \rightarrow 0$, Equation (B.7) can be written as

$$\frac{\partial U_S}{\partial h_w} = - \frac{M_\omega^2}{2EI_\omega} \left(\frac{I_\omega}{I_\omega^C} - 1 \right) \tag{B.8}$$

The energy release $\partial U_S/\partial a$ due to crack extension is related to the energy release $\partial U_S/\partial h_w$ due to crack widening which can be written as [101]

$$\frac{\partial U_S}{\partial a} = 2\beta \frac{\partial U_S}{\partial h_w} \tag{B.9}$$

According to linear fracture mechanics theory [199], the strain energy release rate J is related to $\partial U_S/\partial a$ as follows,

$$J = -\frac{1}{t_f} \frac{\partial U_S}{\partial a} \tag{B.10}$$

Utilizing Equations (B.8) and (B.9) in Equation (B.10) and thereafter making use of Equation (B.4), the following relation can be obtained.

$$K_{IM_\omega} = M_\omega \sqrt{\frac{\beta E^*}{t_f E I_\omega} \left(\frac{I_\omega}{I_\omega^C} - 1 \right)} \tag{B.11}$$

Substituting E^* from Eq. (B.6) in to the Eq. (B.11), one obtains

$$K_{IM_\omega} = M_\omega \sqrt{\frac{\beta_{M_\omega}}{t_f I_\omega} \left(\frac{I_\omega}{I_\omega^C} - 1 \right)} \tag{B.12}$$

where $\beta_{M\omega} = \beta$ for plane stress condition. I_ω and I_ω^C are the warping constant of uncracked and cracked section respectively, obtained numerically using the procedure given elsewhere [185, 203].

Appendix C

Newmark - β Algorithm

The Newmark method is based on the assumption that the acceleration varies linearly within the interval (t_j, t_{j+1}) as illustrated in Figure C.1. This provides

$$\ddot{d} = \ddot{d}_j + \frac{1}{\Delta t}\left(\ddot{d}_{j+1} - \ddot{d}_j\right)\tau \qquad \text{for } 0 \le \tau \le \Delta t \tag{C.1}$$

Integrating yields,

$$\dot{d} = \dot{d}_j + \ddot{d}_j\,\tau + \frac{1}{2\Delta t}\left(\ddot{d}_{j+1} - \ddot{d}_j\right)\tau^2 \tag{C.2}$$

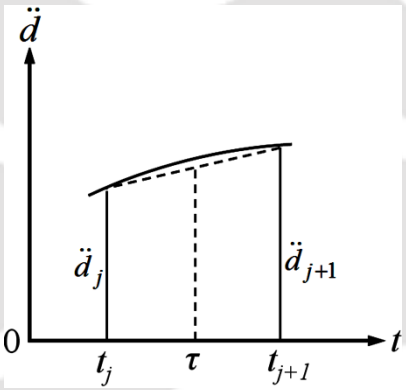

Figure C.1: Linear acceleration approximation

When $\tau = 0, \dot{d} = \dot{d}_j$. Integrating Equation (C.2) again gives,

$$d = d_j + \dot{d}_j\,\tau + \frac{1}{2}\,\ddot{d}_j\,\tau^2 + \frac{1}{6\Delta t}\left(\ddot{d}_{j+1} - \ddot{d}_j\right)\tau^3 \tag{C.3}$$

Since, $d = d_j$ when $\tau = 0$.

Calculating, Equation (C.2) and Equation (C.3) at $\tau = \Delta t$ yields,

$$\dot{d}_{j+1} = \dot{d}_j + \frac{\Delta t}{2}\left(\ddot{d}_j + \ddot{d}_{j+1}\right) \tag{C.4}$$

and

$$d_{j+1} = d_j + \dot{d}_j \Delta t + \frac{1}{2}\ddot{d}_j \tau^2 + \frac{(\Delta t)^2}{6}\left(2\ddot{d}_j + \ddot{d}_{j+1}\right) \quad \text{(C.5)}$$

In the Newmark method, the resulting expressions for the velocity and displacement vectors Equations (C.4) and (C.5) are assumed to take the form

$$\dot{d}_{j+1} = \dot{d}_j + \Delta t\{(1-\gamma)\ddot{d}_j + \gamma \ddot{d}_{j+1}\} \quad \text{(C.6)}$$

and

$$d_{j+1} = d_j + \dot{d}_j \Delta t + (\Delta t)^2\{(\tfrac{1}{2}-\beta)\ddot{d}_j + \beta \ddot{d}_{j+1}\} \quad \text{(C.7)}$$

Considering γ = 1/2 and β = 1/6, Equations (C.6) and (C.7) reduce to Equations (C.4) and (C.5). Therefore, linear acceleration method is a special case of the Newmark method. It can be similarly shown that taking γ = 1/2 and β = 1/4 conforms to assuming that the acceleration is constant and equal to the average value $(\ddot{d}_j + \ddot{d}_{j+1})/2$ within the interval (t_j, t_{j+1}).

$$M\ddot{d}_{j+1} + D\dot{d}_{j+1} + K d_{j+1} = F_{j+1} \quad \text{(C.8)}$$

The method is also known as implicit method.

In order to get $\ddot{d}_{j+1}$ in terms of d_{j+1}, Equation (C.7) can be used and the resulting expression can be substituted into Equation (C.6) to exhibit $\dot{d}_{j+1}$ in terms of d_{j+1}.

$$\ddot{d}_{j+1} = \frac{1}{\beta(\Delta t)^2}\left(d_{j+1} - d_j\right) - \frac{1}{\beta(\Delta t)}\dot{d}_j - (\tfrac{1}{2\beta}-1)\ddot{d}_j \quad \text{(C.9)}$$

$$\dot{d}_{j+1} = \dot{d}_j + (1-\gamma)\Delta t\,\ddot{d}_j + \beta \Delta t\,\ddot{d}_{j+1} \quad \text{(C.10)}$$

Now, substituting the Equations (C.9) and (C.10) into Equation (C.8) one can obtain a relation for obtaining d_{j+1}:

$$\begin{aligned} d_{j+1} = [\ & \tfrac{1}{\beta(\Delta t)^2}M + \tfrac{\gamma}{\beta(\Delta t)}C + K\ ]^{-1} \times \{F_{j+1} + M\,(\tfrac{1}{\beta(\Delta t)^2}d_j + \tfrac{1}{\beta(\Delta t)}\dot{d}_j \\ & + (\tfrac{1}{2\beta}-1)\ddot{d}_j\,) + C\,(\tfrac{\gamma}{\beta \Delta t}d_j + (\tfrac{\gamma}{\beta}-1)\dot{d}_j + (\tfrac{\gamma}{\beta}-2)\tfrac{\Delta t}{2}\ddot{d}_j\,)\} \end{aligned} \quad \text{(C.11)}$$

It is important to note that, the constant average acceleration method is unconditionally stable, whereas the linear acceleration method is conditionally stable.

Appendix D

Regression Co-efficient for Different Configuration of Beams

Table D.1: Estimated regression co-efficient for model equations of natural frequency for single cracked channel section straight beam

Regression co-efficient	Model equation number.				
	1	2	3	4	5
c_0	49.180	105.930	206.180	466.860	603.320
c_1	1.270	2.030	5.420	14.490	4.960
c_2	-1.180	-1.930	-8.710	-13.320	-8.140
c_{11}	-	-	-	-12.280	-
c_{22}	-	-	- 6.900	-	-5.790
c_{12}	1.700	2.680	7.010	18.060	6.280

Table D.2: Estimated regression co-efficient for model equations of natural frequency for single cracked angle section straight beam

Regression co-efficient	Model equation number.				
	1	2	3	4	5
c_0	23.30	50.16	80.14	134.16	263.85
c_1	2.30	0.35	1.74	6.58	6.24
c_2	-2.67	-0.34	-2.25	-10.79	-7.64
c_{11}	-	-	-	-	-
c_{22}	-2.27	-	-	-7.25	-
c_{12}	3.10	0.39	1.74	8.10	6.09

Table D.3: Estimated regression co-efficient for model equations of natural frequency for double cracked channel section straight beam

Regression co-efficient	Model equation number.				
	1	2	3	4	5
c_0	49.95	107.08	203.82	467.20	600.40
c_1	0.91	1.46	3.91	11.00	3.77
c_2	-0.88	-1.43	-4.97	-10.60	-4.81
c_3	0.54	0.91	1.65	3.28	2.12
c_4	-1.28	-2.08	-5.58	-11.45	-5.68
c_{11}	-0.77	-1.15	2.56	-7.54	2.76
c_{22}	-0.51	-0.87	-6.99	-3.95	-6.56
c_{33}	-0.66	-0.95	3.50	-3.35	3.61
c_{44}	-0.47	-0.74	-3.89	-4.59	-3.29
c_{12}	0.98	1.56	4.17	11.51	4.03
c_{13}	0.73	1.12	2.85	6.55	2.25
c_{14}	0.13	0.22	0.66	2.48	0.89
c_{23}	-0.73	-1.12	-2.85	-6.55	-2.25
c_{24}	-0.13	-0.22	-0.66	-2.48	-0.89
c_{34}	1.43	2.31	5.25	12.34	5.40

Table D.4: Estimated regression co-efficient for model equations of natural frequency for double cracked angle section straight beam

Regression co-efficient	Model equation number.				
	1	2	3	4	5
c_0	23.60	50.18	80.31	130.98	262.62
c_1	2.25	0.31	1.50	6.14	5.37
c_2	-2.38	-0.31	-1.67	-7.50	-5.37
c_3	2.09	0.26	0.84	3.95	2.43
c_4	-2.13	-0.26	-0.94	-5.05	-3.15
c_{11}	-1.00	-0.13	-0.12	3.37	0.13
c_{22}	-2.10	-0.10	-1.66	-8.82	-3.35
c_{33}	-0.92	-0.10	0.68	4.67	3.99
c_{44}	-1.23	-0.053	-0.20	-5.23	-2.45
c_{12}	2.46	0.34	1.50	6.64	5.39
c_{13}	0.64	0.055	0.23	1.46	0.70
c_{14}	-0.64	-0.055	-0.23	-1.46	-0.70
c_{23}	-0.64	-0.055	-0.23	-1.46	-0.70
c_{24}	0.64	0.055	0.23	1.46	0.70
c_{34}	2.29	0.28	0.86	4.33	2.53

Table D.5: Estimated regression co-efficient for model equations of natural frequency for single cracked channel section curved beam (θ_s = 25°)

Regression co-efficient	Model equation number.				
	1	2	3	4	5
c_0	40.81	79.14	198.81	408.42	765.50
c_1	0.96	0.89	2.37	6.93	17.60
c_2	-0.83	-0.90	-2.47	-6.94	-16.77
c_{11}	-0.11	0.71	2.00	2.78	1.93
c_{22}	0.29	0.69	1.68	2.76	4.43
c_{12}	0.94	0.75	2.04	6.50	17.52

Table D.6: Estimated regression co-efficient for model equations of natural frequency for single cracked angle section curved beam (θ_s = 25°)

Regression co-efficient	Model equation number.				
	1	2	3	4	5
c_0	17.63	24.60	89.55	128.48	233.95
c_1	1.78	0.79	2.06	0.94	1.25
c_2	-1.46	-0.70	-1.74	-1.30	-2.40
c_{11}	0.095	0.20	0.29	0.66	2.88
c_{22}	1.07	0.47	1.24	-	-
c_{12}	1.50	0.69	1.74	1.02	1.35

Table D.7: Estimated regression co-efficient for model equations of natural frequency for double cracked channel section curved beam (θ_s = 25°)

Regression co-efficient	Model equation number.				
	1	2	3	4	5
c_0	40.68	78.87	197.96	406.51	761.50
c_1	0.77	0.55	1.49	5.07	14.08
c_2	-0.73	-0.55	-1.52	-5.07	-13.80
c_3	0.52	0.49	1.37	4.01	9.96
c_4	-0.49	-0.49	-1.38	-4.01	-9.85
c_{11}	-0.34	0.24	0.76	0.18	-2.92
c_{22}	0.064	0.22	0.45	0.17	-0.37
c_{33}	-0.14	0.27	0.84	1.07	0.20
c_{44}	0.086	0.28	0.69	1.09	1.17
c_{12}	0.81	0.60	1.64	5.44	14.99
c_{13}	0.13	0.15	0.41	1.06	2.53
c_{14}	-0.13	-0.15	-0.41	-1.06	-2.53
c_{23}	-0.13	-0.15	-0.41	-1.06	-2.53
c_{24}	0.13	0.15	0.41	1.06	2.53
c_{34}	0.55	0.54	1.51	4.35	10.74

Table D.8: Estimated regression co-efficient for model equations of natural frequency for double cracked angle section curved beam (θ_s = 25°)

Regression co-efficient	Model equation number.				
	1	2	3	4	5
c_0	17.22	24.33	88.79	127.30	231.37
c_1	1.22	0.55	1.52	0.94	1.28
c_2	-1.11	-0.52	-1.41	-1.04	-1.58
c_3	0.80	0.46	0.83	0.61	0.80
c_4	-0.76	-0.44	-0.81	-0.69	-1.06
c_{11}	-0.48	-0.071	-0.37	0.56	2.14
c_{22}	0.50	0.20	0.57	-0.35	-0.52
c_{33}	0.086	0.042	0.48	0.83	2.61
c_{44}	0.52	0.22	0.62	0.082	0.25
c_{12}	1.23	0.57	1.54	0.97	1.35
c_{13}	0.27	0.12	0.20	0.055	0.00
c_{14}	-0.27	-0.12	-0.20	-0.055	0.00
c_{23}	-0.27	-0.12	-0.20	-0.055	0.00
c_{24}	0.27	0.12	0.20	0.055	0.00
c_{34}	0.84	0.48	0.88	0.63	0.86

Table D.9: Estimated regression co-efficient for model equations of natural frequency for single cracked channel section curved beam (θ_s = 50°)

Regression co-efficient	Model equation number.				
	1	2	3	4	5
c_0	21.56	89.36	208.27	407.99	736.75
c_1	0.55	1.61	3.08	5.40	14.01
c_2	-0.47	-1.49	-3.05	-5.75	-13.91
c_{11}	-0.11	0.30	1.57	4.07	4.49
c_{22}	0.15	0.67	1.65	3.02	4.79
c_{12}	0.55	1.52	2.82	4.83	13.59

Table D.10: Estimated regression co-efficient for model equations of natural frequency for single cracked angle section curved beam (θ_s = 50°)

Regression co-efficient	Model equation number.				
	1	2	3	4	5
c_0	9.22	24.73	72.49	130.33	216.74
c_1	1.21	0.28	4.56	1.40	3.44
c_2	-1.01	-0.23	-3.73	-1.61	-4.13
c_{11}	0.21	-0.18	0.47	0.35	2.79
c_{22}	0.80	-	2.95	-0.25	-
c_{12}	1.00	0.29	3.75	1.44	3.17

Table D.11: Estimated regression co-efficient for model equations of natural frequency for double cracked channel section curved beam (θ_s = 50°)

Regression co-efficient	Model equation number.				
	1	2	3	4	5
c_0	21.49	89.04	207.36	406.11	732.95
c_1	0.45	1.22	2.17	3.58	10.61
c_2	-0.42	-1.18	-2.16	-3.70	-10.56
c_3	0.30	0.79	1.57	3.29	8.83
c_4	-0.28	-0.78	-1.58	-3.34	-8.79
c_{11}	-0.22	-0.22	0.29	1.45	-0.37
c_{22}	0.031	0.15	0.39	0.41	0.00
c_{33}	-0.10	0.095	0.75	1.71	1.11
c_{44}	0.042	0.24	0.65	1.24	1.45
c_{12}	0.47	1.30	2.35	3.92	11.39
c_{13}	0.073	0.22	0.46	0.91	2.20
c_{14}	-0.073	-0.22	-0.46	-0.91	-2.20
c_{23}	-0.073	-0.22	-0.46	-0.91	-2.20
c_{24}	0.073	0.22	0.46	0.91	2.20
c_{34}	0.31	0.86	1.72	3.61	9.57

Table D.12: Estimated regression co-efficient for model equations of natural frequency for double cracked angle section curved beam (θ_s = 50°)

Regression co-efficient	Model equation number.				
	1	2	3	4	5
c_0	8.93	24.61	71.34	128.98	213.41
c_1	0.80	0.26	3.18	1.38	3.06
c_2	-0.73	-0.25	-2.91	-1.42	-3.18
c_3	0.55	0.22	1.72	0.65	1.10
c_4	-0.52	-0.20	-1.66	-0.74	-1.42
c_{11}	-0.23	-0.16	-1.14	0.056	0.96
c_{22}	0.37	-0.018	1.34	-0.33	-0.15
c_{33}	0.11	-0.12	0.88	0.98	3.60
c_{44}	0.38	0.00	1.39	0.12	0.71
c_{12}	0.81	0.26	3.23	1.39	3.12
c_{13}	0.19	0.029	0.53	0.045	0.055
c_{14}	-0.19	-0.029	-0.53	-0.045	-0.055
c_{23}	-0.19	-0.029	-0.53	-0.045	-0.055
c_{24}	0.19	0.029	0.53	0.045	0.055
c_{34}	0.58	0.22	1.84	0.67	1.21

Table D.13: Estimated regression co-efficient for model equations of peak value of acceleration response for single cracked channel section straight beam

Regression co-efficient	Model equation number.				
	1	2	3	4	5
c_0	5.640	16.159	23.008	22.101	17.409
c_1	-0.100	0.107	0.043	0.007	0.145
c_2	0.100	-0.095	-0.025	0.003	-0.107
c_3	4.590	8.836	7.146	12.331	24.290
c_4	4.570	8.149	5.283	11.349	25.633
c_{11}	0.013	-0.133	-0.086	-0.103	-0.012
c_{22}	0.008	-0.028	0.075	-0.013	0.323
c_{33}	-0.046	-0.113	0.022	-0.029	-0.216
c_{44}	-1.050	-7.749	-17.697	-10.563	8.225
c_{12}	-0.092	0.154	0.075	0.003	0.132
c_{13}	-0.090	0.151	0.074	0.003	0.129
c_{14}	-0.092	0.155	0.076	0.004	0.133
c_{23}	0.090	-0.151	-0.074	-0.003	-0.129
c_{24}	0.092	-0.155	-0.076	-0.004	-0.133
c_{34}	4.470	7.950	5.182	11.107	25.123

Table D.14: Estimated regression co-efficient for model equations of peak value of acceleration response for single cracked angle section straight beam

Regression co-efficient	Model equation number.				
	1	2	3	4	5
c_0	8.09	18.79	18.12	15.76	39.64
c_1	0.21	0.28	0.27	0.10	0.60
c_2	-0.25	-0.36	-0.31	-0.10	-0.69
c_3	2.91	5.49	5.17	8.26	21.96
c_4	2.32	3.92	3.58	7.38	20.08
c_{11}	0.24	0.40	0.26	0.00	0.38
c_{22}	-0.16	-0.28	-0.16	0.00	-0.38
c_{33}	-0.047	-0.093	-0.07	0.00	-0.13
c_{44}	-5.80	-14.84	-14.48	-8.24	-19.25
c_{12}	0.18	0.18	0.20	0.12	0.52
c_{13}	0.18	0.18	0.19	0.12	0.51
c_{14}	0.18	0.18	0.20	0.12	0.52
c_{23}	-0.18	-0.18	-0.19	-0.12	-0.51
c_{24}	-0.18	-0.18	-0.20	-0.12	-0.52
c_{34}	2.27	3.84	3.51	7.23	19.66

Table D.15: Estimated regression co-efficient for model equations of peak value of acceleration response for double cracked channel section straight beam

Regression co-efficient	Model equation number.				
	1	2	3	4	5
c_0	6.37	17.87	24.65	22.58	13.49
c_1	-0.28	-0.06	0.03	-0.16	0.29
c_2	0.29	0.07	-0.02	0.14	-0.31
c_3	-0.27	-0.13	0.02	-0.16	0.28
c_4	0.27	0.14	-0.02	0.16	-0.28
c_5	4.78	8.35	5.72	11.64	24.62
c_6	4.90	8.32	5.17	11.56	25.34
c_{11}	-0.48	-0.84	-0.32	-0.09	1.48
c_{22}	-0.40	-0.51	0.28	-0.48	0.74
c_{33}	-0.54	-0.94	-0.22	-0.59	0.97
c_{44}	-0.48	-0.73	0.03	-0.52	0.88
c_{55}	-0.32	-0.21	0.71	-0.41	-1.09
c_{66}	0.68	-6.41	-19.91	-8.92	9.05
c_{12}	-0.28	-0.03	0.06	-0.14	0.25
c_{13}	0.19	0.19	0.00	0.14	-0.11
c_{14}	-0.19	-0.19	0.00	-0.14	0.11
c_{15}	-0.27	-0.03	0.06	-0.14	0.24
c_{16}	-0.28	-0.03	0.07	-0.14	0.25
c_{23}	-0.19	-0.19	0.00	-0.14	0.11
c_{24}	0.19	0.19	0.00	0.14	-0.11
c_{25}	0.27	0.03	-0.06	0.14	-0.24
c_{26}	0.28	0.03	-0.07	0.14	-0.25
c_{34}	-0.27	-0.11	0.06	-0.16	0.21
c_{35}	-0.26	-0.10	0.06	-0.16	0.21
c_{36}	-0.27	-0.11	0.06	-0.16	0.22
c_{45}	0.26	0.10	-0.06	0.16	-0.21
c_{46}	0.27	0.11	-0.06	0.16	-0.22
c_{56}	4.74	8.05	5.09	11.26	24.91

Table D.16: Estimated regression co-efficient for model equations of peak value of acceleration response for double cracked angle section straight beam

Regression co-efficient	Model equation number.				
	1	2	3	4	5
c_0	4.45	11.20	13.34	15.60	29.88
c_1	0.12	0.13	0.15	0.08	0.38
c_2	-0.13	-0.13	-0.15	-0.08	-0.38
c_3	0.20	0.25	0.22	0.09	0.54
c_4	-0.20	-0.25	-0.22	-0.09	-0.54
c_5	2.20	3.95	3.73	7.52	19.75
c_6	2.16	3.77	3.43	7.28	19.64
c_{11}	-0.59	-1.43	-0.88	0.02	-1.76
c_{22}	-0.62	-1.42	-0.86	0.03	-1.65
c_{33}	1.36	2.69	1.71	0.09	3.52
c_{44}	1.34	2.71	1.73	0.10	3.60
c_{55}	-0.62	-1.44	-0.86	0.04	-1.74
c_{66}	-3.11	-8.46	-10.64	-8.45	-11.95
c_{12}	0.13	0.14	0.15	0.09	0.39
c_{13}	0.05	0.04	0.05	0.03	0.12
c_{14}	-0.05	-0.04	-0.05	-0.03	-0.12
c_{15}	0.13	0.14	0.15	0.09	0.38
c_{16}	0.13	0.14	0.15	0.09	0.39
c_{23}	-0.05	-0.04	-0.05	-0.03	-0.12
c_{24}	0.05	0.04	0.05	0.03	0.12
c_{25}	-0.13	-0.14	-0.15	-0.09	-0.38
c_{26}	-0.13	-0.14	-0.15	-0.09	-0.39
c_{34}	0.14	0.13	0.14	0.09	0.39
c_{35}	0.14	0.13	0.14	0.09	0.38
c_{36}	0.14	0.13	0.15	0.09	0.39
c_{45}	-0.14	-0.13	-0.14	-0.09	-0.38
c_{46}	-0.14	-0.13	-0.15	-0.09	-0.39
c_{56}	2.13	3.71	3.37	7.14	19.28

Table D.17: Estimated regression co-efficient for model equations of peak value of acceleration response for single cracked channel section curved beam (θ_s = 25°)

Regression co-efficient	Model equation number.				
	1	2	3	4	5
c_0	9.17	22.26	21.64	17.45	39.35
c_1	0.14	0.38	0.31	0.07	0.35
c_2	-0.16	-0.38	-0.30	-0.07	-0.35
c_3	4.32	8.09	6.56	11.21	27.42
c_4	3.79	6.50	4.71	10.36	25.99
c_{11}	0.62	1.10	0.86	0.05	1.04
c_{22}	0.49	1.07	1.01	0.09	1.02
c_{33}	-0.43	-1.19	-0.99	0.07	-0.92
c_{44}	-5.97	-16.58	-17.58	-6.99	-13.82
c_{12}	0.06	0.15	0.09	0.09	0.20
c_{13}	0.06	0.14	0.09	0.09	0.19
c_{14}	0.06	0.15	0.10	0.11	0.22
c_{23}	-0.06	-0.14	-0.09	-0.09	-0.19
c_{24}	-0.06	-0.15	-0.10	-0.11	-0.22
c_{34}	3.76	6.41	4.66	10.18	25.54

Table D.18: Estimated regression co-efficient for model equations of peak value of acceleration response for single cracked angle section curved beam (θ_s = 25°)

Regression co-efficient	Model equation number.				
	1	2	3	4	5
c_0	4.10	9.41	8.02	13.66	29.70
c_1	-0.25	-0.30	-0.15	0.37	0.61
c_2	0.24	0.30	0.15	-0.37	-0.61
c_3	1.98	4.28	3.63	8.77	21.96
c_4	1.74	3.54	2.81	7.50	20.03
c_{11}	-0.64	-1.23	-0.46	0.57	1.14
c_{22}	-0.70	-1.28	-0.47	0.60	1.08
c_{33}	0.63	1.51	0.45	-0.05	-0.45
c_{44}	-1.71	-4.88	-4.44	-6.42	-9.92
c_{12}	-0.12	-0.01	-0.07	0.33	0.49
c_{13}	-0.12	-0.01	-0.07	0.33	0.48
c_{14}	-0.12	0.01	-0.03	0.42	0.62
c_{23}	0.12	0.01	0.07	-0.33	-0.48
c_{24}	0.12	-0.01	0.03	-0.42	-0.62
c_{34}	1.67	3.45	2.73	7.46	19.79

Table D.19: Estimated regression co-efficient for model equations of peak value of acceleration response for double cracked channel section curved beam (θ_s = 25°)

Regression co-efficient	Model equation number.				
	1	2	3	4	5
c_0	12.24	29.20	26.95	18.49	48.69
c_1	-0.07	-0.05	-0.09	0.03	-0.15
c_2	0.07	0.05	0.10	-0.03	0.15
c_3	-0.06	-0.06	-0.08	0.03	-0.14
c_4	0.05	0.06	0.09	-0.03	0.14
c_5	4.03	7.09	5.46	10.66	26.75
c_6	3.84	6.47	4.75	10.33	26.04
c_{11}	-0.54	-1.42	-1.30	-0.16	-1.82
c_{22}	-0.64	-1.29	-0.97	-0.15	-1.68
c_{33}	-0.56	-1.34	-1.16	-0.24	-1.89
c_{44}	-0.65	-1.30	-0.98	-0.21	-1.81
c_{55}	1.34	3.27	2.53	0.31	3.93
c_{66}	-7.37	-20.68	-20.24	-7.44	-18.93
c_{12}	-0.01	0.09	0.01	0.05	0.04
c_{13}	0.07	0.06	0.08	0.04	0.16
c_{14}	-0.07	-0.06	-0.08	-0.04	-0.16
c_{15}	-0.01	0.09	0.01	0.05	0.04
c_{16}	-0.01	0.09	0.02	0.06	0.06
c_{23}	-0.07	-0.06	-0.08	-0.04	-0.16
c_{24}	0.07	0.06	0.08	0.04	0.16
c_{25}	0.01	-0.09	-0.01	-0.05	-0.04
c_{26}	0.01	-0.09	-0.02	-0.06	-0.06
c_{34}	0.01	0.08	0.02	0.05	0.04
c_{35}	0.01	0.08	0.02	0.05	0.04
c_{36}	0.01	0.08	0.02	0.06	0.05
c_{45}	-0.01	-0.08	-0.02	-0.05	-0.04
c_{46}	-0.01	-0.08	-0.02	-0.06	-0.05
c_{56}	3.75	6.33	4.63	10.12	25.48

Table D.20: Estimated regression co-efficient for model equations of peak value of acceleration response for double cracked angle section curved beam (θ_s = 25°)

Regression co-efficient	Model equation number.				
	1	2	3	4	5
c_0	4.41	10.11	8.20	13.57	29.34
c_1	-0.09	0.00	-0.05	0.24	0.35
c_2	0.09	0.00	0.05	-0.24	-0.35
c_3	-0.09	-0.01	-0.05	0.26	0.37
c_4	0.09	0.01	0.04	-0.26	-0.37
c_5	1.85	3.77	3.27	8.10	20.96
c_6	1.80	3.53	2.82	7.30	19.73
c_{11}	-0.04	-0.04	-0.08	0.13	0.23
c_{22}	-0.08	-0.06	-0.06	0.17	0.18
c_{33}	-0.03	0.00	0.00	0.13	0.21
c_{44}	-0.06	-0.03	-0.04	0.16	0.19
c_{55}	-0.04	0.01	-0.01	0.16	0.21
c_{66}	-2.35	-6.34	-4.85	-6.22	-9.23
c_{12}	-0.09	0.00	-0.05	0.25	0.36
c_{13}	-0.03	-0.01	-0.02	0.09	0.12
c_{14}	0.03	0.01	0.02	-0.09	-0.12
c_{15}	-0.09	0.00	-0.05	0.24	0.35
c_{16}	-0.09	0.01	-0.02	0.32	0.48
c_{23}	0.03	0.01	0.02	-0.09	-0.12
c_{24}	-0.03	-0.01	-0.02	0.09	0.12
c_{25}	0.09	0.00	0.05	-0.24	-0.35
c_{26}	0.09	-0.01	0.02	-0.32	-0.48
c_{34}	-0.09	-0.01	-0.05	0.27	0.38
c_{35}	-0.09	-0.01	-0.05	0.26	0.37
c_{36}	-0.09	-0.01	-0.04	0.29	0.43
c_{45}	0.09	0.01	0.05	-0.26	-0.37
c_{46}	0.09	0.01	0.04	-0.29	-0.43
c_{56}	1.76	3.46	2.76	7.17	19.37

Table D.21: Estimated regression co-efficient for model equations of peak value of acceleration response for single cracked channel section curved beam (θ_s = 50°)

Regression co-efficient	Model equation number.				
	1	2	3	4	5
c_0	10.15	26.68	21.35	13.56	43.38
c_1	0.44	0.48	0.35	0.07	0.45
c_2	-0.33	-0.39	-0.30	-0.09	-0.43
c_3	5.03	9.13	7.63	9.97	28.94
c_4	4.46	7.05	5.67	8.71	25.81
c_{11}	-0.34	0.25	0.53	0.24	0.81
c_{22}	0.61	1.03	0.94	0.05	0.98
c_{33}	0.02	-0.66	-0.70	-0.08	-0.68
c_{44}	-5.95	-20.07	-15.94	-4.01	-16.61
c_{12}	0.28	0.19	0.11	0.09	0.25
c_{13}	0.28	0.19	0.11	0.09	0.25
c_{14}	0.28	0.19	0.14	0.15	0.35
c_{23}	-0.28	-0.19	-0.11	-0.09	-0.25
c_{24}	-0.28	-0.19	-0.14	-0.15	-0.35
c_{34}	4.40	6.94	5.59	8.56	25.38

Table D.22: Estimated regression co-efficient for model equations of peak value of acceleration response for single cracked angle section curved beam (θ_s = 50°)

Regression co-efficient	Model equation number.				
	1	2	3	4	5
c_0	2.42	6.73	4.47	11.05	34.69
c_1	-0.24	-0.25	-0.41	0.03	0.34
c_2	0.23	0.25	0.42	-0.03	-0.34
c_3	1.16	3.14	2.96	7.79	24.42
c_4	1.03	2.35	1.72	4.69	18.54
c_{11}	-0.42	-0.78	-0.29	0.76	2.10
c_{22}	-0.48	-0.77	-0.16	0.71	2.14
c_{33}	0.24	0.87	-0.37	-0.49	-1.83
c_{44}	-0.76	-3.40	-0.77	-4.42	-13.17
c_{12}	-0.18	-0.10	-0.51	-0.12	-0.13
c_{13}	-0.18	-0.09	-0.50	-0.12	-0.12
c_{14}	-0.16	0.04	-0.13	0.67	1.23
c_{23}	0.18	0.09	0.50	0.12	0.12
c_{24}	0.16	-0.04	0.13	-0.67	-1.23
c_{34}	0.95	2.28	1.58	4.68	18.36

Table D.23: Estimated regression co-efficient for model equations of peak value of acceleration response for double cracked channel section curved beam (θ_s = 50°)

Regression co-efficient	Model equation number.				
	1	2	3	4	5
c_0	11.95	31.09	25.45	13.89	48.00
c_1	0.06	0.04	-0.11	0.02	-0.15
c_2	-0.06	-0.03	0.13	-0.03	0.15
c_3	-0.11	0.00	-0.13	0.02	-0.17
c_4	0.10	0.00	0.13	-0.02	0.17
c_5	4.72	7.71	6.66	9.65	28.00
c_6	4.61	7.01	5.80	8.68	26.03
c_{11}	-0.54	-1.24	-1.56	0.06	-1.77
c_{22}	-0.63	-1.03	-1.02	-0.20	-1.50
c_{33}	-0.48	-0.88	-1.08	-0.05	-1.38
c_{44}	-0.57	-0.89	-0.91	-0.19	-1.36
c_{55}	0.52	2.19	1.93	0.03	1.71
c_{66}	-5.68	-22.16	-16.67	-3.81	-15.79
c_{12}	0.09	0.11	-0.05	0.04	-0.08
c_{13}	0.19	0.08	0.16	0.05	0.33
c_{14}	-0.19	-0.08	-0.16	-0.05	-0.33
c_{15}	0.09	0.11	-0.05	0.04	-0.08
c_{16}	0.09	0.12	-0.03	0.09	0.01
c_{23}	-0.19	-0.08	-0.16	-0.05	-0.33
c_{24}	0.19	0.08	0.16	0.05	0.33
c_{25}	-0.09	-0.11	0.05	-0.04	0.08
c_{26}	-0.09	-0.12	0.03	-0.09	-0.01
c_{34}	-0.08	0.08	-0.05	0.03	-0.09
c_{35}	-0.08	0.08	-0.05	0.03	-0.09
c_{36}	-0.08	0.09	-0.04	0.06	-0.04
c_{45}	0.08	-0.08	0.05	-0.03	0.09
c_{46}	0.08	-0.09	0.04	-0.06	0.04
c_{56}	4.48	6.85	5.63	8.50	25.41

Table D.24: Estimated regression co-efficient for model equations of peak value of acceleration response for double cracked angle section curved beam (θ_s = 50°)

Regression co-efficient	Model equation number.				
	1	2	3	4	5
c_0	2.56	7.14	4.29	10.72	33.61
c_1	-0.16	-0.12	-0.30	-0.04	-0.03
c_2	0.16	0.12	0.31	0.04	0.03
c_3	-0.15	-0.09	-0.22	0.13	0.24
c_4	0.15	0.09	0.22	-0.13	-0.24
c_5	1.09	2.69	3.37	7.70	23.81
c_6	1.03	2.18	2.00	4.54	18.17
c_{11}	-0.08	-0.11	-0.21	0.19	0.23
c_{22}	-0.12	-0.08	-0.08	0.14	0.28
c_{33}	-0.05	0.00	-0.05	0.16	0.31
c_{44}	-0.10	-0.06	-0.07	0.15	0.28
c_{55}	-0.09	-0.03	-0.05	0.16	0.29
c_{66}	-1.06	-4.26	-0.42	-3.75	-11.01
c_{12}	-0.16	-0.12	-0.32	-0.04	-0.03
c_{13}	-0.05	-0.04	-0.09	0.03	0.05
c_{14}	0.05	0.04	0.09	-0.03	-0.05
c_{15}	-0.16	-0.12	-0.31	-0.04	-0.03
c_{16}	-0.15	-0.01	-0.01	0.59	1.03
c_{23}	0.05	0.04	0.09	-0.03	-0.05
c_{24}	-0.05	-0.04	-0.09	0.03	0.05
c_{25}	0.16	0.12	0.31	0.04	0.03
c_{26}	0.15	0.01	0.01	-0.59	-1.03
c_{34}	-0.15	-0.10	-0.23	0.14	0.25
c_{35}	-0.15	-0.09	-0.22	0.13	0.25
c_{36}	-0.15	-0.06	-0.11	0.41	0.73
c_{45}	0.15	0.09	0.22	-0.13	-0.25
c_{46}	0.15	0.06	0.11	-0.41	-0.73
c_{56}	0.99	2.12	1.94	4.47	17.85

References

[1] A. Rytter, Vibrational based inspection of civil engineering structures, PhD thesis, Dept. of Building Technology and Structural Engineering, Aalborg University, Aalborg. Fract. Dyn. R9314 (1993).

[2] P.J. Shull, Nondestructive evaluation: theory, techniques and applications, Dekker, Inc., Newyork, 2002.

[3] V.M. Malhotra, N.J. Carino, Handbook on nondestructive testing of concrete, Second, CRC press, Boca Raton, London, 2003.

[4] W.S. Burkle, L.P. Lemle, The effect of order-of-film placement in composite film radiography, Mater. Eval. 51 (1993) 327-329.

[5] K.T. Tan, N. Watanabe, Y. Iwahori, X-ray radiography and micro-computed tomography examination of damage characteristics in stitched composites subjected to impact loading, Compos. Part B Eng. 42 (2011) 874–884.

[6] B. Aidi, M.K. Philen, S.W. Case, Progressive damage assessment of centrally notched composite specimens in fatigue, Compos. Part A Appl. Sci. Manuf. 74 (2015) 47–59. doi:10.1016/j.compositesa.2015.03.022.

[7] N.G.H. Meyendorf, P.B. Nagy, S.I. Rokhlin, Nondestructive materials characterization: with applications to aerospace materials, Springer Berlin Heidelberg, 2013. doi:10.1007/978-3-662-08988-0.

[8] T. Światczak, M. Tomczyk, B. Wiecek, R. Pawlak, R. Olbrycht, Defect detection in wire welded joints using thermography investigations, Mater. Sci. Eng. B. 177 (2012) 1239–1242.

[9] Y. Li, Z. Yang, J. Zhu, A. Ming, W. Zhang, J. Zhang, Investigation on the damage evolution in the impacted composite material based on active infrared thermography, NDT E Int. 83 (2016) 114–122. doi:10.1016/j.ndteint.2016.06.008.

[10] Y.Y. Hung, H.P. Ho, Shearography: an optical measurement technique and applications, Mater. Sci. Eng. R Reports. 49 (2005) 61–87.

[11] W.J. Martin, Test piece for inspection penetrant performance assessment and comparison, US 6,311,538 B1, 2001.

[12] N.P. Kalinichenko, A.N. Kalinichenko, I.S. Lobanova, S.S. Borisov, Methods for the manufacture of nonmetallic reference specimens for liquid-penetrant inspection, Russ. J. Nondestruct. Test. 49 (2013) 668–672.

[13] U. Diederichs, U. Schneider, M. Terrien, Formation and propagation of cracks and acoustic emission wave of concrete, in: F.H. Wittmann (Ed.), Fract. Mech. Concr., Elsevier, Amsterdam, 1983.

[14] W. Peng, Y. Zhang, B. Qiu, H. Xue, A brief review of the application and problems in ultrasonic fatigue testing, AASRI Procedia. 2 (2012) 127–133.

[15] J.F. Chaix, V. Garnier, G. Corneloup, Concrete damage evolution analysis by backscattered ultrasonic waves, NDT E Int. 36 (2003) 461–469.

[16] E.K. Rahani, T. Kundu, Z. Wu, H. Xin, Mechanical damage detection in polymer tiles by THz radiation, IEEE Sens. J. 11 (2011) 1720–1725.

[17] P.Y. Joubert, E. Vourc'h, A. Tassin, Y. Le Diraison, Source separation techniques applied to the detection of subsurface defects in the eddy current NDT of aeronautical lap-joints, NDT E Int. 43 (2010) 606–614.

[18] A. Rosell, G. Persson, Finite element modelling of closed cracks in eddy current testing, Int. J. Fatigue. 41 (2012) 30–38. doi:10.1016/j.ijfatigue.2011.12.003.

[19] A. Aoukili, A. Khamlichi, Modeling an eddy-current probe for damage detection of surface cracks in metallic parts, Procedia Technol. 22 (2016) 527–534.

[20] H. Liebowitz, H. Vanderveldt, D.W. Harris, Carrying capacity of notched columns, Int. J. Solids Struct. 3 (1967) 489–500.

[21] H. Liebowitz, W.D. Claus Jr., Failure of notched columns, Eng. Fract. Mech. 1 (1968) 379–383.

[22] H. Okamura, H.W. Liu, C.S. Chu, H. Liebowitz, A cracked column under compression, Eng. Fract. Mech. 1 (1969) 547–564.

[23] M. Sanayei, S.F. Scampoli, Structural element stiffness identification from static test data, J. Eng. Mech. 117 (1991) 1021–1036.

[24] M. Sanayei, O. Onipede, Damage assessment of structures using static test data, AIAA J. 29 (1991) 1174–1179. http://arc.aiaa.org/doi/pdf/10.2514/3.10720.

[25] S.T. Quek, Q. Wang, L. Zhang, K.K. Ang, Sensitivity analysis of crack detection in beams by wavelet technique, Int. J. Mech. Sci. 43 (2001) 2899–2910.

[26] M. Rucka, K. Wilde, Crack identification using wavelets on experimental static deflection profiles, Eng. Struct. 28 (2006) 279–288.

[27] T. Sain, J.M. Chandra Kishen, Damage assessment in beams using inverse method, J. Eng. Mech. 132 (2006) 337–344. doi:10.1061/(ASCE)0733-9399(2006)132:4(337).

[28] G. Buda, S. Caddemi, Identification of concentrated damages in euler-bernoulli

beams under static loads, J. Eng. Mech. 133 (2007) 942–956.

[29] S. Caddemi, A. Morassi, Crack detection in elastic beams by static measurements, Int. J. Solids Struct. 44 (2007) 5301–5315. doi:10.1016/j.ijsolstr.2006.12.033.

[30] S. Caddemi, A. Morassi, Detecting Multiple Open Cracks in Elastic Beams by Static Tests, J. Eng. Mech. 137 (2011) 113–124. doi:10.1061/(ASCE)EM.1943-7889.0000209.

[31] Q.W. Yang, B.X. Sun, Structural damage localization and quantification using static test data, Struct. Health Monit. 10 (2010) 381–389.

[32] M.A.B. Abdo, Parametric study of using only static response in structural damage detection, Eng. Struct. 34 (2012) 124–131. doi:10.1016/j.engstruct.2011.09.027.

[33] B.K. RaghuPrasad, N. Lakshmanan, N. Gopalakrishnan, K. Sathishkumar, R. Sreekala, Damage identification of beam-like structures with contiguous and distributed damage, Struct. Control Heal. Monit. 20 (2013) 496–519.

[34] A. Kaushik, B.A. Sundaram, S. Parivallal, A.K.F. Ahmed, K. Ravisankar, Numerical studies on the damage locating vector approach for damage detection using static load data, Procedia Eng. 86 (2014) 693–700.

[35] I.Š. Grandić, D. Grandić, Estimation of damage severity using sparse static measurement, J. Civ. Eng. Manag. (2015) 1–9.

[36] J.M. Lifshitz and A. Rotem, Determination of Reinforcement Unbonding of Composites by a Vibration Technique, J. Compos. Mater. 3 (1969) 412–423.

[37] S.W. Doebling, C.R. Farrar, M.B. Prime, D.W. Shevitz, Damage identification and health monitoring of structural and mechanical systems from changes in their vibration characteristics: a literature review, 1996.

[38] H. Sohn, C.R. Farrar, F.M. Hemez, D.D. Shunk, D.W. Stinemates, B.R. Nadler, J.J. Czarnecki, A Review of Structural Health Monitoring Literature : 1996-2001, LA-13976-MS, February 2004.

[39] D.N. Thatoi, H.C. Das, D.R. Parhi, Review of techniques for fault diagnosis in damaged structure and engineering system, Adv. Mech. Eng. 2012 (2012) 1–11. doi:10.1155/2012/327569.

[40] W. Fan, P. Qiao, Vibration-based damage identification methods: a review and comparative study, Struct. Health Monit. 10 (2011) 83–111.

[41] A.D. Dimarogonas, Vibration of cracked structures: A state of the art review, Eng. Fract. Mech. 55 (1996) 831–857.

[42] Z.A. Jassim, N.N. Ali, F. Mustapha, N.A. Abdul Jalil, A review on the vibration

analysis for a damage occurrence of a cantilever beam, Eng. Fail. Anal. 31 (2013) 442–461. doi:10.1016/j.engfailanal.2013.02.016.

[43] J. Fasl, T. Helwig, S.L. Wood, P. Pasupathy, D.P. Neikirk, F. Raffaeli, Factors affecting wireless network communication in monitoring systems for steel bridges, J. Civil Struct. Health Monit. 2 (2012) 87–95. doi:10.1007/s13349-012-0019-y.

[44] O.S. Salawu, Detection of structural damage through changes in frequency: a review, Eng. Struct. 19 (1997) 718–723.

[45] J.K. Vandiver, Detection of structural failure on fixed platforms by measurement of dynamic response, in: Offshore Technol. Conf., 1975: pp. 243–252.

[46] M.E. Wojnarowski, S.G. Stiansen, N.E. Reddy, Structural integrity evaluation of a fixed platform using vibration criteria, in: Offshore Technol. Conf., 1977.

[47] R.D. Adams, P. Cawley, C.J. Pye, B.J. Stone, A vibration technique for non-destructively assessing the integrity of structures, J. Mech. Eng. Sci. 20 (1978) 93–100. doi:10.1243/JMES_JOUR_1978_020_016_02.

[48] P. Cawley, R.D. Adams, The location of defects in structures from measurements of natural frequencies, J. Strain Anal. 14 (1979) 49–57.

[49] M.M.F. Yuen, A numerical study of the eigenparameters of a damaged cantilever, J. Sound Vib. 103 (1985) 301–310.

[50] H. Sato, Free vibration of beams with abrupt changes of cross-section, 89 (1983) 59–64.

[51] Y. Narkis, Identification of crack location in vibrating simply supported beams, J. Sound Vib. 172 (1994) 549–558. doi:10.1006/jsvi.1994.1195.

[52] M.H.H. Shen, J.E. Taylor, An identification problem for vibrating cracked beams, J. Sound Vib. 150 (1991) 457–484.

[53] D. Armon, Y. Ben-Haim, S. Braun, Crack detection in beams by rank-ordering of eigenfrequency shifts, Mech. Syst. Signal Process. 8 (1994) 81–91.

[54] R.Y. Liang, F.K. Choy, J. Hu, Detection of cracks in beam structures using measurements of natural frequencies, J. Franklin Inst. 328 (1991) 505–518.

[55] P.G. Nikolakopoulos, D.E. Katsareas, C.A. Papadopoulos, Crack identification in frame structures, Comput. Struct. 64 (1997) 389–406.

[56] B.P. Nandwana, S.K. Maiti, Detection of the location and size of a crack in stepped cantilever beams based on measurements of natural frequencies, J. Sound Vib. 203 (1997) 435–446. doi:10.1006/jsvi.1996.0856.

[57] S. Chinchalkar, Determination of crack location in beams using natural frequencies, J. Sound Vib. 247 (2001) 417–429. doi:10.1006/jsvi.2001.3748.

[58] A.C. Chasalevris, C.A. Papadopoulos, Cross coupled bending vibrations of rotating shaft due to a transverse breathing crack, in: Seventh IFToMM Conf. Rotor Dyn., Vienna, Austria., 2006.

[59] M.L. Kikidis, C.A. Papadopoulos, Slenderness ratio effect on cracked beam, J. Sound Vib. 155 (1992) 1–11.

[60] Y. Narkis, E. Elmalah, Crack identification in a cantilever beam under uncertain end conditions, Int. J. Mech. Sci. 38 (1996) 499–507.

[61] J.A. Loya, L. Rubio, J. Fernández-Sáez, Natural frequencies for bending vibrations of Timoshenko cracked beams, J. Sound Vib. 290 (2006) 640–653.

[62] A. Labib, D. Kennedy, C. Featherston, Free vibration analysis of beams and frames with multiple cracks for damage detection, J. Sound Vib. 333 (2014) 4991–5003. doi:10.1016/j.jsv.2014.05.015.

[63] A.A. Elshafey, H. Marzouk, M.R. Haddara, Experimental damage identification using modified mode shape difference, J. Marine Sci. Appl. 10 (2011) 150–155.

[64] H.R. Öz, In-plane vibrations of cracked slightly curved beams, Struct. Eng. Mech. 36 (2010) 679–695. doi:http://dx.doi.org/10.12989/sem.2010.36.6.679.

[65] M.N. Cerri, M. Dilena, G.C. Ruta, Vibration and damage detection in undamaged and cracked circular arches: Experimental and analytical results, J. Sound Vib. 314 (2008) 83–94. doi:10.1016/j.jsv.2008.01.029.

[66] A.K. Pandey, M. Biswas, Damage detection in structures using changes in flexibility, J. Sound Vib. 169 (1994) 3–17. doi:10.1006/jsvi.1994.1002.

[67] A.K. Pandey, M. Biswas, Experimental verification of flexibility difference method for locating damage in structures, J. Sound Vib. 184 (1995) 311–328.

[68] J.K. Sinha, M.I. Friswell, S. Edwards, Simplified models for the location of cracks in beam structures using measured vibration data, J. Sound Vib. 251 (2002) 13–38. doi:10.1006/jsvi.2001.3978.

[69] D.Y. Zheng, N.J. Kessissoglou, Free vibration analysis of a cracked beam by finite element method, J. Sound Vib. 273 (2004) 457–475.

[70] S. Weng, H.P. Zhu, Y. Xia, L. Mao, Damage detection using the eigenparameter decomposition of substructural flexibility matrix, Mech. Syst. Signal Process. 34 (2013) 19–38. doi:10.1016/j.ymssp.2012.08.001.

[71] T.C. Tsai, Y.Z. Wang, The vibration of a multi-crack rotor, Int. J. Mech. Sci. 39

(1997) 1037–1053.

[72] Z. Xiaoqing, H. Qiang, L. Feng, Analytical Approach for Detection of Multiple Cracks in a Beam, J. Eng. Mech. 136 (2010) 345–357. doi:10.1061/(ASCE)0733-9399(2010)136:3(345).

[73] M. Attar, A transfer matrix method for free vibration analysis and crack identification of stepped beams with multiple edge cracks and different boundary conditions, Int. J. Mech. Sci. 57 (2012) 19–33.

[74] A.K. Pandey, M. Biswas, M.M. Samman, Damage detection from changes in curvature mode shapes, J. Sound Vib. 145 (1991) 321–332.

[75] M.M. Abdel Wahab, G. De Roeck, Damage detection in bridges using modal curvatures: application to a real damage scenario, J. Sound Vib. 226 (1999) 217–235. doi:10.1006/jsvi.1999.2295.

[76] C.P. Ratcliffe, Damage detection usign a modified laplacian operator on mode shape data, J. Sound Vib. 204 (1997) 505–517. doi:10.1006/jsvi.1997.0961.

[77] A. Dutta, S. Talukdar, Damage detection in bridges using accurate modal parameters, Finite Elem. Anal. Des. 40 (2004) 287–304. doi:10.1016/S0168-874X(02)00227-5.

[78] M. Kisa, Free vibration analysis of a cantilever composite beam with multiple cracks, Compos. Sci. Technol. 64 (2004) 1391–1402.

[79] M. Kisa, M. Arif Gurel, Free vibration analysis of uniform and stepped cracked beams with circular cross sections, Int. J. Eng. Sci. 45 (2007) 364–380.

[80] E.T. Lee, H.C. Eun, Structural damage detection by power spectral density estimation using output-only measurement, Shock Vib. 2016 (2016) 1-13. Article ID 8761249, doi.org/10.1155/2016/8761249.

[81] B. Nanda, D. Maity, D.K. Maiti, Damage assessment from curvature mode shape using unified particle swarm optimization, Struct. Eng. Mech. 52 (2014) 307–322. doi:10.12989/sem.2014.52.2.307.

[82] K.V. Nguyen, Mode shapes analysis of a cracked beam and its application for crack detection, J. Sound Vib. 333 (2014) 848–872. doi:10.1016/j.jsv.2013.10.006.

[83] Y. Wang, M. Liang, J. Xiang, Damage detection method for wind turbine blades based on dynamics analysis and mode shape difference curvature information, Mech. Syst. Signal Process. 48 (2014) 351–367. doi:10.1016/j.ymssp.2014.03.006.

[84] E. Çam, S. Orhan, M. Lüy, An analysis of cracked beam structure using impact echo method, NDT E Int. 38 (2005) 368–373. doi:10.1016/j.ndteint.2004.10.009.

[85] C. Hsiao, C.C. Cheng, T. Liou, Y. Juang, Detecting flaws in concrete blocks using the impact-echo method, NDT E Int. 41 (2008) 98–107.

[86] M. Rezaee, R. Hassannejad, Free vibration analysis of simply supported beam with breathing crack using perturbation method, Acta Mech. Solida Sin. 23 (2010) 459–470. doi:10.1016/S0894-9166(10)60048-1.

[87] K. Aydin, Free vibration of functionally graded beams with arbitrary number of surface cracks, Eur. J. Mech. A/Solids. 42 (2013) 112–124.

[88] A. Gupta, M. Talha, B.N. Singh, Vibration characteristics of functionally graded material plate with various boundary constraints using higher order shear deformation theory, Compos. Part B Eng. 94 (2016) 64-74.

[89] S. Rucevskis, M.A. Sumbatyan, P. Akishin, A. Chate, Tikhonov's regularization approach in mode shape curvature analysis applied to damage detection, Mech. Res. Commun. 65 (2015) 9–16. doi:10.1016/j.mechrescom.2015.01.006.

[90] K.E. Bikri, R. Benamar, M.M. Bennouna, Geometrically non-linear free vibrations of clamped-clamped beams with an edge crack, Comput. Struct. 84 (2006) 485–502. doi:10.1016/j.compstruc.2005.09.030.

[91] E. Carrera, A. Pagani, M. Petrolo, Free vibrations of damaged aircraft structures by component-wise analysis, AIAA J. 54 (2016) 3091–3106.

[92] E.Z. Moore, J.M. Nichols, K.D. Murphy, Model-based SHM: Demonstration of identification of a crack in a thin plate using free vibration data, Mech. Syst. Signal Process. 29 (2012) 284–295. doi:10.1016/j.ymssp.2011.09.022.

[93] D. Wei, Y. Liu, Z. Xiang, An analytical method for free vibration analysis of functionally graded beams with edge cracks, J. Sound Vib. 331 (2012) 1686–1700. doi:10.1016/j.jsv.2011.11.020.

[94] E. Viola, E. Artioli, M. Dilena, Analytical and differential quadrature results for vibration analysis of damaged circular arches, J. Sound Vib. 288 (2005) 887–906. doi:10.1016/j.jsv.2005.01.027.

[95] C.W. Bert, M. Malik, Differential quadrature method in computational mechanics: A review, Appl. Mech. Rev. 49 (1996) 1–28. doi:10.1115/1.3101882.

[96] P. Ricci, E. Viola, Stress intensity factors for cracked T-sections and dynamic behaviour of T-beams, Eng. Fract. Mech. 73 (2006) 91–111.

[97] E. Viola, P. Ricci, M.H. Aliabadi, Free vibration analysis of axially loaded cracked Timoshenko beam structures using the dynamic stiffness method, J. Sound Vib. 304 (2007) 124–153. doi:10.1016/j.jsv.2007.02.013.

[98] R. Kienzler, G. Herrmann, An elementary theory of defective beams, Acta Mech. 62 (1986) 37–46.

[99] W.H. Müller, G. Herrmann, H. Gao, Elementary strength theory of cracked beams, Theor. Appl. Fract. Mech. 18 (1993) 163–177. doi:10.1016/0167-8442(93)90042-A.

[100] T. Yokoyama, M.-C. Chen, Vibration analysis of edge-cracked beams using a line-spring model, Eng. Fract. Mech. 59 (1998) 403–409.

[101] H. Gao, G. Herrmann, On estimates of stress intensity factors for cracked beams and pipes, Eng. Fract. Mech. 41 (1992) 695–706.

[102] H.R. Öz, M.T. Daş, In-plane vibrations of circular curved beams with a transverse open crack., Math. Comput. Appl. 11 (2006) 1–10.

[103] M. Krawczuk, W. Ostachowicz, Natural Vibrations of a Clamped-Clamped Arch With an Open Transverse Crack, J. Vib. Acoust. 119 (1997) 145–151.

[104] T. Wolff, M. Richardson, Fault detection in structures from changes in their modal parameters, in: Proc. 7th Int. Modal Anal. Conf., 1989: pp. 87–94.

[105] J.M. Ko, C.W. Wong, H.F. Lam, Damage detection in steel framed structures by vibration measurement approach, in: Proc. 12th Int. Modal Anal., 1994: pp. 280–286.

[106] C.H.J. Fox, The location of defects in structures: A comparison of the use of natural frequency and mode shape data, in: Proc. 10th Int. Modal Anal. Conf., 1992: pp. 522–528.

[107] J.M. Ndambi, J. Vantomme, K. Harri, Damage assessment in reinforced concrete beams using eigenfrequencies and mode shape derivatives, Eng. Struct. 24 (2002) 501–515. doi:10.1016/S0141-0296(01)00117-1.

[108] K.A. Alnefaie, A finite element analysis of idealized damage in beam structures, Proc. Inst. Mech. Eng. Part C J. Mech. Eng. Sci. 218 (2004) 921–929. doi:10.1243/0954406041991251.

[109] B. Samali, J. Li, F.C. Choi, K. Crews, Application of the damage index method for plate-like structures to timber bridges, Struct. Control Health Monit. 17 (2010) 849–871. doi:10.1002/stc.347.

[110] D.P. Patil, S.K. Maiti, Experimental verification of a method of detection of multiple cracks in beams based on frequency measurements, J. Sound Vib. 281 (2005) 439–451. doi:10.1016/j.jsv.2004.03.035.

[111] A. Eraky, A.M. Anwar, A. Saad, A. Abdo, Damage detection of flexural structural

systems using damage index method - Experimental approach, Alexandria Eng. J. 54 (2015) 497–507. doi:10.1016/j.aej.2015.05.015.

[112] M.M. Rezaei, M. Behzad, H. Moradi, H. Haddadpour, Modal-based damage identification for the nonlinear model of modern wind turbine blade, Renew. Energy. 94 (2016) 391–409. doi:10.1016/j.renene.2016.03.074.

[113] S. Hosseini-Hashemi, H. Roohi Gh, H. Rokni D.T. Exact free vibration study of rectangular Mindlin plates with all-over part-through open cracks, Comput. Struct. 88 (2010) 1015–1032. doi:10.1016/j.compstruc.2010.06.004.

[114] V.S. Sokolinsky, H.F. von Bremen, J.J. Lesko, S.R. Nutt, Higher-order free vibrations of sandwich beams with a locally damaged core, Int. J. Solids Struct. 41 (2004) 6529–6547. doi:10.1016/j.ijsolstr.2004.05.059.

[115] J. Xiang, M. Liang, Y. He, Experimental investigation of frequency-based multi-damage detection for beams using support vector regression, Eng. Fract. Mech. 131 (2014) 257–268. doi:10.1016/j.engfracmech.2014.08.001.

[116] M. Solís, M. Algaba, P. Galvín, Continuous wavelet analysis of mode shapes differences for damage detection, Mech. Syst. Signal Process. 40 (2013) 645–666. doi:10.1016/j.ymssp.2013.06.006.

[117] C.Y. Kao, S.L. Hung, Detection of structural damage via free vibration responses generated by approximating artificial neural networks, Comput. Struct. 81 (2003) 2631–2644. doi:10.1016/S0045-7949(03)00323-7.

[118] M. Sahin, R.A. Shenoi, Quantification and localisation of damage in beam-like structures by using artificial neural networks with experimental validation, Eng. Struct. 25 (2003) 1785–1802. doi:10.1016/j.engstruct.2003.08.001.

[119] N. Impollonia, I. Failla, G. Ricciardi, Parametric statistical moment method for damage detection and health monitoring, J. Risk Uncertain. Eng. Syst. Part A Civ. Eng. 2 (2016) 1–12. doi:10.1061/AJRUA6.0000863.

[120] R.H. Myers, D.C. Montgomery, C.M. Anderson-Cook, Response surface methodology: process and product optimization using designed experiments, Third ed., John Wiley and Sons, Inc., Hoboken, New Jersey, 2009.

[121] D.C. Montgomery, Design and Analysis of Experiments, Seventh ed., John Wiley and Sons, Inc., Hoboken, New Jersey, 2009.

[122] D.C. Montgomery, G.C. Runger, Applied statistics and probability for engineers. Fourth ed., John Wiley and Sons, New Delhi, 2010.

[123] R. Sen, T. Swaminathan, Application of response-surface methodology to evaluate

the optimum environmental conditions for the enhanced production of surfactin, Appl. Microbiol. Biotechnol. 47 (1997) 358–363. doi:10.1007/s002530050940.

[124] K.S.C.R. dos Santos, H.S.R.C. Silva, E.I. Ferreira, R.E. Bruns, 3^2 Factorial design and response surface analysis optimization of *N*-carboxybutylchitosan synthesis, Carbohydr. Polym. 59 (2005) 37–42. doi:10.1016/j.carbpol.2004.08.020.

[125] K. Ravikumar, K. Pakshirajan, T. Swaminathan, K. Balu, Optimization of batch process parameters using response surface methodology for dye removal by a novel adsorbent, Chem. Eng. J. 105 (2005) 131–138.

[126] L. Deng, C.S. Cai, Bridge model updating using response surface method and genetic algorithm, J. Bridge Eng. 15 (2010) 553–564.

[127] A.N. Kallias, M. Imran Rafiq, Performance assessment of corroding RC beams using response surface methodology, Eng. Struct. 49 (2013) 671–685.

[128] J.J. Del Coz Diaz, P.J. Garcia-Nieto, F.P. Alvarez-Rabanal, M. Alonso-Martínez, J. Dominguez-Hernandez, J.M. Perez-Bella, The use of response surface methodology to improve the thermal transmittance of lightweight concrete hollow bricks by FEM, Constr. Build. Mater. 52 (2014) 331–344.

[129] S.C. Mohan, D.K. Maiti, Structural optimization of rotating disk using response surface equation and genetic algorithm, Int. J. Comput. Methods Eng. Sci. Mech. 14 (2013) 124–132. doi:10.1080/15502287.2012.698712.

[130] L. Ye, M. Yang, L. Xu, C. Guo, L. Li, D. Wang, Optimization of inductive angle sensor using response surface methodology and finite element method, Measurement. 48 (2014) 252–262. doi:10.1016/j.measurement.2013.11.017.

[131] H.M. Hasanien, A.S. Abd-rabou, S.M. Sakr, Design optimization of transverse flux linear motor for weight reduction and performance improvement using response surface methodology and genetic algorithms, IEEE Trans. Energy Convers. 25 (2010) 598–605.

[132] T. Mukhopadhyay, T.K. Dey, R. Chowdhury, A. Chakrabarti, Structural damage identification using response surface-based multi-objective optimization: A comparative study, Arab. J. Sci. Eng. 40 (2015) 1027–1044. doi:10.1007/s13369-015-1591-3.

[133] S.E. Fang, R. Perera, Damage identification by response surface based model updating using D-optimal design, Mech. Syst. Signal Process. 25 (2011) 717–733. doi:10.1016/j.ymssp.2010.07.007.

[134] A. Rahai, F. Bakhtiari-Nejad, and A. Esfandiari, Damage assessment of structure

using incomplete measured mode shapes, Struct. Control Health Monit. 14 (2007) 808-829.

[135] L. Faravelli, Response-surface approach for reliability analysis, J. Eng. Mech. 115 (1989) 2763–2781.

[136] M.R. Rajashekhar, B.R. Ellingwood, A new look at the response surface approach for reliability analysis, Struct. Safe. 12 (1993) 205–220.

[137] X.L. Guan, R.E. Melchers, Effects of response surface parameter variation on structural reliability estimates, Struct. Safe. 23 (2001) 429–444.

[138] S. Moradi, P. Razi, L. Fatahi, On the application of bees algorithm to the problem of crack detection of beam-type structures, Comput. Struct. 89 (2011) 2169–2175. doi:10.1016/j.compstruc.2011.08.020.

[139] M.N. Cerri, G.C. Ruta, Detection of localised damage in plane circular arches by frequency data, J. Sound Vib. 270 (2004) 39–59.

[140] M.T. Vakil-Baghmisheh, M. Peimani, M.H. Sadeghi, M.M. Ettefagh, Crack detection in beam-like structures using genetic algorithms, Appl. Soft Comput. 8 (2008) 1150–1160. doi:10.1016/j.asoc.2007.10.003.

[141] S.A. Moezi, E. Zakeri, A. Zare, M. Nedaei, On the application of modified cuckoo optimization algorithm to the crack detection problem of cantilever Euler-Bernoulli beam, Comput. Struct. 157 (2015) 42–50.

[142] Z. Ding, Z. Lu, M. Huang, J. Liu, Improved artificial bee colony algorithm for crack identification in beam using natural frequencies only, Inverse Probl. Sci. Eng. (2016) 1–21. doi:10.1080/17415977.2016.1160391.

[143] N.T. Khiem, T. V. Lien, The dynamic stiffness matrix method in forced vibration analysis of multiple-cracked beam, J. Sound Vib. 254 (2002) 541–555.

[144] S. Loutridis, E. Douka, A. Trochidis, Crack identification in double-cracked beams using wavelet analysis, J. Sound Vib. 277 (2004) 1025–1039.

[145] N. Dharmaraju, R. Tiwari, S. Talukdar, Identification of an open crack model in a beam based on force-response measurements, Comput. Struct. 82 (2004) 167–179. doi:10.1016/j.compstruc.2003.10.006.

[146] S. Loutridis, E. Douka, L.J. Hadjileontiadis, Forced vibration behaviour and crack detection of cracked beams using instantaneous frequency, NDT E Int. 38 (2005) 411–419. doi:10.1016/j.ndteint.2004.11.004.

[147] Q. Gao, C. Duan, H. Fan, Q. Meng, Rotating machine fault diagnosis using empirical mode decomposition, Mech. Syst. Signal Process. 22 (2008) 1072–1081.

doi:10.1016/j.ymssp.2007.10.003.

[148] M. Behzad, A. Meghdari, A. Ebrahimi, A continuous model for forced vibration analysis of a cracked beam, in: ASME 2005 Int. Mech. Eng. Congr. Expo., American Society of Mechanical Engineers, Orlando, Florida USA, 2005: pp. 1849–1855.

[149] H.P. Lin, S.C. Chang, Forced responses of cracked cantilever beams subjected to a concentrated moving load, Int. J. Mech. Sci. 48 (2006) 1456–1463.

[150] D.M. Joglekar, M. Mitra, Analysis of flexural wave propagation through beams with a breathing crack using wavelet spectral finite element method, Mech. Syst. Signal Process. 76-77 (2016) 576-591. doi.org/10.1016/j.ymssp.2016.02.010.

[151] M. Karthikeyan, R. Tiwari, S. Talukdar, Development of a novel algorithm for a crack detection, localization, and sizing in a beam based on forced response measurements, J. Vib. Acoust. 130 (2008) 021002 (1-14). doi:10.1115/1.2827357.

[152] Z. Yang, L. Wang, H. Wang, Y. Ding, X. Dang, Damage detection in composite structures using vibration response under stochastic excitation, J. Sound Vib. 325 (2009) 755–768. doi:10.1016/j.jsv.2009.03.040.

[153] M. Karthikeyan, R. Tiwari, Detection, localization, and sizing of a structural flaw in a beam based on forced response measurements - An experimental investigation, Mech. Mach. Theory. 45 (2010) 584–600.

[154] Y.C. Huh, T.Y. Chung, S.J. Moon, H.G. Kil, J.K. Kim, Damage detection in beams using vibratory power estimated from the measured accelerations, J. Sound Vib. 330 (2011) 3645–3665. doi:10.1016/j.jsv.2011.03.007.

[155] E. bekkaye Merrimi, K. El bikri, R. Benamar, Geometrically non-linear steady state periodic forced response of a clamped-clamped beam with an edge open crack, Comptes. Rendus. Mec. 339 (2011) 727–742.

[156] U. Andreaus, P. Baragatti, Cracked beam identification by numerically analysing the nonlinear behaviour of the harmonically forced response, J. Sound Vib. 330 (2011) 721–742. doi:10.1016/j.jsv.2010.08.032.

[157] M. Heydari, A. Ebrahimi, M. Behzad, Forced vibration analysis of a Timoshenko cracked beam using a continuous model for the crack, Eng. Sci. Technol. 17 (2014) 194–204. doi:10.1016/j.jestch.2014.05.003.

[158] H. Chen, T.S. Maung, Structural damage evolution assessment using the regularised time step integration method, J. Sound Vib. 333 (2014) 4104–4122. doi:10.1016/j.jsv.2014.04.044.

[159] R. Rangaraj, B. Pokale, A. Banerjee, S. Gupta, Investigations on a particle filter algorithm for crack identification in beams from vibration measurements, Struct. Control Health Monit. 22 (2015) 1049–1067. doi:10.1002/stc.1733.

[160] S. Wang, Y. Zi, Z. Wan, B. Li, Z. He, Effects of multiple cracks on the forced response of centrifugal impellers, Mech. Syst. Signal Process. 60-61 (2015) 326–343. doi:10.1016/j.ymssp.2014.12.013.

[161] N. Wu, Study of forced vibration response of a beam with a breathing crack using iteration method, J. Mech. Sci. Technol. 29 (2015) 2827–2835.

[162] X. Zhao, Y.R. Zhao, X.Z. Gao, X.Y. Li, Y.H. Li, Green's functions for the forced vibrations of cracked Euler-Bernoulli beams, Mech. Syst. Signal Process. 68–69 (2016) 155–175. doi:10.1016/j.ymssp.2015.06.023.

[163] L. Hu, L. Huang, Z.R. Lu, Crack identification of beam structures using homotopy continuation algorithm, Inverse Probl. Sci. Eng. (2016) 1–19.

[164] J.H. He, Homotopy perturbation method: a new nonlinear analytical technique, Appl. Math. Comput. 135 (2003) 73–79. doi:10.1016/S0096-3003(01)00312-5.

[165] P. Cacciola, N. Impollonia, G. Muscolino, Crack detection and location in a damaged beam vibrating under white noise, Comput. Struct. 81 (2003) 1773–1782. doi:10.1016/S0045-7949(03)00201-3.

[166] D. Wang, W. Xiang, H. Zhu, Damage identification in beam type structures based on statistical moment using a two step method, J. Sound Vib. 333 (2014) 745–760. doi:10.1016/j.jsv.2013.10.007.

[167] D. Wang, Z. Chen, W. Xiang, H. Zhu, Experimental investigation of damage identification in beam structures based on the strain statistical moment, Adv. Struct. Eng. (2016) 1–12. doi:10.1177/1369433216664349.

[168] Z.D. Zheng, Z.R. Lu, W.H. Chen, J.K. Liu, Structural damage identification based on power spectral density sensitivity analysis of dynamic responses, Comput. Struct. 146 (2015) 176–184. doi:10.1016/j.compstruc.2014.10.011.

[169] S. Orhan, Analysis of free and forced vibration of a cracked cantilever beam, NDT E Int. 40 (2007) 443–450. doi:10.1016/j.ndteint.2007.01.010.

[170] M. Karthikeyan, R. Tiwari, S. Talukdar, Crack localisation and sizing in a beam based on the free and forced response measurements, Mech. Syst. Signal Process. 21 (2007) 1362–1385. doi:10.1016/j.ymssp.2006.06.002.

[171] C. Mei, Y. Karpenko, S. Moody, D. Allen, Analytical approach to free and forced vibrations of axially loaded cracked Timoshenko beams, J. Sound Vib. 291 (2006)

1041–1060. doi:10.1016/j.jsv.2005.07.017.

[172] M. Shafiei, N. Khaji, Analytical solutions for free and forced vibrations of a multiple cracked Timoshenko beam subject to a concentrated moving load, Acta Mech. 221 (2011) 79–97. doi:10.1007/s00707-011-0495-x.

[173] K.R. Collins, R.H. Plaut, J. Wauer, Free and Forced Longitudinal Vibrations of a Cantilevered Bar With a Crack, J. Vib. Acoust. 114 (1992) 171–177.

[174] J. Yang, Y. Chen, Y. Xiang, X.L. Jia, Free and forced vibration of cracked inhomogeneous beams under an axial force and a moving load, J. Sound Vib. 312 (2008) 166–181. doi:10.1016/j.jsv.2007.10.034.

[175] V.Z. Vlasov, Thin-Walled Elastic Beams, Israel Program for Scientific Translations, Jerusalem, Israel, 1961.

[176] T.H.G. Megson, Linear Analysis of Thin-Walled Elastic Structures, John Wiley & Sons, New York, 1974.

[177] E. Dokumaci, An exact solution for coupled bending and torsion vibrations of uniform beams having single cross-sectional symmetry, 119 (1987) 443–449.

[178] J.R. Banerjee, F.W. Williams, Coupled bending-torsional dynamic stiffness matrix for timoshenko beam elements, Comput. Struct. 42 (1992) 301–310.

[179] J.R. Banerjee, S. Guo, W.P. Howson, Exact dynamic stiffness matrix of a bending-torsion coupled beam including warping, Comput. Struct. 59 (1996) 613–621.

[180] A.K. Noor, J.M. Peters, B.J. Min, Mixed finite element models for free vibrations of thin-walled beams, Finite Elem. Anal. Des. 5 (1989) 291–305.

[181] M. Ohga, H. Takao, T. Hara, Natural frequencies and mode shapes of thin-walled members, Comput. Struct. 55 (1995) 971–978.

[182] C. Mei, Coupled vibrations of thin-walled beams of open section using the finite element method, Int. J. Mech. Sci. 12 (1970) 883–891.

[183] M. Tanaka, A.N. Bercin, Finite element modelling of the coupled bending and torsional free vibration of uniform beams with an arbitrary cross-section, Appl. Math. Model. 21 (1997) 339–344. doi:10.1016/S0307-904X(97)00030-9.

[184] L. Jun, S. Rongying, H. Hongxing, J. Xianding, Response of monosymmetric thin-walled Timoshenko beams to random excitations, Int. J. Solids Struct. 41 (2004) 6023–6040. doi:10.1016/j.ijsolstr.2004.05.030.

[185] D.M. Lue, J. Liu, C. Lin, Numerical evaluation on warping constants of general cold-formed steel open sections, Steel Struct. 7 (2007) 297–309.

[186] H.H. Chen, K.M. Hsiao, Coupled axial-torsional vibration of thin-walled Z-section

beam induced by boundary conditions, Thin-Walled Struct. 45 (2007) 573–583. doi:10.1016/j.tws.2007.05.001.

[187] T.P. Vo, J. Lee, K. Lee, N. Ahn, Vibration analysis of thin-walled composite beams with I-shaped cross-sections, Compos. Struct. 93 (2011) 812–820. doi:10.1016/j.compstruct.2010.08.001.

[188] M. Obst, D. Kurpisz, P. Paczos, The experimental and analytical investigations of torsion phenomenon of thin-walled cold formed channel beams subjected to four-point bending, Thin-Walled Struct. 106 (2016) 179–186.

[189] C.G. Culver, Natural frequencies of horizontally curved beams, J. Struct. Div. 93 (1967) 189–203.

[190] S.K. Chaudhuri, S. Shore, Dynamic analysis of horizontally curved I-girder bridges, J. Struct. Div. 103 (1977) 1589–1604.

[191] Y. Yang, S. Kuo, Static stability of curved thin-walled beams, J. Eng. Mech. 112 (1986) 821–841.

[192] J.M. Snyder, J.F. Wilson, Free vibrations of continuous horizontally curved beams, J. Sound Vib. 157 (1992) 345–355.

[193] K. Kang, C. Bert, A. Striz, Vibration analysis of horizontally curved beams with warping using DQM, J. Struct. Eng. 122 (1996) 657–662.

[194] K.Y. Yoon, Y.J. Kang, Y.J. Choi, N.H. Park, Free vibration analysis of horizontally curved steel I-girder bridges, Thin-Walled Struct. 43 (2005) 679–699.

[195] K. Nam-ll, K. Moon-young, Thin-walled curved beam theory based on centroid-shear center formulation, J. Mech. Sci. Technol. 19 (2005) 589–604.

[196] H. Duan, Nonlinear free vibration analysis of asymmetric thin-walled circularly curved beams with open cross section, Thin-Walled Struct. 46 (2008) 1107–1112.

[197] N. Peres, R. Gonçalves, D. Camotim, First-order generalised beam theory for curved thin-walled members with circular axis, Thin-Walled Struct. 107 (2016) 345–361. doi:10.1016/j.tws.2016.06.016.

[198] O.C. Zienkiewicz, R.L. Taylor, J.Z. Zhu, The Finite Element Method: Its Basis and Fundamentals, sixth ed., Published by Elsevier, Reprint ISBN: 978-81-312-1118-2, 2013.

[199] T.L. Anderson, Fracture Mechanics: Fundamentals and Applications, second ed., CRC Press., 1995.

[200] H. Tada, P.C. Paris, G.R. Irwin, The Stress Analysis of Cracks Handbook, third ed., ASME, New York, 1985.

[201] I.S. Gradshteyn, I.M. Ryzhik, Tables of Integrals, Series and Products, seventh ed., Academic Press, San Diego, CA, 2007.

[202] A. Jeffrey, Mathematics for Engineers and Scientists, fourth ed., Chapman and Hall, 1989.

[203] D.P. Walter, D. P. Formulas for stress, strain and structural matrices, second ed., John Wiley & Sons, Inc., Hoboken, New Jersey, 2005.

[204] R.W. Clough, J. Penzien, Dynamics of Structures, McGraw-Hill, Inc., 1993.

[205] J.H. Holland, Adaptation in natutal and artificial system, Ann Arbor, MI: University of Michigan Press, pp. 406.

[206] D.E. Goldberg, Genetic Algorithm in Search, Optimization and Machine Learning, Addison-Wesley, Reading. MA., 1989.

[207] D.J. Inman, Engineering vibration, fourth ed., Prentice Hall, Indian International ed. in Softcover, 2013.

[208] M. Pastor, M. Binda, T. Harčarik, Modal assurance criterion, Procedia Eng. 48 (2012) 543–548. doi:10.1016/j.proeng.2012.09.551.

[209] J.C. Castro-Palacio, L. Velázquez-Abad, M.H. Giménez, J.A. Monsoriu, Using a mobile phone acceleration sensor in physics experiments on free and damped harmonic oscillations. Am. J. Phys. 81 (2013) 472-475.

[210] M. Oprea, C. Miron, Mobile phones in the modern teaching of physics. Rom. Rep. Phys. 66 (2014) 1236–1252.

Publications from the Thesis

International Journal

[1] Palash Dey, S. Talukdar and D. J. Bordoloi (2015), Multiple crack identification in a channel section steel beam using a combined response surface methodology and genetic algorithm, *Structural Control and Health Monitoring*, Wiley, 23, 938-959.

[2] Palash Dey, S. Talukdar (2016), Modal characteristics of cracked thin walled unsymmetrical cross- sectional steel beams curved in plan, *Thin-Walled Structures*, Elsevier, 108, 75-92.

[3] Palash Dey, S. Talukdar (2016), A hybrid approach to detect crack parameters using measured natural frequencies in thin walled angle section beam, *International Journal of Steel Structure*, Springer, 16, 163-175.

[4] Palash Dey, S. Talukdar, Damage assessment of unsymmetrical thin-walled beams based on free, forced and heterogeneous vibration data, under review in *Mechanical Systems and Signal Processing*. Paper ID: MSSP16-119.

International Conference

[1] Palash Dey, S. Talukdar, Influence of warping on modal parameters of thin-walled channel section steel beam, *Procedia Engineering*, Elsevier, 144 (2016) 52-59.

[2] Palash Dey, S. Talukdar and D. J. Bordoloi, Crack identification in thin walled channel section beam using combined three level factorial design response surface and genetic algorithm, Paper ID 173, *8th International Conference on Advances in Steel Structures*, July 21-24, 2015, Lisbon, Portugal.

[3] Palash Dey, S. Talukdar, Free vibration analysis of cracked thin walled channel section beam with warping effect, *5th International Congress on Computational Mechanics and Simulation*, Dec 10-13, 2014, SERC, Chennai, pp 363-372, doi: 10.3850/978-981-09-1139-3_028.

[4] Palash Dey, S. Talukdar, Natural frequencies of thin-walled channel section beam with multiple cracks, *6th International Conference on Theoretical, Applied, Computational and Experimental Mechanics*, Dec 29-31, 2014, Paper Id: 289, Indian Institute of Technology Kharagpur, India.

[5] Palash Dey, S. Talukdar, Health monitoring of an open section thin-walled curved beam based on crack parameters, *2nd International Conference on Fatigue, Durability and Fracture mechanics,* Indian Institute of Science, Bangalore, India**,** September 2016, pp. 28.

[6] Palash Dey, S. Talukdar, Vibration Based Damage Detection in a Channel Section Steel Beam using Response Surface and Genetic Algorithm, *Structural Engineering Convention,* 21-23 December 2016, Paper Id:221, CSIR-SERC, Chennai.